ORNL-3670
UC-25 – Metals, Ceramics, and Materials
TID-4500 (34th ed.)

METALS AND CERAMICS DIVISION
ANNUAL PROGRESS REPORT
FOR PERIOD ENDING JUNE 30, 1964

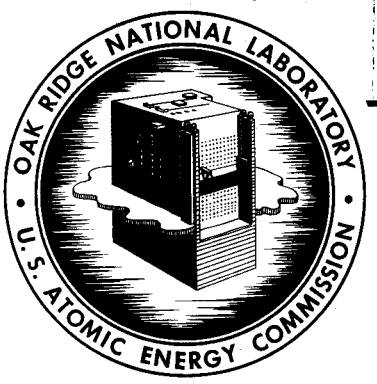

OAK RIDGE NATIONAL LABORATORY
operated by
UNION CARBIDE CORPORATION
for the
U.S. ATOMIC ENERGY COMMISSION

Printed in USA. Price $7.00. Available from the Clearinghouse for Federal Scientific and Technical Information, National Bureau of Standards, U.S. Department of Commerce, Springfield, Virginia

ORNL-3670

Contract No. W-7405-eng-26

METALS AND CERAMICS DIVISION ANNUAL PROGRESS REPORT

for Period Ending June 30, 1964

J. H Frye, Jr., Director
J. E. Cunningham, Assistant Director

Section Heads

G. M. Adamson, Jr.
B. S. Borie
D. A. Douglas, Jr.
C. J. McHargue
P. Patriarca

OCTOBER 1964

OAK RIDGE NATIONAL LABORATORY
Oak Ridge, Tennessee
operated by
UNION CARBIDE CORPORATION
for the
U. S. ATOMIC ENERGY COMMISSION

ACKNOWLEDGMENT

This report was edited by Sigfred Peterson of the Metals and Ceramics Division.

Foreword

For the most part, the work of the Metals and Ceramics Division may be divided into three parts. These are fundamental investigations supported by the AEC Division of Research, research on potential and actual reactor materials supported by the Division of Reactor Development, and research and development programs in support of specific reactor projects or other programs. Occasionally these lines cross as members of diverse programs find common problems or methods. Although substantial progress is reported in many areas, there are a few where special achievements deserve separate mention.

Our fundamental program includes both theoretical and experimental investigations of the structure of both solids and liquids and research on sintering, metal oxidation, superconducting alloys, and physical properties. In the x-ray diffraction of some thin films formed by oxidation of copper single crystals, we found that different reflections were shifted differently by the lattice strain; we related this phenomenon to the atomic configurations at the interfaces. Understanding of the technologically important molten salts has been hampered by the difficulty of experimentation with high-temperature liquids and the complexity of the interactions that occur in them. By a combination of sophisticated spectroscopic techniques, computerized data reduction, and ingenious theoretical interpretation, we have substantially increased our contribution to the knowledge and understanding of the geometric and electronic structures of species that exist in high-temperature ionic media. We are growing crystals of several rare-earth compounds, seeking ferromagnetic materials that can serve as transparent magnets. Although we have not yet achieved this, we have found a very unusual form of strong paramagnetism in a new series of compounds, the rare-earth germanomolybdates, R_2GeMoO_8. Our capabilities for growing single crystals of silicates have led to a novel technique for observing phase transformations. By growing crystals of $ThSiO_4$ at different temperatures, we found that tetragonal thorite is stable below and monoclinic huttonite above 1225°C; this transformation temperature and even its existence were previously in doubt. By measurements of unprecedented precision in our radial heat flow apparatus, we have found previously unknown features in the thermal conductivity of Armco iron, the customary standard for thermal-conductivity measurements.

Looking ahead to the needs of future reactors, our long-range applied research is exploring fundamental properties, methods of evaluation, and novel fabrication techniques for traditional and new reactor materials, with the emphasis on the increasingly important materials required for service at very high temperatures. We have discovered aided-sintering techniques that should lead to easier and more economical fabrication of uranium monocarbide; this high-temperature fuel has been sintered to very high densities at temperatures much lower than those required in more conventional methods. When stainless steel is used in a reactor, the radiation present reduces the ductility. We have discovered a preirradiation heat treatment that introduces a radiation-stable substructure into stainless steel and decreases the irradiation embrittlement. Eddy-current coils, which are customarily designed by trial and error, are used in many nondestructive inspections, including the measurement of channel spacings in reactor fuel elements. With a high-speed computer, we have related eddy-current coil impedance to design and application, so that future inspection development may be made systematically. In our zirconium development program, we had previously shown that knowledge of how preferred orientation develops during fabrication of zirconium alloys can be utilized to optimize the distribution of strengths in the fabricated product. We have now devised techniques for

measuring this preferred orientation in anisotropic materials without the expense and time required by x-ray methods; one uses microhardness measurement and the other metallography. With the latter we measured the stress reorientation of hydride precipitated in Zircaloy-2, a property that limits the useful life of reactor components. Among our advances toward the pyrolytic fabrication of fuel elements, we have prepared UO_2 in a variety of forms from gaseous reactants. Simulating an outer-space environment, we measured the contamination of refractory metals by residual gases in vacuum and devised means for decreasing it.

We are continuing the development and evaluation of fuels and other materials in support of reactor projects and other programs. We have completed fuel-element assignments for the Advanced Test Reactor, the Experimental Gas-Cooled Reactor, and the Enrico Fermi Fast Breeder, and we are continuing others. A major achievement has been the semiremote fabrication, by vibratory compaction of sol-gel oxide, of 1100 thorium-^{233}U oxide fuel elements for a critical experiment at Brookhaven. Our experience is aiding the development of remote fabrication methods, which are desirable to permit recycle of incompletely decontaminated fuel and necessary because of the inevitable presence of ^{232}U and its daughters in the recycled fuel. Using several innovations in technique to overcome the problems of arc melting oxide ceramics, we have melted europium oxide and molybdate. Thus, we have achieved superior properties in these reactor control materials and demonstrated the feasibility of consolidating ceramics by arc melting.

Two particularly interesting achievements have resulted from interactions between these major areas. Our solid reactions studies in the long-range program have included studies of diffusion in tantalum and niobium; our fundamental research on oxidation has found that anodic oxide films on these metals are uniform and easily stripped. In a joint effort this fact has been utilized to develop a new and precise sectioning technique that has enabled extension of diffusion measurements to much lower temperatures than heretofore and discovery of anomalous diffusion behavior near the specimen surfaces. In our development of thorium oxide fuels, observed fission-gas release rates resembled remarkably the densification rates found in our basic research on the sintering of thoria. This led to a joint program that has shown that stress sufficient to cause creep accelerates the release of fission gases from ceramic fuels.

Summary

PART I. FUNDAMENTAL RESEARCH

1. Basic Research on Sintering

We started to study creep on specimens of ThO_2 and ThO_2–0.60% CaO to obtain data for correlation with densification rates. The initial creep rates of the two materials differed markedly at 1465°C, but after 500 hr, the rates were about equal. The changes in the creep rate of the ThO_2–0.60% CaO specimens were probably caused by a redistribution of the calcium. The densification rate of UO_{2+x} was investigated at oxygen-to-uranium ratios of 2.05 to 2.25 in the temperature range of 900 to 1400°C. The maxima and minima that were present in the initial densification rate of ThO_2 were not found in the urania specimens. Beginning studies of grain growth in thoria show that the growth rate is higher in air than in argon.

2. Crystal Physics

A series of lanthanide germanomolybdates of the general formula R_2GeMoO_8, where R is a lanthanide, has been synthesized as single crystals and characterized. Significant paramagnetic anisotropy has been observed in these and in crystals of ErOOH. Small additions of B_2O_3 to the solvent $Li_2O \cdot 2WO_3$ enhanced the growth rate of ThO_2 crystals fivefold with only a small decrease in crystal quality. The crystalline mosaic spread on (111) faces of ThO_2 crystals was determined to be about 2′ of arc by x-ray methods. Crystals of ThO_2 doped with rare-earth ions are being grown, and the electronic character of the rare earths in this host lattice is being studied by electron-spin resonance and by optical absorption methods. Crystals of tri- and tetravalent metal silicates have been grown greater than 1 mm on an edge from $Li_2O \cdot 2WO_3$ solutions. The phase transformation temperature of $ThSiO_4$, a sluggish system, from tetragonal (thorite) to monoclinic (huttonite) was determined to be 1225 ± 10°C by growth of the individual phases just above and below this temperature. Two broad areas of crystal synthesis by the hydrothermal method are being studied. The first includes silicates, ferrisilicates, and similar compounds – germanates, ferrigermanates, and aluminogermanates. The other area includes oxides and multiple oxides, especially those containing elements of the lanthanide series or the first transition series. The temperature dependence of the magnetic susceptibility of Er_2GeMoO_8 has been measured from 50 to 400°K. Optical absorption spectra of crystals whose diameters are greater than 0.13 mm are being obtained with a newly developed sample holder.

3. Deformation of Crystalline Solids

The yield drop was investigated in tantalum, Cu–16 at. % Al, and Ag–6 at. % Al as a function of temperature and strain rate. Analysis of the data indicated that the yield drop results from the multiplication of dislocations at small strains.

A series of measurements of the flow characteristics of an iron-carbon alloy as a function of strain rate and temperature provided direct evidence for the interaction of the strain field of a carbon atom with the stress field of a dislocation, leading to increased resistance to motion in a critical velocity range.

The formation of a double kink in a dislocation occupies a prominent place in the interpretation of the flow properties of body-centered cubic metals at low temperatures. Previous calculations have neglected the applied stress and have obtained results that contradict experimental observations. The present calculations are expected to give a more correct solution.

Investigating the effects of alloying on flow parameters, we found that the addition of molybdenum to nickel increases the effect of temperature by decreasing the stacking fault energy.

The development of compression textures was qualitatively as expected in common metals and alloys except for nickel and Cu–14 at. % Al. The rate of texture formation has been studied during compression and tension of copper, and we hope to deduce the effect of initial orientation on the rate of reorientation of individual grains.

We are developing an isothermal calorimeter that can measure the recovery energy prior to recrystallization. The results have been promising although no satisfactory measurements have yet been possible. We obtained a value for the recrystallization energy for copper that agreed with accepted values in the literature.

4. Electron Microscopy

Transmission electron microscopy of deformed foils of body-centered cubic metals and alloys has shown that the effect of solid-solution alloying is similar to that of a lowered temperature of deformation. In both cases microstructures are dominated by straight joggy screw dislocations. We feel that a frictional stress composed of an inherent Peierls-Nabarro stress and effects of mismatch in atomic size and modulus increases the resistance to motion of screw dislocations.

We have obtained electron microstructures of pyrolytic carbon coatings on nuclear fuel particles and have correlated them with physical properties of the coatings. In addition, we have followed steps in the graphitization that occur during annealing of massive pieces of pyrolytic carbon.

5. Metallurgy of Superconducting Materials

The new Superconducting Materials Laboratory was completed and occupied. Almost all of the equipment necessary for the studies of the effects of metallurgical variables on the superconducting properties has been obtained. The glove-box complex designed for the metallurgical study of technetium and its alloys was installed, along with most of the necessary equipment.

The transformation kinetics study of the Nb-Zr superconducting alloys has continued, using homogenized materials. The homogenization produced a large grain size and contamination by oxygen and silicon, causing severe cracking during fabrication and affecting the transformation kinetics. The pearlitic transformation ceased 10 to 15 μ from the nucleation site at microscopic defects, such as grain boundaries and slip bands; a second type of transformation consumed the remaining material.

In evaluating the superconducting properties of short specimens, one difficulty is making certain that the properties of the specimen are being tested, not those of the joint between the specimen and normal-state current leads. We are investigating variables of joint design and manufacture. The lowest joint resistances obtained to date range from 1.6 to 1.9 microhm, with a reproducibility of manufacture of only three in four.

6. Physical Properties

We have continued to study accurate methods of measuring the thermal conductivity, k, and other physical properties of solids over a broad temperature range to improve the understanding of heat transfer mechanisms. Our measurements on UO_2 showed that the observed maximum in k at room temperature is explained by the rapid decrease in specific heat. The thermal resistance, $1/k$, was linear between 200 and 1000°C, as expected for pure phonon conduction in an insulator above its Debye temperature. The temperature dependence of k of Armco iron was largely controlled by the electronic contribution, but a 4% decrease in k at the α-γ transformation was due to a 20% decrease in the lattice contribution to the thermal conductivity.

By the thermal comparator method, we measured k at 75 and 300°C for US, ThS, and UN; with auxiliary measurements and theory, reasonable extrapolations were made to 1000°C. We perfected a technique to measure the total hemispherical emittance of conductors to 1500°C and measured the emittance and electrical resistivity of a number of refractory metals and alloys. We started using the direct-heating apparatus, which measures k to 2000°C. Finally, we organized and hosted the 1963 Thermal Conductivity Conference and published the proceedings.

7. Reactions at Metal Surfaces

Studies of fundamental oxidation mechanisms of metals have continued to occupy our attention. Several correlations were found between the rate of oxidation and the degree of disregistry in the crystal lattice of the oxide on copper, and these findings led to the speculation that the oxidation rate anisotropy exhibited by copper was caused by a corresponding anisotropy in the oxide lattice disregistry. We discovered that thin anodic oxide films on tantalum and niobium suppressed the formation of additional surface oxide during subsequent thermal oxidation, yet permitted the dissolution of oxygen in the substrate metal. This made it possible to study in detail the effect that the stresses accompanying oxygen solution have upon the oxidation mechanism. The extension of techniques developed during these anodization studies produced a highly sensitive method for studying the diffusion of radioactive tracers in tantalum and niobium. The method made possible the detailed determination of penetration curves within 1 to 2 μ of the specimen surfaces and has proved particularly useful in studying low-temperature diffusion.

8. Spectroscopy of Ionic Media

We have made computer calculations on the electronic states of some molecular and crystal systems, utilizing our previously developed general-purpose one-center expansion code. Problems investigated in this manner include the electronic states of the H_2^+ molecule, the potential energy surface of the H_3 system, the ground state of the carbon atom, the ground state of the CH_3^- molecule, and the electronic states of the *F*-center defect in alkali halide crystals. The *F*-center study included effects of lattice distortions and electronic structure on neighboring ions.

Calculations are being made on the helium atom to test the utility of expansion forms having angular (rather than radial) interelectronic coordinates and many exponential parameters. A study of the construction of sets of orthogonal orbitals led to a technique of orthogonalization in such a way as to produce a wave function of minimum energy. The possible use of this technique to find natural-orbital expansions is being examined. A nonstandard least-squares method derived from numerical variational techniques has been applied in the interpretation of ligand-field spectra.

The optical spectra of $NiCl_4^{2-}$, $NiBr_4^{2-}$, and NiI_4^{2-} in various liquid media were measured from 4000 cm^{-1} in the near infrared to about 40,000 cm^{-1} in the ultraviolet. These results give the most clear-cut evidence to date for geometrically regular complex ions in molten salts, and they were used to test theories of electronic spectra of transition-metal complexes. Of particular current interest are the ultraviolet spectra that provide information on the electron orbitals that are strongly associated with the halide ions.

The optical spectra of solutions of $CuCl_2$ in molten chloride salts with large cations indicated the presence of tetrahedral or mildly distorted tetrahedral $CuCl_4^{2-}$ complexes. Although such entities are well known in crystals, previous attempts to find them in liquid media had been unsuccessful.

9. Structure of Metals

Studies on preferred orientation and inhomogeneous deformation were continued on face-centered cubic metals. While swaging, extruding, and drawing of aluminum rod all resulted in duplex <100>-<111> fiber textures, the proportions of the components were significantly different. Specimens of fine-grained, randomly oriented aluminum and copper developed the same texture when extruded at room temperature.

Preliminary results showed that the dislocation velocity varies as the eighth power of stress in zone-refined niobium. The exact value of the exponent was very sensitive to impurities.

We examined the details of an unusual non-steady-state grain growth occurring in early stages of annealing in aluminum and proposed a model based on interactions between point defects and grain boundaries.

Annealing of deformation twins in niobium single crystals showed that the twins can either contract or expand by the migration of noncoherent twin boundaries. Recrystallization occurred at 1000°C at twin intersections.

10. Theory of Alloying

We investigated the galvanomagnetic properties at 4.2°K of high-purity single crystals of zirconium and beryllium with the current directions $[2\bar{1}\bar{1}2]$ and $[3\bar{1}\bar{2}2]$, respectively, in steady magnetic fields to 31 kilogauss. Both metals showed anisotropy and field dependence characteristic of even-valent metals with equal numbers of holes and electrons and with closed sections of the Fermi surface. Transverse even properties indicated that the Fermi surfaces of both metals were open in certain directions.

The low-temperature specific heats of the continuous hafnium-zirconium solid solution showed that the density of electronic states and the Debye temperatures are nearly linear with composition. However, in the similar titanium-zirconium solid solution a maximum in density of states occurred at 0.6 Ti–0.4 Zr, and corresponding maxima occurred in superconductivity and in electrical resistivity. This maximum is not due to long-range order of the atoms. A variation typical of random solid solutions occurred in the electrical resistance.

The low-temperature specific heats of the continuous solid solution of the system scandium-zirconium and of dilute solid solutions of niobium and molybdenum in zirconium were measured. The density of electronic states showed a minimum at 0.9 Zr–0.1 Sc and rose to a high value for pure scandium. Superconductivity was absent at 1.2°K in scandium and zirconium-scandium alloys. The drop in density of states in zirconium with additions of scandium was approximately equal and opposite to the effect of silver. The additions of molybdenum and niobium produced much larger effects on the density of states than silver and were accompanied by large increases in superconducting transition temperature. The electrical resistivity of alpha-zirconium increased slightly with dilute additions of niobium.

The Mössbauer spectrum of aluminum alloys with dilute cobalt additions showed significant changes in these alloys during precipitation heat treatment.

11. Theory of Electronic States in Solids

We are studying the nature of the electronic states of liquid metals and random alloys by considering soluble one-dimensional models, developing and evaluating techniques for making reliable three-dimensional calculations for such systems, and investigating the application of existing theories to certain experimental work in the Division.

12. X-Ray Diffraction Research

Analysis of diffraction data from BeO single crystals irradiated at a variety of dose levels and temperatures has led to a qualitative understanding of the general radiation-damage mechanisms operating. Models involving displacement faults and spacing anomalies caused by defect clusters currently produce the best agreement with experimental observations.

Work on the structure of thin cuprous oxide films on copper has continued with the extension of the diffraction model to include nonuniform film thicknesses. Significant improvement was thereby obtained in the agreement between observed and computed Fourier coefficients of oxide reflections and between average film thicknesses computed from line shape and integrated intensity measurements. An unusual effect of film structure on the Bragg spacings of 110 and 220 oxide reflections has also been described in terms of particular atomic configurations at the metal-oxide and the oxide-gas interfaces.

PART II. LONG-RANGE APPLIED RESEARCH

13. Fuel Element Development

We have shown vapor deposition, or pyrolytic decomposition, to be an effective and relatively simple technique for fabricating both fuel and cladding materials. Using this technique, high-purity UO_2 has been formed from UF_6 in a one-step conversion process. Many of the deposition parameters have been investigated.

Other vapor-deposition studies have led to the successful fabrication of high-quality tungsten tubing, rhenium and tungsten-rhenium alloy tubing, and boron carbide and silicon carbide bodies. While good quality tungsten-rhenium deposits were achieved, the composition and thickness varied. Boron-carbon alloys were deposited with a wide range of composition and properties. Near-stoichiometric deposits of silicon carbide were

obtained both as tubing and as a thermal-cycle resistant coating on graphite or tungsten.

Miniature aluminum-base dispersion plates suitable for irradiation testing were fabricated from both U_3O_8 and niobium-coated UO_2 with excellent dimensional control and no cracking of the coating.

Fabrication techniques were developed by which UC was sintered to high theoretical densities at temperatures much below those usually used. Sintering the UC was improved by the addition of small quantities of UBe_{13}, which cleaned the surface of the UC particles. Conditions that permit sintering to 95% of theoretical density were established.

14. High-Temperature Materials

The weldability of sheet specimens of the advanced niobium and tantalum alloys D-43, B-66, FS-85, C-129Y, and T-111 was evaluated by measuring bend transition temperatures after fusion welding by either gas tungsten-arc or electron-beam methods. Transition temperatures were generally below room temperature, testifying to the good weldability of these materials. Postweld aging treatments demonstrated that D-43, B-66, and C-129Y were susceptible to embrittlement under certain conditions. A study of the systems Nb-V-Ti and Ta-V-Ti has indicated that several compositions in these ternaries are useful for brazing of refractory metals to produce joints capable of high service temperatures.

Irradiation of Mo–0.5% Ti sheet at 60 to 160°C to integrated fast-neutron doses of approximately 10^{20} neutrons/cm^2 increased the bend transition temperature from 20 to 130°C. Postirradiation annealing at temperatures to 1200°C partially restored the ductility. Irradiation of Nb–1% Zr and D-43 did not embrittle these materials (as determined by the bend test) but did increase the yield strength by 50 to 70%. A postirradiation anneal for 1 hr at 1000°C restored the preirradiation yield strength of both alloys. Creep of D-43, B-66, T-111, and unalloyed tantalum has been tested over the temperature range from 1000 to 1600°C. At 1200°C the 1000-hr rupture strengths for tantalum, B-66, D-43, and T-111 are in the ratio 1:1.9:3.2:6.5. Pretest annealing markedly enhanced the creep properties of Nb–1% Zr at 982 and 1204°C.

The contamination of refractory metals and alloys by the residual gases in vacuum systems has been systematically studied as a function of pressure, temperature, time, alloy composition, and metal surface-to-volume ratio. Empirical equations were developed to represent the effect of these variables on the contamination of Nb–1% Zr over the temperature range 750 to 1200°C. Low partial-pressure additions of CH_4 (approximately 10^{-7} torr) to the vacuum system reduced the contamination of TZM and unalloyed niobium but not that of the Nb–1% Zr alloy. We measured the weight losses of several stainless steels and superalloys caused by evaporation in high vacuums at 760 to 980°C and found that they depended on temperature and the chromium and manganese contents of the alloys. Postevaporation creep testing of type 316 stainless steel demonstrated that thermally induced structural changes within the alloy rather than evaporation controlled the creep behavior. We observed no aging effects in Cb-752, but D-43 showed a marked aging tendency, which was attributed to changes in the morphology and composition of carbide precipitates in this alloy.

Tungsten, molybdenum, and molybdenum-alloy tube shells with excellent surfaces have been produced by high-temperature extrusion, using no lubricant other than the self-produced volatile trioxides. The molybdenum-base materials were successfully warm drawn to defect-free tubing, and no significant contamination occurred during processing. Procedures are under development for the room-temperature flow turning of Nb–1% Zr and T-111 alloy tube hollows.

Oxygen rendered the Nb–1% Zr alloy susceptible to rapid penetration by lithium at 815°C, but attack could be prevented by appropriate heat treatments in which the oxygen combined with zirconium to form ZrO_2. Protection was afforded for all oxygen levels up to that required to produce stoichiometric ZrO_2 (approximately 3500 ppm in Nb–1% Zr). Similar protection was not observed in a Nb–40% V alloy even though oxygen-contaminated unalloyed vanadium was inert to lithium.

The electrical resistivity and total hemispherical emittance of rhenium, T-111, D-43, and Nb–1% Zr were measured to temperatures as high as 1500°C. Several conventional noble- and refractory-metal thermocouples drifted less than ±10°C in 1000 hr in vacuum at 1450°C.

15. Materials Compatibility

The distribution of oxygen between potassium and alpha-zirconium was investigated at 815°C for times of 100 and 500 hr. Where no oxide scale was visible on the specimens after test, the final weight fraction of oxygen in the zirconium varied from 3 to 30 times that in the potassium. For a specific thickness, the ratio of the weight fractions increased with time, whereas, at a constant time, the ratio decreased with increasing specimen thickness. The rate of oxygen uptake by zirconium is controlled by diffusion of oxygen through the zirconium, so we could calculate oxygen profiles in the metal that were in fair agreement with experiment.

Using experimentally determined distribution coefficients for oxygen between zirconium and potassium and a mass balance for oxygen, we determined the total oxygen content of potassium by a gettering–vacuum-fusion technique. This technique gave complete recovery of oxygen from potassium samples doped with K_2O, while amalgamation and vacuum-distillation methods yielded low values. Essentially complete recoveries of oxygen from doped potassium samples were found, using a fast-neutron activation technique that employed the reaction $^{16}O(n,p)^{16}N$. However, the analytic precision of this method was poor.

16. Mechanical Properties

Our objective is the study of the effects produced by reactor environments on the mechanical properties of materials. These environments consist of thermal and mechanical stresses imposed on the reactor structure, chemically reactive coolants, and neutrons produced by fissioning. Our work in the past year has emphasized the study of problems associated with hydrogen and carbon dioxide as potential coolants and the problem of radiation damage to stainless steel.

A hydrogen environment weakens some metals. It reduces the creep strength of Inconel, nickel, and copper, but does not affect that of iron and austenitic stainless steel. The mechanism by which hydrogen affects these materials is not clear; but we have obtained evidence, using the electron microscope, that a hydrogen-dislocation interaction may be involved.

A carbon dioxide environment strengthens and reduces ductility of alloys at elevated temperatures by carburizing them. Carburization may be inhibited in the stainless steels by an increase in the chromium content to above 20%, which leads to formation of a protective Cr_2O_3 film at the metal-oxide interface.

Irradiation at 200 to 400°C increases the strength and decreases the ductility of stainless steel tested in the same temperature range. We have verified that this effect, which is not observed when the irradiation or test temperature reaches 600°C, is caused by fast neutrons. Irradiation at higher temperatures decreases high-temperature ductility without affecting strength; this we have found is caused by thermal neutrons, very likely by the $^{10}B(n,\alpha)$ reaction introducing helium into the metal. We have found a preirradiation heat treatment that can significantly improve the low-temperature postirradiation ductility of stainless steel.

17. Nondestructive Test Development

We are developing new techniques and equipment for the nondestructive evaluation of materials and components. The major emphasis has been on eddy-current, ultrasonic, and penetrating-radiation methods.

Analytical methods have been developed and implemented with computer programming to calculate impedance of eddy-current coils to facilitate their design and application. Improved circuitry has been designed and fabricated to enhance the usefulness of the phase-sensitive eddy-current instrument. Detailed instructions have been prepared on the design and construction of coolant-channel spacing probes.

We have continued to study techniques for the detection of nonbond in clad structures and have designed and built a number of new experimental devices. Preliminary work shows promise for the ultrasonic evaluation of roll-swaged joints common to several fuel elements. New and improved instrumentation has been designed and built for the processing of ultrasonic data signals.

We have microradiographed minute specimens after in-pile testing. In continued studies on techniques and standards for the determination of fuel inhomogeneities in fuel plates and rods, we

have provided design criteria for production scanners for the HFIR fuel plates. We are examining x-ray imaging television systems for use in hot cells. The method also shows promise for precision measurement of component expansion during thermal testing.

In our development on problem materials including molybdenum, tungsten, tantalum, and graphite, we are trying to use ultrasonics to measure the strength of graphite.

A principal part of the development of remote inspection techniques has been the work on radiography in the presence of a radiation background. Use of photographic reduction on the fogged film greatly increases the tolerance to background.

Five exhibits related to nondestructive testing developments were prepared for display at the Third Geneva Conference on Peaceful Uses for Atomic Energy.

18. Reactions in Solids

We found that Arrhenius-type expressions adequately describe the temperature variations of volume diffusion coefficients in niobium and tantalum but not in β-zirconium, β-titanium, or vanadium. Bombardment with 10^{11} 2.2-Mev alpha particles per square centimeter per second increases diffusion coefficients of lead in silver single crystals by 6×10^{-18} cm^2/sec in the temperature range of 360 to 480°C. The thermal-gradient redistribution of antimony in silver can be described in terms of a kinetic theory and an unusually large negative heat of transport ($Q^* = -29 \pm 3$ kcal/mole).

19. Tungsten Metallurgy

We are fabricating and characterizing shapes of pyrolytic tungsten produced by the reduction of tungsten hexafluoride. Both sheet and tubular deposits have been produced under optimum conditions, and an evaluation of these deposits as to weldability and elevated-temperature stability has been undertaken. In addition, data have been obtained on the weldability, ductile-brittle transition temperature, and creep strength of powder-metallurgy tungsten to provide a base line for comparison with the pyrolytic material. We are also exploring the feasibility of using a dispersed second phase to provide sources of mobile dislocations to enhance the ductility of tungsten.

20. Uranium Nitride

We are evaluating uranium mononitride (UN) as a fuel for high-temperature reactors with high power densities. Several pertinent physical properties, including coefficient of thermal expansion, electrical resistivity, thermal conductivity, and fission-gas release after neutron activation, have been measured and are reported. Preliminary measurements of the pressure-temperature-composition relationships in the uranium-nitrogen binary system are described.

21. Zirconium Metallurgy

The transformation kinetics in a series of Zr-Mo alloys and in a Zr–0.9 wt % Fe alloy were studied by electrical resistivity and metallography. The Zr-Mo alloys behaved much as the Zr-Nb alloys previously reported. The Zr–0.9 wt % Fe alloy results are difficult to interpret because three phases are observed over an appreciable temperature range.

The effect of applied stress on the preferred orientation of hydrides precipitated during cooling was examined. The data were analyzed by use of a hydride pole figure. Stress reorientation of hydrides occurred only if the applied elastic stress was parallel to a high concentration of basal poles. Plastic strain caused the hydrides to precipitate parallel to tensile strain components and perpendicular to the compressive strain components.

A technique for the rapid determination of an approximate (0001) crystallographic pole figure for Zircaloy-2 by use of Knoop microhardness measurements was developed. Only 36 impressions are required, if they are made in a specified pattern. The resulting pole figure is in excellent agreement with figures prepared from x-ray diffraction data.

A technique and an analysis were developed for rapidly determining hydride and crystallographic (0001) pole figures in Zircaloy-2 by the use of a polarized-light microscope and quantitative metallography.

The refractive indices were determined as a function of wavelength for the first time for anodized films formed on zirconium foil. The method also yielded accurate measurements of film thicknesses, but it failed for films formed by reaction with air, oxygen, or water, because these films intrinsically absorb in the ultraviolet and visible spectra.

Single crystals of zirconium and Zircaloy-2 were grown in sizes up to 13 mm in diameter and 10 cm long by use of an electron-beam furnace. Many of the variables of the growth process were investigated, and most of the necessary requirements for reproducible growth of large quantities of single-crystal material are now determined.

As-deposited bars of zirconium and titanium as large as 0.5 in. in diameter were successfully zone melted as many as ten successive passes. Appreciable purification was obtained in as few as four passes, and resistivity ratios as high as 450 were measured.

PART III. REACTOR DEVELOPMENT SUPPORT

22. Advanced Test Reactor

The Advanced Test Reactor Aluminum-Base Fuel Element Program was completed during the past year. The majority of effort was directed at the collection and publication of the detailed results obtained in developing this mechanically joined 19-plate, wedge-shaped fuel element.

Evaluation of the homogeneity of the fuel in the ATR plates by x-ray attenuation techniques was completed. Mixtures containing 34.57% U_3O_8 in aluminum made acceptable fuel-plate cores when the U_3O_8 particle size was restricted to $-170 + 325$ mesh.

23. Army Reactors Program

Procedures developed previously for making 30-g batches of high-density Eu_2O_3 and europium molybdate were used with slight modification in scaling up to a 500-g quantity. Compatibility of these arc-melted compounds with stainless steel was indicated in preliminary tests.

Full-size neutron absorbers containing 37% Eu_2O_3 in stainless steel did not change significantly in dimensions on irradiation in the SM-1 to estimated exposures of 5.9 and 13.5 Mwyr. Experimental fuel elements and neutron absorbers in test in the SM-1 were undamaged by limited exposure. Hot-cell inspection of type 403 stainless steel control-rod-drive pressure thimbles used in the PM-1 and PM-3A showed pitting and cracking after relatively low exposures. The frequency of cracks in the cladding and the susceptibility to waterlogging of fuel elements from the SM-1 (first core loading) increased with reactor exposure.

We have evaluated irradiation test specimens containing spheroidal UO_2 "ideally" distributed in stainless steel, which represent the fuel material planned for core 3 of PM-1, and we are testing them in the ORR pressurized-water loop.

24. Enrico Fermi Fast Breeder Reactor

During the past year, work on the current phase of the Fermi Project was completed and the final report issued. By selection of spacers, both the plate-spacing and element-stackup specifications could be met.

25. Gas-Cooled Reactor Program

Part of our effort is in support of the Experimental Gas-Cooled Reactor. We have completed receipt of the reactor fuel and the fabrication of instrumented fuel assemblies, we have assisted the construction contractor with welding problems, and we have measured stress-rupture properties of the fuel cladding material. The creep of the graphite moderator material under irradiation was found to help the material accommodate in-service strains and to be predictable by a theoretical model. We found the effect of irradiation on several physical properties of graphite.

A major effort is the development of unclad fuels for advanced gas-cooled reactors, especially graphite-base fuels containing dispersed pyrolytic-carbon-coated fuel particles. We have related the properties of the coating to the conditions of deposition. We have mathematically analyzed the strain caused in the coating by irradiation. An improved etching technique was found for preparing particles for metallography. Poison particles are also under study. Spherical graphite

fuel elements have been tested by abrasion, crushing, impact, thermal shock, radiography, eddy-current methods, and infrared emission, and prepared for reactor irradiation. Our results have been related to design and fabrication. A phenolic resin was a better binder for graphite fuel elements than a furan. High-temperature chlorination removed exposed thorium and uranium from the surface of graphite fuel elements. Fueled beryllium oxide has been irradiated to 1.6% burnup of the fuel atoms. Uranium can be leached from fueled beryllium oxide with nitric acid.

Supporting research for gas-cooled reactors has been in diverse areas. Using x-ray diffraction and other techniques, we have prepared a phase diagram for the system UC_2-ThC_2. We have devised methods for welding new high-strength nickel alloys. Creep-rupture properties of a British stainless steel were measured under irradiation. The ratchetting of stainless steel cladding on ceramic fuel was studied, and we found the effect could be decreased by use of copper foil as a lubricant between the fuel and cladding. We have investigated the mechanism of structural changes in UO_2 irradiated at high temperatures, and we have measured the thermal conductivity of graphite from 50 to 1000°C.

26. High Flux Isotope Reactor

We have been developing fuel and control elements for the High Flux Isotope Reactor, a reactor being built to operate at a flux of 5×10^{15} neutrons cm^{-2} sec^{-1} to produce transplutonium elements. Development of the novel fuel element has progressed to the point that a contract has been issued for the first year's supply.

We achieved excellent bonding and dimensional control in two complete sets of fuel plates, one for a critical experiment and one for the first reactor core. Excellent control was achieved on both plate dimensions and nonbond. In general, no difficulty was encountered in meeting the +30% tolerance for any $^5/_{64}$-in.-diam area, but some relaxation will be required for the ±10% tolerance for the "average" in short strips. The set for the critical experiment has been formed to the required involute shape and assembled without difficulty into the element.

Perfecting the welding procedures continues to be one of the major HFIR problems. Attachment of fuel plates into the element was improved by an increase in the root thickness and new sequences for the start and finish of each weld.

A new instrument has been developed, built, and demonstrated for measuring uranium homogeneity in fuel plates. From the x-ray attenuation it continuously measures concentration in areas as small as $^5/_{64}$ in. in diameter at scanning speeds of 130 in./min or "average" concentration in short lengths.

Cylindrical control assemblies containing separate dispersions of europium oxide and tantalum in aluminum were fabricated to close tolerances. Control plates were roll clad, mechanically formed into approximately the desired cylindrical quadrants, explosively formed to the specified dimensions, and welded in groups of four to form the cylindrical elements. During preforming, cracking in the europium section was prevented by use of a backup plate to keep the section in compression.

27. Molten-Salt Reactor

Grade CGB graphite specimens were evaluated to determine the acceptability of this material for use as moderator in the Molten-Salt Reactor Experiment. Bulk density ranged from 1.83 to 1.87 g/cm^3. The spectrum of pore-entrance diameters was determined over the range from 100 to 0.02 μ. Lattice constants were measured to be a_0 = 2.464 A and c_0 = 6.746 A. Oxygen concentration in this graphite averaged less than 20 ppm and did not change with exposure to the atmosphere. Material intended for structural purposes was examined radiographically and found to meet the requirement specified.

We successfully sealed stubs remaining in the MSRE heat exchanger after some of the tubes had been cut off.

Tensile properties were measured on welded specimens of INOR-8. When specimens had been stress relieved for 2 hr at 1600°F in hydrogen, the tensile strength below 1000°F was lowered; ductility was lowered at room temperature but not at higher temperatures; the yield strength was lowered; and the specimens failed in the base metal rather than in the weld.

Tensile properties of irradiated and unirradiated INOR-8 are reported for test temperatures from ambient to 900°C. Ductility was reduced at

temperatures above 600°C. The effect of irradiation increased with decreasing strain rate. Postirradiation anneals did not affect the radiation-induced properties.

Creep rates were measured on heats of INOR-8 for the MSRE, and tensile properties of this alloy were measured after various heat treatments.

Specimens and capsule components from in-pile experiments were examined metallographically. Some INOR-8 and molybdenum specimens carburized in contact with graphite and fuel salt. Graphite and INOR-8 capsule components showed no evidence of attack. Autoradiography of graphite demonstrated a slight penetration at the surfaces.

28. Space Power Program

Materials assistance is being provided for the Medium Power Reactor Experiment, a compact boiling-potassium system for electric power generation. Work has included fabrication of components for experimental devices, preparation of fuel element specifications as well as associated fabrication development, and posttest metallurgical analyses of various items of hardware.

29. Thorium Utilization Program

We are cooperating with the Chemical Technology Division to simplify and reduce the cost of the Th-^{233}U fuel cycle. We have developed new processes for applying pyrolytically deposited carbon coatings to fuel particles at markedly reduced costs and demonstrated that these coatings are compatible with oxide particles produced by a new Chemical Technology Division technique.

We completed successfully the remote fabrication of 1100 fuel pins in the Kilorod Facility, vibratorily compacting bulk oxides, prepared by sol-gel techniques, into zircaloy tubes. Our experience is being used to develop the remote fabrication equipment to be installed in the Thorium-Uranium Fuel Cycle Development Facility that we are designing.

From numerous irradiation tests on bulk oxides, we found that the sol-gel produced oxide is an excellent nuclear fuel and that mixed oxides of thorium and uranium perform satisfactorily at much higher heat ratings than UO_2 alone. We found that stress is one of the more important parameters controlling the rate at which fission gas is released from ceramic fuels. Work has continued on the strengthening of metal fuels by alloying and dispersions. Irradiation tests of thorium-zirconium alloys were discontinued because of experimental difficulties.

30. Water Desalination and General Reactor Economic Evaluations

Our study of the problem of producing pure water from sea water at a low cost through nuclear heat was continued. We studied elements contributing to the cost of fuel element fabrication and surveyed the literature to collect available information on the irradiation performance of metal fuels.

Six reactor concepts were evaluated for central power stations. Five of these were based on advanced converter concepts utilizing a thorium fuel cycle. Our task was to analyze the status of the development of the fuel elements for such reactors and to calculate the cost of fabricating the various fuel elements.

PART IV. OTHER PROGRAM ACTIVITIES

31. SNPO-C NERVA Program Assistance

We have evaluated brazing alloys and conditions for René 62 and weldability of Inconel X-750. These nickel-base alloys are nozzle materials for nuclear rockets.

32. Thermonuclear Project

We found that electron bombardment of metallic surfaces releases sorbed gases and appears to be a way of obtaining very clean surfaces without heating or causing radiation damage.

33. Transuranium Program

Process development work was successfully completed for the various steps in the remote fabrication and inspection of target elements for the High Flux Isotope Reactor. Designing and testing of the equipment for the three cells of Transuranium Facility are 60% complete. The

equipment for the glove-box line, in which an initial loading of plutonium-bearing targets will be fabricated, has been assembled and tested. One test consisted of fabricating seven prototype elements, which were subsequently inserted into one of the reactors at Savannah River.

We are developing remote welding procedures and obtaining basic data on welding parameters, so that a suitably programmed welding cycle can be specified.

The first of four prototype elements being irradiated in the ETR was removed and examined after some six months of irradiation. With 40 at. % burnup of the original plutonium at a heat flux comparable to that expected in the HFIR, the target exhibited no serious design or fabrication deficiencies. One of the remaining three elements being tested will be moved to a higher flux position to achieve a heat flux from 1 to 1.6×10^6 Btu hr^{-1} ft^{-2}.

Contents

PART II. LONG-RANGE APPLIED RESEARCH

PART III. REACTOR DEVELOPMENT SUPPORT

PART IV. OTHER PROGRAM ACTIVITIES

PAPERS, ORAL PRESENTATIONS, AND OPEN-LITERATURE PUBLICATIONS

Part I.
Fundamental Research

1. Basic Research on Sintering

C. S. Morgan C. S. Yust

Continued advances in nuclear and other technologies require improved materials suitable for use at high temperatures. Many ceramic materials that have great potential for high-temperature application are most conveniently fabricated into useful shapes by pressing and sintering. Our studies of sintering fundamentals are intended to advance the knowledge of the mechanism of material transport during sintering of ceramics, particularly UO_2 and ThO_2.

Previous studies have indicated[1] that during the initial sintering of thoria, material is transported primarily by dislocation movement. We report here our continued effort to elucidate the factors influencing material transport, including results of related grain-growth and creep studies.

CREEP OF THORIA

To gain further information on the deformation properties of thoria that may be related to the sintering mechanism, we are investigating its compressive creep. High-temperature creep was measured with moderate stresses on ThO_2 bushings. Considerable scatter in the results was apparently caused by variation in the powder-pressing process and by uneven stress distribution due to imperfect matching of the bushing surfaces and the compressing surfaces. Figure 1.1 shows the creep results for a ThO_2 bushing and a ThO_2–0.60% CaO bushing. At 1465°C a stress of 7800 psi caused creep of approximately 0.008%/hr in the ThO_2 bushings. Specimens that contained calcium oxide deformed at much lower stresses at 1465°C; a bushing containing 0.84% CaO showed

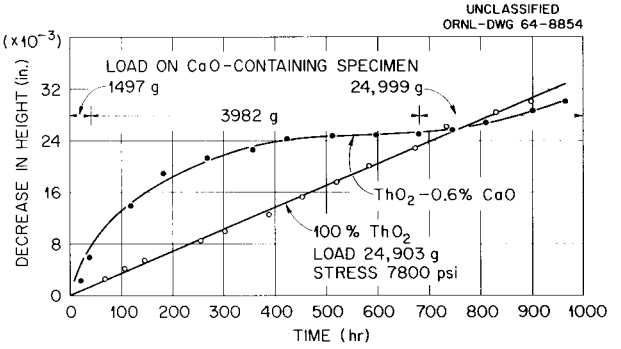

Fig. 1.1. Creep of ThO_2 and ThO_2–0.60% CaO Bushings at 1465°C.

appreciable creep at 500 psi. At approximately 100 hr the ThO_2-CaO specimens became more resistant to creep, and at approximately 500 hr they usually showed about the same facility for creep as pure thorium oxide specimens. X-ray and petrographic examinations showed that initially the calcium was substituted for thorium ions in the lattice, but after long residence in the creep equipment the calcium oxide had segregated substantially.

The activation energy of thoria creep was usually in the range of 70 to 90 kcal/mole for temperatures of 1400 to 1600°C.

DENSIFICATION OF UO_{2+x}

We have measured the densification rate of UO_2 with oxygen-to-uranium ratios ranging from 2.05 to 2.25 in the temperature range of 900 to 1400°C. The material was cold compacted into pellets, reduced in hydrogen, homogenized, and fired in argon. The oxygen-to-uranium ratio of the compact was then determined by firing in air to U_3O_8. The principal object was to investigate the existence

[1] C. S. Morgan and C. S. Yust, *J. Nucl. Mater.* 10(3), 182 (1963).

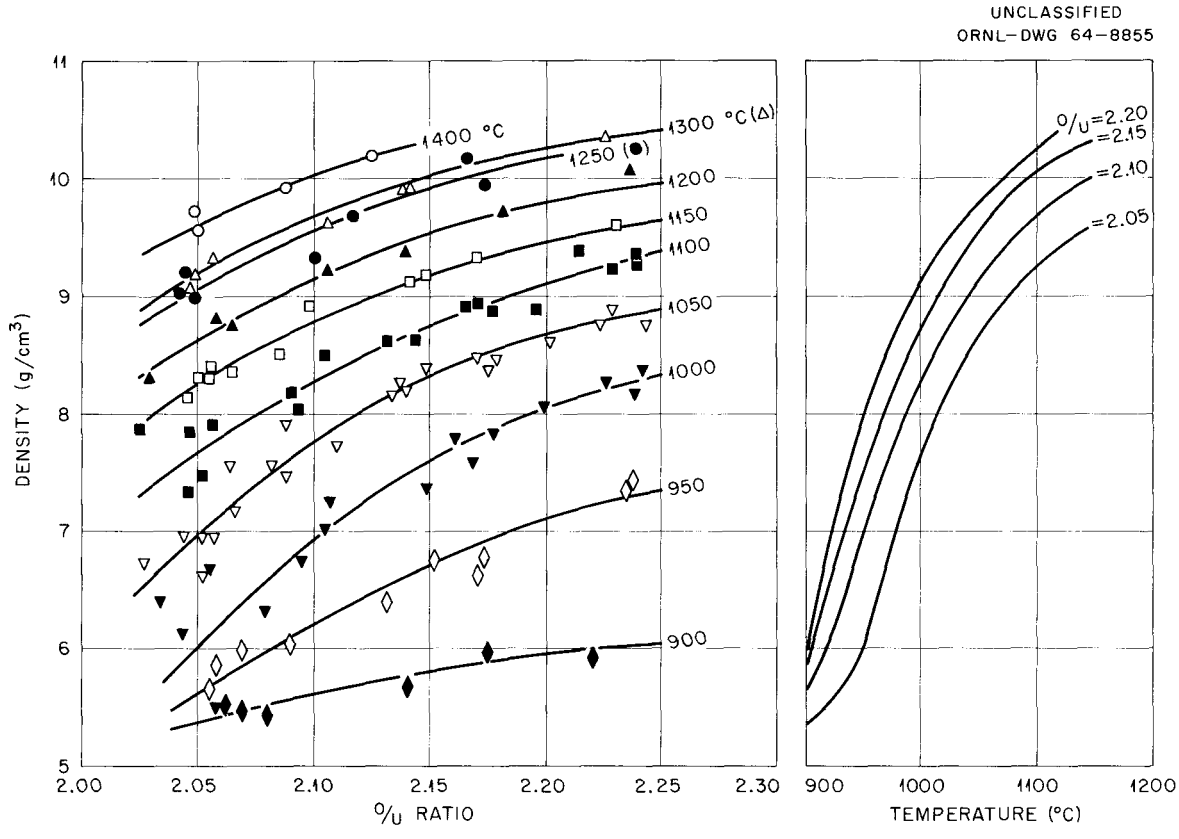

Fig. 1.2. Densification of UO_2 as a Function of Oxygen-to-Uranium Ratio.

of maxima and minima in the densification rate curves for UO_2 of different oxygen contents. The results are presented in Fig. 1.2. Plots of density against densification time at fixed oxygen-to-uranium ratios failed to reveal a maximum or minimum in the densification rate during the sintering of UO_2. In ThO_2 such changes in the densification rate had been found to depend on the impurity content of the material and were evident only in certain ranges of impurity concentration. Thus deviations from stoichiometry in the absence of impurities apparently do not cause this effect.

GRAIN GROWTH IN ThO_2

We started studies of the rate of grain growth in ThO_2 to fulfill two purposes: (1) to determine the relationship between residual porosity in a sintering compact and grain boundaries and (2) to provide additional grain-growth data for oxides, since information of this type is not at present well represented in the literature.

Grain growth in metals and in oxides to the extent that they have been investigated are usually described by the equation $D^2 - D_0^2 = kt$, where D is the average grain diameter at time t, D_0 is the initial grain size, and k is a constant. In general, the data fit the equation only when t is raised to a power other than unity. Lyons *et al.*,[2] examining the results of several investigations of grain growth in UO_2, find that the grain growth is best described by the relationship $D^3 - D_0^3 = kt$.

One of the factors preventing better correlation of the data with the theoretical relations may be the difficulty of calculating the true average diameter of the grains. If this is the case, measurement of grain growth with a parameter that does not depend on average grain diameter might be advantageous. Such a parameter is grain-boundary surface area. Assuming that the rate of change of grain-boundary surface area is proportional to the

[2]M. F. Lyons, D. H. Coplin, and B. Weidenbaum, *Analysis of UO_2 Grain Growth Data from Out-of-Pile Experiments*, GEAP-4411 (November 1963).

fourth power of this surface area leads to the expression $G^{-3} - G_0^{-3} = kt$, where G is the grain-boundary surface area per unit volume at time t, G_0 is the initial grain-boundary surface area per unit volume, and k is a constant.

We plotted our data on grain growth in thorium oxide in argon and air at temperatures ranging from 1720 to 2220°C as $D^2 - D_0^2$, $D^3 - D_0^3$, and $G^{-3} - G_0^{-3}$ vs time on logarithmic scales. The plot based on grain-boundary surface area, shown in Fig. 1.3, yielded slopes more nearly 1.0, as required by the theoretical equation. The data for growth in argon in each plot are compared to the least-squares line through the points. Because of the scatter of the points, the in-air data are compared with dashed lines having a slope of 1.0.

The activation energies for grain growth in argon indicated by these plots are: $D^2 - D_0^2$, 100 kcal/mole; $D^3 - D_0^3$, 136 kcal/mole; and $G^{-3} - G_0^{-3}$, 120 kcal/mole. The data are insufficient for the calculation of the activation energy for grain growth in air. The values of these activation energies are probably higher than would be encountered in pore-free material. The thoria used in the present work had approximately 3 vol % voids in the form of finely distributed pores. The data are incomplete but do reveal that the rate of grain growth is greater in air than in argon. Thoria heated in argon darkens, becoming progressively grayer with increasing temperature and finally black at temperatures in excess of 2000°C. An oxygen ion deficiency is said to be responsible for this darkening. If so, such an ionic variation in the lattice might be expected to influence the grain-boundary migration rate.

At present, we have drawn no conclusions concerning the interrelationship of residual porosity and grain boundaries. The porosity is fine and widely distributed; much of it apparently is at grain boundaries. The etching technique used for delineation of grains, however, produces numerous pits on the grain surfaces, preventing an unambiguous evaluation of the distribution of the porosity with respect to the grain boundaries.

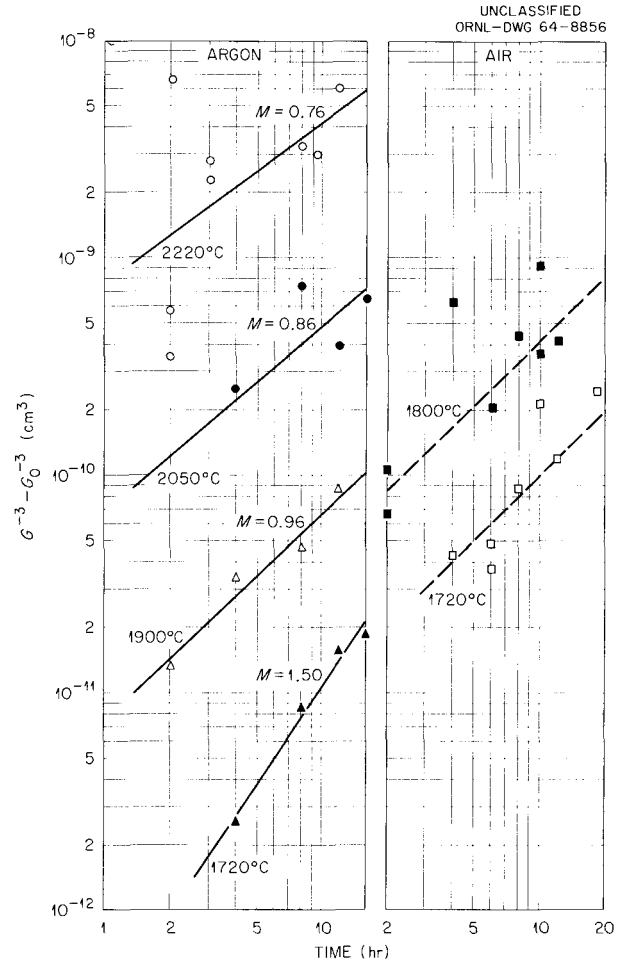

Fig. 1.3. Grain Growth of Thoria in Argon and Air Evaluated by Means of Grain-Boundary Surface Area.

2. Crystal Physics

G. W. Clark

Material technology of tomorrow is dependent upon improved understanding of presently known materials and upon insight into new and novel materials. The use of single crystals is required to characterize unambiguously many physical phenomena. As suitable crystals are frequently difficult to obtain, particularly of refractory substances, we are conducting a continuing program, both to provide crystals needed in research and to devise and improve methods for growing them. Also, we are investigating select physical properties, both those that relate to the crystal growth process and those important for characterizing crystals of new compounds. Crystals are being grown by several methods – from molten-salt solvents, from supercritical aqueous systems, by traveling-solvent techniques, and by the general Verneuil method. More than twenty compounds have been synthesized in single-crystal form within the past year. Some of these crystals have been used in x-ray analysis of neutron damage and others in magnetic, electron-spin resonance, and optical investigations.

GROWTH OF CRYSTALS FROM MOLTEN-SALT SOLUTIONS

Lanthanide Germanomolybdates[1]

C. B. Finch G. W. Clark
L. A. Harris[2]

We have synthesized a series of lanthanide germanomolybdates as single crystals greater than 1 mm on edge. The general formula for the compounds is R_2GeMoO_8, where R = Pr, Nd, Gd, Tb, Dy, Ho, Er, Yb, or Eu. The crystals all have a body-centered tetragonal (scheelite-type) structure with space group $I4_1/a$. Table 2.1 presents the unit cell parameters, densities, and magnetic

[1]Part of this work was presented in a paper, "Single-Crystal Synthesis and Properties of Lanthanide Germano-Molybdates," at the Fourth Rare Earth Research Conference, Phoenix, Arizona, April 22–25, 1964, and will be published in the proceedings.

[2]X-Ray Diffraction Group.

Table 2.1. Properties of the Heavy Lanthanide Germanomolybdates

Composition	Color (25°C)	Lattice Parameters for Unit Cell of Space Group $I4_1/a$		Measured Density[a] (g/cm^3)	Average X-Ray Density (g/cm^3)	χ, Magnetic Susceptibility[b] (emu/g)
		a_0 (A)	c_0 (A)			$\times 10^{-4}$
Gd_2GeMoO_8	Pale blue-green	5.136 ± 0.001	11.275 ± 0.006	6.59	6.801	0.85
Tb_2GeMoO_8	Ocher	5.1175 ± 0.0005	11.211 ± 0.002	c	6.983	1.20
Dy_2GeMoO_8	Light green	5.0976 ± 0.0006	11.156 ± 0.002	7.01	7.122	1.56
Ho_2GeMoO_8	Brownish green	5.0839 ± 0.0004	11.101 ± 0.001	7.07	7.251	1.52
Er_2GeMoO_8	Lavender	5.0686 ± 0.0002	11.0509 ± 0.0007	7.11	7.375	1.17

[a]Pycnometer. Values ± 0.10 g/cm^3.

[b]Faraday method. Values ± 5%.

[c]Insufficient sample.

susceptibilities for the first five compounds synthesized. We have failed to prepare Ce_2GeMoO_8 and La_2GeMoO_8 by similar methods and have achieved only minor incorporation of iron into this structure. Analysis of x-ray data indicated that the iron ion probably substituted for gadolinium. We are trying to form a compound in which transition elements substitute for either the germanium or molybdenum in this structure. This would then give us a material with a greater density of unpaired electrons and concomitant more probable magnetic spin coupling.

An important question relating to this family of compounds is what is the origin of the paramagnetic anisotropy that we have observed. To get to the root of this question, we are measuring the temperature dependence of the magnetic susceptibility, electron-spin resonance spectra, optical absorption spectra, and optical Faraday effect.

Thorium Dioxide

C. B. Finch G. W. Clark

The growth of thorium dioxide crystals up to 3 mm on an edge from $Li_2O{\cdot}2WO_3$ melts was reported last year.[3] More recently we found that the addition of approximately 1 wt % B_2O_3 to the solvent increased the growth rate fivefold without significant impairment of crystal quality; the present growth rate is 0.02 mm/hr.

Thorium dioxide crystals doped with rare-earth ions are being grown also. The ThO_2 acts as a host lattice in whose crystalline symmetry the electronic character of the rare-earth ions may be studied by electron-spin resonance and by optical absorption methods.

Beryllium Oxide

C. B. Finch G. W. Clark

We have reported[3,4] the growth of BeO crystals from the solvents V_2O_5 and $Li_2O{\cdot}2WO_3$. Through the desire to grow larger, purer, and more perfect crystals, we have been evaluating other possible solvent systems. Though the solvent $V_2O_5{\cdot}PbO$ has been one of the most promising, we have not yet found the conditions that yield more perfect crystals than those grown from $Li_2O{\cdot}2WO_3$ melts. Effects of irradiation on the structure of these crystals are reported in Chap. 12.

Tri- and Tetravalent Metal Silicates

C. B. Finch G. W. Clark

Well-formed crystals, greater than 1 mm on an edge, of several tri- and tetravalent metal silicates have been grown from $Li_2O{\cdot}2WO_3$ solutions, using mass transfer at temperatures in the range 1050 to 1250°C with thermal gradients of 10 to 20°C/cm. By x-ray diffraction methods, we have identified one product as identical with the mineral thortveitite, monoclinic $Sc_2O_3{\cdot}2SiO_2$. Both forms of $ThO_2{\cdot}SiO_2$, tetragonal (thorite) and monoclinic (huttonite), have been prepared (see following subsection). Four other compounds formed have been tentatively assigned the following compositions and crystal systems: $Y_2O_3{\cdot}2SiO_2$ (monoclinic), $La_2O_3{\cdot}2SiO_2$ (monoclinic or tetragonal because of possible phase transformation), $Er_2O_3{\cdot}2SiO_2$ (monoclinic), and $HfO_2{\cdot}SiO_2$ (tetragonal). Additional crystallographic data for the erbium silicate are presented in Chap. 12 of this report.

The Thorite → Huttonite Phase Transformation as Determined by Growth of Synthetic Thorite and Huttonite Single Crystals[5]

C. B. Finch L. A. Harris[2] G. W. Clark

The transformation of $ThSiO_4$ from tetragonal (thorite) to monoclinic (huttonite) was investigated by growing single crystals from alkali ditungstate or dimolybdate solutions. Only thorite formed below 1225°C, while above this temperature only huttonite grew. Our data suggest that the equilibrium transformation temperature at 1 atm is 1225 ± 10°C. Crystals of each phase greater than 2 mm on an edge were grown. This technique should be applicable to other systems, especially sluggish ones, where a more direct approach becomes uncertain.

[3] C. B. Finch and G. W. Clark, *Metals and Ceramics Div. Ann. Progr. Rept. May 31, 1963*, ORNL-3470, p. 3.

[4] G. W. Clark, C. B. Finch, O. C. Kopp, and J. J. McBride, *Metals and Ceramics Div. Ann. Progr. Rept. May 31, 1962*, ORNL-3313, p. 181.

[5] Abstracted from a note published in *Am. Mineralogist* **49**, 782 (1964).

HYDROTHERMAL SYNTHESIS

O. C. Kopp[6] G. W. Clark
S. D. Fulkerson

Silicates and Related Compounds

Our crystal syntheses by the hydrothermal method include silicates, ferrisilicates, and similar compounds such as germanates, ferrigermanates, and aluminogermanates. In general, these materials are analogous to natural silicate minerals that contain Al^{3+} substituted for Si^{4+} in tetrahedral coordination with oxygen. Possible phases include those having structures like quartz, feldspar, feldspathoid, zeolite, and mica. We have reported previously[7] the formation of micas, feldspathoids, and zeolites in the system Fe_2O_3–SiO_2–alkali hydroxide.

Further study of the RbOH system suggests the presence of a steep boundary curve passing through the points 405°C, 17,500 psi and 380°C, 9,000 psi. On the low-temperature side of the boundary only the mica phase has been observed. The relationship on the high-temperature side is not as clear. The analcite phase is present, but in some experiments the mica phase is also produced. The boundary between phases depends not only on temperature and pressure but also on the partial pressure of hydrogen in the system. Hydrogen is produced through the reaction between the steel liner of the autoclave and the solvent. The partial pressure of hydrogen increases as temperature increases, but we have not measured it.

Micas, zeolites, and feldspathoidal phases have been produced in the systems Fe_2O_3–GeO_2–alkali hydroxide and Al_2O_3–GeO_2–alkali hydroxide within the temperature range 370 to 450°C and the pressure range 10,000 to 25,000 psi. Under similar conditions, the size of the alkali ion (K < Rb < Cs) influences the phases produced. The dominant phase observed in systems containing KOH is mica. Both micas and zeolites have been prepared in all rubidium-bearing systems studied. Among the cesium-bearing systems, micas have been produced in the Fe_2O_3-SiO_2 and Fe_2O_3-GeO_2 systems but not in the Al_2O_3-GeO_2 system. Cesium-bearing feldspathoids have been produced in all systems. Detailed study of the relationship of the size of the alkali ion to the identity of the stable phases produced (as iron is substituted for aluminum and germanium for silicon in these systems) should provide some clues to the factors that determine the phase or phases stable under a specific set of physical conditions.

Quartz has been grown at 15,000 psi and 410°C from 0.5 *M* KOH in a graphite capsule within a stainless steel liner. This crystal (about 1 cm on an edge) is being used in electron-spin resonance (ESR) studies of the paramagnetic centers formed upon irradiation. Commercially grown quartz is contaminated with sodium, which complicates the interpretation of ESR data. Attempts to grow hemimorphite [$Zn_4Si_2O_7(OH)_2H_2O$] which is very strongly piezoelectric and pyroelectric, have not been successful. Instead, we obtain the phase stable at higher temperatures in this system, willemite ($ZnSiO_4$).

Multiple Oxides

Another broad area of study includes materials that are oxides and multiple oxides, especially those containing the rare-earth elements and the elements from the first transition series.

Erbium manganate(III), $ErMnO_3$, has been grown as thin (0.001–0.003 mm) platelets at 420°C and about 25,000 psi. Both LiOH and CsOH (0.5 *M*) appear to be good solvents. Preliminary evaluation of optical spectra obtained from these crystals lends support to the premise that Mn^{3+} is present. However, a more detailed analysis will be required before we can firmly conclude this.

Additional phases that have been prepared and identified by x-ray diffraction include $ErFeO_3$, $NdFeO_3$, $Nd(OH)_3$, and ErOOH. The latter compound appears to have significant paramagnetic anisotropy.

Studies of the hydrothermal growth of ferrites have continued. Seeded growth has been successful. However, spurious seeding and spontaneous nucleation have interfered with more rapid and better quality growth. We are determining the effect of several additives on the quality of crystal growth.

---

[6]Consultant from the University of Tennessee.

[7]O. C. Kopp and G. W. Clark, *Metals and Ceramics Div. Ann. Progr. Rept. May 31, 1963*, ORNL-3470, p. 4.

PHYSICAL STUDIES

G. W. Clark A. T. Chapman

Perfection of ThO_2 Crystals

G. W. Clark H. L. Yakel[2]

As was stated previously in this chapter, ThO_2 crystals have been grown from melts of $Li_2O{\cdot}2WO_3$ and have been grown five times faster from this same melt with 1 wt % B_2O_3 added. Using an x-ray double-crystal diffractometer, we analyzed the crystalline mosaic spread of selected crystals grown from $Li_2O{\cdot}2WO_3$ with and without the B_2O_3 addition and estimated their defect densities (defects/cm^2). The monochromatized x-ray beam was incident on (111) faces and the system was aligned so as to give Bragg diffraction for (111), (222), and (333) planes. The line width at half maximum of the detected diffraction intensity for the (111) planes was 1.6′ of arc for the crystal grown in $Li_2O{\cdot}2WO_3$. For this same geometry on a crystal grown in $Li_2O{\cdot}2WO_3$ containing 1% B_2O_3, the line width was 2.7′ of arc. The estimated defect density for each of these crystals was $10^{9\pm2}$/cm^2. An active program to identify conditions that will yield crystals of higher quality continues.

Magnetic Susceptibility of Er_2GeMoO_8 (ref. 8)

G. W. Clark E. Sonder[9]
A. T. Chapman

Crystals of Er_2GeMoO_8 tend to orient in a magnetic field contrary to their shape anisotropy, suggesting interesting magnetic properties. The temperature dependence over the range 50 to 400°K and the magnetic-field dependence at room temperature of the magnetic susceptibility of this compound were measured. The volume susceptibility at room temperature was $8.7 \pm 0.3 \times 10^{-4}$ cgs units/cm^3. From the plot of the temperature dependence of the susceptibility using powdered samples, it was concluded that Er_2GeMoO_8 acts like a normal paramagnetic substance between 50 and 400°K. Measurements of the susceptibility of oriented single crystals are now necessary to determine the magnitude of the paramagnetic anisotropy.

Apparatus for Spectrophotometric Study of Small Crystals[10]

J. P. Young[11] G. W. Clark

A sample holder for obtaining spectra of small crystals, of appropriate thickness and whose diameter is greater than 0.13 mm, has been built. This holder was designed for and tested with an unmodified Cary Recording Spectrophotometer, Model 14M. Using an auxiliary high-intensity light source and a holder aperture of 0.13 mm, the measured absorbance was 2.7 and was essentially independent of wavelength over the Model 14M range (0.19 to 2.6 μ) for slit widths less than 0.3 mm. When using the standard light source and a a holder aperture of 0.33 mm, the absorbance was 1.7 and essentially independent of wavelength for slits less than 0.4 mm. Absorption spectra of samples (such as ruby) were well above the background and faithfully reproduced intensity ratios within 10% of spectra obtained from much larger samples.

Electron-Spin Resonance of Rare-Earth Ions[12] in ThO_2: Ytterbium and Erbium

M. Abraham[9] R. A. Weeks[9] G. W. Clark
C. B. Finch

The paramagnetic resonance spectrum of Yb^{3+} and Er^{3+} in ThO_2 has been investigated at 10.5 kMc/sec over the temperature range of 4 to 2°K.

---

[8]Abstract of a more detailed contribution to the *Solid State Div. Ann. Progr. Rept. May 31, 1964*, ORNL-3676 (in press).

[9]Solid State Division.

[10]Abstract of note to be submitted to *Analytical Chemistry*.

[11]Analytical Chemistry Division.

[12]Abstract of paper to be submitted to *Physical Review*.

Sites of cubic symmetry as well as axial sites due to nearby charge compensation were observed. Both cubic spectra gave isotropic g values with $g = 3.423 \pm 0.001$ for Yb^{3+} and $g = 6.752 \pm 0.005$ for Er^{3+}, and these values are in good agreement with the predicted values for Γ_7 doublets. Temperature variation showed that these were the lowest states. For both ions in dilute crystals the line width was $\leq$ 0.5 gauss and in heavily doped crystals the line width was 3 to 4 gauss. Nearby charge compensation in the Yb^{3+} case produces four sites of trigonal symmetry with [111] axes, while in the Er^{3+} case the preponderant axial site had tetragonal symmetry with three [100] axes. For Yb^{3+}, $g_{||} = 4.772 \pm 0.002$, $g_{\perp} = 2.724 \pm 0.001$, and one-third the trace of the g tensor was 3.406. For Er^{3+}, $g_{||} = 3.462 \pm 0.003$, $g_{\perp} = 7.624 \pm 0.005$, and one-third the trace of the g tensor was 6.24. The line widths obtained for the axial sites were broader than those for cubic sites and varied with angle. Evidence for macroscopic crystalline imperfections was also found.

3. Deformation of Crystalline Solids

R. O. Williams

The plastic deformation that can occur when a metal is stressed enables fabrication of the metal and permits it to maintain its integrity during use. The methods by which metals deform are incompletely understood. We have been using several approaches to investigate these mechanisms. These include studies of yield drop in selected alloys, stress-induced ordering of carbon atoms in iron, low-temperature deformation in body-centered metals, the temperature dependence of yielding, development of preferred orientation, and deformation energies.

EFFECTS OF STRAIN RATE AND TEMPERATURE ON YIELD POINTS[1]

R. J. Arsenault

The yield drop that occurs in tantalum, Cu–16 at. % Al, and Ag–6 at. % Al was investigated as a function of strain rate and temperature. From the strain-rate dependence of the yield drop, an activation volume was calculated and found to agree with that obtained from differential strain-rate tests. The temperature dependence of the yield drop can be explained in terms of the parameter temperature divided by activation volume, as illustrated by Figs. 3.1 and 3.2. We attribute the yield drop to the rapid multiplication of dislocations during their motion.

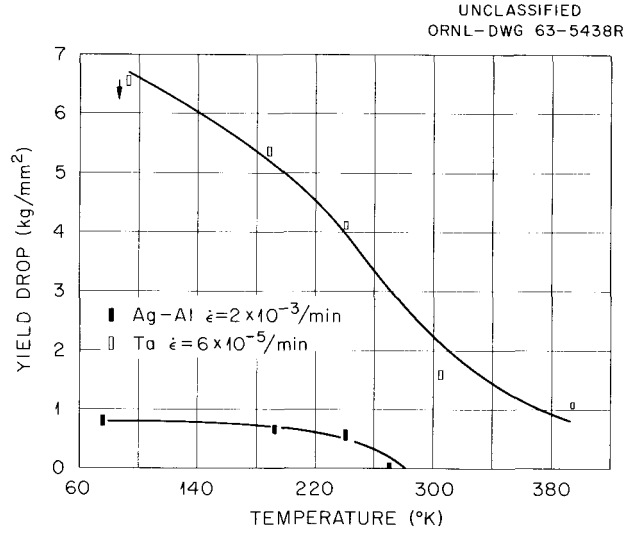

Fig. 3.1. Yield Drop vs Temperature for Tantalum and Silver-Aluminum. Strain rates are shown for the tests represented.

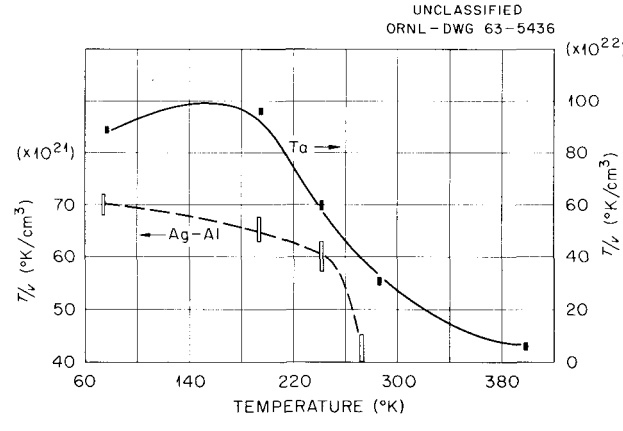

Fig. 3.2. The Parameter T/v^* vs Temperature for Tantalum and Silver-Aluminum.

[1]Abstract of paper accepted for publication in *Transactions of the Metallurgical Society of AIME.*

REARRANGEMENT OF INTERSTITIAL ATOMS DUE TO DISLOCATION MOTION[2]

R. J. Arsenault

We investigated the dependence of activation energy on strain rate in iron-carbon alloys. The experimental results are described and examined in terms of rearrangement interstitials induced by the stress field of moving dislocations.

The activation energy, measured directly by a differential-temperature technique, increased from about 13 kcal/mole to 20 kcal/mole with a reduction in the strain rate. The relationship between activation energy and strain rate was also investigated as a function of interstitial concentration, prestrain, temperature, and grain size. The strain rate was found to be a linear function of stress in the low strain-rate range and a logarithmic function of stress in the high strain-rate range. We suggest that our experimental data are direct evidence for stress-induced ordering.

ENERGY OF FORMATION OF A DOUBLE KINK

R. J. Arsenault G. Czjzek

To a large extent, experimental data obtained from the low-temperature deformation of body-centered cubic metals have been explained in terms of the formation of a double kink over the Peierls' stress barrier. This explanation is based on a model that was developed by Seeger,[3] who assumed that the effective stress was zero. In a detailed discussion of attempts to use the model of Seeger[3] and Seeger and Schiller,[4] we have shown[5] that these models would predict that the activation volume is independent of stress; this contradicts our experimental data.

As a consequence of these discrepancies, the energy of formation of a double kink was calculated as a function of the effective stress from zero to a stress equal to the Peierls' stress. We first made a force balance of the dislocation line, obtaining a second-order nonlinear differential equation. Solving it numerically produced the configuration of the double kink. An expression for the energy of the configuration was then obtained and solved numerically. Two approaches, using different sets of boundary conditions, were used in the numerical solutions and agreed well. Figure 3.3 illustrates the variation in potential energy of a dislocation with the displacement of the center of the double kink for various effective stresses. The energy of formation of a double kink is the difference in energy between the maximum and minimum configurations. We take this energy as the activation energy for the motion of the dislocations, since we assume that the lateral motion of the kinks is an athermal process. Figure 3.4 shows for iron both the theoretical and experimental activation energies plotted vs stress. We found similar agreement between the theoretically calculated and experimentally determined activation volumes.

However, in the above formulation several assumptions were made. The one that is probably the least valid is that continuum elasticity theory can be applied. The reason for this conclusion

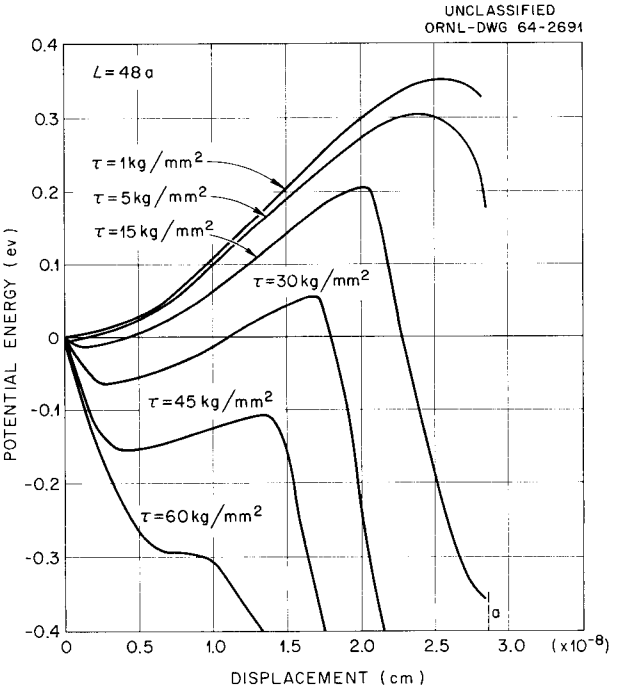

Fig. 3.3. Variation in Potential Energy of the Dislocation Configuration with the Displacement of the Center of the Double Kink for Various Stresses.

[2]Abstract of paper submitted for publication to *Philosophical Magazine*.

[3]A. Seeger, *Phil. Mag.* 1, 651 (1956).

[4]A. Seeger and P. Schiller, *Acta Met.* 10, 348 (1962).

[5]R. J. Arsenault, *Acta Met.* 12, 547 (1964).

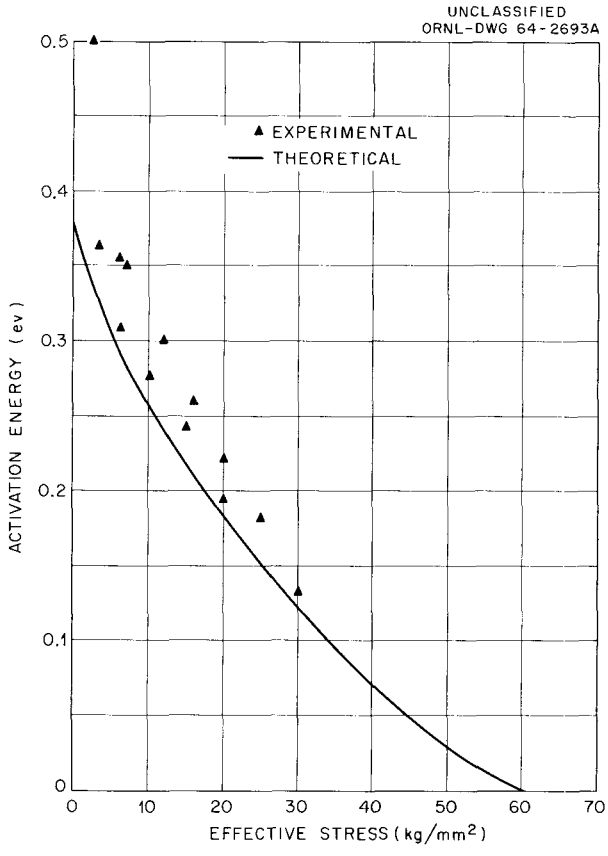

Fig. 3.4. Theoretical and Experimental Values of Activation Energy vs Effective Stress.

is that we are dealing with configuration changes that are essentially within the core of the dislocation. Also the interaction between the kinks was not taken into account.

We calculated the interaction energy for configurations produced at various effective stresses and found it large compared to the energy of formation of a double kink, calculated without considering the interaction of the kinks. Since the interaction force now appears to be repulsive and not attractive as previously found,[4,6] the energy of formation of a double kink may be reduced. The exact magnitude for any particular configuration has not been determined. We are calculating the potential energy of the configurations for different numbers of jumps as a function of the distance between pinning points. When the dislocation line undergoes several jumps, preliminary results indicate that the difference between the potential energy at a maximum and at the next minimum decreases with an increase in the number of jumps and practically becomes nonexistent after two to three jumps. After that, the process becomes athermal.

LOW-TEMPERATURE DEFORMATION OF BODY-CENTERED CUBIC METALS AND ALLOYS[7]

R. J. Arsenault

We are determining the effect of alloying additions on the low-temperature deformation parameters in body-centered cubic metals. The difference between the activation energies and volumes of a body-centered cubic metal and a solid solution of the metal would be small if the rate-controlling mechanism is the formation of a double kink over the Peierls' stress barriers. The main reason is that the Peierls' stress, which would be a major factor in determining the activation energy and volume, is nearly a linear function of the shear modulus. Small alloying additions change the modulus only slightly.

We have investigated tantalum and Ta–9.1 at. % W alloy. The activation energies and volumes were measured by differential-temperature and strain-rate techniques. In Fig. 3.5 are plotted the activation energies vs effective stress. The addition of tungsten decreased the activation energy at a given stress but the modulus was increased approximately 2%. However, in copper alloying with 10 at. % Al increased the activation energy at zero effective stress by a factor of 4. At zero effective stress, the activation volumes are 70×10^{-22} and 25×10^{-22} cm^3 for tantalum and Ta–9.1 at. % W respectively. As shown in Fig. 3.6, these values drop to 2.8 and 5×10^{-22} cm^3 at an effective stress of 17 kg/mm^2.

We are also investigating Ta–10 at. % Nb.

[6] F. Kroupa and L. M. Brown, *Phil. Mag.* **6**, 1267 (1961).

[7] Abstract of paper submitted for presentation at the AIME Fall Meeting, Philadelphia, Pa., Oct. 18–22, 1964.

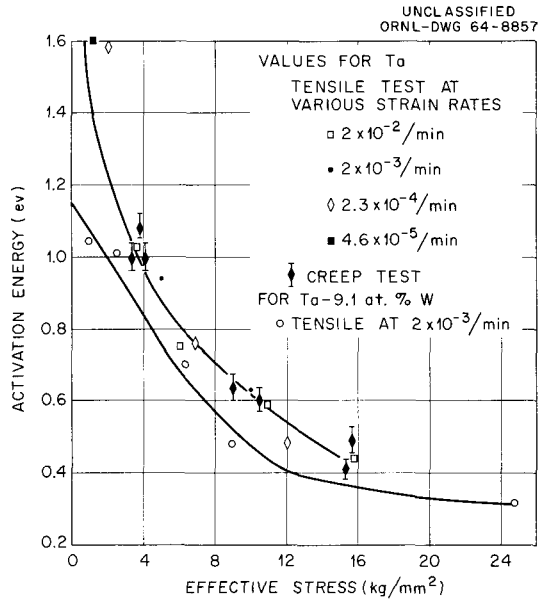

Fig. 3.5. Activation Energy vs Effective Stress for Tantalum and Ta–9.1 at. % W.

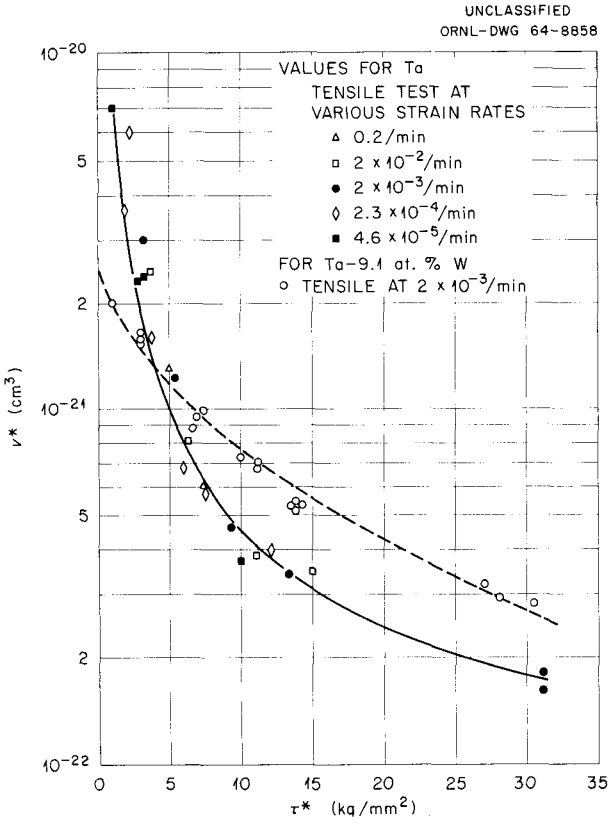

Fig. 3.6. Activation Volume vs Effective Stress for Tantalum and Ta–9.1 at. % W.

EFFECT OF PRESTRAIN AND ALLOYING ON THE TEMPERATURE DEPENDENCE OF YIELDING[8]

R. J. Arsenault J. H Frye, Jr.

Our purpose was to determine whether the increase in the temperature dependence of the yield stress of an alloy over that of a pure face-centered cubic metal could be accounted for by an increase in dislocation density or whether the increase in the temperature dependence was due to other causes of solid-solution strengthening. High-purity Mond nickel and Ni–15% Mo alloy made from high-purity nickel and molybdenum were used.

Prestraining nickel 4.5% and increasing the prestrain to 10% each increased both the athermal and thermal components of stress as shown in Fig. 3.7. The alloy addition also increased both

[8]Abstract of paper accepted for publication in *Acta Metallurgica*.

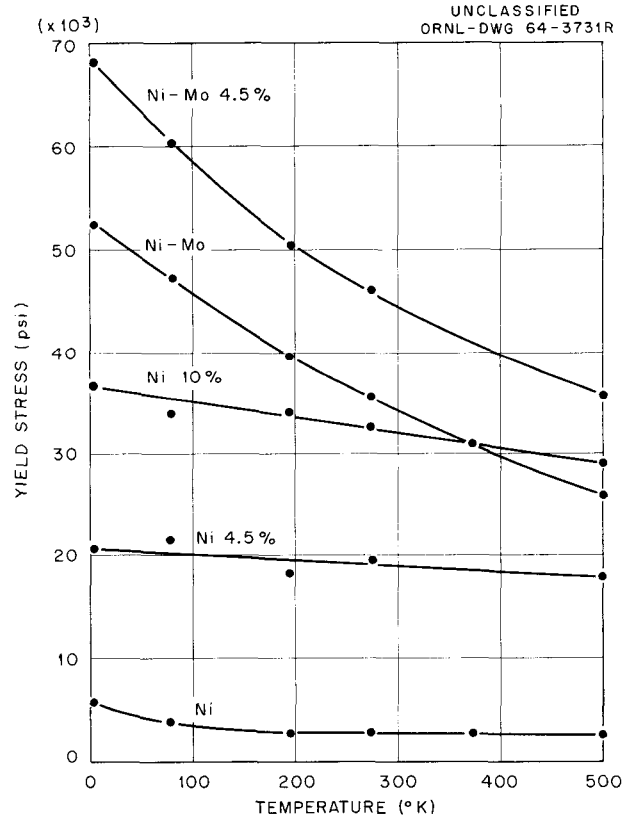

Fig. 3.7. Yield Stress vs Temperature for Annealed and Prestrained Nickel and Ni–15% Mo. Percentages refer to prestrain.

components, as shown in Fig. 3.7, but it increased the thermal component four times as much as did prestraining pure nickel 10%. Prestraining the nickel-molybdenum alloy also increased the temperature dependence of the yield stress. Electron transmission micrographs showed that the change in dislocation density due to alloying was negligible. The most significant change that resulted from the alloy addition was in the dislocation configuration. Piled-up dislocations were not observed in pure nickel, but they were observed in the alloy, indicating, as shown by Swann,[9] that the solute reduced the stacking fault energy.

We can see from the experimental results just described that an increase in the dislocation density does increase the temperature dependence of the yield stress. However, the major effect of the addition of molybdenum is the reduction in the stacking fault energy, which results in wider dislocations. Since they are wider, they are more difficult to intersect, and conservative motion of the jogs is more difficult. Thereby the thermal component of the yield stress is increased.

DEVELOPMENT OF PREFERRED ORIENTATION DURING DEFORMATION

R. O. Williams

We have studied the preferred orientation that results from compression in copper, nickel, silver, iron, 70-30 brass, and Cu–14 at. % Al alloy. The silver, copper, and brass all develop (110) poles in the compression direction, in agreement with the usual behavior of face-centered cubic metals, although there are minor details that are different in each case. Rather unexpectedly, the (320) and (661) orientations were the most preferred in nickel and the copper-aluminum alloy. The iron had a duplex texture of (100) and (111), as expected.

The rate of texture formation in copper in tension, compression, and a combination of tension and compression has been studied. We hope to deduce from the data the rate of reorientation of grains as a function of orientation and compare it with the rate calculated from assumed conditions of deformation.

[9]P. R. Swann, *Electron Microscopy and Strength of Crystals*, p. 131, Interscience, New York (1963).

CALORIMETRY OF DEFORMED METALS

R. O. Williams

Comparatively little work has been done with our liquid-gas film calorimeter[10] during the last year. We have designed, constructed, and tested a high-precision gas volumeter that improves the operation of this calorimeter. Basically this volumeter consists of a metal bellows that is extended or contracted by means of a servomotor, which is controlled by a pressure transducer. This device can detect volume changes of 0.02 cm^3 and has a total capacity of 680 cm^3.

We have completed measuring the effect of grain size on the stored energy of copper using the film calorimeter, and a report has been submitted for publication.[11] Our principal results were that a tenfold increase in grain size decreased the stored energy by about 8%. Also a significant fraction of the flow stress of copper appeared to be required to create the dislocations required for the deformation. A comparison with earlier results showed that changing the strain rate by a factor of 10^6 has little effect on the amount of energy stored.

It has been recognized for some time that the stored energy, measured as the difference between the work required to deform the metal and the released heat (as found by the film calorimeter), is roughly double the observed heats of recrystallization. While this difference can be reasonably attributed to the recovery that takes place prior to recrystallization, no measurements have conclusively proved this. For this reason, we wanted to measure the isothermal heat release at successively higher temperatures until the metal recrystallized, to measure the entire release of stored energy. We have made some progress on this problem.

Basically our method depends upon a careful measurement of the temperature of a sample relative to a closely controlled furnace. The rate of energy release is then given by the expression

$$dQ/dt = C_p(dT/dt) + k(T_s - T_t)$$

where dT/dt is the rate of temperature change,

[10]R. O. Williams, *Rev. Sci. Instr.* 34, 639–43 (1963).

[11]R. O. Williams, "The Stored Energy of Copper Deformed at 24°C," submitted to *Acta Metallurgica*.

k is a constant that depends upon the temperature and sample, and T_s and T_f are the sample and furnace temperatures. Since the amounts of energy released are small, many conditions must be met for the experiment to be a success. The most critical and experimentally the most difficult is to be able to very rapidly raise the temperature of the sample and the furnace so as to maintain the rate of energy release at a measurable level.

The method that we tried is illustrated in Fig. 3.8. The furnace is a copper block that has a low-inertia winding silver-soldered to the outside. The furnace has adequate temperature uniformity, closeness of control, and heating rate. Originally, we planned to heat the sample by pulling it into thermal contact with the furnace walls, but adequate thermal contact could not be made. The present calorimeter was designed so that helium could be introduced to promote heat transfer. While the helium does help, the rate is still not adequate. The method that has been used with reasonable success depends upon the tungsten filament shown in Fig. 3.8. Basically there is no problem with this arrangement provided the furnace is massive enough so that the sample heats faster than the furnace; any additional heat can be supplied to the furnace by its windings. However, a major difficulty with the present arrangement is that the tungsten filament is not in adequate thermal contact with the furnace wall and it would cool to some lower temperature after having been heated. This causes the sample to see a nonuniform changing temperature and thus prevented reliable measurements. Another calorimeter is being constructed and is expected to adequately solve this and other lesser problems. The present apparatus did, however, work well enough to measure a value of the recrystallization energy for copper in good agreement with accepted work.

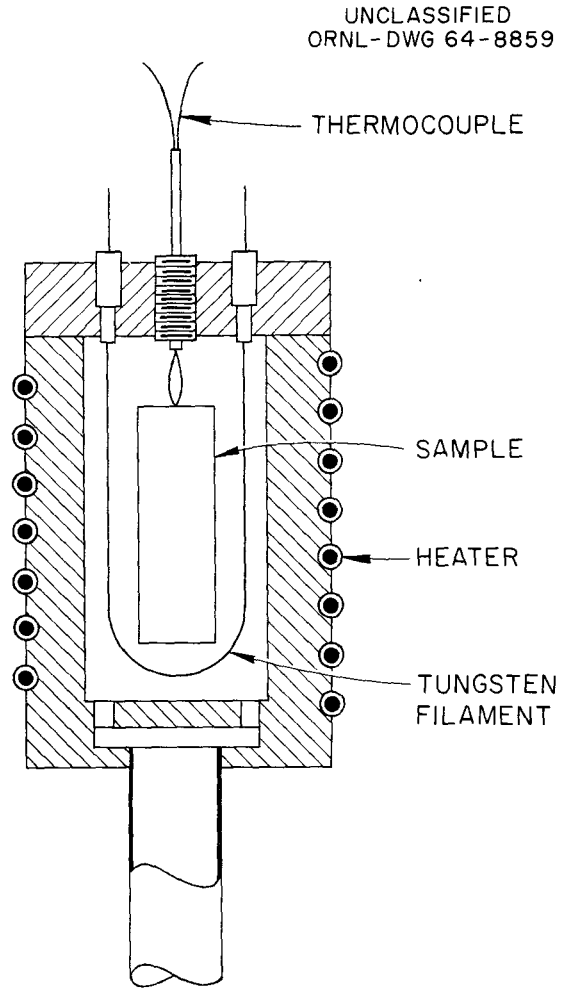

Fig. 3.8. Isothermal Calorimeter Designed for Rapid Increases in Temperature.

4. Electron Microscopy

J. O. Stiegler

We are using transmission electron microscopy as a primary research tool in an attempt to correlate structural features of materials with their mechanical and physical properties. Once we understand how impurities and changes in substructure affect the properties of materials, we feel that we can control these properties through control of the microstructure.

DEFORMATION OF BODY-CENTERED CUBIC METALS AND ALLOYS

J. O. Stiegler C. K. H. DuBose

Our major effort is in a study of the changes that take place in dislocation configuration when metals pass through the transitions between ductile and brittle or twinning and nontwinning behavior. At sufficiently low temperatures of deformation, the microstructures are dominated by screw dislocations that are long and straight but not smooth. In addition, numerous loops and other debris are scattered throughout the material. Tangling and cell formation occur only at relatively high temperatures. This implies that as the temperature of deformation is decreased, the resistance to motion of screw dislocations increases.

For solid-solution alloys, the temperature at which the transition between these structures occurs is higher than for the pure metals. In fact, Nb–55 at. % V and W–26% Re alloys act at room temperature much as pure niobium does at liquid-nitrogen temperature; straight screw dislocations predominate and twinning easily occurs. Typical microstructures illustrating the effects of lowering the temperature of deformation and substitutional alloying of niobium are shown in Figs. 4.1–4.4.

Hamer and Hull[1] recently have demonstrated conclusively that slip does precede twinning and fracture. Our electron microscope observations of metals and alloys that do twin during deformation all show microstructures of straight screw dislocations often grouped together in bands. If dislocations multiply suddenly and rapidly without significant cross slip to distribute the dislocations throughout the grain, narrow bands of highly localized slip result. When blocked by grain boundaries, these bands could produce sufficiently high stress concentrations in adjacent grains to nucleate twins.

Although the transition between twinning and nontwinning behavior occurs over a narrow temperature range (20°C), we find no corresponding sudden change in dislocation substructure. We have observed densely populated slip bands both below and above the transition, although a more homogeneous distribution predominates above the transition.

Several mechanisms have been advanced to explain the rapid increase in flow stress that occurs as the temperature of deformation is lowered and that evidently is related to the observed resistance to motion of screw dislocations.[2] These are (1) breaking away from interstitial atmospheres, (2) overcoming the Peierls-Nabarro stress, (3) nonconservative motion of jogs, (4) overcoming interstitial precipitates, and (5) cross slip.

We would not expect breaking away from interstitial atmospheres and overcoming interstitial precipitates to lead to the very straight dislocations that are observed, and thus they are inconsistent with the experimental evidence. The

[1]F. M. Hamer and D. Hull, *Acta Met.* 12, 682 (1964).

[2]H. Conrad, *Nat. Phys. Lab. G. Brit. Proc. Symp.* 15, 476–516 (1963).

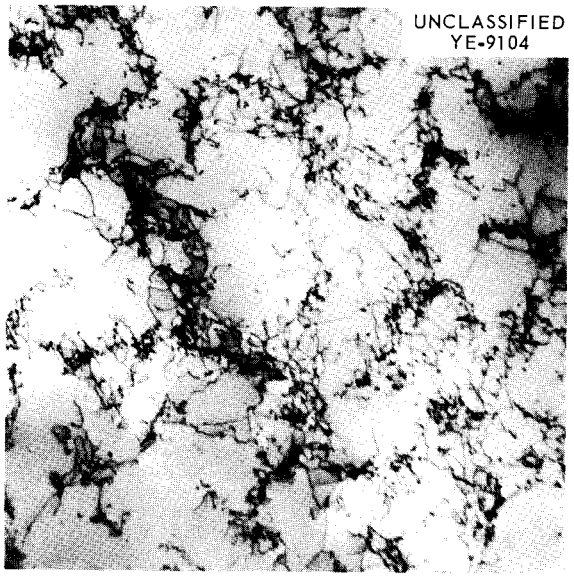

Fig. 4.1. Dislocation Distribution in Pure Niobium Strained Approximately 5% in Tension at Approximately 300°K. 15,000×.

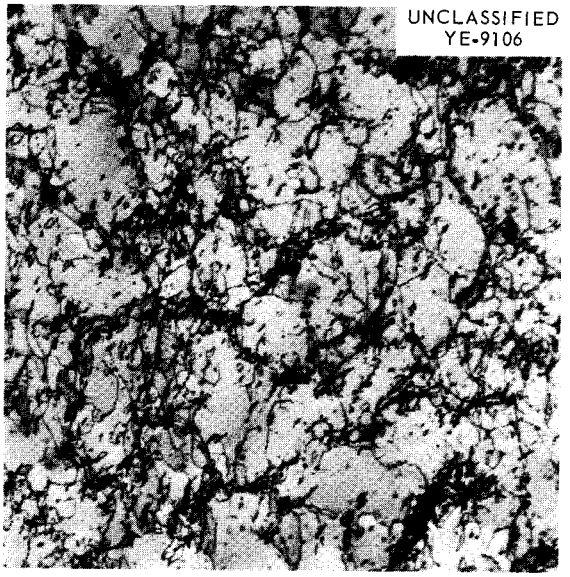

Fig. 4.3. Dislocation Distribution in a Nb–5 at. % W Alloy Strained 5.9% in Tension at Approximately 300°K. Note the extremely small cells having small loops and straight-dislocation segments within them. 30,000×.

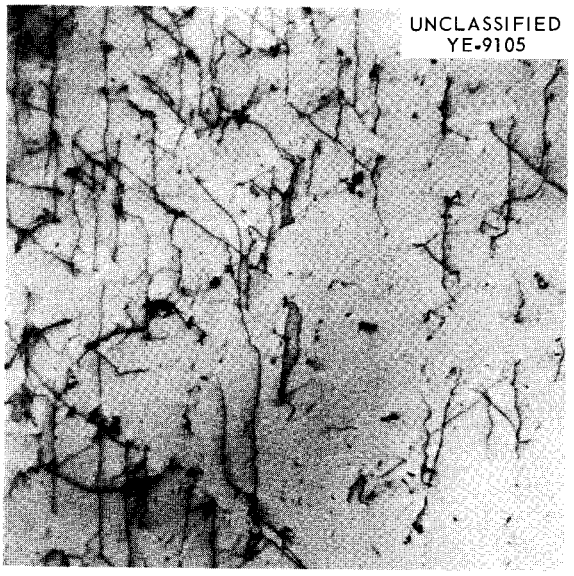

Fig. 4.2. Dislocation Distribution in Pure Niobium Strained in Tension at 78°K. The straight dislocations are almost pure screw segments. 20,000×.

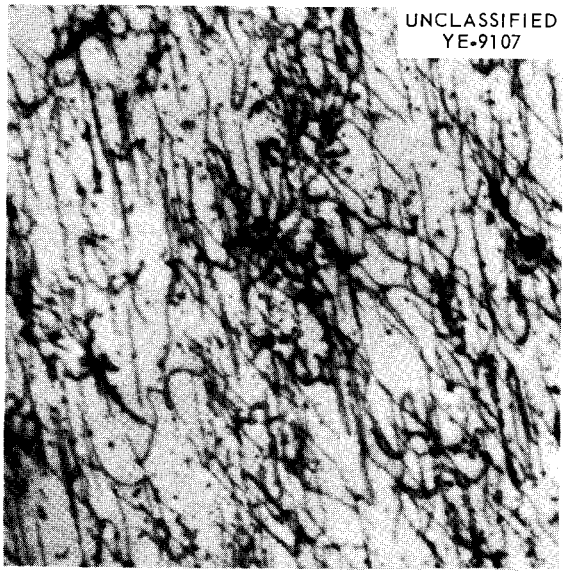

Fig. 4.4. Dislocation Distribution in a Nb–7.5 at. % W Alloy Strained 2% in Tension at Approximately 300°K. There is no tendency toward cell formation in this alloy. 30,000×.

dislocations are heavily jogged, but the jogs are not obviously responsible for the resistance to motion. One would expect the density of jogs to vary statistically along the length of the dislocation, leading to different velocities for different segments of the dislocation line. The continuous and uniform resistance due to the Peierls-Nabarro stress would, however, lead to the straight dislocations actually observed. If motion occurs by the double-kink expansion model advanced by Conrad,[2] the jogs could arise because kinks could expand on different slip planes. Comment on the cross slip proposal is difficult because cross slip is obviously suppressed but not eliminated. This is evidenced by the high density of small loops and other debris, which most likely arise from cross slip of screw segments.

Most interestingly, solid-solution alloying affects the dislocation distribution in the same way that lowering the temperature of deformation does. Fleischer,[3] however, has shown that the substitutional hardening of copper is a result of elastic interactions of solute atoms with screw dislocations that occur due to the different modulus and size of the impurity atoms. For all but extremely dilute solutions this will have the form of an almost continuous frictional stress superimposed on the already present Peierls-Nabarro stress. The fact that similar dislocation distributions are produced in body-centered cubic solid-solution alloys at room temperature and in pure body-centered cubic metals at liquid-nitrogen temperature lends support to the idea that overcoming the Peierls-Nabarro stress is the factor limiting screw dislocation motion in pure metals at low temperatures. We are currently determining atomic-size, electronic, and modulus effects on dislocation distributions in body-centered cubic solid-solution alloys.

STRUCTURAL FEATURES OF PYROLYTIC CARBONS

J. O. Stiegler C. K. H. DuBose

Pyrolytic carbon currently is being developed as a coating material for fuel particles for nuclear reactors; consequently, there is considerable interest in structural features of the various carbons. Pyrolytic carbon basically consists of monolayer sheets on the order of 100 A in diameter having the hexagonal Bernal graphite structure. Detailed descriptions of the structural features of the various carbons are given in recent work being published.[4] As opposed to graphite, in which the stacking of the sheets follows strict rules, the stacking in pyrolytic carbon is nearly random; that is, the layers are twisted and translated randomly with respect to one another.

By altering the deposition variables, deposits can form having densities ranging between 1.4 and 2.2 g/cm^3. Optical and replica electron microscopy show no significant differences between deposits having the extremes in density, so direct electron transmission through cleavage flakes is necessary to show the size, shape, and distribution of the micropores. Figures 4.5 and 4.6 are transmission micrographs of high-density (2.08 g/cm^3) and low-density (1.4 g/cm^3) laminar deposits. The low-density material clearly consists of blocks of carbon and voids, both on the order of 100 A in diameter, packed together. A void network in the high-density deposits, if present, is below our limit of resolution. Particle size did not differ appreciably throughout a series of laminar deposits encompassing the entire range of densities. We detected small differences, however, in a similar series of columnar deposits.

We have studied structural changes during the annealing of blocks of massive deposits. Both lateral growth and ordering of the layers in the graphite structure occurred during anneals at temperatures above the deposition temperature. In addition, the microvoids were consumed during this graphitization process. Annealing at temperatures of 2500 to 3000°C produced graphite crystallites on the order of 1 μ in diameter and a few hundred angstroms thick.

---

[3] R. L. Fleischer, *Acta Met.* 11, 203 (1963).

[4] J. O. Stiegler, C. K. H. DuBose, and J. L. Cook, *An Electron Optical Study of Structural Features of Pyrolytic Carbons*, ORNL-TM-863 (in press).

Fig. 4.5. Transmission Electron Micrograph of a High-Density Deposit of Laminar Pyrolytic Carbon. 100,000×.

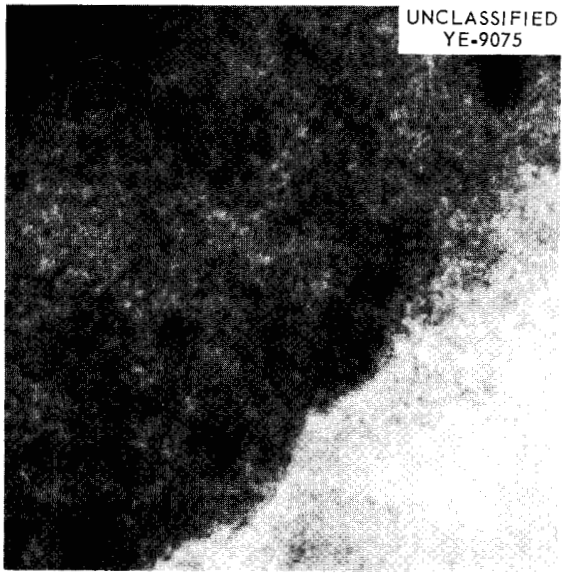

Fig. 4.6. Transmission Electron Micrograph of a Very Low-Density Deposit of Laminar Pyrolytic Carbon. 100,000×.

5. Metallurgy of Superconducting Materials

M. L. Picklesimer

We have been studying metallurgical variables and the superconducting properties of superconducting alloys and intermetallic compounds for three years. We are concerned with the effects of such things as microstructural morphology, compositions, and spacings of two-phase structures; aging reactions; mechanical strain; preferred orientation; and fabrication procedure and heat treatment and their effects on the current-carrying capacity in a magnetic field and at several temperatures. To successfully accomplish such work, first we need to establish a background of information on transformation kinetics and products, morphologies, phase diagrams, precipitation and aging reactions, and rates of formation of intermetallic compounds in the systems of interest. Such work has been conducted and reported previously on Zr-Nb, Nb-Sn, Tc, and Tc-Zr alloys and compounds.

The principal effort of the past year has been the design, construction, and occupancy of the Superconducting Materials Laboratory. The uncontaminated laboratory has been outfitted with essentially all the necessary laboratory equipment for the metallurgical and superconducting studies. The glove-box area designed for the metallurgical study of technetium alloys is complete except for a few remaining items of equipment already purchased or under construction. The glove-box system will permit these operations on technetium alloy specimens: canning in evacuated Inconel to permit fabrication of ingot materials by hot working in air without contamination of either the specimen material or the working area; decanning of these specimens after fabrication; spark machining of specimens for heat treatment, metallography, or superconducting property testing; sawing, filing, and grinding operations; vacuum encapsulation in quartz for furnace heat treatment in air to 1200°C; eventual vacuum melting in beryllia crucibles for purification of starting stock and preparation of 10- to 15-g melts of alloys; electrical-resistivity measurement and thermal analysis for studying transformation kinetics and phase diagrams; and metallographic specimen preparation. The laboratory is sufficiently outfitted to permit concentration in the coming year on the planned metallurgical studies.

TRANSFORMATION KINETICS IN Nb-Zr ALLOYS

G. R. Love M. L. Picklesimer

Preliminary time-temperature-transformation data for Nb-Zr alloys containing 25 to 50 wt % Zr were reported last year.[1] The data were obtained on specimens with 0- to 25-μ-diam grains and known to contain significant amounts of macro- and microsegregation of zirconium. To avoid this segregation, we have subjected arc-cast alloys to a homogenizing heat treatment. This treatment produced large grains, 100 to 200 μ in diameter, and caused some contamination by oxygen and silica. These two factors made our present time-temperature-transformation data not strictly comparable to the previously obtained data, but these contaminated specimens led to some significant observations regarding the transformations in this system. At rather high levels of contamination, Widmanstätten side plates formed in the grain boundaries; and the pearlitic reaction $\beta \rightarrow \beta_1 + \beta_2$ was suppressed. The pearlitic reaction nucleated only at the microscopic defects such as grain boundaries, pronounced slip bands, and free surfaces and not at atomic defects, and growth stopped

[1] G. R. Love and M. L. Picklesimer, *Metals and Ceramics Div. Ann. Progr. Rept. May 31, 1963*, ORNL-3470, pp. 45–46.

within 10 to 15 μ of the defects. In the centers of sufficiently large grains, the high-temperature beta phase decomposed by some type of an aging reaction. The morphology of the aging reaction product changes drastically with transformation times. The precipitate particles are too fine to be sufficiently resolved at 1000×. Bright-field examination of etched specimens yields little information, and anodizing is required to produce sufficient color contrast between the phases of the transformation product to permit fruitful microstructural observation. Possibly, the pearlitic reaction stops because the aging reaction is nucleated homogeneously throughout the untransformed material, or an appreciable time interval may intervene between the cessation of the pearlitic transformation and the aging reaction. In addition to producing difficulties in the transformation studies, high-temperature homogenization and/or the contamination picked up during such treatment embrittled all of the alloys; as little as 15 to 20% reduction produced severe cracking of the homogenized ingot materials. Further work on these problems is under way.

JOINTS BETWEEN SUPERCONDUCTING AND NORMAL-STATE MATERIALS

G. R. Love J. A. Wheeler

One of the significant difficulties encountered in an experimental superconducting program is ensuring that the superconducting properties of the test specimen are being examined, rather than the current-field properties of the joint between the superconducting specimen and the normal-state lead material. This problem is also of appreciable importance in the manufacture of superconducting magnet coils. Most superconducting materials have very low specific heats, very low thermal conductivities, and relatively marked variations of critical current with sample temperature. In practice, this means that microwatts of power dissipated at a joint carrying several tens of amperes of test current may cause the specimen to transform to the normal state at a current level appreciably lower than that characteristic of the specimen itself. Values reported in the literature for the minimum joint resistances between copper (normal state) and Nb-Zr alloys (superconducting state) at 4.2°K in liquid helium range from 0.5 to 5 μohms. We investigated fairly extensively the several types of joints reported in the literature. The best results reported have been obtained with the compression joints of copper on the test wire suggested by R. W. Boom, formerly with the Electronuclear Division, ORNL. Most of the present work has been conducted on variations of the Boom joint. The variables investigated include: (1) pickling of the as-received wire (found desirable); (2) copper plating the test wire (of doubtful utility); (3) tinning with conventional soft solder or indium (may be desirable but the data are not conclusive); and (4) several methods of compressing the copper around the superconductor wire. In all tests, we used the same lot of 0.010-in.-diam Nb–50% Zr wire and the same lot of 0.109-in.-diam copper wire. Joint-resistance values ranged from 1.6 to 1.9 μohms for the best joints, from 2 to 20 μohms for other combinations of the variables, and 50 to 1000 μohms in some cases. The best reproducibility of the low-resistance joints is three out of four having values less than 2 μohms. There are some indications that, even for the joints having the lowest resistance, the electrical resistance increases with increasing current at the higher current levels in zero magnetic field. Since a program such as we have planned demands a reproducibility of low-resistance joint manufacture of at least 99%, the investigation of joint resistances as a function of manufacturing method is critical and will continue.

6. Physical Properties

D. L. McElroy

We are accurately measuring thermal conductivity (k) and other physical properties of solids over a wide temperature range to improve the understanding of heat transfer, particularly at high temperatures. All types of solids are included: metallic, nonmetallic, homogeneous, heterogeneous, isotropic, and anisotropic. Our ultimate objective is the prediction of thermal conductivity either from first principles or from related properties that are easier to measure than k.

One method used in seeking this understanding is the separation of the total thermal conductivity into parts, each dependent on a particular heat-transport mechanism, and subsequent scrutiny of each part with regard to theory. For example, in electrical conductors (metals, semimetals, and semiconductors) k may be separated into an electronic portion and a lattice or phonon portion, where the electronic part can be calculated from measured values of the electric resistivity with the Wiedemann-Franz-Lorenz relation. The electronic contribution is subtracted from the measured thermal conductivity to obtain the lattice contribution. Having made the separation, we can then investigate the effect of variables such as temperature, impurity contents, grain size, and stoichiometry on each part and thereby learn something about the scattering mechanisms affecting each type of heat carrier. The following paragraphs give some examples of the progress we are making with this work.

THERMAL CONDUCTIVITY OF URANIUM DIOXIDE[1,2]

W. Fulkerson T. G. Godfrey[3]

We completed measurements of the thermal conductivity of polycrystalline UO_2 using the radial heat flow apparatus in the temperature range −57 to 1100°C. The technique yielded results with a probable accuracy of ±1.5% and a precision of ±0.1% in the range 50 to 1100°C. Meaningful measurements were limited to 1100°C by the instability of the Pt–10% Rh, Pt thermocouples, although the apparatus was structurally sound to 1400°C. The thermal-conductivity data up to 1000°C could be explained on the basis of heat transport solely by phonons. The thermal resistance, $1/k$, showed the linear dependence with temperature from 200 to 1000°C that is expected for an insulator well above the Debye temperature. The slope of the $1/k$-temperature plot was 0.0223 cm/w, is independent of impurity content, and is indicative of three-phonon *umklapp* processes. The intercept was sensitive to impurity content, as indicated by the fact that it was decreased by a decrease in the oxygen-to-uranium ratio. Between 1000 and 1100°C there was a slight negative departure of $1/k$ from linearity, which may be due to the onset of an electronic contribution. The value of k for uranium dioxide has a maximum near room temperature, apparently caused by the rapid decrease in specific heat below this temperature.

[1] T. G. Godfrey *et al.*, *Thermal Conductivity of Uranium Dioxide and Armco Iron by an Improved Radial Heat Flow Technique*, ORNL-3556 (June 1964).

[2] T. G. Godfrey *et al.*, "Thermal Conductivity of Uranium Dioxide from −57 to 1100°C by a Radial Heat Flow Technique," submitted to the *Journal of the American Ceramic Society*.

[3] Ceramics Laboratory.

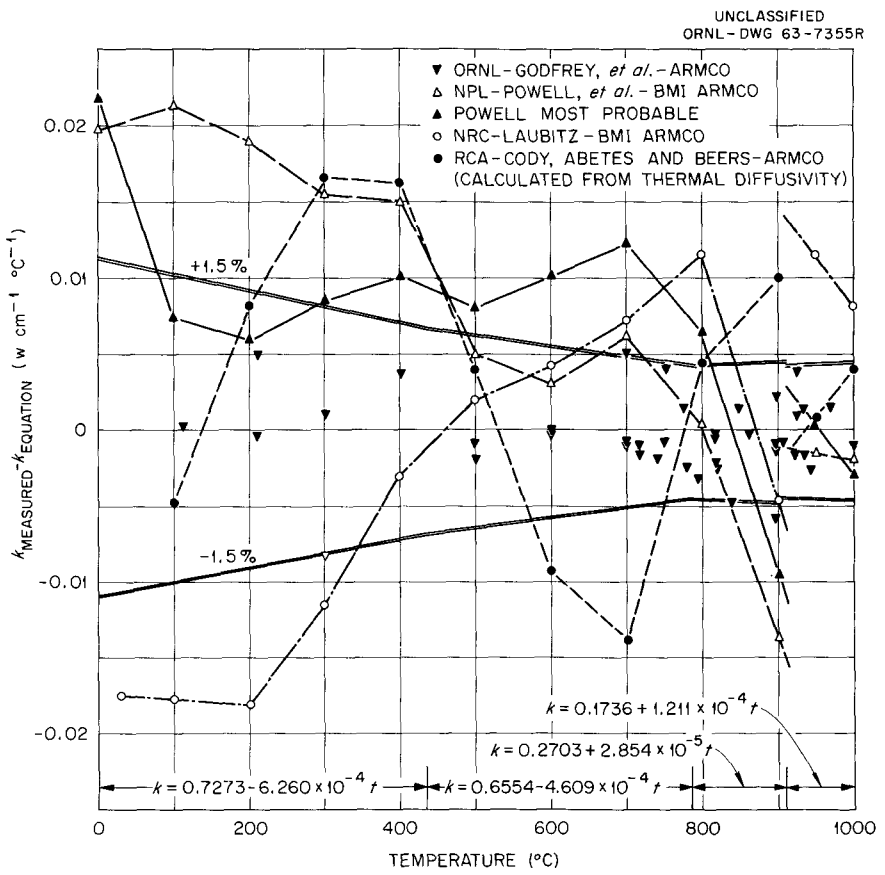

Fig. 6.1. Comparison of Various Measurements of the Thermal Conductivity of Armco Iron to the Four Equations that Represent the ORNL Results from 0 to 1000°C. The equations give k in w cm^{-1} $°C^{-1}$ for Celsius temperature t.

THERMAL CONDUCTIVITY OF ARMCO IRON[1,4]

W. Fulkerson J. P. Moore

We measured the thermal conductivity of polycrystalline Armco iron by the radial heat flow technique between 100 and 1000°C. As shown in Fig. 6.1, all of the best values reported in the literature are within ±3% of our results.[1] The results were compared with measurements from the National Physical Laboratory (NPL),[5] the National Research Council (NRC),[6] and the Radio Corporation of America (RCA),[7] and with data termed by Powell[8] as the most probable values. We deduced from electrical-conductivity measurements, using the Wiedemann-Franz-Lorenz relation, that the temperature dependence of k is largely controlled by the electronic contribution. The four linear equations of Fig. 6.1 represent the temperature dependence of the thermal-conductivity data to within ±1.5% for the ranges 0 to 436, 436 to 786, 786 to 910, and 910 to 1000°C. A slope change of 30% is observed at 436°C and

[4]J. P. Moore *et al.*, *The Thermal Conductivity of Iron from 100 to 1000°C by a Radial Heat Flow Method*, paper presented at the Annual Meeting, AIME, New York, Feb. 16–20, 1964.

[5]R. W. Powell *et al.*, "Armco Iron as a Thermal Conductivity Standard. New Determinations at the National Physical Laboratory," pp. 466–73 in *Progress in International Research on Thermodynamic and Transport Properties* (ed. by J. F. Masi and D. H. Tsai), The American Society of Mechanical Engineers and Academic Press, New York, 1962.

[6]M. J. Laubitz, *Can. J. Phys.* **38**(7), 887 (1960).

[7]G. D. Cody, B. Abeles, and D. S. Beers, *Trans. Met. Soc. AIME* **221**(2), 25 (1961).

[8]R. W. Powell, "Armco Iron as a Thermal Conductivity Standard. Review of Published Data," pp. 454–65 in *Progress in International Research on Thermodynamic and Transport Properties* (ed. by Joseph F. Masi and Donald H. Tsai), The American Society of Mechanical Engineers and Academic Press, New York, 1962.

is possibly related to the minimum in the thermoelectric power of iron vs platinum that occurs near this temperature. The change in sign of the temperature coefficient near 786°C is associated with the Curie transformation. A 4% decrease in the thermal conductivity at the α-γ transformation (910°C) is associated with a 20% decrease in the lattice contribution.

THERMAL COMPARATOR MEASUREMENTS[9]

T. G. Kollie R. S. Graves
D. L. McElroy

We have developed a rapid comparative thermal-conductivity method based on the Powell comparator.[10] Our method consists of measuring the temperature change of a small silver sphere after it is brought in contact with a small specimen initially at a higher temperature. The rate of temperature change of the sphere was calibrated by measuring on samples of known thermal conductivity in the range 50 to 400°C. The accuracy of this technique was better than ±10% with a reproducibility of at least ±2.5%. We measured US, ThS, UN (Part II, Chap. 20, this report), and UO_2 at 75 and 300°C. With the electrical resistivity of US, ThS, and UN and the Wiedemann-Franz-Lorenz relation, we extrapolated the low-temperature k data to higher temperatures, using the assumption that the lattice portion of the thermal resistance, $1/k$, is linear in temperature. The extrapolation of the data for US to 1000°C was within 8% of known values[11] and that for UN within 20% of reported values[12] at 1000°C. Our measurements of k of ThS and the extrapolations to 1000°C are shown in Fig. 6.2; no literature values for comparison were found.

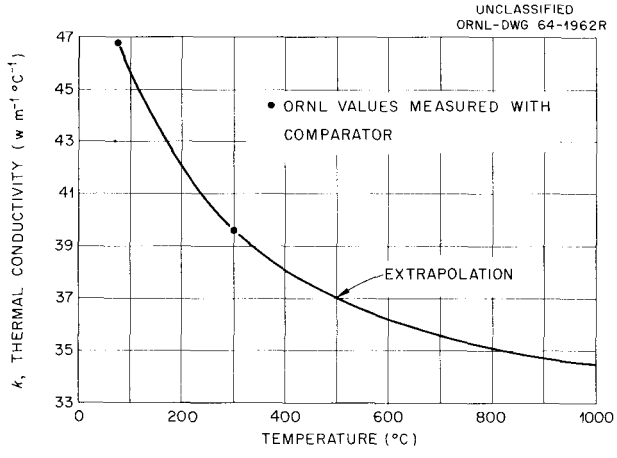

Fig. 6.2. The Thermal Conductivity of Thorium Monosulfide, Corrected to 100% Density, Between 0 and 1000°C.

THE THIRD CONFERENCE ON THERMAL CONDUCTIVITY

The Physical Properties Group organized the 1963 Conference on thermal conductivity, which was held October 16–18, 1963, in Gatlinburg, Tennessee. This conference promotes free and frank exchange of ideas and approaches among the conferees and produces a permanent record of the papers presented. This record is an informal two-volume collection of the papers presented and is made available only to attendees and other contributors to the field of thermal-conductivity measurement. This series of meetings allows our research to be coordinated with all other programs on thermal conductivity and promotes exchange of standard reference specimens.

OTHER MEASUREMENTS RELATED TO THERMAL CONDUCTIVITY

J. P. Moore T. G. Kollie
W. Fulkerson

Since erratic thermocouple behavior above 1100°C is a major limitation to high-temperature thermal conductivity measurements, we are testing the stability of high-temperature thermocouples. Our results are reported in Part II, Chap. 14, of this report.

---

[9] T. G. Kollie *et al.*, "A Thermal Comparator for Thermal Conductivity Measurements from 50 to 400°C," summary of a paper presented at the AIME Symposium on Compounds of Interest in Nuclear Reactor Technology, Boulder, Colo., Aug. 3–5, 1964.

[10] R. W. Powell, *J. Sci. Instr.* **34**, 485–92 (1957).

[11] R. J. Dunworth, Argonne National Laboratory, private communication, October 1963.

[12] E. O. Speidel and D. L. Keller, *Fabrication and Properties of Hot-Pressed Uranium Mononitride*, BMI-1633 (May 1963).

At high temperatures, having more than one temperature transducer is very useful; for example, the core heater of the radial heat flow apparatus proved to be a good resistance thermometer to check the thermocouples, since its electrical resistivity was readily measured.

To complement k measurements in other apparatus, we built a simple longitudinal heat flow apparatus that operated at low temperatures. This device operates in a vacuum and allows directional measurements on small specimens without the need for thermocouples attached to the specimen. Two gold-plated iron heat-meter bars are tandem mounted on the apparatus and are instrumented with Chromel-P/Constantan thermocouples; a compressive load is applied to the specimen sandwiched between the bars with indium foil at the surfaces to reduce interfacial resistance. We calibrated this apparatus with several specimens that had been measured in the radial heat flow apparatus and found it accurate to within 3% between 20 and 90°C for $k > 2$ w m^{-1} $°C^{-1}$. Results from this apparatus and the radial heat flow apparatus on CGB graphite are given in Part III, Chap. 25, of this report. The radial heat flow measurements were made from 100 to 1000°C in a direction perpendicular to the extrusion direction; and using the longitudinal apparatus, results were obtained at 30 and 75°C in directions both parallel and perpendicular to the extrusion direction. We measured the electrical resistivity from room temperature to 1000°C for both directions and found that the lattice portion was greater than 94% of the total k. The lattice portion of the thermal resistance is a linear function of temperature, which indicates that three-phonon *umklapp* processes are the controlling temperature-dependent scattering mechanism.

We are continuing to try to understand the radiative properties of solids and their relation to other physical properties. The total hemispherical emittance apparatus measured emittance as well as electrical resistivity to as high as 1500°C at pressures as low as 1×10^{-7} torr. The electrical resistivity of Armco iron, which was needed to analyze k measurements, was measured to 1000°C in this apparatus. Similar measurements on a number of high-temperature materials are reported in Part II, Chap. 14, of this report. We studied, by electrical-resistivity measurements, physical property changes due to order-disorder transitions in INOR-8. This property could be altered 5 to 10% by rapid cooling and reduced 25% by cold working. These changes serve as a starting point for the study of the effects of order-disorder on other physical properties, such as specific heat. Based on initial results on iron and INOR-8, our apparatus appears to be adaptable to yield specific-heat data.

7. Reactions at Metal Surfaces

J. V. Cathcart

It has long been recognized that superficial oxide films on metals provide a protective barrier that hinders additional oxidation. Of major interest in our research are the factors that control the *degree* of protectiveness of these oxide films. Our previous work established the fact that during oxidation large stresses are generated in the oxide and, in some cases, in the metal as well. Our efforts during the past year have been devoted largely to understanding the influence on the oxidation mechanism of these stresses and of the resultant disarray induced in the oxide lattice. We have continued investigations having this aim and involving the oxidation of copper and the refractory metals niobium and tantalum.

Considerable attention was also given to the study of the diffusion of radioactive niobium and tantalum in specimens of tantalum and niobium. As a result of the development of experimental procedures pertinent to our oxidation research, a highly sensitive sectioning technique for these metals was devised and enabled detailed determination of the penetration curves within 1 to 2 μ of the specimen surfaces. The method has been particularly useful in investigating low-temperature diffusion in these metals.

COPPER OXIDATION

J. V. Cathcart G. F. Petersen

This investigation represents a joint effort with the X-Ray Diffraction Group, whose contribution is given in Chap. 12 of this report. Results during the past year emphasized the importance of regions of disregistry or disarray in the crystal lattice of the oxide film as paths of easy diffusion; in several instances we correlated a variation in the degree of lattice disregistry with a corresponding variation in the rate of oxidation. For example, the presence of 1000 ppm CO_2 in the oxygen increased the rate of oxidation of the (111) of copper by 50% while the lattice disregistry, as measured in terms of the mosaic spread of the films, doubled.

Conversely, the presence of trace quantities of CCl_4 reduced both the rate of oxidation and the degree of lattice disregistry in the oxide on the (111) of copper by altering the amount of twinning that normally occurs in the oxide. The effect on the oxidation rate of changing the fraction of twinned oxide is illustrated in Fig. 7.1, in which the oxide thickness is plotted as a function of the time of oxidation for 12 different (111) specimens. From 50 to 60% of the oxide was twinned with respect to the metal (the crystal lattice of the remaining oxide was essentially parallel to

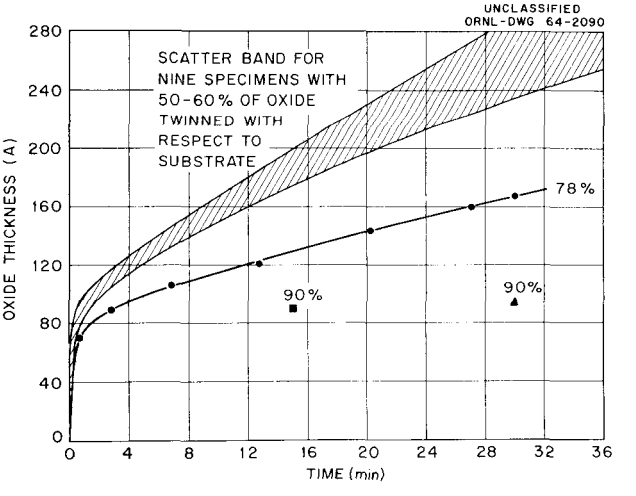

Fig. 7.1. Oxidation Rate Curves for 12 (111) Copper Specimens Showing the Effect of the Amount of Twinning in the Oxide on the Oxidation Rate.

that of the substrate) in nine of the samples, and their oxidation-rate curves all lie in a relatively narrow scatter band shown in the upper part of the figure. For the other three specimens, 75 to 90% of the oxide was in the twinned orientation, and as may be seen, these specimens oxidized considerably more slowly. We believe this decrease in oxidation rate can be attributed to a decrease in the degree of lattice disregistry in the oxide occasioned by a reduction in the effective area of the incoherent twin boundaries in the oxide.

A third correlation between oxidation rate and degree of lattice disregistry was established through a consideration of the marked oxidation-rate anisotropy exhibited by copper. The major crystallographic planes of copper listed in the order of decreasing oxidation rates are (100), (111), (110), and (311); at 250°C the (100) oxidizes 25 times as rapidly as the (311). A qualitatively similar variation in the degree of lattice disregistry in the oxides on these four faces was also noted.

REFRACTORY-METAL OXIDATION

R. E. Pawel J. V. Cathcart

The study of the effect of the solution of oxygen in the metals tantalum and niobium on the morphology and protective qualities of the resulting oxide layer formed during gaseous oxidation continued to be an important phase of our present work. Our previous research[1] correlated the presence of oxygen gradients and stress gradients in the metal during oxidation. We found that in the early stages of oxidation the high stress levels in the surface layers of the metals (e.g., approximately 50,000 psi for tantalum) can influence the mechanism of oxide nucleation. In the case of tantalum this influence was manifested in the formation of platelets of oxide, which grow into the metal, rather than the usual uniform surface oxide film.[2] Thus a complete description of the oxidation process for these metals must consider the development of stresses in the metal as well as in the oxide film.

[1]R. E. Pawel, J. V. Cathcart, and J. J. Campbell, *J. Electrochem. Soc.* 110, 551 (1963).

[2]R. E. Pawel, J. V. Cathcart, and J. J. Campbell, *Acta Met.* 10, 149 (1962).

Study of the properties of anodically formed oxide films has been useful to evaluate further the characteristics of the gaseous oxidation process and, in particular, to establish the events that lead to the breakdown of the initial protective oxide film on refractory metals. The anodic oxide films on suitably prepared surfaces of niobium and tantalum are originally uniform amorphous layers of the pentoxides and grow without appreciable solution of oxygen in the substrate metals. The films are also surprisingly stable when heated to a moderate temperature in oxygen. For example, on tantalum an anodic film as thin as 250 A did not change in thickness when held at 500°C for many hours, although quantitative measurements showed that considerable oxygen was being taken up by the specimen. Thus oxygen apparently penetrated the amorphous oxide film and dissolved in the metal without additional oxide being formed. X-ray and flexure measurements confirmed this interpretation.

An example of how anodic films affect the kinetics of oxygen consumption is shown in Fig. 7.2, which compares the rate of oxygen uptake by several anodized specimens with that by untreated tantalum. Since the anodic films do not thicken during these experiments, the decrease in the rate of oxygen consumption was probably associated with the establishment of oxygen concentration gradients in the metal.

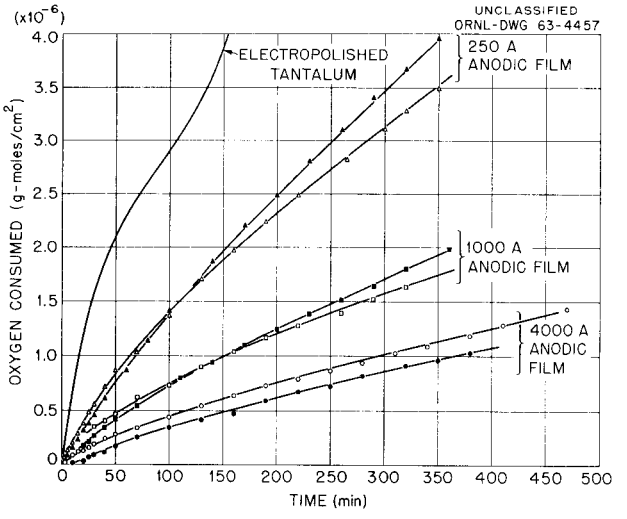

Fig. 7.2. Oxidation Rates of Polycrystalline Tantalum Before and After Anodization.

Because of these unusual characteristics, the anodic treatments permitted observations of the Ta-O system over extended periods of time during which solution of oxygen in the metal remained the principal event. These results have helped to verify some of our earlier arguments concerning the nature of stress development in the metal.

DIFFUSION STUDIES

R. E. Pawel T. S. Lundy[3]

The development of the technique for repeated mechanical stripping of anodic oxide films from suitably prepared specimens of tantalum and niobium[4,5] has provided an extremely sensitive microsectioning technique for examining the near-surface regions of these metals. Using this technique, films of uniform thickness from 100 to 1000 A can be removed consecutively from an electropolished tantalum surface (about 200 to 1000 A for niobium). The stripped films are ideally suited to the determination of their radioactive contents, while the remaining metal specimen retains its integrity for additional measurements. Apparently, the anodizing-stripping sequence can be continued almost indefinitely without significant surface roughening or the development of other difficulties.

Thus far, this technique has been applied with spectacular success to the study of tracer diffusion in tantalum and niobium. Because of the high sensitivity of the method, due as much to the uniformity of the sections as to their small thicknesses, accurate penetration profiles have been obtained for these metals at temperatures as low as 900°C, and diffusion coefficients less than 10^{-17} cm^2/sec have been measured. We expect that refinements of the experimental procedures will permit useful measurements at still lower temperatures. Application of this method to diffusion in tantalum follows; application to niobium is reported in Part II, Chap. 18, of this report.

[3]Solid Reaction Studies Group.

[4]R. E. Pawel and T. S. Lundy, *J. Appl. Phys.* 35, 435–38 (1964).

[5]R. E. Pawel, "Procedure for Stripping Anodic Oxide Films from Tantalum and Niobium," accepted for publication in the *Review of Scientific Instruments*.

Penetration profiles for the diffusion of ^{95}Nb into tantalum single crystals at temperatures from about 1000 to 1600°C were obtained.[4,6] In addition, ^{182}Ta and ^{95}Nb diffusion in both mono- and polycrystalline tantalum was studied at selected temperatures.[6]

An example of typical near-surface penetration profiles is shown in Fig. 7.3, which compares the penetration of ^{95}Nb into single-crystal and polycrystalline tantalum specimens after 2 hr at 1250°C. As is evident from the figure, the profile for each specimen may be conveniently divided into two regions. The penetration plot for the single crystal remained linear (region I) for about four decades of activity, while that for the polycrystal quickly "tailed off" onto a long, relatively high-activity curve (region II), which was not precisely linear when plotted as ln A vs

[6]R. E. Pawel and T. S. Lundy, "Diffusion of Nb^{95} into Tantalum Single Crystals," accepted for publication in *Acta Metallurgica*.

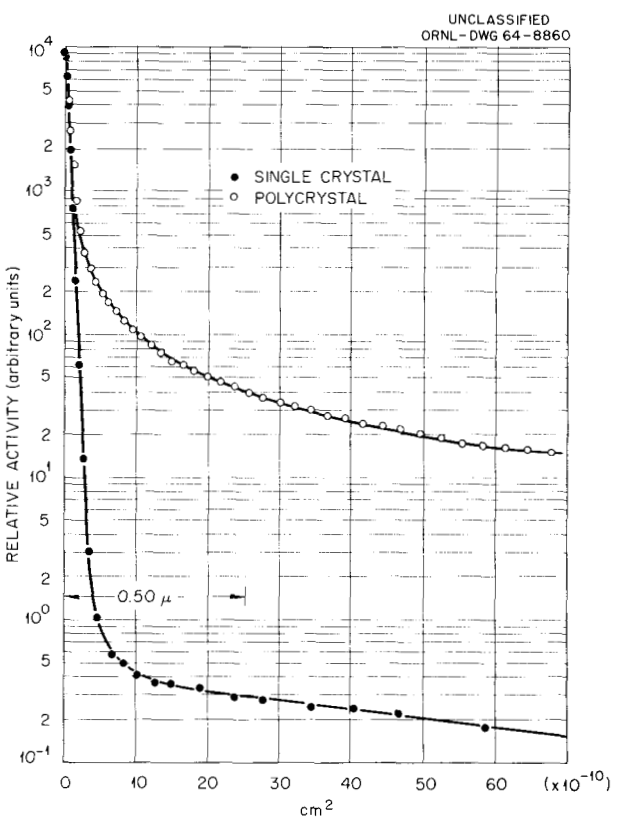

Fig. 7.3. Penetration Profiles for the Diffusion of ^{95}Nb into Mono- and Polycrystalline Tantalum Specimens Annealed for 2.0 hr at 1250°C.

either x^2 or x (here, A is the activity of the ^{95}Nb and x is the penetration distance). We established that region I was the part of the profile representing lattice diffusion, while region II was a result of mechanisms involving short-circuit diffusion.

These results point out the need for care in interpreting low-temperature diffusion data in terms of overly simplified mathematical models. Apparently, even in single crystals the concentration of short-circuit diffusion paths can be high enough to contribute significantly to the observed penetration profile. At low temperatures, therefore, pure lattice diffusion is very difficult to measure in experiments using polycrystalline specimens. Even with single crystals, sectioning techniques unable to resolve the extreme near-surface region may lead to a misinterpretation of the data.

The diffusion results obtained thus far are extremely encouraging. The anodic sectioning technique may be a suitable method for studying many phenomena that occur in the surface regions of metals and for establishing their relationship to the diffusion process.

8. Spectroscopy of Ionic Media

G. P. Smith

This group is subdivided into a theoretical unit and an experimental unit. The theoretical research is concerned largely with the development of techniques for computing electronic wave functions and the application of these techniques to a wide range of problems in the molecular sciences. The experimental research is a study of the optical electronic spectroscopy of ions in condensed phases with emphasis on comparison between the liquid and solid states.

The scope of the theoretical research is amply illustrated by the topical summaries that follow.

The scope of the experimental research is substantially broader than might be surmised from the research summaries, since the only topics described are those that were completed during the reporting period. Other topics of investigation included the following: (1) Ions of posttransition metals in molten salts including the normal Tl(I), Pb(II), and Bi(III) states and the highly abnormal Pb(I) and Bi(I) states. A report on the normal states will appear shortly, but interpretation of the spectra of the abnormal states is still in a preliminary stage. (2) Ions of Ni(II) in a far wider variety of molten-salt environments than are reported here. This research displays many complex facets of the coordination geometry of Ni(II) in liquid ionic systems. Several publications will be submitted during the coming year. (3) Experimental phases of a long continuing study of the influence of cations on the exciton spectrum of molten nitrates were concluded during the year. Analysis of the results will follow along paths we have previously reported.

CONSTANT ENERGY AND MINIMUM ENERGY ORTHOGONALIZATION[1]

H. W. Joy L. J. Schaad[2]
G. S. Handler[3]

Use of an orthogonal set is a great convenience in many of the variational calculations in which atomic and molecular wave functions are approximated as expansions in terms of some set of orbitals. However, a physically or computationally convenient set is often not orthogonal. Though it can be made so by a linear transformation, the choice of such a transformation is not unique; in fact, it is unlimited.

We are considering, first, whether the transformation to orthogonal orbitals can be carried out in such a way that it has no effect on the computed energy of an approximate wave function, and second, whether it is possible to find the transformation that has the best effect, that of lowering the computed energy as much as possible. We have succeeded at both. For the first, we have used a special application of the Schmidt procedure, which we call "constant-energy orthogonalization"; for the second, we have used a computer-oriented procedure that we have named "minimum-energy orthogonalization." Our examples suggest that the latter technique may be

[1]Condensed from a paper accepted for publication by the *Journal of Chemical Physics*.

[2]ORINS summer participant in 1963 from Vanderbilt University, Nashville, Tenn.

[3]Consultant to the Metals and Ceramics Division from Tufts University, Medford, Mass.

useful in finding analytic Hartree-Fock[4] functions and in directly constructing natural-orbital[5] expansions as well as in more ordinary applications.

RADIAL CORRELATION IN HELIUM[6]

G. S. Handler[3] H. W. Joy

Computations of the "s-limit" [the best energy obtainable from an expansion having only s-type ($l = 0$) terms] in helium have commonly used, when done in "configuration interaction," an expansion of the wave function of a form like

$$\Psi = \exp\left[-\alpha(r_1 + r_2)\right] \sum_{n,m} C_{nm}(1 + E_{12}) r_1^m r_2^n ,$$

where E_{12} is the operator that exchanges the coordinates of electrons 1 and 2, m and n are integers, and α and C_{nm} are variational parameters. The computations normally require some 21 or more terms to approach the convergence limit adequately.[7] By simply giving each term in the expansion its own exponential parameters,

$$\Psi = \sum_{n,m} C_{nm}(1 + E_{12}) r_1^m \exp(-\alpha_{nm} r_1) r_2^n \exp(-\beta_{nm} r_2) ,$$

we have greatly improved convergence, nearly reaching the 21-term value with only four terms.

ONE-CENTER EXPANSIONS IN H_2^+

H. W. Joy G. S. Handler[3]

The expansion on one center of the electronic wave function of H_2^+ has been treated several times recently.[8] To resolve seeming discrepancies in these works and to compare several alternative expansion schemes, we have reexamined the problem, using much of our[9] general-purpose computer program for one-center expansions.

We find that the use of a multitude of exponential parameters compared to the use of only one or a very small number (unavoidable when computations are not done by an electronic computer) is very helpful in improving convergence, that Gaussian exponentials ($e^{-\beta r^2}$) are decidedly poorer than ordinary exponentials ($e^{-\beta r}$), and that Slater-type orbitals with noninteger principal quantum numbers[10] do not greatly improve convergence, although they are useful as an aid in computation.

DATA FIT SEARCHING

G. P. Smith H. W. Joy

Very often, one needs to adjust a small set of parameters to a set of data in such a way as to give the smallest possible deviation between computation and observation. The parameters may be found in an expression derived from theory or in an assumed analytical form for a curve to represent the data. In either case, the parameters are refined by the method of least squares. Basically this means only that the sum of the squares of the deviations between corresponding computed and observed points is to somehow be made small. But the name "method of least squares" is often used to describe a particular technique for doing this, which involves Taylor-series expansion of the "sum of squares," truncation of it, numerical evaluation of derivatives when analytical evaluation is not possible, and solution of a set of simultaneous linear equations, sometimes followed at the end of several iterations by statistical analyses of "goodness of fit."

---

[4] C. C. J. Roothaan, *Rev. Mod. Phys.* **23**, 69 (1951); **32**, 179 (1960).

[5] P. O. Löwdin, *Phys. Rev.* **97**, 1474 (1955).

[6] Reported more fully by G. S. Handler and H. W. Joy, *J. Chem. Phys.* **40**, 2408 (1964).

[7] H. Shull and P. O. Löwdin, *J. Chem. Phys.* **30**, 617 (1959).

[8] K. M. Howell and H. Shull, *J. Chem. Phys.* **30**, 627 (1959); M. Cohen and C. A. Coulson, *Proc. Cambridge Phil. Soc.* **57**, 96 (1961); and T. J. Hauser, P. G. Lykos, and E. L. Mehler, *J. Chem. Phys.* **38**, 583 (1963).

[9] H. W. Joy, *Metals and Ceramics Div. Ann. Progr. Rept. June 30, 1963*, ORNL-3470, p. 11.

[10] R. G. Parr and H. W. Joy, *J. Chem. Phys.* **26**, 424 (1957).

Since convergence of this particular approach is not likely to be optimum in every case, alternative techniques are worth pointing out.[11] One is a modified form of method of steepest descent or gradient search which was originally used only in the theoretical work of this group where analytical evaluation of derivatives is, in general, out of the question. It has now been applied in interpretation of ligand-field spectra[12] (where derivatives cannot be found analytically either), with results that seem to be superior to those obtained with the more common least-squares techniques. Our gradient-search computer program seeks a minimum in an arbitrary function of any number of variables by repetitively evaluating its gradient numerically at some point and searching along the gradient direction until further improvement cannot be obtained. For any particular application, it is merely necessary to write a subprogram that will provide the searching program with a numerical value of the function to be minimized. In this case we provided it with values of the sum-of-squares function.

THE THEORY OF THE ABSORPTION AND EMISSION OF THE *F* CENTER IN ALKALI HALIDE CRYSTALS[13]

R. F. Wood[14] H. W. Joy

The states of the *F* center have been computed in a kind of "ligand-field" approximation. Starting with the Hartree-Fock model, we described the defect electron by a single Slater-type orbital at the defect site, made orthogonal to the wave functions of the electrons of the six first-nearest-neighbor ions. The second- and third-nearest neighbors were assumed to be point ions, and the remainder of the crystal was treated classically. We minimized the total energy of the crystal with respect to *F*-electron orbital parameters and first-nearest-neighbor distortions. Computer programs for the necessary integrals were kindly provided by J. C. Browne of the University of Texas. For a variety of crystals, computed and observed transitions agreed to within 10 to 20%.

We are extending the *F*-center work by expanding the *F*-electron wave function in a series of defect-centered Slater-type orbitals and by including up through sixth-nearest neighbors in the quantum-mechanical part of the calculation. We are not yet explicitly taking into account any of the electronic structure of the neighbors, since we are trying to determine the convergence limits of the pure point-ion model. These calculations are being done with the general computer program for one-center expansions described previously.[9]

THE SPLIT-*P* ORBITAL (SPO) METHOD

A. F. Saturno[15] H. W. Joy

We are extending our previous[16] computations and analyses in criticism of the SPO method. The method is equally bad for *ab initio* calculations on the carbon atom and on CH_3^- in one-center expansion. While the SPO method appears to be useful in semi-empirical calculations because it gives an optimum value to an important electron repulsion integral and thus allows better for electron correlation, our analyses show instead that it is successful because it gives a better value to one of the kinetic-energy integrals in the calculation.

THE LOWEST TWO *S* STATES OF HELIUM

G. S. Handler[3] H. W. Joy

The expansion of a two-electron wave function seems to give adequate convergence, contrary to

[11] D. J. Wilde, *Optimum Seeking Methods*, Prentice-Hall, Englewood Cliffs, New Jersey, 1964.

[12] G. P. Smith, C. H. Liu, and T. R. Griffiths, "Charge-Transfer and Ligand-Field Spectra of Tetrahedral Tetrahalonickel(II) Ions in Molten Dimethylsulfone and Molten Organic Halide Salts," submitted to the *Journal of the American Chemical Society*, and abstracted in a later section of this chapter.

[13] Part of this section is condensed from R. F. Wood and H. W. Joy, "On the Theory of the Absorption and Emission of the *F* Center in Alkali Halide Crystals," paper accepted for publication by the *Physical Review*.

[14] Solid State Division.

[15] Consultant to the Metals and Ceramics Division from the University of Tennessee.

[16] A. F. Saturno, H. W. Joy, and L. C. Snyder, *J. Chem. Phys.* **38**, 2494 (1963).

some current opinion.[17] This expansion is

$$\Psi = \sum_{n,m,l} C_{nml}(1 + E_{12})r_1^m \exp(-\alpha_{nml} r_1) \times r_2^n \exp(-\beta_{nml} r_2) P_l(\cos\theta_{12}),$$

where E_{12} is the exchange operator, m, n, and l are integers, θ_{12} is the angle between the radius vectors r_1 and r_2, and α_{nml}, β_{nml}, and C_{nml} are variational parameters. We are attempting to find accurate convergence limits for each group of terms with the same value of l.

THE H_3 POTENTIAL ENERGY SURFACE

A. F. Saturno[15] H. W. Joy

With our general computer program for one-center expansions, we are trying to construct an accurate potential energy surface for the $H + H_2 \rightleftharpoons H_2 + H$ reaction. In addition to attempting to find whether H_3 is stable relative to H_2 and H, we expect to compute the total energy of the system over a considerable variety of nuclear configurations.

DIRECT NATURAL-ORBITAL EXPANSIONS

H. W. Joy

Our minimum-energy orthogonalization technique will probably make it possible to construct a natural-orbital[18] expansion directly rather than by conversion of some other form of expansion, as is now the case. Further, it may be possible to do so for systems with more than two electrons, again surpassing present methods. We are now concerned with finding a good minimum-energy-orthogonalized expansion for the S-limit in helium and seeing whether it is changed by the standard techniques for conversion to natural-orbital form.

[17] C. Schwartz, *Phys. Rev.* **126**, 1015 (1962).

[18] P. O. Löwdin, *Phys. Rev.* **97**, 1474 (1955).

CHARGE-TRANSFER AND LIGAND-FIELD SPECTRA OF TETRAHEDRAL TETRAHALONICKEL(II) IONS IN MOLTEN DIMETHYLSULFONE AND MOLTEN ORGANIC HALIDE SALTS[19]

G. P. Smith T. R. Griffiths[20]
C. H. Liu[21]

Ligand-field (LF) and charge-transfer (CT) spectra of tetrahedral tetrachloro-, tetrabromo-, and tetraiodonickelate(II) were measured in a number of media. The energy ranges investigated were 4,000 to 47,000, 39,000, and 34,000 cm^{-1} for chloride, bromide, and iodide respectively. The systems examined include crystalline tetra-*n*-butylammonium tetrabromonickelate(II) in a KBr disk and dilute solutions of nickel(II) halides in two kinds of systems: molten dimethylsulfone with excess lithium halides added and a number of molten substituted-ammonium, -phosphonium, and -arsonium halides. Molten dimethylsulfone proves to be an excellent solvent for studying transition-metal ion complexes; it is transparent over wide energy ranges, and the solvent molecules coordinate only very weakly with these metal ions. The "organic" melts provide some of the most clear-cut examples of complex formation in molten salts.

Assignments of spin-forbidden LF bands were attempted on the basis of a four-parameter model. The estimated LF parameters are: for $NiCl_4^{2-}$, $Dq = (354 \pm 10)$ cm^{-1}, $B = (734 \pm 6)$ cm^{-1}, $C/B = 3.96 \pm 0.02$, and $\lambda = (-275 \pm 50)$ cm^{-1} (limits fixed by the uncertainty in λ); for $NiBr_4^{2-}$, $Dq = \sim 330$ cm^{-1}, $B = \sim 680$ cm^{-1}, and $C/B = \sim 3.9$; and for NiI_4^{2-}, $Dq = \sim 330$ cm^{-1}, $B = \sim 540$ cm^{-1}, and $C/B = \sim 5.5$. The limits and uncertainties of these parameters were discussed.

A few tentative assignments of the CT bands were made in terms of molecular orbital theory. The optical electronegativity of nickel(II), derived from the lowest energy CT band, was 2.1 for all complexes.

[19] Abstract of paper submitted to the *Journal of the American Chemical Society*.

[20] On leave of absence from N. E. Essex Technical College, Colchester, England, in 1963.

[21] Summer research participant in 1963 from Brooklyn Polytechnic Institute, Brooklyn, N.Y.

TETRAHEDRAL $CuCl_4^{2-}$ COMPLEX IN MOLTEN SALTS[22]

G. P. Smith T. R. Griffiths[20]

The absorption spectra of solutions of copper(II) chloride in melts of cesium chloride and tributyl-2,4-dichlorobenzylphosphonium chloride (Phosphon[23]) indicate the presence of tetrahedral or mildly distorted tetrahedral $CuCl_4^{2-}$ complexes. The importance of this result lies in the fact that only a few examples of copper(II) complexes of this conformation are known;[24,25] and, of these, only the distorted bromo complex has been found previously[25] in liquid solutions. Tetracoordinated chlorocopper(II) complexes have been reported to occur in liquid solvents with excess chloride ions,[26] but a comparison of their spectra with those reported below shows that they are not tetrahedral.

Copper(II) chloride, when dissolved in molten Phosphon at 128°C, had a *d-d* band at 8000 cm^{-1} with a molar extinction coefficient, ϵ, of 79 liters $mole^{-1}$ cm^{-1} and the lowest energy charge-transfer band at 22,200 cm^{-1} (ϵ = 732 liters $mole^{-1}$ cm^{-1}). In molten cesium chloride as solvent, the *d-d* band was also at 8000 cm^{-1}, while the lowest energy charge-transfer band was a shoulder near 24,600 cm^{-1} ($\epsilon \sim 775$ liters $mole^{-1}$ cm^{-1}). No other maxima or shoulders indicative of other *d-d* bands were found, but the 8000-cm^{-1} band was broad and could possibly encompass unresolved components.

These spectra are attributed to tetrahedral or mildly distorted tetrahedral $CuCl_4^{2-}$ on the basis of a comparison of the position of the *d-d* band with those[27] of crystalline Cs_2CuCl_4 at 9000 cm^{-1} and copper(II)-doped Cs_2ZnCl_4 at 8300 cm^{-1}. The band energy shifts toward lower values with decreasing distortion of the $CuCl_4^{2-}$ complex, and presumably the $CuCl_4^{2-}$ complex is less distorted in the melts than in the crystals. These results were rationalized in terms of ligand-field theory.

The lowest energy charge-transfer band in crystalline Cs_2CuCl_4 is reported[24] at about 24,000 cm^{-1}, in agreement with our molten-salt spectra. A similar band of $CuBr_4^{2-}$ has been assigned by Braterman[28] in a reasonable way to an electron jump from a nonbonding ligand orbital into a *d*-type orbital.

---

[22] Condensed from G. P. Smith and T. R. Griffiths, *J. Am. Chem. Soc.* **85**(24), 4051 (1963).

[23] Kindly donated by the Virginia-Carolina Chemical Co.

[24] (a) L. Helmholz and R. F. Kruh, *J. Am. Chem. Soc.* **74**, 1176 (1952); (b) E. Prince, *Acta Cryst.* **13**, 544 (1957); (c) B. Morosin and E. C. Lingafelter, *Acta Cryst.* **13**, 807 (1960); (d) B. Morosin and E. C. Lingafelter, *J. Phys. Chem.* **65**, 50 (1961); (e) D. M. Adams, J. Chatt, J. M. Davidson, and J. Gerratt, *J. Chem. Soc.* 2189 (1963).

[25] J. C. Barnes and D. N. Hume, *Inorg. Chem.* **2**, 444 (1963).

[26] See, for example: (a) J. Bjerrum, *Kgl. Danske Videnskab. Selskab, Mat. Fys. Medd.* **22**(18) (1946); (b) J. Bjerrum, C. J. Ballhausen, and C. K. Jörgensen, *Acta Chem. Scand.* **8**, 1275 (1954); (c) C. J. Ballhausen, *Kgl. Danske Videnskab. Selskab, Mat. Fys. Medd.* **29**(4) (1954); (d) N. S. Gill and R. S. Nyholm, *J. Chem. Soc.* 3997 (1959).

[27] W. E. Hatfield and T. S. Piper, unpublished data.

[28] P. S. Braterman, *Inorg. Chem.* **2**, 448 (1963).

9. Structure of Metals

C. J. McHargue

Our studies are intended to show the principles underlying the atom movements that occur during deformation, annealing, and phase transformations of solids. We use these principles to correlate the physical and mechanical properties with the microstructure and to obtain structures with specific properties by suitable thermal and mechanical treatments. During this report period, we studied deformation of both face-centered and body-centered cubic metals and the behavior of grain boundaries and twin boundaries during annealing.

DEVELOPMENT OF DOUBLE FIBER TEXTURE IN ALUMINUM

R. E. Reed C. J. McHargue

As reported last year,[1] we had developed techniques to extrude a 1-in.-long, 0.750-in.-diam specimen to 0.250-in. diam (an extrusion ratio of 9). We have now extruded a series of aluminum single crystals with starting orientations shown in Fig. 9.1 at room temperature at speed of about 1 in./min. In addition, specimens with columnar grains parallel to the rod axis were extruded, swaged, and drawn. These specimens initially had a diffuse [100] fiber texture. Fine-grained specimens of aluminum and copper with a random starting texture were also extruded at room temperature.

Spherical specimens 0.200 in. in diameter were cut from the 0.250-in.-diam deformed rods. These spheres were then electropolished to 0.190-in. diam. Texture data were obtained using the ORNL technique.[2] A small computer program for the CDC-1604 computer was designed to calculate the component percentages.

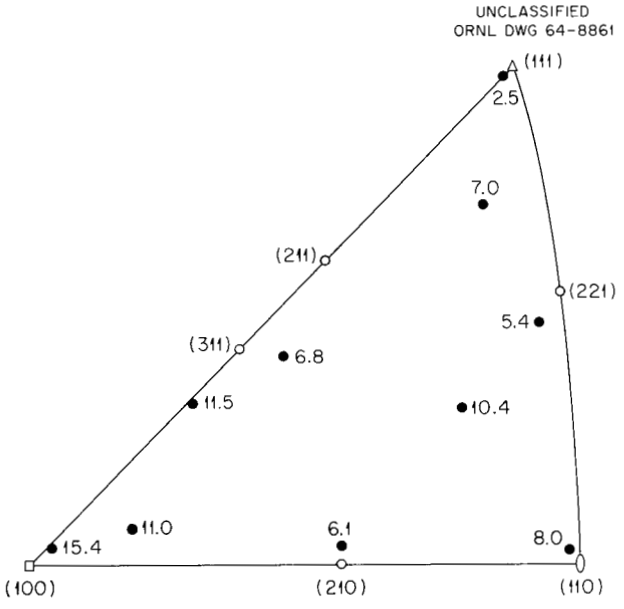

Fig. 9.1. Percentage of Twins Having the <100> Direction Within 20° of the Extrusion Direction in Aluminum Rod Extruded 90% at Room Temperature from Single Crystals of the Orientation Shown.

All of the rods had a ⟨100⟩-⟨111⟩ double fiber texture. Figure 9.1 shows the amount of the ⟨100⟩ component within 20° of the rod axis for each single-crystal orientation used. All orientations had from 3 to 15% ⟨100⟩ component. This is quite different from the results reported by Harsha and Cullity[3] for single crystals of aluminum swaged 96%. They reported no ⟨100⟩ for

[1] R. E. Reed, *Metals and Ceramics Div. Ann. Progr. Rept. May 31, 1963*, ORNL-3470, p. 16.

[2] L. K. Jetter, C. J. McHargue, and R. O. Williams, *J. Appl. Phys.* **27**, 368 (1956).

[3] K. S. Sree Harsha and B. D. Cullity, *Trans. Met. Soc. AIME* **224**, 1189 (1962).

starting orientations near (111) and 85 to 97% for orientations near (100).

To check further this difference in quantities of the ⟨100⟩ and ⟨111⟩ components in double fiber textures developed by swaging and by extrusion, the specimens with diffuse ⟨100⟩ starting texture were examined. The material extruded 90% at room temperature had 15% ⟨100⟩, while material swaged 90% at room temperature had 86% ⟨100⟩, in agreement with the trend indicated in the single-crystal results. In addition, when this same starting material was drawn 90% at room temperature, 32% of the ⟨100⟩ component was within 20° of the rod axis. These data show that care must be taken when textures developed by different forming methods are compared. While swaging, extruding, and drawing of aluminum rods all result in a duplex ⟨100⟩-⟨111⟩ fiber texture, the proportions of these components are significantly different.

Brown[4] has suggested that the stacking fault energy plays an important part in determining relative amounts of ⟨100⟩ and ⟨111⟩ texture in a particular face-centered cubic metal. Since aluminum and copper are examples of face-centered cubic metals having high and low stacking fault energies, respectively, they should have different relative amounts of ⟨100⟩ and ⟨111⟩ components in their deformation textures. However, when we extruded fine-grained aluminum and copper specimens with random starting textures 90% at room temperature, each had 18% ⟨100⟩ component within 20° of the rod axis. For cold drawn wire, Brown[4] gives values of 0 and 40% ⟨100⟩ component for aluminum and copper respectively. This again shows the dangers in generalizing deformation texture results to include different forming operations.

An analysis could explain why there are differences in the relative amounts of ⟨100⟩ and ⟨111⟩ components in deformation fiber textures resulting from extruding, drawing, and swaging of face-centered cubic metals. In this analysis we need to assume that the textures evolve mostly by the development of inhomogeneous deformation during working of the metal. This inhomogeneous deformation consists largely of different types of deformation bands.

Several factors that affect the development of deformation bands contribute to texture evolution. In single crystals, the orientation of the tensile axis determines both the type and density of deformation bands. Also, the orientation range for a particular type of deformation band is different in compression than in tension. Another factor is that constraints during deformation increase the density of deformation bands. These constraints may be internal (e.g., grain boundaries) or external, such as the die walls during forming. Increasing the strain rate probably increases the density of deformation bands, although little work has been done on this factor.

If the friction forces at the die walls are neglected by considering only center textures in the rod, then the extrusion process can be considered as a compressive stress along the extrusion direction plus a radial compressive stress perpendicular to it at the die. Similarly, drawing can be considered a tensile stress along the rod axis plus a radial compressive stress at the die. Swaging introduces a new factor in that it consists of a rotating compressive stress at the die, and it deforms the metal at much higher strain rates.

Therefore, if the formation of deformation bands contributes a major part in the development of the duplex fiber textures in face-centered cubic metals, drawing, extruding, and swaging should all result in different proportions of ⟨100⟩ and ⟨111⟩ components.

[4]N. Brown, *Trans. Met. Soc. AIME* **221**, 236 (1961).

STRESS DEPENDENCE OF THE AVERAGE DISLOCATION VELOCITY IN NIOBIUM SINGLE CRYSTALS

R. E. Reed

In view of the recent interest in the theory of dislocation dynamics as applied to body-centered cubic refractory metals, we decided to find out if this analysis applies to niobium single crystals. Dislocation dynamics theory is based upon the simple equation:

$$\dot{\epsilon} = \bar{b}nv$$

where $\bar{b}$ is the Burger's vector of the dislocations involved, n is the number of mobile dislocations, v is the average velocity of dislocations, and $\dot{\epsilon}$ is the strain rate. To evaluate the validity of this theory, we need two types of experimental data.

One is the stress dependency of the average dislocation velocity. The other is the mobile-dislocation density as a function of strain.

The stress dependence of the dislocation velocity has been determined directly by etch-pitting experiments for such materials as LiF,[5] silicon iron,[6] and tungsten.[7] It has the form

$$v = A\tau^m ,$$

where A and m are constants for a given material and temperature and τ is the resolved shear stress. If we define m' by

$$m' = \partial \ln \dot{\epsilon}/\partial \ln \tau,$$

then

$$m' = \partial \ln v/\partial \ln \tau + \partial \ln n/\partial \ln \tau ,$$

or

$$m' = m + \partial \ln n/\partial \ln \tau .$$

Guard[8] and Johnston and Stein[9] have pointed out that $m' = m$ if the second term of the above equation is negligible. If the strain-rate sensitivity is measured at low enough strains, the resulting value of m' should be equal to m. This is obviously true if the strain is so small that only one dislocation is moving. Therefore, the constant m can be measured indirectly from strain-rate sensitivity data as a function of strain by extrapolation to zero strain.

We tried to develop etch-pitting techniques for niobium to permit direct determination of the stress dependence of the dislocation velocity. Two types of material were used. One was an MRC zone-refined 0.250-in.-diam single crystal. The other was a large-grained specimen cut from a Wah Chang electron-beam-melted ingot and annealed at 1300°C for 1 hr in vacuum.

We first attempted chemical etch pitting. Either of two solutions would etch pit grown-in dislocation networks: (1) 60 parts concd HNO_3, 40 parts concd HF, and (2) (ref. 10) 10 parts (by volume) H_2SO_4, 10 parts concd HF, 10 parts H_2O, and 1 part 30% H_2O_2. However, neither of these nor several variations of them would etch "fresh" dislocations.

The electrolytic methods reported by Evans[11] were then tried. The solution for both electropolishing and electroetching was 90 parts H_2SO_4 and 10 parts concd HF, and it was used at 35 to 40°C. Again, grown-in dislocation substructure could be etched, but not "fresh" dislocations, even after an aging treatment at 300°C. Evans, in personal correspondence, admitted that he could not etch pit large-grained niobium that had been annealed at temperatures around 2000°C. In personal correspondence with R. M. Rose at MIT, we learned that he could etch pit only dislocations that were heavily decorated with particles that he believes are niobium oxide. New attempts to etch pit "fresh" dislocations will be made on niobium single crystals grown in our newly acquired equipment.

Specimens for the dislocation dynamics studies were prepared by electron-beam zone refining at ORNL in a carefully maintained ultrahigh vacuum. The starting material was a Wah Chang electron-beam-melted 3-in.-diam ingot, which was swaged to the size needed. The annealed starting material had a resistivity ratio of 80. Along a 0.250-in.-diam bar zoned 4 passes at 4 in./hr in a vacuum of 1.5×10^{-6} to 6.0×10^{-7} torr, resistivity ratios were 200 to 265, as shown in Fig. 9.2.

We made preliminary strain-rate sensitivity tests on niobium single crystals of two orientations near $\langle 011 \rangle$. Two compression specimens were taken from one crystal and three from the other. The resistivity ratios for compression specimens 7 and 8 were 205 and 193 respectively. Niobium No. 6, from which specimens 9 through 11 were cut, was a single crystal that had been electron-beam zoned three times in the MRC module. The resistivity ratio was 164 at a point on the rod that should be the purest, according to the trend shown in Fig. 9.2.

---

[5] W. G. Johnston and J. J. Gilman, *J. Appl. Phys.* **30**, 129 (1959).

[6] D. F. Stein and J. R. Low, *J. Appl. Phys.* **31**, 362 (1960).

[7] H. W. Schadler and J. R. Low, *Low Temperature Brittleness of Refractory Metals*, Final Rept. GE-62-GC-206 (April 1962).

[8] R. W. Guard, *Acta Met.* **9**, 163 (1961).

[9] W. G. Johnston and D. F. Stein, *Acta Met.* **11**, 317 (1963).

[10] A. B. Michael and F. J. Huegel, *Acta Met.* **5**, 339 (1957).

[11] T. J. Koppenael and P. R. V. Evans, "Microstraining in Polycrystalline Niobium," unpublished paper (also, personal correspondence with P. R. V. Evans).

Compression tests were made at room temperature on an Instron tensile machine at crosshead speeds ranging from 0.002 to 0.2 in./min. These were incremental tests (i.e., the strain rate was changed instantaneously during plastic deformation, and the load change was measured). Tests were generally discontinued after 10% strain. The results are plotted as m' vs strain in Fig. 9.3. The value for m ranges from 8 to 16, depending upon the specimen tested.

It appears that m is sensitive to impurity content. For example, compression specimen No. 9 was cut from next to the starting point of the zone, while specimens Nos. 10 and 11 were successively nearer to the center of the zoned length. Therefore, the resistivity ratios of these specimens should range from about 80 to 164 in that order. The same order was true for compression specimens Nos. 7 and 8, from the niobium No. JW crystal. In any case, these preliminary results show that m is probably 8 or lower for purer crystals and ranges up to 16. Tests have not been made at temperatures other than room temperature as yet.

Schadler and Low[7] report for tungsten that m is 5 at 298°C and 11 at 77°K. Silicon iron[6] has m equal to 40 to 45 at 298°K. For iron, Michalak[12] has reported that m is 4.5 at 370°K and 50 at 78°K.

[12] J. T. Michalak, *J. Metals* **16**, 121 (1964).

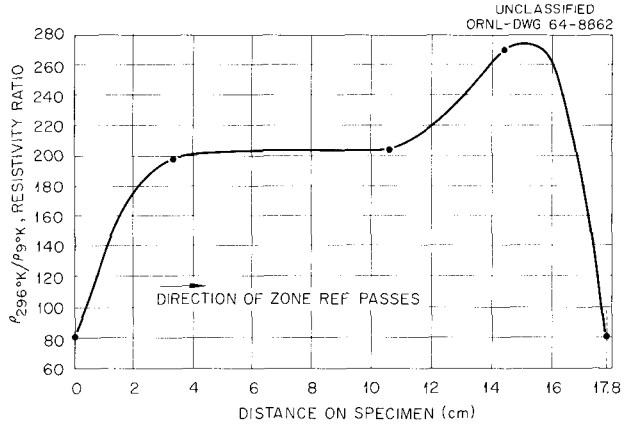

Fig. 9.2. Resistivity Ratio as a Function of Position in a Zone-Refined Niobium Single Crystal.

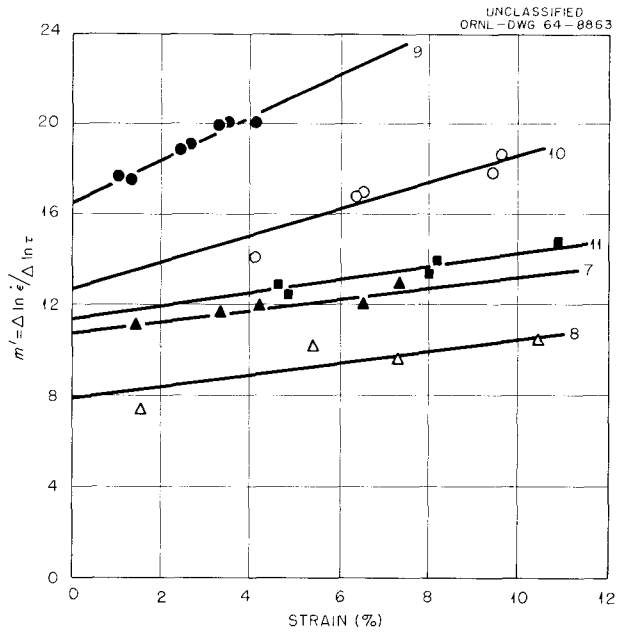

Fig. 9.3. Variation of the Parameter m′ with Strain for Several Niobium Single Crystals of Different Purities.

RECRYSTALLIZATION STUDIES

R. A. Vandermeer

One of the recrystallization fiber-texture components of extruded aluminum rods may be described with reference to the standard stereographic triangle as a scattered $\langle\bar{1}14\rangle$ to $\langle 012\rangle$ orientation. The recrystallized grains that make up this texture component in rods originally extruded near -195°C exhibited rather unusual growth kinetics during the very early stages of recrystallization. To gain a better understanding of principles dictating the migration behavior of grain boundaries, we have undertaken a concentrated effort both to characterize the unusual kinetic features of the growth of these grains experimentally and to explore the interpretation of these results in terms of current theoretical knowledge.

Some of the more important experimental findings resulting from this investigation may be summarized as follows:

1. Initially the $\langle\bar{1}14\rangle$-$\langle 012\rangle$ recrystallized grains exhibited a transient burst of growth when annealed in the temperature range 65 to 187°C. Significant growth apparently took place even

during the time necessary to heat test specimens from the deformation temperature, -195°C, to the annealing temperature (the grain diameter reached 100 μ in the 15 sec needed to reach 100°C).

2. Immediately after the annealing temperature was attained, the growth rate decreased very rapidly and seemingly continuously from a maximum value. The actual rates measured during this time were much higher than expected for aluminum of this impurity level.

3. The growth rate varied by more than a factor of 10^4 in these early heat-treatment times at certain temperatures. At 100°C the variation of the growth rate with time could be represented by the equation

$$v = 2.2 \times 10^{-2}\, t^{-3/2} ,$$

where v is the growth rate in centimeters per second, and t is the time in seconds.

4. A very slow apparently steady-state growth followed this initial transient period of rapid growth.

5. Both the duration of the transient and the magnitude of the growth burst that occurred depended upon the annealing temperature. The higher the temperature, the shorter was the duration but also the larger was the grain diameter achieved during this growth period. For example, at 187°C the transient period lasted no more than 30 sec, during which time the grain diameter reached 225 μ, whereas at 100°C the transient period lasted about 2 hr, giving a grain size of 185 μ.

6. This observed growth behavior is apparently very sensitive to deformation conditions, particularly temperature. Rods extruded at room temperature showed no evidence of this transient growth behavior. Strain rate, impurities, and the severity of deformation may also influence the extent to which these unusual growth kinetics occur.

7. These recrystallized grains could be related to the deformed matrix into which they grew in terms of coincident-lattice-site orientation relationships.

8. Preannealing at 24°C prior to the recrystallization heat treatments carried out at the higher temperatures diminished the growth burst (i.e., the longer the duration of preannealing, the smaller the grain size at the end of the period of transient fast growth).

9. The growth rate was divided by 10^5 with only a corresponding 30% decrease in the strain contained in the cold-worked matrix as determined from x-ray line-broadening measurements. Thus the growth rate is obviously not directly proportional to strain (driving force). This was substantiated by transmission electron microscopic observations of the dislocation substructure (i.e., large decrease in growth rate with little or no detectable change in the dislocation density of the cold-worked matrix).

In most theories of grain-boundary migration during recrystallization, the rate of growth can usually be expressed as a product of the mobility of the rate-determining process and the driving force (in this case, strain energy). The rate of growth would then be, barring any changes in mobility, directly proportional to the strain energy in the deformed matrix. The mobility of the boundary is assumed to be governed by the diffusion of atoms in and around the grain-boundary regions. Thus, any decrease in the growth rate during annealing must be attributable to decreases in either strain energy or atomic diffusivity. In view of the results discussed under item 9 above, the tremendous decrease in growth rate observed during the transient period must be due mainly to a decrease in the rate-determining step in the boundary-migration process.

We have proposed a mechanism that involves the excess vacancies created during deformation and frozen in due to the low deformation temperature and their role in influencing the atomic diffusivity in grain-boundary regions. The model considers that, during annealing, some of the frozen-in excess vacancies impinge upon the grain boundary of a recrystallization nucleus and increase, at least for a time, the concentration of vacancies in the boundary. This decrease in density makes it easier for boundary atoms to diffuse and permits a greater flux of atoms to cross the grain boundary under the influence of the driving force. In this manner the mobility of the boundary is enhanced, and a high instantaneous growth rate would be observed. Accordingly, annihilation processes in the deformed matrix diminish the supply of vacancies available to the boundary, decreasing the mobility of the boundary and hence the growth rate of the grain. The initial burst of growth is ascribed to the rapid accumulation of vacancies in the grain boundary during heating to temperature, while the observed slowdown in growth during the

transient period is attributed to the diminution of vacancies. Preannealing at 24°C annihilates some of the excess vacancies and thus diminishes the growth burst that occurs when the temperature is again raised (see item 8 above). The theory thus seems able to qualitatively account for some of the grosser features of the unusual growth kinetics that were observed. It should, however, be more firmly based and experimentally tested more rigorously and qualitatively before it can be accepted, since other explanations cannot yet be completely discarded.

ANNEALING OF DEFORMED NIOBIUM SINGLE CRYSTALS

J. C. Ogle C. J. McHargue

Recrystallization of Twinned Niobium Crystals

New recrystallized grains were formed during annealing at 1000°C in crystals that contained extensive cross twinning. The new grains were always associated with twin intersections. In the early stages of annealing, the recrystallized grains were approximately equiaxed, and most of the boundaries between the new grains and parent crystal were quite straight. As annealing continued, the grains grew more rapidly in directions parallel to the twins and seemed to favor the direction parallel to the major twin system. The boundaries between the grains and the parent crystal appeared to become curved, but examination at high magnification revealed that these boundaries were made up of several straight segments. The one surface method of analysis showed these straight segments to be along the {112} and the {110} planes of the parent crystal. The new grains have their greatest rate of growth in directions parallel to the twins; however, when the new grain has absorbed a deformation twin, the rate of growth along that twin is greatly decreased.

The recrystallized grains formed at 1000°C have an orientation different from the parent crystals, but the orientations are related by a common crystallographic direction. Approximately 70% of the new grains studied have common ⟨110⟩ directions with the parent crystal and 20% have common ⟨112⟩ directions. A rotation of 20° around the common ⟨110⟩ direction will bring over half of the recrystallized grains into coincidence with the parent crystal. The remaining grains with common ⟨110⟩ directions require rotations of 50.5, 70.5, 80.5, or 90°. The grains with common ⟨112⟩ directions require rotations of 20, 51.8, 111.8, or 149.5°.

Since the deformation twins also have common ⟨110⟩ directions with the parent crystal, the recrystallized grains, in many cases, are also related to the twins by the same common ⟨110⟩ direction. When the relationship between the new grain and the parent crystal is not by the ⟨110⟩ direction that is common to the parent crystal and the intersecting twins, the recrystallized grain usually is related to the twin by either another ⟨110⟩ or a ⟨112⟩ direction. The preferred relationship between the recrystallized grain and the major twin system, which is the direction of the most rapid grain growth, is a rotation of 149.5° around a common ⟨112⟩ direction. All the recrystallized grains that had their greatest length along the twin had this relationship. The recrystallized grains were related to the remaining twin systems by rotations around a common ⟨110⟩ direction of 50.5 and 90° or around a common ⟨112⟩ direction.

The angular rotations mentioned above also correspond to positions of fairly high density of coincident sites with respect to both the parent crystal and the deformation twins. This means that, if the crystallographic lattice of the recrystallized grain is extended into either the parent crystal or the twin, a fairly high fraction of the lattice sites will coincide. The two densities found most frequently for grains with common ⟨110⟩ directions were one coincident lattice site in 11 and one in 33. The density of coincident lattice sites for rotations around ⟨112⟩ directions has not been determined.

Behavior of Twin Boundaries in Niobium During Annealing

Deformation twins in single crystals of niobium may either contract or expand during annealing. When annealed at 1000°C, a twin contracts or expands by the migration of the noncoherent twin boundaries. When contraction occurs, the twin divides into segments, and the noncoherent boundaries at the ends of these segments migrate toward their centers of curvature until the twin is absorbed by the parent crystal. Twins expand in

areas where two or more twins are very close together; they join to form one twin by migration of a noncoherent boundary between the two twins. This contraction and growth are illustrated in Fig. 9.4, where *A* and *B* mark migrating boundaries that are absorbing the twin, and *C* and *D* mark migrating boundaries that are absorbing the parent crystal between parallel twins. At *E* in this micrograph is a very straight coherent twin boundary, which is characteristic of deformation twin boundaries after long anneals. Before annealing, these coherent boundaries contained many sharp notches. These became rounded on annealing and eventually migrated outward to form the straight coherent boundary. The migration of a coherent boundary at 1000°C has not been observed.

At an annealing temperature of 1600°C the twins rapidly disappeared, and after 1 hr the only remaining twins were those that intersected a surface of the crystal. The direction of migration for these remaining twins was toward the crystal surfaces. At this temperature, two types of migration of coherent twin boundaries were observed. Along one face of the crystal the twins exhibited a tendency to expand along the surface. This can be seen in Fig. 9.5. The growth of twins near the face of this crystal was the only indication of twin growth by the migration of coherent boundaries. Also, coherent twin boundaries in the interior were observed to move in a direction that decreased the thickness of the twins; an example of this contraction is shown in Fig. 9.6. The twin boundaries before and after annealing are revealed by thermal etching. Apparently only one coherent boundary (arrow) moved, and it moved a very small distance compared to the noncoherent boundary at the end of this twin.

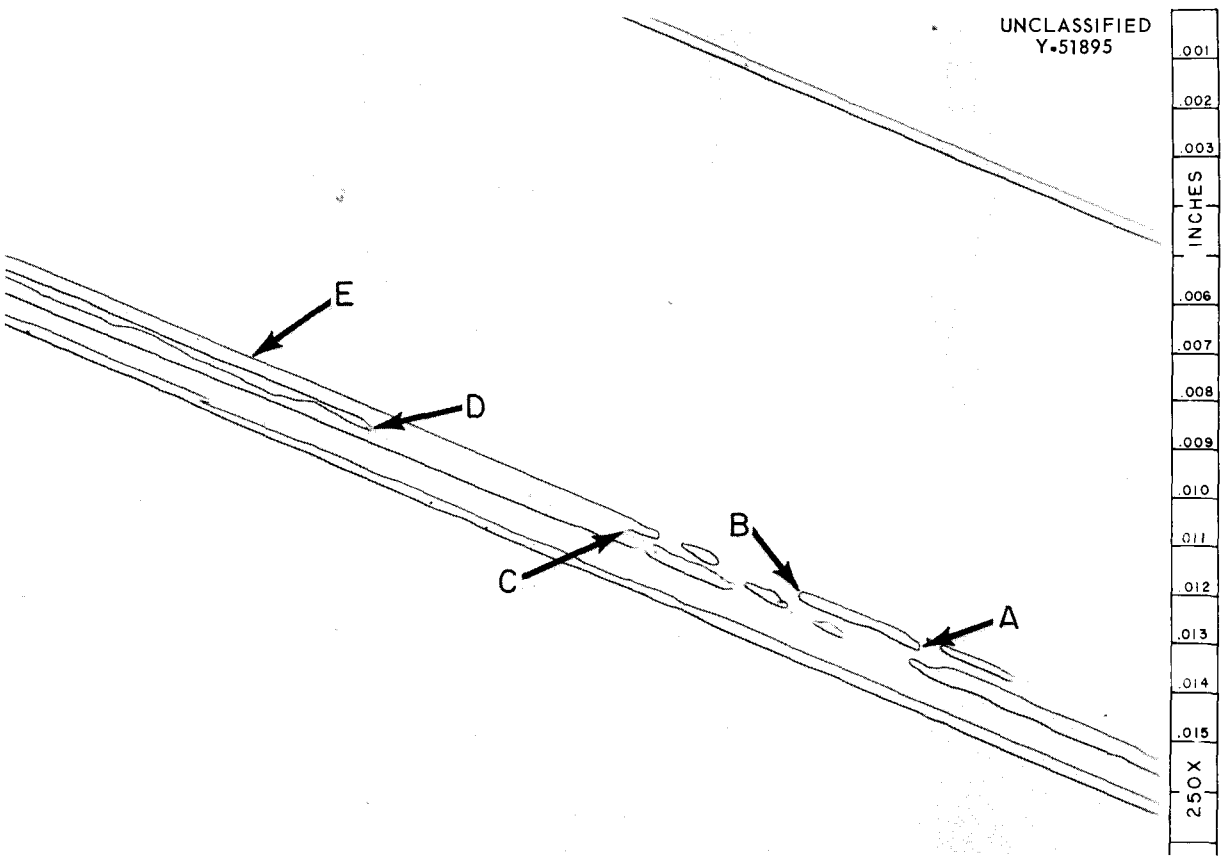

Fig. 9.4. Photomicrograph Showing the Contraction and Growth of Niobium Deformation Twins on Annealing. Annealed 24 hr at 1000°C. 250×.

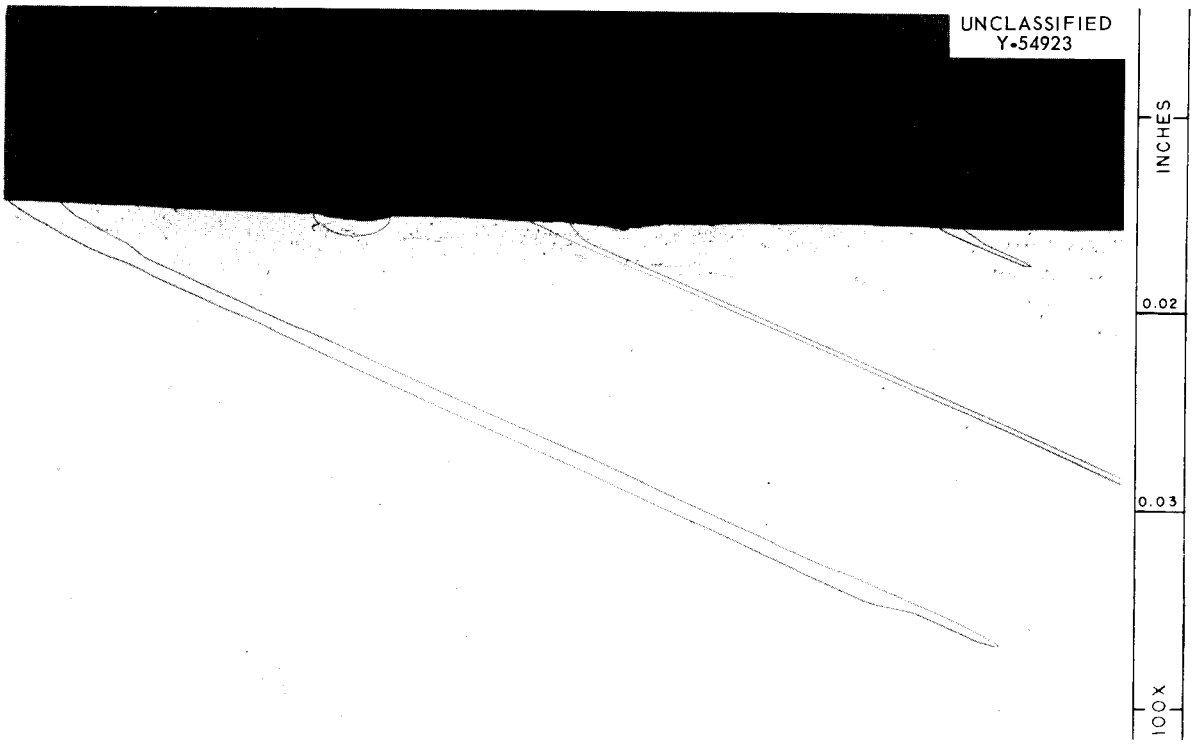

Fig. 9.5. Photomicrograph Showing Deformation Twins Expanding Along One Surface of a Niobium Crystal. Annealed 1 hr at 1600°C. 100×.

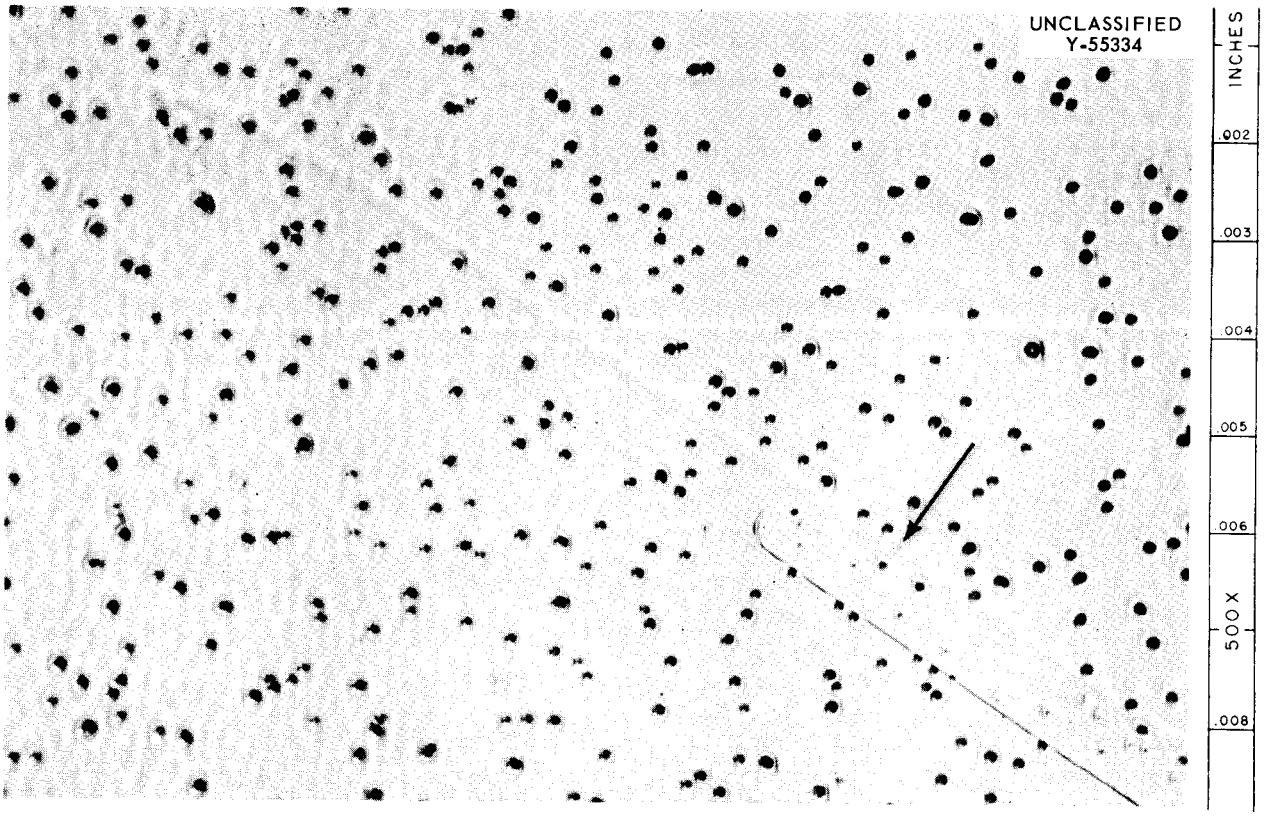

Fig. 9.6. Photomicrograph Showing Migration of Noncoherent and Coherent Twin Boundaries During Annealing. Annealed for 5 hr at 1600°C. Thermally etched. 500×.

10. Theory of Alloying

J. O. Betterton

Our objects are to measure and understand the important factors governing the alloys of early transition metals. We have undertaken experimental studies of the topology of the Fermi surfaces of pure metals such as zirconium, tungsten, and beryllium for comparison to the alloying properties of these metals. We are studying the alloys in several ways: measuring low-temperature specific heats to show density of electronic states and Debye temperatures, observing Mössbauer spectrum to show local electronic and magnetic structure, and measuring electrical resistivity and, with x rays, crystalline dimensions to show scattering of transport current and changes in volume due to alloying. Observations concerning the superconducting and normal states and their interrelations will be utilized wherever possible, to establish better understanding of the factors governing alloy behavior in these materials. The present report includes results on galvanomagnetic properties of zirconium and beryllium; low-temperature specific heat measurements of the alloy systems Ti-Zr, Sc-Zr, Nb-Zr, and Mo-Zr; electrical resistivities for Ti-Zr and Nb-Zr alloys; and results on the Mössbauer spectrum of ^{57}Fe as an impurity in a dilute solution of cobalt in aluminum and in the Co_2Al_9 precipitate.

GALVANOMAGNETIC PROPERTIES OF ZIRCONIUM AND BERYLLIUM

J. O. Betterton D. S. Easton

Transverse galvanomagnetic properties of two cylindrical crystals[1] of zirconium were measured at 4.2°K in magnetic fields to 31 kilogauss. The current was in the direction of the geometric axes of the crystals which were near $[2\bar{1}\bar{1}2]$ and $[4\bar{1}\bar{3}1]$. Results interpreted according to Lifshitz theory[2-4] show that for cross sections containing these directions the Fermi surface of zirconium is closed and compensated (number of electrons equal to number of holes). The magnetic field dependences of the resistivity and of the Hall field deviate from the relations predicted by the Lifshitz theory for pure compensated metals in a manner that suggests imperfect compensation due to impurities.[5] This is shown in Fig. 10.1 for the resistivity, which has been fitted by an expansion $A + BH^2 - CH^4$ and in Fig. 10.2 for the transverse Hall component, which has been fitted by an expression $\alpha H + \beta H^3$. In these expressions, H is the magnetic field and the coefficients are positive. The Hall field is fairly large, about two to three times that of copper, and it changes in sign during rotation of the magnetic field. This anisotropy is shown in Fig. 10.3 which also shows the similar Hall voltage that exists in the longitudinal direction, parallel to the magnetic field.

Although Lifshitz's theory does not interpret the anisotropy of the Hall field for closed compensated metals, one can qualitatively note that the rotation of the magnetic field reverses the

[1]The $[2\bar{1}\bar{1}2]$ crystal was provided by J. C. Wilson, Zirconium Alloy Development Group. Growth of zirconium crystals is described in Part II, Chap. 21, of this report.

[2]I. M. Lifshitz, M. Ia Azbel', and M. I. Kaganov, *Zh. Eksperim. i Teor. Fiz.* **31**, 63 (1956); *Soviet Phys. JETP (English Transl.)* **4**, 41 (1957).

[3]I. M. Lifshitz and V. G. Peschanskii, *Zh. Eksperim. i Teor. Fiz.* **35**, 1251 (1958); *Soviet Phys. JETP (English Transl.)* **12**, 875 (1959).

[4]I. M. Lifshitz and M. I. Kaganov, *Usp. Fiz. Nauk* **69**, 419 (1959); *Soviet Phys.-Usp. (English Transl.)* **2**, 831 (1960).

[5]M. I. Kaganov and V. G. Peschanskii, *Zh. Eksperim. i Teor. Fiz.* **35**, 1052 (1958); *Soviet Phys. JETP (English Transl.)* **8**, 734 (1959).

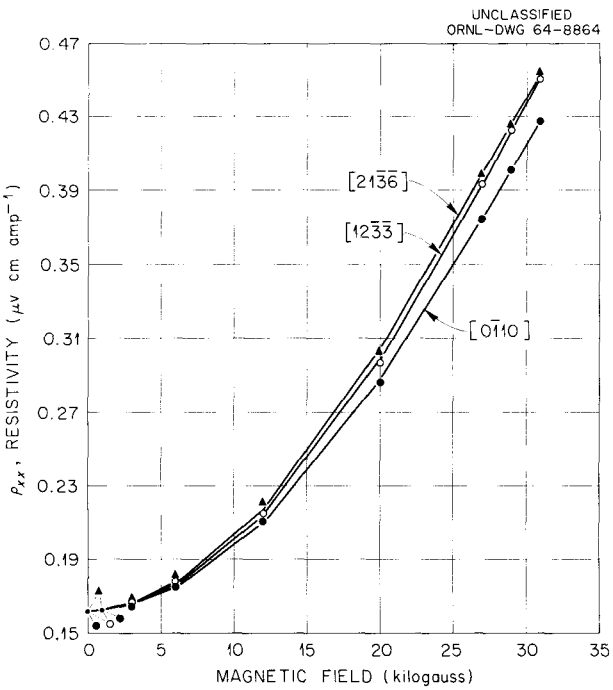

Fig. 10.1. Magnetic Field Dependence of the Resistivity (ρ_{xx}) of Single-Crystal Zirconium for Three Orientations of the Magnetic Field. Measured with current direction [2$\bar{1}\bar{1}$2]. Resistivity ratio 300. Temperature 4.2°K.

relative Hall contribution of the hole and electron portions of the Fermi surface as it might do for any compensated surface. The existence of a large transverse odd voltage parallel to the magnetic field indicates high distortion in the Fermi surface of zirconium. In support of closed surfaces, the magnetoresistivity is nearly isotropic. As shown in Fig. 10.3*a*, it varies by a factor of only 1.11 during magnetic field rotation.

There is a small transverse even voltage in zirconium which may support the open orbits in <10$\bar{1}$0> directions as predicted by band theory calculations for zirconium by Altmann and Bradley.[6] These calculations, which interpret successfully four of the five deHaas van Alphen periods given by Thorsen and Joseph,[7] show open surface only in the fifth and sixth bands in the form of four narrow tubes normal to and passing through the centers of {10$\bar{1}$0} faces of the Brillouin zone. The transverse even peaks for zirconium with the current direction [2$\bar{1}\bar{1}$2] occur when the magnetic field is approximately in certain directions of the type <11$\bar{2}a$>, where *a* is any integer, as shown in Fig. 10.4. Planes in reciprocal k-space normal to these magnetic fields always contain a direction of the type <1$\bar{1}$00>. On the basis of a theory by Klauder and Kunzler,[8] Fig. 10.4 appears to support the open orbits of the Altmann and Bradley Fermi surface. The zirconium measurements are not conclusive in this respect. Confirmation will require tests of additional crystals, since the open orbits in the <1$\bar{1}$00> directions were not observed as resistivity minima at the two field directions [2$\bar{1}\bar{1}$6] and [$\bar{2}$116] in Fig. 10.3*a* at which the magnetic field and the current become coplanar

[6] S. L. Altmann and C. J. Bradley, Department of Metallurgy, Oxford University, Oxford, England, private communication to J. O. Betterton, ORNL.

[7] A. C. Thorsen and A. S. Joseph, *Phys. Rev.* 131, 2078 (1963).

[8] J. R. Klauder and J. E. Kunzler, *Phys. Rev. Letters* 6, 179 (1961).

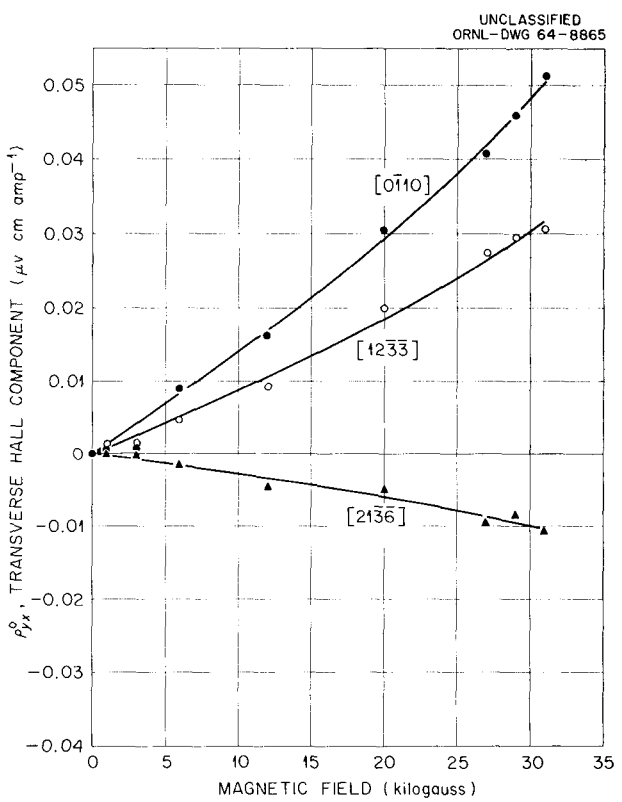

Fig. 10.2. Magnetic Field Dependence of the Transverse Hall Component (ρ^0_{yx}) in Zirconium with Current Direction [2$\bar{1}\bar{1}$2] and with Three Orientations of the Magnetic Field. Temperature 4.2°K.

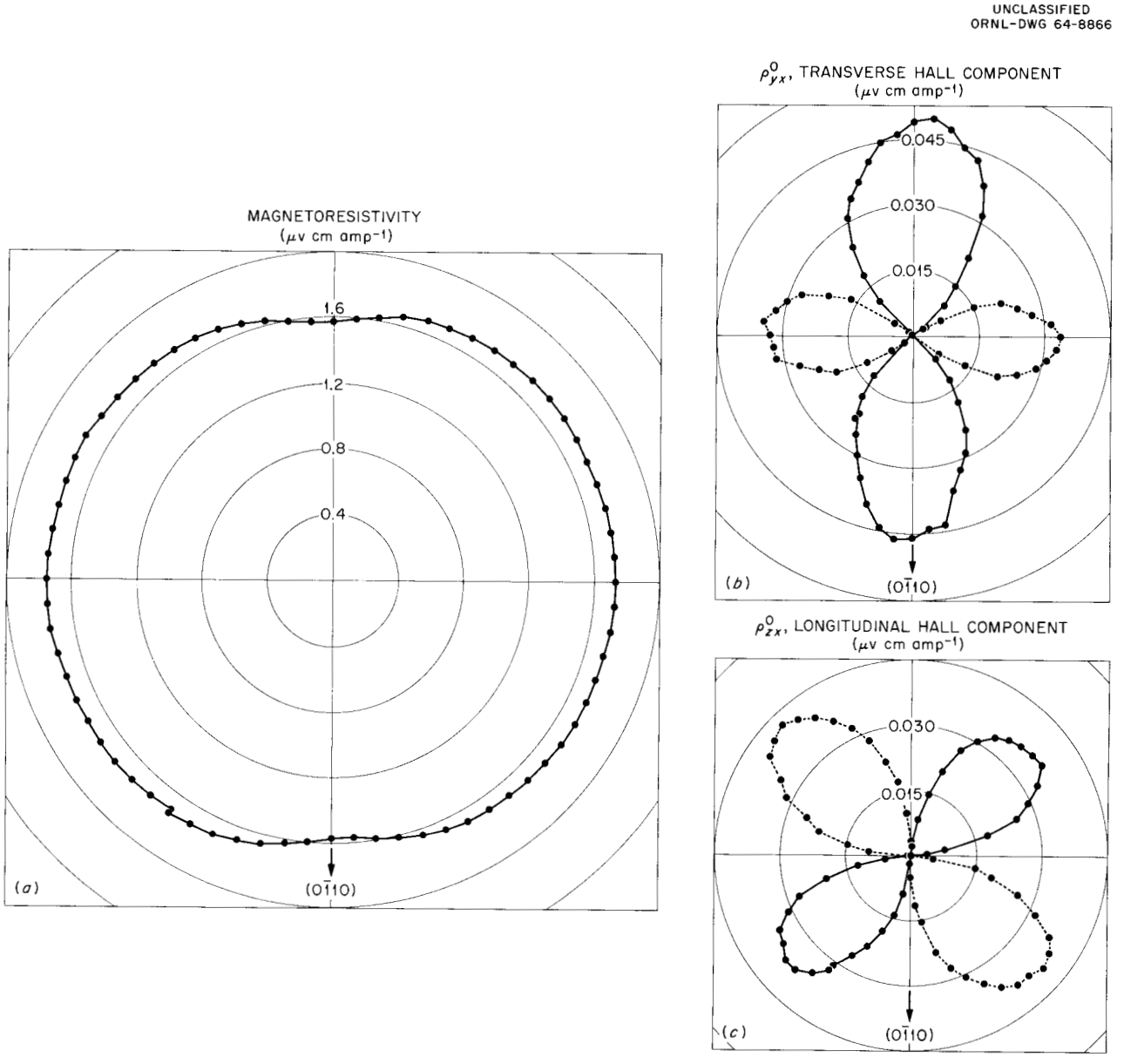

Fig. 10.3. Polar Diagrams Showing the Dependence on Magnetic Field Direction of (a) the Magnetoresistivity and the (b) Transverse and (c) Longitudinal Hall Components in Zirconium with Current Direction [2$\bar{1}\bar{1}$2]. Magnetic field 30 kilogauss. Temperature 4.2°K. Resistivity ratio 300. The dashed lines in the Hall-component plots represent negative values.

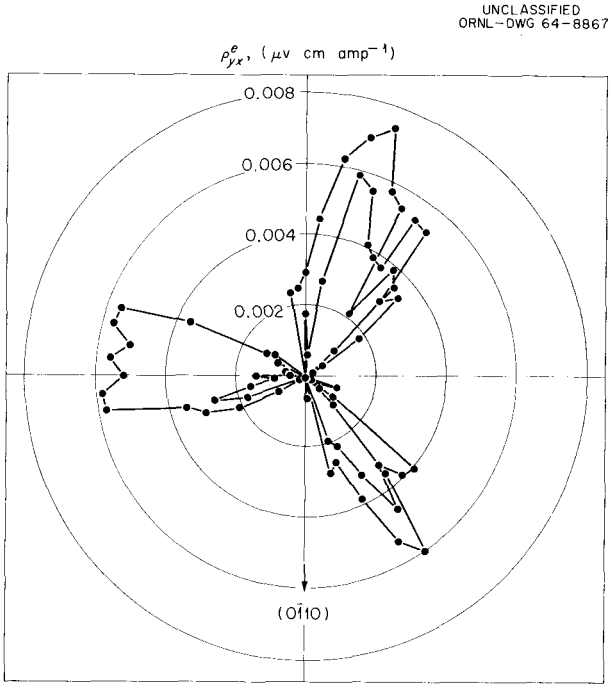

Fig. 10.4. Polar Diagram of the Transverse Even Component ρ^e_{yx} in Zirconium with Current Direction [2$\bar{1}\bar{1}$2] in Magnetic Field of 30 kilogauss at 4.2°K. Note peaks of this property near magnetic field directions of the type $<\bar{1}\bar{1}2a>$ for which an open orbit of the type $<1\bar{1}00>$ could lie in the k-space plane normal to the magnetic field.

with the c axis. Thus the resistivity measurements do not support the open orbits. Klauder and Kunzler[8] have suggested that transverse even voltages are more sensitive to higher order orbits than resistivity, and higher order orbits may be involved here.

The galvanomagnetic properties of a high-purity crystal (geometrical axis [3$\bar{1}\bar{2}$2]) of beryllium[9] have been investigated at 4.2°K in magnetic fields up to 30 kilogauss. The results show that for most field directions the Fermi surface consists of two parts – a closed electron surface and a closed hole surface, which compensate or balance each other. This is shown, for example, by (1) the odd Hall field, which is moderately anisotropic with magnetic field rotation (Fig. 10.5) and has positive coefficients confirming the presence of a hole surface, and (2) the magnetoresistivity, which is nearly quadratic with magnetic field strength (Fig. 10.6) and is only moderately anisotropic (variation by factor of 1.26 as shown in Fig. 10.7). The electrical voltages transverse to the current were not always odd, and a large transverse voltage peak occurred that was even with respect to magnetic field reversal when the magnetic field was simultaneously perpendicular to both the current and the c axis of beryllium. This is shown by the large maximum on Fig. 10.8 when the field is either in direction 4$\bar{1}$30 or $\bar{4}$130.

This peak suggested that open orbits exist in the c direction. Recently Alekseevskii and Egorov[10]

[9]Courtesy of Nuclear Metals, Incorporated.

[10]N. E. Alekseevskii and V. S. Egorov, *Zh. Eksperim. i Teor. Fiz.* **45**, 388 (1963).

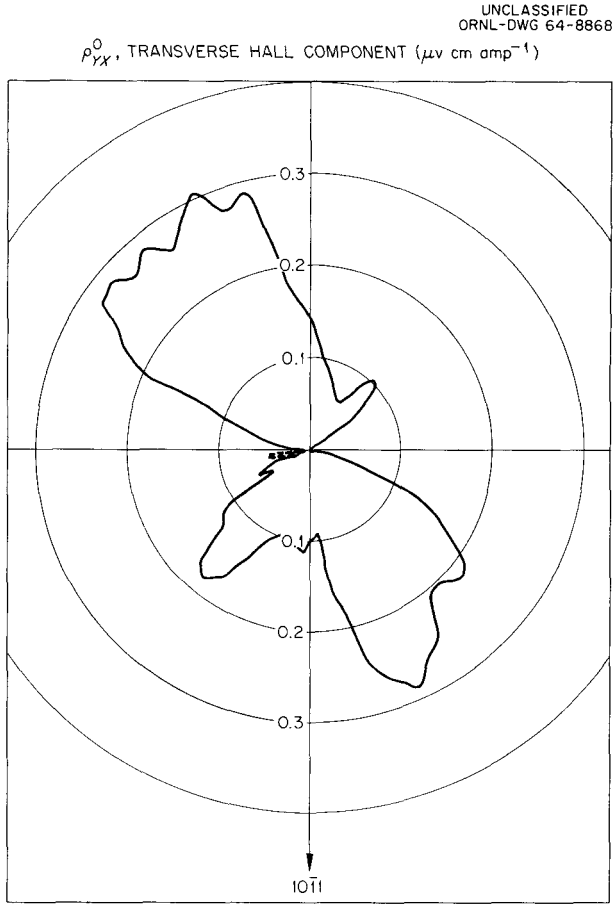

Fig. 10.5. Polar Diagram of the Anisotropy of the Transverse Hall Component in Beryllium with Rotation of the Magnetic Field in a Plane Normal to the Current Direction [$\bar{1}$3$\bar{2}\bar{2}$]. Magnetic field 29.55 kilogauss. Temperature 4.2°K.

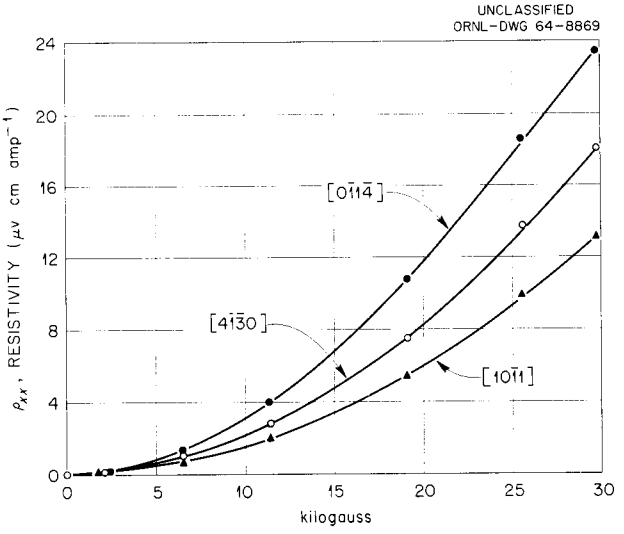

Fig. 10.6. Field Dependence of the Resistivity, ρ_{xx}, in Beryllium with Current Direction $[\bar{1}3\bar{2}\bar{2}]$ for Three Directions of the Magnetic Field. Temperature 4.2°K.

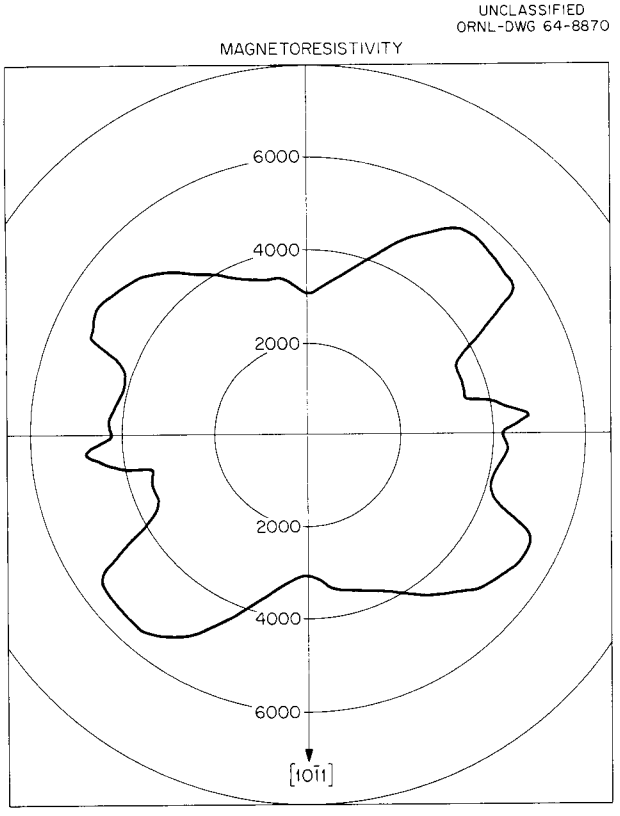

Fig. 10.7. Polar Diagram of the Effect of Field Direction on the Magnetoresistivity of Beryllium. Current Direction $[\bar{1}3\bar{2}\bar{2}]$. Magnetic Field 29.55 kilogauss. Temperature 4.2°K. Resistivity Ratio $\rho_{300}/\rho_{4.2°K}$ 1058.

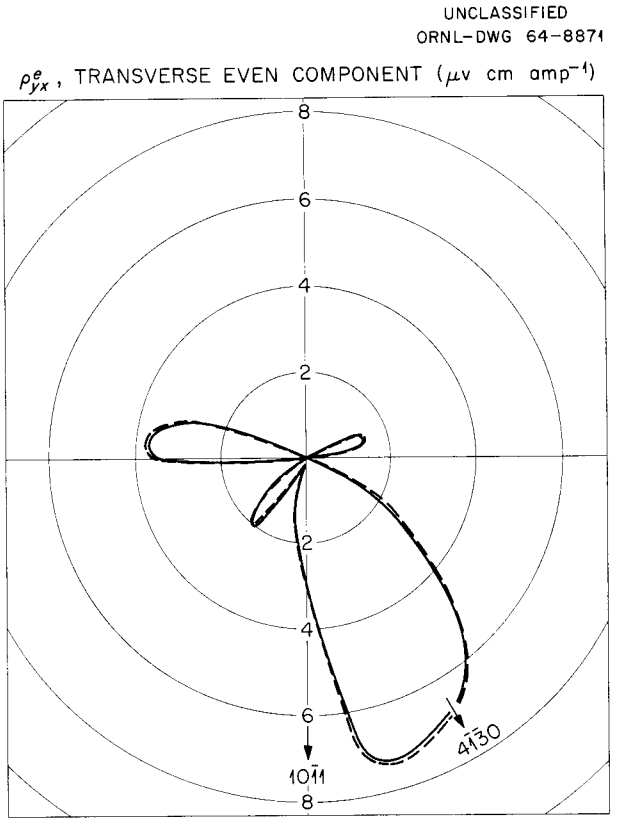

Fig. 10.8. Polar Diagram Showing the Transverse Even Hall Component ρ^e_{yx} of Beryllium as the Magnetic Field is Rotated Normal to the Current Direction $[\bar{1}3\bar{2}\bar{2}]$. Magnetic field 29.55 kilogauss. Temperature 4.2°K. Within experimental error, the curve is traced twice during a complete rotation of the magnetic field, since for opposite directions the values are equal in magnitude but opposite in sign. Negative values are shown by the dashed curve.

have reported such open orbits on the basis of two beryllium crystals, but in their experiment the open orbits occurred only at field strengths exceeding 50 kilogauss. They believe these open orbits are due to magnetic breakdown at this field strength of a small energy gap in the c direction. The results in Fig. 10.8 at 29.55 kilogauss then suggest that in beryllium either the small energy gap at low fields vanishes with the increased purity of our specimen or the transverse even peak arises not from open orbits but simply from the high anisotropy of the closed compensated surface. Calculations of the electronic structure

of beryllium by Loucks and Cutler[11] show closed electron and hole surfaces, which are consistent with galvanomagnetic properties. These calculations show cigar-shaped sections of the Fermi surface pointing in the c direction, which with a minor adjustment would permit open orbits along the c axis.

Apparatus for electrolytic machining of single crystals to cylindrical form was less useful for preparation of zirconium and niobium than it had been previously for tungsten, and a new apparatus was built for trepanning and planing these metals by spark erosion. The rate of spark erosion increased considerably and a much greater range of metals could be used as tools when the tool was vibrated mechanically during spark erosion. Typical improvements are shown in the following cutting rates (mil/min) for 0.0485-in.-thick aluminum with $\frac{1}{16}$-in.-thick tools:

Tool Material	With Vibration	Without Vibration
Tantalum	64	0.87
Brass	42	4.4
Stainless steel	46	1.0

LOW-TEMPERATURE SPECIFIC HEATS OF ZIRCONIUM ALLOYS

J. O. Betterton, Jr. J. O. Scarbrough

Titanium, zirconium, and hafnium are transition metals in the fourth group in the Periodic Table with two *s* and two *d* valency electrons on the free atom. When these elements are alloyed with *B*-subgroup solutes along the same row of the Periodic Table, valency effects are produced, which in the case of zirconium are nearly linear in both atomic composition and solute valency. These effects,[12,13] although not completely understood, can be thought of as electron additions to zirconium in a rigid band approximation with resistivity effects per solute atom that are large and nearly constant because of the *d*-band perturbations from the filled $4d^{10}$ shells on each solute atom. In other words, the $4d^{10}$ shells are assumed not to intermix with the $4d$ electrons of zirconium but to generate "holes" by virtue of excluding these zirconium $4d$ conduction electrons from the vicinity of the nuclear cores of these solutes.

Our more recent measurements have been of low-temperature specific heats, electrical resistivity, and superconducting transition temperatures in the alloy systems Ti-Zr, Nb-Zr, Sc-Zr, and Mo-Zr, in which the solute ion does not have completed $4d^{10}$ shells. The hafnium-zirconium alloys reported last year[14] are part of this study. The alloys between titanium, zirconium, and hafnium show effects of changes in nuclear charge, atomic mass, volume, and potential under conditions where the ratio of valency electrons to atoms remains constant. We have measured the electronic and lattice specific heats of titanium-zirconium and hafnium-zirconium alloys from 1.1 to 4.2°K over the entire range of composition in these continuous solid-solution systems.[15] The results are shown in Fig. 10.9. The lower plot represents superconducting transition temperatures where our results, determined from specific heat data, for certain titanium-zirconium alloys are compared to the previous values determined by Hulm and Blaugher,[16] using an inductive technique. The electronic specific heat and the Debye temperature in the hafnium-zirconium system both vary nearly linearly with hafnium content. In the titanium-zirconium system a pronounced maximum occurs in the electronic specific heat at 60 at. % Ti. In agreement with the BCS theory of superconductivity,[17] this corresponds to the maximum in superconducting transition temperature at this composition. The average interaction parameter in this theory, determined from our measurements, remains constant

[11] T. L. Loucks and P. H. Cutler, *Phys. Rev.* **133**, A819 (1964).

[12] G. D. Kneip, Jr., J. O. Betterton, Jr., and J. O. Scarbrough, *Phys. Rev.* **130**, 1687 (1963).

[13] G. D. Kneip, Jr., J. O. Betterton, Jr., and J. O. Scarbrough, *Phys. Rev.* **131**, 2425 (1963).

[14] J. O. Betterton, Jr., and J. O. Scarbrough, *Metals and Ceramics Div. Ann. Progr. Rept. May 31, 1963*, ORNL-3470, pp. 23–26.

[15] J. O. Betterton, Jr., and J. O. Scarbrough, "Low-Temperature Specific Heats of Ti-Zr and Hf-Zr Alloys," talk presented at Fall Meeting of the Metallurgical Society of AIME, Cleveland, Oct. 21–24, 1963. Abstract published in *J. Metals* **15**, 686 (1963).

[16] J. K. Hulm and R. D. Blaugher, *Phys. Rev.* **134**, A1407 (1964).

[17] J. Bardeen, L. N. Cooper, and J. R. Schrieffer, *Phys. Rev.* **108**, 1175 (1957).

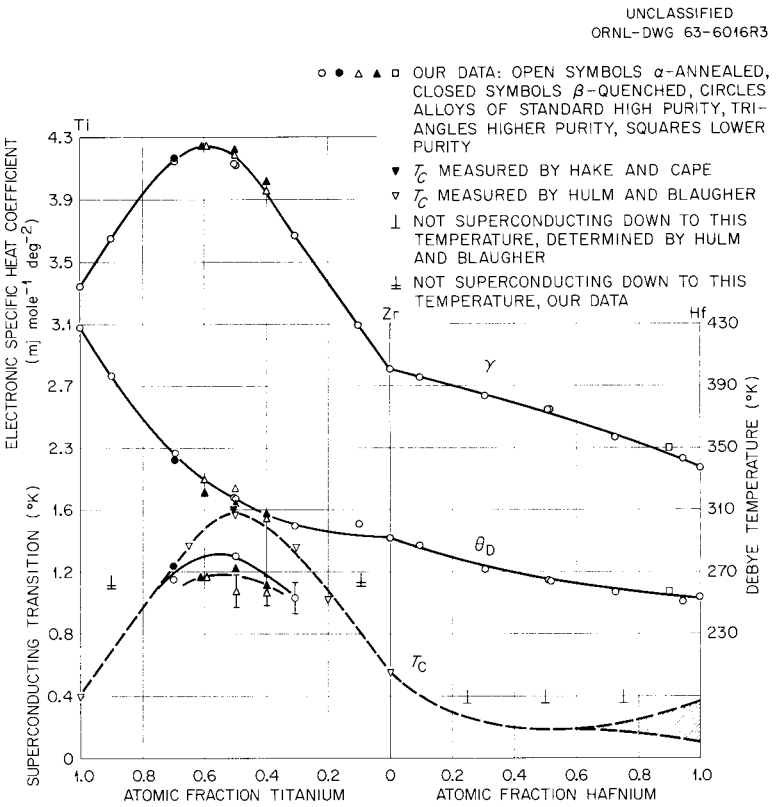

Fig. 10.9. The Low-Temperature Specific Heat Coefficients and Superconducting Transition Temperatures of Titanium-Zirconium and Zirconium-Hafnium Alloys.

from titanium to 60 at. % Zr and then rises to the value for zirconium. Although the Debye temperatures rise monotonically from zirconium to titanium, they deviate negatively from a linear dependence on composition. The effects in the titanium-zirconium system apparently correspond to significant relative energy shifts in the multiband electronic structure of these alloys. The electrical resistivity[18] of titanium-zirconium alloys at low temperatures and at room temperature shows maxima at 60 at. % Ti, typical of disordered solutions (see Fig. 10.10), and we believe no significant long-range ordering occurs in the hexagonal solid solutions to account for the maxima in superconductivity and density of electronic states. We also found, as shown in the first two lines of Table 10.1, that minor impurities affected the superconducting transition temperature and the resistivity of titanium-zirconium alloys significantly but changed the density of states, the hardness, and the Debye temperature only slightly. The impurity effects in titanium-zirconium alloys were previously observed by

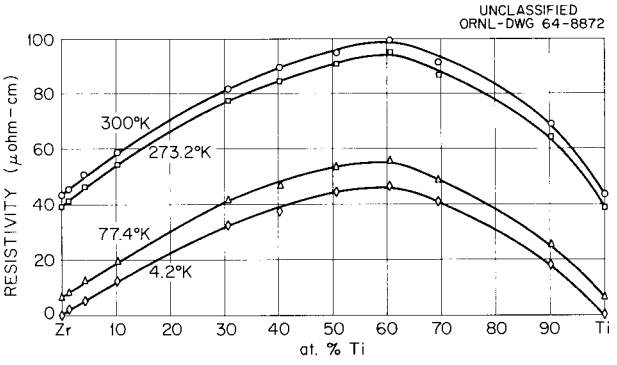

Fig. 10.10. The Electrical Resistivities of Titanium-Zirconium Alloys That Have Been Annealed in the Hexagonal Region.

[18] These electrical resistivity measurements were made by D. S. Easton.

Table 10.1. Impurity Effects in 50% Ti–50% Zr

Material	Electrical Resistivity at 4.2°K (μohm-cm)	Superconducting Transition (°K)	Electronic Specific Heat Coefficient (mj mole^{-1} deg^{-2})
Alloy of greater purity	42.7	1.08	4.19
Alloy of lesser purity	44.1	1.30	4.12
Alloy of Hake and Cape	51	1.60	4.21

Hake and Cape,[19] whose data for 50% Ti–50% Zr are included in Table 10.1.

Higher superconducting transition temperatures (T_c) and higher resistivities are observed in titanium-zirconium alloys with only minor increases in transition-metal impurity content. In this respect our results differ from the conclusion of Hake and Cape that manganese-type impurities decrease T_c of titanium-zirconium but agree with their conclusions that iron-type impurities raise T_c in pure titanium. Our results also agree with the conclusion of Heiniger and Muller[20] that bulk effects rather than second-phase effects are involved in these increases in T_c, since specific heats arise from all parts of the alloy.

We measured the low-temperature specific heats of zirconium alloyed with scandium, which has one less electron per atom than zirconium, and niobium and molybdenum with one or two more electrons per atom than zirconium. The results are shown in Fig. 10.11. In the continuous hexagonal solid solution of the zirconium-scandium system the density of electronic states decreases to a minimum at 10% Sc and then rises nearly linearly to a value for pure scandium that is 3.8 times the value for pure zirconium. In spite of this increase, no superconductivity was observed for the alloys tested down to 1.2°K. This shows that the average interaction potential, which is responsible for superconductivity in the BCS theory, must diminish significantly with scandium additions. The initial decrease of the density of electronic states of alpha-zirconium in dilute alloys with scandium seems to be approximately equal and opposite to the electron addition effects of dissolved Ag, Cd, In, Sn, or Sb. Additions of niobium and molybdenum, which are immediately to the right of zirconium in the Periodic Table, increased the experimental density of electronic states, raised the superconducting transition temperature, and lowered the Debye temperature more per added electron per atom than did Ag, Cd,

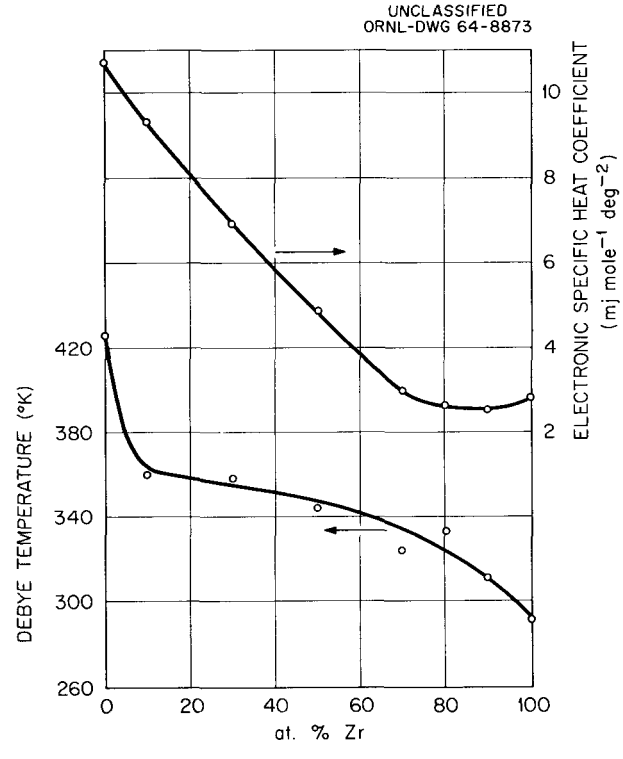

Fig. 10.11. The Low-Temperature Specific Heat Coefficients of Zirconium-Scandium Alloys.

[19] J. A. Cape and R. R. Hake, *Bull. Am. Phys. Soc.* 8, 1962 (1963) and private communication to J. O. Betterton, Jr., ORNL.

[20] F. Heiniger and J. Muller, *Phys. Rev.* 134, A1407 (1964).

In, Sn, and Sb. The niobium and molybdenum effects appear to occur with approximately constant BCS interaction potential; that is, the density of electronic states and the superconducting transition temperature change together. These properties are shown in Table 10.2. To ascertain whether the steep gain in density of states could be associated with localized states about the solute atoms rather than with electrons shared collectively by the whole crystal, the resistivities of the niobium-zirconium alloys were investigated. The change of resistance, 1.4 μohm-cm/at. % Nb (Table 10.2) was lower than would normally[21] be expected from an impurity that causes a high density of localized states at the Fermi surface.[21] Silver presumably contributes one extra electron per atom, increases the resistivity by 14 μohm-cm/at. %, and increases the density of states only slightly. Niobium also contributes one extra electron, but it increases the resistivity by only 1.4 to 4.7 μohm-cm/at. % and increases the density of states five to ten times as much. The reason for the difference is an important question that we have not yet answered.

We have measured the low-temperature specific heats of hexagonal Zr–2% Mo; its properties are compared in Table 10.3 with those of unalloyed zirconium and Zr–3% Nb. The effect of molybdenum with its greater number of electrons appears to be less than expected from the effect of niobium, assuming a simple dependence upon electron-to-atom ratio.

[21] J. Friedel, *Proc. Intern. Conf. Electron Transport in Metals and Solids*, Supplementary number 12A of the *Can. J. Phys.* **34**, 1190 (1956).

Table 10.2. Low-Temperature Properties of Zirconium Alloyed with Low Concentrations of Niobium

Property	Niobium Content (at. %)				
	0	1[a]	2	3[a]	4
Electronic specific heat coefficient (mj mole^{-1} $^{\circ}$K^{-2})	2.81	3.05	2.93	3.98	
Debye temperature ($^{\circ}$K)	292	275	274	263	
Superconducting transition temperature ($^{\circ}$K)	0.55	1.2	1.1	2.7	>4.6
BCS interaction potential (ev)	0.274	0.287	0.296	2.64	
Electrical resistivity at 77.4°K (μohm-cm)	6.4	10.4	8.8	20.6	11.8

[a] These alloys were heat treated by quenching from the beta-phase region, while the remaining alloys were annealed 30 to 45 days at 600 to 620°C.

Table 10.3. Comparison of Low-Temperature Properties

Material	Electronic Specific Heat Coefficient (mj mole^{-1} $^{\circ}$K^{-2})	Debye Temperature ($^{\circ}$K)	Superconducting Transition Temperature ($^{\circ}$K)	BCS Interaction Potential (ev)
Zr	2.8	292	0.5	0.27
Zr + 3 at. % Nb	4.0	263	2.7	0.27
Zr + 2 at. % Mo	3.7	265	1.8	0.26

APPLICATION OF THE MÖSSBAUER EFFECT: PRECIPITATION OF COBALT IN ALUMINUM

Gordon Czjzek

The Mössbauer effect allows investigation of precipitation processes at a concentration that is not accessible by other methods. We are using this effect to study the precipitation of trace amounts of cobalt in aluminum. A series of specimens were annealed at 335 and 400°C. After each anneal the specimen was quenched in water to room temperature and a Mössbauer spectrum was taken. At the present stage of the experiments the following results have been established.

Depending on the annealing treatment, cobalt occurs in at least three different states in aluminum: (1) After quenching the specimens from 630°C a single sharp line was observed with an isomer shift of 0.5 mm/sec with respect to stainless steel. (2) After annealing at 335 and 400°C a second state developed gradually, giving rise to a pair of lines with much smaller isomer shift but 1.5 times as intense. (3) A transient state was observed after short anneals (1 to 2 hr) at 400°C. This state caused a single line with a high isomer shift (1.4 mm/sec). This line disappeared after longer annealing treatments.

A clear picture of the nature of the states will require further investigation. Probably, state 1 can be ascribed to cobalt dissolved in the aluminum lattice, state 2 can be a precipitate of Co_2Al_9 or cobalt atoms segregated at defects, and state 3 may be interpreted as an intermediate state of precipitation, analogous to Guinier-Preston zones.

New equipment is being constructed to give better resolution of the lines and to permit measurements down to liquid-helium temperatures. We plan to study the magnetic moment of iron impurities dissolved in various transition metals and compounds in conjunction with measurements of the transition temperature to the superconducting state.

11. Theory of Electronic States in Solids

J. S. Faulkner

ELECTRONIC STATES OF DISORDERED SYSTEMS

Many of the physical properties of solids can best be understood in terms of the dynamical behavior of their electrons, for which one needs to know the energy and momentum states available to the electrons. The art of calculating the electronic states of ordered crystalline solids has progressed rapidly in recent years, but relatively little is known about the electrons in disordered systems such as random alloys or liquid metals. For this reason we have concentrated much of our attention on the latter problem. The search for reasonable approximation for this problem has followed two main paths: (1) calculations on realistic physical models are carried out on the basis of intuitive assumptions and the results are compared with experiment; (2) calculations on idealized models are carried out in as exact a fashion as possible in order to obtain qualitative information about the nature of the solutions, and the effect of simplifying assumptions on these solutions is noted. The first path should lead to the desired results most directly but encounters the difficulties that the electronic states seem to be different from what intuition suggests and that the experimental information about these states is obtained rather indirectly. The second path is less direct, but it seems to yield some useful information and is the one we have been following recently.

During the past year, we extended a method that we had developed for calculating the electronic states of one-dimensional random alloys[1] and adapted it to treat the problem of one-dimensional liquid metals.[2] Since others have reported considerable work on this problem, we had an opportunity to compare our methods and results with others. In particular, Lax and Phillips[3] carried out some exact numerical calculations for finite chains of atoms; these calculations were substantiated by Frisch and Lloyd's[4] treatment of infinitely long chains using the methods of probability theory. Klauder[5] used a type of perturbation theory in which the contributions of certain types of terms to the Green's function of the system are summed to infinite order. Our results for this liquid-metal problem differ in some ways from the exact results, but they are identical with certain results of Klauder's that he calls the Brueckner approximation. He uses this name because the structure of the terms that he summed is the same as that used by Brueckner in a well-known treatment of the nuclear many-body problem. Since our methods are formally quite different from Klauder's, we were able to investigate the physical interpretation of the Brueckner approximation as applied to this problem and at the same time to gain an understanding of the level of approximation that our method gives.

The Green's function method for the problem of electronic states in disordered systems seems to offer a systematic approach that can be used to treat realistic three-dimensional models. It has, in fact, been used for this purpose, although the treatments do not include as many terms as

---

[1] J. S. Faulkner and J. Korringa, *Phys. Rev.* **122**, 390 (1961).

[2] J. S. Faulkner, "Electronic States of Kronig-Penney Crystal with Random Atomic Positions," accepted for publication in *Physical Review*, July 6, 1964.

[3] M. Lax and J. C. Phillips, *Phys. Rev.* **110**, 41 (1958).

[4] H. L. Frisch and S. P. Lloyd, *Phys. Rev.* **120**, 1175 (1960).

[5] J. R. Klauder, *Ann. Phys. (N.Y.)* **14**, 43 (1961).

Klauder's Brueckner approximation. We have thus been interested in how the Green's function method will work on the random alloy problem if one goes to the level of the Brueckner approximation and what the effect is of making rougher approximations. We have started by assuming that the formula already available from applying our method to one-dimensional models of random alloys yields results that are identical with those that would be obtained using the Brueckner approximation on this problem. We have also carried out some exact calculations for finite chains using a method similar to that of Lax and Phillips. Figure 11.1 compares the integrated density of states plotted against energy for a model of a random binary alloy made up of equal numbers of A and B atoms as calculated from our formulas (solid curve) and by the numerical method (cross marks). The general agreement is very good, but the variations about the solid curve are not simply statistical; they are quite reproducible from chain to chain and do not become smaller as the chain length is increased. We have not yet compared the rougher approximations with these results.

OTHER WORK

We have concluded[6] work on certain mathematical problems in the application of quantum mechanics to physical problems, in collaboration with J. O. Nordling of Uppsala University, Sweden. We have also done some work on the application of existing theories to certain experimental work that is going on in the Division.

[6] J. O. Nordling and J. S. Faulkner, *J. Mol. Spectr.* **12**, 171 (1964).

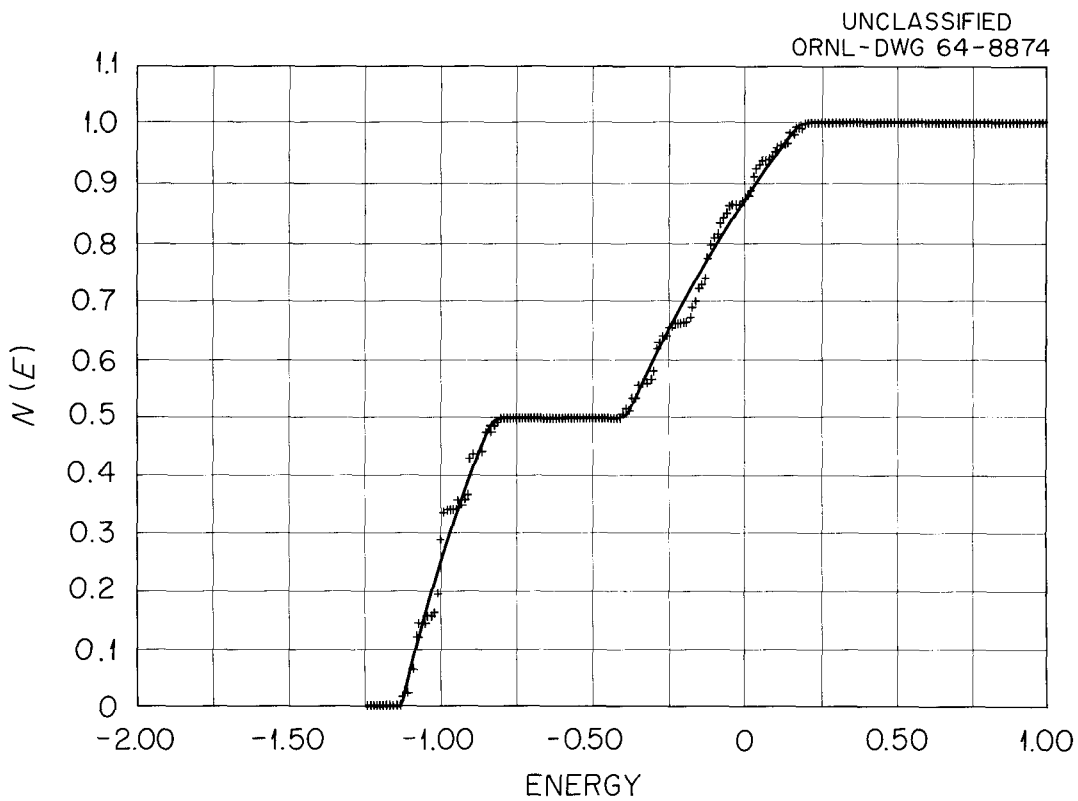

Fig. 11.1. The Integrated Density of States vs Energy in Dimensionless Units Defined in Terms of Lattice Spacing and Fundamental Constants. Solid curve: calculated from our approximate formulas. Crosses: calculated numerically.

12. X-Ray Diffraction Research

B. S. Borie

Our mission is twofold: We function as a service group, supporting other research programs both within the Division and without and we pursue our own basic research independently of other groups. The division of effort between these two activities is approximately equal.

A wide range and large volume of service problems are regularly submitted to us. Most, though not all, of these are routine in nature. Problems varying in sophistication from simple lattice-constant measurements to crystal structure determinations have been undertaken in this reporting period.

Our basic research program is primarily concerned with the study of crystalline imperfections by diffraction techniques. Radiation damage in BeO and measurements of strain and thickness in thin Cu_2O films have been of primary interest during the past year.

ROUTINE ANALYSIS

O. B. Cavin
L. A. Harris
R. M. Steele
H. L. Yakel

Over 800 samples were submitted to the X-Ray Diffraction Group in the period of this report for analyses that could be described as routine. These included phase identification, lattice-parameter determination, determination of crystal orientation, and preferred orientation measurements. Much of this effort is in support of other programs of the Division and is reported elsewhere in this report. Table 12.1 lists structural information derived from previously unreported analyses of materials submitted by groups outside the Metals and Ceramics Division.

Crystallographic data for a series of rare-earth germanomolybdates with the general formula R_2GeMoO_8 have been recorded and are presented in Chap. 2 of this report. The compound Er_2SiO_5 has been prepared and single crystals obtained. The unit cell is monoclinic, space group I2/c or Ic, with $a_0 = 10.24$ A, $b_0 = 6.68$ A, $c_0 = 12.38$ A, $\beta = 102°$. Single-crystal diffraction data from this compound do not agree with powder diffraction data reported previously for a material of similar composition.[1]

Determination of the atom positions in the $Ca_2Be_3O_5$ crystal structure[2,3] has continued with the tentative location of 96 of the 120 oxygen atoms in the unit cell. Further refinement of the structure has proven difficult, possibly due to disorder among the oxygen positions or an error in the assumed composition.

Diffraction data[3] from crystals of $Y_2Be_2O_5$ have shown that the space group is either P*mcn* or $P2_1cn$. Intensity statistics suggest the centered group, but spatial restrictions in the **a** direction indicate that, unless all yttrium and oxygen atoms are located on the mirror planes of P*mcn*, the space group is probably $P2_1cn$. These two results are compatible if the *x* coordinates of the two sets of yttrium atoms in 4(c) positions of $P2_1cn$ are nearly equal. Yttrium atom *y* and *z* coordinates have been deduced from an **a**-axis Patterson projection. Data are currently being processed for a three-dimensional Patterson calculation, which may suggest possible oxygen atom positions.

The shielded x-ray diffractometer for the HRLEL facility has been appended to the cell structure

[1] N. A. Toropov *et al.*, *Izv. Akad. Nauk SSSR, Otd. Khim. Nauk* 1961, 1365–71.

[2] L. A. Harris, *Met. Div. Ann. Progr. Rept. May 31, 1961*, ORNL-3160, p. 29.

[3] L. A. Harris *et al.*, *Metals and Ceramics Div. Ann. Progr. Rept. May 31, 1963*, ORNL-3470, p. 41.

Table 12.1. Crystallographic Data for New Alloys and Compounds

Composition	Crystal System	Lattice Parameters (A)	Comments
Ni_2MnIn	Cubic	6.068 ± 0.004	$L2_1$-type Heusler alloy structure[a]
Tb_2CuZn	Cubic	3.55 ± 0.01	B2(CsCl)-type structure
TbCu	Cubic	3.480 ± 0.005	A2-type bcc structure
TbZn	Cubic	3.57 ± 0.01	B2(CsCl)-type structure
TbAg	Cubic	3.62 ± 0.01	A2-type bcc structure
TbHg	Cubic	5.37 ± 0.01	B1(NaCl)-type structure
ErCu	Cubic	3.43 ± 0.01	B2(CsCl)-type structure
$TbPd_3$	Cubic	4.08 ± 0.01	$L1_2(Cu_3Au)$-type structure
Mn_2V	Cubic	2.91 ± 0.01	A2-type bcc structure
$ScMnO_3$	Hexagonal	$a_0 = 5.826 \pm 0.003$ $c_0 = 11.18 \pm 0.02$	$LuMnO_3$-type structure[b]

[a]O. Heusler, *Ann. Physik.* **19**, 155 (1934).

[b]H. L. Yakel, W. C. Koehler, E. F. Bertaut, and E. F. Forrat, *Acta Cryst.* **16**, 957 (1963).

and has operated successfully with a limited number of radioactive diffraction samples.

A detailed high-temperature x-ray diffraction study of the UC_2-ThC_2 system has been carried out in cooperation with the Ceramics Group of the Metals and Ceramics Division and is described in Part III, Chap. 25, of this report.

X-RAY SCATTERING FROM IRRADIATED BERYLLIUM OXIDE CRYSTALS

H. L. Yakel B. S. Borie

Beryllium oxide single crystals,[4] grown from melts of $Li_2O \cdot 2MoO_3$, $Li_2O \cdot 2WO_3$, $Cs_2O \cdot 2MoO_3$, and V_2O_5, have been recovered after neutron irradiation to doses of 1 to 60×10^{20} neutrons/cm^2 ($E > 1$ Mev) at temperatures of 54 to 1075°C. Physical densities and, for some crystals, refractive indices have been measured and x-ray diffraction patterns have been recorded. Table 12.2 summarizes the results of these experiments; physical appearances of crystals irradiated under various conditions may be compared in Fig. 12.1.

While attention still centers on the detailed explanation of the various diffraction effects observed after irradiation to a given dose at a given temperature, the following general conclusions may be drawn from the total data observed to date:

[4]Crystals were grown by C. B. Finch of the Crystal Physics Group.

Table 12.2. Crystallographic Data for Irradiated BeO Crystals

Crystal Growth Solvent	Fast Neutron Dose (neutrons/cm^2)	Irradiation Temperature (°C)	Observed Density (g/cm^3)	Lattice Parameters		Unit-Cell Volume	Changes in Parameters, Volume, and Density[a]				Refractive Index
				a_0(A)	c_0(A)	V(A^3)	$\Delta a/a$	$\Delta c/c$	$\Delta V/V$	$\Delta \rho/\rho$	
	$\times 10^{20}$										
$Cs_2O \cdot 2MoO_3$	36 ± 5	54 ± 5	2.880 ±0.001	2.702 ±0.001	4.42 ±0.02	27.9_5 ±0.1_7	0.0015 ±0.0004	0.11 ±0.005	0.013 ±0.006	0.0424 ±0.0005	n_w = 1.698 ±0.003
$Li_2O \cdot 2WO_3$	41 ± 5	650 ± 10	2.902 ±0.001	2.701 ±0.002	4.387 ±0.005	27.72 ±0.08	0.0011 ±0.0007	0.002_2 ±0.001_1	0.004 ±0.002	0.0357 ±0.0005	n_w = 1.705 ±0.003 $n_{iso} < 1.700$[b]
$Li_2O \cdot 2WO_3$	7 ± 3	650 ± 10	2.979 ±0.001	2.699 ±0.003	4.384 ±0.004	27.66 ±0.08	0.000_4 ±0.001_0	0.0016 ±0.0009	0.002 ±0.003	0.0100 ±0.0005	n_w = 1.705 ±0.003 $n >$ 1.718 $n_{iso} < 1.700$[b]
$Li_2O \cdot 2WO_3$	8 ± 3	110 ± 5	2.966 ±0.001	c	c					0.0143 ±0.0005	c
$Li_2O \cdot 2WO_3$	12 ± 5	110 ± 5	2.945 ±0.002	c	c					0.0213 ±0.0005	c
$Li_2O \cdot 2WO_3$	14 ± 5	110 ± 5	2.933 ±0.002	c	c					0.0253 ±0.0005	c
$Li_2O \cdot 2MoO_3$	15 ± 2	1075 ± 25	2.997 ±0.001	c	c					0.0040 ±0.0005	c
$Li_2O \cdot 2MoO_3$	57 ± 5	1075 ± 25	2.986 ±0.001	2.699 ±0.003	4.39_5 ±0.01_0	27.7_2 ±0.1_4	0.000_4 ±0.001_0	0.004_1 ±0.002_3	0.005 ±0.004	0.0077 ±0.0005	c c
V_2O_5	9 ± 3	147 ± 5	2.924 ±0.001	2.7018 ±0.0007	4.400 ±0.002	27.81 ±0.03	0.0015 ±0.0003	0.0051 ±0.0005	0.008 ±0.001	0.0282 ±0.0005	c
V_2O_5	9 ± 3	670 ± 10	2.990 ±0.001	2.7007 ±0.0004	4.3843 ±0.0008	27.69 ±0.01	0.0010 ±0.0002	0.0016 ±0.0002	0.0037 ±0.0006	0.0063 ±0.0005	c c
V_2O_5	0.5 ± 0.2	147 ± 5	3.002 ±0.001	2.6987 ±0.0002	4.3828 ±0.0003	27.644 ±0.006	0.0003 ±0.0001	0.0013 ±0.0001	0.0019 ±0.004	0.0023 ±0.0005	c
V_2O_5	0.5 ± 0.2	670 ± 10	3.008 ±0.001	2.6983 ±0.0002	4.3801 ±0.0003	27.618 ±0.006	0.0002 ±0.0001	0.0007 ±0.0001	0.0009 ±0.0004	0.0003 ±0.0005	c

[a]Values for unirradiated BeO are a_0 = 2.6979 A, c_0 = 4.3772 A.

[b]Optically isotropic phase found in crystal crushings.

[c]Not measured.

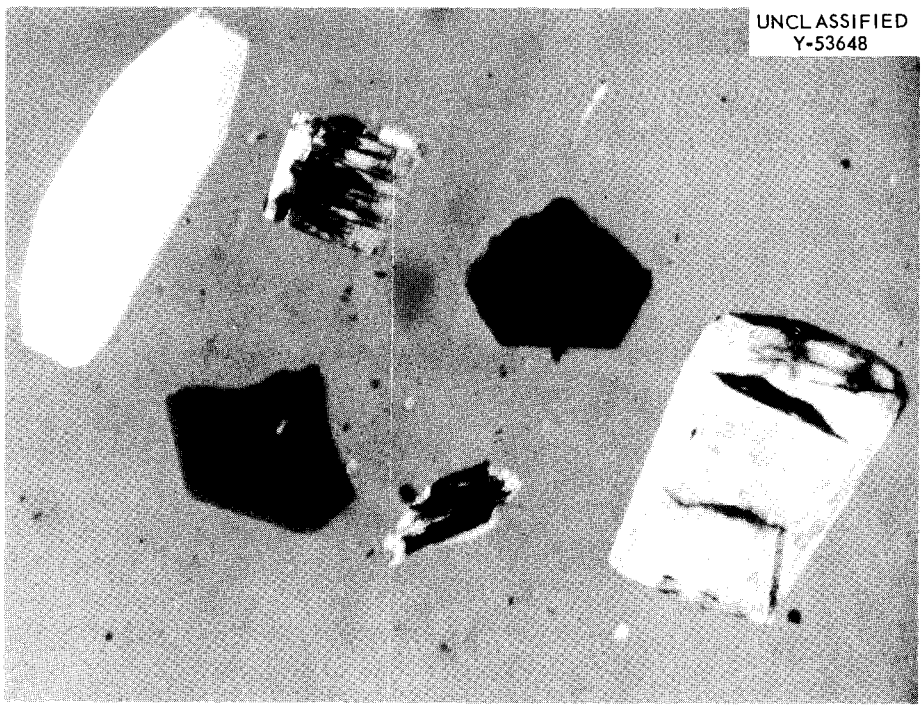

Fig. 12.1. Left: Unirradiated $Li_2O \cdot 2MoO_3$-Grown BeO Crystal. Lower left center: $Cs_2O \cdot 2MoO_3$-grown BeO crystal irradiated to 3.6×10^{21} neutrons/cm^2 (fast) at 54°C. Upper left center: $Li_2O \cdot 2WO_3$-grown BeO crystal irradiated to 0.7×10^{21} neutrons/cm^2 (fast) at 650°C. Upper and lower right center: $Li_2O \cdot 2WO_3$-grown BeO crystals irradiated to 4.1×10^{21} neutrons/cm^2(fast) at 650°C. Right: $Li_2O \cdot 2WO_3$-grown BeO crystal irradiated to 5.7×10^{21} neutrons/cm^2 (fast) at 1075°C. Crystals viewed in 1.68 refractive index oil under crossed Nicol prisms. Crystal on extreme left is about 2 mm long.

(1) For doses greater than 5×10^{20} neutrons/cm^2, crystals irradiated at temperatures below 450°C produce diffraction effects broadly compatible with our model of basal-plane spacing anomalies caused by interstitial clusters coherent with the crystal matrix.[5] Such crystals are as hard as but more brittle than unirradiated BeO crystals.

(2) For doses greater than 5×10^{20} neutrons/cm^2, crystals irradiated at about 650°C produce diffraction effects compatible with a structure highly strained and expanded in the **c** direction but without coherent defect clusters. Other physical properties point to the growth of macroscopic incoherent clusters, which severely fragment the crystal of its basal planes.

(3) For doses greater than 3×10^{21} neutrons/cm^2, crystals irradiated near 1000°C produce diffraction effects compatible with a structure slightly strained due to isolated defects. Neither coherent nor incoherent defect clusters are suggested by the x-ray scattering patterns or by other physical properties. Mechanical properties of these crystals are not easily differentiated from those of unirradiated crystals.

(4) For doses less than 5×10^{20} neutrons/cm^2, crystals irradiated at 147 and 670°C produce sharp diffraction maxima consistent with a structure slightly expanded in the **c** direction. Diffuse scattering maxima are seen however near both 00·2 and 10·1 reflections and may be due to short-range order among defect cluster nuclei.

[5] H. L. Yakel and B. S. Borie, *Acta Cryst.* **16**, 589 (1963).

(5) At all irradiation temperatures and doses studied, the persistence of diffuse scattering streaks parallel to **c*** for $h-k$ not divisible by 3 may be related to the occurrence of random displacement faults in the layer sequence of the ideal BeO structure.[6] The origin of these faults over the entire range of irradiation parameters is not understood. Similar effects are never seen in unirradiated crystals.

These conclusions are oversimplifications of actual structural conditions whose details, if thoroughly understood, should be as important as their broad outline. Outstanding areas of disagreement between theory and experiment or between different experiments include:

(1) The failure of postulated models of spacing anomalies and/or displacement faults to explain such detailed diffraction observations as the minima in a given $hk \cdot l$(l odd) intensity distribution and the deflection of the diffuse streaks toward the origin of reciprocal space near $l = 0$.

(2) The lack of agreement in physical properties and x-ray scattering effects of BeO crystals of nominally similar irradiation history as observed in several laboratories.[7]

The possible influence of neutron dose estimation methods in contributing to the disagreement noted in (2) cannot be denied, but even a liberal allowance for dose errors cannot remove all discrepancies.[7] The sensitivity of radiation damage processes in BeO to chemical impurities may be significant here, so the availability of crystals grown from various melts with a concomitant variety of impurities should aid in assessing such effects.

[6]Intensities of the streaks decrease monotonically with increasing $|h_3|$ values. Faults that produce octahedrally coordinated beryllium atom layers agree with this intensity distribution; faults that preserve tetrahedral beryllium atom coordination do not.

[7]For example, c_o lattice parameters as high as 4.48 A have been reported for BeO crystals irradiated to 6×10^{20} neutrons/cm^2 (fast) by Australian workers (B. S. Hickman, D. G. Walker, and R. Hemphill, Paper 17, "International Conference on Beryllium Oxide, Sydney, Australia, Oct. 21–25, 1963." Deep red colorations have been reported in BeO crystals irradiated to less than 1×10^{21} neutrons/cm^2 (fast) by workers at Atomics International (S. B. Austerman, private communication), whereas even after irradiation to 3 to 4×10^{21} neutrons/cm^2 the crystals described here have only an amber color.

DIFFRACTION STUDIES OF Cu_2O FILMS ON COPPER

Extension of Diffraction Model to Nonuniformity of Film Thickness

C. J. Sparks, Jr. B. S. Borie
G. V. Czjzek

Our[8] model for thin oxide films formed on copper single crystals included two assumptions, a uniform film thickness and a linear strain gradient. This model fitted well a series of experimentally measured Fourier coefficients from oxide films grown on (110) copper crystals.[9] One consistent deviation occurred, however, between experiment and theory; the experimentally measured higher order coefficients always fell below those calculated from the model. If the film thickness and strain gradient were chosen to better fit the higher order coefficients, then the calculated lower order coefficients fell below experiment. This can be seen by comparing the solid line in Fig. 12.2 with the experimental points.

Another independent x-ray technique for measuring film thickness[10] is based on the total integrated intensity from the Bragg reflection. This rocking-curve measure of the thickness, designated Tr, was always larger than the film thickness measured from the line shape (Ts) by about 10 to 20%. The value of Ts should equal the volume average of the thickness for the lowest order coefficients whose order number (converted to length units by multiplication by the average spacing) is less than the minimum thickness. The volume average of the thickness parameter Ts is precisely the same as that measured by Tr. Thus $Tr = Ts$ if the lower order coefficients are properly fitted by the model. But when Ts is chosen so as to equal Tr there is a noticeable discrepancy for the higher order coefficients.

[8]B. S. Borie, *Acta Cryst.* 13, 542 (1960).

[9]B. S. Borie, C. J. Sparks, Jr., and J. V. Cathcart, *Acta Met.* 10, 691 (1962).

[10]B. S. Borie and C. J. Sparks, Jr., *Acta Cryst.* 14, 569 (1961).

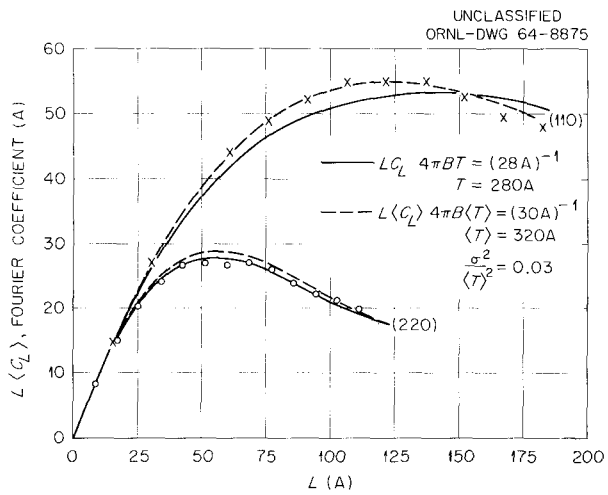

Fig. 12.2. Experimental Fourier Coefficients for Thin Cu_2O Film Grown on (110) Copper Single Crystal Shown as Crosses and Circles. Solid line calculated from model assuming uniform film thickness, dashed line from that assuming nonuniform film thickness.

One of the most probable explanations for this effect is that the assumption of uniform film thickness is not strictly valid. The simplest way to correct the model then is to assume that the films are not uniformly thick and that the strain gradient is the same for all the different thicknesses of the same film. This implies either that the Bragg peak is asymmetric or the average lattice constant is the same for each column of oxide ragardless of thickness. If the films do not vary too greatly in thickness, the peak asymmetries are small and one cannot choose between these two models of variable film thickness.

The expression as previously derived[8] for the Fourier coefficients of uniform film thickness T and linear strain gradient is

$$LC_L = \frac{\sin rL(T - L)}{rT}, \qquad (1)$$

where $r = 2\pi IB$, and the notation is the same as in ref. 8. Let us assume a thickness distribution function $\rho(T)$ such that the observed Fourier coefficients are given by the average

$$L\langle C_L\rangle = L\int_{T=0}^{\infty} C_L(T)\rho(T)dT\,. \qquad (2)$$

If $\rho(T)$ is sharp, the major contributions to $\langle C_L\rangle$ are close to $\langle T\rangle$. If also C_L is a smooth function, we may expand Eq. (2) in a Taylor's series. With $\langle T^n\rangle = \int_0^{\infty} T^n\rho(T)dT$, the result for the first three terms of the expansion is

$$L\langle C_L\rangle = \frac{\sin rL(\langle T\rangle - L)}{r\langle T\rangle} + \frac{\sigma^2}{\langle T\rangle^2}\left[\frac{\sin rL(\langle T\rangle - L)}{r\langle T\rangle} - L\cos rL(\langle T\rangle - L) - \frac{r\langle T\rangle L^2}{2}\sin rL(\langle T\rangle - L)\right], \qquad (3)$$

where $\sigma^2 = \langle T^2\rangle - \langle T\rangle^2$. The fourth term of the series expansion is zero if the thickness distribution function is symmetrical. The first term in Eq. (3) is just the right-hand term of Eq. (1) with the thickness equal to its average value. Since $\sigma^2/\langle T\rangle^2$ is always positive, the quantity in brackets will usually be negative except for the highest order coefficients. Thus, the fact that the thin films are not uniformly thick is manifested by the higher order Fourier coefficients falling below the values predicted for a uniform film with thickness $= \langle T\rangle$. Of course for the highest order terms, say $L \geq \langle T\rangle$, the second term can become positive so that the coefficients may be larger than those predicted by a uniform film.

As an example of the improvement in fit between theory and experiment, Fig. 12.2 compares results from Eq. (1) (solid line) and Eq. (3) (dashed line) with the experimental points for a typical film. Since Eq. (1) is symmetrical about $L = T/2$, it could not account for the decrease in the higher order coefficients. Note that in fitting Eq. (1) to the experimental points, one tends to choose a thickness $Ts < \langle T\rangle$ such that the experimental points lie above the calculated curve for the low-order coefficients and thus do not drop too much below the calculated curve for the higher order coefficients. This type of misfit is most noticeable for the (110) peak, since the lower order reflections are more sensitive to film thickness. The total-integrated-intensity measurement of the thickness gave a value of $Tr = 320$ A, which is exactly the value for the best fit using the series expansion to allow for nonuniform film thickness. In addition, the use of Eq. (1) gives rise to a larger strain gradient $4\pi B = 1.275\ A^{-2}$

compared to the value of 1.042 A^{-2} from Eq. (3). This difference arises because a large strain gradient helps cause the coefficients to decrease more rapidly to match the falloff of the experimental values. Hence, the evidence for the nonuniform film thickness lies in a better match between *Ts* and *Tr*, a better fit to the experimental coefficients, and less scatter in the value of the interplanar spacing at the oxide-air interface in comparison to Fig. 2 of ref. 9.

A similar Taylor's series expansion was made about $r = \langle r \rangle$, in which the thickness was assumed uniform but the strain gradient varied. Coefficients calculated from this model fell off too quickly for the (220) Bragg peak and did not fall off rapidly enough for the (110) peak. We concluded that the films are characterized by nonuniform thickness but that the variation in strain gradient is not large.

An Anomalous X-Ray Diffraction Line Shift for Thin Oxide Films

B. S. Borie C. J. Sparks, Jr.

As part of a joint research program with the Surface Reactions Group, we have for some time been studying the x-ray diffraction patterns of thin films of Cu_2O grown on copper single crystals.[8-10] The diffraction maxima are observed to be broad, partly because the films are thin and partly because they are strained by epitaxial forces. Most of the measurements have been made on films grown on either the 311 or the 110 face of the copper single crystal, in which cases the oxide grows with its 110 planes parallel to the interface. For this situation, with the usual diffractometer geometry, we may observe the 110 and 220 oxide reflections.

In many cases we find that the 110 reflection for the oxide occurs at a 2θ position inconsistent with that of the 220. The shift in $2\theta_{110}$ from that calculated from $2\theta_{220}$ may be as great as several tenths of a degree, and in general it is greater for thinner films. Also, the shift makes d_{110} appear to be less than $2d_{220}$. Described here is an explanation for this anomaly, which provides further insight into the structure of the film as manifested in its x-ray diffraction pattern.

Figure 12.3 illustrates schematically the stacking sequence of planes of atoms for a film whose normal is the 110 direction. We presume each plane to be perfect and to contain *M* copper atoms. Every other plane (those with *n* odd, say) also contains *M* oxygen atoms to maintain stoichiometry. The total number of planes *N* is taken to be even, so that the number of planes containing oxygen is equal to the number with only copper atoms. The average spacing of the planes, $\langle d_{220} \rangle$, determines $2\theta_{220}$. Because of epitaxially induced strain, the spacing of the planes is not constant but varies from a value somewhat larger than $\langle d_{220} \rangle$ at $n = 0$ to a smaller value at $n = N - 1$. For the sake of mathematical simplicity we assume this variation to be linear from one interface to the other. It is described in terms of a strain parameter *A*, which has been defined elsewhere.[8] Then, the scattered intensity in electron units along a line in reciprocal space in the 110 direction for such an assembly of planes is given by

$$I = M^2(f_{Cu}^2 + f_O f_{Cu}) \sum_{\text{all } n} \frac{\sin 2\pi h_3 An(N-n)}{4\pi h_3 An} \exp(2\pi i n h_3) + M^2 f_O^2 \sum_{n \text{ even}} \frac{\sin 2\pi h_3 An(N-n)}{4\pi h_3 An} \exp\{2\pi i n h_3 [1 - A(1 + 2f_{Cu}/f_O)]\} . \quad (4)$$

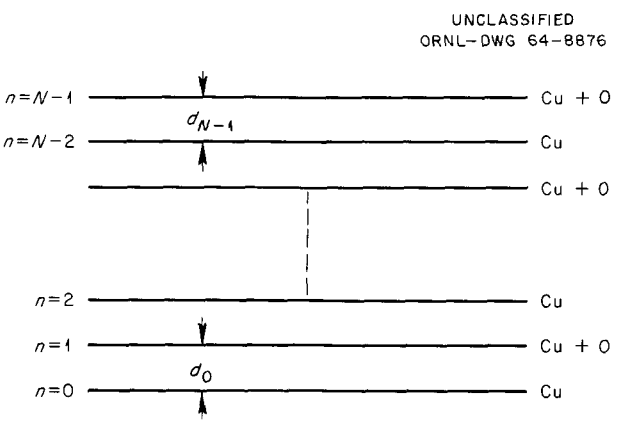

Fig. 12.3. A Schematic Illustration of the Stacking of 110 Planes of Cu_2O.

The atomic scattering factors of copper and oxygen are f_{Cu} and f_O. The continuous variable h_3 is given by $h_3 = 2\langle d_{220}\rangle \sin\theta/\lambda$ and is unity at $2\theta_{220}$.

The first series of Eq. (4) will give rise to broadened peaks at integral multiples of h_3. It will make no contribution near $h_3 = \frac{1}{2}$, the expected position of the 110 reflection. Because the second series of Eq. (4) is summed only over even values of the index n, it will cause peaks near integral multiples of $\frac{1}{2}h_3$. However, note that in the neighborhood of $h_3 = \frac{1}{2}$, the Bragg maximum resulting from this series will not occur precisely at that point, but at $h_3[1 - A(1 + 2f_{Cu}/f_O)] = \frac{1}{2}$. In terms of the more common quantities θ, the film thickness $T = N\langle d_{220}\rangle$, and Δd, the amount by which d_0 exceeds d_{N-1}, the line shift is given by

$$\Delta(2\theta) = (\Delta d/T)(1 + 2f_{Cu}/f_O)\tan\theta . \qquad (5)$$

For the 110 reflection of Cu_2O, this may be written in degrees

$$\Delta(2\theta) = 125\ \Delta d/T \text{ deg} . \qquad (6)$$

Note that $\Delta(2\theta)$ may be positive or negative depending on the sign of Δd. That it is always observed to be positive indicates that near the interface beginning with a copper plane, the interplanar spacing is larger than it is near the other surface terminating with a copper-plus-oxygen plane. If one makes the plausible assumption that the first plane of atoms to scatter coherently as a part of the oxide at the oxide-metal interface is a plane of copper atoms, this result tends to confirm the model for the strained oxide film that we proposed earlier.[9]

If one chooses N, the total number of planes, to be odd, so that the zeroth and $(N - 1)$th planes are identical, the theory predicts no shift in the position of the 110 reflection. Thus if all films begin with a copper plane at the oxide-metal interface and, for reasons at the moment unknown, sometimes terminate at the gas interface with a copper-plus-oxygen plane (N even), and sometimes with a copper plane (N odd), for different films the 110 reflection may or may not be shifted, as observed. If N is even over most of the surface of the film but odd over part of it, the 110 Bragg maximum would be shifted but would be asymmetric with a low angle tail. This also is frequently observed. In all cases theory predicts an essentially symmetric 220 reflection, which is consistent with our measurements.

We have not yet had occasion to apply the above described result in a systematic and quantitative way to our data. However, if we insert plausible values of Δd and T into Eq. (6), say $\Delta d = 0.05$ A and $T = 100$ A, we obtain $\Delta(2\theta) = 0.06°$, a shift in the range generally observed. We expect this interpretation of the 110 shift to contribute usefully to our effort to understand the structure of thin oxide films.

Part II.
Long-Range Applied Research

13. Fuel Element Development

G. M. Adamson, Jr.

The objective of the Fuel Element Development program remains the development of new or improved fabrication techniques for complete fuel elements and for fuel and cladding materials. We are studying a variety of materials, selected to include the best ones for use at temperatures over a wide range.

We are presently emphasizing vapor deposition as a fabrication technique for fuel element materials. Our ultimate goal is the fabrication of a fuel element by a one-step conversion process followed by forming an integral clad, both using the vapor-deposition method. To achieve this goal, efforts have been directed toward the preparation of UO_2 and refractory metals such as tungsten and tungsten alloys in shapes suitable for fuel element applications.

The vapor-deposition process consists essentially of the pyrolytic decomposition or thermochemical reduction of volatile compounds on a heated surface. Since many metal halides are sufficiently volatile to be transferred as gases at low temperatures, these compounds are well suited to use in vapor-deposition techniques. Particular advantages of vapor deposition are the relatively low temperatures and simple equipment that are required as compared to those required for the usual fabrication procedures for refractory metals and compounds. In addition, the process shortens the path from basic raw materials to the finished product and thus may lead to the development of a low-cost fuel cycle.

Improvements in fuel materials are also being sought by improved sintering techniques and development of new fabrication practices. Dispersion hardening is being pursued as a method for improving the strength of cladding materials, primarily the refractory metals.

DEPOSITION OF REFRACTORY URANIUM COMPOUNDS

R. L. Heestand C. F. Leitten, Jr.

Several systems for direct conversion of UF_6 to a refractory fuel compound have been studied. A hot-electrode cold-wall reaction chamber similar to that used for deposition of carbides was used in early survey experiments.[1] However, the reduction always stopped with the formation of UF_4, which condensed on the chamber walls. The only reactions attempted in the cold-wall apparatus were combinations of (1) UF_6, H_2, and CH_4, and (2) UF_4, NH_3, and CH_4. The first combination yielded UF_4 up to 2000°C, and the second combination yielded UF_4 and an unidentified compound of uranium with carbon and nitrogen at 1300°C.

A hot-wall-tube reaction chamber was assembled for reduction-hydrolysis of UF_6 to UO_2 according to the reaction,

$$UF_6 + 2H_2O + H_2 \rightarrow UO_2 + 6HF.$$

This reaction has been proven thermodynamically feasible when accomplished in two steps[2] at atmospheric pressure and at temperatures below 650°C:

$$UF_6 + 2H_2O \rightarrow UO_2F_2 + 4HF$$

[1] R. L. Heestand and C. F. Leitten, Jr., *Metals and Ceramics Div. Ann. Progr. Rept. May 31, 1963*, ORNL-3470, pp. 75–78.

[2] I. E. Knudsen, H. E. Hootman, and N. M. Levitz, *A Fluid-Bed Process for the Direct Conversion of Uranium Hexafluoride to Uranium Dioxide*, ANL-6606 (February 1963).

and

$$UO_2F_2 + H_2 \rightarrow UO_2 + 2HF.$$

However, the resulting UO_2 was of too low density and contained too much fluorine to be of commercial interest.

We are performing experiments on the single-step reduction of UF_6 to determine the effects of proportions of UF_6, H_2O, and H_2 on the reaction products.

DEPOSITION OF TUNGSTEN ALLOYS

J. I. Federer C. F. Leitten, Jr.

Our previous success in the fabrication of tungsten by vapor-deposition techniques[1] has led to a new program directed toward the study and characterization of vapor-deposited tungsten, reported in Chap. 19, this report.

We have shifted our efforts to studies of the feasibility of fabricating tungsten alloys by direct thermochemical deposition techniques. The specific goal is to determine the deposition parameters that will yield homogeneous alloys of a desired composition within a particular system. Alloy constituents of interest include vanadium, niobium, tantalum, titanium, zirconium, hafnium, and rhenium. Alloys containing about 25% Re are of immediate interest; we do not expect to be concerned with the other elements in contents that exceed a few percent. We are depositing these alloys, like pure tungsten, from volatile halides.

Certain elements can disrupt the typical columnar grain structure and promote a fine-grained structure in tungsten deposits. An example of this effect is shown in Fig. 13.1. This tungsten deposit was prepared at 800°C and was previously reported as being a temperature effect. However, higher purity WF_6 produced columnar grains at all deposition temperatures. Chemical analysis revealed that the fine-grained specimen contained 80 ppm V and 40 ppm C, the vanadium arising from a contaminant in the WF_6. We now tentatively attribute the fine-grained structure shown in Fig. 13.1 to the vanadium impurity. Vanadium, which has a high affinity for both carbon and oxygen, may have deposited as minute carbide or oxide particles and, in some manner, caused nucleation of new tungsten grains. Other reactive solutes, such as those elements previously mentioned, may behave in a similar manner.

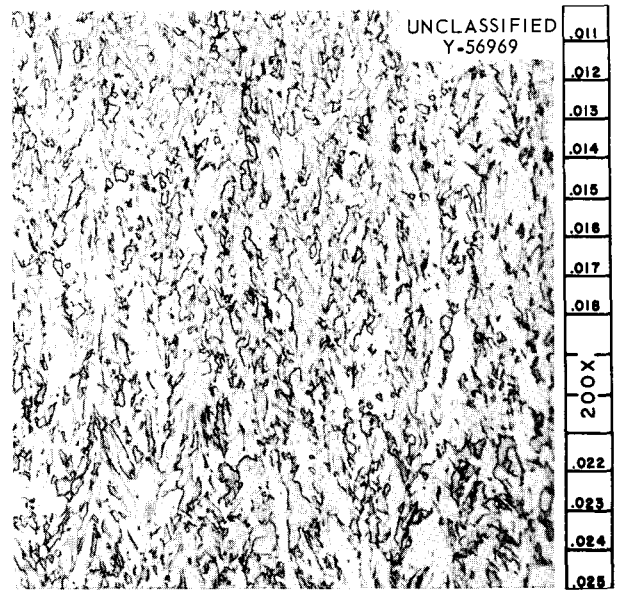

Fig. 13.1. Fine-Grained Structure in Vapor-Deposited Tungsten. Etched in equal volumes concentrated NH_4OH and 30% H_2O_2. 200×.

Our main effort so far has been directed toward the deposition of tungsten-rhenium alloys. A mixture of 29% ReF_6 in WF_6 was prepared by distilling the gases into a common container. Vapor deposition was then conducted under the following conditions: 700°C, 10 torr, 70 moles H_2 per mole of combined fluorides. Good quality deposits were prepared on a tubular copper substrate. The surface texture was smooth, resembling vapor-deposited tungsten. However, the composition and thickness varied along the length of these tubular deposits. In a single deposit, the rhenium content varied from 1.7 to 35.5% over a distance of 10 in. The highest rhenium content and the thickest deposits occurred near the inlet to the reaction zone.

The grain structure of tungsten-rhenium alloy deposits depended upon the rhenium content, becoming less columnar with increasing rhenium content. Figure 13.2*a* compares a specimen containing 6% Re, having a mostly columnar grain structure resembling vapor-deposited tungsten, with a specimen (Fig. 13.2*b*) containing about 22% Re, in which the columnar structure was not dominant, although still present. These preliminary results indicated that the grain structures of

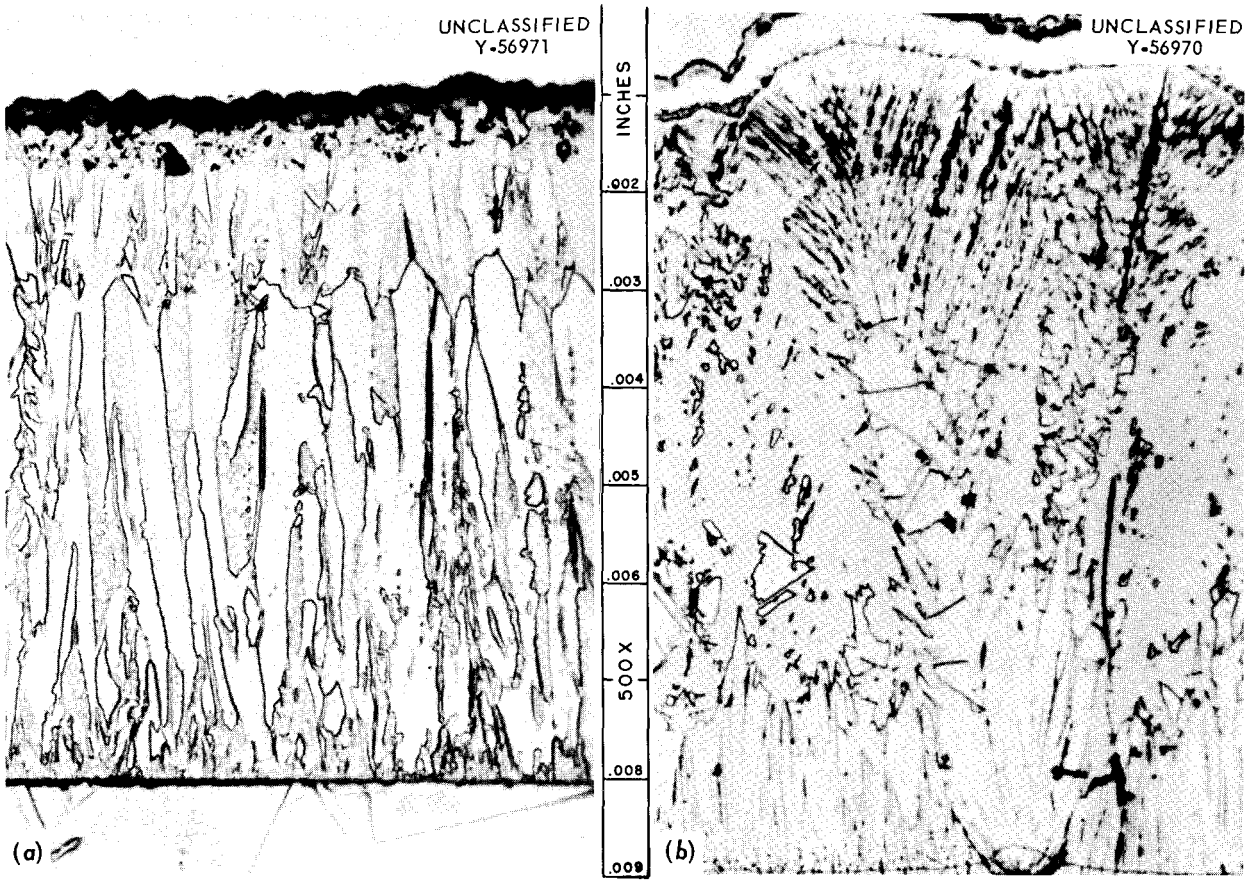

Fig. 13.2. Vapor-Deposited Tungsten-Rhenium Alloys. (*a*) W–6% Re alloy showing columnar grain structure; (*b*) W–22% Re alloy. Etched in equal volumes of concentrated NH_4OH and 30% H_2O_2. 500×.

vapor-deposited tungsten-rhenium alloys will be radically different from those in pure vapor-deposited tungsten. Indeed, approximately equiaxed grain structures may possibly be obtained by control of the deposition parameters.

Since uniform and homogeneous tungsten-rhenium deposits would be expected in the temperature range in which the constituent elements deposit uniformly, we have started to investigate the deposition characteristics of pure rhenium. To avoid corrosion of glass and Kel-F flowmeters by ReF_6, the fluoride was transferred from the supply cylinder directly to the reaction site in a metered stream of hydrogen. The ReF_6 concentration was controlled by its vapor pressure. In the temperature range of 500 to 800°C at a hydrogen flow rate of 3000 cm^3/min and a pressure of 10 torr, the thickness of rhenium deposits was very nonuniform. Thick nodular deposits, shown in Fig. 13.3, occurred near the inlet to the reaction zone, indicating that ReF_6 was readily reduced under these given conditions. The deposit consisted of coarse columnar grains having considerable grown-in porosity at the grain interfaces. Farther downstream the deposits were much smoother in surface texture, although columnar in grain structure. Lowering the temperature to 400°C and decreasing the hydrogen flow to 2000 cm^3/min eliminated the nodular growth near the inlet of the reaction furnace and resulted in a uniform deposit.

Thus, rhenium deposits of uniform thickness were obtained at 400°C, whereas uniform tungsten deposits (see Chap. 19, this report) were obtained at 500 to 600°C. Since nonuniform and heterogenous tungsten-rhenium deposits were obtained at 700°C, these results indicate that better quality alloy deposits will be obtained at lower temperatures at which the two elements deposit uniformly. We are now conducting codeposition experiments at lower temperatures to confirm this hypothesis.

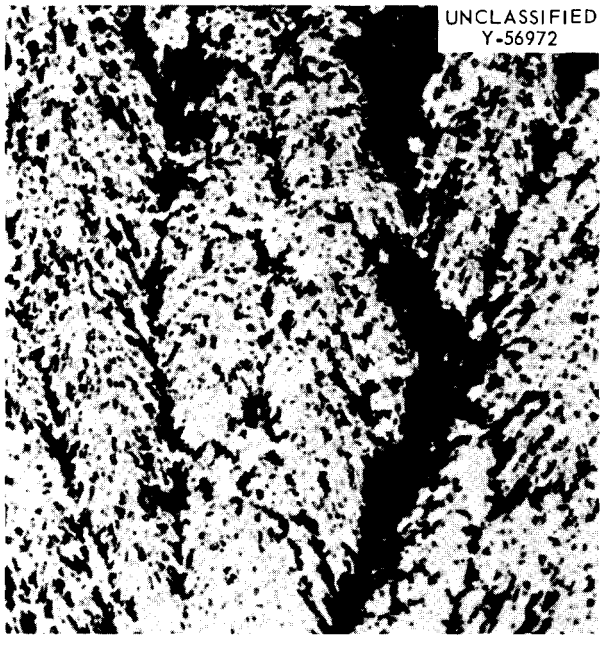

Fig. 13.3. Nodular Rhenium Deposit. Etched in equal parts of concentrated NH_4OH and 30% H_2O_2. 500×.

THERMOCHEMICAL PREPARATION OF CARBIDES

R. L. Heestand J. I. Federer
C. F. Leitten, Jr.

Thermochemical deposition has been investigated as an approach to fabrication of high-quality metal carbides. We have studied deposition parameters of boron-carbon alloys and silicon carbide in the interest of fabricating free-standing shapes and coatings for high-temperature use.[3] Both carbides have application in the nuclear field. Boron carbide is of interest as a neutron-absorbing material due to the high thermal-neutron absorption cross section of boron. The good high-temperature oxidation resistance of silicon carbide promotes the use of this carbide as a fuel coating or cladding material.

In general, these carbides are produced under reduced pressure (10 to 100 torr) by the reduction of the appropriate halides by hydrogen in the presence of a hydrocarbon. Optimum results for deposition of both carbides were obtained in the temperature range of 1200 to 1350°C. Due to differences in their behavior, they will be discussed separately.

We obtained boron-carbon alloys with boron contents ranging from 19 to 81%. Table 13.1 shows the composition of deposits for several different temperatures, pressures, and gas ratios. At constant temperature (1325°C), pressure (35 torr), and flow rates of BCl_3 (30 cm^3/min) and CH_4 (80 cm^3/min), the composition varied from 44 to 65% B as the hydrogen flow rate increased from 1000 to 2960 cm^3/min. Under the same conditions, except for a CH_4 flow rate of 50 cm^3/min, the composition of the deposit varied from 37 to 72% B as the hydrogen flow rate increased from 500 to 2200 cm^3/min.

Temperature also strongly influences the boron content of the deposit. Lowering the temperature from 1325 to 1275°C results in an increase from 72 to 82% B with other conditions being constant. Deposition rates were highly reproducible for any given set of deposition conditions, but varied between 10 and 25 mils/hr for 70 and 50% B respectively. The lack of material balances in Table 13.1 for some of the analyses may be attributed to analytical errors.

Attempts to determine the microstructure of pyrolytic boron carbide have been unsuccessful at present due to the inert nature of the material. Figure 13.4 represents a spectrum of the as-polished structures available. This specimen demonstrates depositing a structure of composition varied by stepwise increases in temperature. The composition varied continuously from 76% B at the outer surface to 50% B at the inner surface. As anticipated, a large hardness difference accompanies the change in composition. Knoop hardnesses (1-kg load) have been measured at 2340 for 72% B and 327 for 44% B. On examination by x-ray diffraction analysis, the material appears to be crystalline with randomly oriented fine grains.

Larger samples were made in a resistance furnace using the same temperatures, pressures, gas ratios, and flow rates to obtain comparable deposits. Figure 13.5 is the end view of a ½-in.-

[3] R. L. Heestand, J. I. Federer, and C. F. Leitten, Jr., *Thermochemical Preparation and Properties of Carbides for Nuclear Applications*, paper to be presented at the AIME Symposium on Compounds of Interest in Nuclear Reactor Technology, Boulder, Colo., Aug. 3–5, 1964, and published by the AIME in a special symposium volume.

Table 13.1 Analyses and Conditions for Deposition of Boron-Carbon Deposits

Boron (wt %)	Carbon (wt %)	Temperature (°C)	Pressure (torrs)	BCl_3 (cm^3/min)	CH_4 (cm^3/min)	H_2 (cm^3/min)
19	81	1350	15–25	30	135	
37.2	60.6	1325	35	30	50	500
43.8	47.2	1325	35	30	80	1000
48.2	50.0	1325	100	30	80	2220
49.2	47.5	1400	35	30	80	2220
59.1	34.9	1325	35	30	80	1800
63.4	31.7	1280	35	30	80	2960
65.3	27.8	1325	35	30	80	2960
66.4	32.6	1325	45	30	80	2960
68.0	29.0	1325	35	30	80	2960
68.2	31.0	1325	40	30	60	2960
69.6	29.4	1280	35	30	80	2960
69.7	26.3	1325	35	30	50	2220
70.5	29.5	1325	40	30	80	2960
72.4	26.7	1325	35	30	50	2220
68.2	30.0	1290	35	30	50	2220
68.7	29.2	1300	35	30	70	2220
76.8	23.2	1275	40	30	50	2220
81.4	17.7	1275	20	20	50	2220
81.0	18.3	1250	20	20	50	2220
81.7	17.1	1250	10	10	50	1400
81.1	18.2	1200	10	10	50	1400
80.7	18.1	1150	10	10	50	1400

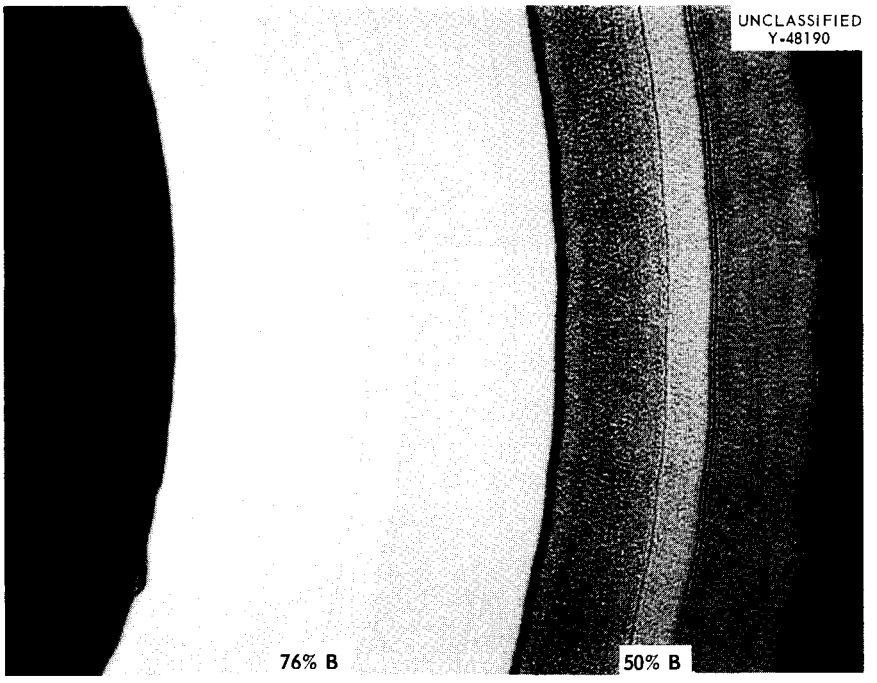

Fig. 13.4. Boron-Carbon $\frac{1}{8}$-in.-ID Tube Deposit 0.040 in. Thick Showing Programmed Composition Change. 100×. Reduced 18%.

diam, 0.030-in.-wall B_4C tube, which was deposited at 1300°C in 4 hr on the inside surface of a graphite tube. The graphite was readily removed, leaving the free-standing tube.

Silicon carbide has been deposited at a rate of approximately 10 mils/hr according to the conditions shown in Table 13.2. Clearly, variations of temperature and hydrogen ratio have little effect on composition. Stoichiometry was generally favored throughout the range of conditions under which continuous deposits were obtained. Deposits formed below 1200°C were nonuniform, while above 1350°C groups of needle-like crystals formed.

Studying the microstructures of silicon carbide was difficult. The as-polished material appeared to be single phase and was not readily etched in acids or fused sodium carbonate. The hardness of the silicon carbide deposits was 2745 Knoop with a 1-kg load. X-ray analyses also indicated that vapor-deposited silicon carbide was crystalline with randomly oriented fine grains.

Coatings of silicon carbide deposited on graphite, tungsten, and alumina were adherent and withstood thermal cycling; however, full evaluation has not been completed.

We have established parameters for deposition of both boron carbide and silicon carbide, and we shall conduct similar studies on other carbides of interest for high-temperature applications.

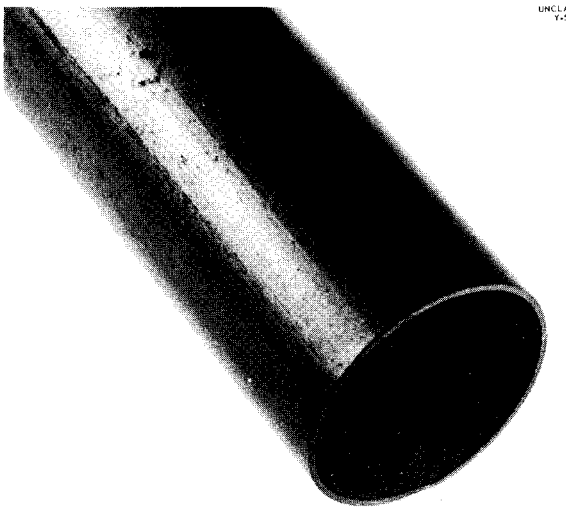

Fig. 13.5. Boron Carbide Tube ½ in. diam × 0.030 in. wall. 3×. Reduced 57%.

FABRICATION OF ALUMINUM-BASE IRRADIATION TEST PLATES

M. M. Martin W. J. Werner

In conjunction with the Phillips Petroleum Company, we are fabricating a series of aluminum-base miniature fuel plates to be used for determining the influence of high-temperature irradiations to high burnup on the dimensional and chemical stability of U_3O_8 and UO_2 dispersions. The final design specifications and the actual rolling parameters used to achieve the core dimensions are presented in Table 13.3. The fissile materials are particles of U_3O_8 and niobium-coated UO_2–15 wt % ZrO_2 dispersed in matrices of X8001 aluminum and roll bonded at 500°C with Alclad 6061 aluminum. Both standard and instrumented plates are included in the program. The instrumented plates are identical in length and width to the standard plates but are thicker and contain two

Table 13.2. Analyses and Deposition Conditions of Pyrolytic Silicon Carbide

	Si (wt %)	C (wt %)	Temperature (°C)	Pressure (torrs)	CH_4 (cm^3/min)	H_2 (cm^3/min)	$SiCl_4$ (cm^3/min)
SC-7	75.03	25.70	1300	100	80	2200	35
SC-8	68.85	29.21	1300	100	80	Varied	35
SC-11	69.62	29.38	1300	100	80	2960	35
SC-12	68.78	29.63	1250	100	80	2960	35
SC-13	70.74	26.68	1300	100	80	2220	35
SC-14	73.27	28.20	1300	100	80	2220	35
SC-24	69.75	30.48	1250	100	80	2960	35

Table 13.3. Design Specification of Miniature Fuel Plates for High-Temperature, High-Burnup Irradiations

	Sample Plates		Instrumented Plates	
	Core A	Core B	Core A	Core B
Materials				
Cladding	Alclad 6061 Al	Alclad 6061 Al	Alclad 6061 Al	Alclad 6061 Al
Frame	Alclad 6061 Al	Alclad 6061 Al	6061 Al	6061 Al
Dispersoid				
Loading	U_3O_8 (42 wt %)	63 wt % Nb-coated UO_2-ZrO_2	U_3O_8 (43 wt %)	64 wt % Nb-coated UO_2-ZrO_2
Particle size	(−170 +325)	(−200 +230)	(−170 +325)	(−200 +230)
Matrix (−100 mesh)	X8001 Al	X8001 Al	X8001 Al	X8001 Al
Number of plates	7	6	1	1
Number of cores per plate	1	1	2	2
Loading of ^{235}U, g	2.205 ± 1%	2.205 ± 1%	2.205 ± 1%	2.205 ± 1%
Plate dimensions, in.				
Length	5.750 ± 0.003	5.750 ± 0.003	5.750 ± 0.003	5.750 ± 0.003
Width	1.250 ± 0.003	1.250 ± 0.003	1.250 ± 0.003	1.250 ± 0.003
Thickness	0.050 ± 0.003	0.050 ± 0.003	0.150 ± 0.003	0.150 ± 0.003
Core dimensions, in.				
Length	5.470 ± 0.061	5.470 ± 0.061	5.250 ± 0.250	5.250 ± 0.250
Width	1.000 ± 0.031	1.000 ± 0.031	1.000 ± 0.031	1.000 ± 0.031
Thickness	0.020 ± 0.003	0.020 ± 0.003	0.010 ± 0.003	0.010 ± 0.003
Rolling schedule, %				
Spread	3.90	3.30	4.0	4.3
Densification	4.30	3.10	5.0	4.5
Elongation	86.40	86.66	86.3	86.3
Total reduction in thickness	87.50	87.50	87.5	87.5

0.010-in.-thick cores per plate with provision for inserting a thermocouple in the aluminum between the cores.

The general appearance of the various fabricated dispersions is shown in Fig. 13.6. The degree of fragmentation and stringering of the dead-burned U_3O_8 and high-fired UO_2 particles, illustrated in Figs. 13.6*a* and 13.6*b*, respectively, are characteristic of these irregularly shaped materials when roll bonded at 500°C with a hot reduction of 84% and a cold reduction in thickness of 20%.

The quality of these dispersions of irregularly shaped U_3O_8 and UO_2 is satisfactory for operation in high-flux, high-power density test reactors. However, further improvements in particle integrity were achieved, as shown in Fig. 13.6c, by use of spherical coated particles of UO_2-ZrO_2 solid solution. No degradation of the individual spherical particles could be observed after the dispersion had been fabricated in the same manner as those bearing irregularly shaped U_3O_8 and UO_2. The distribution of the spherical particles, however, resulted in localized fuel concentrations in excess of those that were encountered in dispersions of equivalent uranium loading containing finer U_3O_8 particles. We are presently studying blending to minimize localized fuel concentrations.

The use of coated-particle fuel in aluminum-base dispersions is being explored primarily to minimize the previously observed[4] chemical reactions that take place under irradiation between the

[4]A. E. Richt, C. F. Leitten, Jr., and R. J. Beaver, "Radiation Performance and Induced Transformations in Aluminum-Base Fuels," p. 469 in *Research Reactor Fuel Element Conference, September 17–19, 1962, Gatlinburg, Tennessee*, TID-7642, Book 2 (1963).

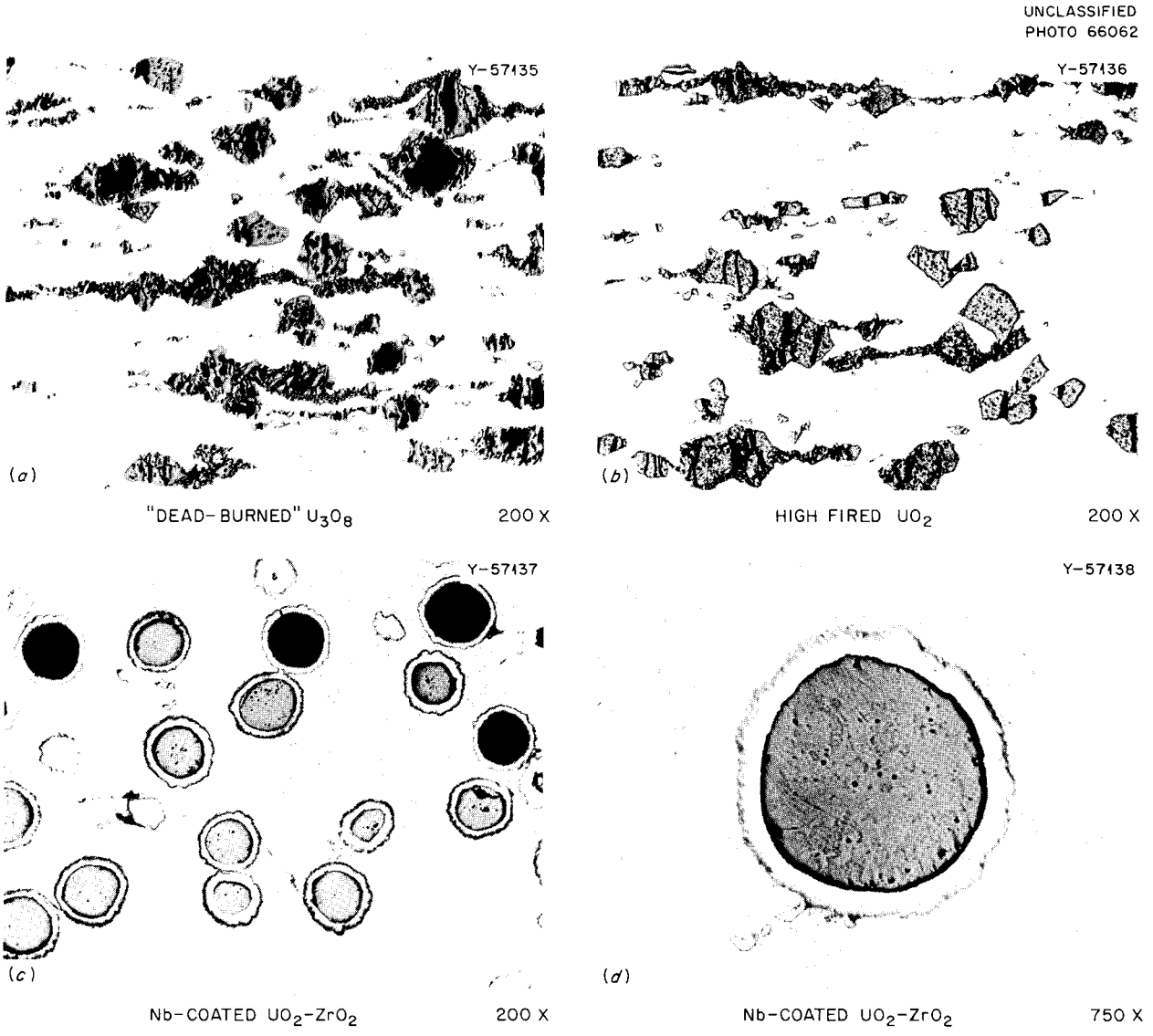

Fig. 13.6. Longitudinal Sections of Developmental Dispersions in Standard Test Plates Rolled at 500°C to an 87.5% Reduction in Thickness, Contrasting the Integrity of an Aluminum-Base Coated-Particle Dispersion to More Conventional Fuels. Reduced 40%.

oxide particles and the matrix. Although these reactions apparently will not cause difficulty under conditions being proposed for present high-performance reactors, this may not be the case with future reactors intended for even higher performance. The metastable nature of the dispersions and the large gas releases that could accompany the reactions under irradiation potentially restrict their use in very high performance test reactors. We have shown that the integrity of a niobium coating on UO_2-ZrO_2 particles can be maintained during fabrication, thus preventing the exposure of the oxide fuel particle to the aluminum matrix. An example of the integrity of the oxide particle coating is shown in Fig. 13.6*d*. We plan heat treatment and irradiation tests to evaluate the effectiveness of the coating in preventing the oxide-aluminum reactions.

HYDROGEN-ABSORPTION STUDIES IN THE WATER-VAPOR ALUMINUM SYSTEM

M. M. Martin

For the past several years, the tendency for blister formation above 500°C has been unpredictable in fuel plates clad with type 6061 aluminum. We have revealed a marked change in the oxide film on this material when it is heated above 515°C in air.[5] However, a quantitative interpretation of the results has been difficult because of the interdependency of blistering on time, temperature, humidity, initial hydrogen content, and surface oxide condition.

Recent studies have suggested that blistering is more sensitive to the water-vapor content of customary annealing atmospheres than previously thought. We are investigating hydrogen absorption by type 6061 aluminum to determine the influence of the parameters (time, 2 to 10 hr; temperature, 450 to 550°C; annealing-air dew point, 0 to 34°C; and initial surface oxide thickness, 20 to 200 μ) on the hydrogen content of the material and to interpret the results in terms of a hydrogen-absorption-blistering mechanism.

FABRICATION OF URANIUM CARBIDE WITH UBe_{13} SINTERING AID

J. P. Hammond

The high thermal conductivity and uranium density of uranium carbide coupled with its good irradiation stability makes this material a desirable fuel for advanced reactor systems. However, production of dense bodies by conventional methods requires excessively high temperatures and still fails to give an entirely satisfactory product. We previously described a method using a sintering aid removable by volatilization[6] for sintering the carbide to high density at substantially lower temperature. This method used $7\frac{1}{2}$ wt % UAl_2 as the additive. Because aluminum must be removed by evaporation, best results were achieved with small batch sizes and pellet diameters below $\frac{5}{16}$ in.

In the past year, we found a method for achieving comparable sintering results without the limitation on batch or pellet size. By using powders prepared from arc-cast uranium monocarbide with approximately $\frac{3}{4}$ wt % UBe_{13} as the sintering aid, 95% of theoretical density was achieved by vacuum sintering in a tungsten-lined tantalum crucible at 1525°C. The UBe_{13} was dissolved within the uranium carbide during sintering. Chemical analyses showed the compacts were stoichiometric in carbon and retained much of the beryllium.

Investigating the UC-UBe_{13} system, we found a quasi-binary phase diagram with a eutectic occurring at 1610°C at 32 wt % UBe. Figure 13.7 shows the UC-rich portion of this diagram (determined metallographically), with theoretical densities obtained by sintering at various temperatures with various UBe_{13} contents superimposed.

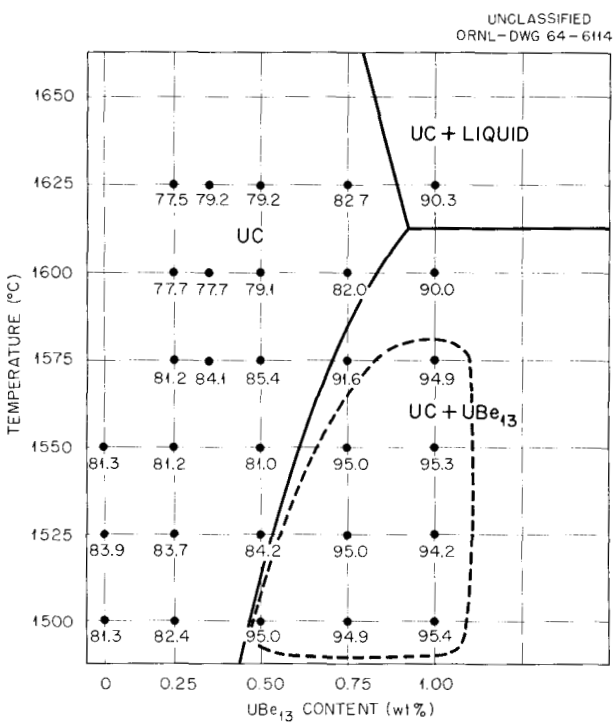

Fig. 13.7. Sintered Density of UC-UBe_{13} System in Relation to Solvus. Densities (percent of theoretical) are average of duplicate tests. Enclosed area indicates optimum sintering conditions.

[5] M. M. Martin and R. L. Heestand, *Metals and Ceramics Div. Ann. Progr. Rept. May 31, 1962*, ORNL-3313, p. 84.

[6] J. P. Hammond, J. D. Sease, and C. Hamby, Jr., "Uranium Monocarbide Fabrication with UAl_2 as Sintering Aid," pp. 145–53 in *The Fourth Uranium Carbide Conference, East Hartford, Connecticut, May 20–21, 1963*, TID-7676 (1964).

We see that the best density is obtained below the eutectic platform and just to the right of the solvus. Figure 13.8 shows a typical microstructure of a compact sintered in this region. Highest density was obtained for UC charged at the 4.8% C level, with the density decreasing rapidly with increasing carbon content. High oxygen and nitrogen contents in the UC charge also impaired densification. Densities as high as those obtained in that region were also achieved for compositions within the solubility limit when a small amount of external silicon vapor was provided along with the beryllide addition.

We believe the primary factor contributing to sintering when fabricating with uranium beryllide as an aid is a scavenging effect. Beryllium vapor appears to permeate the compact during the early stage, reducing the surface oxide responsible for inhibiting the sintering of the particles.

In supplemental experiments, we introduced beryllium vapor externally to the compact as the sintering aid. Sintering for 3 hr at 1600°C aided by beryllium vapor gave densities in excess of 92% of theoretical, whereas unaided uranium carbide sintered only to 89% of theoretical. The intermediate density possibly resulted from sintering and sealing of the surface before the center had been scavenged.

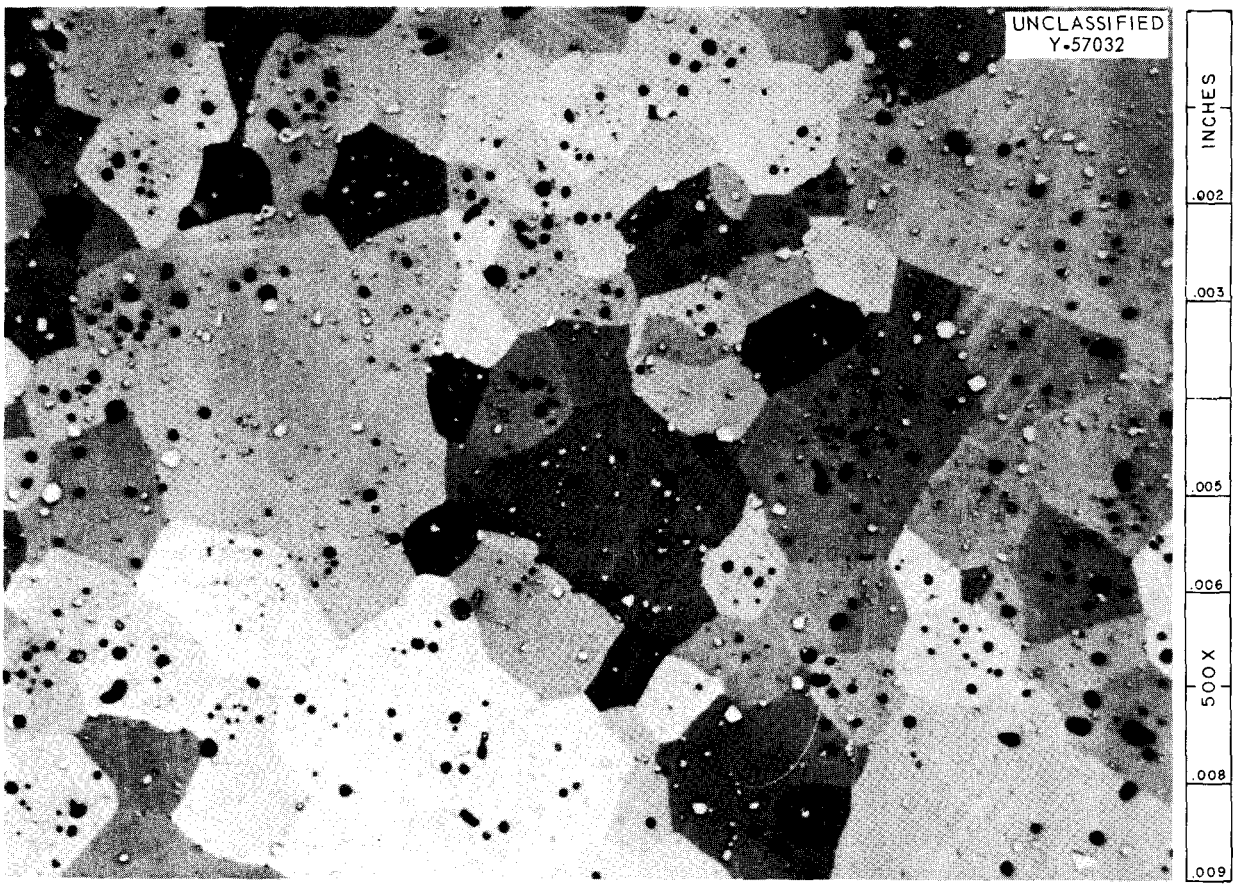

Fig. 13.8. Microstructure of UC–1.0 wt % UBe_{13} Sintered in Vacuum 3 hr at 1550°C. Density is 95.3% of theoretical. Secondary constituent is UBe_{13}. Etched with equal parts concentrated HNO_3, acetic acid, and H_2O. 500×.

14. High-Temperature Materials

W. C. Thurber

The goal of the High-Temperature Materials Program is to develop an advanced materials technology on a sufficiently broad base and an appropriate time scale so that engineers concerned with the design and development of advanced reactor systems will have sufficient information on high-temperature materials when required. This should greatly reduce the amount of development needed for specific systems and accelerate their realization. Within this broad framework we have focused our attention on those high-temperature systems that will require refractory metals for the containment of molten alkali metals. The program includes development and inspection of refractory-metal tubing, studies of joining methods, measurement of the mechanical and physical properties of refractory alloys, studies of physical metallurgy, and an appraisal of the compatibility of refractory metals with alkali metals. Significant portions of this work are covered in detail elsewhere.[1,2]

Table 14.1. Compositions of Refractory-Metal Alloys

Designation	Base	Additives (wt %)
Armour alloy	Niobium	39 V, 1 Ti
B-66	Niobium	5 Mo, 5 V, 1 Zr
C-129Y	Niobium	10 Hf, 10 W, 0.1 Y
Cb-752	Niobium	10 W, 2.5 Zr
D-43	Niobium	10 W, 1 Zr
FS-85	Niobium	27 Ta, 10 W, 1 Zr
T-111	Tantalum	8 W, 2 Hf
TM	Molybdenum	0.5 Ti
TZM	Molybdenum	0.5 Ti, 0.08 Zr

In the text that follows, frequent reference is made to commercial refractory-metal alloys by their trade designations. The nominal compositions of these alloys are listed in Table 14.1.

JOINING OF REFRACTORY MATERIALS

G. M. Slaughter

Welding of Advanced Refractory Alloys

R. G. Donnelly

We are investigating the general weldability of five advanced refractory-metal alloys (D-43, T-111, FS-85, B-66, and C-129Y). Primarily, we are determining and comparing (1) transition-temperature curves for longitudinal face bends ($4T$ bend radius, where T is the sheet thickness), (2) minimum bend radius at room temperature, and (3) room-temperature bend ductility of aged welded specimens of each alloy. Each type of weld (automatic gas tungsten-arc, manual gas tungsten-arc, and electron beam) has been evaluated by radiographic, dye-penetrant, and metallographic inspection as well as by chemical analysis for interstitial impurities. We found that sound welds could be produced in all alloys by each method. One marginal case was the B-66 alloy, which we found would hot-tear on the weld center line unless the specimen blanks were tack-welded securely beforehand. Conditions for welding each alloy are presented in Table 14.2.

The transition-temperature curves are presented in Fig. 14.1. Usually, the transition temperature

[1] W. C. Thurber, ORNL-3571, pp. 93–156, May 1964 (classified).

[2] W. C. Thurber, ORNL-3683, in press (classified).

increased in the order of electron beam, automatic gas tungsten-arc, and manual gas tungsten-arc respectively. However, in C-129Y the bend-transition curve for the electron-beam welded alloy is the same as for the unwelded material, and in D-43 the manual and automatic (10 in./min) gas tungsten-arc curves are approximately the same.

The transition curves for D-43 suggest that increasing the welding speed improves the ductility of the weld, although more data will be required to determine the magnitude of this improvement. The least ductile welds produced in this study were the manual gas tungsten-arc welds in B-66; the room-temperature bend specimen cracked after 100° of bending.

We have not yet tested any specimens in the range of −73 to −196°C, but we plan to in order to more closely define the transition temperature

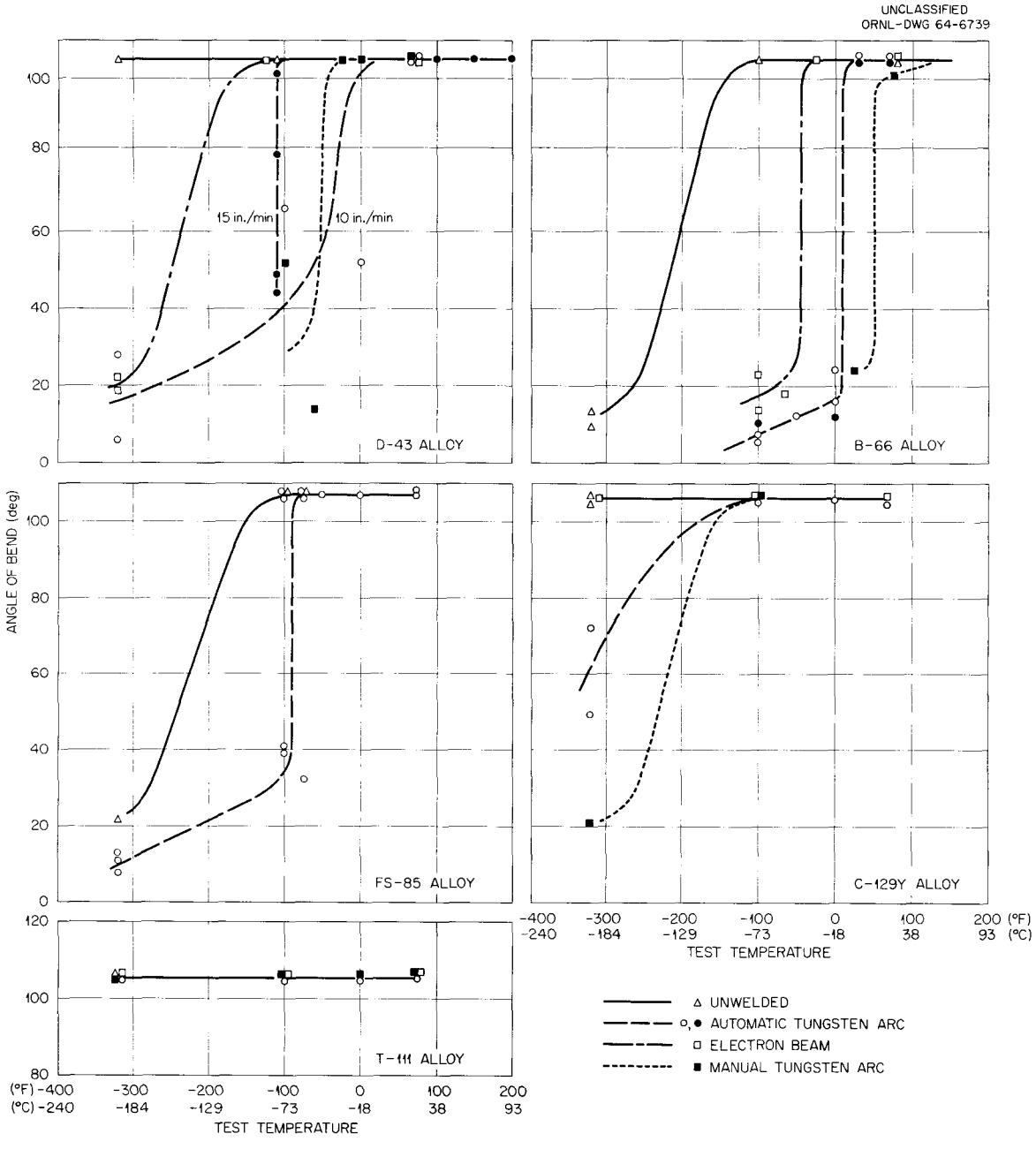

Fig. 14.1. Bend Transition Curves of Welds in Refractory-Metal Alloys D-43, B-66, FS-85, C-129Y, and T-111. Points plotted at 105° indicate completion of the test without failure (4*T* punch radius, 0.5-in./min deflection rate).

Table 14.2. Welding Conditions for Refractory-Alloy Sheet Specimens

Alloy	Sheet Thickness (in.)	Automatic Gas Tungsten-Arc (argon gas, 9-v arc)		Electron Beam (30 in./min)		Manual Gas Tungsten-Arc (argon gas)	
		Welding Speed (in./min)	Welding Current (amp)	Welding Current (ma)	Voltage (kv)	Welding Speed (in./min)	Welding Current (amp)
D-43	0.060	15	210–240				
	0.060	10	200–240	6.5	130	~3	140–150
B-66	0.060	10	190–240	4.5	130	~3	140–150
FS-85	0.050	10	165–175			~4	155–180
C-129Y	0.030	10	70–100	3.5	130	~6	~80
T-111	0.060	10	245–260	6.8	120	~3	190–220

for the specimens that are ductile at −73°C but brittle at −196°C.

We are determining the minimum radius at which the welded alloys can be bent at room temperature at a deflection rate of 0.5 in./min without failure. Like the unwelded alloys, all five alloys with electron-beam welds survived 1*T* bends (radius equal to thickness). The same was true of the alloys T-111, C-129Y, and FS-85 welded by the automatic gas tungsten-arc method, while the alloys D-43 and B-66 required a 2*T* radius. We have not yet tested the alloys welded by the manual gas tungsten-arc method.

We are studying aging in these alloys, and we have completed the basic screening process of aging weldments at 815, 980, and 1205°C for 1, 2, 25, and 100 hr for the three alloys D-43, B-66, and C-129Y. The preliminary results are presented in Fig. 14.2. Here the term ductile means that the specimen survived a full 4*T* bend (105°) at a deflection rate of 0.5 in./min, while brittle means that the specimen cracked before a full bend was attained. In each case an aging reaction is apparent, although the parameters vary. As a result of this study, we shall investigate aging and overaging further, including metallographic examination to provide a more complete understanding of the metallurgical reactions extant. Similar studies on T-111 and FS-85 alloys are in progress.

Brazing Alloy Development

R. G. Gilliland

An application of brazing currently under study requires the joining of potential fin and armor materials, such as pyrolytic graphite and beryllium, to the niobium or stainless steel condensing tubes of space radiators. Aside from the usual difficulties involved with wetting and flow on the composite materials, the markedly different expansion coefficients of the dissimilar materials make the attachment problems particularly troublesome. The brazed joints often tend to separate upon cooling from the brazing temperature.

To combat the problem of thermal expansion, a novel design for producing a sound dissimilar joint is currently being studied. A pin or rivet is placed through a hole in the beryllium or pyrolytic graphite so that after brazing the parts are mechanically locked. Using this design, we brazed finned beryllium tubes to two stainless steel liner tubes. Such a joint is shown in Fig. 14.3. Also, a specimen with the finned beryllium tube brazed to a niobium liner tube is shown in Fig. 14.3. The experimental brazing alloy 49% Ti–49% Cu–2% Be was used in each case.

No joint cracks could be seen in the stainless steel-to-beryllium joint. However, numerous fillet cracks were observed in the niobium-to-beryllium

joint; these probably were caused by the large difference in coefficients of expansion. One of the stainless steel-to-beryllium joints and the niobium-to-beryllium joint are being nondestructively examined for nonbonding. The other stainless steel-to-beryllium joint is being evaluated metallographically.

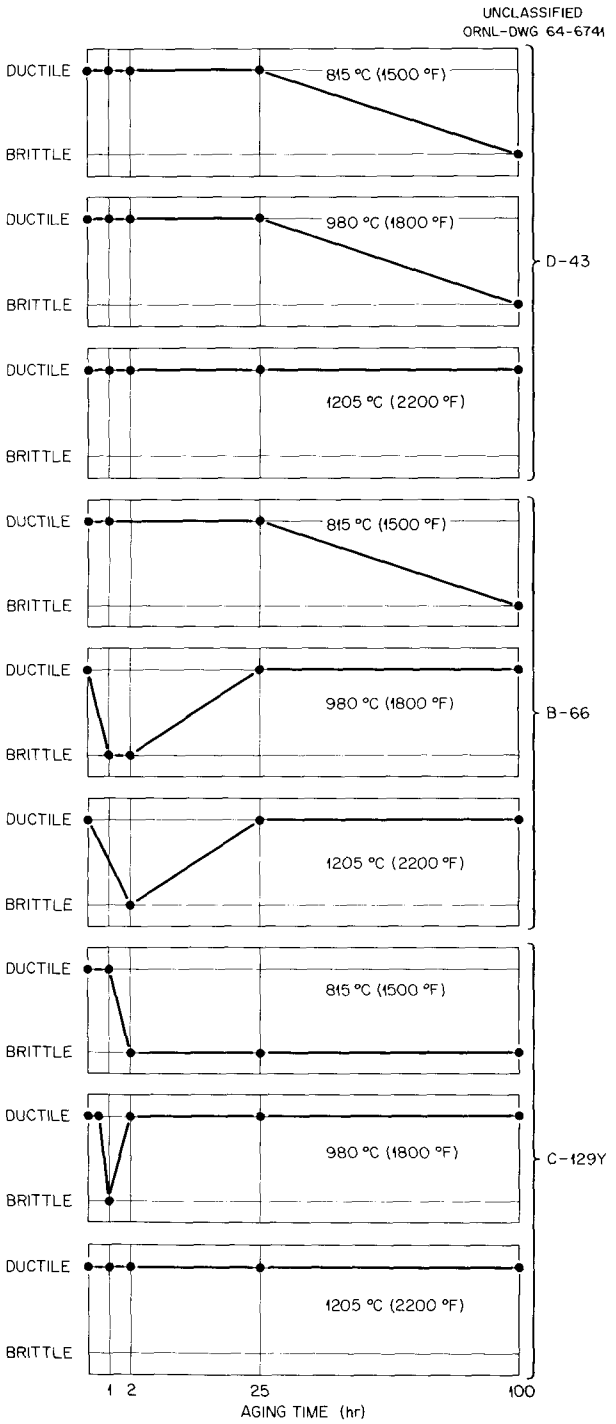

Fig. 14.2. Influence of Aging Time at Various Temperatures on the Bend Ductility of the Refractory-Metal Alloys D-43, B-66, and C-129Y.

Joining of Refractory Metals for Service at Very High Temperatures. – We are developing brazing alloys for joining refractory metals for service up to 1370°C. The ternary systems titanium-vanadium-tantalum and niobium-vanadium-tantalum are promising. The preliminary phase diagrams for these two systems, presented in Fig. 14.4, show our experimentally determined isothermal lines for the flow points of various alloys. It can be seen that the alloy compositions being investigated melt at temperatures of 1650°C and higher.

Alloys in these systems exhibit excellent flowability on niobium, tantalum, and tungsten, with a minimum tendency to react or alloy with these metals. Another attractive property of these systems is their excellent room-temperature ductility. The alloys can be cold rolled to very thin foil from the original arc-melted condition. This high ductility was expected because the binary systems included in these ternary systems exhibit complete solid solubility at high temperatures.[3]

[3] J. J. English, *Binary and Ternary Phase Diagrams of Columbium, Molybdenum, Tantalum, and Tungsten*, DMIC-152, pp. 22, 28, 77 (April 28, 1961).

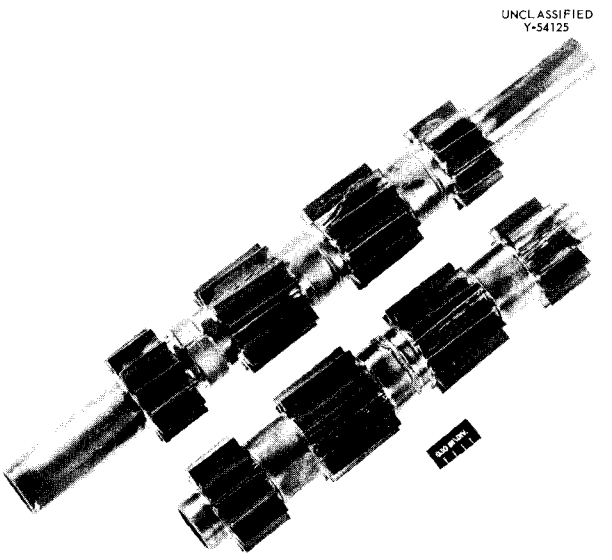

Fig. 14.3. Finned Beryllium Tubing Brazed to a Stainless Steel Liner Tube (Top) and a Niobium Liner Tube (Bottom). These specimens were vacuum-brazed at 1000°C using 49% Ti–49% Cu–2% Be brazing alloy.

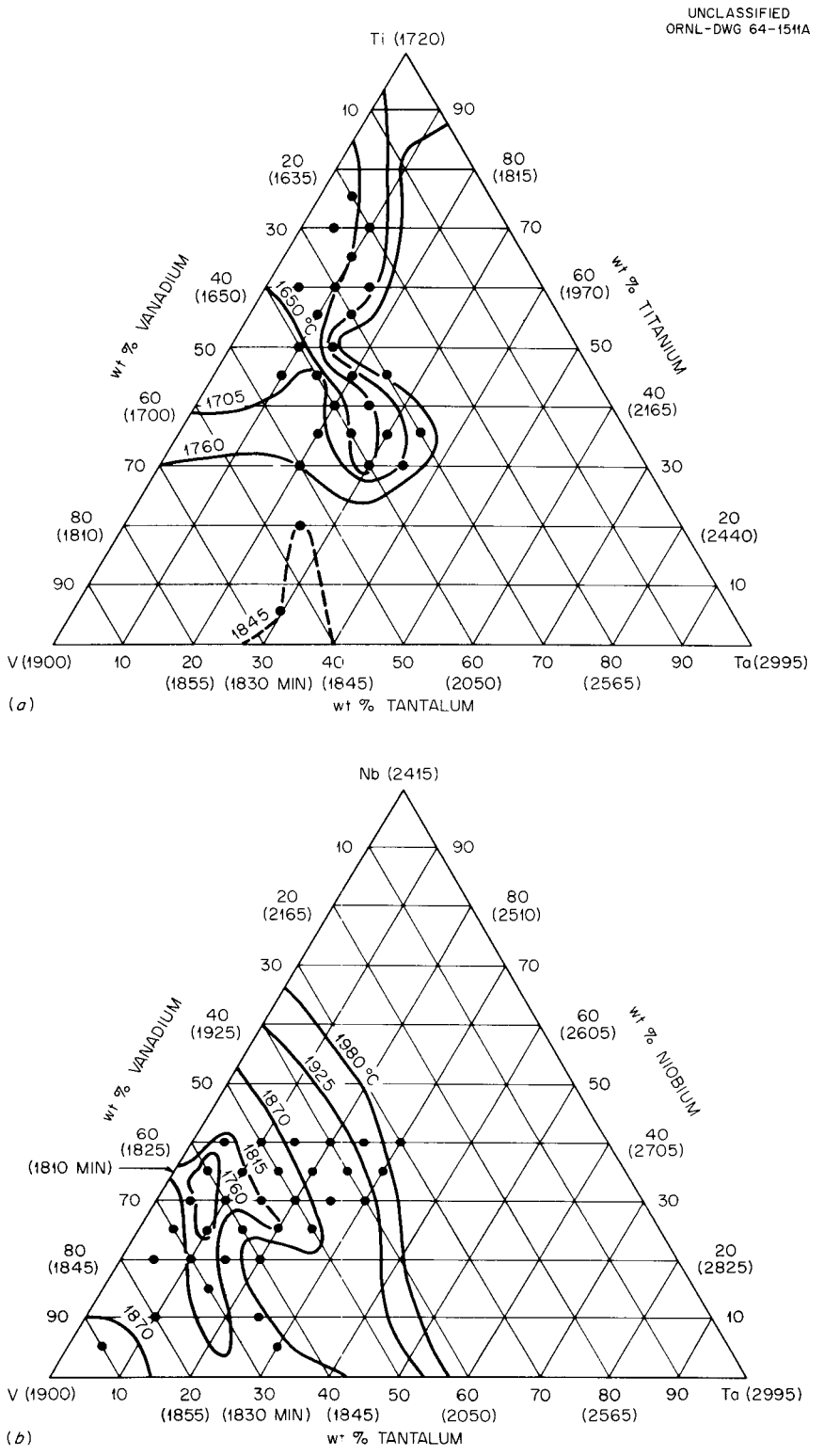

Fig. 14.4. Ternary Diagrams for the Systems (*a*) Titanium-Tantalum-Vanadium and (*b*) Niobium-Tantalum-Vanadium, Showing the Isotherms of Alloy Flow Temperatures. The points denote the actual alloy compositions under investigation. The figures on the graph indicate centigrade melting temperatures; those in parentheses around the edges are melting points of binary alloys with rounded compositions.

Table 14.3. Elevated-Temperature Shear-Strength Data

Composition (wt %)	Brazing Temperature (°C)	Test Temperature (°C)	Shear Strength (psi)	Number of Specimens Tested
		Nb-V-Ta		
65 V–30 Ta–5 Nb	1870	1090	23,400	2
65 V–5 Ta–30 Nb	1820	1090	22,900	2
80 V–10 Ta–10 Nb	1870	1200	13,800	4
30 V–30 Ta–40 Nb	2010	1200	13,400	4
40 V–30 Ta–30 Nb	1930	1200	15,600	4
50 V–25 Ta–25 Nb	1870	1200	16,800	4
90 V–5 Ta–5 Nb	1870	1200	13,900	4
60 V–20 Ta–20 Nb	1870	1200	12,400	4
		Ti-V-Ta		
40 V–10 Ta–50 Ti	1730	1200	12,600	4
25 V–15 Ta–60 Ti	1650	1200	7,800	4
20 V–5 Ta–75 Ti	1650	1200	7,100	4
20 V–10 Ta–70 Ti	1650	1200	7,600	4
35 V–35 Ti–30 Ta	1700	1200	10,000	4
50 V–20 Ta–30 Ti	1760	1200	13,100	4
65 V–30 Ta–5 Ti	1840	1200	13,500	4
55 V–25 Ta–20 Ti	1840	1200	13,800	4

We have tested the shear strength of brazing alloys from these two systems at 1090 and 1200°C. The results shown in Table 14.3 indicate that the joint shear strength is generally greater for the alloys with higher brazing temperatures. These tests were performed in vacuum using Miller-Peaslee shear specimens[4] with Nb–1% Zr as the base metal.

We have studied elevated-temperature aging of tantalum T-joints, brazed with the alloys listed in Table 14.3, for 500 hr at 1370°C in vacuum. The specimens were wrapped in molybdenum foil to reduce contamination during aging. Some titanium collected on the molybdenum foil used to wrap those specimens brazed with alloys of high titanium content. Metallographic examination and T-joint flattening tests revealed no loss in brazing alloy ductility after aging except in the cases of joints brazed with 65% V–30% Ta–5% Nb, 65% V–30% Ta–5% Ti, and 90% V–5% Ta–5% Nb.

[4]F. M. Miller and R. L. Peaslee, *Welding J.* **37**(4), 144s–50s (1958).

Component Fabrication

E. A. Franco-Ferreira

Refractory-Metal Loops. – Several small natural-circulation loops have been fabricated for testing by the Materials Compatibility Group. The general techniques used for loops of this type have been reported previously.[5,6] One of these loops, fabricated of Nb–1% Zr, is shown in Fig. 14.5. The

[5]E. A. Franco-Ferreira, ORNL-3489, pp. 144–45, October 1963 (classified).

[6]A. J. Miller, ORNL-3337, pp. 149–52, October 1962 (classified).

large cylindrical unit on the right vertical leg of the loop is an externally cooled heat sink.

We are developing a small portable inert-atmosphere welding chamber for making some field welds in large refractory-metal corrosion loops. Figure 14.6 shows the prototype of this unit. The glass chamber that carries the welding torch is designed to be evacuated and backfilled with inert gas prior to welding. The unit is automatically rotated around the joint during welding of a straight fusion butt joint. The chamber will be removed from the completed loop through the use of split end fittings and breaking the glass. Initial testing of the prototype has given highly satisfactory results.

Liquid-Metal Pumps. – We are fabricating a liquid-metal pump of Nb–1% Zr alloy designed by the General Electric Company. Welding operations thus far include outside surface buildup of two extruded billets by weld overlay techniques, fabrication of two thin-walled cylinders by rolling from sheet and longitudinal welding, and welding of end caps into two pump cell sleeves. Additional fabrication will proceed as components are received.

We are also performing the entire welding assembly of a second Nb–1% Zr liquid-metal pump, designed by and with components made by Liquid Metals, Inc.

Tube Shell Fabrication. – A Cb-752 tube shell has been fabricated by welding from rolled sheet. The completed unit was $1\frac{1}{2}$ in. in diameter, 15 in. long, and had a wall thickness of 0.136 in. As a result of an extensive welding development program, we found a final welding procedure incorporating three passes to be most suitable and to result in optimum as-welded ductility. The tube shell was manually welded on a copper mandrel with filler wire that had been sheared from the base-metal sheet. After welding, we dissolved away the mandrel in nitric acid.

The outside surface of the weld was machined even with the surface of the surrounding base metal. Then the weld was radiographed. One small root crack was detected at approximately the midpoint of the tube shell, accurately located, and drilled out. The resulting hole was filled by plug welding and the repair radiographed. No further flaws were detected, and the tube shell has been shipped to the Superior Tube Company for redraw on an ORNL subcontract.

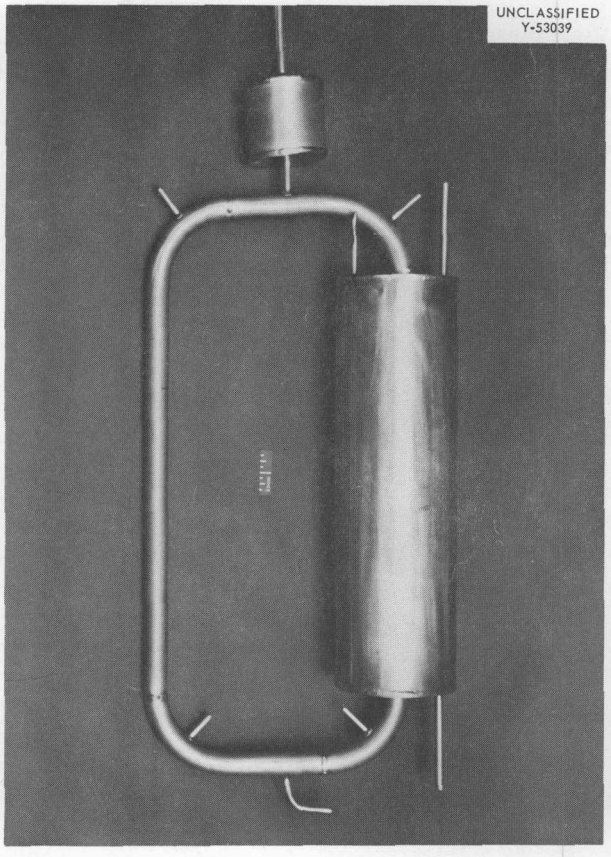

Fig. 14.5. Nb–1% Zr Loop with Externally Cooled Heat Sink.

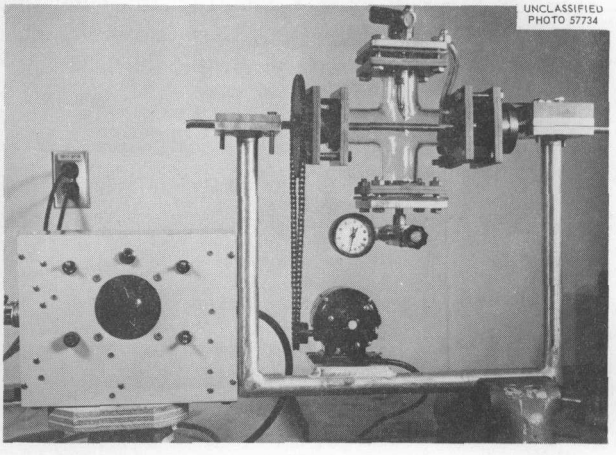

Fig. 14.6. Portable Inert-Atmosphere Welding Chamber for Field-Welding Large Refractory-Metal Loops.

Attachment of Bearing Materials

C. W. Fox

Among the materials that have been proposed for use as bearings at high temperatures in liquid metals are cermets containing major amounts of refractory-metal carbides (e.g., WC). We are developing suitable procedures for attaching these bearing materials to metals and evaluating the resulting joints. Molybdenum is being used as the structural metal in the testing program because it closely matches the low thermal expansion of the cermets. Six refractory-metal carbides and one boride are being investigated.

To choose the best brazing alloy for joining these cermets to metals, we have first studied small disk samples of each cermet. Of the many corrosion-resistant brazing alloys tried, three appear satisfactory: Nicrobraz 50 (Ni-Cr-P), Coast Metals No. 50 (Ni-Si-B), and 48% Ti–48% Zr–4% Be experimental alloy. Figure 14.7 is a photomicrograph of a typical tungsten carbide-to-molybdenum joint brazed with the Ni-Si-B alloy.

To make specimens for testing thermal stability, we brazed each of the different carbide cermets to molybdenum with the same brazing alloy (Ni-Si-B), encapsulated the joints in quartz tubing at 5×10^{-6} torr, heated them 500 hr at 650°C, and metallographically examined them. The results indicate that a stable brazed joint can be made between molybdenum and a carbide cermet if the cermet contains sufficient (>6%) binder (Co, Ni, Mo). However, small cracks in the cermet bodies themselves were occasionally found, probably as a result of the inability to adequately absorb expansion stresses. The metallographic evaluation of these joints is given below:

Cermet (wt %)	Evaluation
96.5 WC–3.5 Co	Limited flow of brazing alloy
94 WC–6 Co	Cracking in brazing alloy and cermet
88 WC–12 Co	No cracking
89 $WTiC_2$–11 Co	Small crack in cermet, no cracking in brazing alloy
70 TiC–10 Nb(Ta,Ti)C–20 Ni	No cracking
90 TiC–10 Mo	Small crack in cermet, no cracking in brazing alloy

Zirconium diboride is also of interest as a bearing material, and we have conducted several brazing studies with it. Of the alloys investigated, 48% Ti–48% Zr–4% Be and 68% Ti–28% Ag–4% Be were the most promising.

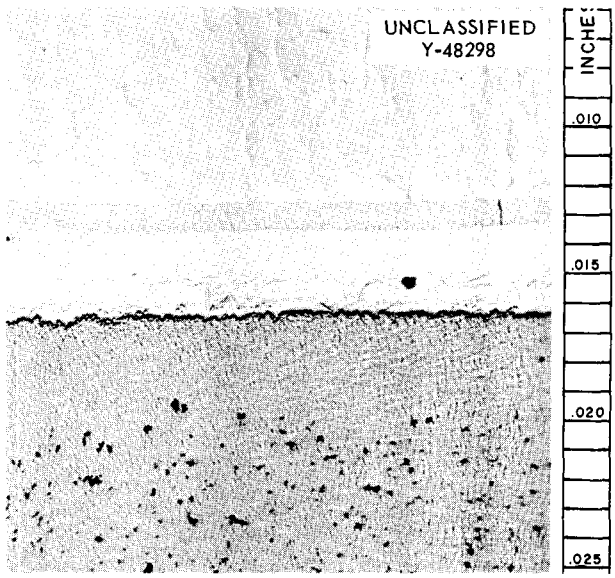

Fig. 14.7. Photomicrograph of Molybdenum(Top)-to-Tungsten Carbide Cermet (Bottom) Joint Brazed with Ni-Si-B Alloy. As polished. 150×.

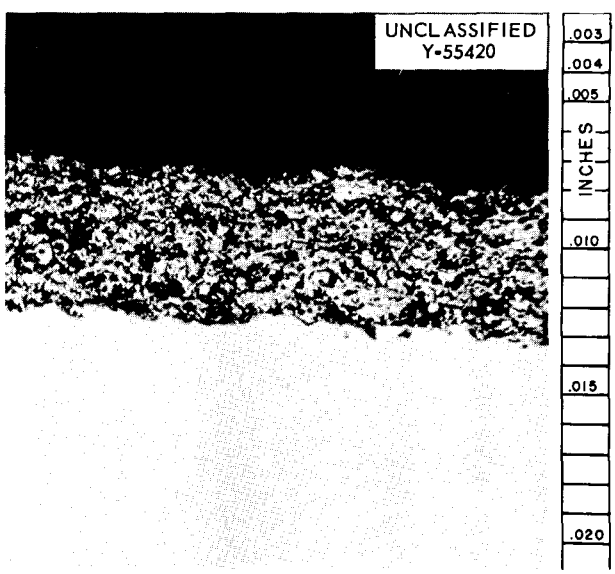

Fig. 14.8. Photomicrograph of Cermet (WC–6% Co) Sprayed on Molybdenum Rod and Then Cycled Thermally (650°C to Ambient) 25 Times. As polished. 150×.

A second approach for producing a metal-cermet composite is the use of plasma-sprayed coatings rather than direct brazing. Several samples of tungsten carbide and zirconium diboride were plasma-sprayed on molybdenum rods by three different laboratories. Specimens from the various plasma-sprayed rods were encapsulated in evacuated (5×10^{-6} torr) quartz tubing and cycled 25 times between 650°C and ambient temperature. The results of this test were quite promising, and a photomicrograph of one of the sprayed coatings after thermal cycling is shown in Fig. 14.8.

MECHANICAL PROPERTIES

J. R. Weir

Creep Properties of Advanced Refractory Alloys

R. L. Stephenson

Long-time creep is a critical criterion for many high-temperature structural applications. In most cases, the only data available on refractory-metal alloys are from high-temperature tensile tests and tests of very short-time creep. The object of this program is to provide creep-rupture data to 1000 hr so that a valid comparison of promising alloys can be made. All tests were performed at pressures less than 2×10^{-7} torr.

During the past year, we have tested unalloyed tantalum and the alloys D-43, B-66, FS-85, and T-111. We have deferred completion of the testing of TM alloy[7] until we complete testing of other alloys. We have started to test Ta–10% W and TZM alloys. We have determined complete creep-rupture properties of stress-relieved D-43 and as-worked B-66 to 1000 hr at 980, 1090, and 1204°C. The 1000-hr rupture stress is shown as a function of temperature in Fig. 14.9 along with preliminary values for T-111 and unalloyed tantalum. Both the rupture life and the creep rate of B-66 are significantly inferior to those of D-43.

The high-temperature mechanical properties of D-43 alloy may be improved[8] by solution annealing at 1650°C, cold working 25%, and aging 1 hr at 1425°C. To verify this, we treated a number of specimens this way before testing. In short-time tests (up to 100 hr) at 980°C there was indeed a substantial improvement in both rupture life and creep rate, although the ductility was reduced considerably. At longer times, however, the stress-rupture curve bent downward, intersecting the curve for stress-relieved material at about 500 hr. Further, when specimens were held at 980°C for 300 hr prior to loading, no improvement in rupture life was observed at short times. Preliminary data indicated that the same effect is present at higher temperatures, although it is not as pronounced. This effect is also observed in specimens that were recrystallized by a 1-hr anneal at 1540°C.

The stress-relieved D-43 alloy appears to be microstructurally stable at the temperatures studied, but the heat-treated and recrystallized conditions both require detailed study before any extrapolations of mechanical property data are prudent.

A quantity of FS-85 alloy in the recrystallized condition has been procured and fabricated into specimens. Only a few short-time tests have been completed at this time, but a program similar in scope to that for alloy D-43 is projected.

Internal Friction in Niobium-Zirconium Alloys

R. L. Stephenson

We are trying to provide a basic understanding of the behavior of interstitials in niobium-zirconium alloys. Our previous report[7] recorded preliminary work to find the actual mechanism of peaks at 380, 480, and 570°C in a niobium-zirconium-nitrogen alloy, which were apparently related to nitrogen.

The peak at 570°C was selected first for detailed study. This peak appears when supersaturated niobium-nitrogen alloys and niobium-zirconium-nitrogen alloys are aged. It rises to a maximum that is roughly proportional to the amount of supersaturation and then it slowly declines in height.

---

[7] R. L. Stephenson and H. E. McCoy, *Metals and Ceramics Div. Ann. Progr. Rept. May 31, 1963*, ORNL-3470, p. 118.

[8] J. S. Clark, A. L. Mincher, and G. N. Villee, *Development of Optimum Manufacturing Methods for Columbium Alloy Sheet, RTD-TDR-63-4236*, E. I. du Pont de Nemours and Co., Inc. (December 1963).

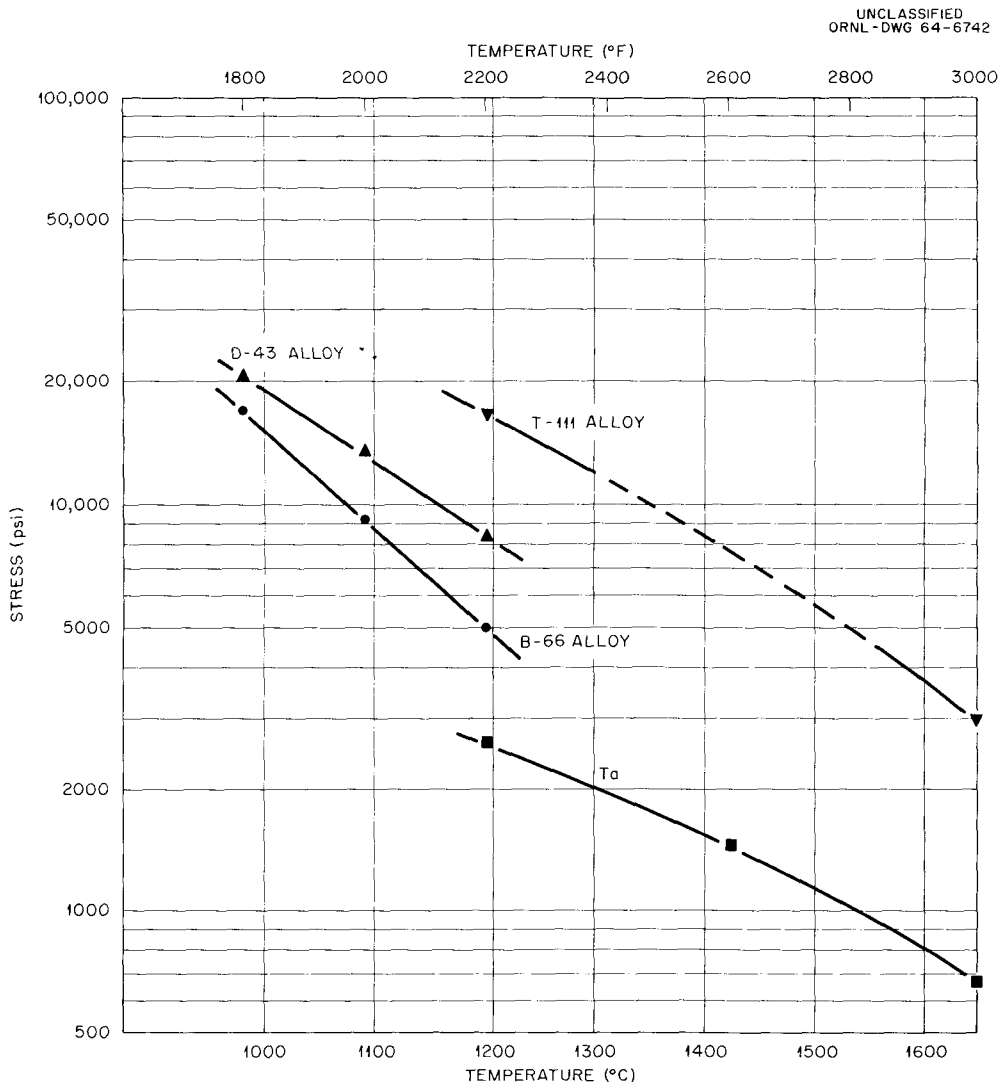

Fig. 14.9. Temperature Dependence of Stress to Produce Rupture in 1000 hr.

Recently Boone and Wert[9] have reported a "cold-work" peak in the niobium-nitrogen system in the same temperature range. We believe these two phenomena are related. To verify this, we prepared specimens for transmission electron microscopy by J. O. Stiegler and C. K. H. DuBose. They report that the annealed specimens were free of precipitates and almost completely free of dislocations. In contrast, the aged specimens showed large numbers of dislocations, even though they had not been mechanically deformed. Additional specimens will be prepared and examined in an attempt to formulate a theory that is consistent with the observed facts of both investigations.

[9]D. H. Boone and C. A. Wert, "Interstitial-Dislocation Interaction in Niobium," *Proc. Intern. Conf. Crystal Lattice Defects, 1962 Symposium, Physical Society of Japan*, vol. 18, suppl. I, 1963.

Effect of Irradiation on the Bend Transition Temperature of Molybdenum- and Niobium-Base Alloys

H. E. McCoy J. R. Weir

Because of the potential use of refractory metals as structural materials in nuclear reactors, the

influence of irradiation on the ductility of materials must be evaluated. We are concerned with the development of test equipment suitable for evaluating the ductile-brittle transition temperature of irradiated specimens and with the use of this equipment to study several alloys. The details of this work may be found elsewhere.[10]

The postirradiation bend properties of several materials have been determined and compared with appropriate unirradiated controls. These materials include TM, Nb–1% Zr, welded Nb–1% Zr, and D-43 alloys. They were irradiated at temperatures over the range of 60 to 157°C to doses of approximately 10^{20} neutrons/cm^2 ($E > 1$ Mev). The rate of bend deflection was 0.5 in./min.

The transition temperature of the TM alloy was increased approximately 110°C by irradiation. Postirradiation anneals of 1 hr at 500, 1000, and 1200°C lowered the transition temperature but did not completely restore the preirradiation properties. Although irradiation caused only slight increases in strength, the magnitude of the yield load was greatly increased. The hardness increased upon irradiation from 174 to 230 DPH. Postirradiation anneals of 500, 1000, and 1200°C yielded hardnesses of 233, 196, and 180 respectively.

In a second experiment, irradiation of TM alloy to twice the dose described above increased the transition temperature approximately 115°C. Hence, the influence of irradiation appears saturated by doses of the order of 10^{20} neutrons/cm^2.

The Nb–1% Zr alloy was irradiated after a 1-hr anneal at 1350°C. At the deflection rate of 0.5 in./min being used, the bend transition temperature could not be determined, so yield strength was used as an evaluation criterion. The yield strength was increased by about 50%, and the material was still ductile at −79°C. Postirradiation anneals of 1 hr at 300 and 500°C increased the yield strength an additional 15%. A postirradiation anneal of 700°C reduced the strength by 25% and a 1000°C anneal returned the material to its original strength. These features are summarized in Fig. 14.10.

Irradiation of Nb–1% Zr alloy to twice the integrated dose of the above experiment increased the yield strength 70% over the unirradiated material. Although this is a larger degree of strengthening than observed in the material with the lower dose, slight differences in the irradiation temperature may account for the variation. Postirradiation annealing gave results similar to those described above.

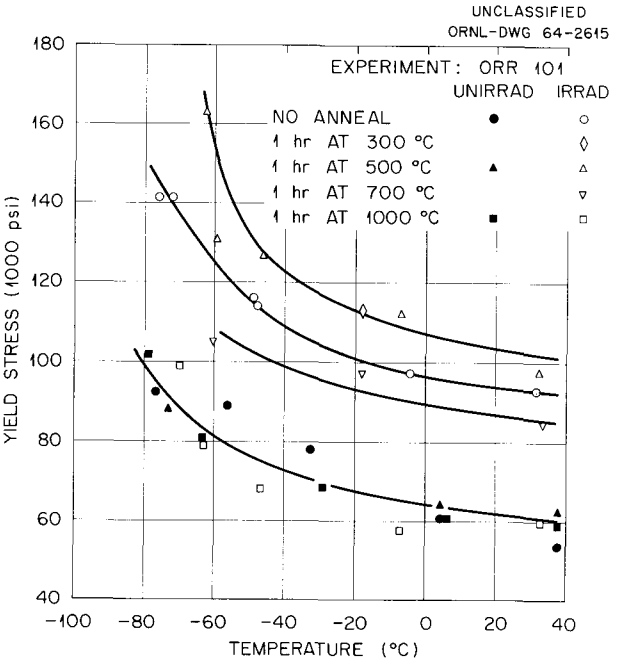

Fig. 14.10. Effect of Irradiation and Postirradiation Annealing on the Yield Strength in Bending of Nb–1% Zr. Irradiated at 60 to 82°C to 0.27 to 1.1 × 10^{19} neutrons/cm^2 ($E > 2.9$ Mev).

The yield strength of Nb–1% Zr that had been cold worked 40% was increased 25% by irradiation, increased another 10% by postirradiation annealing at 500°C, and restored to its preirradiation value by annealing at 1000°C.

Since we found that specimens of Nb–1% Zr containing a transverse weld have properties comparable with the base metal, the weld metal should not be more strongly influenced by irradiation than the base metal.

Annealed D-43 alloy was increased in strength by about 70% as a result of neutron irradiation, but it remained ductile at −79°C. A postirradiation anneal of 1000°C restored the preirradiation properties. The yield strength of D-43 alloy that had been cold worked 20% was increased 40% by irradiation, but good ductility was retained at −79°C.

[10] H. E. McCoy and J. R. Weir, *Effect of Irradiation on the Bend Transition Temperature of Molybdenum- and Niobium-Base Alloys*, ORNL-TM-880 (in press).

We are studying the behavior of other alloys, the rate of saturation of property change with dose, the nature of the defects formed during irradiation, and the change in these defects with postirradiation annealing.

Creep of the Nb–1% Zr Alloy

H. E. McCoy

We have determined creep-rupture properties of two heats of Nb–1% Zr alloy. Although these materials had comparable chemical analyses and were reported to have the same fabrication history, their creep strengths differed considerably. At a test temperature of 982°C and high stresses, a fine precipitate formed and was oriented normal to the applied stress. At 1204°C the precipitate was quite coarse but still preferentially oriented normal to the applied stress. An important observation was that pretest annealing at temperatures up to 1700°C improved the strength without decreasing the rupture ductility.

PHYSICAL METALLURGY

Contamination of Refractory Metals in High Vacuums

H. Inouye

We are concerned with the stability of oxygen, carbon, nitrogen, and hydrogen in refractory metals to high vacuums and temperatures. The study areas have included the characterization of the contamination of numerous alloys resulting from their extended exposure to the residual gases in a vacuum system, the development of techniques to measure reaction rates in the pressure range 10^{-6} to 10^{-10} torr, and finally the exploration of practical methods to control the contamination.

The contamination characteristics of fabricable niobium, tantalum, and molybdenum alloys were determined in terms of the test conditions and the influence of the alloying elements. The results are summarized in a topical report[11] and abstracted in the following paragraphs.

[11] H. Inouye, *Contamination of Refractory Metals by Residual Gases in Vacuums Below 10^{-6} torr*, ORNL-3674 (in press).

The gaseous contamination of niobium, molybdenum, Nb–1% Zr, FS-85, D-43, Cb-752, TZM, and T-111 resulting from their extended exposure to the residual gases in high vacuums was measured by chemical analyses and related to system pressure, metal temperature, exposure time, metal surface-to-volume ratio, and alloy composition. Also, we developed techniques for lowering the contamination of Nb–1% Zr by use of refractory-metal envelopes, vapor-plated molybdenum, and intentional additions of nitrogen or methane to the environment to counteract the noxious gases.

The residual gases in the system between 10^{-6} and 10^{-8} torr were mainly H_2, H_2O, CO, CH_4, N_2, and CO_2. This environment caused significant contamination by oxygen to the above alloys when they were heated for 1000 hr between 600 and 1200°C. Although carburization also occurred, a competing carbon-oxygen interaction became important at the higher temperatures and caused decarburization in alloys that depend on carbon for mechanical strength. The alloying elements titanium, zirconium, and hafnium promoted oxygen contamination while additions of tungsten and tantalum had no influence. Contamination by hydrogen and nitrogen was not a problem.

The oxygen contamination of Nb–1% Zr can be expressed in terms of four variables by two empirical expressions:

at 750 to 1000°C,

$$\Delta C = 90.6 t p^{0.5} X^{-1} \exp(-5500/RT) ;$$

and at 1000 to 1200°C ,

$$\Delta C = 6.89 \times 10^{4} t p^{0.5} X^{-1} \exp(-22{,}400/RT) ,$$

where

ΔC = increase in oxygen contamination (ppm),

t = exposure time (hr),

p = system pressure (torr),

X = metal thickness (in.).

Refractory-metal envelopes effectively stabilized the carbon content of Nb–1% Zr but were erratic in their ability to lower the oxygen contamination. The oxygen content in protected samples varied from 2 to 50% of that in the unprotected metal. Molybdenum deposits less than 5×10^{-5} in. thick, produced from $MoCl_5$ by chemical vapor plating, provided complete protection of the alloy up to 1060°C. Low concentrations of methane added

to the residual gases lowered the oxygen contamination of TZM and niobium but did not improve the situation with Nb–1% Zr.

Our results show that the contamination of refractory metals is controlled by four test variables. For the temperature range investigated, the maximum permissible pressures are estimated to be near 10^{-9} torr for thin metal sections. Through the additional use of secondary control measures, such as metal barriers, metal surface deposits, and additions to the residual gases, the permissible atmospheres for niobium and tantalum alloys could be expanded to higher impurity concentrations and inert-gas environments. Furthermore, our results indicate that control of the interstitial content of the alloys during heat treatment may be feasible.

Sorption Rate of Nitrogen by Nb–1% Zr in Ultrahigh Vacuum

H. Inouye

A technique has been developed to measure the reaction rates of refractory metals with gases up to 1650°C in the pressure range from 10^{-10} to 10^{-6} torr. We measure the flow rates of the low-pressure gas into and out of a reaction vessel containing a resistant-heated filament. To measure the sorption rate, Q_a, of a gas by this technique requires three pressure measurements which are related to Q_a by the equation

$$Q_a = (F_1/A)(P_1 - P_2) - (F_2/A)(P_2 - P_3) ,$$

where

Q_a = sorption rate, $\mu l\ cm^{-2}\ sec^{-1}$;

F_1 = conductance of the gas inlet, cm^3/sec;

F_2 = conductance of the gas outlet, cm^3/sec;

P_1 = inlet manifold pressure, torr;

P_2 = gas pressure over filament, torr;

P_3 = outlet pressure, torr;

A = filament area, cm^2;

$P_1 > P_2 > P_3$.

The filament is absorbing gas when Q_a is positive, degassing when Q_a is negative, and at equilibrium when Q_a is equal to zero. The sorption efficiency or sticking probability, α, which is defined by the ratio of the sorption rate to the arrival rate (Q_i) of the gas, is calculated from

$$\alpha = \frac{Q_a}{Q_i} = \frac{Q_a}{3638\ (T/M)^{1/2} \cdot P_2} ,$$

where

M = molecular weight of the gas,

T = absolute temperature.

To date, the kinetics of reaction of Nb–1% Zr with nitrogen have been determined at 1200°C for nitrogen pressures ranging from 2×10^{-9} to 2×10^{-7} torr. The sorption rates in this pressure range were constant with time and increased linearly with pressure at a rate of 460 $\mu l\ cm^{-2}\ sec^{-1}\ torr^{-1}$, while α remained constant with both test time and pressure. The data for several conditions of pressure and reaction time are listed in Table 14.4. The constant value of α, averaging

Table 14.4. Sorption Rates of Nitrogen by Nb–1% Zr at 1200°C

Run No.	Test Duration (min)	Nitrogen Pressure (torr)	Sorption Rate ($\mu l\ cm^{-2}\ sec^{-1}$)	Sticking Probability (α)	Total N_2 Sorbed	
					($\mu l/cm^2$)	(ppm)
6	450	1.7×10^{-9}	7.70×10^{-7}	0.038	0.020	0.83
7	870	5.2×10^{-9}	2.28×10^{-6}	0.037	0.119	2.0
9	360	5.5×10^{-8}	1.56×10^{-5}	0.024	0.378	6.3
10	1735	1.1×10^{-7}	4.1×10^{-5}	0.032	4.68	78
11	2145	2.2×10^{-7}	1.1×10^{-4}	0.040	13.8	231

about 0.035, indicates that the surface nitrogen concentration remained constant during any one test and increased in proportion to the pressure. Our results suggest that the rate-controlling variable over the tested range of parameters is the arrival rate, Q_i, of the gas.

Preliminary experiments at 1300°C showed the same dependence of sorption rates on pressure and time. At this temperature, however, α was about 0.06. This represents a 70% increase in the reaction rate over that measured at 1200°C.

Nitrogen Solubility in Nb–1% Zr

H. Inouye

Equilibrium pressures of nitrogen over Nb–1% Zr containing nitrogen added by the technique described in the previous section were measured by adjusting P_1 (the manifold pressure) so that the sorption rate was zero. In this case P_2 becomes P_e, the equilibrium pressure. The nitrogen concentration in the alloy was calculated from the nitrogen analysis of the starting material and the added nitrogen calculated by

$$\Delta C = \alpha k t P / X \sigma ,$$

where

ΔC = increase in nitrogen concentration,

α = sticking probability,

t = exposure time,

P = nitrogen pressure,

X = metal thickness,

σ = alloy density,

k = conversion factor.

In practice we could not adjust the sorption rate to zero, but values approaching 1×10^{-9} μl cm^{-2} sec^{-1} (equivalent to ΔC approximately equal to 1 ppm/1000 hr) were readily attained. The measured values from 1200 to 1650°C of P_e for Nb–1% Zr containing 145 and 298 ppm N are tabulated in Table 14.5. The feasibility of using the present technique for the determination of the solubility limits of interstitials in refractory metals will be explored in future experiments.

Table 14.5. Equilibria Between Nitrogen[a] and Nb–1% Zr

Temperature (°C)	Equilibrium Pressure (torr)	
	78 (145)[b] ppm N	231 (298)[b] ppm N
1200	4.4×10^{-10}	1.0×10^{-9}
1250		2.4×10^{-9}
1300	3.1×10^{-9}	6.2×10^{-9}
1350		2.3×10^{-8}
1400	2.2×10^{-8}	6.2×10^{-8}
1450		1.4×10^{-7}
1500	1.2×10^{-7}	3.8×10^{-7}
1550		9.0×10^{-7}
1600		1.7×10^{-6}
1650		3.4×10^{-6}

[a]Nitrogen added at 1200°C and equilibrated at 1650°C; p_e determined on cooling.

[b]Concentrations added are followed in parentheses by estimated total nitrogen concentrations in alloy.

Evaporation of Iron-, Nickel-, and Cobalt-Base Alloys at 760 to 980°C in High Vacuums[12]

D. T. Bourgette

Evaporation rates of types 316, 304, and 446 stainless steels, Inconel, INOR-8, and Haynes alloy No. 25 were measured at pressures ranging from 5×10^{-7} to 1×10^{-9} torr in both the polished and oxidized conditions to determine their suitability for use in high vacuums. The test temperatures for type 316 stainless steel, the alloy most thoroughly studied, ranged from 760 to 980°C. The remaining alloys were tested at 870 and 980°C only.

Evaporation losses increased with chromium and manganese concentrations in the alloys and with temperature but were independent of the pressure in the range investigated. Also, at constant temperature the evaporation rates decreased with

[12]Extracted from report by D. T. Bourgette, *Evaporation of Iron-, Nickel-, and Cobalt-Base Alloys at 760 to 980°C in High Vacuums*, ORNL-3677 (in press).

time and the lower the test temperatures, the greater the decrease in the rates. These effects are illustrated by the weight loss curves of Fig. 14.11.

At 870 and 980°C specimens that had been preoxidized in air evaporated at lower initial rates than did polished specimens. However, long exposures resulted in accelerated rates, due to the decomposition of the oxide.

Pre- and posttest x-ray analyses of the oxide layer on several alloys showed that only Cr_2O_3 remained after several hundred hours under the test conditions. Therefore, we preoxidized type 316 stainless steel in wet hydrogen to yield a layer of only Cr_2O_3. Subsequent evaporation tests again showed that after extended periods of time above 760°C the Cr_2O_3 was not fully protective. Evaporation rates for polished type 316 stainless steel varied from 5.28×10^{-4} mg cm^{-2} hr^{-1} at 760°C to 65.9×10^{-4} mg cm^{-2} hr^{-1} at 982°C. The evaporation rates for preoxidized material (Cr_2O_3 film) varied from 4.44×10^{-4} mg cm^{-2} hr^{-1} at 872°C to 35.7×10^{-4} mg cm^{-2} hr^{-1} at 982°C. At 760°C an oxidized specimen lost no weight in

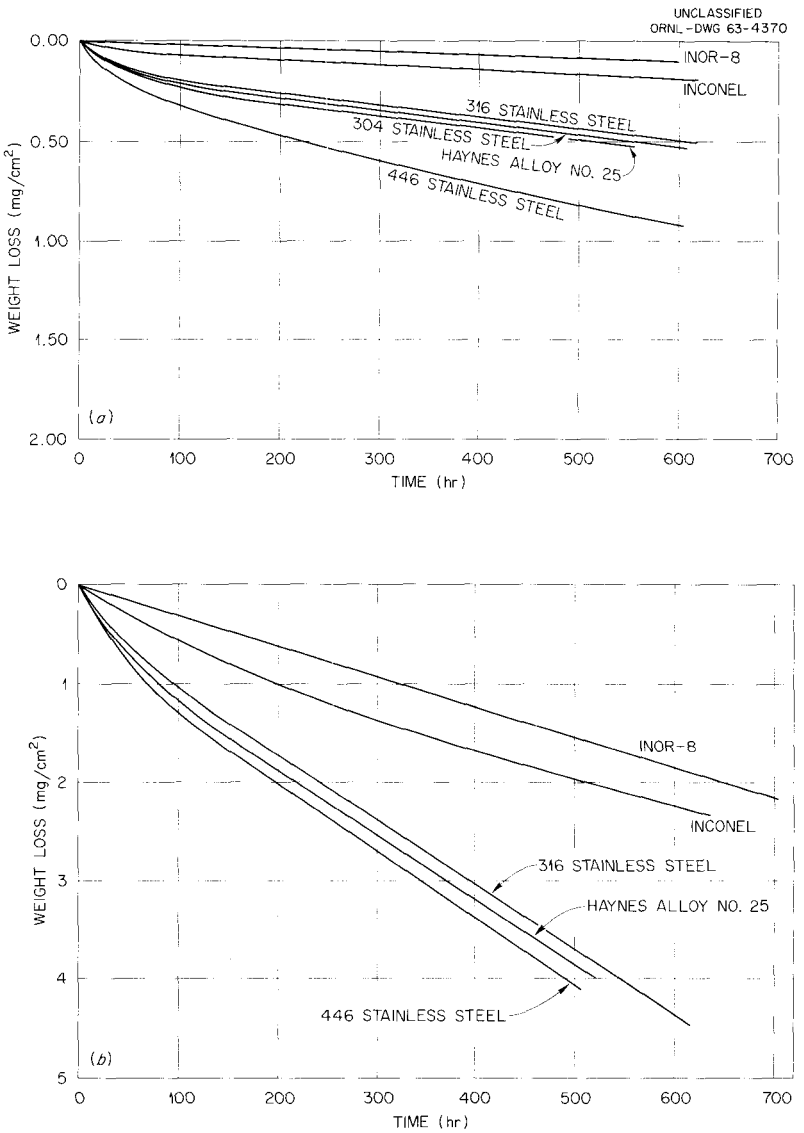

Fig. 14.11. Evaporation Losses of Iron-, Nickel-, and Cobalt-Base Alloys at (*a*) 872°C and Approximately 5×10^{-7} to 5×10^{-9} torr and (*b*) 982°C and Approximately 5×10^{-7} to 5×10^{-8} torr.

Table 14.6. Evaporation Rates at Various Temperatures for Type 316 Stainless Steel with Polished Surfaces and with Surfaces Preoxidized in Wet Hydrogen

Test Temperature (°C)	Polished Surfaces			Oxidized Surfaces				
	Test Duration (hr)	Evaporation Rate (mg cm^{-2} hr^{-1}) × 10^{-4}		Test Duration (hr)	Oxide Thickness (mg/cm^2)	Oxide Identification	Evaporation Rate (mg cm^{-2} hr^{-1}) × 10^{-4}	
		Initial[a]	Final[b]				Initial[a]	Final[b]
982	956	120	65.9	1058	0.2804	Cr_2O_3	26.9	35.7
927	1832	42.3	20.5	1226	0.2983	Cr_2O_3	7.89	12.50
872	3453	26.8	3.90	1456	0.3134	Cr_2O_3; $NiMnO_4$ (trace)	4.42	4.44
760	1321	6.56	0.528	1142	0.2525	Cr_2O_3	0	0

[a]Rate during initial 50 hr of test.
[b]Rate during final 50 hr of test.

1142 hr. Results of these tests are summarized in Table 14.6.

Metallographically, the manifestations of evaporation were subsurface void formation, grain growth at the specimen surface, disappearance of precipitates, grain-boundary grooving, and excessive void formation in the grain boundaries. For type 316 stainless steel these effects are illustrated in Fig. 14.12.

Chromium and manganese were found chemically to be the principal elements lost during evaporation. However, lesser amounts of iron, nickel, cobalt, carbon, and silicon were found in the vapor deposits. Microprobe analysis has revealed the existence of chromium and manganese concentration gradients below 900°C. Above 900°C, these gradients were difficult to detect and in certain specimens nonexistent.

Effect of Evaporation Losses on the Creep-Rupture Properties of Type 316 Stainless Steel

D. T. Bourgette H. E. McCoy

The evaporation of type 316 stainless steel was briefly discussed in the preceding section of this report. We have also tested the creep-rupture properties as affected by evaporation losses during prior exposure at 872°C to pressures ranging from 5×10^{-7} to 5×10^{-8} torr. Surface conditions, vacuum levels, vacuum exposure times, weight changes, and pertinent creep data are summarized in Table 14.7, while the stress-rupture properties are presented in Fig. 14.13.

The data show that the creep properties of type 316 stainless steel change as it is exposed to vacuum for long periods of time at 872°C. If the material is initially in the as-received condition,

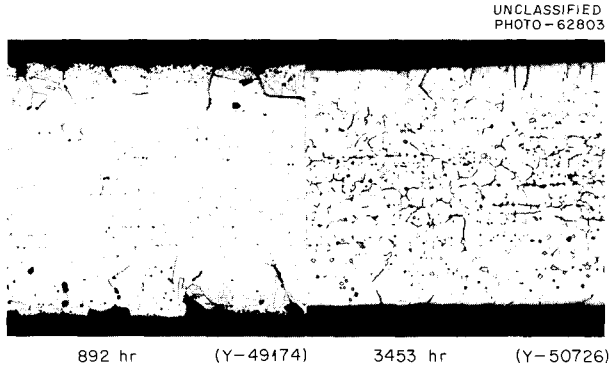

Fig. 14.12. Type 316 Stainless Steel Evaporation Tested at 872°C and 8×10^{-9} torr for 892 and 3453 hr. 500×. Reduced 64%.

Table 14.7. Prior Thermal Treatments and Results of Creep Tests of Type 316 Stainless Steel at 872°C

Specimen and Group Code	Thermal Treatment Prior to Creep Test	Weight Change Due to Thermal Treatment (mg)			Creep Stress (psi)	Rupture Life (hr)	Percent Elongation	Minimum Creep Rate (in./in./hr)
		1040°C	Oxid.	Evap.				
A 1	As received and polished through 4/0 paper	None			900	2071	75	2.8×10^{-4}
2					1400	585	80	1.1×10^{-3}
3					3000	56	83	1.1×10^{-2}
B 1	576 hr at 872°C and 5×10^{-7} torr	−12.2			1400	1237	100	3.8×10^{-4}
2		−11.4			2240	132	50	1.6×10^{-3}
3		−12.0			3000	76	86	5.7×10^{-3}
C 1	550 hr at 872°C and 1 atm of argon	None			3000	121	64	3.7×10^{-3}
D 1	1321 hr at 872°C and 5×10^{-7} torr	−18.6			1400	1199	67	4.6×10^{-4}
2		−19.5			2200	280	80	1.9×10^{-3}
3		−18.8			3000	109	77	4.7×10^{-3}
E 1	1 hr at 1040°C and 5×10^{-6} torr	−4.9			1400	1537	1	5×10^{-7}
2		−5.1			2200	4871	32	2×10^{-5}
3		−5.1			2500	3406	29	2.5×10^{-5}
4		−5.1			4000	667	45	3×10^{-4}
5		−4.5			6000	137	58	2×10^{-3}
6		−5.4			8000	25	73	1.4×10^{-2}
F 1	1 hr at 1040°C and 5×10^{-6} torr, then 550 hr at 872°C in 1 atm of argon	−1.6			3000	Discontinued		9.5×10^{-5}
2		−1.7			3000	1136	39	1.8×10^{-4}
3		−2.1			5000	179	47	1.7×10^{-3}
G 1	1 hr at 1040°C and 5×10^{-6} torr followed by 170 hr at 816°C in wet hydrogen	+5.8			2500	162	83	2.8×10^{-3}
2		+4.1			3000	1207	28	5.8×10^{-5}
3		+3.1			4000	29	83	1.4×10^{-2}
4		+4.0			5000	195	50	1.1×10^{-3}
5		+4.3			8000	21	67	1.5×10^{-2}
H 1	1 hr at 1040°C and 5×10^{-6} torr followed by 170 hr in wet hydrogen at 816°C, followed by 820 hr at 872°C and 5×10^{-7} torr	−6.2	+5.7	−20.7	3000	173	33	1.3×10^{-3}
2		−6.8	+4.7	−18.7	5000	75	92	2.8×10^{-3}
3		−5.4	+5.7	−20.7				

Table 14.7 (continued)

Specimen and Group Code	Thermal Treatment Prior to Creep Test	Weight Change Due to Thermal Treatment (mg)			Creep Stress (psi)	Rupture Life (hr)	Percent Elongation	Minimum Creep Rate (in./in./hr)
		1040°C		872°C				
J 1	1 hr at 1040°C and 5×10^{-6} torr	−5.1		−34.1	2500	1118	39	1.88×10^{-4}
2	followed by 2129 hr at 872°C	−5.0		−32.5	3000	577	42	4.8×10^{-4}
3	and 8×10^{-8} torr	−5.0		−37.4	5000	61	33	5×10^{-3}
		1040°C		872°C				
K 1	1 hr at 1040°C and 5×10^{-6} torr	−5.2		−45.2	1700	800	32	1.4×10^{-4}
2	followed by 3521 hr at 872°C	−5.0		−44.3	3000	164	34	1.6×10^{-3}
3	and 1×10^{-7} torr	−5.1		−44.8	5000	32	40	8.9×10^{-3}
		1040°C	Oxid.	Evap.				
L 1	1 hr at 1040°C and 5×10^{-6} torr	−4.9	+4.2	−40.9	3000	210	23	8.6×10^{-4}
2	followed by 170 hr at 816°C in	−5.1	+4.4	−40.7	5000	63	30	3.2×10^{-3}
3	wet hydrogen followed by 2584 hr at 872°C and 8×10^{-8} torr	−5.0	+4.2	−40.8	8000	6.5	51	4.9×10^{-2}
		1040°C		872°C				
M 1	1 hr at 1040°C and 5×10^{-6} torr	−5.2		60.7	3000	183	49	1.9×10^{-3}
2	followed by 5028 hr at 872°C	−5.1		58.1	5000	82	55	4.0×10^{-3}
3	and 4×10^{-8} torr	−5.1		62.6				

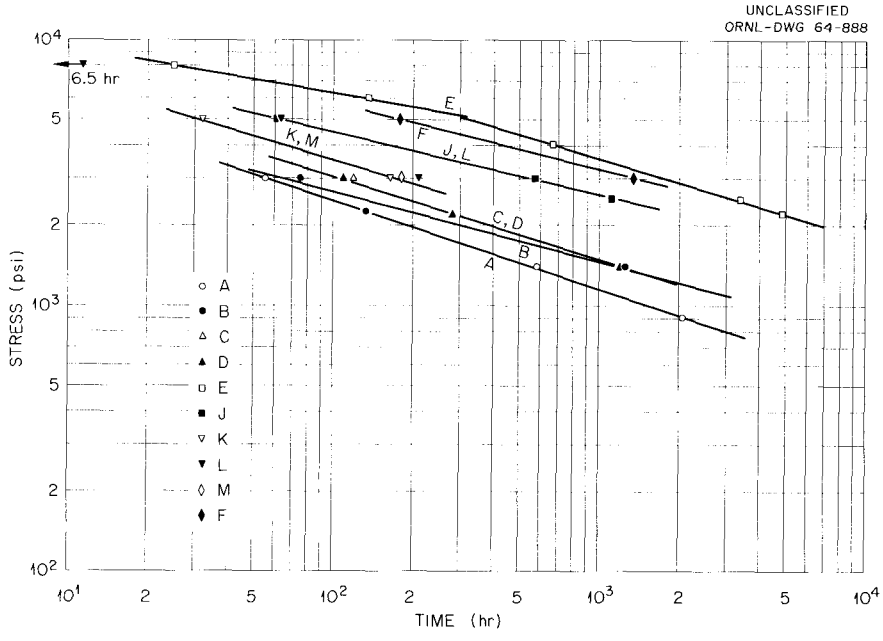

Fig. 14.13. Influence of Evaporation on the Stress-Rupture Properties of Type 316 Stainless Steel at 872°C. Letters refer to treatments in Table 14.7.

it becomes stronger when annealed (i.e., evaporated) at 872°C. If the material is initially annealed 1 hr at 1040°C, it grows weaker upon annealing at 872°C. Although we observed some voids near the surface of the specimens exposed to vacuum for 2129 hr, we believe that all these strength changes can be accounted for in terms of heat treatment rather than the loss of material.

It is a well-established fact that stainless steels containing 18% Cr and 8% Ni can undergo at least two changes with time – the precipitation of complex carbides and the formation of chi or sigma phases. Rosenberg and Irish[13] have shown that the solubility of carbon in an 18% Cr–10% Ni stainless steel at 1040°C is between 0.06 and 0.075%. The solubility at 872°C is between 0 and 0.03%. Koh[14] has studied the formation of chi and sigma phases in type 317 stainless steel and has shown that the tendency for chi formation is a maximum at 872°C. Garofalo *et al.*[15] have found that cold work up to levels of 25% alters the morphology of the carbide precipitate in type 316 stainless steel so that the strength over the temperature range of 600 through 816°C improves significantly.

We do not know exactly the condition of our material in the as-received state, but it quite likely contained some residual cold work. This cold working would give numerous nucleation sites for carbide precipitation, which would in turn improve the strength with holding time at 872°C. At some point, the carbides would have all precipitated or a steady state would be reached between precipitation and agglomeration so that no further strengthening would occur. When the material was annealed at 1040°C, the residual cold working was removed, the carbides were dissolved, and grain growth occurred. Although we do not know the exact reason for this material being stronger than the as-received material, we are not surprised that these two states result in different properties. The precipitates that were formed in the material held at 872°C after annealing at 1040°C were not of satisfactory morphology to strengthen the material, and the loss of impurities from solution reduced the strength.

[13]S. J. Rosenberg and C. R. Irish, *J. Res. Natl. Bur. Std.* **48**(1), 40–48 (1952).

[14]P. K. Koh, *J. Metals* **5**, 339–43 (1953).

[15]F. Garofalo, F. Von Gemmingen, and W. F. Domis, *Am. Soc. Metals, Trans. Quart.* **54**(3), 430–44 (1961).

Forming a thin surface oxide did not observably change the creep properties at 872°C. This we expected, since other experimenters[16] have shown that surface films on a polycrystalline specimen are not effective at elevated temperatures, due to the numerous internal surfaces present in the material.

Although we have failed to show any significant influence of mere exposure to vacuum on the mechanical behavior of 0.040-in.-thick specimens, it is probable that evaporation, *per se*, would be more important in thinner material. Also, the mechanical behavior under conditions of simultaneous stressing and evaporation might be different from that observed under our present conditions. This is because material is preferentially lost from the grain boundaries and this loss might promote grain-boundary motion and thus reduce creep strength.

Effect of Residual System Gases on the Slow-Bend Creep Behavior of Nb–0.6% Zr at 1000°C

T. K. Roche

We have concluded our study[17] of the effect of degree of vacuum (i.e., the partial pressure of residual system gases) on the slow-bend creep behavior of Nb–0.6% Zr at 1000°C. The creep behavior of this alloy was determined in 500-hr cantilever-beam bend tests in the approximate pressure range of 10^{-7} to 10^{-5} torr at a 12,500-psi initial outer fiber stress. The results depended strongly upon the test vacuum as a result of varying amounts of contamination, principally oxygen and carbon, from residual gases in this environment. The alloy was either weakened or strengthened by interstitial contamination, depending upon (1) the rate at which the alloy absorbed interstitials from the test environment, (2) the solubility of interstitials in the alloy, and (3) the concentration of interstitials in the alloy at the time of application of the stress.

When the alloy initially contained 95 ppm C, 495 ppm O, 2 ppm H, and 215 ppm N, a systematic increase in the test pressure within the range 7×10^{-8} to 6×10^{-5} torr increased the contamination rate, leading to a progressive weakening of the alloy during the early test stages. Later the alloy was strengthened by dispersed phases such as ZrO_2 and probably niobium carbides or nitrides and possibly by dissolved interstitials. This strengthening effect was more pronounced at test pressures greater than the system base pressure, which ranged from 7×10^{-8} to 3×10^{-7} torr.

When oxygen contamination became great enough to precipitate NbO, the alloy was weakened; wrapping the specimen with molybdenum foil protected it.

Exposing the alloy in the pressure range of 2.5 to 4×10^{-5} torr before stressing it strengthened the alloy for the early stages of test in the same pressure range.

During a single test, we could alternately accelerate or decelerate the deflection rate of the alloy by systematically varying the pressure in the range of 10^{-5} to 10^{-7} torr.

Vacuums of better than 1×10^{-7} torr are required to minimize the environmental effects at our test conditions.

Aging of Niobium-Base Alloys

T. K. Roche

Since metallurgical stability (i.e., response to aging) can influence the mechanical properties of alloys, we have started to investigate the effect of heat treatment on the aging characteristics of two advanced niobium alloys, Cb-752 and D-43. Coupons of both alloys were annealed at 1315 and 1800°C. For both annealing temperatures, specimens of both alloys were aged for times up to 500 hr at 925°C and specimens of alloy D-43 were also aged at 1095°C. Room-temperature hardness measurements and metallographic studies were performed.

The hardness data and the analyses for interstitial elements for the alloy Cb-752 are listed in Tables 14.8 and 14.9 respectively. Annealing at the higher temperature resulted in a greater grain size, smaller carbon and oxygen contents, and higher hardness than those of the material annealed at the lower temperature. No significant

[16] J. R. Cuthill and W. N. Harrison, *Effect of Ceramic Coatings on the Creep Rate of Metallic Single Crystals and Polycrystalline Specimens*, WADC Technical Report 56-85 (April 1956).

[17] T. K. Roche, *Effect of Degree of Vacuum on the Slow-Bend Creep Behavior of Columbium–0.6% Zirconium at 1000°C*, ORNL-3569 (June 1964).

Table 14.8. Diamond Pyramid Hardness Data for Annealed and Aged Niobium-Base Alloys

Alloy and Aging Temperature (°C)	Aging Time (hr)	Average Diamond Pyramid Hardness	
		Annealed 2 hr at 1315°C	Annealed 2 hr at 1800°C
D-43, 1095	0	156	171
	1	155	180
	5	153	171
	25	149	170
	100	149	167
	200	148	165
	218	149	165
	500	148	167
D-43, 925	0	159	169
	1	151	169
	5.5	159	171
	25	154	171
	50	151	170
	100	159	171
	200	154	172
	500	158	172
Cb-752, 925	0	168	197
	1	168	213
	5	169	218
	25	171	201
	50	168	205
	100	168	201
	200	168	193
	500	169	207

Table 14.9. Analyses for Interstitial Elements in Niobium-Base Alloys, Annealed for 2 hr

Alloy	Annealing Temperature (°C)	Analysis (ppm)			
		C	O	H	N
Cb-752	1315	110	160	<1	80
Cb-752	1800	44	50	<1	68
D-43	1315	950	42	2	13
D-43	1800	740	15	4	25

aging response was detected either by hardness or metallographic examination for the coupons annealed at either temperature. The microstructures of all coupons annealed at 1315°C contained a fine pepper-like precipitate, presumably ZrO_2, distributed in the matrix. Those annealed at 1800°C contained much less precipitate.

Alloy D-43 responded definitely to heat treatment. Two carbide phases are stable in this alloy[18] – a zirconium-rich carbide present as a fine dispersion and stable below about 1650°C and a niobium-rich carbide phase present as platelets or needles and stable above about 1650°C. As a result, the 1800°C anneal promoted formation of the niobium-rich carbide and resulted in a higher hardness than that of the material annealed at 1315°C, as seen in Table 14.8. Specimens annealed at either temperature showed a slight softening trend on aging at 1095°C. As illustrated in Fig. 14.14, the niobium-rich carbide in the microstructure of the high-temperature annealed material redissolved with time. This was accompanied by precipitation of the zirconium-rich carbide. No change was clearly evident in the microstructure of the material annealed at the lower temperature, as shown in Fig. 14.15.

Aging at 925°C resulted in no significant hardness changes in alloy D-43 annealed at either temperature, and the annealed microstructures were essentially retained after 500 hr at the aging temperature. As was the case for the Cb-752 alloy, annealing alloy D-43 at the higher temperature reduced the carbon and oxygen contents. This is indicated in Table 14.9.

Stability of Refractory Alloys in High Vacuums

D. T. Bourgette

Application of refractory-base alloys in space power systems may require thin-walled structural members in which evaporation losses cannot be tolerated because they would lead to loss of mechanical strength and changes in thermal conductivity and emissive properties. To assess these potential problems, several alloys are being studied in the range of 1100 to 1500°C and 5×10^{-7} to 6×10^{-10} torr. The test specimens

[18] E. M. Mahla, E. I. du Pont de Nemours and Co., personal communication with T. K. Roche, ORNL.

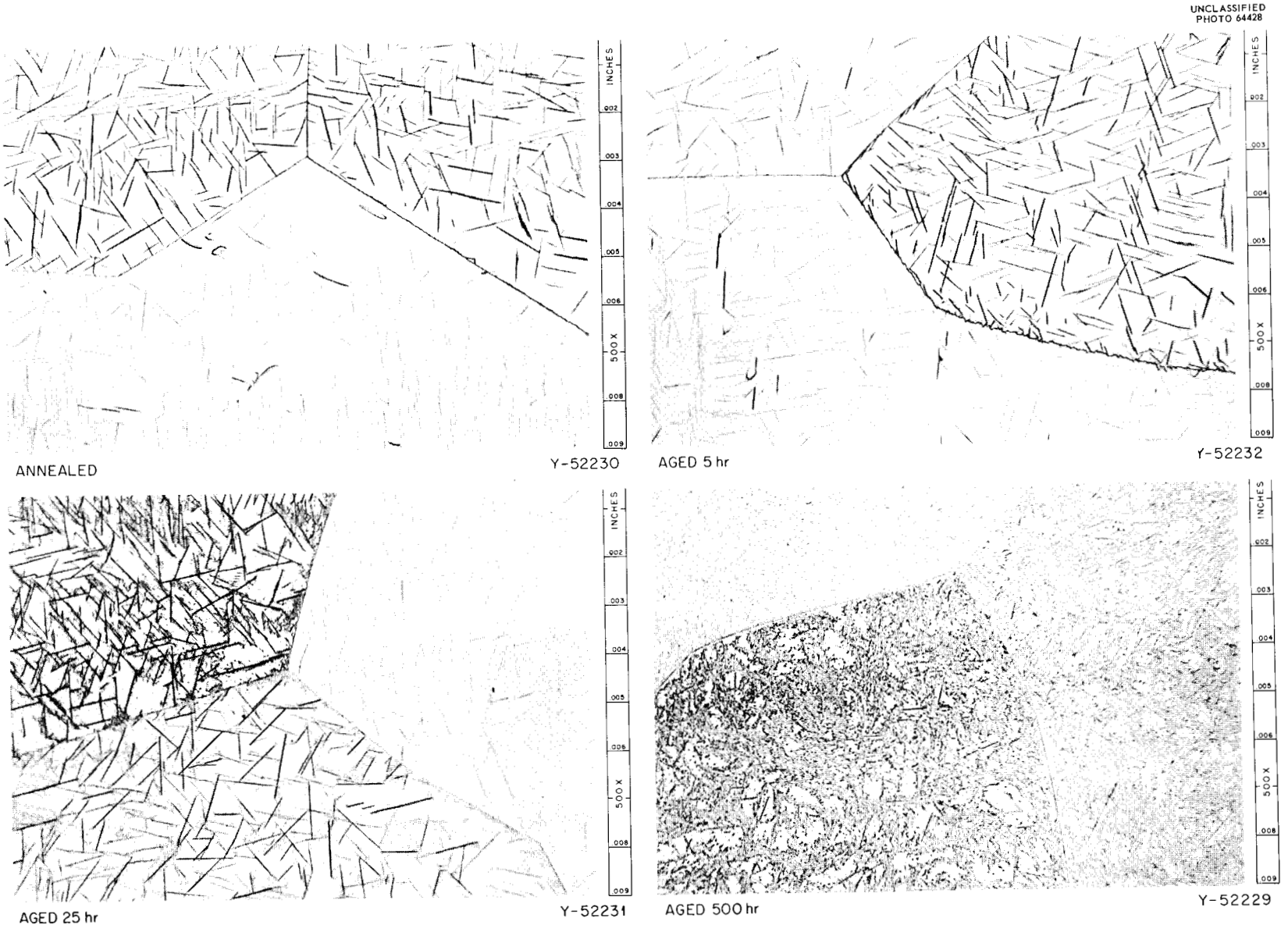

Fig. 14.14. Alloy D-43 Annealed 2 hr at 1800°C and Aged at 1095°C. Etched in 10 ml H_2SO_4, 10 ml HNO_3, 25 ml HF, and 50 ml H_2O. 500×. Reduced 37%.

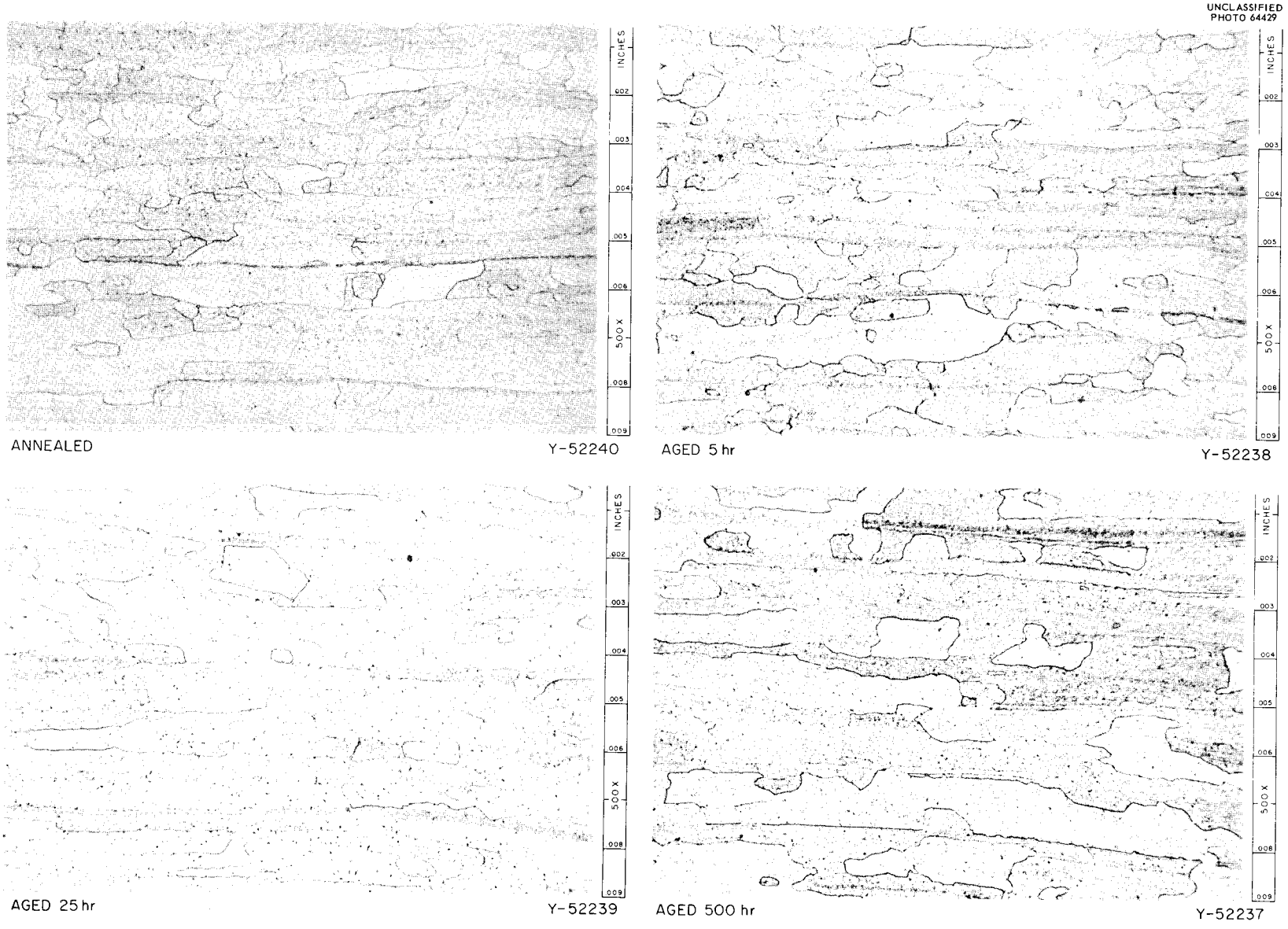

Fig. 14.15. Alloy D-43 Annealed 2 hr at 1315°C and Aged at 1095°C. Etched in 10 ml H_2SO_4, 10 ml HNO_3, 25 ml HF, and 50 ml H_2O. 500×. Reduced 37%.

were 0.013 cm thick and approximately 20 cm^2 in area; all samples were heated by induction in cold-wall systems.

Test conditions and results to date are presented in Table 14.10, while the changes in the contents of interstitial elements are summarized in Table 14.11. At 1100 to 1300°C, no appreciable evaporation losses were encountered in the Nb–1% Zr alloy. At very low pressures (10^{-9} torr) and higher temperatures, drastic losses of oxygen and carbon were measured. The microstructure of the specimen tested at 1500°C and 1×10^{-9} torr showed a clean matrix, free of precipitates. The grain boundaries appeared to have broadened. From these observations, we postulate that evaporation occurs primarily at the edges of the surface grains. This limited area for evaporation can account for the very small weight losses presented in Table 14.10.

Table 14.10. Evaporation Tests of Refractory-Base Alloys in High Vacuums

Alloy	Temperature (°C)	Test Conditions Pressure (torr)	Duration (hr)	Weight Change (mg/cm^2)	Composition of Deposit (%)
Nb–1% Zr	1500	1×10^{-9}	512	−0.098	100 Zr
		5×10^{-7}	512	−0.130	100 Zr
	1300	1×10^{-9}	303	−0.012	Not measurable
		5×10^{-7}	303	+0.043	Not measurable
	1200	1×10^{-9}	1000	−0.024	Not measurable
		5×10^{-7}	1000	+0.051	Not measurable
	1100	1×10^{-9}	300	−0.030	Not measurable
B-66	1500	7×10^{-9}	316	−1.7	83.8V–15.5Zr–0.462Mo–0.251Nb
		5×10^{-7}	316	−1.6	82.9V–12.2Zr–0.467Mo–0.171Nb
	1200	6×10^{-10}	513	−0.077	93V–7Zr
		5×10^{-7}	494	−0.024	93V–7Zr
D-43	1300	1×10^{-9}	276	−0.016	Not measurable
		5×10^{-7}	276	+0.018	Not measurable
T-111	1500	2×10^{-9}	448	−0.079	92.6Hf–5.81Zr
		5×10^{-7}	496	−0.23	100Hf
C-129Y	1500	2×10^{-9}	521	−0.16	30.5Hf–8.10Zr–21.2Y[a]
		5×10^{-7}	521	−0.56	61.5Hf–3.70Zr–1.50Y[a]
FS-85	1500	2×10^{-9}	667	−0.066	100Zr
		5×10^{-7}	667	−0.10	100Zr
Armour alloy	1100	2.8×10^{-9}	672	−0.14	67.0V[b]
		4.6×10^{-7}	672	+0.019	

[a]Sample weight uncertain.

[b]Titanium, niobium, and carbon present but not measured.

Table 14.11. Change in Interstitial Content of Refractory Alloys in High Vacuums

Alloy	Temperature (°C)	Interstitial Concentration After Exposure at Indicated Pressure (torr) — ppm											
		Carbon			Oxygen			Nitrogen			Hydrogen		
		Initial	10^{-9}	10^{-7}	Initial	10^{-9}	10^{-7}	Initial	10^{-9}	10^{-7}	Initial	10^{-9}	10^{-7}
Nb–1% Zr	1500	100	30	3	180	5	18	78	75	170	10	4	4
	1300		90	520		43	140		87	84		3	6
	1200		100	290		160	300		120	92		5	5
	1100		94			155			73			4	2
B-66	1500	100	30	19	97	6	50	250	10	24	4	2	3
	1200		80	18		74	1800		64	120		6	6
D-43	1300	980	960	900	63	61	410	89	26	33			
T-111	1500	70	60	40	53	11	97	23	21	200			
C-129Y	1500	75	90	460	115	76	240	60	29	1200	5	1	1
Armour alloy	1100	460	440	290	270	81	1100	130	130	130	4	3	3

Evaluation of Niobium-Vanadium Alloys for Application in High-Temperature Lithium-Cooled Reactor Systems

T. K. Roche

We have evaluated niobium-vanadium alloys for potential application in lithium-cooled reactor systems for space applications. Alloys for this use must be capable of withstanding high temperatures for relatively long times. Niobium-vanadium alloys appeared to be attractive because of good short-time strength properties as reported by other investigators. The greatest emphasis was placed on alloys with about 40% V and small additions of titanium and zirconium. This concentration of vanadium has been shown to be near optimum for high short-time strength properties. Properties of immediate interest were fabricability, corrosion behavior in lithium, aging response, weldability, strength, and stability in high vacuum.

We did not evaluate the alloys completely because several deficiencies were uncovered early in the testing program. For example, fabricating seamless tubing of the alloy Nb–39% V–1% Ti was difficult, and this same alloy lost metal by evaporation at elevated temperature in high vacuum. The most disappointing result was a lack of creep strength at elevated temperature. Nevertheless, certain properties such as corrosion behavior in lithium and aging response appear to be acceptable for the mentioned application.

We conclude generally that, while niobium-vanadium alloys embrace many attractive properties for short-time high-temperature applications, the major deterrent to the use of these alloys for extended service appears to be the lack of creep strength. As a result, we consider these alloys to be less satisfactory than other niobium alloys presently available for use in lithium-cooled reactors.

FABRICATION DEVELOPMENT

C. F. Leitten, Jr.

Refractory-Metal Extrusion

R. E. McDonald C. F. Leitten, Jr.

Work has continued on the extrusion of refractory-metal tube shells for the subsequent production

of large-diameter thin-wall tubing by warm-drawing and tube-reducing techniques. We completed satisfactorily the extrusion of molybdenum and molybdenum-base alloy tube shells using the floating-mandrel technique.[19]

The pertinent extrusion data are compiled in Table 14.12. Because of the difficulties encountered in obtaining smooth glass-free surfaces on the initial extrusions,[20] we evaluated alternate lubricants. As shown in the table, excellent extrusion surfaces were obtained using the volatile molybdenum trioxide, which formed readily on uncoated molybdenum billets at elevated temperatures. Prior to extrusion, the zirconia-coated die and mandrel were coated with a thin film of graphite. The surface appearance typical of as-extruded uncoated TZM and TM alloy tube shells is illustrated by Fig. 14.16, a close view of the surface of the TM alloy. A thin film of molybdenum trioxide essentially covers the surface.

The use of pyrolytic graphite as a lubricant in the high-temperature extrusion process was also considered because of its excellent insulation properties and favorable glide characteristics. A 0.020-in.-thick sleeve of pyrolytic graphite was placed in the extrusion-press container prior to the transfer of the billet and an uncoated TZM alloy billet was extruded at 2065°C. A TM alloy billet was similarly extruded at 1925°C. Figure 14.17 shows the rough surfaces where the high-strength pyrolytic graphite coextruded with the molybdenum alloys.

The extruded tube shells were sectioned for chemical analysis and metallographic examination

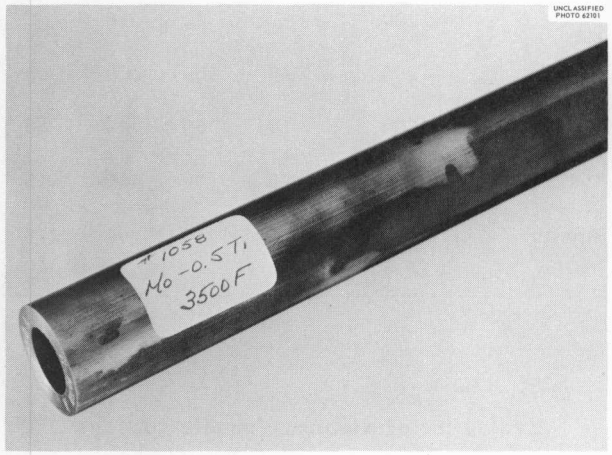

Fig. 14.16. Closeup View of Surface on Extruded TM Alloy Tube Shell.

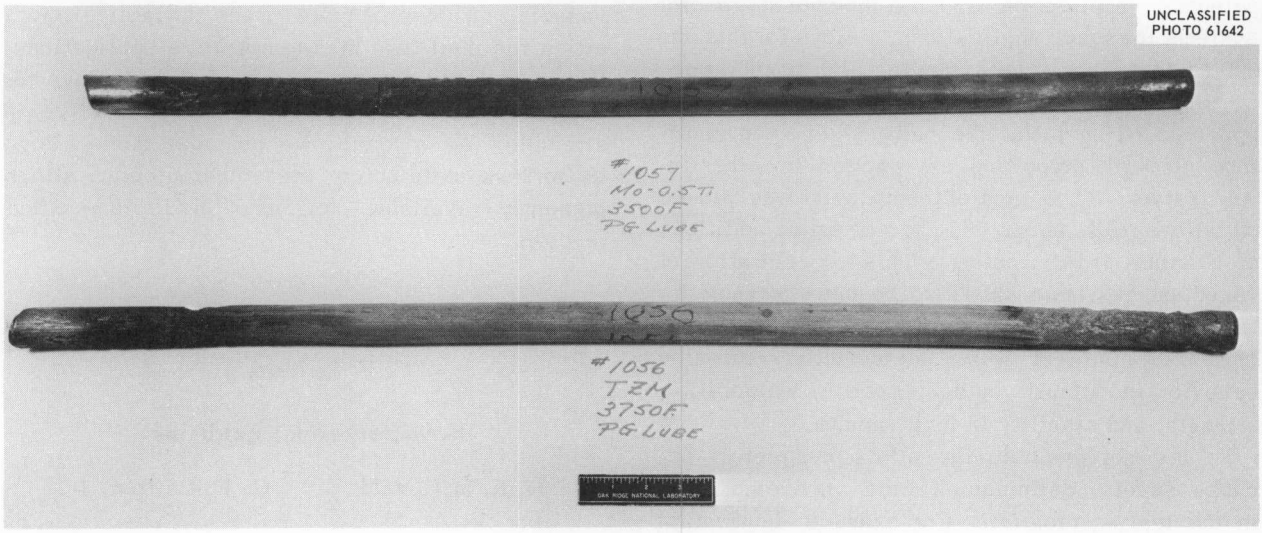

Fig. 14.17. Surface Appearance of TZM and TM Alloy Tube Shells Extruded with Pyrolytic Graphite Liners.

[19]R. E. McDonald and C. F. Leitten, Jr., "Production of Refractory-Metal Tube Shells by Extrusion and Flow-turning Techniques," paper presented at *AIME/IMD Symposium on the Applied Aspects of Refractory Metals*, Los Angeles, Calif., Dec. 9–10, 1963, and to be published in proceedings of the symposium.

[20]R. E. McDonald, *Metals and Ceramics Div. Ann. Progr. Rept. May 31, 1963*, ORNL-3470, pp. 106–108.

Table 14.12. Summary of the Molybdenum-Alloy Tube Shell Extrusion Data

(All reduction ratios approximately 8.8)

Billet	Material	Extrusion Temperature (°C)	Heating Time (min)	Transfer Time (sec)	Load (tons)		Lubricant	Remarks
					Breakthrough	Running		
985	Mo	1815	25	15.5	440	Not available	CG-7810	Surfaces fair; glass rub-in on nose and tail
986	Mo	1590	25	22	550	Not available	CG-7810	Surfaces good
1054	Mo	1650	21	10.9	600	530	CG-7740 outside only	Press stalled on billet tail; outer surface good; inner surface excellent
1055	TM	1925	25	10.6	510	415	CG-7740 outside only	Surfaces good
1056	TZM	2065	25	11.6	520	340	Pyrolytic graphite with nose cone	Nose and tail severely gouged; inner surface good
1057	TM	1925	22	9.7	500	370	Pyrolytic graphite sleeve	Tail severely gouged; inner surface good
1058	TM	1925	22	11.1	535	420	Bare	Outer and inner surfaces good
1059	TZM	2040	22	11.6	550	470	Bare	Outer and inner surfaces good
1060	TZM	2040	23	9.9	Not available	Not available	Bare	Outer and inner surfaces good

and to provide stock for warm drawing and tube reducing. Hollows of each alloy composition were available in the as-extruded condition for drawing and tube reducing. Additional hollows of each alloy composition were prepared for drawing and tube reducing after an optimum heat treatment.

The tube hollows for warm drawing were machined to 1-in. OD × $\frac{1}{8}$-in. wall and nondestructively tested using dye-penetrant, ultrasound, and x-ray techniques. All starting hollows were of sound quality and were shipped to Superior Tube Company to be drawn to $\frac{5}{8}$-in. OD × 0.035-in. wall using their commercial warm-drawing schedule. Figure 14.18 shows the high-quality surfaces on the finished tubing. The drawn tubing was found by extensive nondestructive testing to be free from defects. Table 14.13 compares the analyses of the starting stock and the product. A minor change in the carbon and oxygen contents may be noted.

On the basis of the success achieved in extruding uncoated molybdenum-base alloy tube shells and the subsequent production of high-quality tubing, two sintered unalloyed tungsten billets were extruded to tube shells using the same basic techniques. The billets were extruded uncoated using as the lubricant the volatile WO_3 that formed during the transfer of the billet from the inert-atmosphere furnace to the extrusion-press container. The initial billet was extruded at 1870°C and the second at 1705°C at a reduction ratio of 5.8. The external surfaces of the extruded tube shells are shown in Fig. 14.19. Apparently, good surface finishes were obtained in both extrusions that used the volatile tungsten trioxide

Table 14.13. Chemical Comparison Between Molybdenum-Base Alloy Wrought Stock and Drawn Tubing

Element	Starting Material[a]			Product		
	Mo	TM	TZM	Mo	TM	TZM
C	200	200	260	290	290	290
O	15	4	15	33	32	32
H	1	2	3	2	3	3
N	10	4	3	5	6	6
Ti			5500		4700	4700
Zr			1200			2100[b]

[a]Vacuum arc-melted and hot-rolled bar.
[b]Being rechecked.

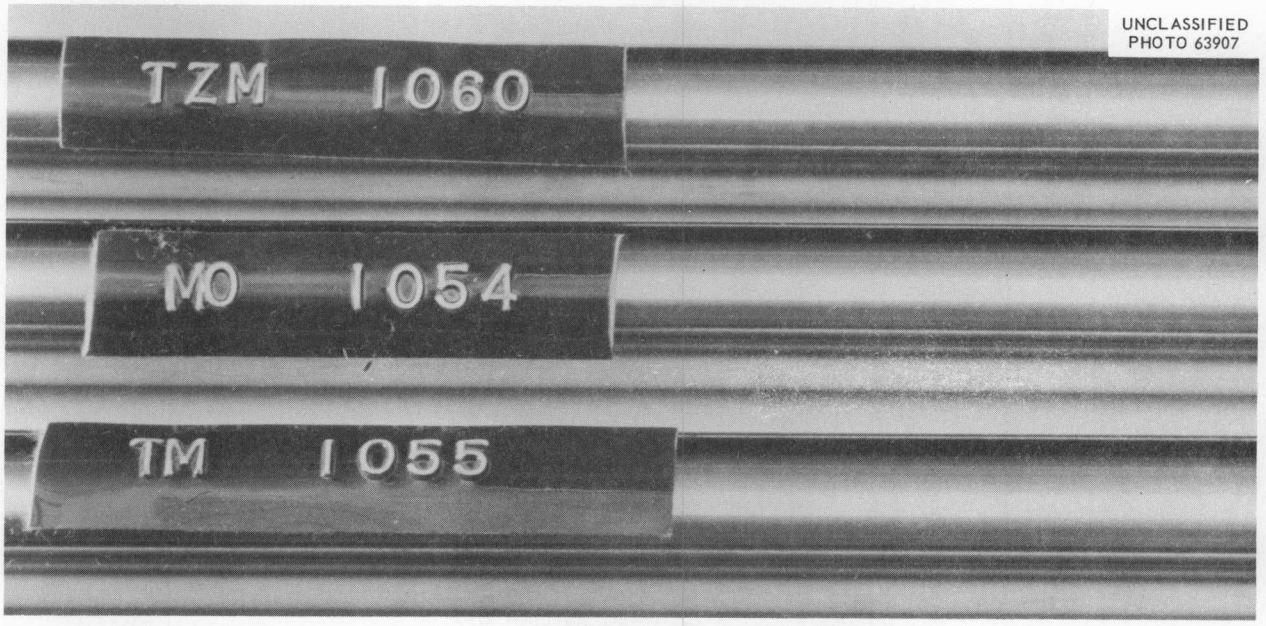

Fig. 14.18. High-Quality Surface Appearance of the Warm-Drawn Molybdenum and Molybdenum-Base Alloy Tubing.

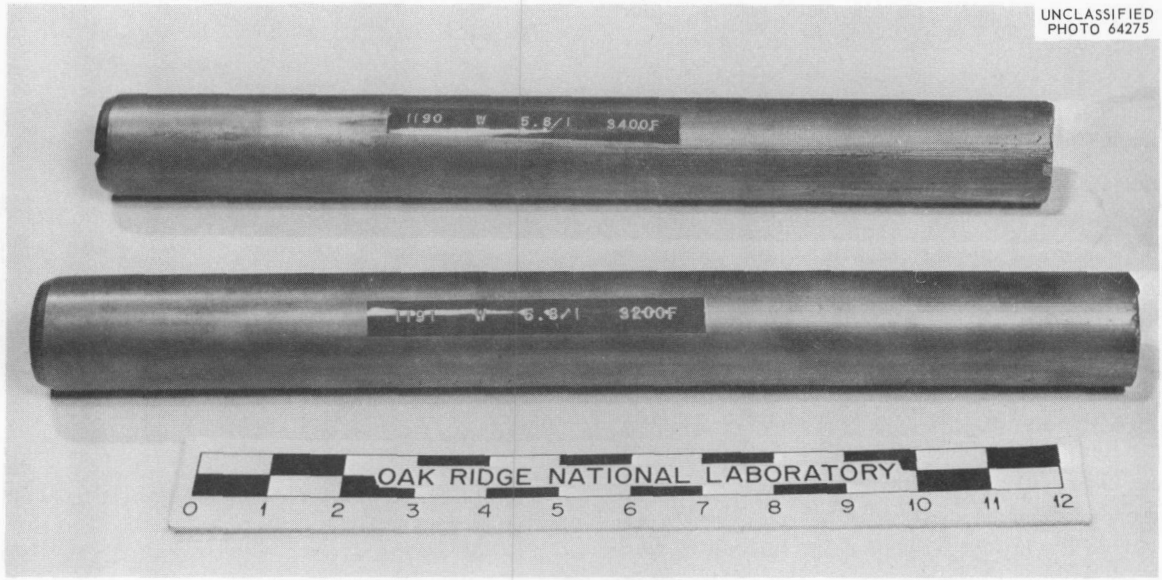

Fig. 14.19. Surface Appearance of Extruded Tungsten Tube Shells.

as the lubricant. As in the molybdenum-base extrusions, only a thin film of oxide was noted on these tungsten tube shells. After removal of this thin film, chemical analyses indicated that the atmosphere did not contaminate the tungsten at the extrusion temperature. Table 14.14 summarizes the interstitial impurity content of the tube shells and the powder-metallurgy starting material.

Table 14.15 is a compilation of the extrusion data. Note that the breakthrough pressure was lower at the lower temperature. The explanation for this seemingly contradictory behavior is that WO_3, which melts at 1473°C, evaporated so rapidly at the higher temperature that a less than ideal amount remained on the surface of the billet. We plan two further extrusions at 1600 and 1500°C to determine the optimum extrusion temperature.

Billets will also be prepared from wrought tungsten bar stock to compare with the sintered billets. Because the breakthrough pressures on the sintered billets were lower than expected, the

Table 14.14. Interstitial Impurity Content of the Tungsten Tube Shells

Impurity Content (ppm)	Tube Number		Starting Material
	1190	1191	
C	20	20	20
O	9	6	38
H	<1	<1	<1
N	<5	<5	7

Table 14.15. Tungsten Tube-Shell Extrusion Data

Billet No.	Billet Temperature (°C)	Time to Temperature (min)	Transfer Time (sec)	Load (tons)		Remarks
				Breakthrough	Running	
1190	1870	25	12.5	480	405	Outer surface good; inner surface superior
1191	1705	23	10.6	405	380	Outer surface superior; inner surface superior

wrought material will be extruded at a higher reduction ratio.

Flow Turning of Refractory-Metal Tube Shells

R. E. McDonald C. F. Leitten, Jr.

Work continued on the feasibility of producing tube shells at room temperature by flow turning.[21] By use of a commercial reducing schedule,[22] two tube shells were reduced to $\frac{7}{8}$-in. OD × 0.100-in. wall in a single pass, then vacuum annealed for 2 hr at 1200°C, and finally drawn at room temperature to final sizes (0.750-in. OD × 0.035-in. wall and 0.675-in. OD × 0.035-in. wall).

Three additional cast billets of Nb–1% Zr, 3-in. OD × $1\frac{1}{2}$-in. ID × about 5 in. in length, were flow turned by back extrusion to 2-in. OD × $\frac{1}{4}$-in. wall tube shells in six passes. Figure 14.20 shows the finished tube shells, which represent material yields of 75 to 80%. This yield should increase as the process is refined and the optimum parameters are developed.

We are investigating the feasibility of flow turning a cast tantalum-base alloy (T-111) at room temperature. A compilation of flow turning data on both the T-111 and Nb–1% Zr alloys is listed below. The higher rate of work hardening for the T-111 alloy requires more in-process anneals whereas the Nb–1% Zr alloy was reduced without intermediate annealing. The preliminary studies show that the T-111 will back extrude at room temperature and that the internal surfaces will be superior to those obtained on the Nb–1% Zr alloy.

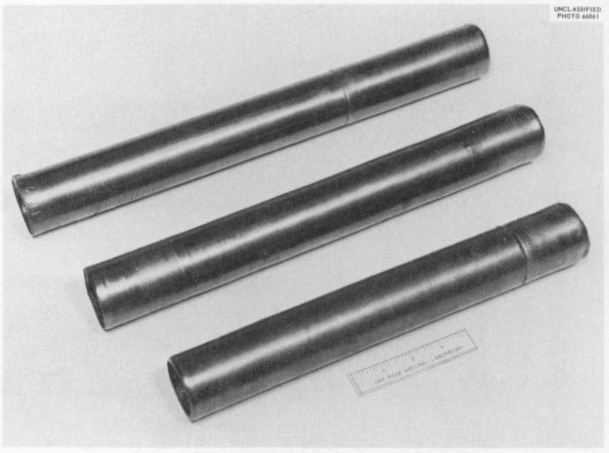

Fig. 14.20. Overall View of the Flow Turned Nb–1% Zr Alloy Tube Shells.

	T-111	Nb–1% Zr
Headstock speed, rpm	250	300–325
Roll feed, in./min	$2\frac{3}{4}$	1
Diameter reduction per pass, in.	$\sim\frac{1}{8}$	$\sim\frac{1}{8}$
Rockwell hardness		
Starting material	R_B 92–95 (vacuum annealed at 1200°C)	R_B 18–24 (vacuum annealed at 980°C)
1st pass	R_C 17–19	R_B 80–85
2nd pass	R_C 35–40 (to be vacuum stress relieved)	R_B 90–91
3rd pass		R_B 91–92
4th pass		R_B 91–92
5th pass		R_B 92–93
6th pass		R_B 94–95

[21] R. E. McDonald and C. F. Leitten, Jr., *Metals and Ceramics Div. Ann. Progr. Rept. May 31, 1963*, ORNL-3470, pp. 108–110.

[22] ORNL Subcontract No. 2316 with Superior Tube Company, Norristown, Pa.

MATERIALS COMPATIBILITY

J. H. DeVan

Corrosion of Refractory Metals by Lithium[2]

J. R. DiStefano

The pure metals niobium, tantalum, vanadium, titanium, and zirconium exhibit excellent resistance to dissolution by lithium at temperatures even in excess of 800°C. However, small quantities of oxygen in either niobium or tantalum can cause the rapid penetration of these metals by lithium over a wide range of temperatures. On the other hand, vanadium, titanium, and zirconium with oxygen concentrations as high as 2000 ppm do not show this susceptibility to lithium penetration.

One possible solution to this problem for niobium or tantalum is the addition of an alloying element that would tie up any oxygen present in the alloy. After systematic additions of oxygen were made to a Nb–1% Zr alloy at 1000°C, exposure to lithium for 100 hr at 815°C resulted in attack of the alloy in a manner similar to unalloyed niobium. However, we found later that at 815°C lithium did not penetrate niobium-zirconium alloys with less than two oxygen atoms per zirconium atom if the alloy had been heat treated for 2 hr at 1300°C after oxidation at 1000°C. Since the limiting proportion corresponds to the stoichiometry of ZrO_2, we postulate that corrosion protection results from the formation of this oxide during the heat treatment at 1300°C. Further tests showed that heat treatments of 1 hr at 1600°C or 5 hr at 1000°C were equally effective in producing a corrosion-resistant alloy. Our theory is supported by the results of Stephenson and McCoy,[24] who used mechanical-relaxation measurements, and Hobson,[25] who identified ZrO_2 in Nb–1% Zr specimens that had been heat treated under similar conditions.

Although treatment at temperatures from 1000 to 1600°C stabilized oxygen in Nb–1% Zr alloys, a specimen containing 900 ppm O was attacked after heat treatment at 2000°C. Similarly, specimens welded after oxygen additions did not resist penetration by lithium. These latter treatments apparently redissolved ZrO_2, leaving the oxygen in a form that rendered the alloy susceptible to attack.

The addition of 40% V to niobium did not alter the corrosion resistance to lithium even after heat treatments at 1300°C. Therefore, oxygen is not preferentially associated with vanadium in a form that prevents attack by lithium.

[23]Condensed from the University of Tennessee M.S. thesis of J. R. DiStefano, *Corrosion of Refractory Metals by Lithium*, ORNL-3551 (March 1964).

[24]R. L. Stephenson and H. E. McCoy, *Metals and Ceramics Div. Ann. Progr. Rept. May 31, 1962*, ORNL-3313, pp. 42–44.

[25]D. O. Hobson, *Aging Phenomenon in Columbium-Base Alloys*, ORNL-3245, p. 7 (March 1962).

NONDESTRUCTIVE TESTING

R. W. McClung

Refractory-Metal Evaluation

K. V. Cook R. W. McClung

We have nondestructively evaluated rod, bar, sheet, plate, tubing, and tube hollows of several refractory materials including Mo, W, and the alloys Nb–1% Zr, Cb-752, D-43, T-111, TM, TZM, and W–26% Re. The specific techniques have been selected according to the materials and their configurations. Fluorescent penetrants were used to evaluate the outer surfaces of all material, and generally speaking, no significant discontinuities were detected by this inspection procedure. At least one ultrasonic technique was used for the detection of internal flaws. In some instances radiography was also applied.

A large portion of the inspection work was devoted to the evaluation of three groups of developmental tubing. One group was fabricated under an ORNL developmental contract; the other two resulted from a joint AF-NASA-AEC project on refractory-metal tubing. The ORNL tubing ($\frac{3}{8}$-in. OD × 0.065-in. thick) was duplex material with an outer molybdenum or TM alloy sheath and an inner Nb–1% Zr alloy liner. Fluorescent penetrant examination disclosed only two small pinhole indications on the molybdenum-Nb–1% Zr alloy tubing, but cracks were detected in the outer surface of most of the tubes in the other lot.

Ultrasonic inspection was applied to each group. However, the presence of only a mechanical bond between layers of the composite tubing restricted the evaluation to the outer layer of molybdenum or TM alloy. A number of cracks were found in

Fig. 14.21. Flaws Ultrasonically Detected on the Inside Surface of D-43 Alloy Tubing. As polished. 75×.

tubing from each group, in agreement with metallographic observations, which revealed some cracks extending as much as 80% through the sheath.

Nondestructive evaluation has been completed on 79 ft of $\frac{1}{2}$-in. OD × 0.062-in. wall, 78 ft of $\frac{3}{8}$-in. OD × 0.062-in. wall, and 358 ft of $\frac{1}{4}$-in. OD × 0.018-in. wall D-43 alloy tubing produced under Air Force contract for a joint AF-NASA-AEC project. Analysis of the inspection results indicated that 80 to 90% of the material met stringent quality specifications. Typical flaws on the inside surface of a tube are shown in Fig. 14.21. We have reported[26] the results of the evaluation program in detail.

Nondestructive evaluation is nearing completion on a quantity of T-111 and B-66 alloy tubing also produced on a joint AF-NASA-AEC project. In general, the quality of the B-66 is somewhat superior to that of the T-111. This is somewhat surprising, since the latter alloy has demonstrated fabricability, while problems have frequently occurred with the former.

PHYSICAL PROPERTIES

D. L. McElroy

We are concerned with the measurement and correlation of needed high-temperature thermophysical properties of materials of interest. Information useful in the design, execution, and analysis of high-temperature experiments was obtained, including a meaningful series of thermocouple stability tests and measurements of properties such as total hemispherical emittance, electrical resistivity, and thermal conductivity.

High-Temperature High-Vacuum Thermocouple Drift Tests[27]

J. W. Hendricks D. L. McElroy

A facility for prolonged testing of the thermal-emf stability of thermocouples at high temperature and high vacuums was constructed. Using a Pt–10% Rh, Pt referee thermocouple and an optical pyrometer referee, tests in the range 1200 to 1450°C for times up to 1000 hr at pressures between 10^{-6} and 10^{-8} torr have shown a lack of drift in the thermal emf of platinum, rhodium, and tungsten-rhenium-base thermoelements. Commercial thermocouples of the types Pt–10% Rh, Pt; Pt–6% Rh, Pt–30% Rh; W, W–26% Re; and W–5% Re, W–26% Re were stable within ±10°C for the test conditions. Wire size and alloy content were not important variables within this stability range. Posttest examinations revealed only minor changes in surface appearance for the stable thermocouples.

[26] K. V. Cook and R. W. McClung, *Nondestructive Evaluation of D-43 Alloy Tubing*, ORNL-TM-843 (June 1964).

[27] J. W. Hendricks and D. L. McElroy, *High-Temperature High-Vacuum Thermocouple Drift Tests*, ORNL-TM-883 (in press).

One test at 1450°C did show that drift of thermal emf could be expected in Pt–6% Rh, Pt–30% Rh thermocouples if the hot junction is joined to niobium and exposed to a severe temperature gradient. This drift is apparently due to variations in composition resulting from diffusion of niobium into the wires. Severe changes in thermal emf were observed at 1200°C in MgO-insulated Pt–10% Rh, Pt thermocouples sheathed with tantalum or niobium; these changes were apparently caused by a reaction between the thermoelements and MgO.

Emittance of Type 316 Stainless Steel

T. G. Kollie D. L. McElroy

The total hemispherical emittance and the electrical resistivity of type 316 stainless steel in bright, oxidized, and evaporated conditions were measured in the range 200 to 1025°C. Since the specimens studied were designed to optimize measurement of emittance rather than electrical resistivity, our values of electrical resistivity for this particular alloy are higher than nominal literature values. The emittance is influenced by surface preparation, temperature, and vacuum of the measuring system. The emittance of polished, lapped, or cold-worked surfaces that had been held at 900°C for a few hours at 5×10^{-7} torr could be represented to ±0.5% in the range 200 to 1000°C by

$$E_t = 0.1345 + 1.6\,(t - 200) \times 10^{-4} ,$$

where t is in degrees Celsius. Polished or lapped surfaces measured at 5×10^{-6} torr did not obey this relation in the range 600 to 900°C. Holding a specimen for several hours between 600 and 750°C at 5×10^{-6} torr doubled the emittance; the higher value persisted on cooling and was due to a readily observable oxide film. However, if any initially bright specimen was heated above 800°C at 5×10^{-6} torr, this film decomposed, and at 1000°C the emittance returned to the value predicted by the above equation, even though initial differences of 15% may have existed.

Up to 900°C the emittance of the oxidized specimens was two to three times that of the unoxidized specimens, depending on the amount of oxide present. Holding at 900°C for several hours resulted in large increases in emittance for two oxide coating thicknesses; after approximately 5 hr, the emittances became essentially equal. Both oxidized samples gave values within 1% of each other on cooling, although they differed initially by 12% on heating. The emittance of these oxidized specimens may be represented by

$$E_t = 0.57 + 2.37\,(t - 200) \times 10^{-4} ,$$

where t is in degrees Celsius. The emittance of a specimen with an initial oxide film of 0.12 mg/cm^2 decreased 6% at 1025°C and 1×10^{-6} torr. This specimen was left overnight with power applied to observe the extent of this decrease. The decrease was apparently due to oxide decomposition, because the next morning the specimen had melted, and the oxide was missing from most of the specimen. The decomposition of the oxide had lowered the emittance and thus raised the temperature sufficiently to cause melting. This experiment was repeated with identical results.

Emittance, Electrical Resistivity, and Thermal Conductivity of Refractory Metals and Alloys

T. G. Kollie D. L. McElroy

A knowledge of the total hemispherical emittance, the electrical resistivity, and the thermal conductivity of refractory metals and alloys is needed to design equipment to operate at high temperatures. In addition, the measurement of several thermophysical properties on the same material aids the understanding of a single property. Initially we are studying rhenium, niobium, and the alloys Nb–1% Zr, D-43, T-111, and FS-85. We shall measure thermal conductivity in the thermal comparator apparatus to 400°C and in the longitudinal heat-flow apparatus to at least 100°C on specimen disks $\frac{1}{4}$ in. thick by 1 in. diam. We are measuring emittance and electrical resistivity in the emittance apparatus from −200 to 1500°C at pressures less than 5×10^{-7} torr. The emittance measurements are best performed on strips $0.010 \times 1.0 \times 12$ in., and the electrical resistivity measurements on $\frac{1}{16}$- to $\frac{3}{32}$-in.-diam rod. The electrical resistivity measurements allow the low-temperature thermal conductivity data to be extrapolated to high temperatures and may also

allow prediction of the total hemispherical emittance if present theoretical approaches[28] can be developed. The following paragraphs relate the results that we have obtained on some of the above-mentioned materials.

We obtained electrical resistivity data from −200 to 1000°C and meaningful emittance data from 600 to 1000°C using an $\frac{1}{8}$-in.-diam rod of rhenium. The electrical resistivity measurements were fitted to a fourth-degree equation covering this temperature region, and the values calculated from the equation are tabulated in 100°C increments in Table 14.16. For comparison, data of Powell[29] and Taylor[30] are included in this table. To 200°C, our results are 0.3 to 0.5 μohm-cm below Powell's, probably because we used a slightly purer specimen. Powell's measurements to 1400°C are reported graphically, but the values read from his graphs scatter less than ±0.4 μohm-cm from ours through 1000°C. Taylor's results are 4 to 6 μohm-cm above ours and indicate either a very impure specimen or a systemic measurement error. We calculated the electronic portion of the thermal conductivity, using the Wiedemann-Franz-Lorenz relation, from our electrical resistivity data and include it in Table 14.16. These values predict a minimum in the electronic portion of the thermal conductivity at 300°C. The total hemispherical emittance values of this rhenium rod are also listed. However, the rod geometry is not ideal for emittance measurements, since it permitted thermal conduction down the rod and led to spurious values below 600°C. Above 600°C this effect is negligible, and the measured emittance increased linearly with temperature to 1000°C. The values listed below 600°C were obtained by linear extrapolation of the high-temperature results.

[28]W. J. Parker and G. L. Abbott, "Total Emittance of Metals," paper presented at the *Symposium on Thermal Radiation of Solids*, sponsored by ASD-USAF, NBS, and NASA, San Francisco, Calif., March 4–6, 1964, and to be published in proceedings.

[29]R. W. Powell, R. P. Tye, and M. J. Woodman, *J. Less-Common Metals* **5**, 49–55 (1963).

[30]R. E. Taylor and R. A. Finch, *J. Less-Common Metals* **6**, 283–94 (1964).

Table 14.16. Thermophysical Properties of Rhenium

Temperature (°C)	Electrical Resistivity (μohm-cm)	Total Hemispherical Emittance	Thermal Conductivity[a] (w cm^{-1} $°C^{-1}$)	Electrical Resistivity (μohm-cm)	
				R. W. Powell	R. E. Taylor
−200	2.290				
−100	9.335			9.6	
0	16.837	0.123	0.397	17.2	25.6
100	24.476	0.130	0.373	24.9	31.6
200	31.993	0.138	0.362	32.6	37.6
300	39.189	0.145	0.358	39.3	43.6
400	45.926	0.152	0.359	45.9	49.6
500	52.125	0.160	0.363	51.8	55.5
600	57.766	0.167	0.370	57.8	61.4
700	62.894	0.175	0.379	63.1	67.4
800	67.608	0.182	0.389	68.0	71.8
900	72.073	0.189	0.399	72.3	76.2
1000	76.510	0.197	0.408	76.6	80.6

[a]Calculated electronic portion.

We have niobium specimens that we shall soon start to measure.

Table 14.17 lists our electrical resistivity and total hemispherical emittance values for the alloys Nb–1% Zr, D-43, and T-111. Since these measurements were made on rods, the emittance results are not valid below about 500°C because of thermal conduction. The emittance of these alloys decreased with increased thermal cycling, as if thermal polishing of the surfaces was occurring at the high temperatures. The emittance values reported are those for the final cycle and are 25 to 50% below the values obtained on first heating. Theory[28] predicts the emittance to be proportional to $(\rho_T)^{1/2}$, and the data for Nb–1% Zr and D-43 are consistent with this postulate.

The electrical resistivity values obtained on an Nb–1% Zr rod are consistently 0.7 to 0.5 μohm-cm greater than the existing values for niobium, and the D-43 values are 0.8 to 1.7 μohm-cm greater than those of Nb–1% Zr. This represents a surprisingly small increase in electrical resistivity for the 10% W addition, especially when one considers that the addition of 8% W and 2% Hf in T-111 alloy raises the resistivity 8 μohm-cm above that of unalloyed tantalum. Ordering in the niobium-tungsten system could explain the low magnitude of the increase. The electronic portion of the thermal conductivity of these alloys increases with increasing temperature. From 0 to 1500°C, it increases 40% for Nb–1% Zr, 50% for D-43, and 60% for T-111. The results for Nb–1% Zr agree well with the reported[31] increase of 37% in thermal conductivity between 0 and 1200°C.

[31] A. W. Lemmon, Jr., *et al.*, *The Specific Heat, Thermal Conductivity and Viscosity of Liquid Cesium*, NASA CR-54018 (BATT-4673-T7) (Feb. 29, 1964).

Table 14.17. Electrical Resistivity and Total Hemispherical Emittance of Nb–1% Zr, D-43, and T-111 Alloys

Temperature (°C)	Electrical Resistivity (μohm-cm)			Total Hemispherical Emittance		
	Nb–1% Zr	D-43	T-111	Nb–1% Zr	D-43	T-111
−200		6.9				
−100		11.3				
0	14.7	15.7	18.5			
100	20.0	20.1	23.0		0.205	
200	23.7	24.5	27.2		0.150	
300	27.6	28.5	31.2		0.129	
400	31.5	32.3	35.2		0.120	
500	35.3	35.9	39.0	0.103	0.124	0.081
600	38.9	39.3	42.8	0.110	0.133	0.096
700	42.2	42.8	46.6	0.117	0.143	0.111
800	45.4	46.0	50.3	0.130	0.154	0.126
900	48.4	49.2	54.1	0.142	0.167	0.141
1000	51.6	52.3	57.8	0.154	0.178	0.156
1100	54.7	55.4	61.3	0.167	0.190	0.170
1200	57.7	58.7	65.0	0.179	0.202	0.184
1300	60.8	61.8	68.6	0.192	0.214	0.199
1400	63.8	65.0	72.3	0.204	0.226	0.213
1500	67.0	68.2	75.9	0.215	0.238	0.227

15. Materials Compatibility

J. H. DeVan

Since refractory metals have exhibited better corrosion resistance to liquid alkali metals than have the more conventional metals and alloys, they are being considered as containment materials for alkali metals in high-temperature nuclear reactor systems. However, impurities such as oxygen, nitrogen, and carbon can significantly impair the corrosion resistance of these metals to several of the alkali metals.[1] Small concentrations of oxygen are particularly harmful. Meaningful corrosion studies have been difficult because it is difficult to obtain, maintain, and assay low levels of oxygen in these systems. We are continuing studies[2] that will enable us to accurately detect oxygen in the alkali metals, especially potassium, and to remove it. Our studies on oxygen in the container alloy, Nb–1% Zr, are reported in Chap. 14 of this report.

THE PARTITIONING OF OXYGEN BETWEEN ZIRCONIUM AND LIQUID POTASSIUM

A. P. Litman J. W. Prados[3]

We have utilized the observation that certain active metals will getter oxygen from alkali metals predictably to develop a method for determining oxygen in potassium. Previously, we showed[2] that oxygen could be quantitatively recovered from potassium by a technique that combined gettering by zirconium with vacuum fusion.

In the present work, the distribution of oxygen between dilute solutions in liquid potassium and α-zirconium at 815°C was studied in greater detail. Chemically polished zirconium specimens 0.010 to 0.065 in. thick were equilibrated with purified potassium for 100 to 500 hr in molybdenum capsules. The molybdenum was essentially inert, so the oxygen lost from the potassium was completely taken up by the zirconium and could be accurately determined by a mass balance for oxygen.

When no oxide scale was visible on the specimens after equilibration, the final weight fraction of oxygen in the zirconium varied from approximately 3 to 30 times that in the potassium. For a specific thickness, the ratio of the weight fractions increased with time, whereas for the same exposure time, the ratio decreased with increasing specimen thickness (Table 15.1). These results indicated that under the test conditions the system had not reached equilibrium.

There are good reasons to believe that oxygen diffuses approximately 1×10^5 times as fast in liquid potassium as in solid zirconium at 815°C. Hence, we suggest that the rate of oxygen uptake by zirconium is controlled by diffusion of oxygen through the zirconium. For oxygen uptake so controlled, one may calculate theoretical oxygen profiles using literature values for the diffusion coefficient of oxygen in zirconium and the solution given below for the diffusion equation with the boundary conditions of our experimental tests.

$$y = \frac{\kappa^0 y_{l0}}{1+k} + 2k\kappa^0 y_{l0} \sum_{n=1}^{\infty} \frac{\cos\left[\alpha_n (1 - x/l)\right] \exp\left(-\alpha_n^2 Dt/l^2\right)}{\left[\alpha_n^2 + k^2 + k\right] \cos \alpha_n},$$

[1] J. R. DiStefano and A. P. Litman, "The Effect of Impurities in Some Refractory Metal-Alkali Metal Systems," accepted for publication in *Corrosion*.

[2] A. P. Litman and J. R. DiStefano, *Metals and Ceramics Div. Ann. Progr. Rept. May 31, 1963*, ORNL-3470, pp. 63–66.

[3] Consultant from the University of Tennessee.

Table 15.1. The Partitioning of Oxygen Between Zirconium and Liquid Potassium at 815°C

Specimen Thickness (in.)	Time (hr)	Oxygen Contents (ppm)			Ratio of Final Oxygen Concentrations Zr/K
		Initial[a] in K	Initial[b] in Zr	Final[b] in Zr	
0.010	100	135	87	1400	24
0.010	500	135	87	1400	30
0.021	100	135	52	760	19
0.0215	100	135	52	720	13
0.022	100	135	52	650	12
0.021	500	135	52	800	20
0.040	100	135	38	420	9.6
0.065	100	135	32	190	2.7
0.065	500	135	32	190	2.9

[a]Gettering–vacuum-fusion analysis.
[b]Vacuum-fusion analysis.

where

y = weight fraction of oxygen in the solid,

y_{l0} = weight fraction of oxygen in the liquid at time $t = 0$,

$k = \frac{lA_s\kappa^0}{V_l}$, a capacity ratio,

l = half the thickness of the solid,

A_s = half the surface area of the solid,

V_l = half the volume of the liquid,

$\kappa^0 = y(0 \text{ in solid})/y_l(0 \text{ in liquid})$, equilibrium distribution coefficient,

x = distance from the solid surface,

D = diffusivity of oxygen in the solid, and

α_n = the roots of $\alpha_n \cot \alpha_n + k = 0$.

Using this result, we found that the ratio of the weight fraction of oxygen at the surface of the 0.010-in. specimen to that in the center should be approximately unity after 500 hr. Therefore, this specimen should not have exhibited an oxygen concentration gradient. The surface-to-center distribution ratio for the 0.065-in. specimen after 100 hr was calculated to be approximately 8, which was in fair agreement with experiment. Hardness traverses, although inconclusive, tended to support these calculations. Calculations of the average concentrations of oxygen in zirconium were also consistent with the experimental results. Although the experimentally measured equilibrium distribution coefficient for oxygen in this system was approximately 30, computations based purely on thermodynamic considerations give a value many orders of magnitude larger.[2]

DETERMINATION OF OXYGEN IN POTASSIUM

A. P. Litman G. Goldberg[4]
J. E. Strain[4]

In engineering systems using potassium as the working fluid, the most probable sources of oxygen contamination for the alkali metal are dissolved or adsorbed oxygen in the container material. The oxygen will usually redistribute from the solid metal into the alkali metal. However, there is evidence[5] that oxygen can also enter into the formation of metal-oxygen-potassium complexes in the potassium. Therefore, we must evaluate the analytical techniques for oxygen in terms of their

[4]Analytical Chemistry Division.

[5]S. Blecherman and J. Corlis, PWAC-1011, pp. 41–43 (classified).

ability to detect *total* oxygen in potassium irrespective of the chemical form of oxygen.

The source of oxygen in the tests described below was oxygen in solid solution in niobium. Earlier studies[6] demonstrated that oxygen in this form was strongly gettered by potassium at 815°C. The experimental sequence included oxidizing niobium specimens in a modified Sievert's apparatus, equilibrating the specimens at 815°C with purified potassium for 100 hr in molybdenum containers, and analyzing the potassium baths for refractory-metal impurities and for oxygen by several methods.

Table 15.2 shows the results of the recovery tests using amalgamation, vacuum distillation, and gettering–vacuum fusion (GVF). Both the amalgamation and distillation methods yielded low oxygen recoveries under these test conditions. Calculation of the oxygen content by either method is based on the intrinsic assumption that any oxygen in the residue after amalgamation or distillation is present as K_2O.

The determination of oxygen in potassium by GVF depends upon accurate knowledge of the distribution ratio for oxygen between potassium and an active metal, such as zirconium. Recent tests indicate that oxygen will distribute itself between 0.050-in.-thick zirconium specimens and liquid potassium in 100 hr at 815°C in accordance with the partition coefficient

$$C_{fZr}/C_{fK} = 5 ,$$

where C_{fZr} is the final concentration of oxygen in zirconium and C_{fK} that in potassium. Accordingly, the initial oxygen concentration C_{iK} in potassium can be determined by equilibrating the sample with a zirconium specimen initially containing oxygen at concentration C_{iZr}, determining the gain ΔC_{Zr} in oxygen concentration of the zirconium specimen, and solving for C_{iK} in the equilibrium expression:

$$C_{fZr}/C_{fK} = \frac{C_{iZr} + \Delta C_{Zr}}{C_{iK} - \Delta C_{Zr}(W_{Zr}/W_K)} = 5 ,$$

where W_{Zr}/W_K is the weight ratio of zirconium to potassium. Table 15.2 shows that complete recovery was attained using the GVF method to determine the oxygen content of potassium after equilibration with niobium. We conclude that amalgamation and distillation analyses, in their present state, are inadequate but the GVF procedure is satisfactory for determining total oxygen in potassium.

Table 15.2. Recovery of Oxygen from Potassium by Amalgamation, Vacuum-Distillation, and Gettering–Vacuum-Fusion Analyses

Method of Analyzing O in K	Oxygen Content (ppm)				Recovery (%)
	in Nb[a]		in K[b]		
	Initial	Final	Calculated	Found	
GVF	1500	130	746	742	99.5
Amalgamation	1400	110	881	305	35
Vacuum distillation	1400	170	741	280	38

[a]By vacuum fusion.

[b]Initial concentration of O in K was 135 ppm, determined by GVF.

Another analytical procedure that is specific for oxygen is neutron activation. Small concentrations of oxygen have been assayed in various materials using the reaction $^{16}O(n,p)^{16}N$, where the neutron source is a machine generator[7,8] producing neutrons of approximate energy 14 Mev. There are few interferences encountered in measuring the induced ^{16}N decay, but a disadvantage of the method is the extremely short ^{16}N half-life (7.4 sec), which requires rapid transport of the activated sample to a counting device. Another problem is the selection of a suitable sample container (rabbit). For determining small quantities of oxygen in potassium, the container should have: (1) a low oxygen concentration, (2) resistance to attack by potassium, and (3) low induced activity during exposure. High-density polyethylene rabbits have been used[9] for the determination of elements other than oxygen and for the determination of oxygen in high concentration. However,

[6]A. P. Litman and J. R. DiStefano, ORNL-3420, pp. 219–20 (classified).

[7]E. L. Steele and W. W. Meinke, *Anal. Chem.* 34(2), 185–87 (1962).

[8]D. J. Veal and C. F. Cook, *Anal. Chem.* 34(2), 178–84 (1962).

[9]J. E. Strain, W. L. Hampton, and G. W. Leddicotte, *The ORNL Analytical Chemistry Division's 150-KV Cockcroft-Walton Generator*, ORNL TM-362, p. 12 (Sept. 10, 1962).

polyethylene contains up to 1000 ppm O and so was deemed unsuitable for our application. We chose molybdenum and nickel capsules, using different end closures for the containers, to examine both accuracy and precision of the method.

The results of analyses by this method are summarized in Table 15.3. In the first three test series, essentially complete recovery of oxygen was obtained from samples of potassium doped with known amounts of K_2O. However, repeated analyses of a single sample gave scattered results. The percentage recovery in eleven determinations of one doped sample varied from 95 to 170%. Several possible reasons for this variance are being considered.

Apparently, total oxygen can be determined in potassium by activation analysis. The problem of a container seal suitable for routine work remains unsolved. However, we have designed a system to evade this problem in future studies by using a completely enclosed irradiation and counting cubicle, in which the potassium is protected by inert gas from contamination. This system should be in operation soon.

Table 15.3. Analysis of Oxygen in Potassium by Activation[a]

Sample Container		Sample Weight (g)	Initial[b] Oxygen (ppm)	Final Oxygen[c] (ppm)		Recovery (%)
Material	Oxygen Content (ppm)			Calculated	Analyzed	
Molybdenum	58	2.9	230	750	700	93
Molybdenum	58	2.6	230	560	550	98
Molybdenum	57	2.3	190	785	795	101
Nickel	155	0.7	212	2515	2380–4285[d]	95–170[d]

[a]Neutron flux, 2×10^8 neutrons cm^{-2} sec^{-1}; sensitivity, approximately 100 counts/mg.

[b]By activation.

[c]Additional oxygen added as $K_2O(s)$ and the solutions thermally equilibrated at 100 or 200°C.

[d]Eleven determinations.

16. Mechanical Properties

J. R. Weir, Jr.

Our objective is the study of the effects produced by reactor environments on the mechanical properties of materials. These environments consist of thermal and mechanical stresses imposed on the reactor structure, chemically reactive coolants, and neutrons produced by fissioning. Our work in the past year has emphasized the study of problems associated with hydrogen and carbon dioxide as potential coolants and the problem of radiation damage to stainless steel.

EFFECT OF HYDROGEN ON THE MECHANICAL PROPERTIES OF METALS[1]

H. E. McCoy, Jr.

We are evaluating the high-temperature mechanical behavior of several metals in hydrogen, primarily by comparative creep-rupture testing in hydrogen and in argon. The materials studied included two heats of Inconel, Nickel 200, Nickel 270, an electron-beam zone-refined melt of nickel, high-purity copper, Armco iron, electrolytic iron, and type 304 stainless steel. All of the nickel-base materials and the copper exhibited inferior creep resistance in hydrogen, while the iron-base materials were not influenced by this environment. Hydrogen had a large effect on pure nickel and copper; the magnitude of this effect decreased with decreasing purity of the metals. This effect was characterized, in general, by these observations. (1) At the same stress and temperature, the minimum creep rate was greater in hydrogen than in argon. (2) The rupture life was less in hydrogen than in argon at an equivalent stress and temperature. (3) The rupture ductility was the same in both.

We have run several additional experiments to determine the responsible mechanism. These experiments have included measurement of permeation of hydrogen through Inconel; measurement of the surface energy of nickel in argon and in hydrogen; comparison of sintering rates of nickel powder in argon, hydrogen, and vacuum; comparison of void formation in diffusion couples of iron and nickel annealed in argon and in hydrogen; comparison of diffusion of carbon in nickel in environments of hydrogen and argon; measurements of the rate of diffusion of ^{60}Co in nickel in argon and hydrogen; and transmission electron microscopy on thin nickel creep specimens. The mechanism that we think is most consistent with the experimental observations is based on the interaction of hydrogen with dislocations. Although several details of the mechanism are lacking, it qualitatively accounts for most of the experimental observations.

REACTIONS OF TYPE 304 STAINLESS STEEL WITH FLOWING CO_2 AT ATMOSPHERIC PRESSURE AND ELEVATED TEMPERATURES[2]

H. E. McCoy, Jr.

We have measured the oxidation of type 304 stainless steel in CO_2 over the temperature range of 590 to 980°C. Although the oxidation rate was usually parabolic, in several cases there was a transformation from parabolic to approximately

[1] Condensed from the University of Tennessee Ph.D. Dissertation of H. E. McCoy, Jr., *Effects of Hydrogen on the High-Temperature Flow and Fracture Characteristics of Metals*, ORNL-3600 (June 1964).

[2] Condensed from article by H. E. McCoy, Jr., "Reactions of Type 304 Stainless Steel with Flowing CO_2 at Atmospheric Pressure and Elevated Temperatures," submitted to *Corrosion*.

linear. These transformations were reproducible and we believe they are associated with changes in the rate-controlling step of the oxidation process. Type 304 stainless steel became carburized during exposure to CO_2. We studied several other alloys to determine the mechanism of carburization. These included type 406 stainless steel, a British niobium-stabilized steel (20 Cr–25 Ni), Inconel, iron, Fe–1% Cr, Fe–3% Cr, and Fe–10% Cr. We found that the carburization was dependent on the chromium content; a low chromium content favored carburization and higher chromium contents inhibited carburization. We explained this effect in terms of the influence of chromium on the type of surface oxide formed.

RADIATION EFFECTS ON THE MECHANICAL PROPERTIES OF STAINLESS STEEL

W. R. Martin

The influence of irradiation at elevated temperatures on the mechanical properties of structural materials is not well understood. A number of investigators have shown that the rupture life and fracture ductility of several materials are reduced by irradiation. We are evaluating the effect of irradiation on the ductility of stainless steels at elevated temperatures.

Figure 16.1 compares typical stress-strain curves for material irradiated and tensile-tested in each of two temperature ranges. Material irradiated at temperatures less than 450°C is stronger and less ductile (as measured by uniform elongation). At elevated temperatures irradiation does not affect the strength. The ductility at temperatures above one-half of T_m, the absolute melting temperature, is reduced, and this reduction in ductility is sensitive to the strain rate.

Figure 16.2 illustrates the effect of irradiation to 7×10^{20} neutrons/cm^2 (E > 1 Mev) at 200°C as a function of deformation temperature. The magnitude of the effect of irradiation on the properties increases to a maximum and then decreases as the deformation temperature is increased to approximately 0.5 T_m. Above 0.5 T_m, the effect is the same as observed for material irradiated at elevated temperatures and is shown in Fig. 16.3. Thus the irradiation temperature does not significantly alter the irradiation effect observed for stainless steel tested at elevated temperatures.

The general effects we have observed may be summarized as follows:

1. Irradiation affects the stress-strain relationship of material irradiated and then tested at low temperatures; irradiation results in increased strength and reduced ductility, as measured by uniform elongation. The true tensile stress (true stress at maximum load) and the true fracture stress and strain are not altered. Thus, the deformation process and not the fracture process is affected.
2. Irradiation at elevated temperature does not affect the stress-strain relationship. Ductility, as measured by uniform and fracture strains, is reduced for deformation temperatures above 0.5 T_m. The loss of ductility results in reductions in the true tensile and fracture stresses. The reduction in ductility is more significant at test conditions that result in intergranular failure, such as low strain rates at elevated temperature.

The loss of ductility of irradiated material deformed at elevated temperature is complex.

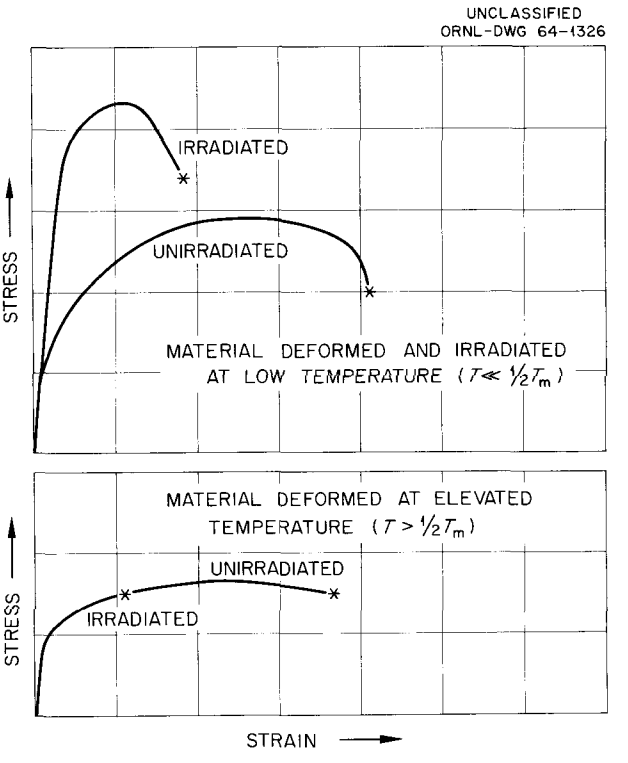

Fig. 16.1. Effect of Irradiation on the Stress-Strain Curves of Stainless Steels.

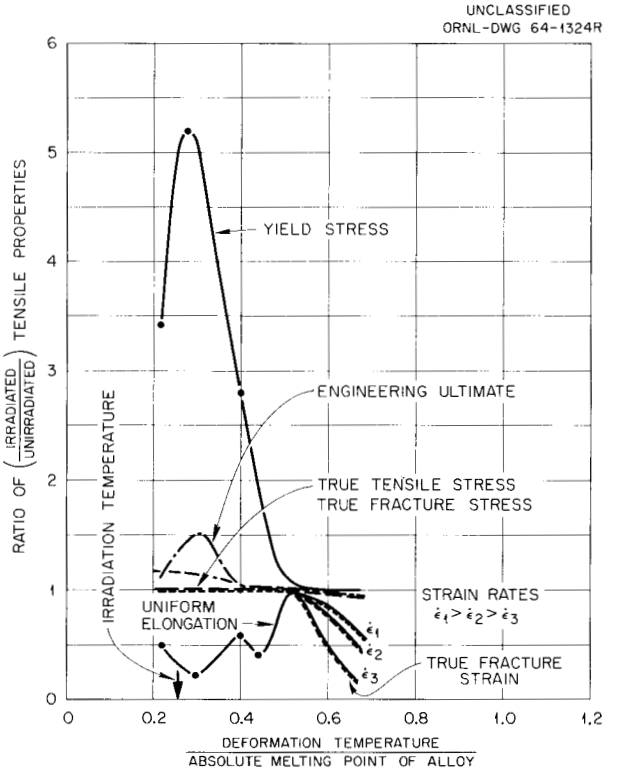

Fig. 16.2. Dependence on Test Temperature of the Effect of Irradiation at Approximately One-Fourth the Absolute Melting Point on the Tensile Properties of Stainless Steel.

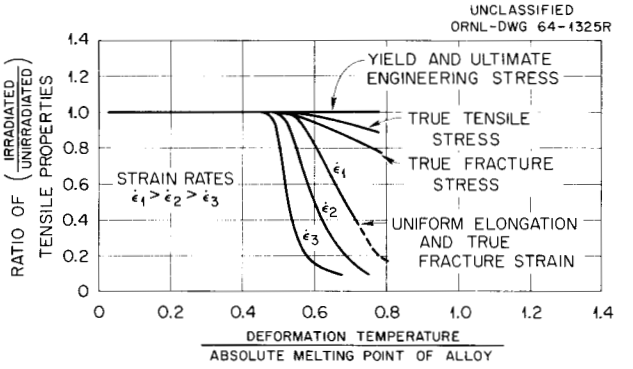

Fig. 16.3. Influence of Irradiation at Temperatures Above Half the Absolute Melting Point on the Post-irradiation Tensile Properties of Stainless Steel.

Damage from fast neutrons has been shown[3] to anneal at temperatures as low as 450°C, so one would expect that at a flux of 10^{14} neutrons cm^{-2} sec^{-1} the damage would anneal within the reactor at irradiated temperatures of 600°C and above. However, Roberts and Harries[4] indicate that the low ductility at elevated temperatures is caused by thermal neutrons, and our results for type 304 stainless steel (Table 16.1) are in agreement. We have reported[5] that the damage causing the low ductility at elevated temperatures does not anneal at approximately 1000°C.

Postirradiation examination of stainless steel shows that the low ductility at elevated temperature is due to grain-boundary embrittlement. Metallographic examination shows that the deformation temperature at which the irradiated alloy becomes embrittled is the temperature of transition from transgranular to intergranular mode of fracture. Grain-boundary cracks are found at smaller strains in the irradiated material than in the unirradiated alloy. In the irradiated material, these cracks propagate along the boundary rather than widen and cause complete specimen rupture at a considerably reduced strain. The dependence of the number of cracks per unit grain-boundary area on fracture strain supports these observations. Both nucleation and propagation of microcracks above 0.5 T_m were affected by irradiation.

The general characteristics of the effect of irradiation on the deformation of stainless steels at elevated temperatures are (1) yield stress and tensile strength are not affected; (2) ductility is reduced; (3) the reduction in ductility is more significant at test conditions that result in intergranular failure, such as low strain rates at elevated temperatures; (4) the reduction of ductility is due to grain-boundary embrittlement; (5) post-irradiation heat treatments, including those that anneal the damage caused by low-temperature irradiation, do not improve the ductility at elevated temperature; and (6) the loss in ductility appears to be related to doses of thermal and epithermal neutrons and not fast neutrons.

These observations are consistent with the hypothesis that the high-temperature damage is due to helium produced by the $^{10}B(n,\alpha)$ reaction. The helium may agglomerate into grain-boundary bubbles, which act as crack nuclei at elevated temperature.

---

[3] R. E. Bailey and M. A. Silliman, "Effect on Irradiation on Type 347 Stainless Steel Flow Separator in the EBR-I Core," pp. 84–102, *Symposium on Radiation Effects on Materials*, Vol. 3, *Am. Soc. Testing Mater. Spec. Tech. Publ. 233* (1958).

[4] A. C. Roberts and D. R. Harries, *Nature* **200**, 773 (1963).

[5] W. R. Martin and J. R. Weir, *Nature* **202**, 997 (1964).

Table 16.1. Comparison of Dose Effect on Mechanical Properties of Type 304 Stainless Steel at Room Temperature and 842°C

Deformation Temperature (°C)	Dose neutrons/cm^2		0.2% Offset Yield Stress (psi)	True Tensile Strength (psi)	True Uniform Strain (%)	Total Elongation (%)
	Fast E > 1 Mev	Thermal				
			$\times 10^3$	$\times 10^3$		
20	0	0	26.9	155.0	61.5	89.8
	3×10^{19}	1.6×10^{20}	58.1	144.0	45.7	65.4
	3×10^{19}	Cd covered	58.5	148.1	47.3	70.6
	5×10^{20}	7×10^{20}	91.0	140.0	40.6	50.6
842	0	0	9.3	16.1	13.5	47.4
	3×10^{19}	Cd covered	9.0	18.4	12.8	20.0
	3×10^{19}	1.6×10^{20}	9.0	17.9	9.2	14.0
	5×10^{20}	7×10^{20}	10.3	22.8	7.7	9.4

INFLUENCE OF PREIRRADIATION HEAT TREATMENT ON THE STRENGTH AND DUCTILITY OF IRRADIATED TYPE 304 STAINLESS STEEL

W. R. Martin

Observations of the interaction of dislocations at low temperatures with point defects generated by fast neutrons suggest that the introduction of a dislocation substructure into the material before irradiation may increase the coefficient of work hardening in irradiated material and consequently improve the ductility. Several heat treatments selected for type 304 stainless steel are given in Table 16.2. We believe that treatment 2 develops a substructure that is stable in the absence of radiation for a period greater than 2000 hr at 700°C and that treatment 3 does not develop a stable substructure. Both these treatments conclude with heating 24 hr at 482°C and 100 hr at 704°C, a treatment discussed previously by Garofalo and co-workers.[6] This treatment stabilizes the dislocation structure by precipitation of carbides of the type $M_{23}C_6$. Treatments 4 and 5 are anneals that result in grain sizes of ASTM 5–6 and 1–2 respectively. Table 16.2 also gives the influence of these preirradiation heat treatments on the strength and ductility of type 304 stainless steel at 20°C after irradiation to a dose level of 7×10^{20} nvt (E > 1 Mev).

Except after treatment 2, the pre- and postirradiation strengths of the alloy are in the same sequence after the various treatments. The effect of irradiation, as measured by the ratio of post- to preirradiation strengths, decreases as the preirradiation dislocation density in the alloy increases. Similar effects of cold working have been noted earlier.[7] However, the magnitude of the increase in yield stress of the alloy given treatment 2 is less than expected for cold-worked material. In fact, its postirradiation yield stress is less than that of the most annealed material (treatment 5).

Comparing the effect of irradiation on the stress-strain curve after treatments 4 and 5, we find that the influence of grain size is the same as that found by Chow[8] for iron at room temperature. However, the offset yield stress of the irradiated alloy does not have the grain-size independence

[6]F. Garofalo, F. von Gemmingen, and W. F. Domis, *Trans. Am. Soc. Metals* **54**, 430 (1961).

[7]T. H. Blewitt and R. R. Coltman, *Phys. Rev.* **82**, 769 (1951).

[8]J. G. V. Chow, *Quart. Progr. Rept. May–July, 1962: Irradiation Effects on Reactor Structural Materials*, HW-74679, pp. 5–7.

Table 16.2 Influence of Preirradiation Heat Treatment on the Postirradiation Room-Temperature Tensile Properties of Type 304 Stainless Steel[a]

Preirradiation Heat Treatment		0.2% Offset Yield Stress (psi)		Ratio of Post/Pre Yield Stress	Increase in Yield Stress (psi)	Ductility		Ratio of Post/Pre Strain	Difference in Strain (%)
						True Uniform Strain (%)			
No.	History	Postirradiated	Preirradiated			Postirradiated	Preirradiated		
		$\times 10^3$	$\times 10^3$		$\times 10^3$				
1	As received (equivalent to ~30% cold work)	106.0	69.2	1.5	36.8	29.0	44.0	0.66	15.0
2	Annealed 1 hr at 1038°C in H_2; strained uniaxially 25% at room temperature; finally heat treated 24 hr at 482°C and 100 hr at 704°C	74.0	53.0	1.4	21.0	35.0	44.0	0.80	9.0
3	Annealed 1 hr at 1038°C in H_2; strained 10% at room temperature; finally heat treated 24 hr at 482°C and 100 hr at 704°C	95.0	43.0	2.2	52.0	35.0	50.0	0.70	15.0
4	Annealed 1 hr at 1038°C in H_2	90.0	28.0	3.2	62.0	39.0	59.0	0.66	20.0
5	Annealed 5 hr at 1260°C in H_2	79.0	26.0	3.0	53.0	42.0	63.0	0.67	21.0

[a]Irradiated to 7×10^{20} nvt (>1 Mev). During irradiation the specimens were exposed for 2000 hr in the temperature range 120 to 170°C.

shown by Chow for iron but is similar to that observed by Hull and Mogford[9] for steels.

The ductility of the unirradiated alloy, as given by the true uniform elongation, is altered significantly by preirradiation heat treatment. The effect of irradiation, measured as the ratio of post- to preirradiation strain, is within the range of 0.66 to 0.70 for all treatments except treatment 2. Thus, another benefit of the development of the stable substructures appears to be a smaller loss of ductility, since the corresponding ratio is 0.8 after treatment 2. The data also suggest that treatments that improve the preirradiation ductility will also increase the postirradiation ductility of the alloy.

NEUTRON FLUX DOSIMETRY

J. C. Zukas

Routine activation sampling to monitor the neutron flux has been an adjunct of all experiments operated in the ORR by the Mechanical Properties Group of the Metals and Ceramics Division. We measure the activity of dilute cobalt alloy specimens, irradiated both bare and shielded by cadmium to obtain the necessary data for calculation of the thermal and resonance flux. We have chosen the model of Stoughton and Halperin[10] for these computations, which provide values for calculating burnout of other nuclide species. We measure the fast flux with various threshold detector materials. The reaction scheme that has provided the best internal consistency to date, based on the use of ^{58}Ni, is shown in Fig. 16.4. In theory, we should be able to measure the flux with unshielded samples and calculate the reaction rate, making corrections for thermal burnout of the high cross-section isomers, ^{58}Co and ^{58m}Co. However, uncertainties in cross sections, resonance integrals, and branching yields of these isomers limit the accuracy of such calculations.

The cross sections that have been reported for a single nuclide in many cases differ widely. Therefore, we are measuring thermal neutron cross sections using separated ^{58}Ni and high-purity iron along with the cobalt specimens. The ^{58m}Co is measured directly (as opposed to by difference). We are analyzing data from short irradiations while carrying out the long-time exposures.

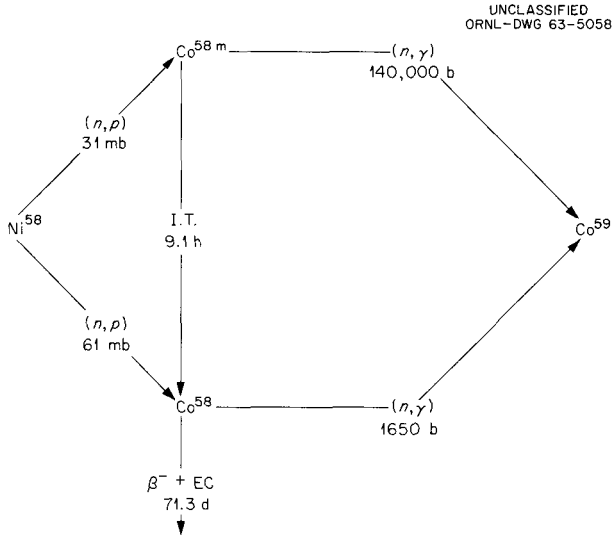

Fig. 16.4. Nickel-58$(n,p)^{58}$Co Reaction Scheme.

[9] D. Hull and I. L. Mogford, *Phil. Mag.* 8, 1213 (1958).

[10] R. W. Stoughton and J. Halperin, *Nucl. Sci. Eng.* 6, 100–18 (1959).

17. Nondestructive Test Development

R. W. McClung

The nondestructive test development program has been designed to develop new and improved methods of evaluating reactor materials and components. To achieve this we have conducted studies on the various physical phenomena, developed instrumentation and other equipment, devised application techniques, and designed and fabricated reference standards. Among the methods being actively pursued are electromagnetics (with major emphasis on eddy currents), ultrasonics, and penetrating radiation. In addition to the programs with method orientation, there are programs which use these and other methods to evaluate problem materials and to develop techniques for remote inspection.

ELECTROMAGNETIC TEST METHODS

C. V. Dodd

We have continued research and development concerning electromagnetic phenomenon on analytical and empirical bases. As part of the program we are studying the determination of impedance of an eddy-current probe coil as a function of coil dimensions, frequency, specimen conductivity and permeability, and coil-to-specimen spacing or "lift off." The mathematical solution has been programmed for computer operation[1] and values for several typical cases have been determined. A family of curves of coil impedance as a function of frequency (ω), conductivity (σ), permeability (μ), coil radius (R), and lift off (S) is shown in Fig. 17.1. The figure demonstrates that frequency, coil radius, or conductivity can be interchanged. The computer program also allows the eddy-current density and the field (vector potential) of the coil

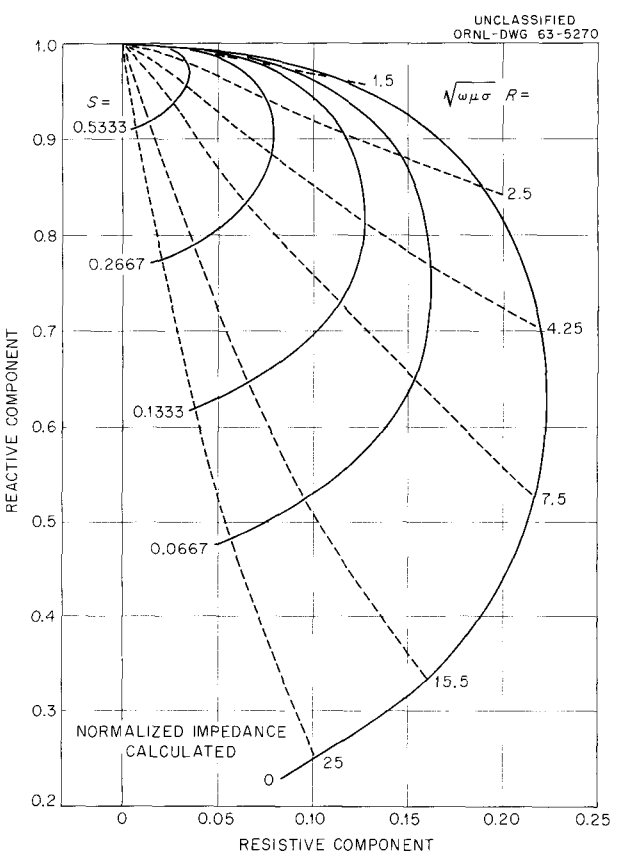

Fig. 17.1. Example of Calculated Normalized Impedance. The impedance components are plotted in reduced dimensionless units. The solid curves are for indicated constant values of the lift-off, and the dashed curves are for constant values of the combined parameter $R\sqrt{\omega\mu\sigma}$.

[1] C. V. Dodd and W. E. Deeds, "Eddy-Current Coil Impedance Calculated by a Relaxation Method," pp. 300–14 in *Symposium on Physics and Nondestructive Testing*, Southwest Research Institute, San Antonio, Tex., 1964.

to be calculated. Figure 17.2 shows equipotential contours of the field of a coil and eddy-current densities, superimposed on a cross section of the coil that is creating them. Both the currents and the field flow around the axis of the coil. From values of these, other information such as ohmic-heating density and eddy-current-force distribution may be obtained. We are seeking more versatile calculation methods with associated computer programming.

Development has continued on the phase-sensitive eddy-current instrument.[2] Several new circuits have been designed and constructed for the modular instrument. These include a low-distortion high-power amplifier, video amplifiers with high gain and low distortion and noise, and stable voltage-height discriminators. These coupled with the development of a new method for nulling the probe coils allow more accurate metal thickness measurements, since there is less error due to variations in lift off. In addition, a time-differential filter has been incorporated into the instrument to allow the detection of defects in materials in the presence of changes in wall thickness or conductivity. Included among the applications have been detection of core edge in flat fuel plates and detection of cracks in graphite spheres.

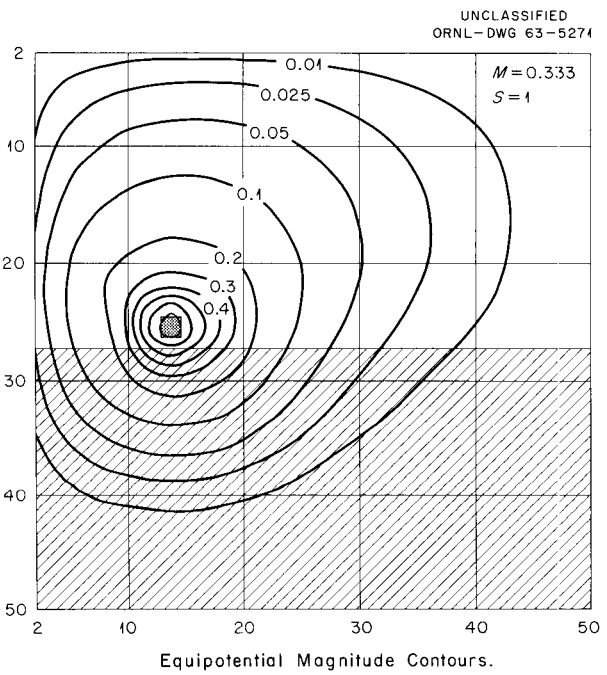

Fig. 17.2. Example of Equipotential and Current Magnitude Contours. Abscissa and ordinate scales are arbitrary lattice points used for the computer calculations and related to distances. The small cross-hatched square represents the cross section of the coil, and the large cross-hatched area represents the nearby metal specimen.

Continued studies of spacing measurements have culminated in a report[3] describing in detail our method of designing and fabricating coolant-channel spacing probes. The report describes the needed compromises and provides detailed instructions for constructing an optimum spacing probe.

ULTRASONIC TEST METHODS

K. V. Cook R. W. McClung

Our studies of ultrasonic behavior in thin sections have been directed primarily toward development of techniques to detect nonbond areas in clad structures. Studies of through transmission in flat fuel plates and sheet have continued. One- and two-crystal reflection methods have been demonstrated to be very useful for solving a number of difficult inspection problems. For instance, a two-crystal system was developed to detect nonbond in brazed tube-to-header joints.[4,5]

Many of these techniques need a reliable method of establishing the appropriate inspection angles. In order to simplify this problem a two-crystal angle manipulator (shown in Fig. 17.3) has been designed and fabricated in cooperation with the Plant and Equipment Division. We shall use this precise mechanical system to study both reflection and Lamb-wave ultrasonic techniques. The principal advantage to this system is that each transducer can be varied through a 45° angle without changing either the distance from crystal to

---

[2] C. V. Dodd, *Mater. Eval.* 22(6), 260 (1964).

[3] C. V. Dodd, *Design and Construction of Eddy-Current Coolant-Channel Spacing Probes,* ORNL-3580 (April 1964).

[4] K. V. Cook and R. W. McClung, *Metals and Ceramics Div. Ann. Progr. Rept. May 31, 1963,* ORNL-3470, p. 95.

[5] K. V. Cook and R. W. McClung, "An Ultrasonic Technique for the Evaluation of Heat Exchanger Brazed Joints," paper submitted for presentation at the Annual Meeting of the Society for Nondestructive Testing, Philadelphia, Pa., Oct. 19–23, 1964, and for publication in *Materials Evaluation.*

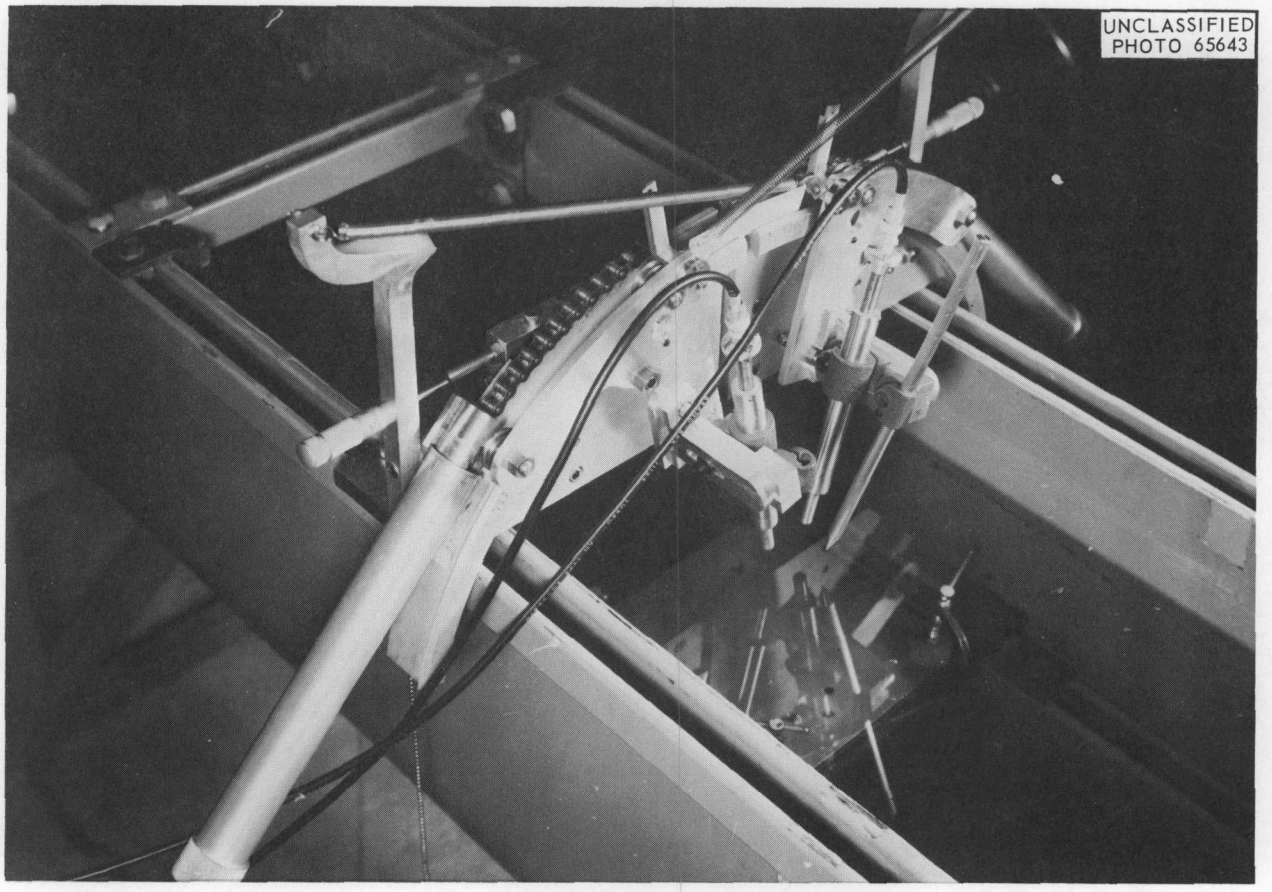

Fig. 17.3. Angle Manipulator for Two Independent Ultrasonic Crystals.

specimen or the point at which the ultrasound enters the specimen.

Another advance has been the design and fabrication of a two-crystal probe in which the angle of each crystal is variable. The probe, shown in Fig. 17.4, allows each crystal to be pivoted about a diameter. Hence, the probe can be used both to establish proper angles for reflection or Lamb-wave techniques and to perform the inspection. The illustrated probe has a minimum outside diameter of 0.370 in.; we feel that smaller probes are possible.

We have designed and constructed a transistorized ultrasonic dual-channel analyzer using the latest semiconductor and integrated circuitry. This instrument performs better than the old vacuum-tube model for the detection, gating, and processing of ultrasonic signals generated during nondestructive testing.

We have started to study the evaluation of fuel-plate-to-side-plate joints, such as those in ATR fuel assemblies, that have been pressure bonded by roll swaging. We used both sonic and ultrasonic methods on test samples of aluminum sheet that had been pinned at different roll pressures. No conclusive results were observed with the sonic method, but transmission of ultrasound (although very small) was possible through the bonded joints and seemed to be increased by increasing the roll pressure. Twelve swaged joints rolled at different pressures were evaluated first ultrasonically and then destructively. Destructive results and ultrasonic data could be correlated. However, further study showed that this technique will demonstrate variation in the bond strength of joints up to a certain value above which variations in sound transmission can no longer be detected. These preliminary studies show that a technique using ultrasonics probably could be developed to evaluate the fuel-plate-to-side-plate pressure bonds.

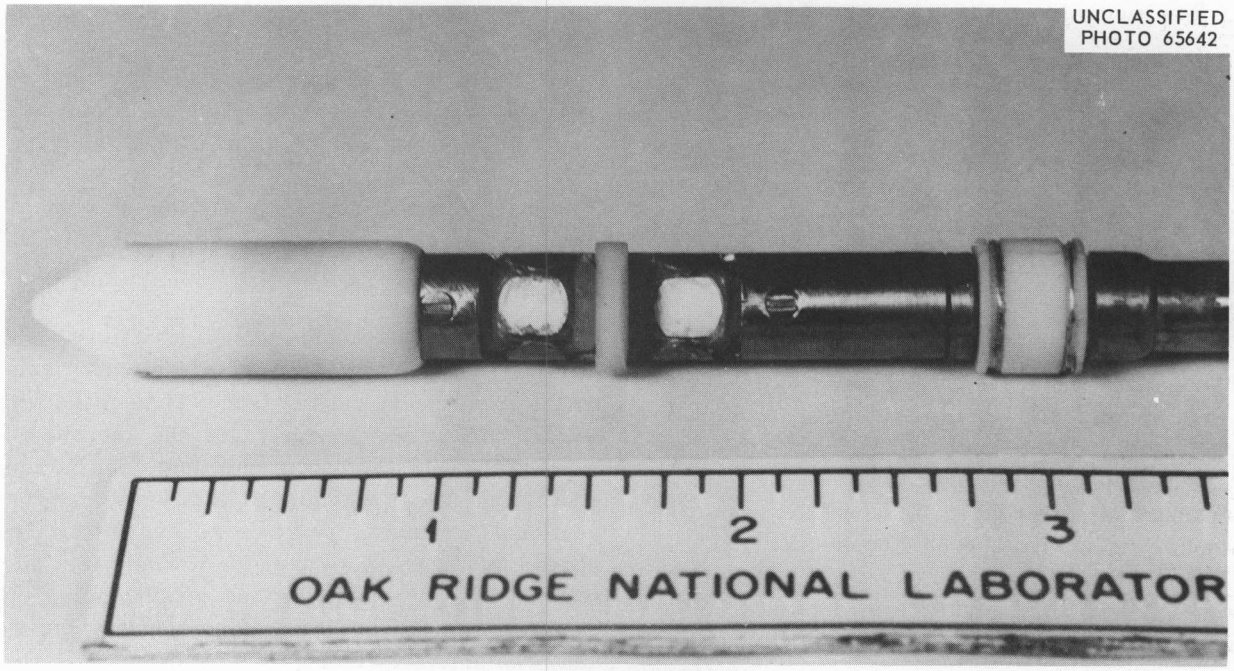

Fig. 17.4. Variable-Angle Dual-Crystal Probe.

PENETRATING RADIATION METHODS

Low-Voltage Radiography and Microradiography

R. W. McClung

We have applied the low-voltage radiographic and contact microradiographic technique[6] to evaluate a wide variety of specimens of thin or lightweight material. Of particular interest has been the use of the microradiographic technique on miniature samples of materials such as UC_2 and graphite that had undergone in-pile testing and were radioactive. Use of an internal dimensional standard in microradiography is described in Part III, Chap. 25, this report.

Gamma Scintillation Gaging

B. E. Foster S. D. Snyder

The versatile mechanical scanner[7] was successfully installed and modified slightly to facilitate its operation. Its successful use in developing techniques for measuring fuel inhomogeneities in fuel plates provided necessary design criteria for the fabrication of a pilot-model scanner and two production scanners, which will be used for homogeneity evaluation of the HFIR fuel plates. Details of this application are reported in Part III, Chap. 26, this report. Application to rods is reported in Part III, Chap. 29, this report.

We are continuing to develop calibration standard for x and gamma-ray attenuation measurement of fuel concentration variations, including the fabrication and use of alternate attenuation standards.[7]

We are expanding the use of the scanning system and technique toward determination of total fuel content. The results of some initial evaluations of fuel content in HFIR fuel plates have been in excellent agreement with those obtained by chemical analysis using total dissolution. Several problems are associated with this new application, but the results thus far are quite promising.

---

[6]R. W. McClung, *Mater. Res. Std.* 4(2), 66–68 (1964).

[7]B. E. Foster and S. D. Snyder, *Metals and Ceramics Div. Ann. Progr. Rept. May 31, 1963*, ORNL-3470, p. 96.

X-Ray Imaging with Closed-Circuit Television

W. H. Bridges

Several years ago we investigated the capabilities and performance of a closed-circuit television system for imaging x rays.[8] At that time the only x-ray sensitive vidicons were experimental tubes with glass windows that markedly impaired their use with x-ray energies below about 90 kv constant potential. Since then, interest has increased worldwide, and a beryllium-window vidicon was developed.[9] This vidicon is more sensitive to x rays, particularly to low-voltage x rays. As some welds in thin-wall tubing need to be inspected in a hot cell, procuring one of the new vidicons and determining its characteristics and potential application appeared advisable.

The first task was to determine the sensitivity of the vidicon to x rays. With 100- and 150-kv constant potential x rays, the signal current from the beryllium-window vidicon was about 1.6 times that of the glass-window vidicon. The greatest benefit with the beryllium-window vidicon is the low attenuation of the long-wavelength low-voltage x rays. We have obtained very good images of masking tape and graphite at 12 kvp. There was every indication that much lower voltages could be used with an adequate helium environment.

The major shortcoming of the vidicon is the small size of the active area – only $\frac{3}{8}$ by $\frac{1}{2}$ in. This is ameliorated to a great extent, however, by moving the specimen that is being examined. In fact, the motion aids the observation of a defect. With a proper mechanical drive, a specimen can be scanned about as rapidly as a radiograph can be examined. Another advantage is a magnification of 10 to 30×, depending on the monitor used.

The system was tested for resolution by examination of screens of various mesh sizes, transistors and diodes, welds in tubes of different sizes and materials, and wires. A 0.0005-in. tungsten wire was plainly visible. A 200-mesh screen was clearly resolved, but resolution of 400 mesh was marginal, probably the result of the lack of response of the 8-yr-old closed-circuit television system. Defects in aluminum plug welds up to $\frac{1}{2}$-in. diam were clearly discernible, but with materials of greater atomic number, techniques for masking and orienting must be developed for maximum resolution.

We have recently begun a series of experiments that provides an excellent example of the potential use of an x-ray-sensitive television system. We want to measure the movement of a specimen as it is subjected to very rapid thermal excursions. The annular specimen surrounds a resistance heater and is enclosed in a metal tube that is filled with helium and water-jacketed. As the thermal excursions may proceed at a rate up to 550°C/min, equilibrium is not established and the use of conventional measuring devices is negated. The speed precludes the use of radiographic film techniques. By observing and photographing the monitor screen of the x-ray television system, we can continuously record the specimen motion. Incorporation of an oscilloscope permits a relatively precise (<0.002 in.) direct reading of the specimen position. The oscilloscope is triggered by the television vertical-synchronization signal and the video output is fed to the vertical-deflection amplifier. By introducing a delay between the trigger impulse and the time the oscilloscope sweeps, the information contained in a horizontal line or group of lines from any position on the television screen may be presented on the cathode-ray tube. Now, insertion of the delayed trigger pulse of the oscilloscope sweep into the television video amplifier can put a marker on the television screen. By maintaining the marker at some distinctive specimen feature and reading the amount of delay, we may readily ascertain the movement.

[8] J. W. Allen and R. W. McClung, *An Electronic, High-Resolution, X-Ray Imaging System*, ORNL-2671 (Aug. 11, 1959).

[9] J. P. Mitchell, M. L. Rhoten, and R. C. McMaster, *X-Ray Image System for Nondestructive Testing of Solid Propellent Missile Case Walls and Weldments Final Report*, WAL TR 142.5/1-5, AD-299 987 (August 1962).

INSPECTION DEVELOPMENT OF PROBLEM MATERIALS

K. V. Cook R. W. McClung

We are developing nondestructive tests for materials that are difficult to inspect, including molybdenum, tungsten, tantalum, and graphite. Ultrasonics have been of particular value in the inspection of refractory-metal rod, bar, sheet, plate, tubing, and tube shells or hollows. Some applications of our methods are reported in Chap.

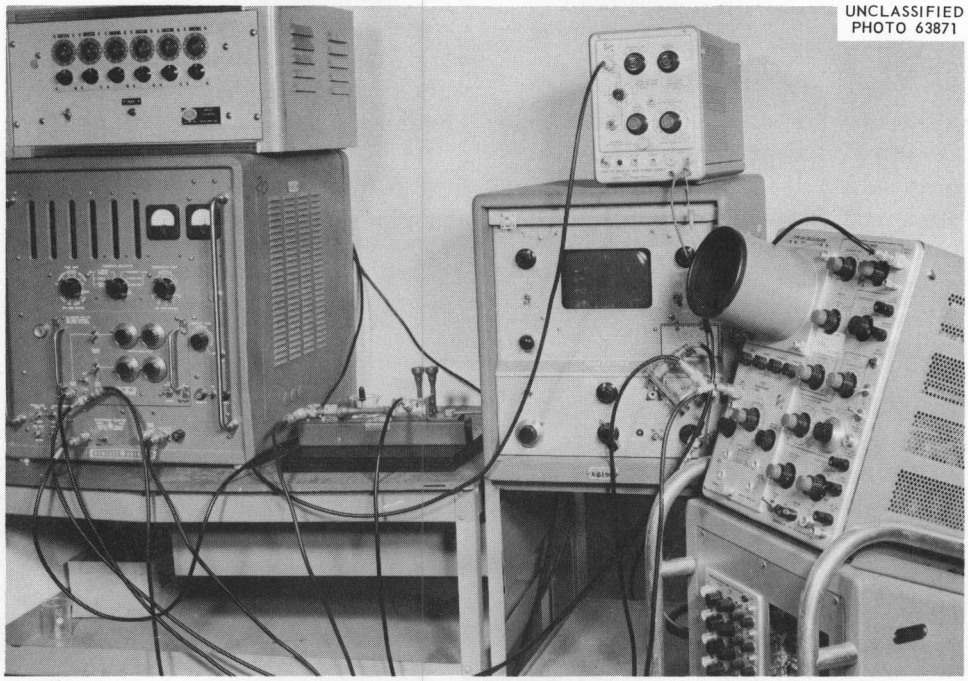

Fig. 17.5. System for Through-Transmission Ultrasonic Evaluation of Tensile Specimens.

14, this report. To avoid damaging the very expensive alloys, we have been concerned with the use of alternate materials as reference standards.

Two similar methods for ultrasonically evaluating graphite have been developed. One method is an immersion through-transmission technique that can be applied to large samples. The other method is a contact through-transmission technique that is limited to tensile specimens. Both methods were used to evaluate material from three large graphite blocks. The blocks were thinly coated with latex rubber to seal out moisture and evaluated by the immersion technique in the X, Y, and Z planes for velocity and attenuation. We selected 242 tensile specimens for all three planes to cover a good distribution of ultrasonic velocity values over a complete high-to-low range, cut them from the blocks, and evaluated them by the contact ultrasonic method, using the system shown in Fig. 17.5.

Mechanical properties will be obtained from the specimens and correlated with ultrasonic data. The Mechanical Properties Group is determining specimen properties, such as Young's modulus, resistivity, and fracture stress and strain. These properties will be compared with the ultrasonic velocity and attenuation data to see if a usable correlation exists.

DEVELOPMENT OF REMOTE INSPECTION TECHNIQUES

R. W. McClung

We have continued to develop techniques for radiography of materials in the presence of a radioactive background.[10] We have evaluated the first sets of radiographs of the aluminum step wedge after application of the fogging background. Use of photographic chemical reduction[11] increased tenfold the tolerance to background fogging radiation.

Many of our ultrasonic and eddy-current techniques and other penetrating-radiation techniques are being developed with the added criterion that they can be applied in a hot cell or other remote environment.

---

[10] R. W. McClung, K. V. Cook, and C. V. Dodd, *Metals and Ceramics Div. Ann. Progr. Rept. May 31, 1963*, ORNL-3470, pp. 96–97.

[11] R. W. McClung, "Radiography in the Presence of a Radioactive Background," paper submitted for presentation at the Annual Meeting of the Society for Nondestructive Testing, Philadelphia, Pa., Oct. 19–23, 1964, and for publication in *Materials Evaluation*.

THIRD GENEVA CONFERENCE EXHIBITS

S. D. Snyder

Five exhibit items were prepared for showing at the Third Geneva Conference held from August 28 through September 11, 1964. The displays are a phase-sensitive eddy-current flaw detector, a penetrating-radiation homogeneity scanner, an eddy-current gage for coolant-channel spacings, a metal identification meter, and a display of work done with contact microradiography. The four working-model items are shown in Fig. 17.6. Each of these was accompanied by a pictorial display in the form of back-lighted transparencies assembled into modules.

UNCLASSIFIED
PHOTO-66146

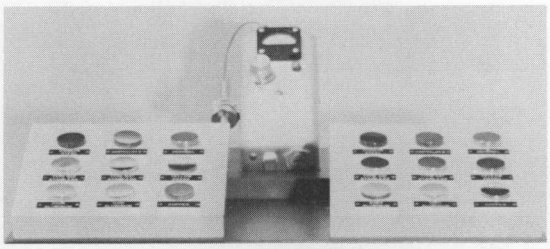

METAL IDENTIFICATION METER

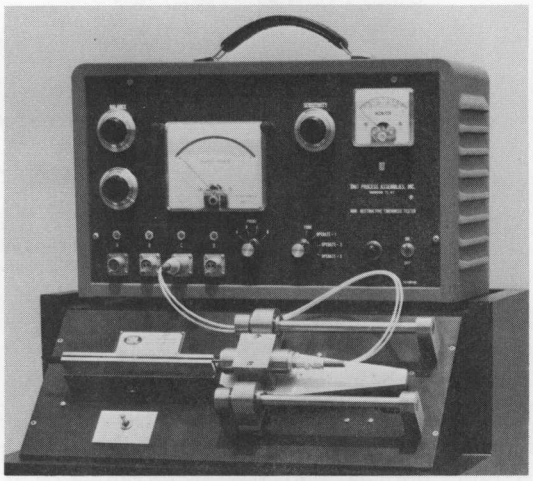

CHANNEL-SPACING MEASURING DEVICE

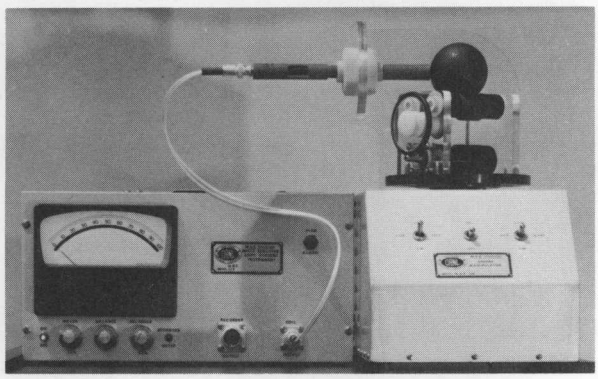

PHASE-SENSITIVE EDDY-CURRENT FLAW DETECTOR

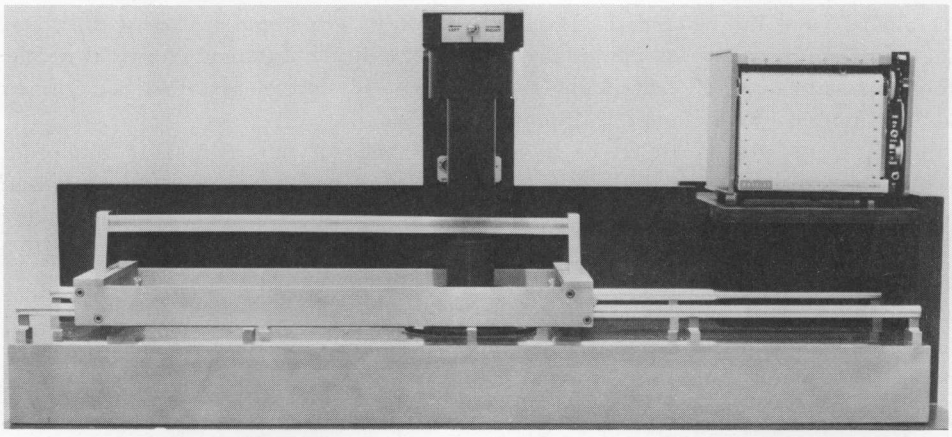

HOMOGENEITY SCANNER

Fig. 17.6. Nondestructive Testing Instruments Displayed at the Third Geneva Conference.

18. Reactions in Solids

T. S. Lundy

Our purpose is to provide information concerning solid-state reactions of importance in the development of materials for high-temperature application. We are emphasizing the study of mechanisms of these reactions by measuring diffusion rates in the solid state by various methods. In particular, we have studied (1) diffusion rates in various body-centered cubic refractory metals over wide ranges of temperatures, (2) the effect of alpha-particle bombardment on the diffusion of lead in silver, and (3) the thermal diffusion of antimony and ruthenium in silver.

DIFFUSION IN BODY-CENTERED CUBIC METALS

T. S. Lundy D. Heitkamp[1]
W. K. Biermann[1] J. F. Murdock
F. R. Winslow

Our investigation of diffusion in certain body-centered cubic metals has continued. This year we emphasized measurement of diffusion coefficients in niobium and tantalum over very wide ranges of temperature. Present indications are that in both of these metals the Arrhenius-type expression $D = D_0 \exp(-Q/RT)$ with constants D_0 and Q adequately describes the temperature variation of volume diffusion coefficients. This, of course, is in direct contrast to the inadequacy of this expression in describing diffusion coefficients in β-zirconium, β-titanium, and vanadium.[2]

[1]Visitor from Germany.

[2]T. S. Lundy *et al., Metals and Ceramics Div. Ann. Progr. Rept. May 31, 1963*, ORNL-3470, p. 67.

Diffusion of ^{44}Ti and ^{48}V in Titanium[3]

J. F. Murdock T. S. Lundy
E. E. Stansbury[4]

The diffusion of ^{44}Ti and ^{48}V in the body-centered cubic phase of iodide titanium was studied over the temperature range 900 to 1550°C. The resulting Arrhenius-type plots show curvature with the apparent activation energies and frequency factors increasing with temperature. The various possible interpretations of this behavior are considered.

Diffusion of ^{48}V in Vanadium[5]

T. S. Lundy C. J. McHargue

The diffusion rate of ^{48}V in single crystals of body-centered cubic vanadium was determined at temperatures from 1002 to 1888°C. The lower temperature data are enhanced on an Arrhenius-type plot relative to values expected by extrapolation of the high-temperature diffusion coefficients. Above 1600°C the equation

$$D = 58 \exp(-91{,}500/RT) \text{ cm}^2/\text{sec}$$

[3]Abstract of paper accepted for publication in *Acta Metallurgica* and based on the University of Tennessee M.S. Thesis of J. F. Murdock, *Diffusion of Titanium-44 and Vanadium-48 in Titanium*, ORNL-3616 (June 1964).

[4]Consultant from the University of Tennessee.

[5]Abstract of paper accepted for publication in *Transactions of the Metallurgical Society of AIME* and based on part of the University of Tennessee Ph.D. Dissertation of T. S. Lundy, *Diffusion in the Body-Centered Cubic Metals Zirconium, Vanadium, Niobium, and Tantalum*, ORNL-3617 (June 1964).

describes the data while at temperatures below about 1400°C the temperature dependence of the diffusion coefficient is

$$D = 1.1 \times 10^{-2} \exp(-61{,}000/RT) \text{ cm}^2/\text{sec} .$$

Submicron Sectioning Technique

R. E. Pawel[6] T. S. Lundy

A microsectioning technique for tantalum and niobium, based on the formation and subsequent stripping of an anodic oxide film, is described along with some applications in Part I, Chap. 7, of this report. Another application is in the following section.

Diffusion of ^{95}Nb and ^{182}Ta in Niobium[7]

T. S. Lundy F. R. Winslow
C. J. McHargue

We have measured the volume diffusion coefficient of ^{95}Nb in both mono- and polycrystalline niobium over the temperature range of 1000 to 2400°C. The high-temperature specimens (T > 1500°C) were sectioned by conventional lathe and precision-grinding techniques. The anodizing-and-stripping technique described above was used for the lower temperature specimens. The logarithm of the diffusion coefficient is a linear function of reciprocal absolute temperature down to 1200°C but deviates from linearity below this temperature. Over a diffusivity range of almost 10^7, the diffusion coefficient D is well described by the equation

$$D = 1.66 \exp(-97{,}600/RT) \text{ cm}^2/\text{sec} .$$

The low-temperature enhancement is probably due to short-circuit diffusion along lattice defects.

In a limited number of measurements, we found the diffusivity of ^{182}Ta in niobium to be about half that of ^{95}Nb in niobium, and the activation energies to be approximately the same for the two cases.

[6]Reactions at Metal Surfaces Group.

[7]T. S. Lundy, *Diffusion in the Body-Centered Cubic Metals Zirconium, Vanadium, Niobium, and Tantalum, ORNL-3617 (June 1964).*

EFFECT OF ALPHA BOMBARDMENT ON THE DIFFUSION OF LEAD IN SILVER

D. Heitkamp[1] W. Biermann[1]
T. S. Lundy

We measured the diffusion of ^{212}Pb in silver single crystals in the temperature range of 360 to 480°C by using the recoil method of Hevesey and Seith,[8] a surface-counting technique. Experiments were performed both with and without alpha-particle bombardment from a 10-curie source of ^{210}Po. In the absence of such bombardment the temperature dependence of the diffusion coefficient in the near-surface region may be described by

$$D = 600 \exp(-61{,}700/RT) \text{ cm}^2/\text{sec} .$$

Bombardment with 10^{11} 2.2-Mev alpha particles per square centimeters per second produces approximately 9.6×10^{-8} defects per second per atom site in silver and increased the diffusion coefficient by 6×10^{-18} cm^2/sec at all temperatures. Such an enhancement agrees satisfactorily with theoretical predictions based on analyses by Lomer[9] and Dienes and Damask.[10]

THERMAL DIFFUSION OF ANTIMONY AND RUTHENIUM IN SILVER[11]

W. Biermann[1] D. Heitkamp[1]
T. S. Lundy

The thermal-gradient redistribution of antimony and ruthenium in very dilute solid solutions in silver was investigated by radioactive tracer techniques. The concentration of antimony increased considerably at the hot side of the specimens and decreased at the cold side. The steady-state concentration was given by a straight line

[8]G. v. Hevesy and W. Seith, *Z. Physik.* **56,** 790 (1929).

[9]W. M. Lomer, "Defects in Pure Metals," p. 255 in *Progress in Metal Physics,* vol. 8, Pergamon, New York, 1959.

[10]G. J. Dienes and A. C. Damask, *Proc. U. N. Intern. Conf. Peaceful Uses At. Energy, 2nd, Geneva, 1958* **29,** 340 (1959); *J. Appl. Phys.* **29,** 1713 (1958).

[11]Abstract of paper submitted to *Acta Metallurgica.*

on a plot of the logarithm of the antimony concentration vs the reciprocal absolute temperature. The redistribution can be described by an unusually large negative heat of transport $Q = (-29 \pm 3)$ kcal/mole. The kinetic treatment of Wirtz can explain the data if it is assumed that most of the activation energy for migration of antimony atoms is necessary to open up the vacancy into which the atom jumps. This treatment, however, allows a very wide variation in the predicted heat of transport. The concentration profile for ruthenium in silver annealed under a temperature gradient was quite different from any redistribution that could be explained by thermal diffusion alone. No heat of transport could be calculated from the ruthenium distribution.

19. Tungsten Metallurgy

W. C. Thurber

For service at maximum temperature, tungsten represents the ultimate in pure metals. Exploitation of this potential has been sorely hampered by its limited ductility, which creates severe fabrication problems when the material is wrought at reasonable temperatures. To circumvent these problems, we are examining chemical vapor deposition as a fabrication technique, in which tungsten can be formed directly from the gaseous state into the desired final shape. We are emphasizing the preparation of pyrolytic tungsten deposits, particularly sheet stock, which can be subsequently evaluated by welding, mechanical testing, and measurement of the ductile-brittle transition. Preliminary studies of joining and characterization of the stability of pyrolytic tungsten have been undertaken. Base-line data have been obtained on tungsten sheet prepared by powder metallurgy.

We are also examining the possibility of enhancing the ductility of tungsten by introducing a dispersed second phase, which will provide mobile dislocations to promote plastic flow. Experiments on the extrusion of tungsten are reported in Chap. 14 of this report.

PYROLYTIC-TUNGSTEN DEVELOPMENT

D. O. Hobson C. F. Leitten, Jr.

We have completed preliminary experimental deposition of pyrolytic tungsten and scaled up the process. Previously, we studied[1,2] deposition of tubing over a wide range of variables. Tungsten was formed as internally deposited tubes ranging from $\frac{3}{4}$- to $\frac{1}{2}$-in. OD with lengths up to 14 in. We are continuing to study effects of temperature, pressure, and rate; and we are now assessing the effects of varying the ratio of hydrogen to tungsten hexafluoride as well. Typical results are shown in Fig. 19.1. The data represented by these curves were obtained by deposition with a hydrogen-to-tungsten hexafluoride ratio of 140 at a pressure of 20 torr on the inner surface of a $\frac{3}{4}$-in.-diam tube. Hydrogen reduced the WF_6 rapidly at 800 and 1000°C; the residual gas became so depleted in WF_6 at short distances from the injector that deposition became very nonuniform. At 600°C, the deposition rate depended less on distance, while at 500°C no deposit was obtained.

Typical microstructures of pyrolytic tungsten are shown in Fig. 19.2. The columnar grains extend through the entire specimen thickness.

To better evaluate pyrolytic tungsten, we want to perform both mechanical and physical tests on large pieces. So far, our experimental deposition

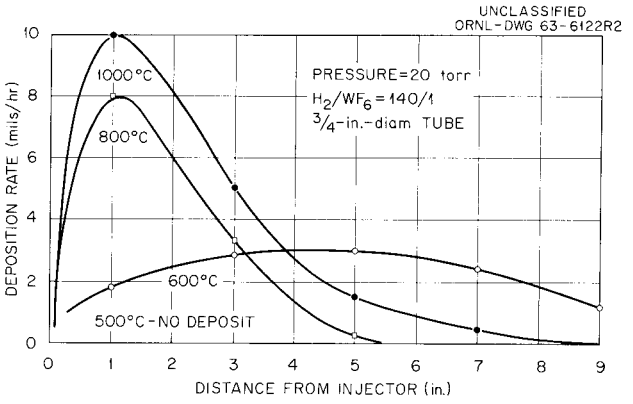

Fig. 19.1. Dependence of Deposition Rate upon Distance from the Hydrogen-WF_6 Injector in Tests at a Pressure of 20 Torr and H_2-to-WF_6 Ratio of 140:1.

[1]R. L. Heestand and C. F. Leitten, Jr., *Metals and Ceramics Div. Ann. Progr. Rept. May 31, 1963*, ORNL-3470, p. 75.

[2]R. L. Heestand, J. I. Federer, and C. F. Leitten, Jr., *Preparation and Evaluation of Vapor-Deposited Tungsten*, ORNL-3662 (in press).

equipment can produce large tubes with substantial wall thicknesses, but not shapes with extended surface area. In view of these requirements, a pilot plant production facility, shown in Fig. 19.3, was designed and placed in operation. This system again uses the reaction

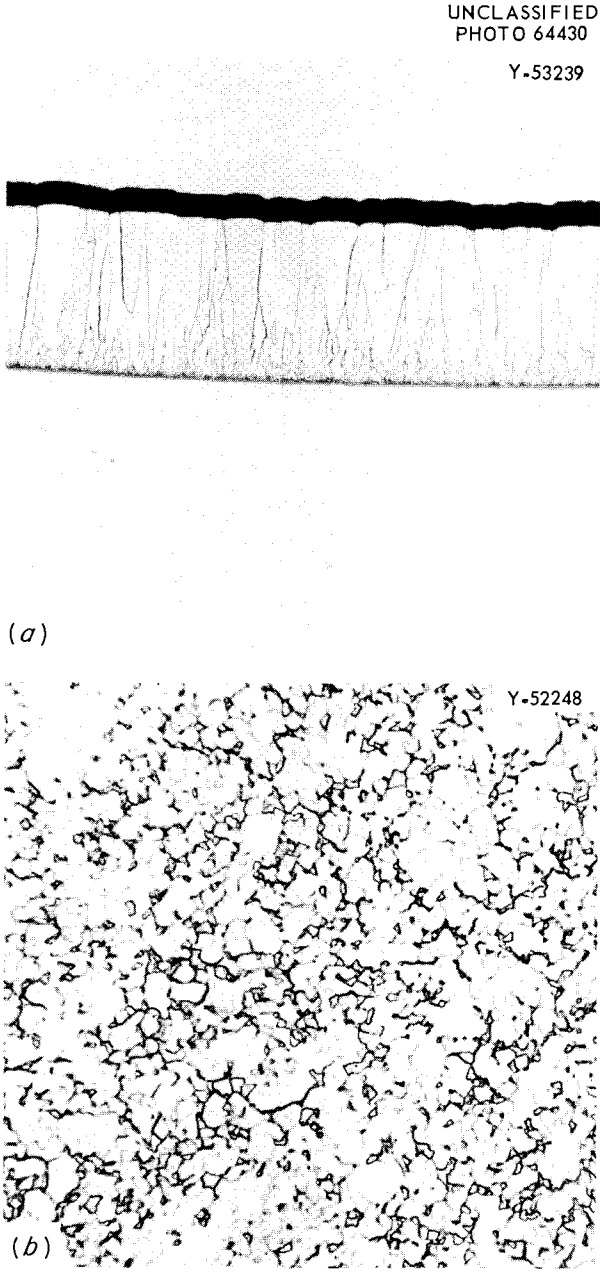

Fig. 19.2. Typical Microstructures of Vapor-Deposited Tungsten. Etchant: Equal parts concd NH_4OH and 30% H_2O_2. (a) Perpendicular to substrate. 100×. (b) Parallel to substrate. 500×.

$$WF_6 + 3H_2 \xrightarrow[\text{Excess } H_2]{\text{Heat}} W + 6HF$$

to deposit tungsten metal. At first we deposited it on the inner surface of a large copper right-hexagonal prism with a total usable flat area of approximately 320 in.^{2}, shown in Fig. 19.4. The heart of the equipment is a furnace containing a stainless steel chamber in which the copper deposition mandrel is suspended from a stainless steel cover flange. This arrangement creates two unconnected volumes, each of which can be evacuated independently of the other. The reactant gases are introduced through a water-cooled injector at controlled flow rates.

Since the strength of the copper mandrel is low at the deposition temperature (approximately 700°C), the pressure differential across the mandrel walls is controlled by a balance system capable of holding a pressure differential less than 1 torr across the mandrel wall at any system pressure.

Although we have used this mandrel, the results have not been satisfactory. To deposit sheet of needed thickness on it in a reasonable time would require a gas flow greater than our present capability. In addition, an internal arrangement of baffles would be needed to modify the flow pattern to ensure uniform deposition. To obtain sheet specimens for testing without making the required modifications, we have substituted a smaller mandrel and deposition furnace in our apparatus of Fig. 19.3. With them, we have produced sheet material $8 \times 1\frac{1}{4} \times 0.060$ in. in runs lasting 12 to 14 hr at WF_6 flow rates of 200 cm^3/min. This material is being evaluated chemically and metallographically and subsequently will be examined for its response to heat treatment and to tests of mechanical properties.

Typical chemical analyses of vapor-deposited tungsten, depending on deposition parameters, have the following ranges: C, 18 to 50 ppm; O, 12 to 60 ppm; H, 1 to 11 ppm; N, < 5 to 13 ppm; F, 10 to 40 ppm; and Cu, 1 to 10 ppm. Before a Kel-F flowmeter had been installed in the WF_6 line, spectrographic traces of B, Mg, and Si were found. These impurities resulted from attack on the glass flowmeters originally used.

In addition, a tubing-deposition furnace was built for the production of small ($\frac{1}{4}$- to $\frac{3}{4}$-in.) tungsten tubes by external deposition on copper tube mandrels. As in the sheet production

UNCLASSIFIED
Y-53631

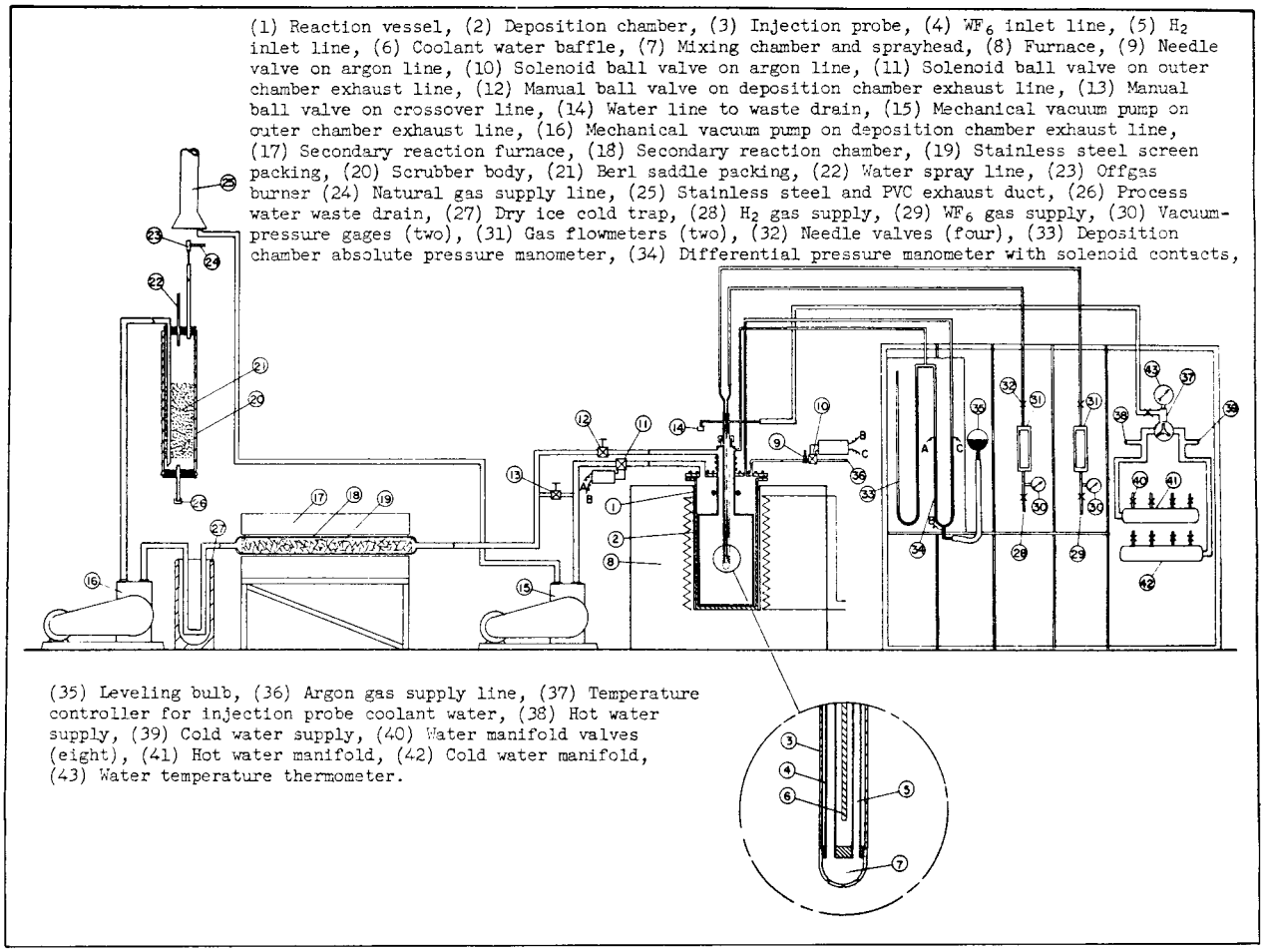

Fig. 19.3. Pyrolytic-Tungsten Deposition Setup.

discussed above, uniformity of wall thickness has been a problem, and several techniques have been used to obtain it. Previously,[1,2] tungsten was internally deposited by use of a three-zone furnace in which successive zones were cooled so as to transfer the deposition area down the length of the mandrel. The high thermal conductivity of the copper mandrel hampered the use of this method with external deposition. Although the furnace temperature was varied as the zones were operated, the tube remained at an essentially uniform temperature. To counteract this tendency, we tried external deposition on an internally resistance-heated mandrel and found that a heater wound to give maximum heating to the front and rear sections of the mandrel produced the most uniform depositions. At the front the incoming gas is cooled, and at the rear the outgoing gas is depleted in WF_6. The best tube obtained to date was 6 in. long with a wall thickness varying from 0.031 to 0.037 in.

BRITTLE BEHAVIOR OF TUNGSTEN

A. C. Schaffhauser

The embrittlement of body-centered cubic metals at low temperatures by small quantities of interstitial impurities is well known. Weakening of the grain boundaries by segregation of impurities is the accepted cause of this embrittlement, but the mechanism is not understood.

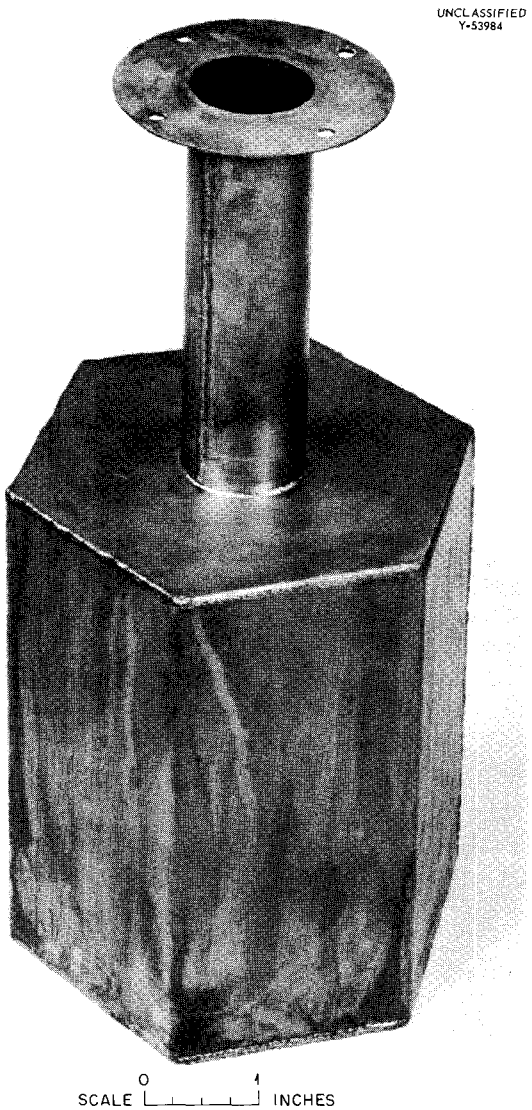

Fig. 19.4. Prismatic Copper Mandrel Used in First Attempts to Deposit Pyrolytic-Tungsten Sheet.

Recent electron-microscope studies[3] have shown that in impure body-centered cubic metals the grain boundaries cannot act as dislocation sources. Thus, very high stresses may be built up in the material without significant plastic flow until grain-boundary rupture ultimately occurs and the specimen fractures. From studies by Johnston and Gilman[4] of the dynamics of yielding and flow, extended to body-centered cubic metals by Hahn,[5] we know that the yield behavior depends on the number of mobile dislocations present prior to yielding.

The ductility of tungsten can be increased by increasing the purity, alloying to tie up the interstitial impurities, promoting other modes of deformation, or producing additional sources of dislocations. The purity level necessary for substantial increases in ductility is unrealistically high; the transition temperature for tungsten with less than 5 ppm C and O is still over 150°C. The improvement in ductility through the addition of alloying agents intended to scavenge the interstitial impurities may be limited, since these additions may not appreciably change the small concentration of interstitials in solution at the grain boundaries. The room-temperature ductility of the W–26% Re alloy is attributed to the ability of the rhenium to alter the concentration of interstitial impurities in the grain boundaries and to relieve the stresses built up during deformation by twinning. The high cost and limited supply of rhenium limit application of this alloy.

In view of these observations, we believe that the most attractive approach to lowering of the ductile-to-brittle transition temperature is by introduction of additional dislocation sources. We have started to study increasing the ductility of recrystallized tungsten by introducing particles that will act as dislocation sources during deformation. The dilute ternary alloys W-C-(Hf, Nb, or Ta) have been chosen for the initial stages of this investigation because of their strong tendency to form carbide particles, the size and distribution of which may be controlled by heat treatment.

Experimental quantities of the alloys have been produced as pancakes (800 g) by electron-beam melting. The results of chemical analysis of the alloys are given below:

Nominal Composition (wt %)	Analyzed Composition (wt %)
W–0.6 Nb–0.02 C	0.55 Nb–0.002 C
W–0.3 Ta–0.02 C	0.28 to 0.35 Ta–0.002 C
W–0.4 Hf–0.01 C	0.25 Hf–<0.002 C

[3]J. O. Stiegler, ORNL-3571, pp. 230–35 (May 1964) (Classified).

[4]W. G. Johnston and J. J. Gilman, *J. Appl. Phys.* **31**, 632 (1960).

[5]G. T. Hahn, *Acta Met.* **10**, 727 (1962).

Since we anticipated difficulty in retaining the alloying elements during melting, we had doubled the alloying content of the melting stock. Evidently the overcharge was sufficient to obtain the desired metallic alloying composition, but most of the carbon was lost during melting.

We believe that we can retain the desired carbon content by reducing the large surface area of the molten alloy exposed to the vacuum system. Consequently, a $1\frac{1}{8}$-in.-diam retractable mold was designed and installed by the Metal Forming and Casting Group[6] for this purpose. The carbides have been prealloyed in an arc furnace and will be drip melted with the tungsten into the water-cooled mold. The new melting procedure is also expected to aid in fabrication of the alloys. The ingots will be encased in molybdenum and extruded prior to further processing.

The effectiveness of varying amounts, sizes, distributions, and compressibilities of particles as dislocation sources will be evaluated by electron microscopy and etch-pitting techniques on compression samples.

Exploratory compressions tests have been conducted on commercially available 2% thoriated tungsten, which had been consolidated by powder metallurgy and contained a uniform dispersion of thoria particles having an average diameter of 1 μ. The compression samples were cut and centerless ground to 0.15-in.-diam × 0.300-in.-long cylinders, and then annealed at 1×10^{-5} torr for 1 hr at either 1800 or 2300°C. Either annealing treatment resulted in a recrystallized grain size of 30 μ without altering the thoria particle size and distribution. The data obtained in these tests are compared in Table 19.1 with data obtained on commercially pure polycrystalline tungsten. Apparently, the fine-particle dispersions represented here do not reduce the yield strength. The primary role of the thoria particles in this case appears to be stabilization of the substructure of the alloy.

[6]R. E. McDonald, ORNL-3683 (in press) (Classified).

PYROLYTIC-TUNGSTEN EVALUATION

A. C. Schaffhauser

A major factor preventing the use of pyrolytic tungsten for many applications is its brittleness, even at temperatures well above room temperature. Preliminary studies at ORNL, "Pyrolytic-Tungsten Development," this chapter, and elsewhere[7,8] of the microstructures and mechanical properties of vapor-deposited tungsten have defined the general characteristics of this material. However, the factors influencing the annealing characteristics and brittle behavior of the pyrolytically produced material are not known.

[7]*Summary Progress Report*, High Temperature Materials, Inc., Brighton, Mass., Contract NOw 61-0876-C(FBM) (March 1962).

[8]J. L. Taylor and D. H. Boone, *J. Less-Common Metals* 6(2), 157–64 (1964).

Table 19.1. Effect of Heat Treatment on Room-Temperature Yield Strength of Pure and Thoriated Tungsten

Material	Heat Treatment	Grain Diameter (μ)	Strain Rate (sec^{-1})	Average Upper or 0.3% Yield Strength (psi)
			$\times 10^{-4}$	
Pure[a]	As-swaged		1	210,000
	1 hr at 1700°C	50	1	146,000
	4 hr at 2050°C	50	5	99,000
Thoriated	As-swaged			Over 250,000[b]
	1 hr at 1800°C	30	1	188,000
	1 hr at 2300°C	30	1	186,000

[a]C. R. McKinsey *et al.*, *Investigation of Tungsten-Tantalum-Columbium-Base Alloys*, ASD-TR 61-3 (July 1961).

[b]An accurate yield strength for as-swaged thoriated tungsten could not be obtained due to plastic deformation of the compression mandrels at stresses over 250,000 psi. New mandrels to correct this are being ground.

The vapor-deposition process generally produces a columnar grain structure perpendicular to the plane of deposition, as shown in Fig. 19.2. The extent to which the well-known low-temperature brittleness of tungsten is intensified by this grain structure is not known. Limited elevated-temperature impact data[8] show a ductile-to-brittle transition temperature of 900°C. A transition temperature this high is not surprising considering the severity of the test.

Initial studies of the response of pyrolytic tungsten to annealing suggest that the microstructure may be dependent on the strain induced during deposition. Generally, the columnar structure is stable to temperatures over 1800°C (Fig. 19.5a). However, in one sample a fine equiaxed structure was produced by annealing at 1800°C (Fig. 19.5b). At higher temperatures, strain-induced grain-boundary migration resulted in exaggerated grain growth in some areas (Figs. 19.5c and 19.5d). At the highest annealing temperature (2500°C) the columnar structure was completely obliterated. In light of these unexplainable differences in presumably similar deposits, we have started a joint program with the Metals Forming and Casting Group to determine systematically the effect of deposition variables on the ductility and annealing characteristics of pyrolytic tungsten.

An elevated-temperature bend-test rig has been designed according to the recommendations of the Materials Advisory Board[9] to determine the ductile-to-brittle transition temperature of pyrolytic tungsten sheet. Base-line transition-temperature data for wrought and recrystallized powder-metallurgy tungsten are presented in Table 19.2. This information, obtained on material that is representative

[9] *Evaluation Test Methods for Refractory Metal Sheet Materials*, MAB-192-M.

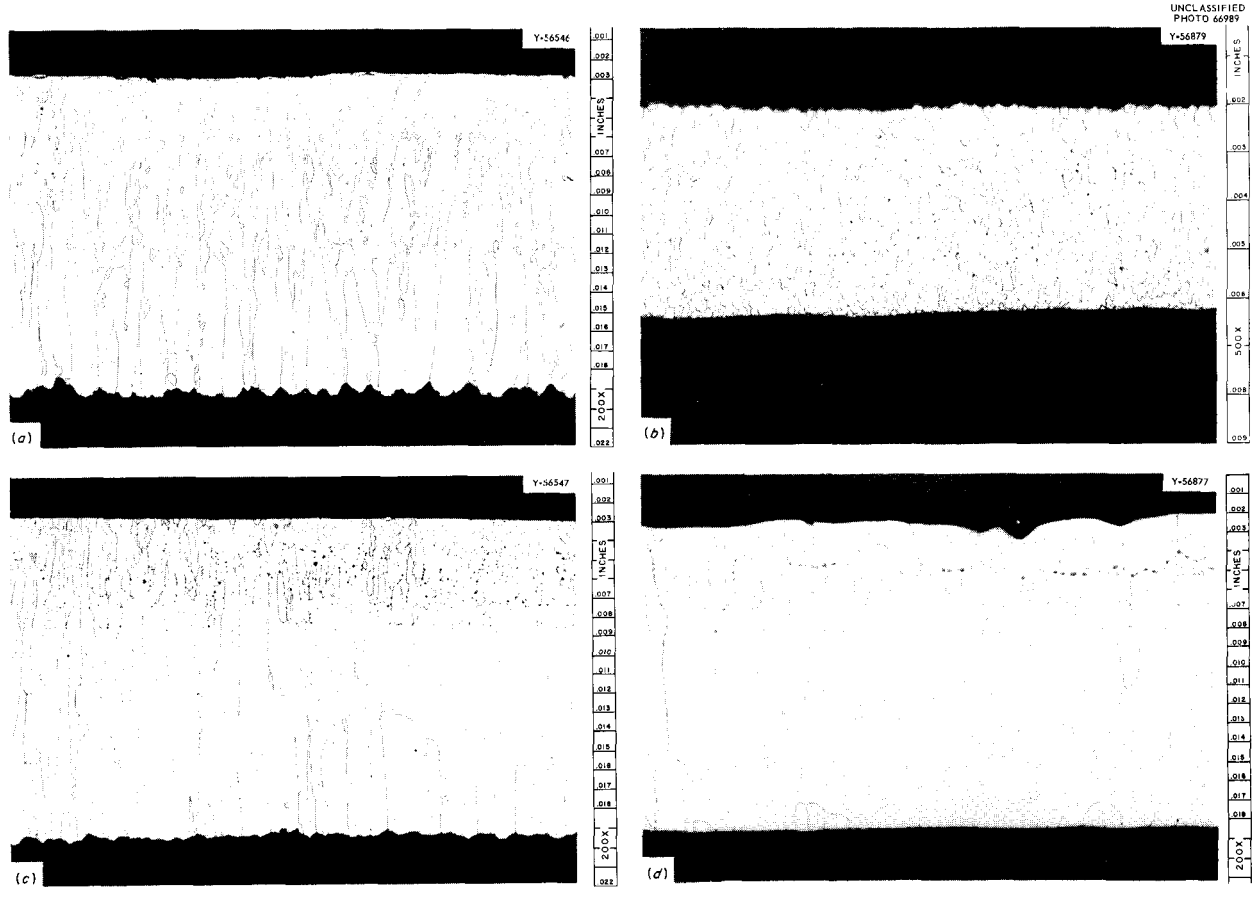

Fig. 19.5. Effect of Heat Treatment on Microstructure of Pyrolytic Tungsten. Etchant: Equal parts concd NH_4OH and 30% H_2O_2. (*a*) W56-HTI, 2 hr at 1800°C. 200×. (*b*) W49A, 4 hr at 1800°C. 500×. (*c*) W56-HT4, 2 hr at 2100°C. 200×. (*d*) W56-HT5, 1 hr at 2500°C. 200×. Reduced 51%.

Table 19.2. Bend-Transition[a] Behavior of Powder-Metallurgy Tungsten Sheet[b]

Specimen No.	Condition	Test Temperature (°C)	Span (in.)	Observation
		Transverse to Rolling Direction		
T–I	As-received	130	1.5	Brittle[c]
T–J	As-received	140	1.5	Brittle
T–M	As-received	140	1.5	Brittle
T–L	As-received	145[d]	1.5	Ductile[e]
T–K	As-received	150	1.5	Ductile
T–C	As-received	200	0.90	Ductile
T–E	As-received	180	0.90	Ductile
T–G	As-received	170	0.90	Ductile
T–F	As-received	160[d]	0.90	Ductile
T–B	As-received	155	0.90	Brittle
T–A	As-received	150	0.90	Brittle
T–R	Annealed[f]	375	0.90	Ductile
T–N	Annealed	350[d]	0.90	Ductile
T–Q	Annealed	350	0.90	Brittle[d]
T–O	Annealed	325	0.90	Brittle
T–P	Annealed	325	0.90	Brittle
		Parallel to Rolling Direction		
L–L	As-received	160	0.90	Ductile
L–H	As-received	150	0.90	Ductile
L–G	As-received	140	0.90	Ductile
L–C	As-received	140[d]	0.90	Ductile
L–A	As-received	135	0.90	Brittle
L–B	As-received	130	0.90	Brittle
L–K	As-received	150	0.90	Brittle[g]
L–J	As-received	150	0.90	Brittle[g]
L–I	As-received	160	0.90	Brittle[g,h]
L–E	As-received	120	0.90	Brittle[i]
L–D	As-received	130[d]	0.90	Ductile[i]
L–M	Annealed[f]	375	0.90	Ductile
L–N	Annealed	350	0.90	Ductile
L–Q	Annealed	350	0.90	Ductile
L–O	Annealed	325[d]	0.90	Ductile
L–P	Annealed	325	0.90	Brittle

[a] $4T$ punch radius, 1.0-in./min deflection rate.

[b] Material produced by Fansteel Metallurgical Corp. on Bureau of Naval Weapons Contract NOw-60-0621-c.

[c] Brittle – approximately 0° plastic bend angle.

[d] Transition temperature.

[e] Ductile – approximately 90° plastic bend angle.

[f] One hour at 1350°C.

[g] Surface rough-conditioned by manufacturer.

[h] Bend angle approximately 70°.

[i] Tension surface metallographically polished.

of current mill practice, will provide a useful comparison to information on the pyrolytic tungsten.

JOINING OF TUNGSTEN

R. G. Gilliland

Fusion Welding

In order to fully utilize the high-temperature structural properties of tungsten, techniques that are suitable for providing high integrity welded and brazed joints are needed.

Recently, we have studied joining of 0.060-in.-thick, powder-metallurgy tungsten sheet obtained from the Fansteel Metallurgical Corporation. We investigated butt welds made by the semiautomatic gas tungsten-arc process without additions of filler metal. A preheat temperature of approximately 650°C was used, and the specimens were welded in a chamber filled with high-purity argon. Samples were then bend tested to determine the ductile-brittle transition temperature for welds made in strips cut both parallel and transverse to the final rolling direction. The results are presented in Fig. 19.6. All bends were around a $4T$ radius and were made essentially in accordance with accepted Materials Advisory Board recommendations, except that the deflection rate was 0.5 in./min. These data indicate that the transition temperatures for welds made parallel and transverse to the rolling direction are approximately 450 and 475°C respectively. These transition temperatures may be compared with 140 and 160°C for the unwelded material parallel and transverse to the rolling direction respectively.

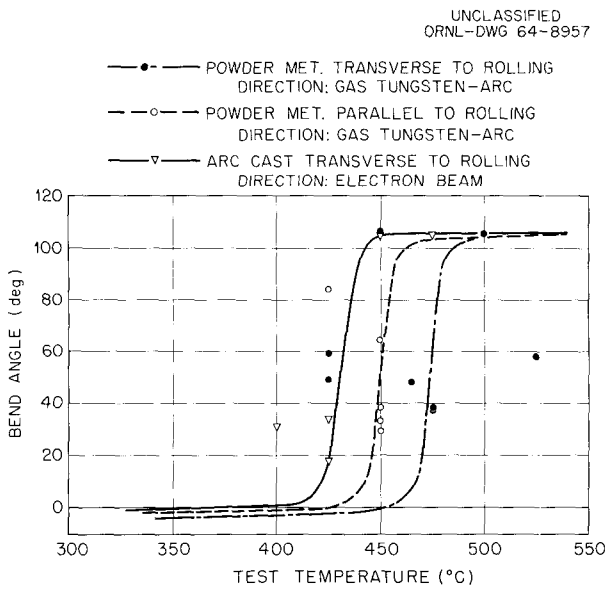

Fig. 19.6. Results of Ductile-Brittle Transition Temperature Tests on Tungsten Welds.

Also, arc-melted 0.060-in.-thick tungsten sheet, obtained from the Universal Cyclops Steel Corporation, has been welded transverse to the final rolling direction using a high-voltage electron-beam welder. Bend tests on these welds, also presented in Fig. 19.6, indicate that the ductile-brittle transition temperature of electron-beam welds in this material is approximately 425°C. The transition temperature of the base metal was 170°C.

We made preliminary studies of welding on early specimens of 0.025-in.-thick pyrolytic tungsten, produced in this Division. The starting material was very brittle at room temperature and cracked during welding. Metallographic examination revealed porosity in the heat-affected zone and some cracks. A cross section of one of these welds is shown in Fig. 19.7. Further studies await material of improved quality.

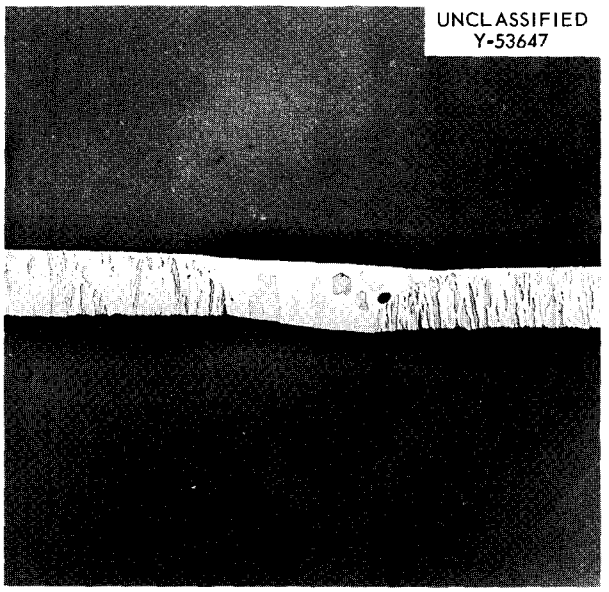

Fig. 19.7. Tungsten-Arc Weld in 0.025-in.-Thick Pyrolytic Tungsten, Showing Porosity and Cracking in the Heat-Affected Zone. Etchant: Equal parts concd NH_4OH and 30% H_2O_2. 11×.

Braze Welding

We have started to investigate the feasibility of braze welding tungsten with a filler metal of a lower melting composition. Calculations have indicated that the energy input to braze welds is only about half that of fusion welds. Therefore, the heat-affected zone and fusion zone should be reduced proportionately. We have tested tantalum, niobium, rhenium, molybdenum, and the binary alloy W–26% Re as filler metals with the gas tungsten-arc process. Bend tests at 525°C, similar to those described above, on these braze welds are reported in Table 19.3. All joint combinations cracked during bending, but embrittlement may have occurred from impurities within the filler metals themselves and from the alloying of the filler metal with the tungsten base metal. We plan to further examine the influence of these variables. Binary and ternary alloys of these refractory metals will also be prepared for use as filler metals.

Brazing

Preliminary vacuum-brazing studies on pyrolytic tungsten were made using the brazing alloys described in Chap. 14 of this report for very high-temperature service. An example of one of these joints is shown in Fig. 19.8. The excellent wetting and flowing characteristics of the Ta-Nb-V brazing alloy on the pyrolytic tungsten can be seen.

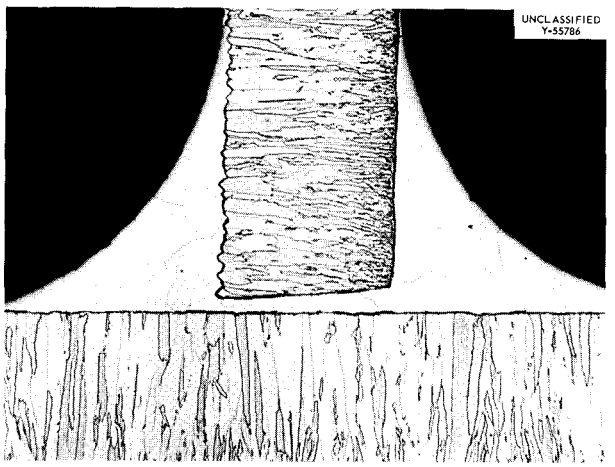

Fig. 19.8. Vacuum-Brazed Pyrolytic-Tungsten T-Joint Made with 65% V–30% Ta–5% Nb Alloy at 1900°C. As polished. 75×. Reduced 48%.

Table 19.3. Results of Transverse Bend Tests Performed at 525°C on Braze-Welded, Powder-Metallurgy Tungsten Using Ta, Nb, Mo, Re, and W–26% Re As Filler Metals

Filler Metal	Bend Angle at Which Crack Occurred (deg)	Remarks
Tantalum strip	53	Cracks in weld, heat-affected zone, and base metal
Rhenium wire	90	Very slight crack in weld metal No heat-affected zone or base-metal cracks
Niobium wire	14	Cracks in weld metal and heat-affected zone; no cracks in base metal
Molybdenum wire	44	Specimen fractured across entire width
W–26% Re wire	17	Cracks in weld metal and heat-affected zone; no cracks in base metal

MECHANICAL PROPERTIES OF TUNGSTEN

J. C. Zukas

The stress-rupture behavior in vacuum (10^{-6} torr) of powder-metallurgy tungsten sheet[10] is being explored. Specimens cut either parallel or transverse to the rolling direction have been tested at three stresses at 2200°C. The data are summarized in Fig. 19.9 with the results of another investigation.[11] Significant grain growth occurred in all the specimens tested.

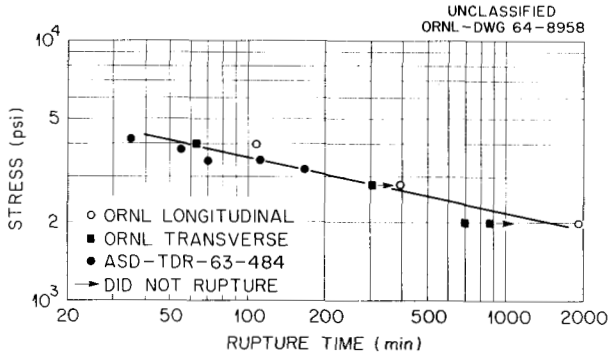

Fig. 19.9. Stress vs Rupture Time for Tungsten at 2200°C in Vacuum.

[10]Produced by Fansteel Metallurgical Corporation under contract NOw-60-0621-c.

[11]Ronald F. Brodrick, *Development of an Electron Beam Heating Facility and Its Use in Mechanical Testing of Tungsten to 6000°F*, ASD-TDR-63-484, p. 38 (July 1963).

20. Uranium Nitride

W. C. Thurber

Uranium mononitride is an attractive nuclear fuel by virtue of its high uranium density and high thermal conductivity. Unlike uranium carbide, it does not hydrolyze rapidly in moist air. Because of these superior properties, we are characterizing this compound further.

Physical properties, such as the coefficient of thermal expansion, thermal conductivity, electrical resistivity, and fission-gas release after neutron activation, have been measured. A study of the pressure-temperature-composition relationships in the uranium-nitrogen system has been initiated. Other portions of this program have been summarized in appropriate progress reports.[1,2]

ELECTRICAL RESISTIVITY AND THERMAL CONDUCTIVITY OF URANIUM MONONITRIDE[3]

T. G. Kollie J. P. Moore

We measured the electrical resistivity of an 86%-dense UN specimen in the range −200 to 1000°C at a pressure of 10^{-5} to 10^{-6} torr, using a four-probe technique. The results are tabulated in Table 20.1. Below 600°C this specimen exhibited a polarization effect, in which the resistance increased with time after current was applied. We think the effect, which is not observed above 600°C, is caused by UO_2 inclusions in the UN grain boundaries. Our electrical resistivity values are approximately 15% greater than those reported by Battelle[4] for 97- and 98%-dense UN; a simple density correction brings the two sets of data into relatively good agreement.

We measured thermal conductivity with the thermal comparator at 75 and 300°C on a 94.5%-dense UN specimen, 1 in. in diameter by ¼ in. thick. The measured values, corrected to theoretical density, are reported in Table 20.1. The total thermal conductivity of many solids can be divided into two portions, the electronic portion due to the transport of heat by electrons and the lattice portion due to the transport of heat by phonons. The electronic portion may be calculated from the electrical resistivity by the Wiedemann-Franz-Lorenz relation. Theory predicts the lattice portion to be an inverse linear function of temperature, but it is not readily calculable from auxiliary measurements. Thus the total thermal conductivity may be expressed as

$$k_T = \frac{1}{A + BT} + \frac{LT}{\rho},$$

where

k_T = thermal conductivity at temperature T in w m^{-1} $(°C)^{-1}$,

A and B = constants,

L = Lorenz constant,

ρ = electrical resistivity in μohm-cm, and

T = temperature in °K.

[1] W. C. Thurber, ORNL-3571, pp. 195–213 (May 1964) (classified).

[2] W. C. Thurber, ORNL-3683 (in press) (classified).

[3] Summary of the pertinent part of a paper to be presented at the AIME Symposium on Compounds of Interest in Nuclear Reactor Technology, Boulder, Colorado, August 3–5, 1964, entitled, "A Thermal Comparator Apparatus for Thermal Conductivity Measurements from 50 to 400°C," by T. G. Kollie, D. L. McElroy, R. S. Graves, and W. Fulkerson.

[4] E. O. Speidel and D. L. Keller, *Fabrication and Properties of Hot-Pressed Uranium Mononitride*, BMI-1633 (May 30, 1963).

Table 20.1. Electrical Resistivity and Thermal Conductivity of UN

Temperature (°C)	Electrical Resistivity (μohm-cm)		Thermal Conductivity w m^{-1} $(°C)^{-1}$		
	Measured	Corrected[a]	Electronic[b]	Lattice[c]	Total[d]
−200	129	111			
−100	177	152			
0	193	166	4.03	9.1	13.1
75	199	171	4.98	8.6	13.6
100	201	173	5.28	8.5	13.8
200	208	179	6.47	7.9	14.4
300	212	183	7.67	7.4	15.1
400	216	186	8.86	7.0	15.9
500	220	189	10.0	6.6	16.6
600	224	192	11.1	6.3	17.4
700	227	195	12.2	6.0	18.2
800	231	198	13.3	5.7	19.0
900	235	202	14.2	5.4	19.6
1000	240	206	15.1	5.2	20.3

[a]Corrected to theoretical density.

[b]Calculated from electrical resistivity by Weidemann-Franz-Lorenz relation.

[c]By difference at 75 and 300°C; from $1/(0.086 + 8.35 \times 10^{-5}\ T)$ at other temperatures.

[d]Experimental values at 75 and 300°C. Summed from calculated electronic and lattice portions at other temperatures.

Using the electrical and thermal measurements on UN at 75 and 300°C, the temperature dependence of the lattice portion of k_T for UN was calculated and yielded a value of $A = 0.086$ m°K w^{-1} and $B = 8.35 \times 10^{-5}$ m/w. These values were used to obtain the extrapolated thermal conductivity values listed in Table 20.1. Although the temperature dependence agrees, our calculated value is 25% below the measured value reported by Battelle[4] at 1000°C. This difference may be due to significant specimen differences. An alumina tube to replace the quartz tube of the electrical resistivity apparatus was procured, and this will allow the electrical resistivity measurements to be extended to 1400°C in the near future.

THERMAL EXPANSION OF UN

F. L. Carlsen, Jr. W. O. Harms

The thermal expansion of pressed-and-sintered UN was determined in the temperature range 20 to 1100°C. A plot of these data and those of Speidel and Keller[4] is shown in Fig. 20.1.

Our specimen was prepared by cold pressing and sintering depleted UN powder.[5] The thermal expansion was measured at a pressure of 6×10^{-6} torr on a stack of three pellets 0.298 in. in diameter and 0.985 in. in total length. The bulk density was 91.5% of theoretical and the UO_2 content was estimated to be 1 wt % from point count in microstructures of control specimens. Dilation was measured by a dial gage (smallest division 0.0001 in.) at approximately 100°C intervals at an average heating rate 2 to 3°C/min. No data were obtained during cooling. Maximum error was estimated to be ±2%. There was no detectable net change in either weight or length during the experiment. The BMI specimen[4] did show a net growth during cycling, and this can be attributed to oxidation of the specimen. Making reasonable estimates of the course of oxidation, we have corrected the BMI results and included the corrected expansion curve in Fig. 20.1.

From our data and from the corrected BMI results, we computed mean coefficients of linear thermal expansion for temperature ranges of 20°C to the

[5]Obtained from Nuclear Materials and Equipment Corporation.

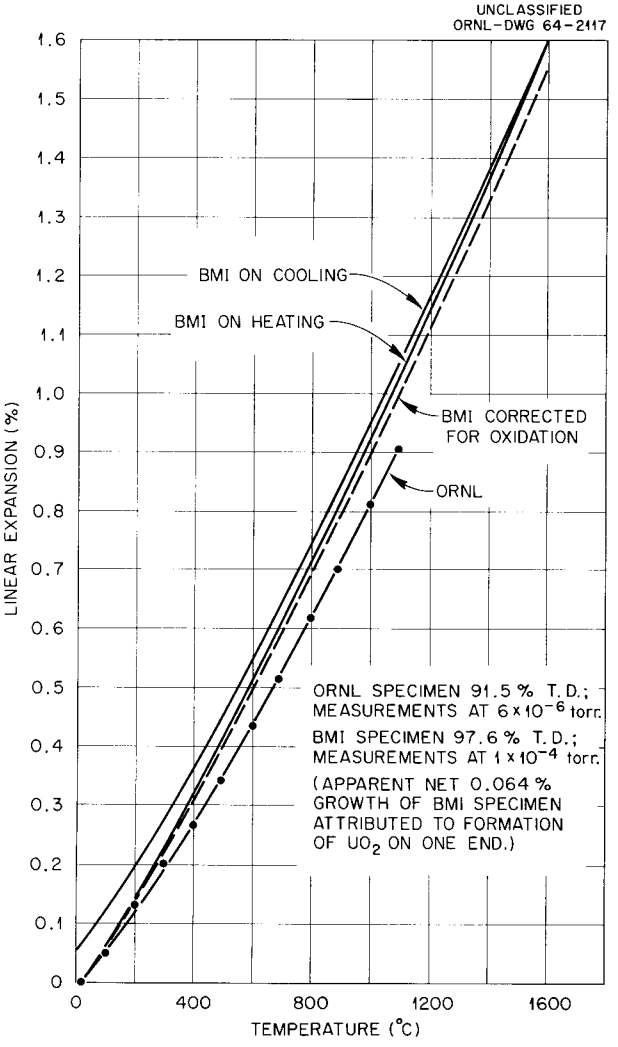

Fig. 20.1. Thermal Expansion Data for Uranium Mononitride.

highest temperature investigated, in 100°C increments; these are shown in Table 20.2. Values read from the best curve drawn through our data points were used, since, especially at the lower temperatures (<500°C), the dial-gage reading errors could introduce as much as 25% error in the derived coefficient. Our values are 10 to 20% lower than the corrected BMI values.

NEUTRON ACTIVATION STUDIES OF UN

R. B. Fitts

We are investigating the fission-gas retention properties of uranium-nitride fuels by the neutron activation method. We shall compare fuel compacts made by various techniques with each other and attempt to correlate their fission-gas release with various material properties.

Tests have been run in vacuums of two qualities, about 100 torr and 10^{-5} to 10^{-6} torr. Tests in the 100-torr vacuum on samples made by the Dynapac process and by cold pressing and sintering indicate that UN is comparable to UO_2 in its fission-gas retention properties. A value of approximately 2×10^{-14} sec^{-1} for $D'_{1400°C}$ (a form of diffusion coefficient corrected for surface area) was obtained for 99.7%-dense Dynapac UN.

Also, irradiated samples of both pressed-and-sintered UN that had been slightly oxidized and almost pure arc-cast UN have also been annealed in vacuums of 10^{-5} to 10^{-6} torr. At 1400°C and above in this vacuum, fission gases were released primarily by the dissociation of UN according to the reaction:

$$UN(s) \rightarrow U(l) + \tfrac{1}{2} N_2(g) .$$

Gas is released by this process at a constant rate much greater than the diffusion rate in this temperature range. The release at lower temperatures (1000–1300°C) was linear with the square root of time, as is expected for a diffusion-controlled mechanism of release. At the first testing temperatures (800–1000°C), the release was linear with time, indicating that some component of each sample dissociated. These components were found by x-ray analysis to be UN_2 and the hexagonal modification of U_2N_3. They were located on grain boundaries, around porosity in the sintered samples, and as a surface layer (0.1- to 0.5-mm thick) on the arc-cast samples. The presence of these phases in the sintered samples was not too surprising, since the pellets were known to be of poor quality. However, this result was unexpected with the arc-cast material, since precautions were taken to prevent unnecessary exposure to air. Preliminary tests indicated that the surface contamination could be removed from arc-cast samples by a 15-hr anneal in vacuum at 1500°C. The pressed-and-sintered samples were partially purified by this treatment but still contained some intergranular contamination.

Future tests will be made on materials that have had surface contamination removed by heat treatment or mechanical means. Storage and testing atmospheres will be carefully controlled for all

Table 20.2. Summary of Thermal Expansion Coefficients for UN

Temperature Range (°C)	Mean Linear Thermal Expansion Coefficients $(^{\circ}C)^{-1}$		
	ORNL Specimen[a]	BMI Specimen[b]	
		During Initial Heating	Corrected for Oxidation Effect
	$\times 10^{-6}$	$\times 10^{-6}$	$\times 10^{-6}$
20–100	6.1	7.5	7.3
20–200	6.4	7.8	7.7
20–300	6.7	8.2	7.8
20–400	7.0	8.4	8.1
20–500	7.3	8.6	8.3
20–600	7.5	8.8	8.5
20–700	7.7	9.0	8.8
20–800	7.9	9.2	8.9
20–900	8.1	9.3	9.0
20–1000	8.3	9.5	9.2
20–1100	8.4	9.6	9.3
20–1200		9.7	9.4
20–1300		9.8	9.5
20–1400		9.9	9.6
20–1500		10.0	9.7
20–1600		10.1	9.8

[a]Cold pressed and sintered to 91.5% of theoretical density. Pressure: 6×10^{-6} torr.

[b]Hot pressed to 97.6% of theoretical density. Pressure: 1×10^{-4} torr.

UN samples. A sweep gas system is being constructed to allow the testing of these samples at temperatures above 1300°C without dissociation of the UN.

THERMAL STABILITY OF URANIUM NITRIDES

J. J. Schwaller T. G. Godfrey
R. E. Meadows

We have started to study the pressure-temperature-composition relations in the uranium-nitrogen system. Of primary interest are the thermal decomposition of uranium mononitride at elevated temperatures and the effects of impurities and additives on this decomposition.

Pressure-Temperature-Composition Relations in the Uranium-Nitrogen System

In initial experiments, we determined equilibrium compositions for uranium-nitrogen combinations over the temperature range 800 to 1200°C at nitrogen pressures of 25, 100, and 400 torr in a thermogravimetric apparatus (TGA). The starting powder contained 5000 ppm O and 700 ppm C as major impurities. The results obtained showed a marked dependence of the nitrogen-to-uranium ratio on the final oxygen content of the sample as determined by chemical analysis.

We corrected for the oxygen effect through the use of a material balance based on chemical analyses performed before and after each experiment, assuming that oxidation occurred only on heating to the reaction temperature. Both the observed and corrected nitrogen-to-uranium ratios are shown in Table 20.3. These results indicate that the correction improves the agreement, although it apparently overcorrects. Similar results were obtained at nitrogen pressures of 100 and 400 torr. However, all results, both corrected and uncorrected, show nitrogen-to-uranium ratios considerably lower than those reported by Bugl

and Bauer[6] and by Lapat and Holden[7] for equivalent pressures and temperatures. Possible causes for these low nitrogen-to-uranium ratios will be investigated after several modifications have been incorporated in the present TGA and gas-handling system.

[6]J. Bugl and A. A. Bauer, "Phase Relationships in the Uranium–Nitrogen System," paper presented at the Washington Meeting of the Basic Science Division, American Ceramic Society, Oct. 7 and 8, 1963. (To be published in the *Journal of the American Ceramic* Society.)

[7]P. E. Lapat and R. B. Holden, "Thermodynamics of the Uranium–Nitrogen System," *Semiann. Progr. Rept. June 15, 1963*, UNC-5060.

UN Vapor-Pressure Determinations

Several attempts were made to determine the apparent vapor pressure of UN by Langmuir and Knudsen experiments in the TGA, but the results were inconclusive because we could not account for the vaporization of uranium arising from the decomposition of UN. However, the method appears feasible for a study of the effects of impurities and additions on the vapor pressure of UN, and we are planning this study.

Table 20.3. Equilibrium Composition of Uranium Nitrides with Two Final Oxygen Contents at Various Temperatures and 25 Torr N_2

Temperature (°C)	Nitrogen-to-Uranium Ratio			
	Observed		Corrected	
	0.95 wt % O	2.24 wt % O	0.95 wt % O	2.24 wt % O
790	1.56	1.61	1.56	1.52
888	1.54	1.59	1.54	1.50
987	1.52	1.58	1.51	1.48
1085	1.49	1.56	1.48	1.46

21. Zirconium Metallurgy

M. L. Picklesimer

We are conducting research along several lines on zirconium-base alloys of potential use as structural materials in several water-cooled and/or -moderated reactor systems. The principal projects presently under way are: (1) studies of the physical metallurgy, consisting of transformation kinetics and morphologies, mechanical properties, phase diagrams where necessary, and heat-treatment response; (2) the development, evaluation, and utilization of preferred orientation and strain anisotropy in α-zirconium alloys during fabrication, and the utilization of the yield-stress anisotropy in increasing maximum permissible design stresses in structures; (3) the determination of the effects of composition, temperature, and environment on the oxidation-corrosion rates in the thin film stages of oxide growth; (4) a study of the effects of alloy composition and oxidation environment on the structural properties of thin oxide films *in situ*; and (5) investigation of stress reorientation of precipitated hydrides in Zircaloy-2.

ZIRCONIUM ALLOYS

P. L. Rittenhouse M. L. Picklesimer

We have followed the transformation kinetics of zirconium alloys containing from 1 to 7.5 wt % Mo by electrical resistivity measurements and also obtained some information on the phase boundaries. The resistivity results obtained were similar to our previous results[1] for zirconium-niobium alloys rich in zirconium. At low alloy content (less than 3 wt % Mo or 10 wt % Nb), we can establish an $\alpha + \beta \rightarrow \beta$ transformation temperature consistent with metallographic results. At no level of alloy content can a eutectoid temperature be unambiguously observed by changes in electrical resistivity.

The transformation of a Zr–0.9 wt % Fe alloy was also studied by measurement of electrical resistivity and by metallography. Resistivity changes near the eutectoid temperature indicated that at least three phases were present in the specimen over appreciable temperature ranges during both heating and cooling cycles. Rates of heating and cooling were from 2 to 8°C/min, and Fig. 21.1*a* shows the typical variation of resistivity with temperature. Zirconium-copper alloys containing less than 2 wt % Cu show similar behavior on cooling but not on heating. Zirconium alloys containing Ni, Cr, or Pd do not show such behavior on either heating or cooling, giving curves shaped as shown in Fig. 21.1*b*, which is typical of a binary alloy system that transforms rapidly. The temperature designated T_1 in Fig. 21.1*a* was 780°C, which is slightly below the presently accepted eutectoid temperature of 790 to 800°C. The temperature T_2, the start of the "bump" that indicates the presence of three phases, was 795°C; and the temperature T_3 for the solvus line was 845 to 850°C, in agreement with the presently accepted phase diagram.[2] Isothermal anneals for 3 hr during both heating and cooling cycles did not appreciably change the resistivity at any temperature above 780°C. Either the alloy has a remarkable metastability in comparison to the Ni, Cr, and Pd alloys, or the oxygen present (about 150 ppm) caused the Zr-Fe alloy to behave as a ternary alloy. This amount of oxygen is apparently insufficient to cause such behavior in the alloys containing Ni, Cr, and Pd.

[1] P. L. Rittenhouse and M. L. Picklesimer, *Metals and Ceramics Div. Ann. Progr. Rept. May 31, 1963*, ORNL-3470, p. 55.

[2] F. N. Rhines and R. W. Gould, "The Zr-Fe System," pp. 62–73 in *Advances in X-Ray Analysis*, vol. 6, ed. by W. M. Mueller and Marie Fay (Proceedings of the Eleventh Annual Conference on Application of X-Ray Analysis, Aug. 8–10, 1962), Plenum Press, New York, 1963.

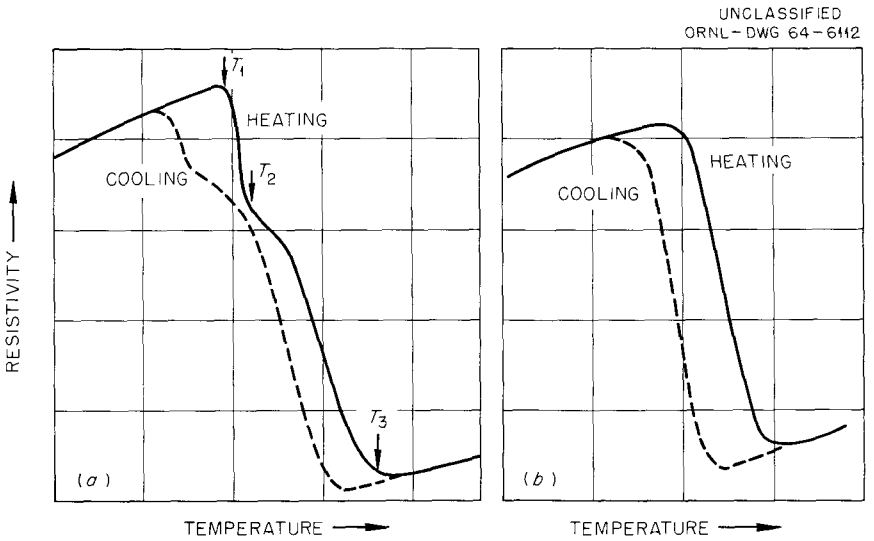

Fig. 21.1. Schematic Electrical Resistivity Curves for (a) Zr–0.9 wt % Fe, (b) Lean Zr-Ni, Zr-Cr, and Zr-Pd Alloys.

To determine if three phases exist in the Zr-Fe alloy at temperatures near 800°C, specimens were heat treated for 30 min at temperatures from 750 to 860°C, water quenched, and metallographically examined. Those held at 860°C were all beta phase at temperature, those at 810 and 840°C showed the normal $\alpha + \beta$ structure, and those held at 750 and 770°C showed fine recrystallized α-zirconium plus a large amount of a precipitate difficult to resolve at 1000×. In those specimens held at 780 and 795°C, the same alpha matrix was observed, the precipitate particles were appreciably larger, and anodizing showed conclusively that three phases were present. According to the presently accepted phase diagram,[2] the two minor phases should be β-zirconium and Zr_4Fe. Our data are in agreement with this phase diagram except that we find a lower eutectoid temperature.

THE EFFECT OF PREFERRED ORIENTATION AND STRESS ON THE DIRECTIONAL PRECIPITATION OF HYDRIDES IN ZIRCALOY-2

P. L. Rittenhouse

Hydrogen pickup associated with the corrosion of α-zirconium alloys is a major deterrent to their use as reactor materials, since the modest concentrations of hydrogen soluble in these alloys are sufficient to precipitate zirconium hydride platelets when the alloys are cooled from operating temperature. The effect of these platelets on ductility depends on their orientation relative to the applied stress and is nearly zero in Zircaloy-2 of relatively low hydrogen content when the stress axis is parallel to the platelets.[3] That stress can reorient the hydrides has been shown;[4] and this reorientation can either enhance or lower ductility, depending on the distribution of the hydrides relative to the stress axis before and after reorientation.

We tested specimens of three lots of Zircaloy-2 of known preferred orientation to determine the effect of stress direction and preferred orientation on the directional precipitation of the hydrides.[5] Controlled amounts of hydrogen were added to all the materials. We heated some specimens to a temperature above the solvus, loaded them elastically in tension to a maximum stress of 20,000 psi,

[3]R. P. Marshall and M. R. Louthan, Jr., *Trans. Am. Soc. Metals* **56**, 693–700 (1963).

[4]R. P. Marshall, *Hydride Orientation and Mechanical Properties of Thin-Walled Zircaloy Tubing*, DPST 63-74-8 (October 1963).

[5]P. L. Rittenhouse and M. L. Picklesimer, *The Effect of Preferred Orientation and Stress on the Directional Precipitation of Hydrides in Zircaloy-2*, ORNL TM-844 (June 1964).

and slowly cooled them to room temperature under stress. A second group of specimens was plastically deformed by bending at room temperature, heated above the solvus, and cooled without load. The angles between a reference direction and the traces of several hundred hydride platelets were measured on three surfaces. These were plotted as histograms such as shown in Fig. 21.2 for one lot of Zircaloy-2 stressed in the transverse direction. A chart of pole distribution of the hydrides, Fig. 21.3, was constructed from the data on three orthogonal planes. This construction presently requires a trial and error synthesis, but a computer program is being written which will give the pole distribution directly from the trace data.

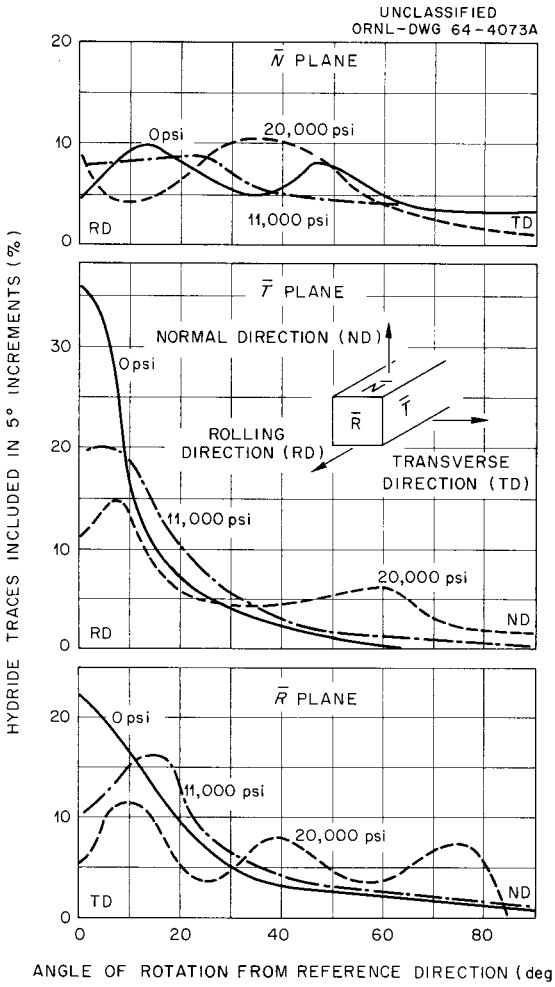

Fig. 21.2. Histograms Showing Hydride Traces on the Three Surfaces of Schedule 18 Zircaloy-2 for Three Stress Levels.

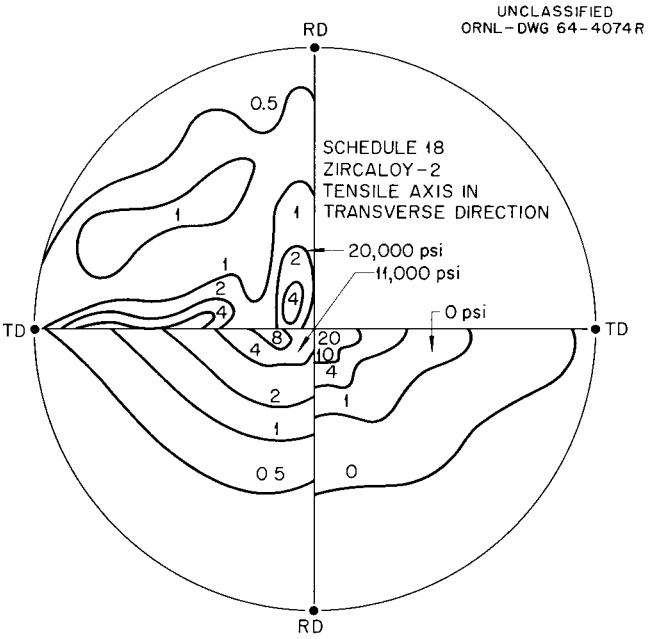

Fig. 21.3. Hydride Pole Figures for Three Stress Levels in Schedule 18 Zircaloy-2.

Although hydride study is still in progress, at least three conclusions may be drawn now. First, the preferred orientation has little if any influence on the orientation of hydride platelets in as-received sheet material, the hydride texture being similar to the orientation of slag inclusions in rolled steels. Second, the hydrides precipitated after plastic deformation tend to align themselves parallel to the tensile strain component and perpendicular to the compressive strain component. Finally, hydrides precipitated under an elastic stress redistributed appreciably only when the stress axis is perpendicular to a high concentration of basal planes.

TEXTURE DETERMINATION BY HARDNESS ANISOTROPY IN α-ZIRCONIUM ALLOYS

P. L. Rittenhouse M. L. Picklesimer

The engineering design of structural members of α-zirconium alloys requires consideration of the anisotropy of mechanical properties resulting from preferred orientation. Rapid and semiquantitative methods of evaluating anisotropy and determining preferred orientation are needed for examining

large numbers of test specimens. A method was developed that uses Knoop microhardness measurements to provide an approximation of the (0001) pole figure, the figure of most importance.

Last year,[6] we reported studying by Knoop microhardness the anisotropy of five schedules of polycrystalline Zircaloy-2 and the $\{10\bar{1}0\}$, $\{11\bar{2}0\}$, and (0001) planes of a single crystal of Zircaloy-2. We have now collected data on additional polycrystalline material, on four more planes of Zircaloy-2 single crystals, and on ten crystallographic planes of iodide-zirconium single crystals. The hardness results for both the Zircaloy-2 and zirconium single crystals are shown in Fig. 21.4 in terms of the coordinate angles α and β. We define angle β as the angle between the basal plane and the plane of examination and angle α as the angle between the long diagonal of the Knoop indenter and the projection of the basal pole on the plane of examination. The hardness was a function of both crystallographic plane and direction, and for any plane was a minimum when the long diagonal of the indenter was parallel to the projection of the basal pole on that plane (i.e., at $\alpha = 0$). The deformation systems of zirconium and Zircaloy-2 differed significantly on planes within 40° of the basal plane ($0 \leqq \beta \leqq 40°$). This difference is shown by the decrease in hardness in zirconium but the continued increase in hardness in Zircaloy-2 as the basal plane is approached.

[6]P. L. Rittenhouse, *Metals and Ceramics Div. Ann. Progr. Rept. May 31, 1963*, ORNL-3470, pp. 56–58.

We have developed an empirical method for determining the texture of polycrystalline Zircaloy-2, using the hardness data obtained from the single crystals and from a specific pattern of hardness measurements on the unknown material. Three metallographic specimens of the polycrystalline unknown are prepared with their planes of examination perpendicular to the rolling direction ($\bar{R}$ plane specimens), the transverse direction ($\bar{T}$ plane), and the normal direction ($\bar{N}$ plane) of the fabricated plate. Twelve Knoop microhardness measurements are made on each specimen, three each at successive 45° intervals from one of the fabrication directions (defined in Fig. 21.2) in the surface of the specimen. As in Fig. 21.5, the Knoop hardness number is plotted against the angle θ, which is defined as the angle between the long diagonal of the Knoop indenter and a reference fabrication direction. Then a second angular coordinate, ψ, of the hardness anisotropy is determined with the use of a hardness contour map, such as Fig. 21.6, constructed from the single-crystal data. In this figure, hardness contours are plotted against the directional coordinate angles α and β. From a plot of the polycrystalline hardness data, such as Fig. 21.5, the angle θ for the minimum hardness in a plane is located and designated θ_1. The corresponding ψ_1 is read from the β scale for $\alpha = 0$ at the hardness corresponding to θ_1. Similarly ψ_2 corresponding to $\theta_2 = \theta_1 + 10°$ is read from the hardness at θ_2 and $\alpha = 10°$. This process is repeated for successive 10° intervals, recognizing that θ and $180° - \theta$ are the same. Finally the

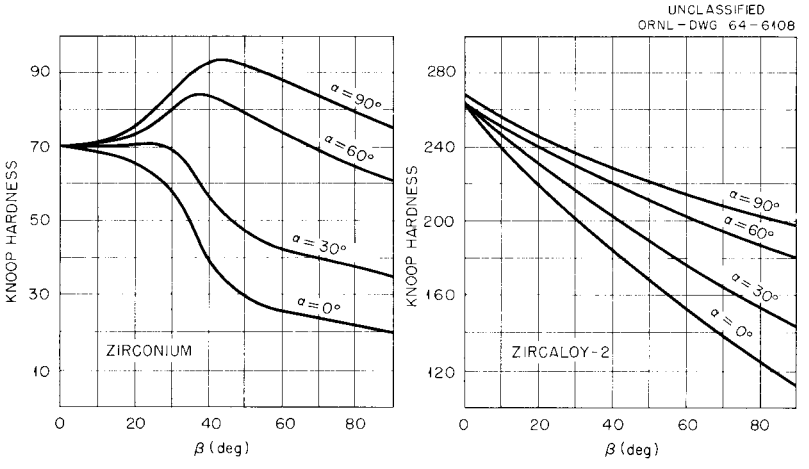

Fig. 21.4. Microhardness Anisotropy in Single Crystals of Zirconium and Zircaloy-2. See text for definition of direction angles.

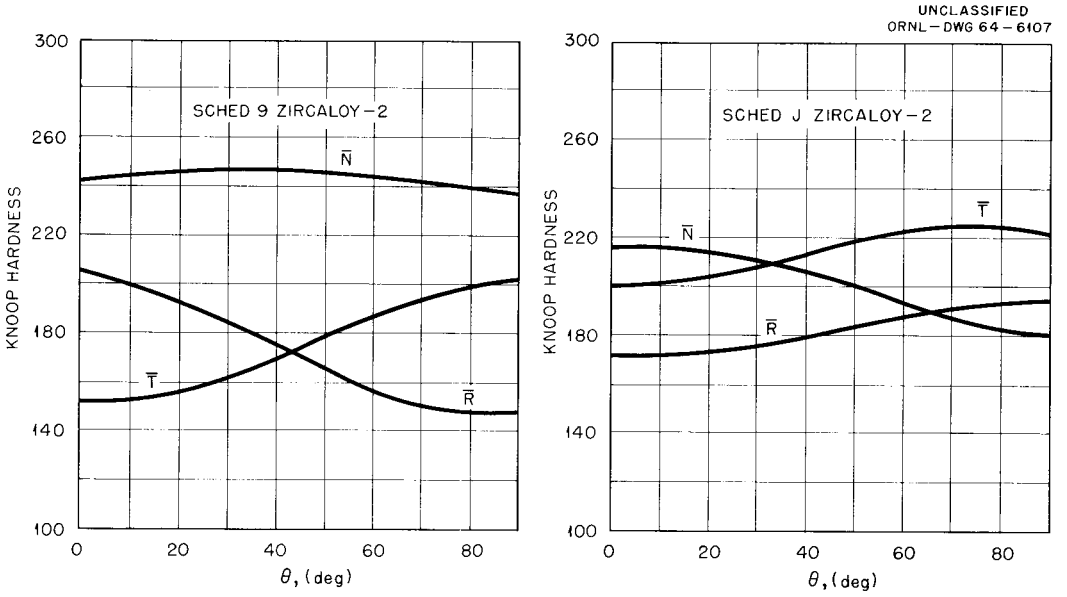

Fig. 21.5. Knoop Hardness as a Function of Direction in Zircaloy-2 Fabricated by Two Selected Schedules. The planes of measurement are $\overline{N}$, normal to the normal direction; $\overline{R}$, normal to the rolling direction; and $\overline{T}$, normal to the transverse direction. Angle θ is between the long diagonal of the Knoop indenter and a reference direction.

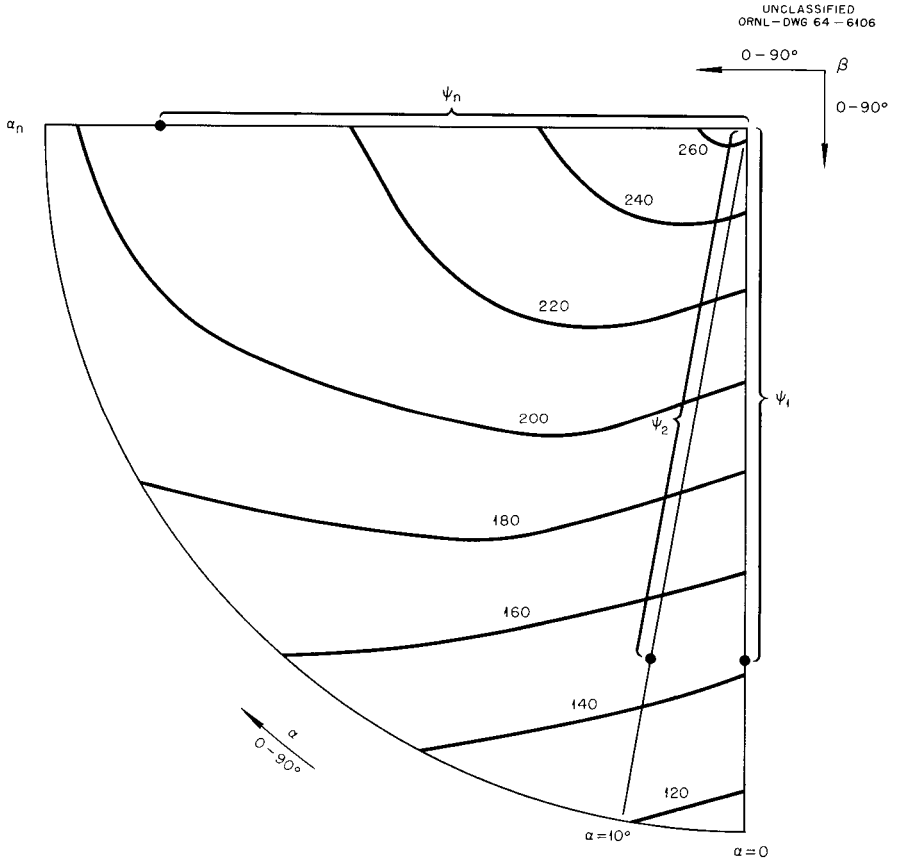

Fig. 21.6. Hardness Map for a Single Crystal of Zircaloy-2.

values of ψ for the different angles are averaged to give $\overline{\psi}$ for the plane.

The procedure is repeated for each of the three specimens, designating each $\overline{\psi}$ by the appropriate symbol for the plane of examination. The values for $\overline{\psi}_{\overline{R}}$, $\overline{\psi}_{\overline{T}}$, and $\overline{\psi}_{\overline{N}}$ are plotted on a Wulff net, as shown in Fig. 21.7, to define two areas that contain equal numbers of basal poles. The line separating these two areas defines an "average" basal pole figure for the material. Figure 21.8 shows typical results for such measurements for two schedules[7] of Zircaloy-2 together with x-ray-

[7]P. L. Rittenhouse and M. L. Picklesimer, *Metallurgy of Zircaloy-2: Part I — The Effects of Fabrication Variables on the Anisotropy of Mechanical Properties*, ORNL-2944 (Oct. 13, 1960); *Part II — The Effects of Fabrication Variables on the Preferred Orientation and Anisotropy of Strain Behavior*, ORNL-2948 (Jan. 11, 1961).

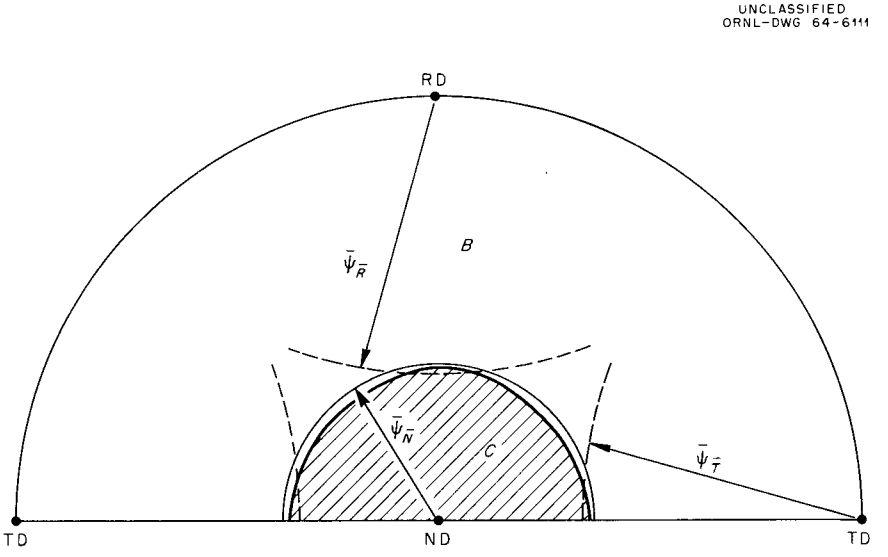

Fig. 21.7. Plotting the Values of $\overline{\Psi}_{\overline{R}}$, $\overline{\Psi}_{\overline{T}}$, and $\overline{\Psi}_{\overline{N}}$ for Determining the Pole Figure.

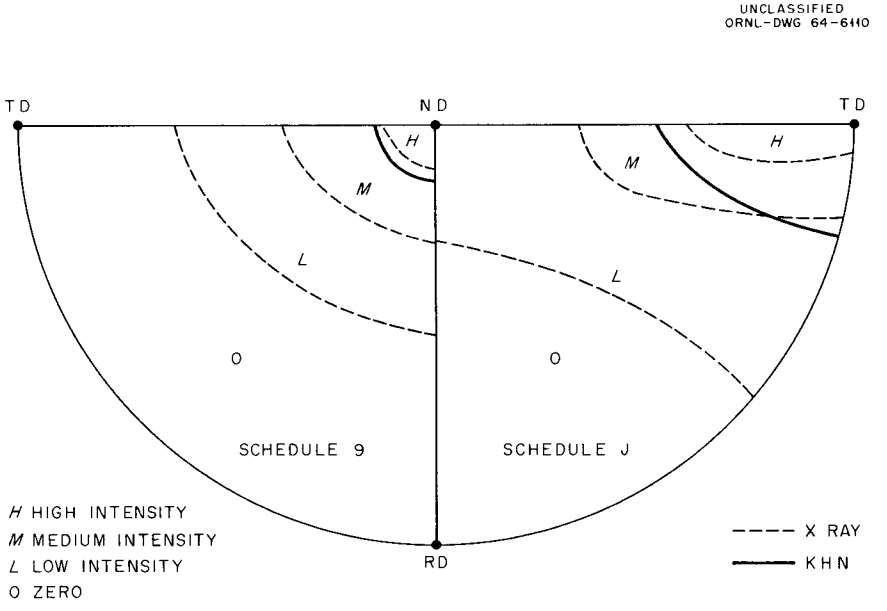

Fig. 21.8. Comparison of Hardness and X-Ray Data Pole Figures for Two Schedules of Zircaloy-2.

diffraction pole-figure data, indicating the satisfactory approximation of the method.

An x-ray diffraction value for $\bar{\psi}$ can be determined using quantitative inverse pole-figure data. The values determined by x-ray and the hardness techniques are compared in Table 21.1.

The smallest number of hardness measurements consistent with satisfactory texture data is 36; these must be made on a specific pattern on three orthogonal planes.

Table 21.1. The Angle $\bar{\psi}$ Determined by X-ray Diffraction and Knoop Hardness

Schedule[a]	$\bar{\psi}_{\bar{R}}$ (deg)		$\bar{\psi}_{\bar{T}}$ (deg)		$\bar{\psi}_{\bar{N}}$ (deg)	
	X-ray	KHN	X-ray	KHN	X-ray	KHN
9	77	77	73	76	16	15
J	77	73	22	32	48	51
1	71	67	43	46	29	26
8	76	70	70	71	17	17
62	72	70	40	44	26	34

[a]Schedules as defined in ref. 7.

DETERMINATION OF POLE FIGURES BY QUANTITATIVE METALLOGRAPHY

M. L. Picklesimer P. L. Rittenhouse

The study of preferred orientation and strain anisotropy in α-zirconium alloys as functions of fabrication variables requires pole figures for many of the specimens studied. The effects of stress on the reorientation of embrittling hydrides in Zircaloy-2 can be effectively evaluated only if the pole figures of the hydride plates can be determined. The preferred orientation of grains can be determined by x-ray diffraction, but specimen preparation is quite difficult and expensive in many cases and the procedure is time consuming. The preferred orientation of hydride plates cannot be determined by x-ray diffraction; some other technique must be used.

We have developed a suitable technique for determining approximately both types of pole figures using a polarizing metallurgical microscope and quantitative metallography. The determinations are rapidly and easily performed, requiring metallographic preparation of only three specimens. In many cases, the total required time is 2 to 3 hr.

Two observations led to the development of the technique. First, the hydride platelets generally grouped into sheets or "cornflakes" in the grain boundaries of well annealed Zircaloy-2 and as thin long plates within the grains of cold-worked Zircaloy-2. Thus, they can be considered, for the present purposes, as thin flat sheets distributed in some pattern in the three-dimensional body of the specimen. Second, the basal plane trace of individual grain of zirconium or Zircaloy-2 can be located in a polarized-light microscope by use of a sensitive tint plate between the specimen and the analyzer disk, since the trace is parallel to the north-south cross hair of the eyepiece just as the color of the grain changes from blue to red on clockwise rotation of the stage.[8] The angles between hydride sheet traces (or the basal plane trace) and selective reference directions can be measured by an eyepiece goniometer or the rotating stage. If a preferred orientation of either kind exists in the material, the measurement of several hundred trace angles on each of the three orthogonal surfaces of the specimen material should indicate an angular preference, which in turn should reveal the three-dimensional texture.

Consider the traces a plane cuts on three mutally orthogonal surfaces formed by three orthogonal reference directions. If the angles between the traces and the reference directions are defined so that different reference directions are used for the three trace angles, the trace angles α, β, and γ are related by the trigonometric relationship

$$\tan \alpha \tan \beta \tan \gamma = 1 .$$

Thus, the selection of values for any two of the trace angles fixes the value for the third.

Since the sheets of hydride platelets are so small that almost none of the sheets cut any two of the specimen surfaces, a statistical approach to the analysis is required. Consider that sheets of precipitate are formed in a specimen such that the individual sheets are small relative to the size of the specimen, but let them have a preferred distribution of orientation in space rather than a random one. Then the measurement of a sufficient

[8]S. L. Couling and G. W. Pearsall, *Trans. AIME* **209**, 939 (1957).

number of traces on each of three orthogonal surfaces of the specimen should show a preferred distribution that should enable an approximation of the preferred orientation in space.

Typical results of such measurements are shown in Fig. 21.2, where the histogram-type data have been smoothed into curves. The smoothed histograms represent intensity curves, each point of which is a normalized sum of the poles along a zone of all planes that could form that particular trace on that surface. The pole figure is determined by a trial and error solution by the same method of approximation that is used for the determination of the inverse pole figure from x-ray diffraction data.[9] Of course, only an approximate (0001) pole figure is given by the basal plane trace method, but this figure is the important one in evaluating strain anisotropy. Typical pole figures for hydride plates are shown in Fig. 21.3.

The associated equipment required (besides the polarized-light microscope) is an eyepiece goniometer and a rotating stage on the microscope, each coupled to a potentiometer to permit electrical measurement of the angle measured, an *x-y* recorder, and a stepping potentiometer. The electrical angle signal is fed to the *x*-axis of the recorder and the stepping potentiometer is used to advance the recorder pen along the *y*-axis so that several points at the same trace angle do not print on each other. With this equipment, the operator can measure between 600 and 800 trace angles per hour in comparison to less than 200 per day by the more conventional manual technique.

OXIDE FILM STUDIES

J. C. Banter

We are determining the optical properties of oxide films formed on zirconium in various corrosion environments to gain information on the oxidation-corrosion mechanisms. Initial experiments have been performed with zirconium foil specimens bearing anodically formed oxide films.

To determine the refractive indices and thicknesses of these films, we developed a new method based on the interference patterns exhibited on transmission of light through the films. The metal was dissolved from the film over a selected area of the specimen, leaving a clear window of the oxide supported by a frame of the remaining metal. The transmission of each film was measured over the spectral range of 2000 to 28,000 A with a double-beam recording spectrophotometer. The transmitted light exhibits interference maxima at those wavelengths where

$$nT \cos r = m\lambda/2$$

and interference minima where

$$nT \cos r = (2m + 1)\lambda/4$$

with n = refractive index of the oxide film at wavelength λ, T = oxide film thickness, r = the angle of refraction into the film, and m = the order of the interference peak. For normally incident light $\cos r = 1$.

As the angle of incidence of the light is increased, the wavelength of the peak for any given order of interference shifts toward shorter wavelengths. At some angle of incidence, this shift is sufficient to cause the minimum for a given order to coincide in wavelength with the maximum for that same order at normal incidence. Since the order of interference is known, values for nT and $nT \cos r$ can be calculated. Then, both n and T can be calculated using these values and Snell's law,

$$n = \sin i/\sin r ,$$

where i = the angle of incidence of the light. Dividing values of nT determined at other wavelengths by T determined as above, the values of n at the other wavelengths can be determined. Figure 21.9 shows results in the visible and ultraviolet regions of the spectrum for two different oxide films approximately 5500 A thick.

As an internal check on the method, we calculated the film thicknesses from the values of $nT \cos r$ at the various wavelengths using values of n taken from curves such as those in Fig. 21.9. In all cases, the individual values agreed to within 2%. Thus, the method also provides an accurate measure of the film thickness.

Attempts to apply the same technique to films formed by oxidation of zirconium foil in air and in high-temperature water were not successful

[9] L. K. Jetter, C. J. McHargue, and R. O. Williams, *J. Appl. Phys.* **27**, 368–74 (1956).

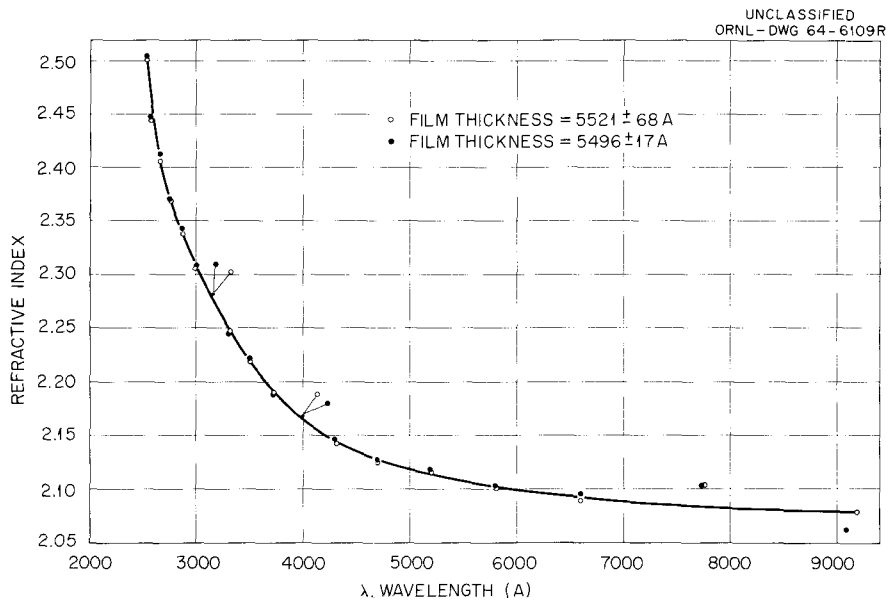

Fig. 21.9. Refractive Index as a Function of Wavelength for Anodized Films on Zirconium Foil.

due to an intrinsic absorption of visible and ultraviolet light by these films. No interference patterns were exhibited, even for films only 1500 A thick. Similar measurements in the infrared region of the spectrum should prove more fruitful, as the thermally formed films do not show the intrinsic absorption there. However, this region can be used only for films several tens of thousands of angstroms thick, as thinner films cannot exhibit interference patterns at these wavelengths.

PREPARATION OF SINGLE CRYSTALS OF ZIRCONIUM AND ZIRCONIUM ALLOYS

J. C. Wilson

A new, rapid, solid-state method for growing single crystals of zirconium and Zircaloy-2 in thin strips was described last year.[10] This year the process has been studied in detail in order to extend the method to thicker sections and reduce the effects of composition variations among different lots of zirconium. In addition, crystals up to 13 mm in diameter and 10 cm long have been produced by zone melting. A paper summarizing much of the work is to be published soon.[11] The following paragraphs describe some of the more important points. Galvanomagnetic measurements on one of these crystals are reported in Part I, Chap. 10 of this report.

The solid-state-growth method consists of forming a narrow, beta-phase zone (by electron-beam heating) and traversing the zone along the length of the specimen. There are at least three steps in the process: (1) production of a few large beta grains across the width and thickness of the specimen in or near the starting zone; (2) growth of *each* large beta grain so formed, in the direction of zone travel, by consuming all the alpha grains in its path at the leading alpha-beta interface; and (3) transformation of each large beta grain to a single alpha grain at the trailing alpha-beta interface. Once growth is well started, the moving beta zone consists of a few elongated grains whose

[10] J. C. Wilson, *Metals and Ceramics Div. Ann. Progr. Rept. May 31, 1963*, ORNL-3470, pp. 59–60.

[11] J. C. Wilson and M. L. Picklesimer, *Variable-Gradient, Electron-Beam Heating Methods for Growing Single Crystals of Zirconium*, paper presented at the 1964 International Conference on Electron and Ion Beam Science and Technology, Toronto, Canada, May 6–8, 1964, under joint auspices of the Electrochemical Society and AIME (proceedings to be published by John Wiley & Sons, Inc., New York).

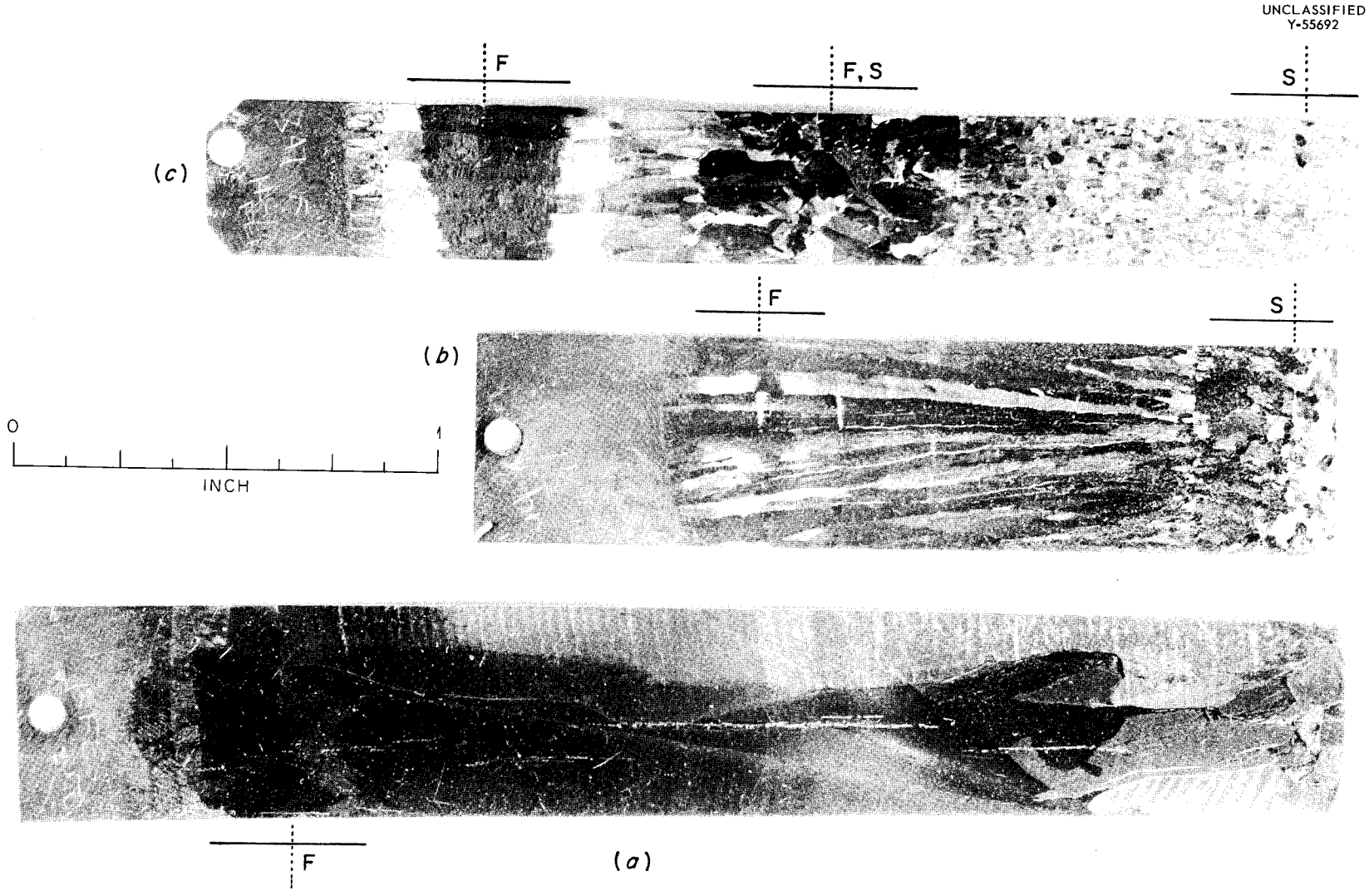

Fig. 21.10. Solid-State Crystal Growth in Three Different Lots of 1 × 25 mm Zirconium Strip at a Maximum Temperature of 1200°C and a Zone Travel Rate of 4 cm/hr. "S" and "F" show extent of beta zones at start and finish respectively. Unetched.

boundaries extend the length of the zone (in the general direction of zone travel). Steps 2 and 3 are rather insensitive to experimental parameters or to which lot of a material is used.

Step 1, the production of grains sufficiently large to grow with the moving beta zone, is the most difficult and variable step in the process. The morphology and growth rates of the grains in the original beta zone differ visibly among the six lots of zirconium metal used. The characteristic behavior of each material is altered by zone refining but not by working or heat-treating processes that might affect the texture. Therefore, the differences in behavior are probably due to variations in composition. These variations must be small, because the composition of all materials used was well within the limits for reactor-grade-I crystal bar. In general, the initial beta zone must be heated to a temperature (from 1100 to 1500°C) at which grains larger than twice the specimen thickness are formed.

Figure 21.10 illustrates the different behavior of three lots of zirconium under identical conditions. In material (c) no elongated grains grew until the specimen was cooled and reheated to a higher temperature (1300°C) and traversed at a slower rate (0.5 cm/hr).

The growth process apparently requires steep temperature gradients; if the surface-to-volume ratio is decreased (as by using a thicker strip), the gradients are made less steep and producing large grains is more difficult. Using higher temperatures, decreasing the zone travel rate, and sometimes cycling through the alpha-beta transformation temperature will often help initiate grain growth. In some material better growth occurs if lateral temperature gradients are superimposed on the predominantly longitudinal gradients normally employed. Multiple individually controlled electron guns have proved useful for producing arbitrary heating patterns on the specimens. One material has proved particularly sensitive to the direction of temperature gradients; each beta grain elongated in the direction of the maximum local temperature gradient, so by manipulation of the heating pattern, we could cause periodic changes in direction of the boundary between adjacent beta grains. This behavior is tentatively attributed to the "temperature gradient zone melting process" postulated by Pfann.[12]

[12]W. G. Pfann, *Zone Melting*, Wiley, New York, 1958.

Two observations suggest that growing large crystals in the alpha phase in zirconium may be practical. Alpha annealing following localized plastic deformation of the temperature-stable structure, material (*b*), illustrated in Fig. 21.10, produced a grain 5 mm wide in a few hours. Also, during annealing of zone-refined crystals at 830°C, boundary migration rates of the order of 1 mm/hr have been observed.

During zone-refining operations, cylindrical single crystals up to 13 mm in diameter and as long as 10 cm have been produced at rates of 2 cm/hr on the first or second zone pass. The yield of large crystals may decrease on subsequent passes, because thin elongated surface grains often form. The crystals that grow from the melt are frequently nucleated back in the solid starting section of the bar. This suggests that seeding may be possible. The composition of the material used apparently has little effect on crystal growth by zone melting.

Crystals produced by both the solid-state and zone-melting methods generally show diffuse or streaked Laue diffraction spots. Annealing at 830°C for periods of 10 to 100 hr usually produces sharp spots. Apparently, crystals with the basal plane parallel to the rod axis (or the basal plane parallel to the face of strip specimens) tend to show a higher degree of as-grown perfection than do other orientations.

ZONE REFINING OF ZIRCONIUM

J. C. Wilson

We purified several pounds of crystal-bar zirconium by floating-zone refining with an electron-beam heat source. Although a crude apparatus designed for 6-mm rods was used, stable zones were produced in rods as large as 13 mm in diameter. The vacuum system blanks off below 10^{-8} torr, but there are signs of occasional contamination with carbon and possibly oxygen. A bakeable ion-pumped system is being assembled to reduce contamination during future refining.

Purification achieved in 4 passes (at 3 cm/hr) of a 7-mm bar 20 cm long may be judged from the analyses in Table 21.2 and the fact that, of the 18 elements sought in the region 3 cm from the head

Table 21.2. Composition of Zirconium Bar Before and After Zone-Refining

Impurity	Position in Bar	Initial Concentration (ppm)	After Zone-Refining (ppm)
Oxygen	Head	5	32
Oxygen	Tail	5	10
Hafnium	Tail	95	80
Nitrogen	Total		<1
Hydrogen	Total		<1
Carbon	Total	20	60

of the bar, all were below either 10 ppm or a detection limit of 20 ppm. In later batches, more careful operation of the system reduced the pickup of carbon so it was not discernible at the 20 ppm level.

Resistivity ratios ($\rho_{300^\circ K}/\rho_{4.2^\circ K}$) as high as 450 have been measured. After a few passes the ratio is usually above 300 over one-third to one-half the bar. The measurements were made on an unannealed specimen by D. S. Easton of the Theory of Alloying Group. The highest resistivity ratios were invariably found toward the tail of the bars, as has been observed by others.[13] This fact, the oxygen distribution from analyses, and the observation that vacuum annealing invariably lowers the resistivity ratio in zirconium[14] suggest that oxygen is primarily responsible for the low ratios observed in the past.

One difficulty in zone refining zirconium stems from the anisotropy of thermal expansion in the alpha phase and perhaps from some kinking at the trailing alpha-beta interface. Under certain conditions the bar becomes skewed with respect to its original axis. The electron gun has a large central aperture, so that a large amount of misalignment can be tolerated. The electron beam is focused to a width much less than a millimeter at the specimen in order to maximize the superheat for volatilization of impurities. Others who have zone refined zirconium with induction heating[15,16] have usually found some collection of iron and nickel in the tail. Since the iron and nickel contents in the tails of our ingots are about the same as in the original bar, the intense heating is apparently effective. Also, increased stirring of the melt probably results from the superheat.

The gun configuration has allowed crystal-bar material to be zone melted directly. Figure 21.11 shows that as-deposited zirconium and titanium can be zone melted without difficulty in spite of variations in diameter and shape. Direct melting without the usual prior machining or mechanical working to a cylinder is much more economical of material and time. The large grains produced in the titanium bar suggest that single crystals can be grown as easily as in zirconium.

[13] J. P. Langeron, *Compt. Rend.* **256**, 5570 (1963).

[14] D. S. Easton, ORNL, personal communication.

[15] G. D. Kneip, Jr., and J. O. Betterton, Jr., *J. Electrochem. Soc.* **103**, 684 (1956).

[16] J. P. Langeron *et al.*, *Compt. Rend.* **248**, 35 (1959).

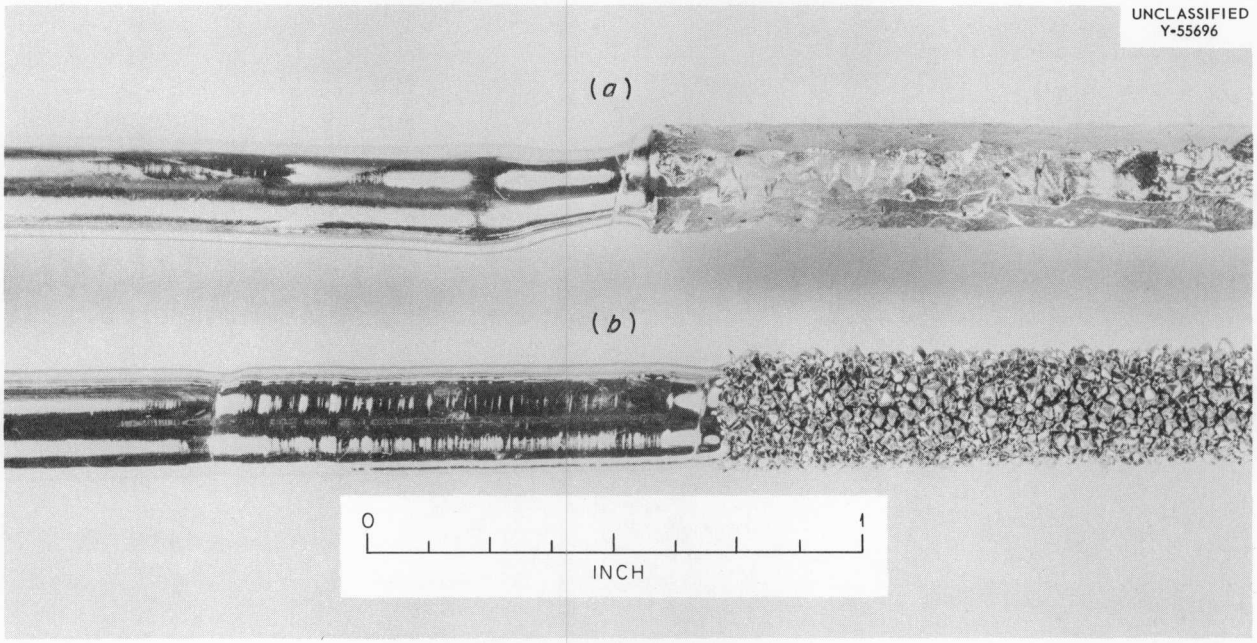

Fig. 21.11. Tails of Zone-Refined As-Deposited Crystal-Bar Zirconium and Titanium. (*a*) Zirconium after nine passes showing typical offsetting that occurs in multipass specimens. (*b*) Titanium bar after one and two passes; the right section is the as-deposited crystal bar, the center section received one zone pass, and the left section received two passes.

Part III.
Reactor Development Support

22. Advanced Test Reactor

R. J. Beaver G. M. Adamson, Jr.

Our effort in this program has been directed to the development of an aluminum-base wedge-shaped fuel element in which each of the 19 plates has its own specific fuel width and radius of curvature.[1] The fuel consists of a dispersion of 34.57% U_3O_8 and 0.2% B_4C in type X8001 aluminum and is clad with type 6061 aluminum. We evaluated plate fabrication parameters and forming characteristics and emphasized joining the plates into a fuel element by a mechanical roll-swaging process.

All work has been phased out with the organization of data and preparation of reports. Four reports have been completed[2–5] and another[6] is in preparation.

Other phases of the overall ATR Fuel Element Development Program have been reported.[7–9]

[1]R. J. Beaver, *Metals and Ceramics Div. Ann. Progr. Rept. May 31, 1963*, ORNL-3470, pp. 213–20.

[2]R. J. Beaver, G. M. Adamson, and P. Patriarca, *Procedure for Fabricating Aluminum-Base ATR Fuel Elements*, ORNL-3632 (June 1964).

[3]W. R. Martin and J. R. Weir, *Mechanical Properties of X8001 and 6061 Aluminum Alloys and Aluminum-Base Fuel Dispersions at Elevated Temperatures*, ORNL-3557 (Feb. 1964).

[4]D. O. Hobson, R. L. Heestand, C. F. Leitten, Jr., *Fabrication Development of U_3O_8-Aluminum Composite Fuel Plates for the Advanced Test Reactor*, ORNL-3644 (in press).

[5]R. W. Knight and C. F. Leitten, Jr., *Development of the Assembly Method for Fuel Elements for the Advanced Test Reactor*, ORNL-3643 (in press).

[6]J. H. Erwin and C. F. Leitten, Jr., *Development of a Forming Method for Curved ATR Fuel Plates* (to be published).

[7]J. C. Griess *et al.*, *Effect of Heat Flux on the Corrosion of Aluminum by Water. Part IV. Tests Relative to the Advanced Test Reactor and Correlation with Previous Results*, ORNL-3541 (Feb. 1964).

[8]H. D. Ferris and J. C. Mayers, *Advanced Test Reactor Fuel Element Hydraulic Buckling Tests*, ATR-FE-100-Ca-2 (Oct. 1963).

[9]M. A. Slominski (B & W) and R. J. Kedl (ORNL), *Advanced Test Reactor Hydraulic Test Program*, ATR-FE-103-Ca-7 (March 1964).

FUEL PLATE FABRICATION AND HOMOGENEITY

D. O. Hobson W. J. Werner

The plate fabrication phase of the ATR Development Program was completed. We explored unique fabricating procedures, proved the feasibility of a fabrication method, and produced plates for subsequent forming, assembling, and testing.

The work centered mainly on the development of procedures for blending mixtures of 34% U_3O_8–0.2% B_4C–bal X8001 aluminum, pressing into compacts, and cladding with type 6061 aluminum by hot-roll bonding. Special innovations included the use of tandem cores and cross rolling to achieve with only three pressing dies the nineteen different required fuel section widths required.

The results were quite encouraging with respect to meeting dimensional specifications desired, as exemplified by the data based on 128 plates fabricated using procedures established from the development work. Of these "production" plates, 98.4% met all dimensional specifications. Out of twenty representative plates that were examined by the through-transmission ultrasonic method for nonbond, only a single defect greater than $\frac{1}{16}$-in. diam was found.[10] More specific details, including a parametric evaluation of core spread and fuel compact characteristics, billet design, and procedures for plate rolling and plate machining, are reported elsewhere.[4]

Total nondestructive inspection for fuel homogeneity was performed on a number of ATR fuel plates to qualify development production procedures. Previous homogeneity inspection had been

[10]K. V. Cook and R. W. McClung, *Feasibility of Ultrasonic Detection of Nonbond in ATR Fuel Plates*, ORNL-TM-888 (in press).

Table 22.1. Percent Deviation of Fuel Concentration in ATR Fuel Plates from Nominal[a]

Plate No.	Plate Average	Range for Longitudinal 48- × 0.078-in. Scans	Local Areas, 0.078-in. diam		
			Maximum Positive	No. of Measurements > +20%	Maximum Negative
2038-5	+3	0 to +4	+26	8	−18
2039-5	+1	0 to +2	+21	2	−18
2040-5	+4	0 to +5	+32	11	−16
2041-5	+3	0 to +5	+30	20	−15
2031B-12	+5	+2 to +6	+23	6	−25
2032-12	+5	0 to +6	+32	19	−20
2033-12	+4	+2 to +6	+32	11	−16
2035-12	+5	+2 to +6	+32	19	−16
2036-12	+5	0 to +6	+36	28	−15
2027-19	+4	0 to +6	+30	19	−40[b]
2028-19	+5	+2 to +6	+30	>50	−22
2029-19	+7	+1 to +10	+36	>50	−45[b]
2030-19	+4	0 to +6	+30	33	−28

[a]Nominal concentration: 34.57% U_3O_8-Al determined nondestructively using x-ray attenuation.

[b]Found at core-to-core interface in plates with tandem cores.

limited to qualitative examination of high-contrast plate radiographs, confirmed in part with chemical analyses from several fabricated plates. Plates were inspected by use of the through-transmission x-ray attenuation technique[11] developed for the High-Flux Isotope Reactor. Entire fueled areas were scanned longitudinally using a $^5/_{64}$-in.-diam collimated x-ray beam with $^1/_{16}$-in. index between scans.

The plates evaluated were fabricated through both hot and cold rolling in accordance with procedures established[2] for plate types 5, 12, and 19. The compacts, which contained −170 +325 mesh U_3O_8, had been prepared by simple dry-blending and then pressing at room temperature to a density of 93.5% of theoretical.

As a precautionary quality control measure, all compacts were radiographed using high-contrast film. Since no significantly high- or low-density regions were visible in the radiographs, good homogeneity of the fuel was indicated.

Table 22.1 summarizes the x-ray attenuation data. In general, the results show a positive bias above the nominal fuel concentration. We believe that this is because the plates tested had slightly thicker fuel sections than the nominal 0.020 in. These data indicate that (1) the average fuel concentration in 48- × $^5/_{64}$-in. longitudinal scans can be maintained to ±4% of nominal, and (2) the variation in fuel concentration in 0.078-in.-diam areas can be controlled to within ±20% of nominal in more than 97% of the total plate area. The maximum variation expected should be no greater than 30%.

FUEL PLATE FORMING

J. H. Erwin

Our studies on forming ATR plates to the proper shapes[12] were culminated with the successful demonstration of the two-step low-pressure marforming process. Using this process, we formed

[11]B. E. Foster and S. D. Snyder, *Metals and Ceramics Div. Ann. Progr. Rept. May 31, 1963*, ORNL-3470, pp. 182–83.

[12]J. H. Erwin and C. F. Leitten, Jr., *Metals and Ceramics Div. Ann. Progr. Rept. May 31, 1963*, ORNL-3470, pp. 216–17.

fuel plates with sufficient accuracy to assemble within dimensional specifications six elements containing depleted uranium.

In addition to developing this two-step forming process, we improved the reproducibility of plate curvature further[13] by increasing the degree of cold rolling during plate fabrication from 7.4 to 20%. A detailed description of the forming development work and recommended procedures is presently being prepared.[6]

FUEL ELEMENT ASSEMBLING AND JOINING

R. W. Knight

This phase of the ATR Development Program was completed with the establishment of mechanical methods for assembling and joining fuel plates into an element. The roll-swaging technique selected has been described previously[1] and has produced joints with strengths in excess of 300 lb per lineal inch. The step-by-step procedures for producing fuel elements[2] and the detailed results of the development[5] have been reported. We showed that a match was very important between the angle of the side plate groove and the entrance angle of the fuel plate. Side plates with 19 different groove angles could be gang-machined and fuel elements of the latest design (Mark IV) could be made to the desired specifications, particularly the nominal 0.078-in. channels between plates. Inspection of the spacings between plates in the last several fuel elements, made after the process had been established, showed that the average channel could be held to within ±0.004 in. and that no individual measurement exceeded ±0.007 in.

---

[13] J. H. Erwin, M. M. Martin, and C. F. Leitten, Jr., *Ibid.* pp. 85–87.

23. Army Reactors Program

R. J. Beaver G. M. Adamson, Jr.

The main objectives of the Army Reactors Program are to (1) develop the technology of materials of interest as neutron absorbers, (2) evaluate the performance of the stainless-steel-base fuel elements, (3) study fuel materials that can meet the performance required of future long-life high-power-generation cores, and (4) provide general support assistance to the Army reactor development programs.

During the past year the work on neutron absorbers was directed at the production, the study of compatibility, and the determination of the irradiation resistance of europium oxide and europium molybdate. Both the fuel element development and the general support work have consisted primarily of hot-cell examinations of materials of interest.

CONSOLIDATION OF EUROPIUM OXIDE

R. E. McDonald C. F. Leitten, Jr.

Optimum parameters were established for melting of europium oxide and various other rare-earth compounds in quantities ranging from 300 to 500 g. As previously reported,[1] we first studied melting of 30-g quantities of Lindsay Mix (45% Gd_2O_3–45% Sm_2O_3–10% other rare-earth oxides) to define the major problem areas. We met considerable difficulties with arc stability, arc scatter, gas evolution, and reaction of the oxide with the copper hearth. The arc scatter was attributed to the low surface tension of the molten rare-earth oxide and was greatly reduced by use of a deep hemispherical mold cavity to prevent the spread of small droplets of the molten material. The arc instability was primarily due to the evolution of gas from the oxide during initial fusion and was minimized by injection of an inert gas through a hollow tungsten electrode to sweep the released gas from the immediate vicinity of the arc.

We also observed significant deposition of copper oxide on the internal surfaces of the melting chamber. We believe that while striking the arc during the initial stages of the melting process, some copper volatilized and deposited as copper oxide. We vapor plated the copper surfaces with tungsten; this apparently prevented this phenomenon because gas evolution during subsequent melting has been greatly reduced and inspection of the hearth surfaces after use has shown no evidence of copper oxide.

Although the small experimental quantities of rare-earth oxide can be arc melted in one operation, a two-step operation is more suitable for melting the larger (300- to 500-g) quantities. In the initial step, low-density cold-pressed pellets are partially fused to remove the major portion of volatiles and to increase the bulk density. In the second step, the material is melted completely. During this later stage of melting, the power is kept low (300 to 400 amp at 30 v) until the entire oxide charge becomes molten and then is increased gradually until a power level of approximately 800 amp at 40 v is reached to assure homogeneity of the oxide. In both melting steps, an equimolar mixture of helium and argon flows through the electrode tip at a system pressure of 300 torr. We also arc melted large pellets of europium molybdate, using the conditions established for europium oxide, with similar success.

[1] C. F. Leitten, Jr. and R. E. McDonald, *Metals and Ceramics Div. Ann. Progr. Rept. May 31, 1963*, ORNL-3470, pp. 221–22.

CHEMICAL COMPATIBILITY OF ARC-FUSED EUROPIUM OXIDE AND EUROPIUM MOLYBDATE IN STAINLESS STEEL, IRON, NICKEL, AND CHROMIUM

C. F. Leitten, Jr.

We have initiated a program to evaluate the chemical compatibility of arc-melted europium molybdate ($Eu_{5.3}MoO_{11}$) with low-silicon iron, nickel, and chromium powders and with types 304L and 302B stainless steel powders. Arc-melted Eu_2O_3 was also tested to compare its compatibility to that of a hydrogen-conditioned Eu_2O_3 type found previously[2] to be incompatible with stainless steels or their constituent elements that contained appreciable silicon. Because of this incompatibility, neutron absorbers now in the SM-1 reactor were made[3] by dispersing Eu_2O_3 in a mixture of low-silicon powders of 71% Fe, 18% Cr, and 11% Ni.

We did not observe reaction of either europium molybdate or arc-melted europium oxide with iron or nickel powder as a result of treatment at 1150°C in vacuum or argon. These oxides reacted with chromium, but we attribute this reaction to faulty chromium powder. Although the compatibility with chromium still remains to be resolved, we feel that the europium molybdate and the arc-melted europium oxide are just as compatible with the low-silicon powder ingredients of stainless steel as is the hydrogen-prepared europium oxide.[4] The arc-melted europium oxide, like the hydrogen-prepared material, can also be sintered in hydrogen. We expected europium molybdate to react when treated in hydrogen, and indeed we found considerable weight loss and other evidence of reaction when we sintered this compound at 1150°C in hydrogen.

As anticipated, neither the europium molybdate nor the arc-melted europia was compatible at 1150°C with types 302B and 304L stainless steel powders. We did notice, however, that the reaction between arc-melted europia and type 304L stainless steel was significantly less than reported previously for hydrogen-prepared oxide.

[2]C. F. Leitten, Jr., *The Stability of Europium Oxide in Silicon-Bearing Stainless Steel*, ORNL-2946 (Aug. 9, 1960).

[3]C. F. Leitten, Jr., R. J. Beaver, and J. E. Cunningham, *Specifications and Fabrication Procedures on Europium-Bearing Absorber Rods for Reactivity Control in Core II of SM-1*, ORNL-2733 (July 29, 1959).

[4]C. F. Leitten, Jr., *Army Reactors Program Ann. Progr. Rept. Oct. 31, 1963*, ORNL-3712 (in press).

IRRADIATION PERFORMANCE OF Eu_2O_3–STAINLESS STEEL NEUTRON ABSORBER SECTIONS

A. E. Richt

Previously, we showed[5] that platelets containing 40% Eu_2O_3 dispersed in and clad with stainless steel were not significantly damaged by relatively long exposures in the ETR at a temperature of approximately 150°F. Also, we have been following the performance in the SM-1 of full-size absorber rods that contain 37% Eu_2O_3 in stainless steel. The design features and fabrication process have been published previously.[3]

Absorber section Eu-SS-4, with a reported exposure of 5.9 Mwyr, was nondestructively examined in the ORNL hot cells. We found no significant changes in appearance or dimensions. Detailed results are reported elsewhere.[6]

Absorber section Eu-SS-8, with an estimated exposure of 13.5 Mwyr, showed no visible evidence of damage when examined in the reactor at the SM-1 site.

POSTIRRADIATION EXAMINATION OF SM-1 CORE I FUEL ELEMENTS

A. E. Richt

An important aspect in the Army Reactors Program during the past several years has been the postirradiation evaluation of fuel elements developed and fabricated at ORNL for the first core loading of the SM-1 reactor. Design and fabrication details on these fuel elements were reported previously.[7] Similarly, data obtained in postirradiation examination of these elements have

[5]A. E. Richt, *Army Reactors Program Ann. Progr. Rept. Oct. 31, 1962*, ORNL-3386, pp. 84–88.

[6]A. E. Richt, *Army Reactors Program Ann. Progr. Rept. Oct. 31, 1963*, ORNL-3712 (in press).

[7]J. E. Cunningham, R. J. Beaver, R. D. Robertson, and E. C. Edgar, *Specifications and Fabrication Procedure for APPR-1 Core II Stationary Fuel Elements*, ORNL-2649 (Jan. 29, 1959).

already been reported.[8-10] We observed both intergranular and transgranular cracking in the type 304 stainless steel cladding. Although the cracking caused no damaging effects (such as fission-product activity), the effect was disconcerting. We studied the frequency of the cracks to identify significant trends. The results are illustrated in Fig. 23.1. In all three fuel elements studied, cracks were most numerous in the region 8 to 17 in. from the lower end of the fuel plate. Also, the rate of cracking increased with irradiation exposure much more than proportionately.

Although the unirradiated UO_2–stainless steel dispersion in the SM-1 plate is not prone to waterlogging, we have started to determine whether irradiation induces it. In the first tests, specimens from fuel element S-81 were alternately exposed for 24 hr in 570°F water at 1200 psi and heated in air for 3 min at 1000°F. The results listed below indicate that at less than 15% burnup of the ^{235}U atoms the fuel does not waterlog. At higher exposures the samples blister, no doubt as a result of waterlogging. This effect is probably related to the porosity developed in the UO_2 during irradiation.

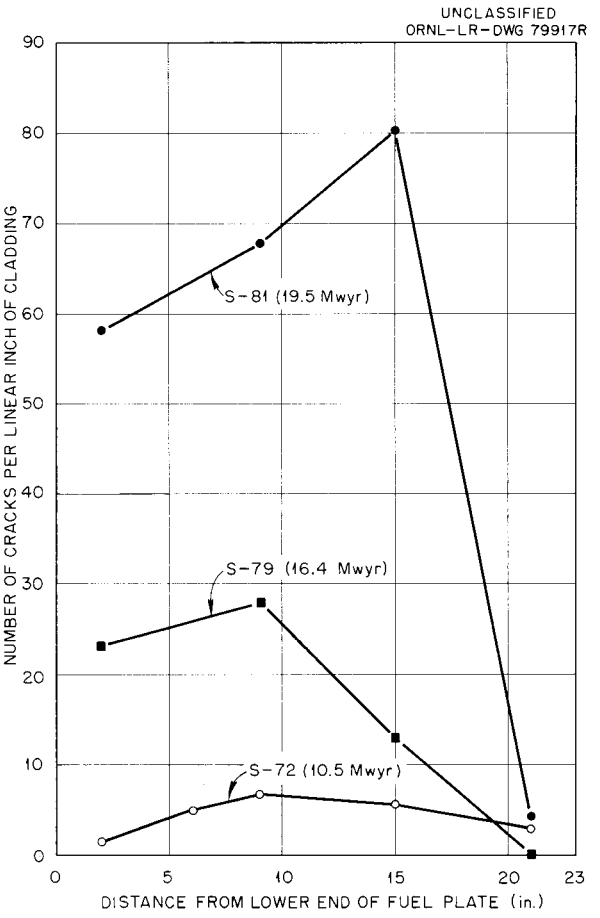

Fig. 23.1. Clad Cracking as a Function of Axial Position in SM-1 Fuel Elements S-72, S-79, and S-81.

Specimen No.	Specimen Burnup (% ^{235}U depletion)	Result
A	Unirradiated	No blisters after 10 cycles
1	9–15	No blisters after 10 cycles
2	15–35	Blistered after 6 cycles
3	35–52	Blistered after 4 cycles
4	52–62	Blistered after 4 cycles

[8]Staff, Oak Ridge National Laboratory, *APPR Ann. Progr. Rept. Jan. 31, 1960*, ORNL-2907, pp. 32–44.

[9]A. E. Richt, *Army Reactors Program Ann. Progr. Rept.*, ORNL-3231, pp. 33–38 (Jan. 31, 1962).

[10]A. E. Richt, *Army Reactors Program Ann. Progr. Rept. Oct. 31, 1962*, ORNL-3386, pp. 82–84.

IRRADIATION OF DISPERSIONS OF SPHEROIDAL UO_2 IN STAINLESS STEEL FOR ADVANCED PM-TYPE REACTOR CORES

R. J. Beaver A. E. Richt

We are cooperating with the Martin-Marietta Company, Baltimore, Maryland, for the purpose of irradiating both tubular and plate-type specimens containing UO_2 dispersed in stainless steel in the ORR pressurized-water loop.[11] The program is aimed at developing advanced fuel cores for PM-type (portable, medium power) reactors. The overall objective is to increase both core lifetime and power output. For example, core 3 of PM-1 is to be capable of a 100-Mwyr core lifetime with a 30-Mw (thermal) power output, a substantial increase over the 16 Mwyr and 9.4 Mw of core 1.

To accomplish this objective, the fuel investment must be increased significantly. Thus, 35% UO_2 must be homogeneously dispersed in stainless steel to form a tubular 0.090-in.-thick fuel core. The centerline fuel temperature is predicted to be in the range of 900 to 1000°F. Because of known burnup limitations of the UO_2–stainless steel system at elevated temperatures[12] (usually observed on dispersions of irregularly shaped UO_2 particles), the Martin Company has chosen to develop a more ideal dispersion using spheroidal UO_2, coated with stainless steel, to improve the irradiation stability. The types of specimens in test are summarized elsewhere.[11]

The major variable under test is the UO_2 concentration, which ranges from 30 to 45%. Other variables of lesser importance but still of significance include particle size of the fissile phase, type of spheroidal UO_2, type of the stainless steel powder dispersant, and differences in the process for preparing this fuel mixture.

Before the irradiation, dimensions were measured and the exterior surfaces of all specimens were replicated. Irradiation started in August 1963, and the fuel burnup is now an estimated 6×10^{20} fissions/cm^3. Fuel burnup at the end of test is expected to be in the neighborhood of 5×10^{21} fissions/cm^3.

[11] C. Eicheldinger, *PM Fuel Specimen Irradiation Program Preliminary Design Report*, MND-MD-2954 (March 15, 1963).

[12] W. C. Thurber and F. R. McQuilkin, *Metals and Ceramics Div. Ann. Progr. Rept. May 31, 1963*, ORNL-3470, pp. 228–31.

FUEL COMPOUNDS FOR ADVANCED CORES

D. M. Hewette II J. P. Hammond

By the use of alternate fuel materials, we are trying to develop fuel elements with capability of higher burnup and thermal performance. The use of a fuel material with higher thermal conductivity than UO_2, higher uranium density, or both would reduce the central temperature for a given power density and increase the permissible burnup. We are testing the compatibility of several fuel materials with the stainless steel matrix and the compatibility of their dispersions with water. These fuels include uranium mononitride (UN), mixed carbides (UC-NbC), uranium silicide (U_3Si_2), and uranium phosphide (UP). Preliminary information shows that the nitride and mixed carbides are compatible with stainless steel but, at least under hydrogen, U_3Si_2 is not. In boiling-water tests, both the UN and U_3Si_2 were acceptable but the mixed carbides were not.

INTERIM EXAMINATION OF EXPERIMENTAL FUEL ELEMENTS AND ABSORBER SECTIONS IN THE SM-1

R. J. Beaver A. E. Richt
L. D. Schaffer[13]

An interim examination was made at the SM-1 reactor of the experimental components listed in Table 23.1. Since the exposure was fairly low in most cases, we anticipated and found no irradiation instability.

EXAMINATION OF PM-1 AND PM-3A CONTROL-ROD-DRIVE PRESSURE THIMBLES

A. E. Richt L. D. Schaffer[13]

At the request of the AEC Division of Reactor Development, we have examined control-rod-drive pressure thimbles from both the PM-1 and PM-3A reactors. Routine inspection at the reactor sites after relatively short periods of service had revealed that the reactor shield tank water was

[13] Reactor Division.

Table 23.1. Components Inspected at the SM-1 Reactor

Component Identity	Type of Element	Exposure (Mwyr)
Fuel Element		
5-83	Brazed, SM-1, Type 1, core 1[a]	3.7
20V	Brazed, SM-1, Type 1, core 2[a]	5.5
SM2A	Welded element for Type 3 core[b]	7.0
SM2B	Welded element for Type 3 core[b]	5.8
PM1-M2	Assembly of Type 1 core PM-1 fuel tubes[c]	3.7
Neutron Absorber		
BG-1	ORNL boron gradient[d]	5.5
SCI	ALCO silver-cadmium-indium[e]	2.5

[a]J. E. Cunningham *et al.*, *Specifications and Fabrication Procedures for APPR-1 Core II Stationary Fuel Elements*, ORNL-2649 (Jan. 29, 1959).

[b]J. Cooke *et al.*, *Hazards Report for SM-1 Core II with Special Components*, APAE No. 84 (March 30, 1961).

[c]J. Cooke *et al.*, *Hazards Report for SM-1 Core II with Special Components*, APAE No. 84, Add. II (Sept. 1, 1961).

[d]R. J. Beaver and T. D. Watts, *Army Reactors Program Progr. Rept.*, ORNL-3231, pp. 24–29 (Jan. 31, 1962).

[e]R. A. Shaw and R. L. Harris, *Silver-Cadmium-Indium Absorber Development*, APAE-116 (June 13, 1962).

corroding the thimbles. Since these pressure thimbles form a part of the reactor pressure vessel, severe corrosion could be dangerous. As shown in Fig. 23.2, the control-rod thimbles consist of two sections. The corrosive attack was restricted to the outer surfaces of the lower section, which was made from type 403 stainless steel. Although the bulk water temperature in this region was about 70°F, we believe that boiling occurred at the stainless steel surfaces, and the surfaces may have reached temperatures as high as 350°F.

The data of the examinations indicate that the type and the maximum depth of attack are distinctly different in the two reactor systems. The results are summarized below:

	PM-1 Thimble	PM-3A Thimble
Total exposure to shield tank water, months	16	18
Total reactor operating time, months	14	9
Maximum depth of corrosive attack, in.	0.003	0.014
Type of corrosive attack	Pitting	Pitting and intergranular

The corrosion of the PM-1 thimble was restricted to the type of pitting illustrated in Fig. 23.3. However, the thimble from the PM-3A reactor was attacked intergranularly, as shown in Fig. 23.4, as well as pitted. The pitting attack is not surprising; it would be expected in type 403 stainless steel exposed to oxygenated water.[14] However, the intergranular attack is disconcerting, particularly since it was found only in the PM-3A thimble. We are trying to obtain more detail of the environmental conditions.

[14]D. J. DePoul (ed.), *Corrosion and Wear Handbook for Water Cooled Reactors*, pp. 105, 155, 156, 162–64, 171, McGraw-Hill, New York, 1957.

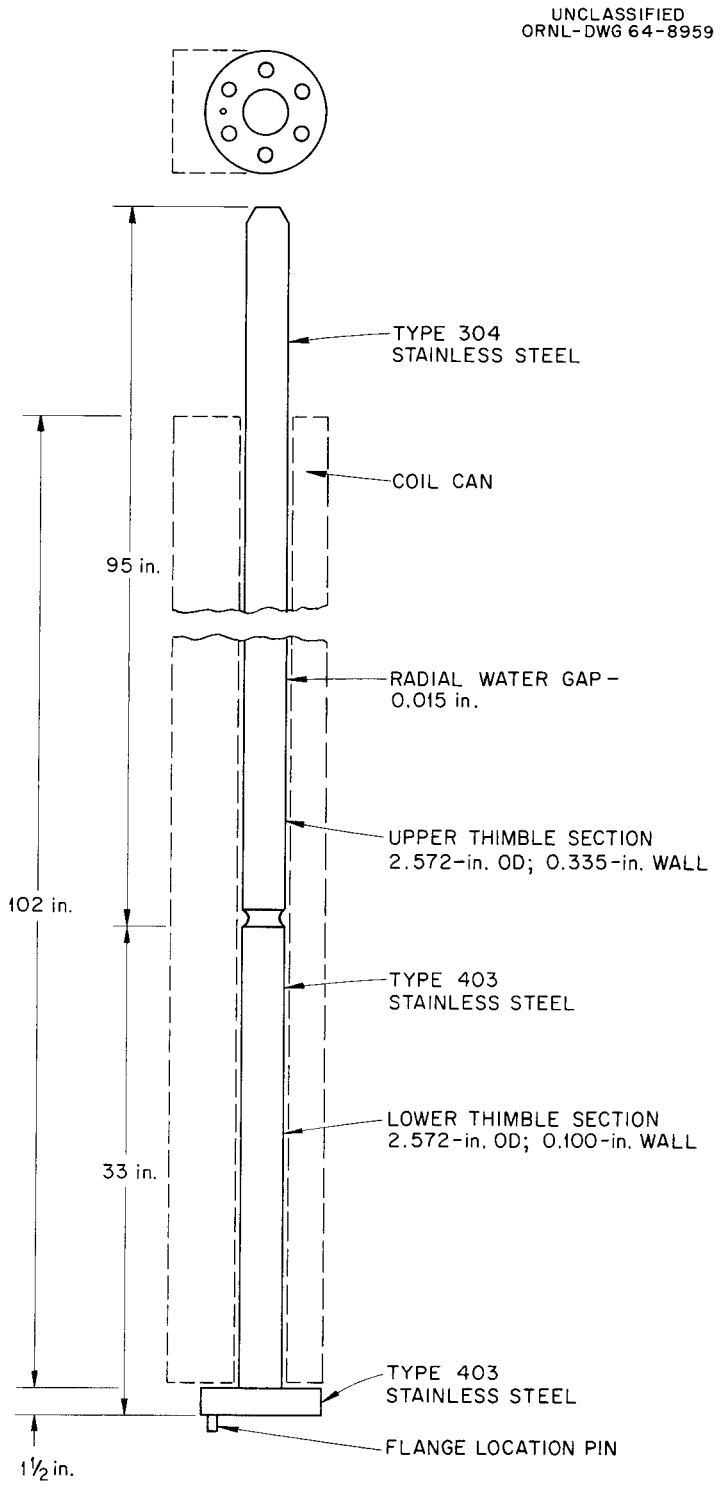

Fig. 23.2. Control-Rod-Drive Pressure Thimble Used in the PM-1 and PM-3A Reactors.

Fig. 23.3. Typical Pitting Attack Found in PM-1 and PM-3A Control-Rod Thimbles. As polished. 250×, reduced 25%.

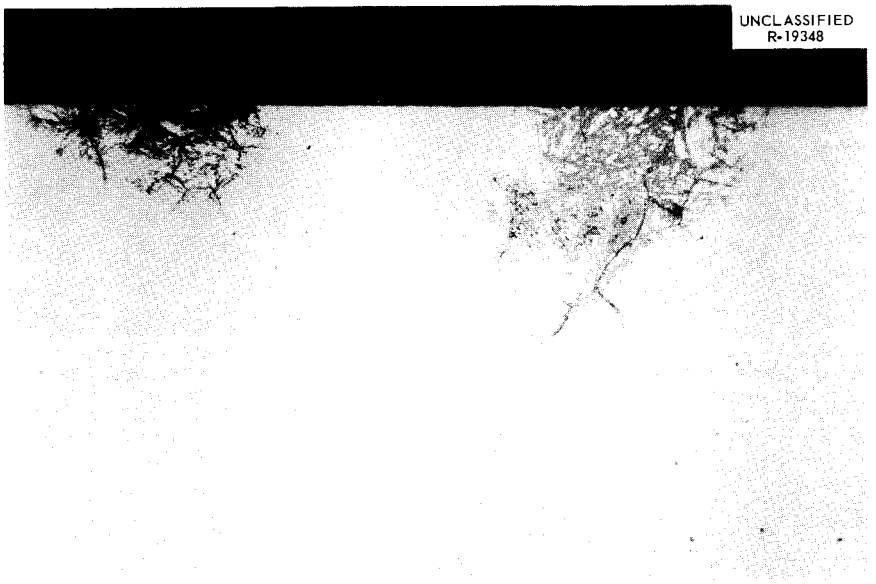

Fig. 23.4. Intergranular Attack Found in PM-3A Control-Rod Thimble. As polished. 250×, reduced 25%.

24. Enrico Fermi Fast-Breeder Reactor

G. M. Adamson, Jr.

We have been given the responsibility for fabrication development of stainless steel-base flat-plate fuel elements for the core B loading of the Enrico Fermi Fast Breeder Reactor. Our concluding efforts are reported below.

FUEL ELEMENT FABRICATION

R. G. Donnelly

As reported previously,[1] the core B fuel elements fabricated during this program had met all tolerances and requirements imposed by APDA except for two problem areas: (1) the stackup height of 2.270 ± 0.005 in., and (2) the coolant channel width of 2.246 ± 0.002 in.

To demonstrate that by using undersize spacers (0.052 to 0.053-in. thick for a nominal 0.054-in. plate spacing) we could build a fuel element that meets both the plate-spacing and the stackup-height tolerances, another test assembly was fabricated. This proof test assembly was built exactly as the later prototype fuel elements with the exception of the undersize spacers. With this modification, the assembly was brought easily to the correct stackup height. After brazing, the plate spacing was within tolerance in all cases. In fact, the distribution of plate spacing values in Fig. 24.1 shows an almost ideal distribution with a peak at the nominal spacing of 0.054 in.

The second problem area involved the width of the coolant channels. As stated previously,[1] instrument readings indicated that only about 50%

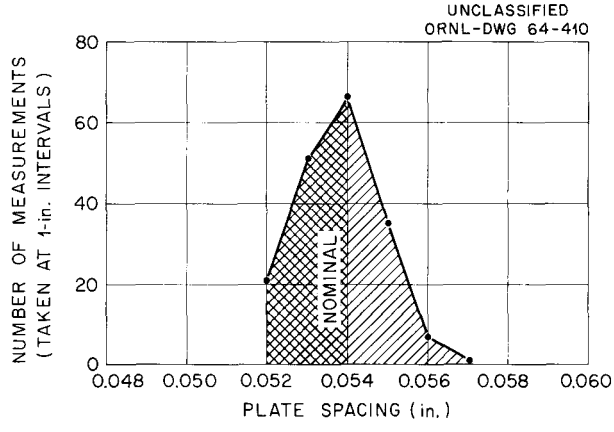

Fig. 24.1. Distribution of Plate-Spacing Measurements in Proof Test Assembly.

of the scanned portion of the latest prototype element was within the 2.246 ± 0.002-in. tolerance limit. However, direct measurements from two random metallographic sections of this same fuel element revealed that this dimension was maintained to a much higher degree than indicated by the eddy-current measuring device. Of the 26 channels measured, two were out of tolerance by 0.001 in., three by 0.002 in., and only one was out by 0.003 in. As a result, we feel that a ±0.005-in. tolerance on this dimension could be met consistently during production of such a fuel element.

The results of this proof test assembly have been incorporated in the topical report on the Core B fabrication procedures.[2]

[1] R. G. Donnelly, *Metals and Ceramics Div. Ann. Progr. Rept. May 31, 1963*, ORNL-3470, p. 227.

[2] R. G. Donnelly, W. C. Thurber, and G. M. Slaughter, *Development of Fabrication Procedures for Core B Fuel Elements for the Enrico Fermi Fast Breeder Reactor*, ORNL-3475 (in press).

25. Gas-Cooled Reactor Program

A. E. Goldman W. O. Harms

Our materials effort in support of the Gas-Cooled Reactor Program consists of support for the Experimental Gas-Cooled Reactor (EGCR), development of unclad ceramic fuel elements, and corollary supporting research. Major activities in each of these areas during the past year are presented below, along with pertinent background information.

EGCR SUPPORT

The EGCR, under construction at Oak Ridge, is an outgrowth of conceptual design studies by Kaiser Engineers, Allis-Chalmers, and ORNL. The reactor core consists of 2.46%-enriched UO_2 fuel clad with stainless steel and supported in a graphite moderator structure contained within a carbon-steel pressure vessel. The plant is being constructed by the H. K. Ferguson Company, and ORNL was responsible for procurement of the fuel and control-rod assemblies.

The fuel assemblies are clusters of seven elements, each of which consists of a column of UO_2 bushings clad with 0.020-in.-thick type 304 stainless steel. The cluster is supported within a 1-in.-thick × 29-in.-long × 5-in.-OD graphite sleeve. The UO_2 bushings are 0.707-in. OD × 0.323-in. ID × 0.740-in. long. The design lifetime of the assemblies is 10,000 Mwd/metric ton. The nominal peak operating temperature of the stainless steel cladding is about 1500°F.

Manufacture of the initial fuel loading and spares for the EGCR was completed at the Atomic Fuel Department of the Westinghouse Electric Corporation. All critical phases of work were monitored to ensure compliance with the standards specified on materials and workmanship. Approximately 1660 fuel assemblies have been received and stored at the Oak Ridge Gaseous Diffusion Plant. The fuel assemblies were fabricated for about $55 per kilogram of contained uranium metal.

Fabrication of Instrumented Fuel Assemblies for the EGCR

E. A. Franco-Ferreira

The Welding and Brazing Laboratory had the responsibility of fabricating 20 instrumented fuel assemblies for the EGCR.[1] The fabrication of all required components was completed, and they have been delivered to the Reactor Division for assembly into complete fuel stringers.[2,3]

Each instrumented fuel assembly consists of a cluster of seven cylindrical stainless steel elements, each containing 36 bushings of 2.46%-enriched UO_2. These stainless steel elements are spaced and supported within a graphite sleeve. The fuel elements within a cluster were instrumented by brazing Chromel-Alumel thermocouples, sheathed with $^1/_{16}$-in.-diam type 347 stainless steel, to the inside of the element tubing. The 20 fuel assemblies for the 5 instrumented stringers contained 125 noninstrumented fuel elements and 15 instrumented fuel elements. A view of a completed fuel stringer, as assembled by the Reactor Division, is shown in Fig. 25.1.

EGCR Construction Assistance

G. M. Slaughter E. A. Franco-Ferreira

Metallurgical assistance was provided to the EGCR project in various phases related to construction.[4] For example, we welded ferritic steel

[1] E. A. Franco-Ferreira, *Metals and Ceramics Div. Ann. Progr. Rept. May 31, 1963*, ORNL-3470, pp. 129–30.

[2] E. A. Franco-Ferreira, *GCR Program Semiann. Progr. Rept. Sept. 30, 1963*, ORNL-3523, p. 60.

[3] R. L. Senn, *GCR Program Semiann. Progr. Rept. Sept. 30, 1963*, ORNL-3523, pp. 47–56.

[4] E. A. Franco-Ferreira and G. M. Slaughter, *GCR Program Semiann. Progr. Rept. Sept. 30, 1963*, ORNL-3523, p. 63.

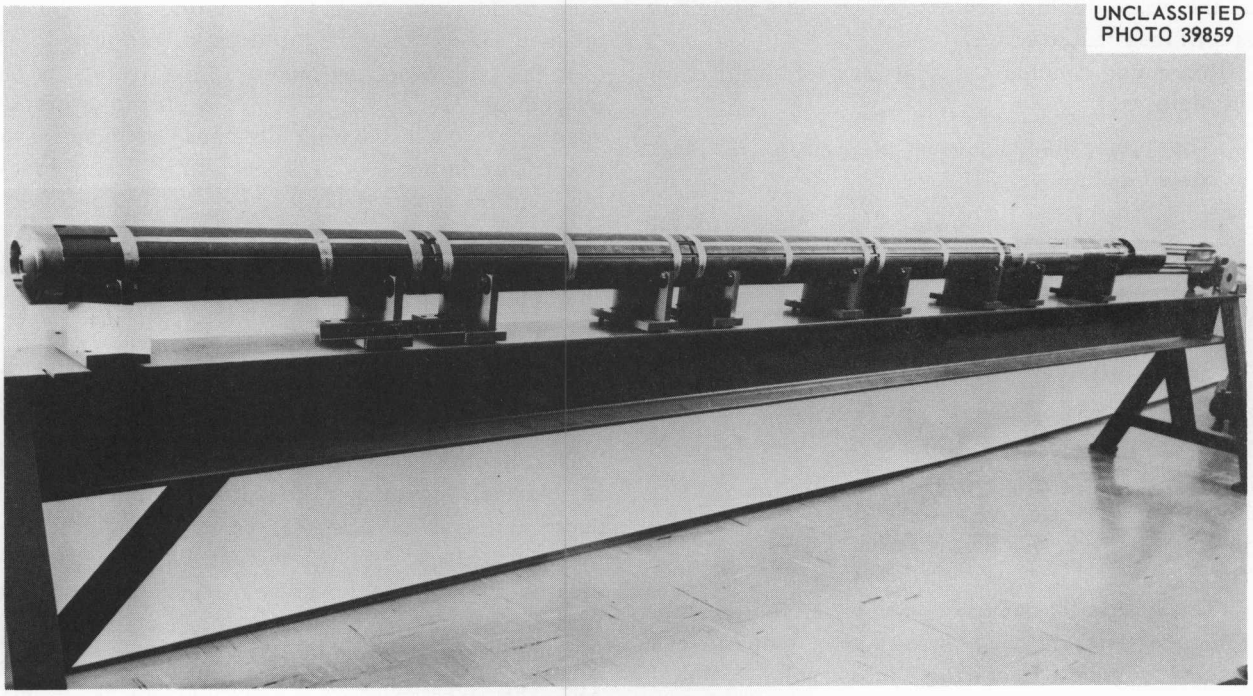

Fig. 25.1. EGCR Instrumented Fuel Assembly on Assembly Fixture.

to stainless steel in the primary coolant piping. The pipes were approximately 3 ft in diameter with a 1-in.-thick wall. The welds were made with Inconel 182 filler metal by our original procedure.[5] A rigid inspection of the welds was maintained, including periodic examinations by an ASME code inspector. The welds were of excellent quality and the pipes have been shipped to the EGCR site for insertion in the reactor system.

Also, we assisted the EGCR contractors with analysis of repair welds on the thermal shield, observation of repair welding on the pressure vessel bottom nozzles, evaluation of stud welds for the attachment of the pressure vessel reflective insulation, and development of thermocouple penetrations through the pressure vessel wall.

Measurement of Inter-Rod Spacing in the Fuel Assembly

C. V. Dodd

An eddy-current probe was designed, fabricated, and used to measure the inter-rod spacing in a number of EGCR fuel assemblies. The head of the probe, about which the induction coil is wound, rotates and has a modified V-shape. Thus, when it is placed between adjacent rods, it aligns itself and the depth of coil insertion is limited by the distance between the rods and by the shape of the probe. The probe permits fast and accurate measurements with a minimum of operator "feel" and should also be useful during postirradiation examination of the assemblies. A technical memorandum is being written to describe the device and its application.

Stress-Rupture Tests on Tubing for EGCR Fuel Cladding

J. T. Venard

Stress-rupture tests begun last year[6] on brazed fuel element tubes from Westinghouse were completed, and the results are plotted as points in Fig. 25.2. The curves shown in the figure are taken from a previously published investigation[7]

[5] G. M. Slaughter and T. R. Housley, *The Welding of Ferritic Steels to Austenitic Stainless Steels*, ORNL-TM-98 (Jan. 4, 1962); to be published in the *Welding Journal*.

[6] J. T. Venard, *Metals and Ceramics Div. Ann. Progr. Rept. May 31, 1963*, ORNL-3470, pp. 131–32.

[7] J. T. Venard, *Stress-Rupture Properties of Type 304 Stainless Steel Tubing*, ORNL-TM-535 (June 7, 1963).

of the stress-rupture behavior of type 304 stainless steel tubes tested in air.

The major conclusions that may be drawn from the data are:

1. The tubing had the same strength as the heat tested before.
2. Tests in air or in flowing argon showed about the same stress-rupture results.
3. Posttest metallography revealed no abnormal grain growth at any of the test temperatures.
4. Strain-at-fracture data are consistent with earlier data[7] on similar material.

Creep of Graphite Under Irradiation

C. R. Kennedy

The irradiation-induced shrinkage of graphite introduces strains much greater than graphite can absorb without fracturing unless the internal stresses can be reduced through irradiation-induced creep.

A second parabolic cantilever-beam in-reactor creep experiment containing specimens of AGOT, CGB, and isotropic grades of graphite has been completed. The experiment was essentially the same as the first[8] except that the beams were thermally insulated from the frame to produce a more uniform specimen temperature. This change reduced the temperature variation to less than 15°C over the 6-in. beam and increased the average beam temperature to 370°C. Creep data for the isotropic specimens could not be obtained because of a transducer failure, a specimen failure during loading, and an apparent blockage of the beam deflection.

The creep curves obtained have the same general characteristics as the earlier ones (i.e., a large amount of primary creep followed by a linear stage). The creep data are given in Figs. 25.3 and 25.4, where the zero intercepts and linear creep rates from both experiments are compared.

The neutron flux in the experimental facility is relatively constant except in the vicinity of the upper three specimens. There is a gradient over these positions with an average flux about five-eighths that of the lower positions. The results from the second experiment were all obtained from the lower positions and can be directly compared. The two specimens at the lowest stress in the first experiment were located in the lower flux positions, and their creep rates are adjusted in Fig. 25.4 for comparison. The specimen at the highest stress in the first experiment operated at

[8] C. R. Kennedy, *Metals and Ceramics Div. Ann. Progr. Rept. May 31, 1963*, ORNL-3470, p. 132.

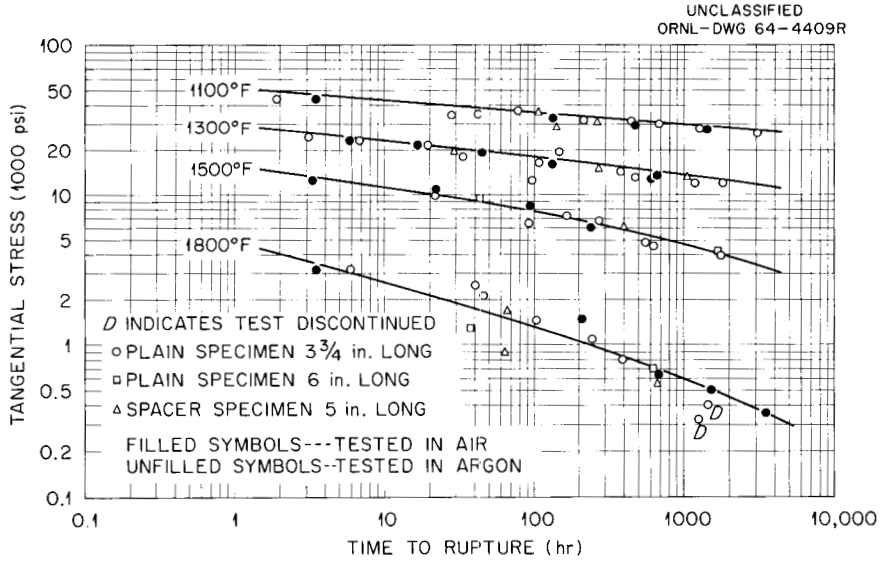

Fig. 25.2. Stress-Rupture Results on EGCR Fuel Element Tubing.

a slightly higher temperature than the others and is compared separately.

The zero-intercept data demonstrate good general agreement with Hesketh's[9] model for primary creep. This model of dislocation climb uses elastic modulus values from unirradiated graphite specimens and predicts that the transient strain should be linear with stress, independent of temperature, and proportional to the elastic strain on loading. Comparing the slopes from Fig. 25.3 with values of the elastic modulus, Table 25.1 shows a much more precise proportionality of the transient creep to the modulus of elasticity of the irradiated specimens. As shown in the table, the transient strain is very close to 95% of the elastic strain calculated from the modulus of elasticity of the irradiated specimens:

$$\epsilon_t = 0.95\ \Delta\sigma/E_I\ , \qquad (1)$$

where ϵ_t = transient creep, $\Delta\sigma$ = applied stress increment, and E_I = modulus of elasticity of irradiated specimens.

[9]R. V. Hesketh, *The Mechanisms of Irradiation Creep in Graphite*, R. D./B/N.188 (November 1963).

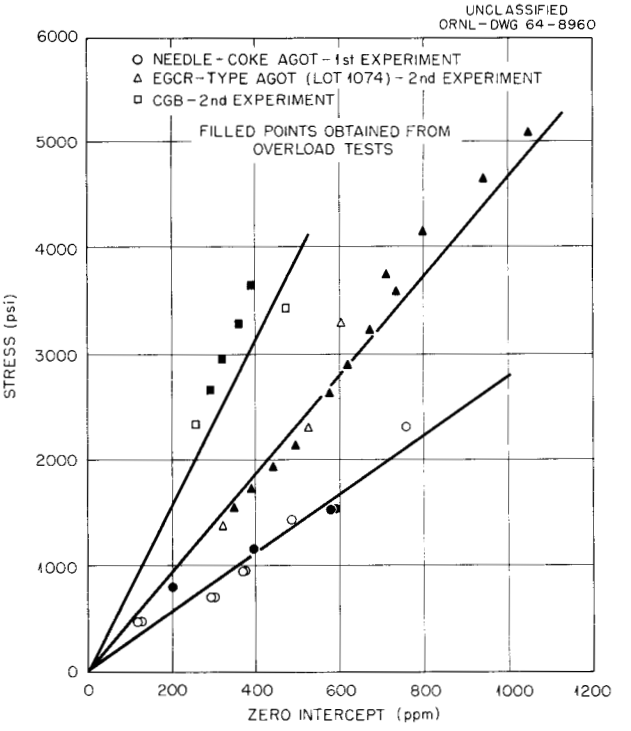

Fig. 25.3. Zero Intercepts for Creep of Graphite Under Irradiation.

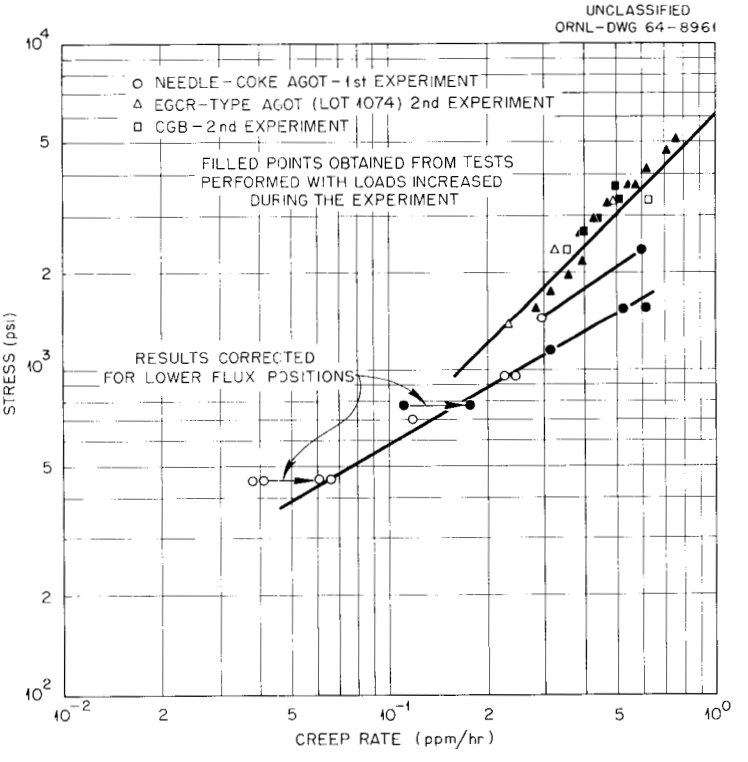

Fig. 25.4. Creep Rate of Graphite Under Irradiation.

Table 25.1. Comparison of Measured Moduli of Elasticity to the Slopes in Fig. 25.3

Grade	Slope in Fig. 25.3 (psi)	Modulus of Elasticity[a] (psi)		Ratio of Modulus to Slope	
		Unirradiated	Irradiated	Unirradiated	Irradiated
	$\times 10^6$	$\times 10^6$	$\times 10^6$		
Needle-Coke AGOT	2.80	1.7	2.60	0.61	0.93
AGOT (lot 1074)	4.70	2.0	4.54	0.43	0.97
CGB	7.90	2.8	7.5	0.35	0.95

[a]Measured in creep apparatus when specimens were loaded.

The overload test results (obtained by increasing the load during the experiment) also demonstrate that Eq. (1) is not affected by prior creep or irradiation history; for every $\Delta\sigma$ overload there was a transient creep calculated by Eq. (1). This behavior is in conflict with the concept of Perks and Simmons[10] and Reynolds[11] that the creep process is that of unpinning dislocations without climb. This hypothesis would predict that the transient creep would be affected by neutron dose and thus be reduced significantly for each overload. This, however, was not observed, as shown in Fig. 25.3.

The linear or second-stage creep rates also confirm the application of Cottrell's[12] irradiation creep model to graphite as proposed by both Hesketh[9] and Williamson and Jenkins.[13] Although these two proposals describe the model differently, they yield the same result in the form:

$$\dot{\epsilon}_c = A\sigma(\dot{G}_c - \dot{G}_a), \qquad (2)$$

where $\dot{\epsilon}_c$ is the linear creep rate, σ is the applied stress, $\dot{G}_a$ and $\dot{G}_c$ are growth rates of the crystallite in the a and c direction, and A is a constant. According to this model, the linear creep rate depends upon the growth rates of the crystallites and therefore should be the same for different grades of graphite. This model also predicts an effect of temperature similar to that on the growth rates. The creep results agree very well with Eq. (2) using the growth rates given by Simmons and Reynolds.[14] In the second experiment, both the AGOT and CGB grades exhibited the same creep rate, which was less than that observed for the AGOT grade in the first experiment. An interesting result is that, in the experiment at the lower temperature, the creep rate was not a linear function of stress. The nonlinearity at the lower temperatures verifies indications by Losty[15] that the creep rate is independent of temperature. At lower stress levels, creep rates would be similar in this temperature range. This effect, coupled with the possible weighting of the temperature-independent primary creep in the linear creep rates, may have resulted in Losty's conclusion that the creep rate is not temperature dependent.

Effect of Irradiation on Graphite

C. R. Kennedy

Specimens of grades CGB and AGOT (lot 1074) graphite were irradiated for one cycle to neutron

[10]A. J. Perks and J. H. W. Simmons, *Radiation Induced Creep in Graphite*, AERE-R-4372 (1963).

[11]W. H. Reynolds, *The Mechanical Properties of Reactor Graphite*, AERE-R-4566 (1964).

[12]A. H. Cottrell, *Radiation Induced Creep in Graphite*, M/M-102 (1955).

[13]G. K. Williamson and G. M. Jenkins, *Irradiation Creep in Graphite*, R. D./B/N.220 (February 1964).

[14]J. H. W. Simmons and W. H. Reynolds, "Dimensional Effects in Graphite on Irradiation," pp. 75–80 in *Proceedings of a Symposium on Uranium and Graphite, London, 1962*, Institute of Metals Monograph No. 27 (1962).

[15]H. H. W. Losty, "The Interpretation of Irradiation Creep Experiments on Graphite Springs," pp. 81–85 in *Proceedings of a Symposium on Uranium and Graphite, London, 1962*, Institute of Metals Monograph No. 27 (1962).

exposures ($E > 2.9$ Mev) of between 0.6×10^{20} and 1.4×10^{20} neutrons/cm^2 in the B-8 position of the ORR. We then measured the effect of irradiation on the electrical resistivity, dimensional stability, and tensile properties of the two materials. Except for the transverse AGOT, the irradiated specimens were so strong that the specimen grips failed before the specimen, so the modulus was the only tensile property that could be obtained.

The neutron dose was determined by nickel and cobalt flux monitors. The neutron energy spectrum is estimated in Fig. 25.5 from calculations furnished by R. E. Dahl[16] for a similar position in

[16]R. E. Dahl, General Electric, Hanford, personal communication to C. R. Kennedy, Oak Ridge National Laboratory, Feb. 10, 1964.

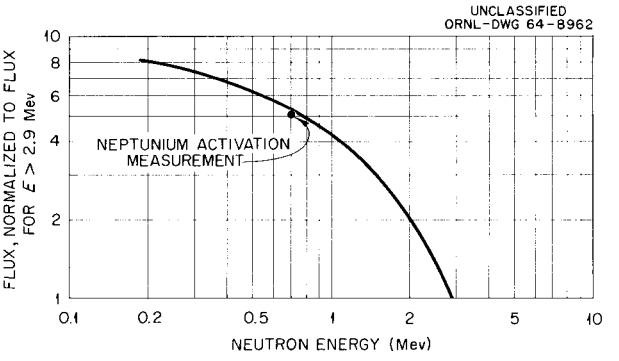

Fig. 25.5. Calculated Flux-Energy Spectrum for ORR B-8 Position. The ordinate represents the flux of neutrons having energy greater than the abscissa value, relative to that for 2.9 Mev.

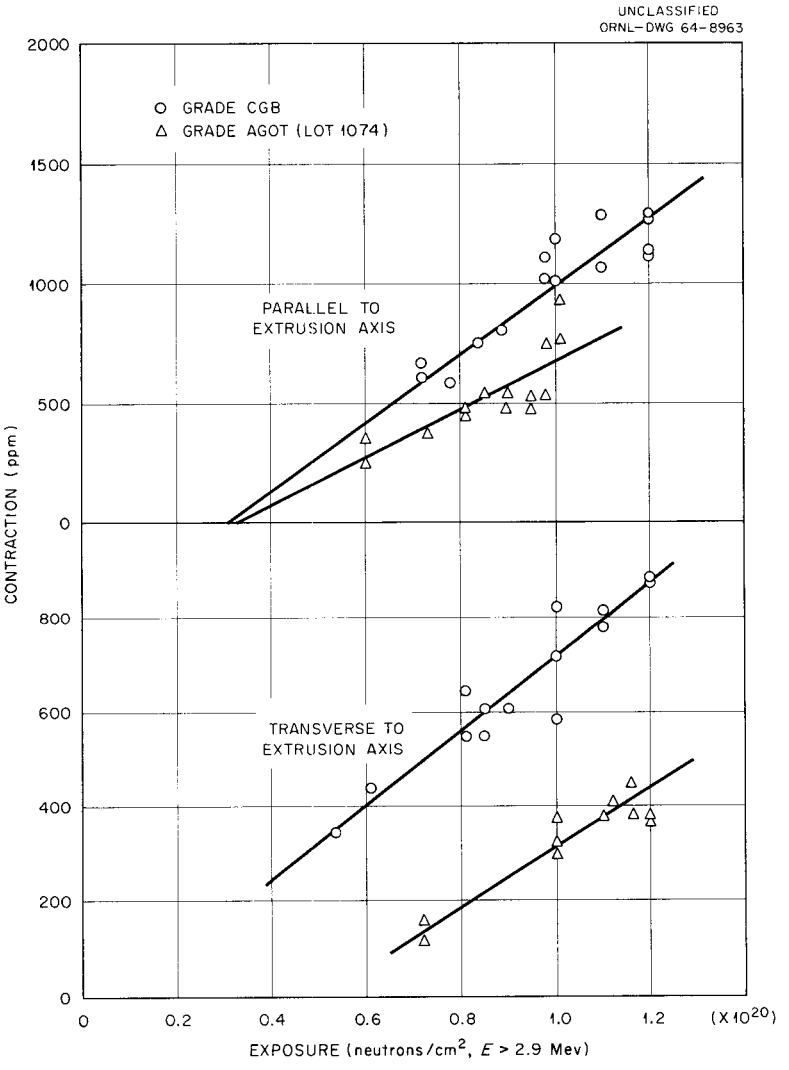

Fig. 25.6. Dimensional Change of Graphite by Irradiation at 350–475°C.

the GETR. Data for comparing results at these low neutron doses are scarce except those from the United Kingdom. The dose units used in the United Kingdom, however, are nickel-activation doses estimated from thermal flux measured by cobalt activation and are not directly comparable to our neutrons per square centimeter ($E > 2.9$ Mev) dose units. Simmons and Reynolds[14] give this conversion based on a comparison of irradiation damage to graphite:

$$3.6 \text{ UK Ni Dose} = \text{Dose } E > 2.9 \text{ Mev} . \quad (3)$$

The contraction results are given in Fig. 25.6. The contraction of AGOT material (in percent per 10^{20} neutrons/cm^2, $E > 2.9$ Mev) is compared to to that of UK PGA graphite below:

Graphite Grade	Parallel	Transverse
AGOT	0.10	0.064
PGA	0.12	0.076

The difference cited above may be due to a real difference in the graphite behavior or to inaccuracy in the dose conversion given by Eq. (3). The comparison of the CGB and AGOT grades is valid, however, and demonstrates an interesting behavior. Although the contraction increases with dose almost identically in both the parallel and transverse directions, contraction of the CGB graphite in the transverse direction appears to become appreciable at a much lower dose.

Our electrical resistivity measurements indicated that the irradiation damage is independent of temperature over the range of 150 to 550°C and does not vary with dose after an initial change. The averages of the values obtained are given in Table 25.2. Irradiation affected the AGOT more than the CGB and the parallel values in both materials more than the transverse.

Our elastic modulus values also appeared to be temperature independent and saturated after an initial dose. The averages of the completed results are given in Table 25.3. Although the tensile properties of the AGOT material differ for two different transverse directions, the average is shown here for comparison. Our only fracture results are for the transverse AGOT samples and are given in Table 25.4. The fracture results show an interesting comparison of the total and elastic energies at fracture. Losty[17] has previously reported that the elastic fracture energy, determined from bend tests, was unchanged by irradiation. The results in Table 25.4 are in fair agreement with this, but the total fracture energy appears to be more nearly unaffected. This disagreement is a reflection of the difference between the bend and tensile tests, since the material acts more like an elastic material under bend testing.

Table 25.2. Effect of Irradiation on the Electrical Resistivity of Graphite

Graphite Grade	Orientation	Average Preirradiation Resistivity, ρ_0 (ohm-cm)	Average Increase ($\Delta\rho/\rho_0$)
		$\times 10^{-4}$	
AGOT (lot 1074)	Parallel	6.166	2.21
	Transverse	9.762	1.88
CGB	Parallel	6.437	1.37
	Transverse	12.558	1.16

Table 25.3. Effect of Irradiation on the Elastic Modulus of Graphite

Grade	Orientation	Average Preirradiation Elastic Modulus, E_0 (psi)	Average Change in Elastic Modulus ($\Delta E/E_0$)
		$\times 10^6$	
AGOT (lot 1074)	Parallel	1.84	1.34
	Transverse	0.92	1.42
CGB	Parallel	3.25	1.59

[17] H. H. W. Losty and J. S. Orchard, "The Strength of Graphite," *Proc. Conf. Carbon, 5th, Univ. Park, Penna., 1961* 1, 519 (1962).

Table 25.4. Effect of Irradiation on Fracture Strength of AGOT Graphite (lot 1074)

Specimen and Orientation[a]	Average Fracture Stress, σ_f (psi)	Average Fracture Strain, ϵ_f (%)	Average Elastic Modulus, E (psi)	Total Energy $\sigma_f \epsilon_f / 2$ (in.-lb)	Elastic Energy $\sigma_f^2 / 2E$ (in.-lb)
			$\times 10^6$		
Unirradiated No. 1	1520	0.206	0.98	1.57	1.18
Irradiated No. 1	2510	0.125	2.42	1.57	1.30
Unirradiated No. 2	1100	0.131	0.87	0.72	0.69
Irradiated No. 2	1550	0.088	1.99	0.68	0.60

[a]Numbers 1 and 2 refer to two perpendicular transverse directions.

DEVELOPMENT OF UNCLAD FUELS

All-ceramic fuels offer the advantages of high-temperature operation, long life, and good neutron economy. A possible disadvantage is that some fission product activity from them may enter the coolant system, although recent observations in this area have been encouraging. We are developing and evaluating all-ceramic fuel elements with major emphasis on fueled-graphite elements containing carbide fuel particles coated with pyrolytic carbon. Other studies have involved fabrication, evaluation, and irradiation testing of fueled BeO and testing the mechanical properties of graphite and the effects of irradiation on them. Some of our efforts on thorium-containing fuels are reported in Chap. 29 of this report.

Pyrolytic-Carbon-Coating Studies

R. L. Beatty

Fuel particles have been coated with carbon produced by the pyrolytic decomposition of hydrocarbon gases in fluidized beds.[18] Deposition conditions have been varied to determine their effect on coating properties. Temperature of application appears to be the dominant variable in that it influences all properties of the coatings, including strength, density, c_0 lattice spacing, apparent crystallite size, and preferred orientation. Another major variable is deposition rate, which is controlled by temperature and by the rate and partial pressure at which hydrocarbon gas is supplied to the coating chamber relative to the surface area of the charge being coated.

Coatings have been applied at temperatures over the range from 1000 to 1800°C, mostly at 1400°C. In general, the coatings deposited at the higher temperature were denser, with 2.10 g/cm^3 being the maximum density obtained. Densities have not been determined on coatings deposited at temperatures below 1400°C. Densities and other properties of coatings deposited at 1400°C, measured as described in the following section, depended on deposition rate as shown in Fig. 25.7. These properties are for coatings deposited with all conditions held essentially constant except the partial pressure and flow rate of methane. The

[18]F. L. Carlsen, Jr., E. S. Bomar, and W. O. Harms, "Development of Fueled Graphite Containing Pyrolytic-Carbon Coated Carbide Particles for Nonpurged, Gas-Cooled Reactor Systems," to be published in *Nuclear Science and Engineering*.

average deposition rates for these coatings ranged from 2.5 to 164 μ/hr. So that the average deposition rate measured for each run would be a meaningful number rather than an average of a wide range of values, the thickness of coating deposited in each run was limited to approximately 50 μ. Thus, during coating of the 150- to 250-μ-diam uranium carbide particles used, the surface area on which carbon was being deposited increased by an average factor of approximately 2 rather than the usual factor of 4 for 100-μ-thick coatings. Even this doubling of charge surface area (and thus presumably halving of deposition rate) hampers the accurate detection of effects of changes in deposition rate. However, we needed to compromise constancy of deposition rate to this extent to obtain sufficient coating material for accurate analysis. To maintain a constant deposition rate, one might vary the rate at which hydrocarbon gas is supplied to the coating chamber continuously or step-wise to compensate for the changing surface area. Programming the hydrocarbon gas supply would have practical advantages in production-scale coating where time economy is an important consideration.

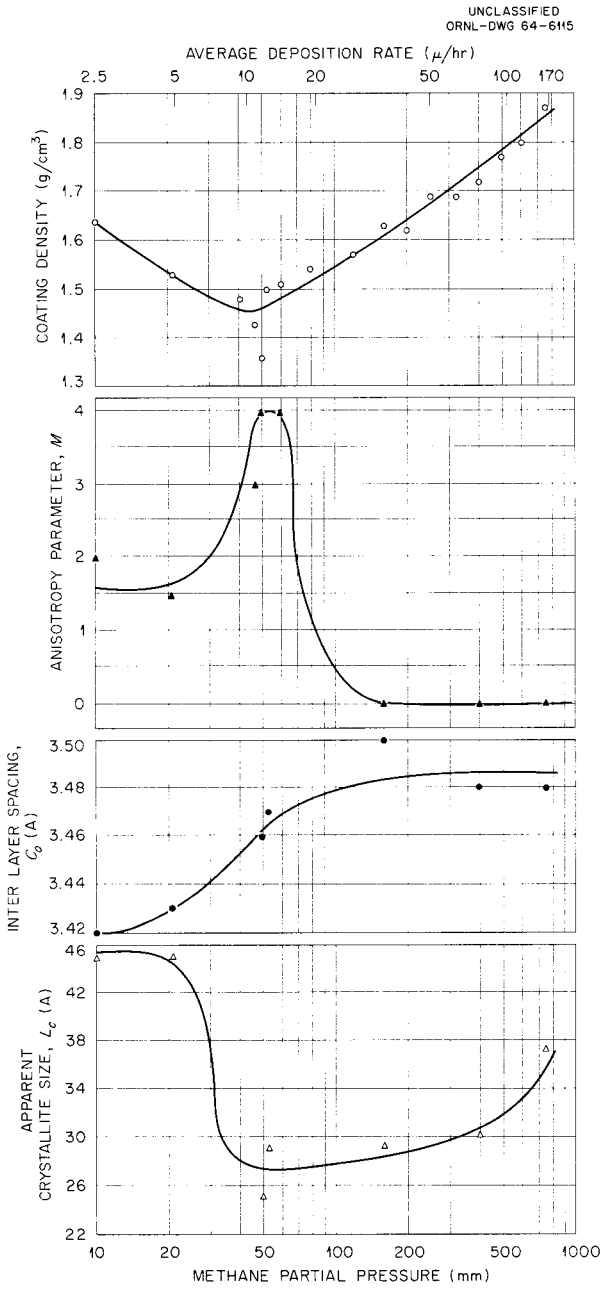

Fig. 25.7. Effect of Methane Partial Pressure on Properties of 50-μ-Thick Pyrolytic Carbon Coatings Deposited on Spheroidal Uranium Carbide Particles in a Fluidized Bed at 1400°C and 1 atm Total Pressure. Average deposition rates represented range from 2.5 to 164 μ/hr.

All coatings prepared in this series were deposited on reference 10-g lots of uranium carbide in a $\frac{3}{4}$-in.-ID graphite tube with a 30°-included-angle cone at the bottom. In each run five graphite disks $\frac{3}{16}$-in. diam × $\frac{3}{64}$-in. thick were also included to obtain deposits representative of the particle coatings for other studies described in the next section. The coating chamber was positioned near the center of the furnace hot zone for temperature uniformity of the fluidized bed. Temperature was monitored by a thermocouple located outside the coating chamber and previously calibrated against another thermocouple immersed in the fluidized bed.

Thoria particles prepared by the ORNL sol-gel process[19] were coated with single layers deposited at 1400°C and with duplex coatings comprising an inner layer applied at 1400°C and an outer layer at 1800°C. In no case did the core react with the coating as a result of the coating operation.

Evaluation of Coated Particles

E. S. Bomar F. L. Carlsen, Jr.
J. L. Cook J. O. Stiegler

During this period, we evaluated 41 lots of pyrolytic-carbon-coated fuel particles from five

[19] O. C. Dean *et al.*, "The Sol-Gel Process for Preparation of Thoria Base Fuels," p. 519 in *Proceedings of the Thorium Fuel Cycle Symposiums, Gatlinburg, Tennessee, December 5–7, 1962*, TID-7650, Book II (July 1963).

commercial suppliers and 32 lots of fuel particles coated in our laboratory. Visual appearance, fuel content, particle and coating dimensions, crushing load, total coated-particle and coating density, surface contamination, and exposed fuel content were reported. Additional evaluation procedures were developed and used to better characterize the pyrolytic carbon coating and the coated particles.

Densities of pyrolytic carbon coatings were measured with the helium pycnometer by an established procedure.[20] Density values from 1.36 to 2.08 g/cm^3 were observed for coatings prepared at 1400°C and values up to 2.18 g/cm^3 were observed on coatings deposited at 2100°C.

Some coatings that were deposited at 1400°C in the range of methane partial pressures shown in Fig. 25.7 were examined for interlayer spacing, c_0; apparent crystallite size, L_c; and degree of preferred orientation. Values of c_0 and L_c were determined with refined diffractometer methods, and we used the technique described by Bacon[21] to evaluate the preferred orientation of coatings stripped from disks. Six of these samples, representing the range of densities and methane partial pressures, were examined to determine the function $I(\Phi)$, the relative number of (00·2) poles per unit solid angle that make an angle Φ with the normal to the substrate. The symmetry around the normal to the substrate allows the data to be presented as a single distribution curve, $I(\Phi)$ vs Φ. Such a curve generally can be fitted to the equation[22]

$$I(\Phi)/I_{max} = \cos^M \Phi .$$

Bacon's anisotropy factor is $\sigma_{oz}/\sigma_{ox} = M + 1$. The variation of M with the methane partial pressure during deposition is shown in Fig. 25.7 along with the variations observed for the crystallite size L_c and the interlayer spacing c_0.

Electron microscopy and x-ray diffraction techniques were used to characterize structural features of various pyrolytic carbons in the as-deposited state and after annealing.[23,24] We established that the as-deposited materials consist of turbostratically stacked monolayers having the hexagonal graphite structure. In low-density deposits, transmission techniques revealed microvoids of of about 100 A in diameter. The density of the microvoids increased as the density decreased, but the crystallite size did not change significantly. Annealing of massive deposits caused lateral growth of the crystallites, which generally sharpened the diffraction patterns but did not change the microstructure. After 3 hr at 2650°C, the massive material was composed of graphite crystallites a few tenths of a micron in diameter and about 100 A thick; microvoids were no longer present.

Using microradiography, we have measured particle dimensions, studied fuel migration qualitatively and quantitatively, evaluated the effectiveness of chlorine and acid leaching, and analyzed shapes of core particles.[25–28] We examined 16 lots of fuel particles; those with unusual shapes were compared with previously prepared standards. The total percentage of unusual shaped particles ranged from 0.74 to 13.3%. We do not know if all of these unusual shapes would perform badly during irradiation, but certain shapes such as doublets and angular particles sometimes crack radially.

A technique was developed for studying the nature of crack propagation in pyrolytic-carbon coatings.[18] We had observed that cracks that initiate at the coating-particle interface of irradiated particles seem to stop at the interface between the laminar and columnar layers of certain duplex particles.[29] Examining 12 lots of multiple-layer coatings, we observed that the coatings with

---

[20] E. S. Bomar, R. L. Beatty, and J. L. Cook, *GCR Program Semiann. Progr. Rept. Mar. 31, 1963*, ORNL-3523, pp. 103–6.

[21] G. E. Bacon, *J. Appl. Chem.* **6**, 477–81 (1956).

[22] O. J. Guntart and C. A. Klein, *Appl. Phys. Letters* 2(7), 125–27 (1963).

[23] J. O. Stiegler, C. K. H. DuBose, and J. L. Cook, *An Electron Optical Study of Structural Features of Pyrolytic Carbons*, ORNL-TM-863 (in press).

[24] J. O. Stiegler, C. K. H. DuBose, and J. L. Cook, *Effects of Heat Treatment on the Structure of Pyrolytic-Carbon Coatings on Uranium Carbide Particles*, ORNL-TM-876 (classified) (in press).

[25] E. S. Bomar *et al.*, *GCR Program Semiann. Progr. Rept. Sept. 30, 1962*, ORNL-3372, pp. 183–85.

[26] E. S. Bomar *et al.*, *GCR Program Semiann. Progr. Rept. Mar. 31, 1963*, ORNL-3445, pp. 111–14.

[27] J. L. Cook and R. L. Hamner, *The Removal of Uranium and Thorium from Fueled-Graphite Materials by Chlorination*, ORNL-3586 (April 1964).

[28] E. S. Bomar, R. L. Beatty, and J. L. Cook, *GCR Program Semiann. Progr. Rept. Mar. 31, 1964*, ORNL-3619, pp. 61–73.

[29] W. O. Harms, "Coated-Particle Fuel Development at Oak Ridge National Laboratory," pp. 71–79 in *Ceramic Matrix Fuels Containing Coated Particles, Proceedings of a Symposium Held at Battelle Memorial Institute, November 5 and 6, 1962*, TID-7654 (1963).

the most pronounced physical discontinuities performed well under irradiation.

Analysis of Strain in Pyrolytic-Carbon Coatings[30]

J. W. Prados[31] J. L. Scott

To assist in the planning and interpretation of tests on pyrolytic-carbon-coated nuclear-fuel particles, a technique was developed for calculating profiles of the tangential stress and strain components in spherical pyrolytic carbon shells under simulated reactor operating conditions. The method is based on a mathematical analysis of stress and strain in a spherically symmetric anisotropic medium with hexagonal crystal symmetry, in which the crystallographic c axes coincide with the axes of geometrical symmetry. Stress-inducing factors considered are (1) thermal expansion, resulting from differences between coating deposition temperature and operating temperature; (2) swelling of the core particle as fuel atoms are converted to fission products; (3) release of gaseous fission products from the fuel particle, leading to buildup of pressure between the particle and the coating; and (4) dimensional changes in the pyrolytic carbon coating itself, caused by fast-neutron or fission-fragment damage.

A digital computer program was developed for calculating and plotting profiles of the tangential stress and strain associated with these factors, acting singly or in combination, in a particle coating. Lack of property data and failure criteria for pyrolytic-carbon coatings preclude absolute calculation of failure conditions at present. However, we believe relative comparisons of calculated behavior are meaningful and should be of considerable assistance in the selection of optimum coated-particle design parameters and test conditions.

As an illustration of our results, Fig. 25.8 shows the thermal strain calculated for a 100-μ pyrolytic-carbon coating applied to a 200-μ-diam UC_2 fuel particle with no initial gap between particle and coating. The abcissa represents fractional distance measured from the inner coating surface, the ordinate represents fractional strain, and the curve parameters are differences between the actual temperature of the coating during operation (assumed uniform) and the temperature at which the coating had been deposited. Note that in these calculated strain profiles we assumed that the coating was anisotropic, so they differ significantly from profiles that would obtain if isotropic coating material were assumed.

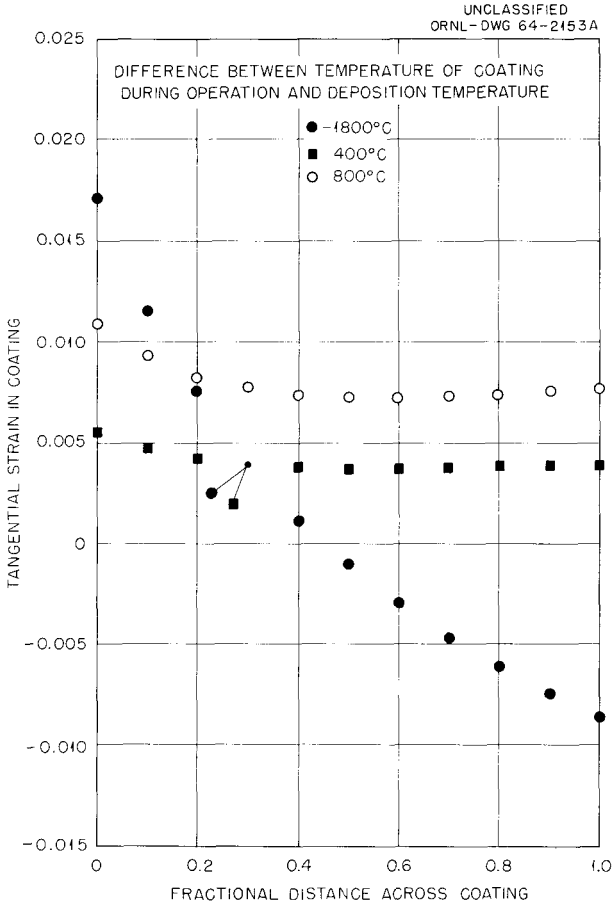

Fig. 25.8. Tangential Thermal Strain Profile in a 100-μ Pyrolytic Carbon Coating with No Initial Gap.

Microradiography of Coated Particles

R. W. McClung

Samples from more than 1350 batches of coated particles were microradiographed for nondestructive

[30] J. W. Prados and J. L. Scott, *Analysis of Stress and Strain in Spherical Shells of Pyrolytic Carbon*, ORNL-3553 (June 1964).

[31] Consultant from the University of Tennessee.

evaluation. The samples included not only as-deposited coated particles but also selected groups that had undergone heat treatment or in-pile testing.[32]

A new calibration scheme was developed to provide positive assurance of the accuracy of dimensional measurements made on coated particles.[32,33] Short lengths of 0.002-in.-diam tungsten wires were coated with pyrolytic carbon to a total diameter of about 10 mils. One of these was placed in a small cylindrical container and microradiographed with standard coated particles. Measured optically, the diameters of both the standard and its radiographic image were 248 μ, assuring that no bias was introduced into the measurements.

Metallography of $(Th,U)C_2$ and ThC_2 Particles

T. M. Kegley, Jr. B. C. Leslie

Special techniques are required in the metallographic preparation of thorium-containing carbides because of the strong tendency of these carbides to hydrolyze. For instance, vibratorily polished specimens must be prepared in a controlled atmosphere of low humidity. Figure 25.9 shows two coated $(Th,U)C_2$ particles of 0.6 thorium-to-uranium ratio from the same batch; one particle was prepared with the vibratory polisher in the room atmosphere and the other in a dry box. The former reacted while the latter did not.

We developed procedures for both vibratory and mechanical polishing of the thorium-containing carbide specimens.[34–36] The choice of methods depends on the time available, the quality of polish desired, and the number of specimens to be processed. Vibratory polishing requires more time than mechanical, but it produces a better quality of polish, with fewer scratches and less surface relief. Mechanical polishing is more expedient since it is quicker and needs no dry box.

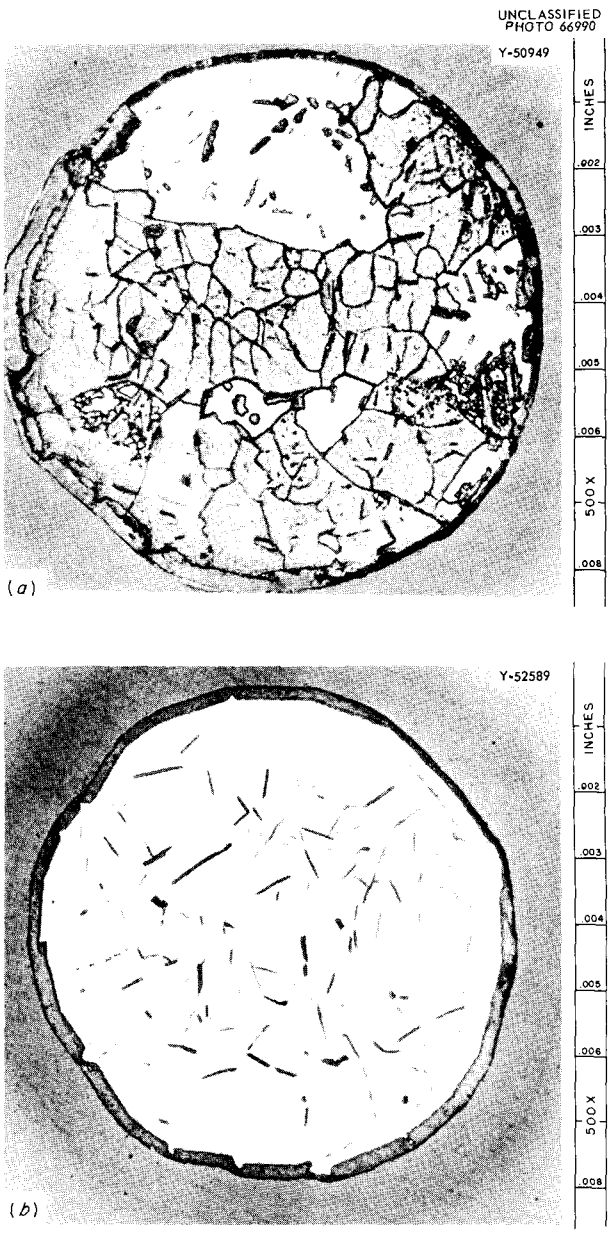

Fig. 25.9. Effect of Atmospheric Environment on Vibratory Polishing of $(Th,U)C_2$ Particles of 0.6 Thorium-to-Uranium Ratio. As polished. (a) Particle with reaction, polished in room atmosphere. (b) Particle without reaction, polished in dry box. Reduced 32%.

[32] R. W. McClung, *GCR Program Semiann. Progr. Rept. Mar. 31, 1964*, ORNL-3619, pp. 73–74.

[33] R. W. McClung, *GCR Program Semiann. Progr. Rept. Sept. 30, 1963*, ORNL-3523, p. 112.

[34] T. M. Kegley, Jr., and B. C. Leslie, "Metallographic Preparation of Dicarbides of Thorium and Thorium-Uranium," technical note submitted to *Journal of Nuclear Materials*.

[35] E. S. Bomar *et al.*, "Thorium-Uranium Carbides for Coated-Particle, Graphite Fuels," paper to be presented at AIME Symposium on Compounds of Interest in Nuclear Technology, Boulder, Colo., Aug. 3–5, 1964.

[36] T. M. Kegley, Jr., and B. C. Leslie, "Metallographic Preparation of Dicarbides of Thorium and Thorium-Uranium," paper to be presented at the 18th AEC Metallography Group Meeting, Atomics International, Canoga Park, Calif., June 22–24, 1964, proceedings will be published.

Our procedures for preparing thorium-containing carbide specimens are somewhat different from those used elsewhere; the principal distinction is that we use nitric acid for passivating and etching pyrolytic-carbon-coated $(Th,U)C_2$ particles instead of the customary air etching employed by other investigators.[37–39] We etched coated particles of $(Th,U)C_2$ and ThC_2 by immersion in equal parts of water and concentrated nitric acid. A short period of immersion in this solution passivates the polished surface and retards subsequent reaction with moisture. Longer periods of immersion also etch by the development of interference colors in the passive film formed on the polished surface.

Figure 25.10 compares air-etched and nitric-acid-etched microstructures for $(Th,U)C_2$ particles of 2.2 thorium-to-uranium ratio from the same batch. The microstructure of the nitric-acid-etched particle is considerably clearer and more definitive than the microstructure of the air-etched particle.

Figure 25.11 shows a pyrolytic-carbon-coated ThC_2 particle that had been passivated by immersion in the nitric acid solution. The particle has a bright metallic appearance similar to that of a specimen in the as-polished condition. Observation

[37]H. A. Wilhelm and P. Chiotti, *Trans. Am. Soc. Metals* 42, 1295–1310 (1950).

[38]N. Brett, D. Law, and D. T. Livey, *J. Inorg. Nucl. Chem.* 13, 44–53 (1960).

[39]G. B. Engle, *Metallography of Carbide Fuel Compounds*, GA-2067 (1961).

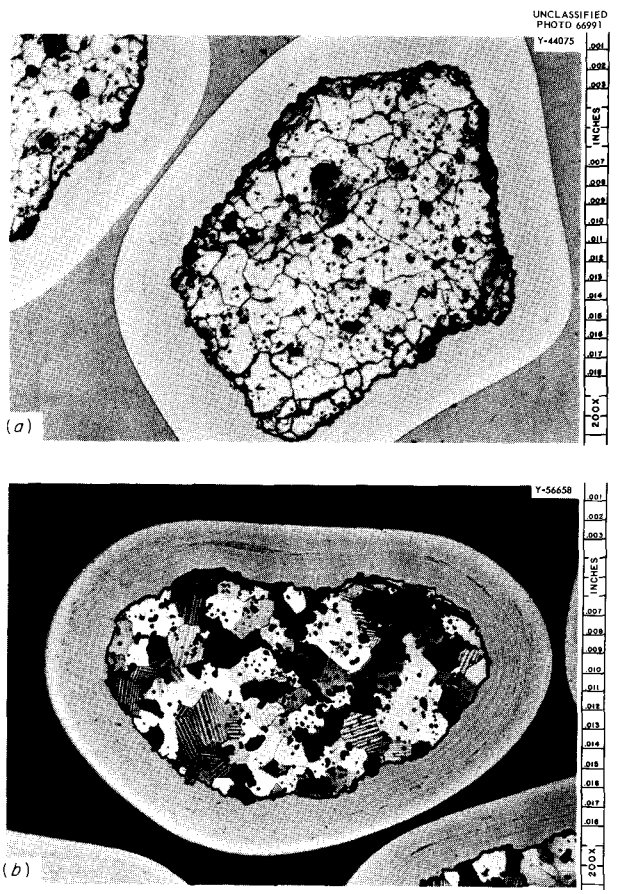

Fig. 25.10. Pyrolytic-Carbon-Coated $(Th,U)C_2$ Particles of 2.2 Ratio from the Same Batch. 200×. (a) Air etched. (b) Etched by immersion in "1:1 HNO_3-H_2O" for 15 min. Reduced 51%.

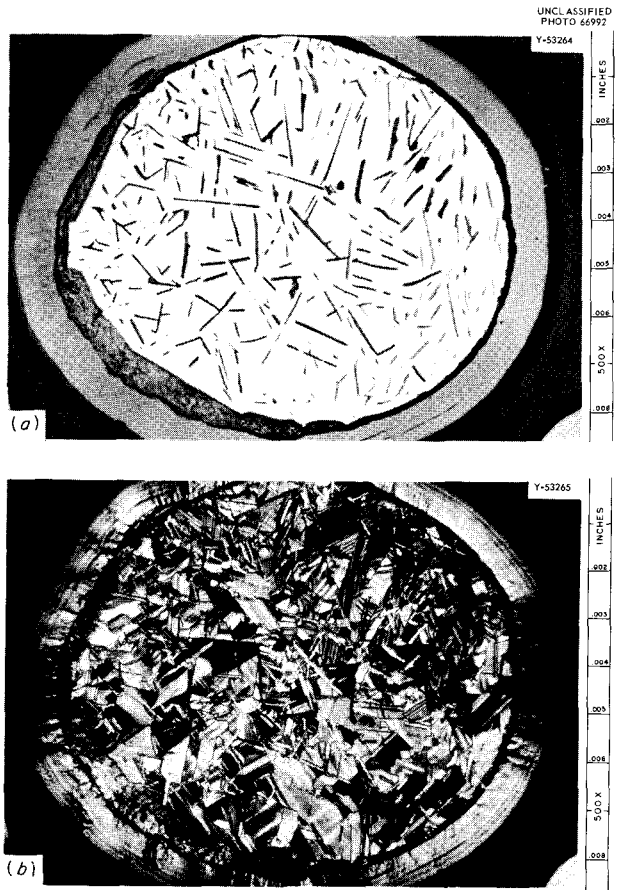

Fig. 25.11. Pyrolytic-Carbon-Coated ThC_2 Particle with Excess Graphite, Passivated by Immersion in "1:1 HNO_3-H_2O" for 1 min. (a) Bright field. (b) Polarized light. Reduced 51%.

with polarized light reveals the complex twinned structure of the ThC_2 particle.

Poison Particles

R. L. Hamner R. L. Beatty
R. E. Meadows

We studied the preparation and thermal behavior of rare-earth poison particles intended for use in fueled-graphite, pebble-bed reactors. Our studies included the compatibility of oxide-carbon mixtures, the thermal stability of pyrolytic-carbon-coated oxide particles, and the preparation of spheroidal carbide particles.

In thermogravimetric studies at a pressure of 10^{-6} torr, intimately mixed powders of Eu_2O_3 and carbon began to react at approximately 1100°C. The data were interpreted in terms of the following reactions above 1100°C:

$$Eu_2O_3(s) + 7C(s) \rightarrow 2\,Eu(l) + 4C(s) + 3CO(g)$$

$$2\,Eu(l) \rightarrow 2\,Eu(g)\,.$$

A rare-earth oxide mixture (45% Gd_2O_3, 45% Sm_2O_3, 10% other rare-earth oxides) also began to react with graphite at approximately 1100°C, but it reacted more slowly in the 1400 to 1500°C temperature range than did Eu_2O_3.

Dense irregular shaped Eu_2O_3 particles, −60 +100 mesh, were coated with 100 μ of pyrolytic carbon at 1400°C and heat treated. After either 1000 hr at 1100°C or 200 hr at 1400°C, both at a pressure of 10^{-5} torr, no significant change from the as-coated state was detected by metallography. After the 1400°C heat treatment, radiography revealed some migration from the Eu_2O_3 particles into the coating. Weight losses in short-term thermogravimetric experiments and metallographic examination showed that the Eu_2O_3 particles reacted appreciably with the pyrolytic carbon coating at higher temperatures (1700 to 1800°C).

Radiographic and metallographic examination of pyrolytic-carbon-coated spheroidal B_4C particles that had been heated for 2 hr at 2200°C in argon at 1 atm revealed essentially complete migration of the boron into the coating.

Attempts to form spheroidal EuC_2 particles by heating granules prepared from mixed Eu_2O_3 and graphite powders were not successful, because an intermediate molten phase formed at approximately 1700°C and exuded from the granules before the dicarbide could be formed at 2300°C. The most promising technique[40,41] for preparing rare-earth carbide particles was to arc melt the oxide-graphite mixtures to form a solid mass, granulate to a given particle size, embed these particles in graphite, and heat at approximately 2500°C.

Fueled Beryllium Oxide

A. T. Chapman R. L. Hamner
R. E. Meadows

We have investigated the feasibility of leaching fuel particles from the surface of BeO–30 vol % UO_2 specimens with acid. Also, we have used acid leaching to evaluate fabrication techniques designed to minimize fission-gas release through open pores and microflaws in the structure during irradiation. The specimens were of two microstructural types (1) conventionally prepared 93%-dense dispersions, representative of those irradiated in the group VI experiment in the ORR (see below), and (2) 94%-dense dispersions prepared[42] from particles coated with BeO. Treatment with 2 *M* HNO_3 at 98°C or 4 *M* HNO_3 at 105°C showed that fuel was leached not only from the surface but, given sufficient time, nearly completely from the matrix. Fuel was probably leached through open pores and microcracks, although the BeO matrix at high magnification appeared to have been damaged by the leaching process.[43]

The group VI irradiation test capsule[42] containing bushings of BeO–30 vol % UO_2 was withdrawn from the ORR poolside facility after 125 operating days at a fuel specimen temperature of approximately 1100°C and after a heavy-metal burnup of 1.6 at. %. Steady-state values of release rate to birth rate (R/B) were about 10^{-3} for ^{87}Kr, ^{135}Xe,

[40] R. L. Hamner *et al.*, *GCR Program Semiann. Progr. Rept. Sept. 30, 1963*, ORNL-3523, pp. 121–26.

[41] R. L. Hamner, R. L. Beatty, and R. E. Meadows, *GCR Program Semiann. Progr. Rept. Mar. 31, 1964*, ORNL-3619, pp. 79–80.

[42] A. T. Chapman, R. L. Hamner, and R. E. Meadows, *Metals and Ceramics Div. Ann. Progr. Rept. May 31, 1963*, ORNL-3470, pp. 78–79.

[43] A. T. Chapman, R. L. Hamner, and R. E. Meadows, *GCR Program Semiann. Progr. Rept. Sept. 30, 1963*, ORNL-3523, pp. 220–21.

^{88}Kr, and ^{85}Kr and 10^{-2} for ^{133}Xe; the values remained essentially constant throughout the experiment. The specimens swelled slightly during irradiation and exhibited both macro- and microcracking. In addition, grain growth was observed[44] in the fuel midway between the inner and outer surfaces.

Evaluation of Fueled-Graphite Bodies

F. L. Carlsen, Jr. E. S. Bomar
J. L. Cook R. E. Adams

The evaluation of graphite-matrix fuel elements[45] has continued with 76 lots during the present reporting period. These fuel elements were spherical, either 1.5 or 2.36 in. in diameter, and were of three basic types: molded without unfueled shells, molded with molded unfueled shells, and molded inserts within machined shells. In addition to the fueled spheres, we tested a large number of unfueled spheres machined from various grades of graphite.

Our aims were to characterize irradiation-test samples and to develop specifications for the fueled-graphite spheres to be used in the AVR (German Pebble-Bed Reactor). This program included nondestructive testing (see next subsection), determination of mechanical and thermal properties, thermal shock tests, and tests to determine the integrity of the contained coated fuel particles.

All spheres were measured, examined visually, and radiographed. The diameters of the molded 1.5-in.-diam spheres were generally 1.500 ± 0.030 in. whereas the machined spheres varied much less. A method was developed for rapidly measuring the sphere diameters by using a rotating fixture and an eddy-current coil to detect the relative position of a Teflon-tipped probe.[46] Radiography of intact spheres qualitatively indicated the fuel distribution. A method was developed[46] for quantitatively measuring fuel distribution by radiography of $\frac{1}{4}$-in.-thick disks machined from the fueled spheres.

The abrasion resistance of fueled and unfueled graphite spheres was determined in three types of tests: simple ball milling, cycling in a mockup of a fuel-handling apparatus, and in the core mockup for the Pebble-Bed Reactor Experiment. The molded spheres resisted abrasion less than the machined spheres. The resistance of the various lots of molded fueled spheres differed considerably since they were made by various fabrication procedures. The crushing strength, determined for many of the 1.5-in. spheres,[46,47] ranged from 775 to 3370 lb load at failure. Oxidation in steam at 900 to 1000°C seriously reduced the crushing strength when the weight loss was greater than 1%. For example, the strength of one lot was reduced from 1400 to 300 lb by an oxidation weight loss of 8.7%.

A graphite-resistor furnace was assembled for thermal-shock tests of fueled-graphite spheres to simulate the thermal stresses that will be generated during reactor operation. The apparatus permits dropping the spheres into the hot furnace, holding them for a period of time, and then quenching them in a graphite crucible at room temperature. The conditions necessary to crack the spheres were determined. Molded 1.5-in.-diam spheres cracked when dropped from temperatures of 2000°C or above. Some of the 6-cm-diam spheres cracked when dropped from 1950°C, but two machined-shell elements heated as high as 2150°C did not. Spheres were measured after thermal treatments to determine whether thermal effects were responsible for dimensional changes that have been observed[48] for irradiated spheres. A heat treatment at 1000°C for 1000 hr did not cause any measurable changes, but thermal shock treatments did, indicating that thermal gradients may have caused the changes observed in irradiated spheres.

The integrity of coated particles in spheres was determined by acid electrolysis and neutron activation.[46,47] The exposed uranium, as determined by acid electrolysis, on neutron-activated spheres correlated very well with the ^{133}Xe release observed during postirradiation annealing of the same spheres.

---

[44] J. G. Morgan, H. E. Robertson, and M. F. Osborne, *GCR Program Semiann. Progr. Rept. Sept. 30, 1963*, ORNL-3523, pp. 221–25.

[45] F. L. Carlsen, Jr., *Metals and Ceramics Div. Ann. Progr. Rept. May 31, 1963*, ORNL-3470, p. 140.

[46] E. S. Bomar *et al.*, *GCR Program Semiann. Progr. Rept. Sept. 30, 1963*, ORNL-3523, pp. 302–18.

[47] F. L. Carlsen, Jr., E. S. Bomar, and J. L. Cook, *GCR Program Semiann. Progr. Rept. Mar. 31, 1964*, ORNL-3619, pp. 203–5.

[48] M. F. Osborne *et al.*, *GCR Program Semiann. Progr. Rept. Sept. 30, 1963*, ORNL-3523, p. 359.

The ratio of fraction of ^{133}Xe released to fraction of uranium exposed ranged from 1.3×10^{-2} to 1.5×10^{-2}. The ratio values varied more when the measurements were made on two separate spheres. Crushing, impact testing, or thermal-shock testing did not increase the exposed uranium content except on impact-tested spheres that did not have unfueled shells.[47]

Thermal expansion coefficients were determined for a number of fueled-graphite samples.[47] The effect of coated particle contents (0 to 40%) was measurable only for hot-pressed samples in the direction parallel to the molding axis. Anisotropy factors of 2 to 3 were observed for hot-pressed and extruded cylinders. The ratio of the coefficient for the fuel insert to that for the ATJ shell material in spheres with machined shells is an important parameter for thermal stress considerations.[49] This ratio varied from 0.53 to 2.2 for hot-pressed cylinders and from 1.0 to 1.5 for specimens cut from spheres.

Nondestructive Testing of Fueled Graphite

C. V. Dodd R. W. McClung

A mechanism was designed and constructed to allow scanning of 6-cm-diam graphite spheres, such as are proposed for the AVR fuel elements. The device rotates the sphere simultaneously about the vertical and horizontal axes and has been used in development of both eddy-current and infrared nondestructive testing techniques.[50,51]

A new low-noise phase-sensitive eddy-current instrument[52] was fabricated for the determination of the integrity of the outer shell in the AVR-type fuel elements. Several new coils were designed and built for use with the new instrument. In addition, we started to apply the eddy-current instrument and scanning device to develop a system for identifying specific spheres or groups of spheres. Some of our eddy-current developments are given in Part II, Chap. 17, of this report.

Considerable effort has been expended toward the development of infrared techniques for the detection of nonbond between the fueled and unfueled sections of graphite spheres. In the most promising technique, shown in Fig. 25.12, a lens system focuses the infrared radiation from a spot on a hot graphite sphere onto a detector. Emissivity variations have caused loss in sensitivity.

Special radiographic techniques[50] using Lucite masks have been developed for high-quality inspection of the graphite from which shells are machined for fueled spheres.

[49] J. G. Merkle, *GCR Program Semiann. Progr. Rept. Sept. 30, 1963*, ORNL-3523, pp. 296–301.

[50] C. V. Dodd and R. W. McClung, *GCR Program Semiann. Progr. Rept. Sept. 30, 1963*, ORNL-3523, pp. 318–24.

[51] C. V. Dodd, *GCR Program Semiann. Progr. Rept. Mar. 31, 1964*, ORNL-3619, pp. 74–77.

[52] C. V. Dodd, *Metals and Ceramics Div. Ann. Progr. Rept. May 31, 1963*, ORNL-3470, p. 94.

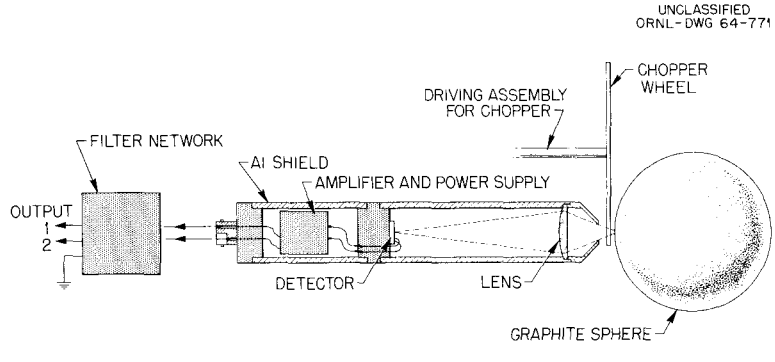

Fig. 25.12. Device Using Infrared Radiation to Detect Nonbond in Spherical Graphite Fuel Elements.

Removal of Uranium and Thorium from Fueled-Graphite Materials by Chlorination

J. L. Cook R. L. Hamner

A nondestructive process was developed for the removal of exposed uranium and thorium from fueled-graphite spheres for gas-cooled pebble-bed reactors.[53] Volatile chlorides were formed and removed by reacting exposed uranium and thorium at high temperature with a dynamic atmosphere of gaseous chlorine diluted with argon. Chlorination experiments were conducted at 800 to 1000°C with uncoated spherical UC_2 and $(U,Th)C_2$ particles, pyrolytic-carbon-coated fuel particles, and graphite matrices containing coated fuel particles. The results were evaluated by radiography, chemical analyses, x-ray diffraction analyses, and alpha assay.

Surface-exposed uranium without thorium was more readily removed by chlorine treatment than surface-exposed uranium-thorium combinations, but both could be removed by treating for 16 hr at 1000°C in a flow of 80 cm^3/min Cl_2 and 125 cm^3/min Ar. Internally exposed fuel was not effectively removed.

Assembly and Impact Testing of Fueled-Graphite Spheres[54]

C. O. Smith J. M. Robbins

More than 300 specimens of eight different designs, made from shells machined from ATJ graphite and simulated fuel inserts machined from CS-312 graphite, were assembled by methods previously reported.[55] In seven of the designs the shell thickness was 0.80 cm while in the eighth it was 1.00 cm. In addition to differences in design, we considered the effects of several fabrication variables. These included the magnitude of the clearance (in most cases ultimately filled with cement) between insert and shell, closure torque, type of cement, need for ultrasonic cleaning, whether the insert was loose (with only threads cemented) or completely cemented, and submission to thermal cycling in vacuum.

The tentative AVR specifications require that finished fuel elements be capable of surviving 50 drops from a height of 4 m onto a 3-deep bed of close-packed 6-cm-diam graphite spheres. The testing procedure used was dropping simulated elements on the bed of graphite spheres until failure or 75 drops, whichever occurred first, then dropping unfailed elements from 4 m onto a steel plate.

Neither a variation in closure torque between 15 and 50 in.-lb nor ultrasonic cleaning of the shell and insert before assembly appeared to affect the impact resistance. An element with a loose insert had a shorter impact life than an element with a completely cemented insert. Elements assembled with three different cements apparently had the same impact life.

Impact life of simulated fuel elements is sensitive to the nominal clearance between shell and insert. All specimens with 0.80-cm-thick shells, 0.005-in. clearance, and threaded closures met the impact requirement. Some with 0.025-in. clearance and none of those with 0.040-in. clearance did. Elements with 1.00-cm-thick shells were superior to those with 0.80-cm-thick shells; all those tested having 0.005-in. and 0.025-in. radial clearances met the requirement and only one element out of ten having 0.040-in. clearance did not.

Thermal cycling ten times in vacuum between room temperature and 1000°C did not change the impact resistance of elements with 0.025-in. clearance and either 0.080- or 1.00-cm-thick shells.

Impact Testing of Graphite Spheres[54]

C. O. Smith

Free-drop, drop-weight, and crushing tests were performed on eight grades of graphite: extruded TSX, AGOT, CS-312, and HLM-85; and molded C-18, 9050, 3499-S, and ATJ. Of these graphites the ATJ grade was the best, and further detailed investigation was performed with this material.[56]

---

[53] J. L. Cook and R. L. Hamner, *The Removal of Uranium and Thorium from Fueled-Graphite Materials by Chlorination*, ORNL-3586 (April 1964).

[54] C. O. Smith and J. M. Robbins, *GCR Program Semiann. Progr. Rept. Mar. 31, 1964*, ORNL-3619, pp. 210–17.

[55] J. M. Robbins and R. L. Hamner, *GCR Program Semiann. Progr. Rept. Sept. 30, 1963*, ORNL-3523, pp. 324–25.

[56] E. S. Bomar *et al.*, *GCR Program Semiann. Progr. Rept., Sept. 30, 1963*, ORNL-3523, pp. 310–15.

Resistance to impact and crushing varied considerably from one sphere to another and from one block of ATJ graphite to another. There was no discernible pattern of variation in results as a function of position in the block and no correlation between the density of an individual sphere and its resistance to impact or crushing.[56]

As might be expected, the number of drops for failure in both the free-drop and drop-weight tests decreased as drop height increased. In the extreme test,[56] nine 6-cm-diam ATJ graphite spheres failed on three to ten drops (average 6.8) from 90 ft.

In all three types of tests with 1-in.-, 1.5-in.-, 6-cm- (2.36-in.-), and 3.5-in.-diam spheres, the resistance decreased with increase in sphere size.[54]

Thermal cycling between room temperature and 1000°C has been postulated to increase the size and number of microcracks and thus decrease the impact resistance. Thermal cycling of ATJ graphite spheres in helium appeared not to affect impact and crushing resistance, but thermal cycling in vacuum decreased the impact and crushing resistance of some lots of spheres.

A number of 6-cm-diam spheres that failed in the free-drop and drop-weight tests were machined to 1.5-in.-diam spheres (concentric with the original sphere) and crushed. The fact that the crushing loads were the same as those of spheres taken from virgin graphite indicated that all damage leading to failure occurred in an outer region not more than $\frac{7}{16}$ in. thick.

Fueled-Graphite Irradiation Tests

J. L. Scott C. Michelson[57]
R. A. Bowman

We are continuing a program[58] for testing fueled-graphite elements. This program has involved the preparation of 21 irradiation capsules and tests, requiring 94 spherical fueled-graphite elements containing pyrolytic-carbon-coated particles of $(U,Th)C_2$ or UC_2. The major areas being investigated are (1) irradiation stability and fission-product retention of fueled-graphite spheres, (2) design and fabrication of shells for fuel elements, (3) irradiation stability of fuel-element materials and dimensions, (4) thermal conductivity of fuel-element materials and irradiation-induced changes in it, and (5) effects of irradiation on the impact and crushing strength of fuel elements fabricated by different processes. Our responsibility is to help in planning the capsule irradiation tests and to load fuel elements into the primary containment prior to irradiation. Capsules that have been loaded during this report period are described below.

First, 1.5-in.-diam spheres were tested in four-ball and eight-ball capsules and in the ORR gas-cooled loop No. 2. The four-ball capsules contained two fueled-graphite spheres in a static (sealed) compartment and two in a sweep compartment that was purged with helium. This feature permitted the sampling of fission gases for analysis during irradiation. This type capsule was positioned in the ORR pool next to the reactor pressure vessel and was cooled by the pool water. Each eight-ball capsule contained eight spheres in a sealed container with no provision for fission-gas analysis. This type capsule was placed in the F-1 position of the ORR core, and its heat was removed by the core cooling water. The assembly for testing 1.5-in.-diam spheres in ORR loop No. 2 held four spheres. It was positioned in a large ORR beam hole and cooled by a continuous flow of helium over the spheres.

Later, we tested 2.36-in.-diam spheres in AVR capsules and in the ORR loop No. 2. The AVR capsules contained two spheres in a static compartment and one in a sweep compartment. The capsule was positioned in the ORR pool at locations formerly occupied by the four-ball capsules. The ORR loop No. 2 assembly for testing 2.36-in.-diam spheres holds three spheres and is positioned in the location formerly occupied by the assembly for testing 1.5-in.-diam spheres.

The 1.5-in.-diam elements were of interest during the development of an ORNL pebble-bed reactor. The larger elements are of interest for use in the AVR. The AVR fuel elements were designed for operation at a maximum surface temperature of 900°C and a maximum power output of 2.1 kw per sphere. We are still testing the smaller spheres because the eight-ball irradiation facility cannot be modified to accommodate the larger spheres and because these subscale prototype tests in a high fast flux region yield much useful information.

[57] On loan from the Tennessee Valley Authority.

[58] F. L. Carlsen, Jr., *Metals and Ceramics Div. Ann. Progr. Rept. May 31, 1963*, ORNL-3470, p. 141.

The design and assembly of each capsule, including a detailed description of the fuel elements and their coated particles, have been reported[59,60] along with the results of test operation and post-irradiation examination. Fabrication of test elements is also reported briefly in the following subsection. A final evaluation of some of the test results is in progress.

Fabrication of Capsules for Fueled-Graphite Irradiation Tests

E. A. Franco-Ferreira

We are concerned with the design and irradiation testing of various advanced fuel elements.[59] The irradiation testing is normally carried out on single capsules in the ORR as described in the previous subsection. Our primary responsibility is the fabrication of these highly complex irradiation capsules.

This year's work has included 2 ORR poolside capsules, 6 ORR loop No. 1 elements, and 16 coated-particle capsules, as well as the gas-shroud assemblies for all the loop elements. Typical of the complex designs encountered is the eight-ball capsule shown in Fig. 25.13. Thermocouples are provided in each capsule for monitoring the central temperature of the top sphere and the graphite container temperature adjacent to each sphere. Six temperature-instrumented tubes were placed in a head space between the graphite tube assembly and the top cap of the capsule to facilitate fission-product deposition studies.

[59]J. L. Scott, C. Michelson, and E. A. Franco-Ferreira, *GCR Program Semiann. Progr. Rept. Sept. 30, 1963*, ORNL-3523, pp. 326–41.

[60]J. L. Scott and C. Michelson, *GCR Program Semiann. Progr. Rept. Mar. 31, 1964*, ORNL-3619, pp. 217–28.

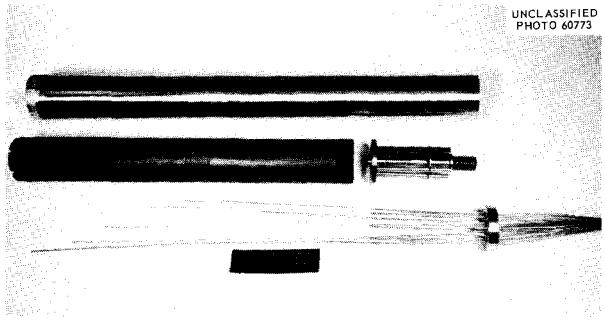

Fig. 25.13. An Eight-Ball Irradiation Capsule Showing Thermocouples, Graphite Column, Fission-Product Deposition Specimens, and Containment Capsule.

Graphite Fabrication

A. J. Taylor

We have essentially completed basic investigations on the fabrication of graphite spheres. The furan resins were abandoned as binders in favor of a liquid phenolic resin. This resin not only was better suited to the fabrication techniques being developed but it also gave a much stronger body at the same baked density. We are studying the expansion characteristics of the bodies containing phenolic resin when cold molded in a spherical cavity die. With understanding of these characteristics we can design a die to form a shape that will, after the remaining fabrication steps, provide a high-quality molded fuel sphere of well-controlled dimensions.

SUPPORTING RESEARCH

The Thorium Dicarbide–Uranium Dicarbide System

N. A. Hill[61] O. B. Cavin

Thorium dicarbide was found by differential thermal analysis and high-temperature x-ray diffraction to transform at 1415 ± 10°C from a low-temperature monoclinic structure to a face-centered cubic structure with a_0 = 5.808 ± 0.003 A at 1500°C.[62] The high-temperature structure could not be retained by quenching.

We identified the phases in a range of arc-melted alloys of uranium dicarbide and thorium dicarbide and found their areas of stability.[63] We used the

[61]On loan from AERE, Harwell, England.

[62]N. A. Hill and O. B. Cavin, *Monoclinic-Cubic Transformation in Thorium Dicarbide*, ORNL-3588 (April 1964).

[63]N. A. Hill and O. B. Cavin, *Phase Equilibrium Studies in the System UC_2-ThC_2*, ORNL-3668 (in press).

results of high-temperature x-ray diffraction, differential thermal analysis, isothermal annealing, and the examination of structures at room temperature by metallography and by x-ray powder patterns. Figure 25.14 is a tentative equilibrium diagram section for these alloys in the presence of excess graphite.

At high temperatures, a single face-centered cubic phase was found at all compositions with a lattice parameter (at 1500°C) that varied linearly with composition (Fig. 25.15) from 5.81 at ThC_2 to 5.51 at UC_2–14% ThC_2 alloy. On cooling to a temperature that depended on composition (1820°C for UC_2, 1420°C for ThC_2, and 1110°C for an equimolar mixture), the cubic phase transformed to a low-temperature structure. From UC_2 to alloys containing 30% ThC_2, this structure was a solid solution having the UC_2 structure; from approximately 30 to 38% ThC_2, a two-phase region was found comprising the UC_2 solid solution and a second phase, which could be indexed most simply as body-centered tetragonal. At 80 to 100% ThC_2, the low-temperature phase had a structure closely related to that of monoclinic ThC_2 and could be considered a solid solution. The x-ray powder data showed no two-phase region between this solid solution and the body-centered tetragonal

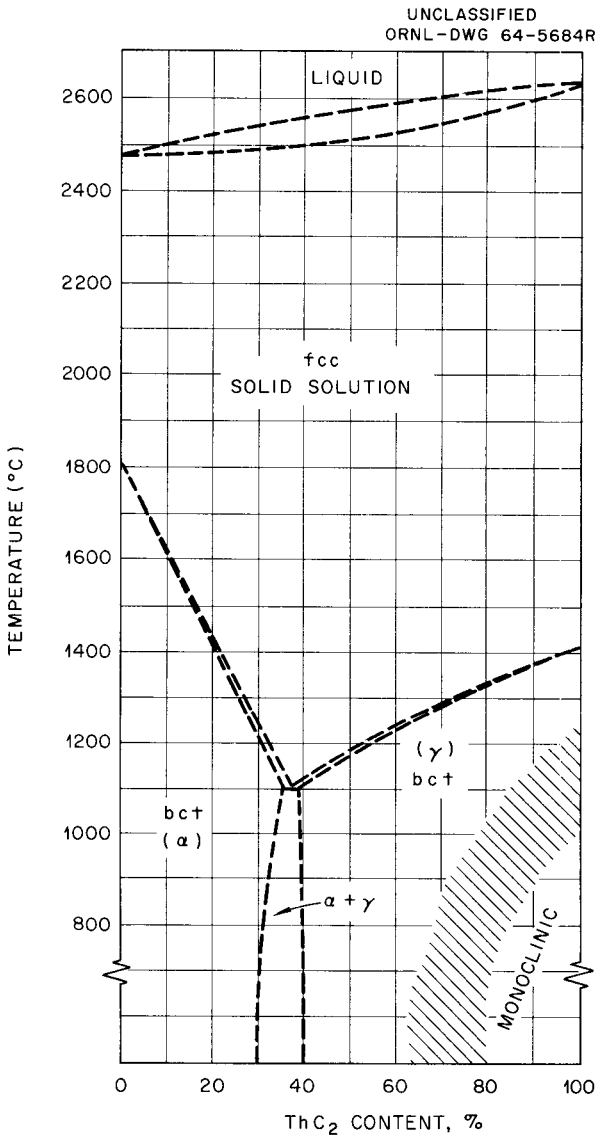

Fig. 25.14. Tentative Equilibrium Phase Diagram for the UC_2-ThC_2 System in the Presence of Excess Carbon.

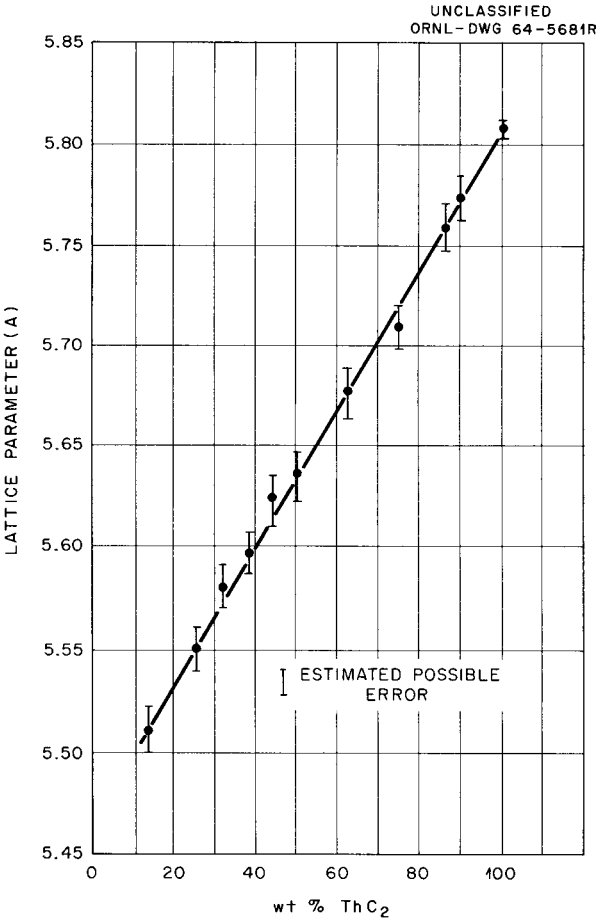

Fig. 25.15. Lattice Parameters of the Face-Centered-Cubic Phase in UC_2-ThC_2 Alloys at 1500°C as a Function of Composition.

phase at 40 to 70% ThC_2. The composition range over which the solid solution structure changes to the higher symmetry structure is indicated by the cross-hatched area in Fig. 25.14.

Welding of Advanced Alloys

R. G. Gilliland

We are investigating the weldability of two new nickel-chromium alloys strengthened with molybdenum, niobium, and tungsten. These alloys were developed by International Nickel Company and are designated IN-102 and A-625-M. The chemical analyses of these alloys are listed below:

Element	Analysis (wt %)	
	IN-102, Heat No. 015502	A-625-M, Heat No. NX-8473
Chromium	15.50	20.70
Niobium	3.19	3.02
Molybdenum	2.61	8.32
Tungsten	4.04	4.07
Iron	7.96	2.38
Carbon	0.05	0.03
Nickel	bal	bal

These alloys possess high-temperature properties that make them attractive for use in gas-cooled reactors.

Welds were made under conditions of high restraint using the shielded metal-arc welding process. After side-bend and metallographic tests showed that high-quality welds had been deposited, we tested room- and elevated-temperature mechanical properties. The tensile properties of welds in these materials are listed in Table 25.5 and the 1200 and 1500°F creep test results are presented in Fig. 25.16. The tensile data indicate no significant difference in the two alloys, although the yield strength of alloy No. A-625-M is higher at both testing temperatures. Interestingly, the total strain of alloy A-625-M is consistently lower than that of IN-102, yet no difference is visible in rupture life. These data indicate a very flat stress-rupture curve at 1200°F, which converges with the curve for wrought metal after 1000 hr; at 1500°F the curves actually cross.

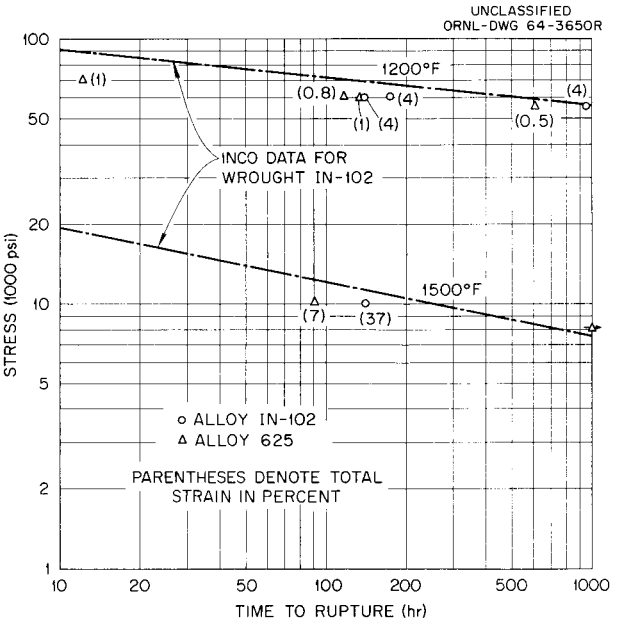

Fig. 25.16. Creep Results on Transverse Weld Specimens of INCO Alloys IN-102 and A-625-M Tested in Air at 1200 and 1500°F.

Current hot-ductility experiments will conclude this study.

In-Reactor Stress Rupture of UK Stainless Steel[64]

J. T. Venard

Interest is widespread in the effect of neutron bombardment on the mechanical properties of the austenitic stainless steels because of the frequent application of these steels in reactor structures and fuel claddings. For this reason, a niobium-stabilized 20% Cr–25% Ni austenitic stainless steel developed in the United Kingdom for gas-cooled reactor service has been tested in-reactor for its stress-rupture characteristics as part of the AGR/EGCR Information Exchange Program.

[64] J. T. Venard and J. R. Weir, "In-Reactor Stress-Rupture Properties of Niobium-Stabilized Steel," paper presented at the 67th Annual Meeting of the American Society for Testing Materials, Chicago, Ill., June 21–26, 1964; also ORNL-TM-881 (in press).

Table 25.5. Room- and Elevated-Temperature Tensile Properties of Transverse Welds in High-Strength Nickel-Base Alloys[a]

Alloy	Test Temperature (°F)	Tensile Strength (psi)	Yield Strength (psi)	Elongation (%)	Reduction in Area (%)
IN-102	Room	115,000	68,700	31.5	35.7
A-625-M	Room	116,400	74,300	34.1	40.1
IN-102	1200	87,300	51,000	21.0	29.7
A-625-M	1200	85,100	55,100	22.6	27.6

[a]Four samples were tested at each condition.

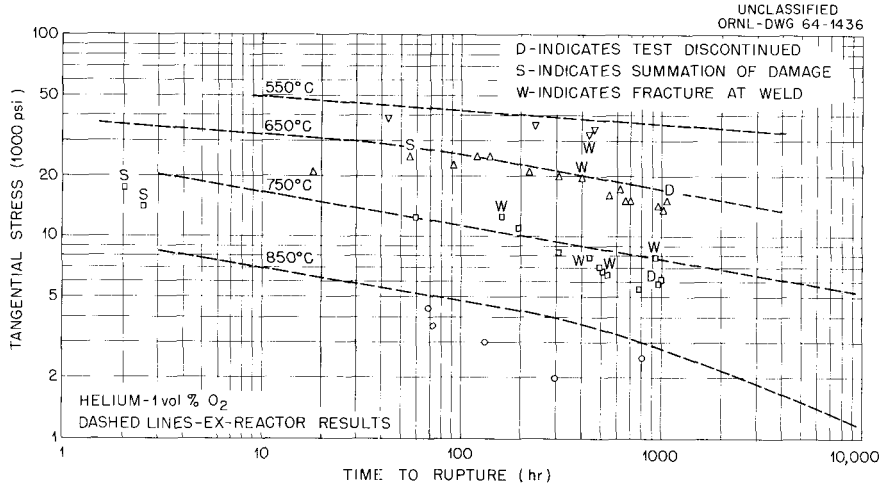

Fig. 25.17. In-Reactor Stress Rupture of 20 Cr–25 Ni, Niobium-Stabilized Stainless Steel Tubing.

The tests were performed by internally pressurizing tubes at temperatures of 550, 650, 750, and 850°C in a neutron flux of approximately 5.0×10^{12} ($E > 2.9$ Mev) and 6.0×10^{13} neutrons/cm^2 thermal. Duplicate tests were performed out-of-reactor.

The results of these experiments did not reveal the mechanism of neutron damage, but the following observations and conclusions can be made:

1. At 650, 750, and 850°C the out-of-reactor stress-rupture behavior was the same in flowing Ar–1 vol % O_2 as in CO_2–5 vol % CO.
2. Within the scatter of individual data points, we found little if any effect of irradiation on the stress to produce rupture in a given time (Fig. 25.17).
3. Within the limits of the experiments, irradiation seemed to have no effect on the average dependence of strain rate on applied stress (Fig. 25.18).
4. As seen in Fig. 25.19, this material exhibited a definite minimum in strain at fracture at 650°C, both out-of- and in-reactor. Neutron bombardment decreased ductility at 550, 650, and 750°C but not at 850°C; the greatest loss occurred at 650°C.

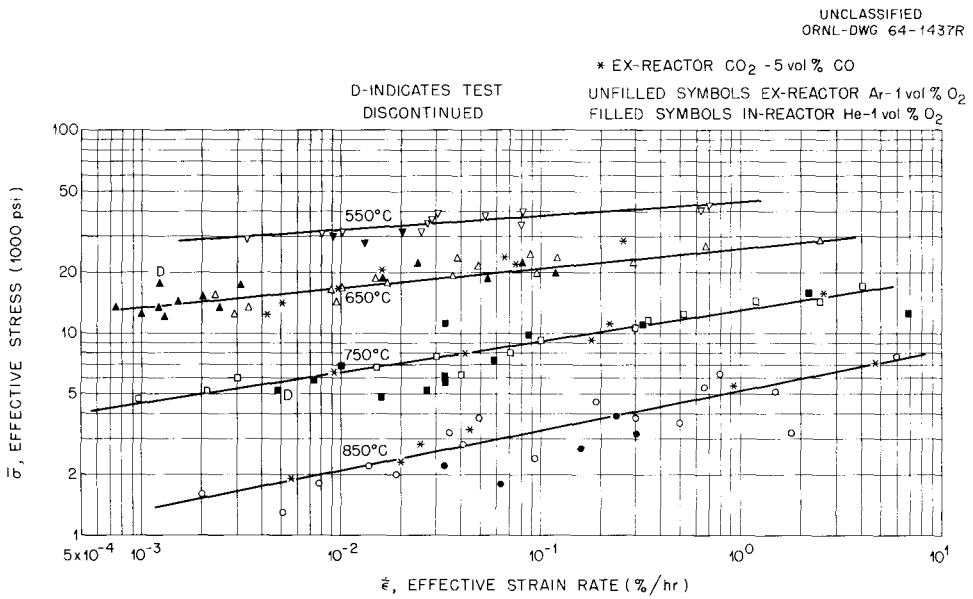

Fig. 25.18. The Effect of Irradiation on Effective Strain Rate in 20 Cr–25 Ni Niobium-Stabilized Stainless Steel Tubing.

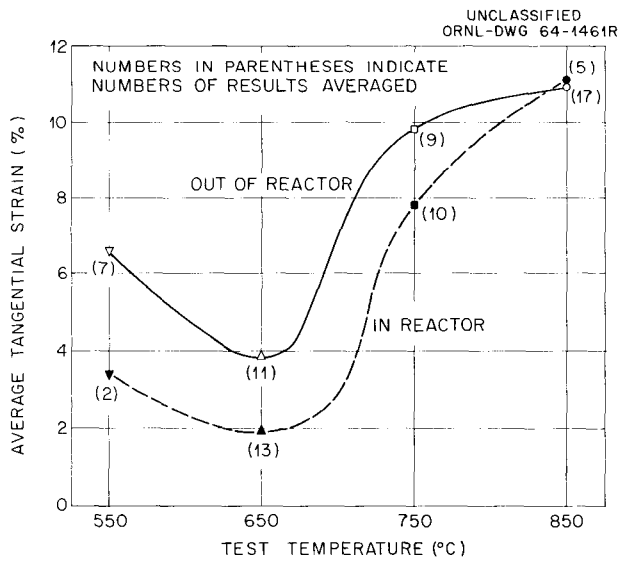

Fig. 25.19. Effect of Temperature and Irradiation on Strain at Fracture for 20 Cr–25 Ni Niobium-Stabilized Stainless Steel Tubing.

The Effect of Bushing Length on the Ratchetting of Metal-Clad Fuel Elements

W. R. Martin

The effect of bushing length on the ratchetting of metal-clad ceramic fuel elements was investigated. An internal heater device was used in out-of-reactor experiments to determine the rate of axial elongation of the cladding during thermal cycling.

Zirconia bushings were used to simulate UO_2. The 95%-dense bushings were either 0.250 or 9.0 in. long. The inside and outside diameters were 0.323 and 0.707 in. respectively. We prepared two simulated fuel capsules using 0.750 × 0.020-in.-wall type 304 stainless steel tubing. One contained a single 9-in.-long bushing while the second contained 36 short bushings. The tubing was partially collapsed about the bushings prior to thermal cycling to initiate mechanical interaction between cladding and bushings. The length of each capsule was monitored continuously during the test, and the rate of plastic deformation computed is given in Fig. 25.20.

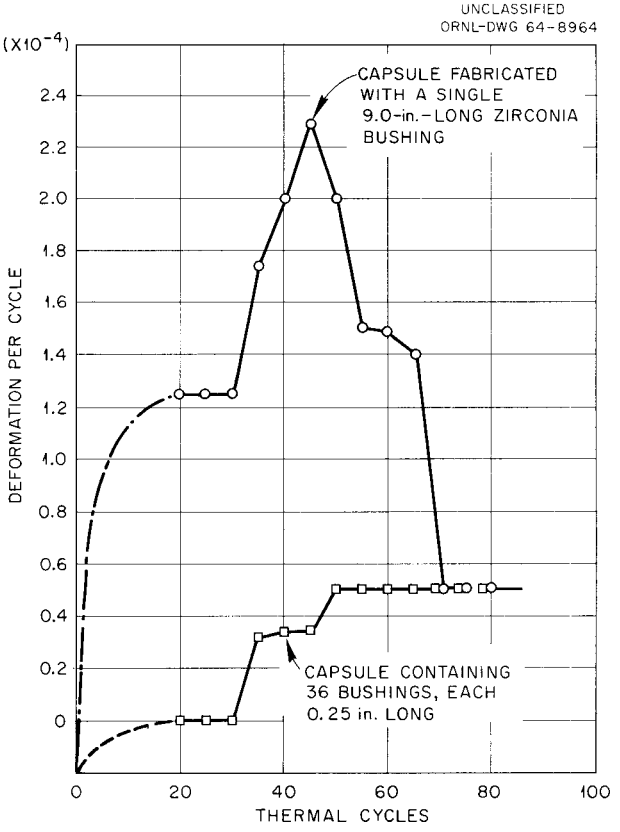

Fig. 25.20. Influence of Bushing Length on the Axial Deformation of Stainless Steel Cladding During Thermal Cycling.

The rate of deformation initially increased with successive thermal cycles because of creep collapse of the tubing about the bushing. The rate of deformation was larger for the capsule containing the longer bushing. The resulting increase in the frictional force between bushings and cladding increased the rate of plastic strain in the cladding. After approximately 50 thermal cycles, the collapse became complete and the rate of deformation became constant for the capsule containing the short bushings. However, at this point the deformation rate for the capsule containing the long bushing had passed its peak and was decreasing. Finally, the rate became equal to the maximum rate of deformation observed for the capsule containing the shorter bushings.

Radiographs of each capsule after test indicated that the long bushing had fractured into quarter-inch segments, while the short bushings, although fractured, did not change in length. The decrease in rate of cladding deformation observed for the capsule originally containing the long bushing was due to fracture of that bushing into smaller segments during cycling.

Thus, we concluded that the rate of clad deformation increases with increasing bushing length. Elsewhere,[65] we suggest that the frictional force between bushing and cladding is directly proportional to bushing length, and that hypothesis is supported by the present results.

Lubrication of Metal-Clad Ceramic Fuel Elements to Reduce Ratchetting

W. R. Martin

The use of a lubricant between the fuel and cladding of metal-clad ceramic fuel elements has been proposed[66] as a method of reducing ratchetting, thus lowering the probability of fuel element failure. Lubricants considered in this investigation were graphite, molybdenum disulfide, mica, calcium fluoride, copper, and gold. Our criteria for selection of the lubricant were low shear strength, good chemical compatibility with fuel, good chemical compatibility with cladding, low neutron absorption and scattering cross sections, simple method of application, and low cost. In view of these criteria, copper was selected.

Two capsules were fabricated using UO_2 bushings and 0.75-in.-OD × 0.020-in.-wall type 304 stainless steel tubing. The bushings in one capsule were wrapped with 0.001-in. copper foil prior to insertion into the stainless steel tubing. Both capsules were thermally cycled in an internal-heater device between identical temperature limits. The rate of axial deformation during cycling was measured for each capsule at pressure differentials across the clad wall of 100, 200, and 300 psi. The rates of axial deformation in the cladding are given below:

	Coolant Pressure (psi)		
	100	200	300
Lubricated with copper foil	$<5 \times 10^{-6}$	$<5 \times 10^{-6}$	5.8×10^{-5}
Without lubrication	$<10 \times 10^{-6}$	2.5×10^{-4}	4×10^{-4}

[65] W. R. Martin, *Mechanical Cladding-Fuel Interactions During Thermal Cycling of Metal-Clad Fuel Elements*, ORNL-3514 (to be published).

[66] W. R. Martin, *GCR Program Semiann. Progr. Rept. Sept. 30, 1963*, ORNL-3523, pp. 193–94.

The results show a significant reduction in the axial deformation of the copper-lubricated capsule.

The success of the copper foil is attributed to its behavior as a boundary lubricant, preventing or greatly reducing the contact area of the fuel and clad. The frictional force, F, at the boundary is given by

$$F = A[\beta\sigma_1 + (1 - \beta)\sigma_2] ,$$

where

A = total area of fuel and lubricant in contact with the cladding,

β = ratio of the cladding-fuel contact area to the total area A,

σ_1 = shear strength of the fuel-cladding junction, and

σ_2 = shear strength of the boundary lubricant.

The shear strength of the lubricant must be less than the shear strength of the fuel-cladding junction before the lubricant will reduce the frictional force. When the lubricant prevents fuel-cladding contact, β is zero and the friction force is governed by the shear strength of the lubricant.

Irradiation of UO_2 Pellets above 1600°C

J. L. Scott C. Michelson[67]

When UO_2 pellets are irradiated at high heat ratings, a columnar-grained structure and a void are observed in the center of the pellets. This columnar structure can arise from the migration of voids in the structure through a temperature gradient. It is generally believed that the mechanism involves UO_2 sublimation from the hotter side of each void and condensation on the cooler side. The net result is void migration to the center of the fuel pellet. The migrating voids sweep fission gases from the affected zone and ultimately transport them to a central void. Thus, a high rate of release of xenon and krypton would be expected to occur during this structural redistribution. Since the resulting structure is free of voids, the subsequent rate of fission-gas release from the densified UO_2 should be much lower. On the other hand, fission gases may continue to be released by the migration of newly formed voids or some other mechanism.

We investigated this problem with four LITR irradiation capsules, each of which had two gas-tight compartments containing three 20%-enriched, bushing-shaped UO_2 specimens (0.076-in. ID × 0.155-in. OD × 0.249 in. long) which were surrounded by depleted UO_2 insulating bushings (0.157-in. ID × 0.288-in. OD × 0.249 in. long). The fuel insulators and bushings were contained in a tantalum sleeve and supported at each end by insulators fabricated from depleted UO_2. The capsules were fabricated from Inconel and were air cooled. At least one compartment of each capsule contained a thermocouple for measurement of the fuel central temperature. Thermocouples were also provided to measure the capsule surface temperatures.

The capsules were irradiated to various burnups as indicated in Table 25.6. The effective thermal neutron flux was approximately 1.7×10^{13} neutrons cm^{-2} sec^{-1} and the fuel power density exceeded 1 kw/cm^3. Although the thermocouple readings are probably in error at the high indicated temperatures, the fuel microstructures show that the central temperature exceeded 1600°C in every case.

Postirradiation examination of each capsule has been completed[68] and the results are now being evaluated. The results suggest that the fission-gas release was virtually complete above 1600°C and that fission gas continued to be released almost completely as long as the high temperature was maintained.

The type of microstructure developed at each specimen location indicated the existence of severe axial as well as radial temperature gradients in the fueled region. This makes it difficult to find specimens with identical thermal histories and correlate the observations with time at power or burnup. However, the metallographic specimens clearly showed the migration of voids to the center of the fueled region and the formation of a columnar grain structure. A somewhat unexpected occurrence was a closing of the gap between the fuel and insulating bushings. A redistribution of fuel through the sublimation-condensation process apparently closed the gap and permitted the columnar structure to extend far into the depleted-uranium region.

[67] On loan from the Tennessee Valley Authority.

[68] J. G. Morgan, M. F. Osborne, and E. L. Long, Jr., *Examination of UO_2 Irradiated at High Temperatures*, ORNL-TM-763 (March 1964).

Table 25.6. Operating Conditions for High-Temperature Irradiations of UO_2 Pellets

Capsule	Compartment	Fuel Central Temperature (°C)				Average Capsule Surface Temperature (°C)	Time at Power (hr)	Burnup	
		Initial[a]	Peak	Final	Average			(Mwd/MT UO_2)	(At. % U)
LHT-1	*a*	2177	2399[b]	2093	2232	371	749.4	3520	0.4
	b	2204	2982[c]	2677	2704	468	749.4	3520	0.4
LHT-2	*a*	2135	2427[d]	1954	2010	538	185.3	830	0.1
	b	2163	2427[d]	1968	2010	677	185.3	830	0.1
LHT-3	*a*	2204	2427[d]	2204	2177	510	19.1	87	0.01
	b	(no central thermocouple)				593	19.1	87	0.01
LHT-4	*a*	2343	2427[d]	1538[e]	1732	510	1844.8	8410	1.0
	b	(no central thermocouple)				566	1844.8	8410	1.0

[a]Approximately 3 hr after startup.
[b]After 72 hr.
[c]After 612 hr.
[d]After <3 hr.
[e]1760°C after 750 hr.

While further work must be done to elucidate the release mechanisms in detail, a comparison of the enriched and depleted zones of the columnar structure, both of which must have been above 1600°C, lends insight into the nature of these mechanisms. The metallographic specimens showed that fission-gas bubbles formed both within grains and at the grain boundaries. As fissioning continued more bubbles were formed at grain boundaries. Eventually the bubbles became interconnected, either by coalescence or by crack formation on thermal cycling, and when this occurred the xenon and krypton (and probably iodine and cesium as well) were released.

The fission-gas bubbles within the grains must also migrate either to the grain boundaries or up the temperature gradient. These bubbles appeared to be spherical, unlike the voids that migrated and produced the initial columnar structure. Undoubtedly the gas pressure was much higher in fission-gas bubbles, so that surface diffusion would be favored as the mode of migration instead of sublimation and condensation. Since the columnar grains were already in the preferred orientation, the movement of fission-gas bubbles left no trail like the initial migration of preexisting voids. It is clear that fission-gas release was quantitative from within the columnar grain growth region at all burnups. This fact must be taken into account in the design of operating fuel elements containing UO_2.

Thermal Conductivity of UO_2

T. G. Godfrey J. P. Moore

Measurements of the thermal conductivity of polycrystalline UO_2 were completed in the radial heat flow apparatus over the temperature range −57 to 1100°C. The results are treated in Part I, Chap. 6, of this report.

Thermal Conductivity of Graphite

J. P. Moore T. G. Godfrey

The total thermal conductivity, k, of CGB graphite (an impregnated grade with a density of 1.824 g/cm^3) was measured normal to the extrusion axis

in a radial heat flow apparatus from 50 to 1000°C. Supplementary electrical resistivity measurements in the normal direction were used with the Wiedemann-Franz-Lorenz relation to calculate the electronic contribution, k_E, to the total thermal conductivity. The lattice component, k_L, was obtained by subtracting k_E from k. The lattice component varied inversely with temperature and all data were within ±4% of values given by the equation:

$$1/k_L = 0.48812 + 1.4060 \times 10^{-3}\ T\ ,$$

where k_L is in w cm^{-1} $°K^{-1}$ and T is the temperature in °K. However, since k_E is so small at these temperatures, the total thermal conductivity can also be represented by an inverse linear equation in temperature:

$$1/k = 0.54436 + 1.2496 \times 10^{-3}\ T\ .$$

Additional thermal conductivity measurements were made in a longitudinal comparative heat flow apparatus. This apparatus consisted of two 1-in.-diam gold-plated Armco iron meter bars mounted coaxially in a vacuum chamber with the disk specimen compressed between them. A temperature gradient was established along the meter bars and the specimen by a Nichrome heater at the top of one meter bar and a water-cooled heat sink at the bottom of the other. The temperatures at known positions along the bars were determined with Chromel-P/Constantan thermocouples and extrapolated to the meter-bar–specimen interface to determine the temperature drop across the specimen. Using the measured gradients along the meter bars and the known thermal conductivity of these bars, we calculated the rate of heat flow through the specimen. Interfacial resistance was minimized with 0.001-in.-thick indium foils and careful lapping of the specimen and meter bar surfaces. This apparatus yields data with a reproducibility of better than 0.25% and a probable accuracy of ±3%.

Thermal conductivity values obtained from measurements with this apparatus on a 2-cm-high CGB graphite specimen that was cut so that the heat flow was normal to the extrusion axis agreed to within 4% with the values from the radial heat flow apparatus. Measurements on a 2-cm-high CGB graphite specimen that was cut so that the heat flow was parallel to the extrusion axis yielded thermal conductivity values of 1.942 and 1.884 w cm^{-1} $°K^{-1}$ at 34 and 75°C respectively. The thermal conductivity along the extrusion axis was 1.79 times that normal to the axis. The ratio of the electrical conductivity parallel to the extrusion axis to that normal to this axis was 2.11 at 23°C and decreased uniformly to 1.96 at 1000°C.

26. High-Flux Isotope Reactor

G. M. Adamson, Jr.

The High Flux Isotope Reactor (HFIR) is being constructed at ORNL to provide a high flux density that may be used to provide research quantities of the transplutonium elements. This reactor is designed to produce 5×10^{15} neutrons cm^{-2} sec^{-1} with an average power density of 2000 kw/liter and a total power of 100,000 kw. In spite of the high power density, aluminum is being used as the structural material for both the fuel element and the control rods.

To minimize flux peaking and thereby reduce the hot-spot temperature, the fuel content of each plate is varied nonlinearly across the width. In addition, the plates are formed into an involute configuration to equalize the coolant channels and provide uniform cooling to all surfaces. Also, a burnable poison (B_4C) is added to each plate and its concentration varies opposite to that of the fuel. Finally, extremely close tolerances are required for both the fuel concentrations and the dimensions.

The control rods for this reactor are also unique. They consist of eight plates arranged in two cylinders, which fit around the fuel element; each cylinder is about 18 in. in diameter × 5 ft long. Limited time has required that full-size components be fabricated simultaneously with the development of the fabrication and forming techniques.

FUEL ELEMENT

The design of the fuel element has changed very little during the past year. The program has progressed from the laboratory phase through the pilot plant and production is now starting. Specifications[1] for fuel elements were prepared and a commercial contract placed for 33 elements. From this cost-plus-fixed-fee contract, we expect sufficient data on recovery rates and other production aspects to permit placing a fixed-price contract for subsequent elements. We procured all the component materials and furnished them along with technical assistance to the fabricator.

The developmental effort was largely directed at solving the problems encountered in scaling up the production. Two complete sets of enriched fuel plates were produced, one for a critical experiment and the second for the first reactor fuel element. The critical plates were inspected for uranium homogeneity using the newly developed production scanner and then assembled into an acceptable element. The homogeneity scanner worked very well and should prove to be a valuable tool in all fuel plate development work.

Fuel Plate Fabrication and Assembly of the HFIR Critical Experiment Element

J. H. Erwin W. J. Werner R. W. Knight

During the year, major emphasis was placed on establishing the basic fabrication and forming parameters for the fuel plates. This development work culminated with the issuing of specifications[1] for the commercial manufacture of the fuel plates.

The production of two complete sets of enriched fuel plates to the required dimensional specifications further confirmed the validity of the fuel-plate fabrication procedures. One of these sets

[1]G. M. Adamson, Jr., and J. R. McWherter, *Specifications for High Flux Isotope Reactor Fuel Elements*, ORNL-TM-902 (in press).

has been assembled into the core for the third HFIR critical assembly and the other will be used in the first reactor core.

Like a HFIR fuel core, the critical assembly consisted of inner- and outer-annulus elements containing 171 and 369 fuel plates, respectively. As illustrated in Fig. 26.1, the outer side plate of the outer-annulus element and the inner support tube of the inner-annulus element extend beyond the normal length of the standard reactor element. Both this difference and the requirement that all fuel plates be removable complicated the assembly of the elements.

Powder-metallurgy duplex fuel compacts[2] containing −170 +325 mesh oxide were used in both the inner- and outer-annulus critical-experiment plates. The compacts were rolled into fuel plates by the conventional "picture frame" method using a combination of hot rolling (500°C) and 20% cold reduction. This combination improved the formability in subsequent low-pressure marforming to the specified shapes. Rolling parameters, which in turn dictate powder-metallurgy die dimensions and compact volumes, were developed to yield plates of the nominal plan dimensions.

Table 26.1 summarizes the results of the production of the critical-element fuel plates. Excellent control was maintained over all fabrication variables, resulting in a high yield (>90%) of nonbond-free plates of specified dimensions. Although analysis is not complete, comparable results were also obtained with the fuel plates for the reactor. This control was further demonstrated by the chemical analyses of entire plates for total ^{235}U and ^{10}B contents, which are included in Table 26.1. Information on uranium homogeneity and its measurement is presented in a separate section of this chapter.

Table 26.2 summarizes the curvature data obtained on the critical-element fuel plates and compares these data with the best previous low-pressure marforming results.[3] The large spread in point duplication for the outer-annulus plates resulted from improper plate handling procedures prior to forming. Subsequent revisions in plate handling procedures improved the point duplication, as manifested by the 6-mil maximum variation in measurements obtained from the inner-annulus plates. Even though the point range in the outer-annulus plates was large, they were easy to insert into the side plates. Differences between standard deviations for all measuring points along a single traverse and for the individual points, as shown in Table 26.2, are caused by a saddle effect at the center of the fueled plates. This saddle, which averaged 0.008 in. in height as viewed from the convex side of the plate, is due to the greater forming springback in the fueled sections of the plates than in the unfueled ends.

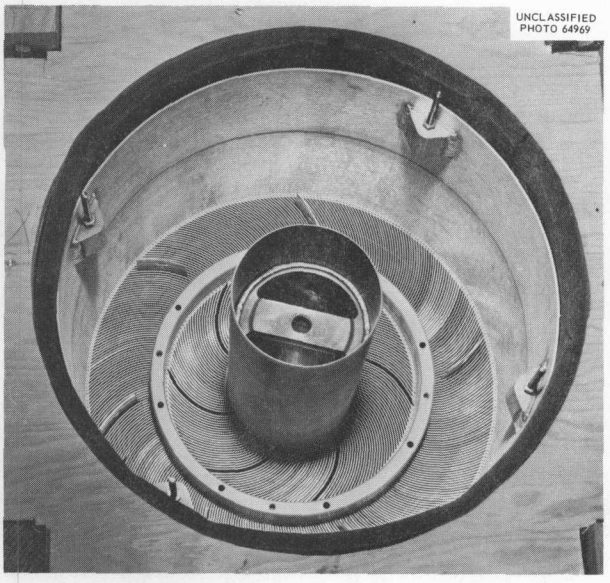

Fig. 26.1. Fuel Core for the Third HFIR Critical Experiment.

The critical-experiment element was assembled with relative ease due to the high quality of the machined side plate tubes and the formed fuel plates. Assembly specifications were complicated by the fact that all fuel plates had to be removable, in particular six inner- and six outer-annulus plates, symmetrically located. The positions of these plates in the assembled element are identified in Fig. 26.1 by the aluminum tabs that extend above the normal fuel plate height. These tabs were welded to the fuel plates to facilitate their removal from the element. Repeated fuel plate insertion was facilitated by the use of a semipermanent Teflon spray lubricant. Alcohol was used as a temporary lubricant to prevent galling of the plate in the side-plate slot.

---

[2]M. M. Martin and C. F. Leitten, Jr., *Metals and Ceramics Div. Ann. Progr. Rept. May 31, 1963*, ORNL-3470, pp. 174–76.

[3]J. H. Erwin and C. F. Leitten, Jr., *Metals and Ceramics Div. Ann. Progr. Rept. May 31, 1963*, ORNL-3470, pp. 175–79.

Table 26.1. *Summary of Critical-Element Fuel Plate Processing Data*

	Inner Annulus	Outer Annulus
Number of fuel plates required	187	385
Duplex powder metal compacts		
Number of compacts pressed	209	456
U_3O_8 in fuel region, wt %	30.16	41.44
B_4C in filler region, %	0.39	0
Dimensions of fuel region in the fabricated plate		
Width, in.	$3.054^{+0.023}_{-0.016}$	$2.773^{+0.013}_{-0.015}$
Length, in.	$20.250^{+0.360}_{-0.281}$	$19.975^{+0.431}_{-0.412}$
Rejection, %		
Duplex compacts		
Weight	0.5	0
Dimensions	0	0
Other	1.0	0
Fabricated plate		
Dimensions	0.5	0.4
Blisters	0	4.6
Nonbond	2.0	2.9
Other	0	0.2
Total fuel and burnable poison content		
Uranium (^{235}U isotope), g		
Specified	15.18 ± 0.15	18.44 ± 0.18
Found[a] (wet chemistry)	$15.27^{+0.04}_{-0.04}$	$18.35^{+0.07}_{-0.08}$
Boron (^{10}B isotope), g		
Specified	0.0124 ± 0.0008	none
Found[a] (wet chemistry)	$0.0123^{+0.0008}_{-0.0010}$	

[a]Content represents data from total dissolution of 10 fuel plates. Reported accuracy of uranium value 0.2% and boron value 5% at the 95% confidence level.

The six special positions in the inner and outer annuli were supplied with three different sets of formed fuel plates. These were: (1) a set of dummy plates (6061-0 aluminum), (2) a set of fueled plates, and (3) a special set of fueled plates with removable punchings in each plate. A special punch, broach, and die were made to punch 28 rectangular holes (1.500 ± 0.005 in. × 0.125 ± 0.002 in.) in the fuel plates. Each punching was inserted in its own hole such that it could be removed easily. With the inserts in position, plates were formed.

Although the channel spacings were not measured on the assembled element, their overall appearance was excellent. The element was subsequently delivered to the critical test facility.

Table 26.2. Forming Duplication of HFIR Fuel Plates as Shown by Deviation in Curvature Comparator Measurements Taken at the Center of the Involute

	Inner Annulus		Outer Annulus	
	Commercial Aluminum Unit	HFIRCE-3 Unit	Commercial Aluminum Unit	HFIRCE-3 Unit
Number of fuel plates measured	20	186	67	393
Number of fuel plates in statistical sample	20	20	37	50
Duplication of all measurements (mils) (7 repetitive equidistant measuring points)				
Maximum to minimum	10	17	8	28
Standard deviation[a]	4.06	7.64	3.00	9.24
Duplication at individual measuring points (mils)				
Maximum range (7 points considered)	9	6	8	24
Average standard deviation[a]	4.20	2.82	3.00	7.28

[a]95% confidence level.

Assembly and Welding

J. W. Tackett

The reactor will use fuel elements assembled by sliding the fuel plates into slotted tubular side plates and then fusing them to the side plates by circumferential welds (the all-welded concept[4]). A complete fuel assembly requires 96 circumferential welds or 25,920 joints of fuel plates to side plates. So far, we have not discovered a nondestructive method of evaluating these joints, which are located on the root side of the welds. The fuel element design requires, however, that the assembly and welding procedures reasonably ensure that each joint has a minimum pullout strength of 100 lb. Also, the volume of weld metal deposited should be sufficient to provide a smooth surface after final machining, and the root penetration must be carefully controlled to prevent melting of the fuel plate cores.

During the past year, a major portion of our effort has involved establishing assembly procedures, joint configurations, welding procedures, and evaluation methods to satisfy the reactor requirements. Several problems involving both assembly and welding arose during this effort, and our efforts were directed at solving them.

In the joint configuration developed for the circumferential welds, the fuel plates protrude into the weld grooves to ensure that they are fused with the weld metal deposited in each groove. However, at the start and end of each circumferential weld, the plates were not attached reliably when welded in the manner found most suitable for the remainder of the weld. We corrected this difficulty by developing an integrated program to control the weld. This program modified the electrode-wire feed speed, the weld travel speed, and the weld voltage to give reliable attachment for the entire weld.

The root penetration is sensitive to the welding variables. Some penetration, approximately 25% of the root thickness, is needed for attachment strength, but melt-through (in excess of 100% of the root thickness) is undesirable. Although

[4]J. W. Tackett and G. M. Slaughter, *Metals and Ceramics Div. Ann. Progr. Rept. May 31, 1963*, ORNL-3470, pp. 177–81.

satisfactory parameters had been established for welding the joint with the originally designed root thickness of 0.075 in., excessive control over the welding parameters was required for consistent plate attachment without excessive penetration or melt-through. For example, the effect of travel speed on root penetration was pronounced. At travel speeds of 20 and 25 in./min, melt-through was observed. At weld speeds less than 14 in./min, root penetration was negligible, and fuel plates were not consistently attached, especially at the weld start. Minor changes in the welding voltage also had a pronounced effect. While the sensitivity of the weld parameters to root penetration decreased gradually with increasing root thickness, a reasonable latitude of welding variables was not obtained until the root thickness reached approximately 0.1 in. Therefore, the specified root thickness was increased to 0.100 in.

To determine whether plate-forming tolerances might be relaxed, we assembled a full-size inner annulus in which 10% of the plates were deliberately formed with off-specification curvature, chord width, and edge angularity. Although these plates were readily inserted between the side plates, marked irregularities were prevalent in the plate-to-plate spacings, especially in the mid-channel positions where measurements varied from greater than 0.080 in. to less than 0.020 in. Figure 26.2 shows this condition in a typical region. The plates were easily fitted into the correct involute positions by Teflon spacer strips. We found a considerable variation in how far the plates protruded into the weld groove; some plates did not even reach the groove. After the Teflon spacers had been removed, all of the 3591 plate spacing measurements in the completed assembly were within the required 0.050 ± 0.010 in. The data are summarized in Table 26.3. Metallographic examination revealed that ample tie-in had been obtained in a vast majority of the fuel-plate-to-side-plate welds but not in a few joints in which the fuel plates did not protrude sufficiently into the weld groove.

We also developed assembly and preweld inspection procedures to assure compliance with the joint criteria. A quality control weld sample was developed which will permit both a joint-strength evaluation and metallographic evaluation of the welds used in making the reactor components. The preweld inspection and the destructive testing of the quality-control specimens will be used to evaluate the integrity of these very critical weld joints.

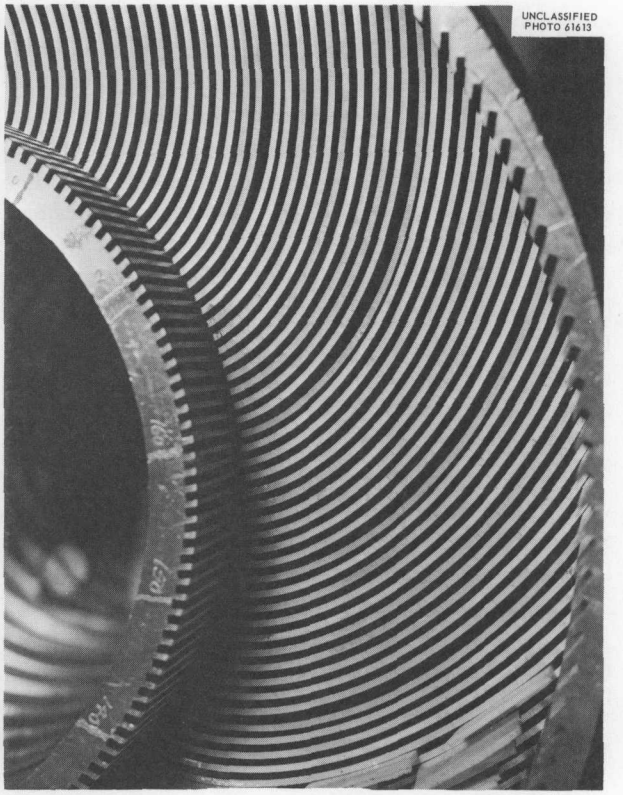

Fig. 26.2. Area of Full-Size Inner Annulus Containing Wide and Narrow Plate Spacings in As-Assembled Condition Prior to Insertion of Teflon Spacers.

Table 26.3. Summary of Plate Spacing Measurements in the Annulus Formed with Off-Specification Plates

Radial Position	Channel Thickness Measurements (in.)		
	Maximum	Minimum	Average
Adjacent to inner tube	0.054	0.043	0.048
Middle	0.056	0.043	0.048
Adjacent to outer tube	0.058	0.045	0.051

Boron Distribution in HFIR Critical Inner-Annulus Fuel Plates

M. M. Martin

To minimize the radial peak-to-average power density ratio in the HFIR, the fuel and poison surface densities in each plate are varied along the arc of an involute curve. The ^{10}B, included only in the inner plates in the form of B_4C of natural isotropic content, is added to the aluminum filler piece for maximum effectiveness rather than to the fuel-bearing portion of the duplex core. Previously, the feasibility of the addition was demonstrated,[5] but analytical procedures for boron were needed to verify the distribution. The specification is complicated in that the loading is different for each longitudinal traverse. Further, the amount of boron in every 0.2-in.^{2} area must be distributed to within ±35% of the nominal loading.

A method was developed[6] to determine boron in $\frac{1}{2}$-in.-diam punchings from HFIR inner fuel plates within ±6% over the range of 50 to 300 μg boron. Six plates were examined for boron distribution, and the data are statistically evaluated in Table 26.4. Row No. 2 is located on the longitudinal traverse of minimum boron content, and rows Nos. 1 and 3 are near the edges of the fuel core. As indicated in the table, the average boron content is appreciably larger near the ends of the core than near the middle; the fuel content exhibits the opposite trend. Although the average boron content was high at the core ends of row No. 2, the samples analyzed met the specification. A correction in the filler piece contour in the region of row No. 2 would bring the average boron content near nominal.

[5] T. D. Watts and M. M. Martin, *Metals and Ceramics Div. Ann. Progr. Rept. May 31, 1963*, ORNL-3470, p. 185.

[6] W. R. Laing, *Anal. Chem. Div. Ann. Progr. Rept. Nov. 15, 1963*, ORNL-3537, p. 124.

Uranium Homogeneity

J. H. Erwin R. W. Knight
B. E. Foster S. D. Snyder
J. Reynolds[7]

One of the unusual features of the HFIR is the very tight and complex specification on uranium homogeneity. These requirements are complicated by the variation in uranium content across the plate width. Demonstrating whether the plates meet these requirements has necessitated the

[7] Instrumentation and Controls Division.

Table 26.4. Statistical Analysis of Boron Distribution in Six Inner-Annulus Fuel Plates for HFIRCE-3

Row No.	Coordinates of Punchings		No. of Replicate Punchings	Boron Content[a] (μg)					Tolerance Limits[b] (%)
	Distance from Reference Edge of Plate (in.)	Distance from Center of Plate (in.)		Specified		Found			
				Min	Max	Min	Max	Av	
1	0.52	0, ±4	18	239	495	337	377	355	8
		±8	12	239	495	343	377	363	8
2	1.92	0, ±4	18	77	159	107	136	127	22
		±8	12	77	159	122	145	138	20
3	2.92	0, ±4	18	138	284	201	225	213	13
		±8	12	138	284	209	233	222	13

[a] Isotopic analysis of boron was 18.5 wt % ^{10}B.

[b] Tolerance limits calculated at the 95% confidence level to include at least 99% of the distribution for a sample of 76.

development of a special instrument using through-transmission x-ray-attenuation techniques.[8-10] This scanner was developed and built through a joint effort with the Instrumentation and Controls Division, and operators of the instrument are furnished by Inspection Engineering. First, a pilot model was fabricated and used for inspecting the critical-assembly plates. After this model performed satisfactorily, a production model was designed and parts were obtained for two units. The fuel element fabricators will use these to inspect the production plates.

The pilot model can completely scan a plate, measuring the uranium concentration in each $\frac{5}{64}$-in.-diam area along the length. Also, it will determine an "average" concentration in $\frac{5}{64}$-in.-wide strips. In this measurement, the concentration signal is fed through a delay circuit, so that the emerging signal is a concentration measure weighted by both duration and magnitude. Simultaneously with the recording of the point concentrations, the instrument can reject plates for out-of-tolerance values of the "average." With the present model, plates can be scanned at a speed of 128 in./min; with changes in width of the standards, this can be increased to 180 in./min. Two ways in which the data are recorded are shown in Figs. 26.3. and 26.4. Figure 26.3 is a typical plot of area concentrations and includes the indicated level of all standards for that particular scan. If desired, the "averages" could be plotted similarly. Plots of these types are used

[8]B. E. Foster, S. D. Snyder, and R. W. McClung, "A Continuous X-Ray Scanning Technique for Determining Minute Inhomogeneities in Solids," paper to be presented at the 24th Annual Convention of Society of Nondestructive Testing in Philadelphia, Pennsylvania, October 19–23, 1964.

[9]B. E. Foster, S. D. Snyder, and R. W. McClung, "Measurement and Application of X- and Gamma-Ray Attenuation to Reactor Materials Evaluation," paper presented at 4th International Conference on Nondestructive Testing, London, England, September 9–13, 1963, to be published in the proceedings.

[10]B. E. Foster and S. D. Snyder, *Metals and Ceramics Div. Ann. Progr. Rept. May 31, 1963*, ORNL-3470, pp. 182–83.

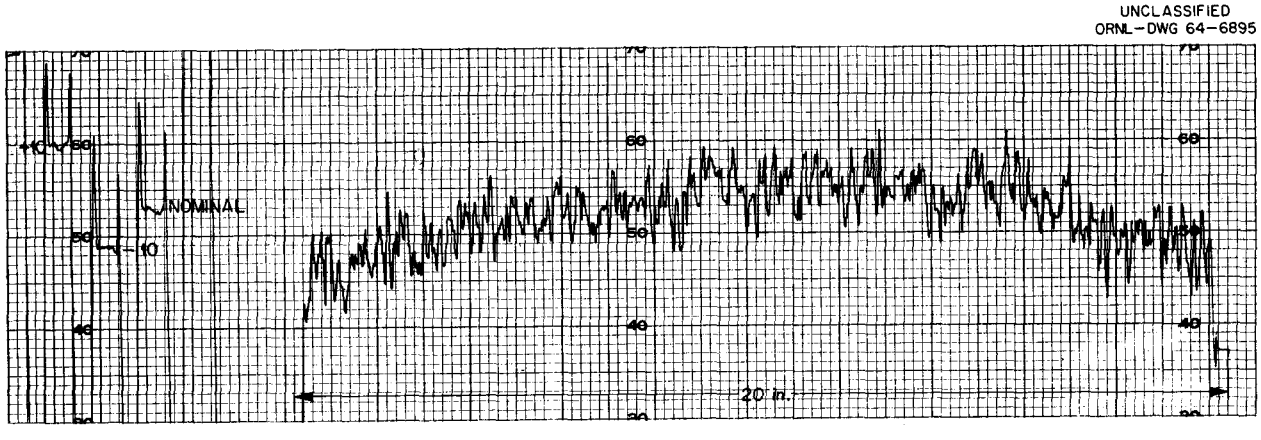

Fig. 26.3. Typical Spot Scan for Uranium Homogeneity in a HFIR Fuel Plate.

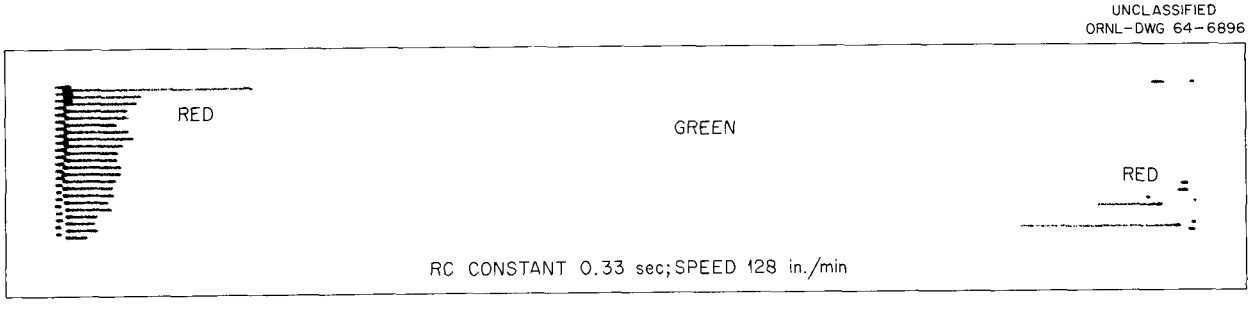

Fig. 26.4. Go-No-Go Homogeneity Scan of a HFIR Fuel Plate.

if detail is needed, as in plates under development or in plates of questionable acceptability. The disadvantage is that a large amount of chart paper must be examined, since each plate requires over 50 scans for complete coverage.

During production, the plate inspection data were condensed into the form shown in Fig. 26.4. In this form, any areas or averages that do not meet tolerance are marked on a map of the plate, with different color inks indicating the different tolerances. In this figure the areas at the ends were red, indicating low "averages," and those in the center were green, indicating high "averages." A disadvantage of this method is that it is strictly go-no-go and tells only what areas are out of tolerance; it cannot be used for interpretation. This figure would indicate that one end is much better than the other. However, spot scans of the same plate show that the "good" end was just under the tolerance level and the "bad" end was just above; actually, the two differed little.

In the determination of the "average" concentrations, the effective length over which the concentration is apparently averaged depends on the rate at which a condenser charges or discharges with fluctuations in the actual concentration. These lengths could be increased by increasing the *RC* time constant for the condenser. Scans made over the same traverse with differing time constants are shown in Fig. 26.5. The value used for inspecting the critical-assembly plates was 0.33 sec.

One difficulty in inspecting HFIR plates has been in obtaining adequate standards. Since the uranium concentration varies across the core width, a separate standard is needed for each scan, and an individual standard is also needed for each of the limits to be checked (i.e., +10, −10, +30, and nominal). Therefore, a standard with a curved surface corresponding to the change in fuel loading was made for each of the limits. Since to obtain the required accuracy and uniformity would have been extremely difficult using a dispersion, we used other materials with thicknesses calculated to give the same attenuation. The original standards were machined from an Al–13% U alloy, but we have learned that type 6061-T6 aluminum is much easier to work with and is satisfactory for the normal variations in spectrum of our x-ray tubes.

All plates for the critical experiment were inspected using the pilot model scanner with very few equipment or operating troubles. The data showed that meeting the +30% tolerance for the 0.005-in.^{2} area will be no problem. No inner plates and only a few outer plates contained variations this large. Most of these can be avoided by adjusting the average uranium content to a value nearer to nominal. Very few plates, however, meet the ±10% tolerance on "average" uranium. When all the data are available from both the critical-experiment plates and the reactor plates, a statistical study will be made and the specification modified accordingly.

An examination of the scans in Fig. 26.5 reveals one of the problems in meeting the 10% tolerance. Each plate for the critical experiment has a longitudinal fuel gradient, with the concentration low at the ends. When the effect of the gradient is superimposed on the other normal variations, areas that are out of tolerance will be found at the ends. This gradient is not completely understood, but it originates in the compact pressing and is accentuated by the rolling. Another problem encountered was that, in general, the average uranium concentrations in the outer plates were well above nominal; this, when combined with the normal variations, caused some high spots. In future plates, this will be minimized by altering the core area so that the average and nominal fuel concentration values are nearly the same.

For both sets of plates, calculations based upon measured uranium surface density and core surface area verified that the total uranium content was within specifications.

HFIR CONTROL ROD

R. J. Beaver

As illustrated previously,[11] the control rods for the HFIR contain 33 vol % Eu_2O_3 and 40 vol % Ta dispersed, respectively, in 22-in.- and 5-in.-long regions in $\frac{1}{4}$-in.-thick aluminum-base composite plates that make up the basic control components. Each plate has approximately 1700 $\frac{1}{4}$-in.-diam holes, spaced at 1-in. intervals, in all portions of the plate except those containing

[11] R. J. Beaver, *Metals and Ceramics Div. Ann. Progr. Rept. May 31, 1963*, ORNL-3470, p. 187.

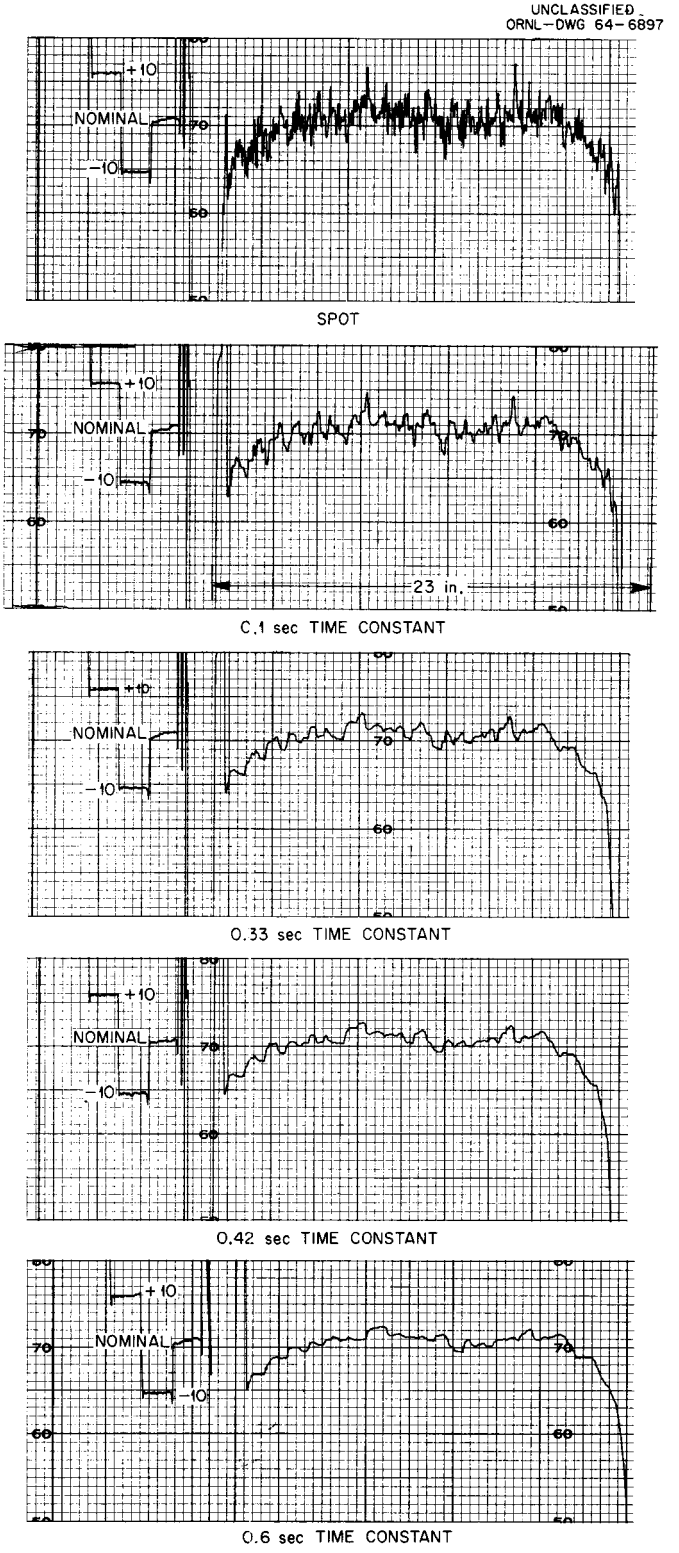

Fig. 26.5. Average Homogeneity Scans of a HFIR Fuel Plate for Different Sampling-Length Ranges. Each scan is for the same area but made with a different condenser and hence different time constant to control the sampling length.

europium oxide. Minimum cladding thickness is 0.025 in. The inner control rod consists of four plates welded together to form a cylinder 17.832-in. OD × $65\frac{9}{16}$ in. long. Surrounding this cylinder and separated by a water gap of 0.170 in. are four outer segments, spaced symmetrically around the inner control rod. These plates are $64\frac{3}{16}$ in. long and are formed to an outer radius of 9.270 in.

Since close control of the annuli between these control rod components, the fuel element, and the beryllium reflector is important, rigorous dimensional tolerances have been specified. To achieve the desired contour, final *sizing* (small adjustment to specified dimensions) of both the outer segment plates as well as the inner cylinder is accomplished by explosive forming techniques.

Much of the preliminary work relating to selection of materials, compatibility, and feasibility of plate fabrication techniques has been reported previously.[12] This year we have tried mainly to scale up from small-size parts to full-size components. Simultaneously with this scale-up development, we started to produce the inner- and outer-control-rod components for the third critical test. Eight plates were fabricated and explosively sized; these operations demonstrated the adequacy of the process.

Pertinent mechanical and physical properties of the control rod plates were measured and a program was initiated to determine the behavior of an Al–33 vol % Eu_2O_3 dispersion under irradiation.

Plate Fabrication and Preforming

M. M. Martin W. J. Werner
R. W. Knight

Our work has been directed mainly at manufacturing prototype plates to firmly establish the essential fabrication parameters and to develop a suitable technique for preforming the composite plates to close tolerances.

The compact stacking arrangement and billet design developed to achieve the desired core dimensions are shown in Fig. 26.6. The billet contains (in tandem) 18 compacts of 33 vol % rare-earth oxide and 10 compacts of 40 vol % Ta in aluminum. The compacts are prepared by powder metallurgy and are pressed at 45 tsi to 91% of theoretical density. Thickness variations within a single compact are limited to ±0.002 in. to minimize deleterious rolling effects. The europium oxide had been prepared using an arc-fusing technique described in Chap. 23 of this report. This method yielded economically a high-density material that was easy to crush, producing very few fines. Therefore, we could use all material −100 mesh, rather than material with sizes in the previously limited range of −100 +325 mesh.[12] Rejection of the fines, which were an appreciable fraction of the starting material, necessitated recycle. Prior to rolling, the billet cavity is evacuated and sealed from the atmosphere. The billets are rolled at 500°C to proper length and width using a combination of cross- and straight-rolling sequences.

Nondestructive inspection of the fabricated plates indicated that a sound bonding was achieved between the core and the cladding. However, during subsequent forming, apparent longitudinal cracks were observed at points corresponding approximately to the original longitudinal core interfaces (Fig. 26.7). Metallographic examination showed that the cladding only thinned and did not rupture; an internal crack extended part way through the core (see inset in Fig. 26.7). Since the defects occurred only on the convex or tension side of the plate, an aluminum plate was glued to the outside of the control plate to ensure that during forming all forces in the control plate were compressive. This eliminated the cracking. The backup plate was readily removed by heating and chemical cleaning.

On the basis of the fabrication and forming developments, the control plate billet specifications shown in Fig. 26.6 were established and eight Eu_2O_3-bearing plates were produced for the inner and outer control rods in the critical experiment. Table 26.5 summarizes the fabrication results for these plates and clearly shows that excellent control of rolling variables, poison loadings, and core dimensions was achieved. These plates were subsequently formed with the help of backup plates to their required radii.

Explosive Sizing

R. J. Beaver C. F. Leitten, Jr.

The $\frac{1}{4}$-in.-thick preformed clad outer-annulus plates are finally shaped by explosive sizing to

[12] W. J. Werner *et al.*, *Metals and Ceramics Div. Ann. Progr. Rept. May 31, 1963*, ORNL-3470, pp. 187–92.

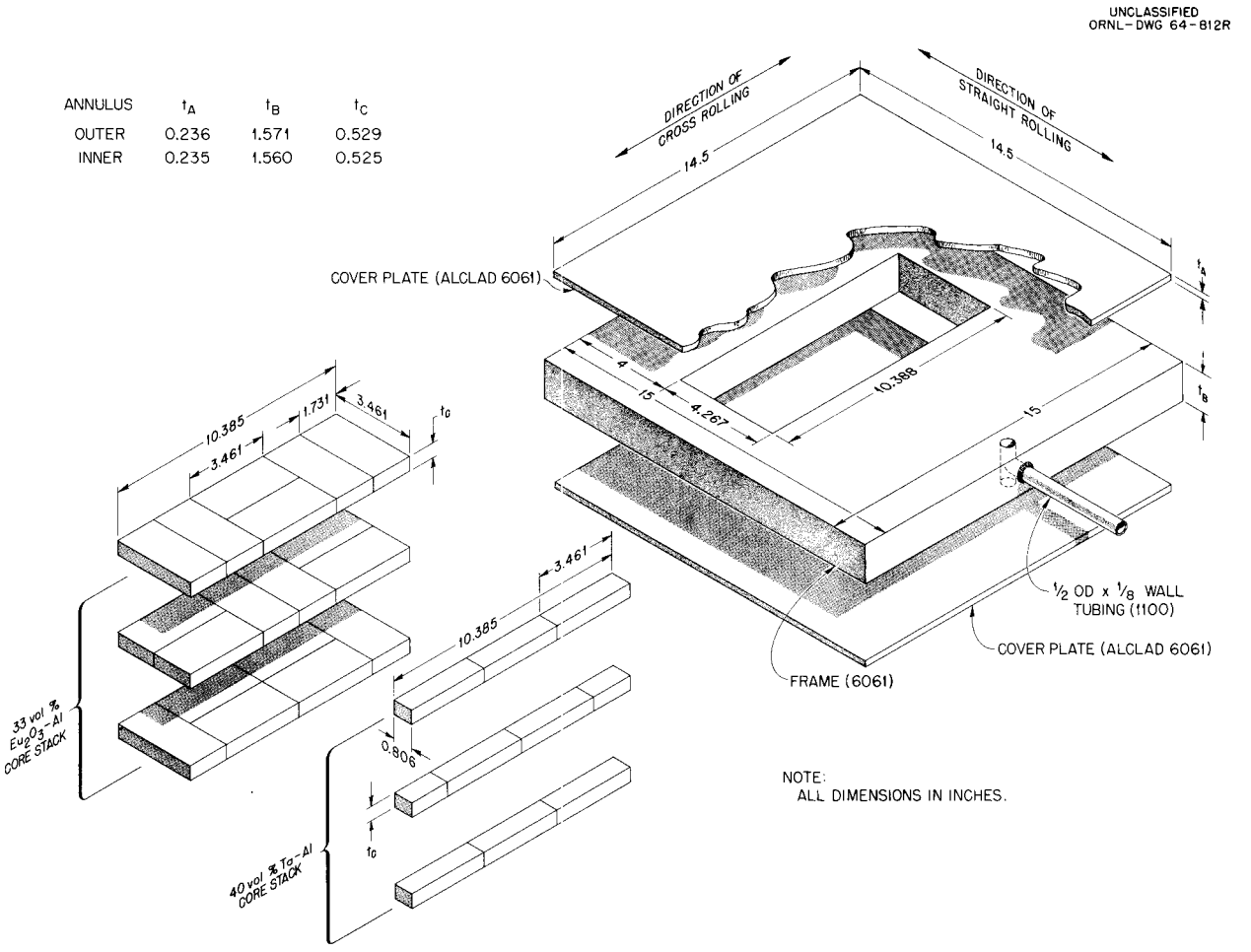

Fig. 26.6. Design of HFIR Control-Rod-Plate Billets.

achieve close control of the 9.270-in. outside radius. The explosive sizing work is conducted at the Y-12 plant by a group under the direction of W. T. Carey.

Figure 26.8 illustrates the explosive sizing equipment ready to be lowered into the water tank. It consists of a large steel die containing the preformed plate. A rubber liner over the plate seals the plate from the water. Holes through the die body permit evacuating the space between the plate and the die. Two strands of Deticord with 50 grains per lineal foot are positioned 4 in. from the longitudinal center line above the die. Two explosive detonations appear necessary for acceptable results. After the first detonation, the second set of Deticord, again with 50 grains per linear foot, is positioned with each strand 5 in. from the longitudinal center line. This second sizing with the Deticord 1 in. closer to the plate edges minimizes the variations in the radius near the edges.

Five full-size plates have been sized by this technique, and the radii of curvature have been measured at points along the longitudinal and transverse directions. The measurements obtained from all plates are summarized in Table 26.6. The majority of the large negative deviations are near the edges, showing that the plates tend to curl inward there.

The inner control rod is a hollow cylinder 17.832-in. OD $\times$ $65\frac{9}{16}$ in. long $\times$ $\frac{1}{4}$-in. thick. It will be prepared by welding together four preformed similarly shaped composite plates with the same europium oxide and tantalum concentrations as the outer control rod plates. The tube will be finished to final size by explosive forming.

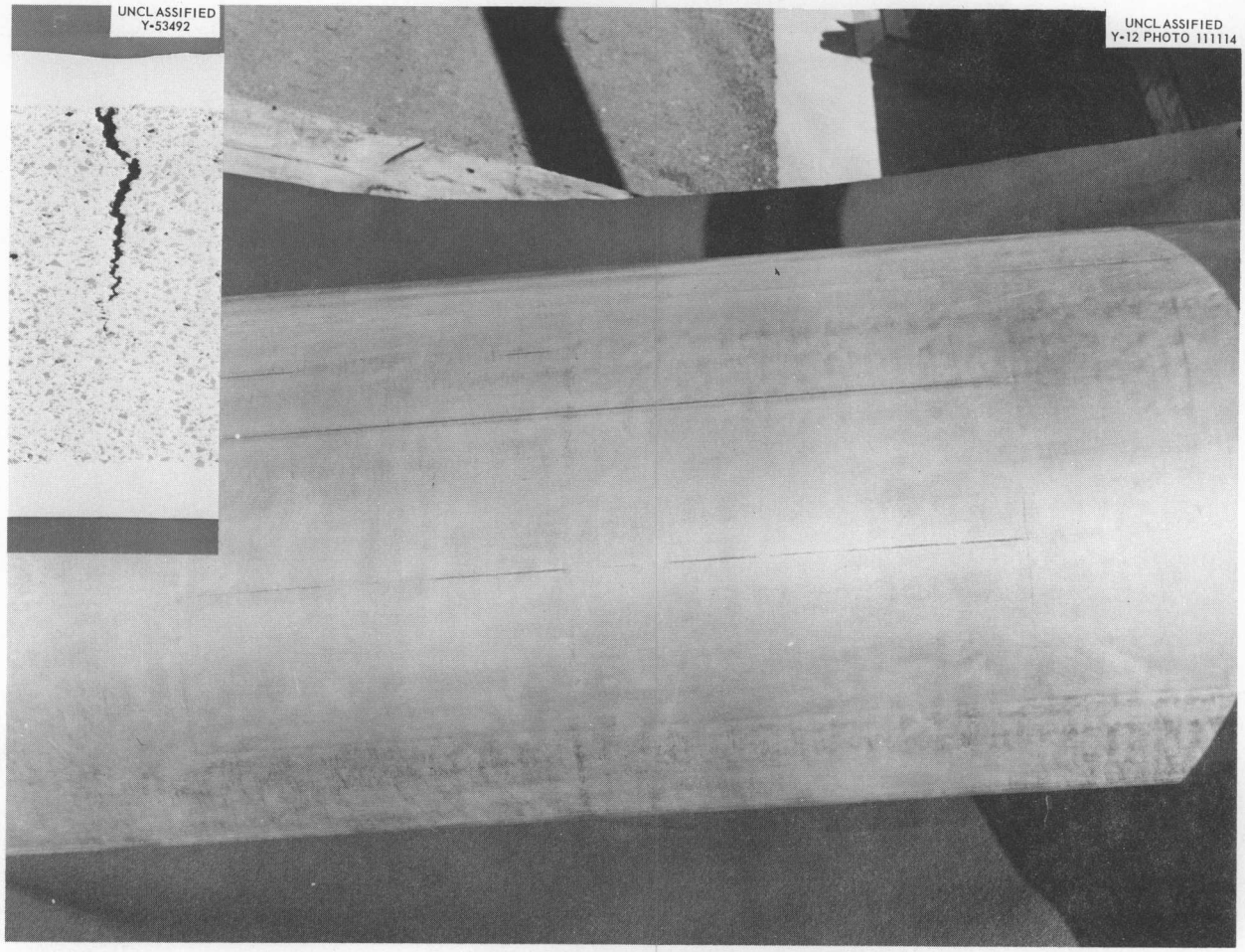

Fig. 26.7. Europium Oxide Section of Formed HFIR Control-Rod Plate Showing Interface Cracking. Insert 15×. Reduced 35%.

Procedures for welding the plates together were developed and one all-aluminum mockup cylinder was welded, mechanically expanded to a diameter approximately 0.030 in. less than the final diameter, and finished by explosive sizing. Two detonations were used to form the cylinder to final size: the first with 100 grains per lineal foot of Primacord, the second with 150 grains per lineal foot of this explosive. The results, although preliminary, are encouraging. After the first shot, the diameter, calculated from pi-tape measurements at intervals along the length, ranged from 17.838 to 17.834 in. and averaged 17.837 in. After the second shot, individual measurements ranged from 17.862 to 17.821 in. and averaged 17.850 in. Our preliminary results indicate that in future explosive forming of composite control plates a smaller second charge should be used to minimize variations in the diameter.

Since Al–33 vol % Eu_2O_3 is not ductile enough to endure the strain necessary in final sizing of a completed cylinder, this sizing will be performed in two steps. The separate plates will be explosively sized to nearly the right radius before welding. After the plates are welded together, the cylinder will be sized a final increment within the range the cermet can withstand.

Properties of HFIR Control Rod Plates

R. J. Beaver

Mechanical and Physical Properties. – To assist the proper design of the control rods, our Mechanical Properties Laboratory and Physical Properties Laboratory have measured some properties of the HFIR control plates, and the results are given in Table 26.7.

Table 26.5. Summary of Data on Core Fabrication for Control Rod Plates for the HFIR Critical Experiment

	Outer Plates		Inner Plates		Tolerance Limits
	Black Section[a]	Gray Section[b]	Black Section[a]	Gray Section[b]	
Specifications					
Dimensions, in.					
Length	22.00	5.00	22.00	5.00	±0.50
Width	13.19	13.19	13.10	13.10	±0.12
Thickness	0.194	0.194	0.194	0.194	±0.005
Loading, g	2230	1300	2215	1295	±22
Preform plate radius, in.	$9\frac{1}{8}$		$8\frac{3}{4}$		$\pm\frac{1}{2}$
Summary of Results					
Average dimensions, in.					
Length	21.96	4.90	21.96	4.90	±0.28
Width	13.20	13.17	13.12	13.09	±0.07
Thickness	0.193	0.197	0.193	0.197	±0.005
Average loading, g	2225		2211		±1
		1305		1292	±16
Preform radius, in.	$9\frac{1}{8}$		$9\frac{1}{8}$		$\pm\frac{1}{4}$
Rolling schedule, %					
Spread	2.14	1.85	2.14	1.85	±0.37
Cross	19.67	19.67	19.14	19.14	±0.37
Elongation	84.24	83.56	84.24	83.56	±0.37
Total reduction in thickness	87.84	87.62	87.71	87.53	±0.37
Estimate of densification	1.83	4.42	1.83	4.42	

[a] 33 vol % Eu_2O_3 in aluminum.
[b] 40 vol % Ta in aluminum.

Corrosion Resistance. – The Reactor Chemistry Division found that when unclad Al–33 vol % Eu_2O_3 in the fabricated HFIR control rod plate was exposed to water at 100°C for 100 hr, the oxide hydrolyzed and swelled. The swelling created sufficient stress to generate cracks throughout the material. A similar phenomenon had been reported previously for dispersions of Eu_2O_3 in stainless steel when exposed to 295°C water.[13] Deliberate defects representing conceivable 0.013-in.- and 0.025-in.-diam pits were made through the cladding into the core of otherwise hermetically sealed roll-clad platelets containing Al–33 vol % Eu_2O_3 mixtures. These specimens were tested for periods of 400 hr (on the 0.025-in.-diam defects) and 600 hr (on the 0.013-in.-diam defects) in water at 100°C pressurized to 600 psi. At one of the 0.013-in.-diam defects, a blister approximately 0.002 in. high developed. At the 0.025-in.-diam defects, blisters 0.025 in. high occurred. Although these results are not surprising, they do indicate that pitting through the cladding should be avoided because of consequent undesirable blistering. On the other hand, such a condition will probably not lead to a catastrophic failure.

[13] A. E. Richt, *Army Reactors Program Progr. Rept.*, ORNL-3231, pp. 41–43 (Jan. 31, 1962).

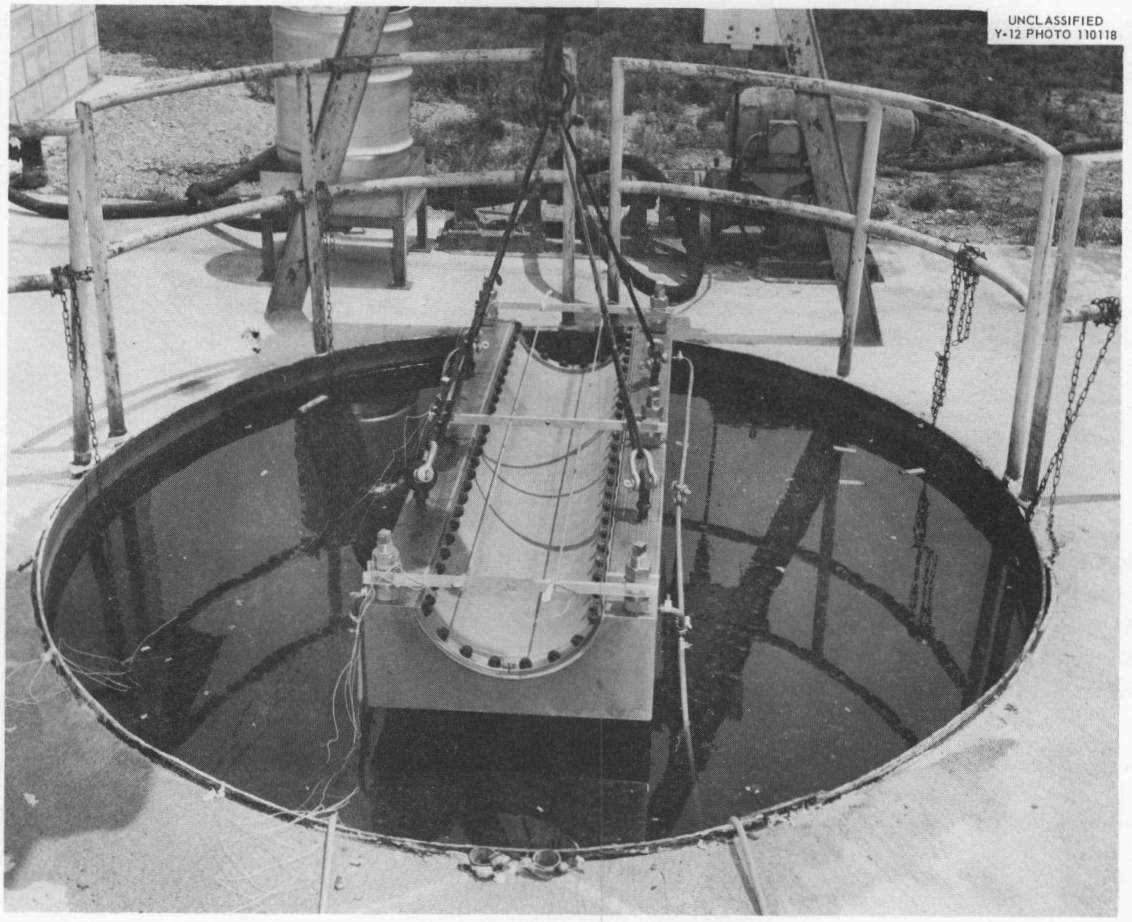

Fig. 26.8. Explosive Forming Equipment.

Table 26.6. Distribution of Deviations from the 9.020-in. Nominal Inside Radius of Explosively Sized HFIR Outer Control Rod Plates

Deviation from Nominal Radius (mils)	Deviations in Each Range (%)				
	Plate HC-28	Plate HC-29	Plate HC-30	Plate HC-31	Plate D-4
0 to +5	46.7	20.3	35.5	43.4	38.6
+6 to +10	0.0	1.7	10.2	15.0	29.8
+11 to +15	0.0	0.0	3.4	1.7	7.0
+16	0.0	0.0	0.0	0.0	0.0
−1 to −5	21.6	40.7	18.6	21.7	15.8
−6 to −10	18.3	5.1	11.7	8.3	5.3
−11 to −15	5.0	15.3	6.9	3.3	3.5
−16 to −20	5.0	15.3	6.9	6.6	0.0
−21 to −25	0.0	1.7	5.1	0.0	0.0
−26 to −30	0.0	0.0	1.7	0.0	0.0
−30	0.0	0.0	0.0	0.0	0.0

Table 26.7. Properties of HFIR Control Plates[a]

Property	33 vol % Eu_2O_3 in Aluminum	40 vol % Ta in Aluminum
Tensile strength (psi)		
Rolling direction	11,800	17,700
Transverse direction	10,300	17,700
Elongation (%)		
Rolling direction	5	6
Transverse direction	3	6
Thermal conductivity (w min^{-1} $°C^{-1}$)		
At 31°C	80.2	112.4
At 71°C	85.8	113.8
Coefficient of thermal expansion between 36 and 200°C ($°C^{-1}$) (bare core)	26.6×10^{-6}	Not measured

[a]0.030-in. cladding – 0.190-in. core – 0.030-in. cladding.

Corrosion resistance of the Al–40 vol % Ta mixture appears to be acceptable. Roll-clad specimens have been tested in 100°C aerated water with a pH of 5.0 for periods up to 11,500 hr. Several $\frac{1}{4}$-in.-diam holes were made through the tantalum-aluminum section in one specimen and part of the cladding was removed to expose the tantalum-aluminum mixture to the environment in another. In neither was there any evidence of dissimilar-metal attack between the tantalum-bearing core and the cladding. Weight changes of the samples were negligible.

IRRADIATION TESTING OF Al-CLAD PLATELETS CONTAINING A DISPERSION OF 33 VOL % Eu_2O_3 IN ALUMINUM

R. J. Beaver C. F. Leitten, Jr.

Although out-of-reactor tests have shown that Eu_2O_3 is compatible with aluminum at the 500°C rolling and heat-treatment temperature,[12] no comprehensive data exist on the behavior of the Eu_2O_3-Al mixture under irradiation. Tests have therefore been initiated in the ORR to obtain exposures at 60°C (based on unperturbed fluxes) to 4.7×10^{21} and 1.3×10^{21} neutrons/cm^2 thermal and fast respectively. The test specimens were made by the procedures established for making the full-size HFIR control-rod plates, except small cylindrical cores were used. Typical specimens before exposure and a radiograph of a core are shown in Fig. 26.9.

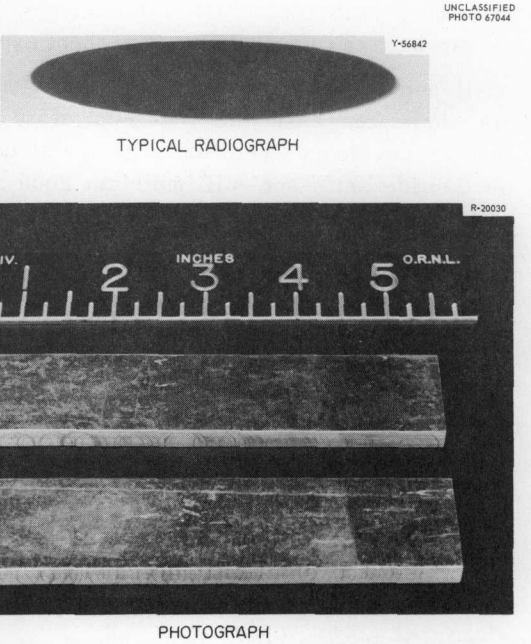

Fig. 26.9. HFIR Control Rod Irradiation Test Specimens Containing 33 vol % Eu_2O_3 in Aluminum.

27. Molten-Salt Reactor

A. Taboada

The major effort of the overall program is presently devoted to the design, construction, and operation of the Molten-Salt Reactor Experiment (MSRE)[1] to demonstrate the feasibility of this reactor type for central power stations and to provide experience with the engineering (operability, dependability, serviceability, and safety) and materials compatibility of the reactor under conditions of long-term operation.

The MSRE is a high-temperature (1300°F), low-pressure (50 psi) system designed to provide a thermal output of 10 Mw. A fuel mixture of LiF, BeF_2, ZrF_4, and UF_4 is circulated through a 5-ft-diam cylindrical reactor vessel, containing a graphite matrix, to a heat exchanger, where heat is transferred to a fuel-free fluoride salt. This secondary salt coolant then discharges heat to the atmosphere through a salt-to-air heat exchanger.

All portions of the reactor in contact with salt are fabricated from the Ni-Cr-Mo alloy INOR-8 that we developed specifically to resist corrosion by fluoride salts and still maintain good strength at elevated temperatures. The core matrix consists of unclad low-permeability graphite stringers that form vertical channels for fuel-salt flow.

Our part of this program has been limited to those problems affecting the successful completion of the MSRE. It includes metallurgical assistance to other divisions working toward this aim, as well as the materials development and testing work that follow.

[1]A. L. Boch *et al.*, "The Molten-Salt Reactor Experiment," pp. 247–92 in *Symposium on Power Reactor Experiments*, Vol. I, International Atomic Energy Agency, Vienna, 1962.

EVALUATION OF MSRE GRAPHITE

W. H. Cook

We continued evaluation of the MSRE graphite, grade CGB. Although our tests were not part of the quality control required in the specification,[2] studies to determine the properties of graphite pertinent to molten-salt reactors are useful in determining the acceptability of the material for reactor use.

The bulk density of specimens from ten different bars ranged from 1.83 to 1.87 g/cm^3. Most specimens had a density of 1.86 g/cm^3, which is slightly higher than the 1.85 g/cm^3 indicated in initial tests.[3]

We determined the spectrum of the open-pore entrance diameters over the range from 100 to 0.02 μ. The accessible porosity was 9.6% of the bulk volume of the small specimens, and more than 96% of the accessible porosity had pore-entrance diameters smaller than 0.2 μ. If the MSRE graphite had no cracks, a pressure of about 600 psia would be necessary to force the nonwetting molten fuel salt into 0.5% of the bulk volume of the graphite, the design limit for the MSRE.

The average accessible porosity for the MSRE core bars appears to be about 4.0%, which is lower than the 9.6% value reported above for the small specimens used in the determination of the spectrum of pore-entrance diameters. Apparently, not all of the pore channels in the graphite are continuous, so if specimen dimensions exceed certain values, some interior pore channels become inaccessible. This has been demonstrated in tests

[2]*Tentative Specification for Graphite Bar for Nuclear Reactors*, MET-RM-1 (May 10, 1961).

[3]W. H. Cook, *Metals and Ceramics Div. Ann. Progr. Rept. May 31, 1963*, ORNL-3470, pp. 165–67.

in which a graphite-wetting fluid, xylene, was used to measure accessible volumes of transverse sections machined from full-sized MSRE core bars and smaller specimens machined from these sections. Therefore, if for any reason the fluoride salt wetted and penetrated the accessible voids of the graphite, relatively little fuel salt would be taken up.

The small pore-entrance diameters and the relatively small accessible porosity of the MSRE graphite are attained through a unique microstructure.[4] This is unusual in that nearly all of the voids in the base stock have been filled through a series of impregnations and heat treatments.

Lattice constants, measured[4] on samples from the graphite, were a_0, 2.464 A and c_0, 6.746 A. The x-ray pattern also indicated a well-graphitized material with a small amount of amorphous material.

Previous measurements[3] of the oxygen concentration in random samples of the core graphite had averaged about 20 ppm. Recently, we measured another set of random samples of the core graphite to determine if oxygen contamination had increased during the interim period. The average value was about 10 ppm O, which is within the normal variation and is still well below the 115 ppm maximum permitted by the specification.

Supporting and retaining graphite bars are used in the reactor at the bottom and around the top of the graphite core bars. Since these serve as part of the support assembly, they must have high structural integrity. Therefore, these were fabricated with a higher permeation than were the core bars, to minimize the cracks common to the core bars.[5] Radiographic examination of several of these bars showed that some had no detectable cracks and the others had only a few short tight ones.[4] These bars contained approximately 40 ppm O, about twice the highest value reported above for the low-permeability core bars. The total surface area of specimens from both kinds of bars was essentially the same. The reason for the higher oxygen content in the more permeable graphite bars has not been determined, but the value is still well within the maximum permitted by the specification.

The thermal conductivity and the effects of irradiation on physical properties and creep of CGB graphite are reported in Chap. 25 of this report.

MSRE HEAT EXCHANGER FABRICATION

R. G. Donnelly

To reduce the pressure drop through the shell side of the MSRE primary heat exchanger,[6] Reactor Division personnel decided that four outer U-tubes from the tube bundle should be removed. Since these were removed by cutting the INOR-8 tubes at the barrier plates, the resultant eight tube stubs had to be sealed.

We designed a tube plug and developed seal-welding procedures for this application. Also, a welder was specially qualified on sample welds of this joint design. The tapered plugs were machined to an interference fit, each being 0.0002 in. greater in diameter than the inside diameter of the tube stub. The design provided an edge-type fusion weld between the plug and the tube-stub end. Metallographic examination of sample welds showed an even weld contour and satisfactory penetration. Since the plug fitted very tightly in the tube, no root cracks were detected in any of the 30 samples welded.

Although the actual gas tungsten-arc welding was complicated by the close proximity of adjacent tubes, the welds were of excellent quality as revealed by dye-penetrant and radiographic inspection. The unit will be rewelded inside its pressure shell for insertion into the MSRE system.

MECHANICAL PROPERTIES OF INOR-8 WELDS

R. G. Gilliland J. T. Venard

We are learning more about the general weldability of INOR-8, in particular about the mechanical properties of welds in MSRE-approved heats of material. Several of these heats were welded under conditions of high restraint, and specimens were machined transverse to the welds. These were then tensile tested in the as-welded condition

[4]R. B. Briggs *et al.*, *MSR Program Semiann. Progr. Rept. Jan. 31, 1964*, ORNL-3626, pp. 67–70.

[5]R. B. Briggs *et al.*, *MSR Program Semiann. Progr. Rept. Jan. 31, 1963*, ORNL-3419, pp. 70–71.

[6]R. G. Donnelly and G. M. Slaughter, *Welding J.* 43(2), 118–24 (1964).

Table 27.1. Room- and Elevated-Temperature Tensile Properties of INOR-8 Transverse Weld Specimens in the As-Welded and Stress-Relieved Conditions

Test Temperature (°F)	Tensile Strength (psi)		Yield Strength (psi)		Elongation in 1½ in. (%)		Reduction in Area (%)	
	As-Welded	Stress-Relieved	As-Welded	Stress-Relieved	As-Welded	Stress-Relieved	As-Welded	Stress-Relieved
Room	102,000	93,800	65,400	44,200	23	21	35	21
600	91,200	88,900	54,800	42,600	24	25	38	34
800	88,600	85,400	52,900	44,400	24	27	28	24
1000	82,600	85,400	48,100	39,400	22	32	37	34
1200	71,200	73,100	46,800	39,400	14	24	28	27
1400	59,900	60,000	43,700	36,900	9	14	15	15
1600	38,400	40,000	36,800	34,800	9	14	5	12
1800	21,700	22,000	21,300	21,600	18	13	13	15

and after stress relief (2 hr at 1600°F in hydrogen), and the results are presented in Table 27.1.

The thermal treatment appears to have lowered the tensile strength at the lower testing temperatures but left that at the higher temperatures unchanged. The yield strength was lowered at nearly all testing temperatures. Ductility at room temperature has been lowered but not at elevated temperatures. In the as-welded tests, failures occurred in the weld area. However, since stress-relieving either embrittled the base metal or strengthened the weld, failures generally occurred in the base metal of stress-relieved specimens. Although the ductility shows a minimum in the 1400 to 1600°F temperature range, the strength appears to decrease with increasing test temperature.

We are testing this material further, including investigation of base-metal hot ductility and the determination of stress-rupture properties of transverse weld specimens.

MECHANICAL PROPERTIES OF INOR-8 IRRADIATED AT ELEVATED TEMPERATURES

W. R. Martin

Subsize tensile specimens of INOR-8 (heat 5081) have been irradiated in the B-8 lattice position of the ORR. The specimens were solid-solution heat treated at 1175°C and then irradiated at 700°C for approximately 2000 hr to doses from 5 to 12×10^{20} neutrons/cm^2 (fast and thermal).

The tensile properties of the irradiated and the unirradiated alloys, given similar thermal histories, are compared in Table 27.2 for several deformation temperatures at one strain rate (0.02/min). No significant differences in the yield stress were observed except slight ones at 300 and 400°C. However, irradiation markedly reduced the ultimate and true tensile stresses for deformation temperatures of 600°C and above. Irradiation reduced the elevated-temperature ductility, as measured by the fracture strain, uniform strain, and total elongation.

The influence of strain rate at elevated temperatures is shown in Table 27.3. The effect of irradiation increases with decreasing strain rate. Figure 27.1 indicates that the effect of irradiation on the uniform elongation and true fracture strain may reach a maximum at a temperature that is sensitive to the strain rate.

We investigated the effect of postirradiation annealing on the elevated-temperature embrittlement. Numerous investigations have shown that postirradiation heat treatments in the range 950 to 1100°C anneal the damage that causes embrittlement of stainless steel irradiated and tensile tested at 20 to 100°C. We heat treated irradiated INOR-8 samples 45 min at 1175°C prior to testing at 700 and 900°C. The properties of the irradiated

Table 27.2. Tensile Strength and Ductility of Irradiated and Unirradiated INOR-8 (Heat 5081)

Deformation Temperature (°C)	Stress (psi)				Ductility (%)			
	Yield Strength		True Tensile Strength		True Uniform Strain		True Fracture Strain	
	Irradiated	Unirradiated	Irradiated	Unirradiated	Irradiated	Unirradiated	Irradiated	Unirradiated
	$\times 10^3$	$\times 10^3$	$\times 10^3$	$\times 10^3$				
Room	46.3	45.5	168.6	166.5	42.3	40.6	42.5	39.0
100	43.9	43.9	159.5	161.0	40.1	40.3	44.6	37.2
200	38.4	40.7	150.6	157.5	40.3	41.9	42.5	50.7
300	36.0	40.7	154.3	147.0	42.2	37.9	44.6	41.4
400	35.0	40.7	146.9	153.0	40.2	39.3	42.5	46.9
500	35.8	35.8	129.5	144.0	35.3	42.4		
600	32.5	36.2	82.4	109.0	11.8	26.7	21.9	31.6
700	31.0	34.1	53.4	102.8	8.0	30.8	11.6	42.1
800	28.5	30.9	38.4	59.9	3.7	12.2	6.9	86.6

Table 27.3. Strain Rate Sensitivity of Irradiated and Unirradiated INOR-8 (Heat 5081)

Deformation Temperature (°C)	Strain Rate (min^{-1})	Stress (psi)				Ductility (%)			
		Yield Strength		True Tensile Strength		True Uniform Strain		True Fracture Strain	
		Irradiated	Unirradiated	Irradiated	Unirradiated	Irradiated	Unirradiated	Irradiated	Unirradiated
		$\times 10^3$	$\times 10^3$	$\times 10^3$	$\times 10^3$				
500	0.2	32.7	34.9	136.1	145.6	41.2	42.3	46.6	53.4
500	0.02	35.8	35.8	129.5	144.0	35.3	42.4		51.4
500	0.002	34.4	37.4	122.5	131.5	32.3	33.3	36.5	34.2
600	0.2	32.9	34.1	112.7	134.4	31.2	38.9	36.5	48.7
600	0.02	32.5	36.2	82.4	109.0	17.7	26.7	21.9	31.6
600	0.002	34.2	34.6	63.1	106.0	10.3	29.9	13.2	29.7
700	0.2	30.5	30.9	66.8	106.5	13.5	32.2	19.2	39.2
700	0.02	31.0	34.1	53.4	102.8	8.0	30.8	11.6	42.1
700	0.002	32.1	33.7	47.0	80.5	5.6	20.0	7.8	29.0
800	0.2	29.3	29.3	45.7	79.8	6.7		11.6	
800	0.02	28.5	30.9	38.4	59.9	3.7	12.2	6.9	86.6
800	0.002	29.3	32.5	32.2	42.9	1.8	6.5	4.9	93.7

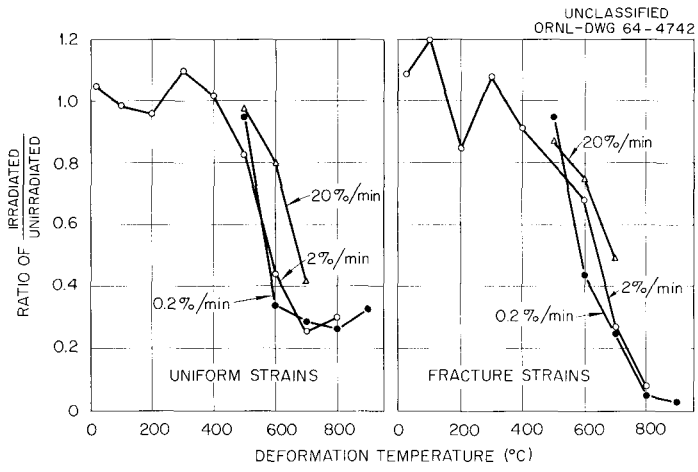

Fig. 27.1. Effect of Irradiation on the Ductility of INOR-8 as a Function of Strain Rate and Deformation Temperature.

alloy with and without the postirradiation heat treatment are compared in Table 27.4. The stability of the irradiation-induced defect that causes poorer properties at elevated temperatures is remarkable.

The effects of irradiation at the lower and upper limits of neutron exposure given the INOR-8 are compared in Table 27.5. We believe the differences in these data, obtained at 700°C and a strain rate of 0.002/min, are insignificant.

In summary, the ductility of unirradiated INOR-8 is low at deformation temperatures of 800 and 900°C. The low uniform elongations decrease with decreasing strain rate. The decrease in uniform strain is accompanied by a large increase in fracture strain and a reduction in true fracture stress. The alloy appears to work-soften at or above a specific elevated temperature that is sensitive to the strain rate.

Irradiation at elevated temperatures affects only the mechanical properties of INOR-8 measured at temperatures in excess of 600°C. The magnitude of the effect increases with decreasing strain rate. The effect is primarily a decrease in ductility. However, the ultimate engineering stress and the true tensile stress are markedly reduced for those deformation temperatures at which the work-hardening coefficient of the alloy is high.

Table 27.4. Influence of Postirradiation Heat Treatment on the Tensile Properties[a] of INOR-8

Deformation Temperature (°C)	Postirradiation Heat Treatment	Yield Stress (psi)	Tensile Strength (psi)		Elongation Measured in 1 in. (%)	
			Ultimate	True	Uniform	Total
		$\times 10^3$	$\times 10^3$	$\times 10^3$		
700	None	32.1	44.3	47.0	5.8	6.1
700	1 hr at 1175°C	30.5	41.5	44.2	6.3	6.4
900	None	23.2	23.2	23.3	0.4	~0.4
900	1 hr at 1175°C	23.5	23.5	23.6	0.6	0.7

[a]Measured at a strain rate of 0.002/min.

Table 27.5. Effect of Neutron Dose on Tensile Properties of Irradiated INOR-8

Neutron Dose (neutrons/cm^2)		Yield Stress (psi)	Ultimate Strength (psi)	True Tensile Strength (psi)	Elongation (%)	
Fast	Thermal				Uniform	Total
5×10^{20}	6×10^{20}	33,300	44,000	46,000	4.5	4.7
1.2×10^{21}	1.2×10^{21}	32,100	44,300	47,000	5.8	6.1

MECHANICAL PROPERTIES OF INOR-8

J. T. Venard

Tensile properties of two heats of INOR-8 MSRE plate and stress-rupture data on a third heat were reported previously.[7] At that time, we pointed out that tensile properties of neither heat 5075 nor 5081 differed between specimens taken parallel or transverse to the plate rolling direction. Also, heat 5075 was somewhat less ductile than heat 5081 in the temperature range 590 to 870°C.

Figure 27.2 shows that the creep behavior of the three heats was quite similar. Heat 5075, however, exhibited a lower rupture strength, as is seen in Fig. 27.3. In stress-rupture tests, as in the tensile tests, heat 5075 was less ductile. For example, at 704°C the elongation at fracture for heat 5075 was 4 to 8%, compared with 16 to 50% for heats 5055 and 5081.

A detailed topical report giving the mechanical properties data on these three heats of MSRE material is in preparation.

[7] J. T. Venard and W. J. Leonard, *Metals and Ceramics Div. Ann. Progr. Rept. May 31, 1963*, ORNL-3470, pp. 162–63.

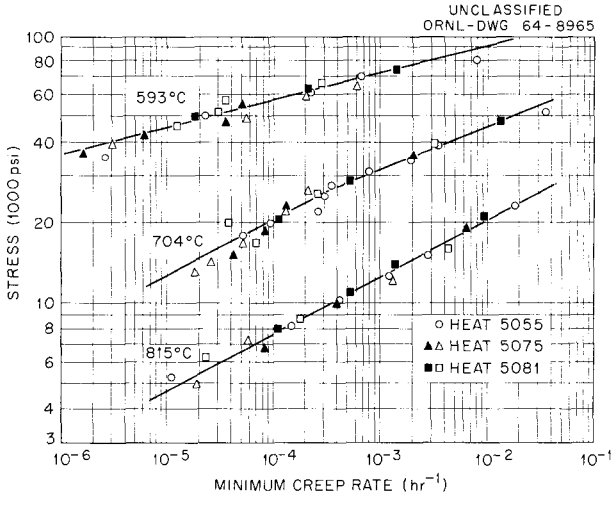

Fig. 27.2. Creep Rate in Air of INOR-8 MSRE Plate. Open symbols represent measurements parallel to the rolling direction and closed symbols transverse.

INFLUENCE OF HEAT TREATMENT ON THE TENSILE PROPERTIES[8] OF INOR-8

H. E. McCoy

The tensile properties of INOR-8 (Hastelloy N) have been evaluated after various heat treatments. Four air-melted heats and one vacuum-melted heat were studied. The vacuum-melted material exhibited good ductility after all heat treatments.

[8] H. E. McCoy, *Influence of Several Metallurgical Variables on the Tensile Properties of Hastelloy N*, ORNL-3661 (in press).

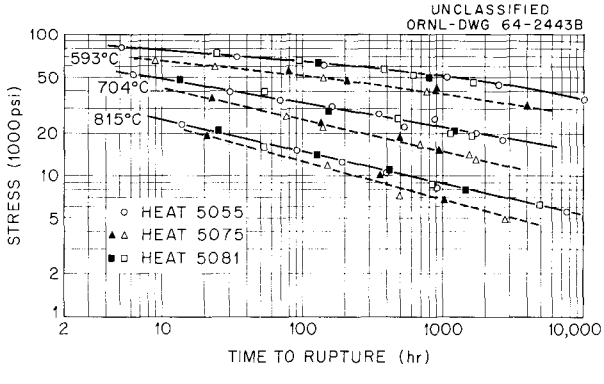

Fig. 27.3. Stress Rupture of INOR-8 MSRE Plate Tested in Air. Open symbols represent measurements parallel to the rolling direction and closed symbols transverse.

Annealing the air-melted material at temperatures in excess of 2150°F reduced significantly the minimum fracture strain exhibited by the alloy. Holding at temperatures of about 1600°F for an extended period recovered the fracture ductility. Aging material in the 1100 to 1200°F range that had been previously annealed at 2150°F reduced the ductility significantly but changed the tensile strength very little.

We believe we can explain these effects in terms of the formation of a brittle grain-boundary layer along which a crack can propagate easily at elevated temperatures. Breaking up the continuity of this layer by aging or cold working recovers good fracture ductility. The formation of this layer is associated with the presence of trace alloying elements.

POSTIRRADIATION METALLOGRAPHIC EXAMINATION OF MSRE IN-PILE TESTS

E. J. Manthos

During the past year, we have examined corrosion coupons from in-pile experiment ORNL-MTR-47-3 and capsule components from in-pile experiment ORNL-MTR-47-4.

Corrosion Coupons from In-Pile Experiment ORNL-MTR-47-3

In-pile experiment ORNL-MTR-47-3 consisted of four INOR-8 capsules that were irradiated[9] at temperatures ranging from 790 to 950°C. Each capsule contained one coupon each of INOR-8, molybdenum, and pyrolytic graphite in MSRE fuel salt. The coupons were clamped to a graphite blade and partially immersed in a static molten-salt fuel mixture. The blade material was R-0025 graphite in the two capsules with fuel at 835°C and AGOT graphite impregnated with fuel in the capsules with fuel at 850 and 945°C.

All four of the INOR-8 coupons carburized, as shown in Fig. 27.4. A precipitate had formed throughout all of the coupons and could not be identified by x-ray diffraction. Subsurface void formation was also seen on one surface and on one end of the coupons. We do not know which surface of the coupon had been in contact with the fuel.

As seen in Fig. 27.5, a reaction layer, probably a molybdenum carbide, formed on one surface of the two molybdenum coupons that had been irradiated at 810 and 900°C (fuel at 850 and 945°C). On the other side voids formed, and the surface was roughened. No reaction layer formed on the

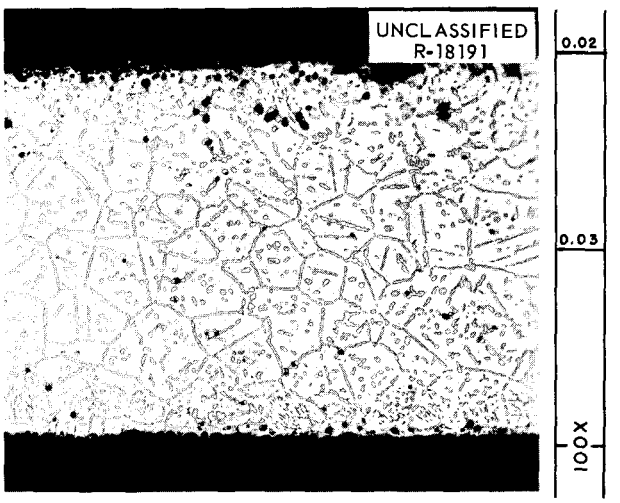

Fig. 27.4. Photomicrograph of INOR-8 Coupon from Capsule 3 of Experiment ORNL-MTR-47-3. One side of the coupon had been in contact with graphite and the entire coupon was carburized. Etchant: Aqua regia.

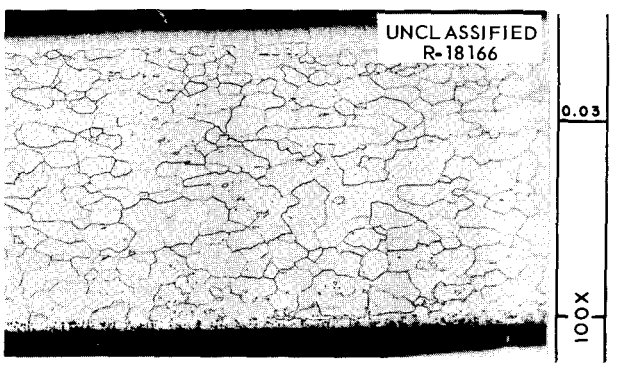

Fig. 27.5. Photomicrograph of Molybdenum Coupon from Capsule 3 of Experiment ORNL-MTR-47-3. A reaction layer, probably a molybdenum carbide, had formed on the surface that had been in contact with graphite. Etchant: Equal parts of 30% H_2O_2 and NH_4OH.

[9]R. B. Briggs *et al.*, *MSR Program Semiann. Progr. Rept. Feb. 28, 1962*, ORNL-3282, pp. 97–101.

other two molybdenum coupons at 790°C (835°C fuel), but the portions of the coupons that had been immersed in molten salt were partially dissolved.

The pyrolytic graphite coupons were apparently unaffected by the molten-salt mixture. We saw no salt permeation into the pyrolytic graphite, and the surfaces of the coupons were smooth.

In-Pile Experiment ORNL-MTR-47-4

Two types of capsules[10,11] were irradiated in ORNL-MTR-47-4. The larger (Nos. 24, 26, and 45) capsules consisted of an INOR-8 jacket that contained molten-salt fuel into which a graphite bullet had been inserted. The smaller capsules (such as No. 4), also of INOR-8, contained the molten-salt fuel in a graphite crucible.

Metallographic examination of the INOR-8 wall from capsule 24 has been reported.[12,13] Sections of the INOR-8 capsule wall from the fuel and vapor-phase regions of capsule 45 were examined metallographically and showed no evidence of corrosive attack or film formation.

Sections of the graphite from capsules 24, 36, and 45 were metallographically prepared under silicone oil. We saw no evidence of attack or permeation of the graphite by the salt mixture. The graphite from capsule 45 had been subjected to a vacuum heat treatment at 600, 800, and 1000°C in a stainless steel container.[14] After the heat treatment, a silvery deposit less than 0.001 in. deep had formed on the surface of the graphite (Fig. 27.6). The identity of the deposit is not known, but iron, nickel, or chromium may have volatilized from the stainless steel container and deposited on the graphite to form carbides. We autoradiographed the metallographic specimens by placing them in contact with a high-resolution, beta-sensitive film.[15] Typical results are shown in Fig. 27.7. A radioactive deposit was present on the outer circumference of the graphite; also, a faint trace of radioactivity was present on the

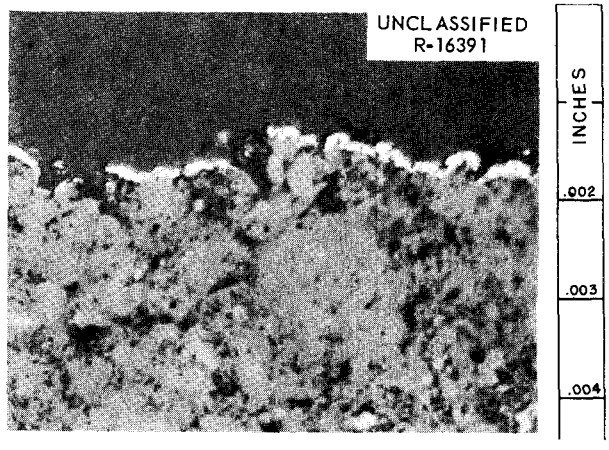

Fig. 27.6. Photomicrograph of Graphite from Capsule 45 of Experiment ORNL-MTR-47-4 Showing Silvery Deposit That Formed on Surface of Bullet. As polished.

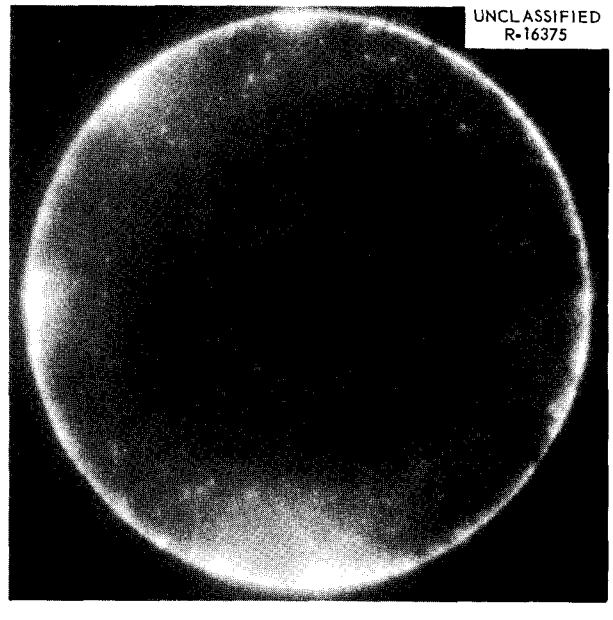

Fig. 27.7. Autoradiographs of Sections of Graphite from Experiment ORNL-MTR-47-4. A radioactive deposit had formed where the graphite had been in contact with molten fuel.

[10]R. B. Briggs *et al.*, *MSR Program Semiann. Progr. Rept. Feb. 28, 1962*, ORNL-3282, p. 111.

[11]R. B. Briggs *et al.*, *MSR Program Semiann. Progr. Rept. Aug. 31, 1962*, ORNL-3369, pp. 100–62.

[12]R. B. Briggs *et al.*, *MSR Program Semiann. Progr. Rept. Jan. 31, 1963*, ORNL-3419, pp. 84–86.

[13]E. J. Manthos, *Metals and Ceramics Div. Ann. Progr. Rept. May 31, 1963*, ORNL-3470, pp. 168–70.

[14]R. B. Briggs *et al.*, *MSR Program Semiann. Progr. Rept. July 31, 1963*, ORNL-3529, p. 81.

[15]Kodak Spectroscopic Safety Film, Type 649.

surface of the thermocouple wells. The deposit was not detected metallographically.[16] It may be uranium metal.

We saw no sign of reaction between the INOR-8 wall from capsule 4 and the graphite crucible. The graphite crucible wall was severely attacked in the vapor phase region (Fig. 27.8); the severity of attack decreased as the fuel level was approached. At the fuel level, the graphite was relatively unaffected. Since fluorine is evolved from the salt mixture during solidification after neutron irradiation, the graphite crucible wall above the solidified fuel was apparently attacked by the fluorine to form CF_4. Both fluorine and CF_4 were found in capsule 4 during postirradiation gas sampling.[17]

---

[16]R. B. Briggs *et al.*, *MSR Program Semiann. Progr. Rept. Jan. 31, 1964*, ORNL-3626, pp. 81–86.

[17]R. B. Briggs *et al.*, *MSR Program Semiann. Progr. Rept. Jan. 31, 1963*, ORNL-3419, pp. 80–84.

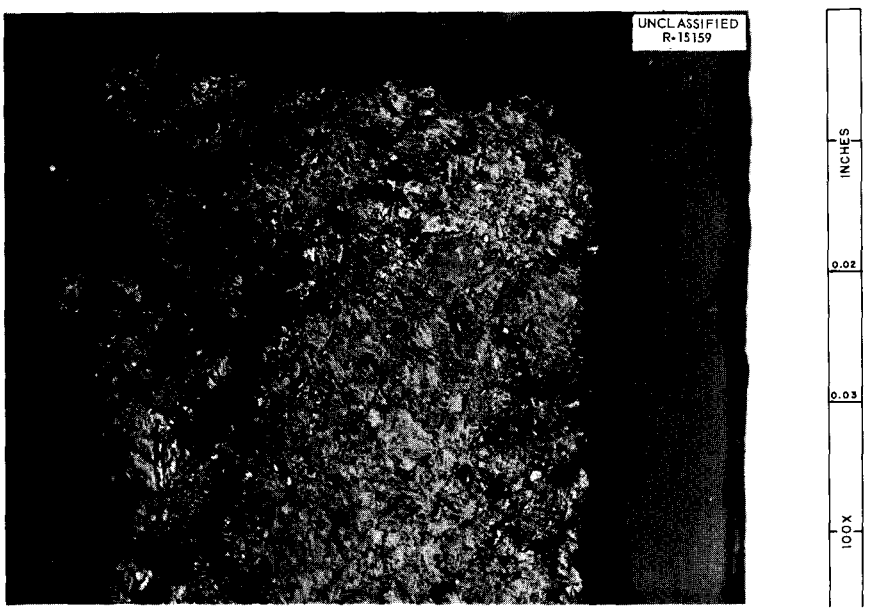

Fig. 27.8. Photomicrograph of Longitudinal Section of Graphite Crucible Wall at Top of Crucible in Vapor-Phase Region. Capsule 4 of experiment ORNL-MTR-47-4. As polished. Reduced 33%.

28. Space Power Program

W. C. Thurber

Our purpose is to provide materials support for the Medium Power Reactor Experiment. This reactor, currently being designed and developed at ORNL, is a single-loop Rankine-cycle system employing boiling potassium as the reactor coolant and thermodynamic working fluid. The reactor system, to be constructed of conventional materials, will operate in the 815 to 870°C temperature range to produce more than 100 kw of electricity to demonstrate its utility for space applications.

Support work has included fabrication of turbine-pump components, a calandria for physics experiments, and radiators for heat transfer experiments. Posttest metallurgical analyses have been performed on various components from experimental test rigs, and specifications and fabrication procedures for fuel elements have been developed. This work is discussed in detail elsewhere.[1,2] Research and development on high-temperature materials with potential space-power application are reported in Part II, Chaps. 14, 19, and 20 of this report.

TURBINE-PUMP FABRICATION

C. W. Fox

One component associated with liquid-metal reactor systems is a turbine pump with cermet bearings. The development of joining procedures for producing cermet-to-metal assemblies has been reported previously.[3] Two assemblies have been produced during this reporting period incorporating a revolution counter and certain design modifications to provide increased reliability for brazing.

Two impeller assemblies and two turbine wheels were successfully brazed in vacuum at 1120°C with a nickel-silicon-boron brazing alloy. Each Mo–0.5% Ti alloy impeller had three tungsten carbide bearings (two radial and one thrust) and a magnetic insert to serve as a revolution counter. Each turbine wheel had a thrust bearing. The brazed assemblies along with the accompanying sleeve-bearing assembly are shown in Fig. 28.1.

FABRICATION OF CALANDRIA FOR CRITICALITY EXPERIMENTS

C. W. Fox

A calandria assembly was fabricated for physics experiments to define potassium reactivity. We developed welding procedures and programmed the welding sequence so that a large number of closely spaced type 347 stainless steel tubes were welded to thin type 304 stainless steel header plates.[4] The completed assembly was reasonably leaktight in that it could be evacuated to 7×10^{-7} torr and required 14 min to leak to 1×10^{-3} torr. Consequently, we filled the unit with potassium without difficulty. The Neutron Physics Division completed the reactivity tests satisfactorily using this calandria.

STATOR BORE SEAL BRAZING

C. W. Fox

Aluminum oxide has been proposed as the stator bore seal in the electrical generators for Rankine-cycle nuclear electric power generation systems.

[1] W. C. Thurber, ORNL-3571, pp. 93–156 (May 1964) (classified).

[2] W. C. Thurber, ORNL-3683 (in press) (classified).

[3] C. W. Fox, *Metals and Ceramics Div. Ann. Progr. Rept., May 31, 1963*, ORNL-3470, pp. 193–94.

[4] C. W. Fox, ORNL-TM-779 (March 1964) (classified).

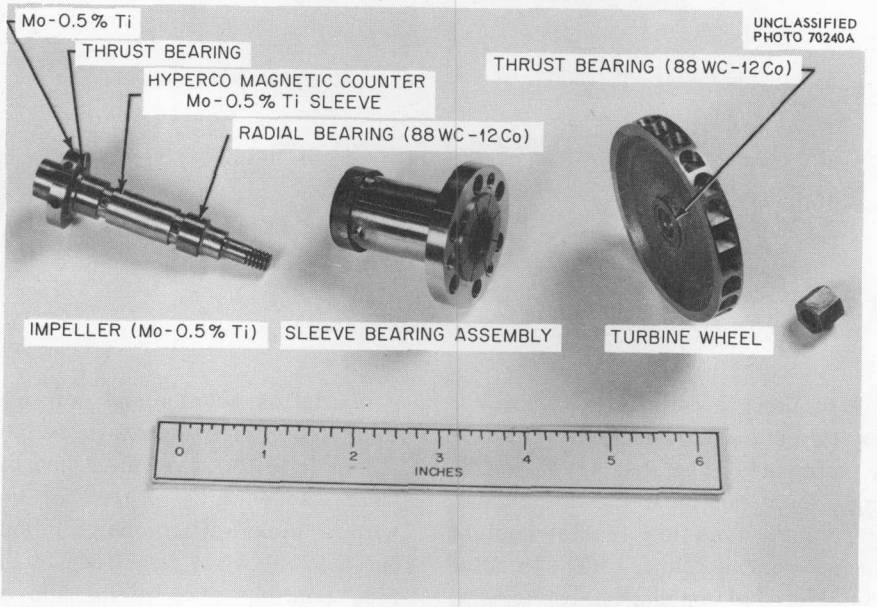

Fig. 28.1. Turbine-Pump Assembly Showing Impeller, Sleeve Bearing, and Turbine Wheel. The tungsten carbide was brazed to Mo–0.5% Ti with a nickel–silicon–boron alloy at 1120°C and 1×10^{-5} torr.

A major area of concern is that of joining a large (approximately 10-in.-diam) ceramic cylinder to the metal supporting structure. The metals of major interest are Nb–1% Zr alloy and a commercially produced nickel-iron-cobalt alloy (Ceramvar) that was developed specifically to have an expansion coefficient near that of aluminum oxide.

A series of general studies has been conducted to accumulate basic information that will in turn permit a realistic evaluation of the problem. We tested wetting by various brazing alloys and produced joints between aluminum oxide and the metals of interest. In general, the niobium alloy appeared more suitable for joining to the ceramic, although sound brazes could be made with both alloys. To further evaluate these joints, a series of small specimens was prepared, encapsulated in quartz tubing under vacuum, and cycled 20 times from ambient to 550°C. The results are shown in Table 28.1. The aluminum oxide was cracked with severity differing among the eight specimens. This cracking suggests that joint design should be of primary concern in the use of such a seal for cyclic service at elevated temperature. This modest study of ceramic-joining techniques is continuing.

FABRICATION OF HEAT TRANSFER EQUIPMENT

E. A. Franco-Ferreira

A large 144-tube finned radiator was fabricated under our supervision for fluid heat transfer studies to be conducted by the Reactor Division. The general design of this unit was similar to that of one reported previously.[5]

The high-conductivity fins were attached to the 7-ft-long tapered tubes of the radiator by an outside vendor, who used a combination of spot welding and furnace brazing. All component parts of the unit were then welded together by ORNL shop personnel. All procedures used for the fabrication of this radiator had been qualified on earlier units and detailed elsewhere.[6]

---

[5]E. A. Franco-Ferreira, *Metals and Ceramics Div. Ann. Progr. Rept., May 31, 1963*, ORNL-3470, pp. 194–95.

[6]E. A. Franco-Ferreira, *Fabrication of Radiators for Boiling Heat-Transfer Experiments*, ORNL-TM-602 (Aug. 23, 1963).

Table 28.1. Results of Thermal Cycling Tests[a] on Al_2O_3-to-Metal Joints

Combination Al_2O_3 to –	Brazing Alloy (wt %)	Flow Point (°C)	Metallographic Observations
Ceramvar	Ni-clad Ti	1040	Cracking in braze alloy and Al_2O_3.
Ceramvar	80 Zr–17 Fe–3 Be	1050	Cracking in braze alloy and Al_2O_3.
Ceramvar	49 Ti–49 Cu–2 Be	980	No cracking in braze alloy. Cracking in Al_2O_3.
Ceramvar	68 Ti–28 Ag–4 Be	1030	Slight erosion of base metal by brazing alloy. No cracking in braze alloy. Cracking in Al_2O_3.
Nb–1% Zr	Ni-clad Ti	1040	No cracking in braze alloy. Cracking in Al_2O_3.
Nb–1% Zr	80 Zr–17 Fe–3 Be	1050	No cracking in braze alloy. Cracking in Al_2O_3.
Nb–1% Zr	49 Ti–49 Cu–2 Be	980	Cracking in braze alloy and Al_2O_3.
Nb–1% Zr	68 Ti–28 Ag–4 Be	1030	No cracking in braze alloy. Cracking in Al_2O_3.

[a]Twenty cycles from room temperature to 550°C.

29. Thorium Utilization Program

D. A. Douglas

Simplification and cost reduction of the fuel cycle as it pertains to bred fuels has been the aim for several years of a joint effort with the Chemical Technology Division. The Th-^{233}U cycle with oxide fuel has received the major attention and we are comprehensively developing processes and equipment. Our work is in three parts: process development, engineering development and demonstration, and product evaluation or irradiation testing.

A major accomplishment of the Chemical Technology Division during the past year was the development of a process to produce nearly perfect uranium and thorium oxide spheres to any specified size between 10 and 1000 μ. Along with this, we have developed new processes for applying pyrolytically deposited carbon coatings at markedly reduced costs and demonstrated that these coatings are compatible with the oxide particles.

We successfully completed the remote fabrication of 1100 fuel pins in the Kilorod Facility, culminating a 2-year effort of process and equipment development. Our experience is being used to develop the remote fabrication equipment to be installed in the Thorium-Uranium Fuel Cycle Development Facility that we are designing.

Also, we are evaluating the results of irradiation tests on bulk oxides, with emphasis on the sol-gel produced oxide, and studying the mechanisms by which fission gas is released from ceramic fuels.

OPERATION OF A Th-^{233}U FUEL ROD FABRICATION FACILITY

J. E. Van Cleve, Jr. A. L. Lotts

A lightly shielded facility[1] (4 in. steel) for fabrication of fuel rods containing low-activity ^{233}U and thorium commenced operation with ^{233}U in June 1963. The facility completed its first objective of remotely fabricating 1100 fuel pins of two lengths containing (Th–3% ^{233}U)O_2 in April 1964. A schematic sketch of the longer fuel pin is shown in Fig. 29.1. The shorter pins have an 18-in. fuel length and are otherwise identical with the longer ones. The fuel rods are now being used in criticality experiments at Brookhaven National Laboratory (BNL).

[1] J. D. Sease and J. E. Van Cleve, Jr., *Metals and Ceramics Div. Ann. Progr. Rept. May 31, 1963*, ORNL-3470, pp. 196–98.

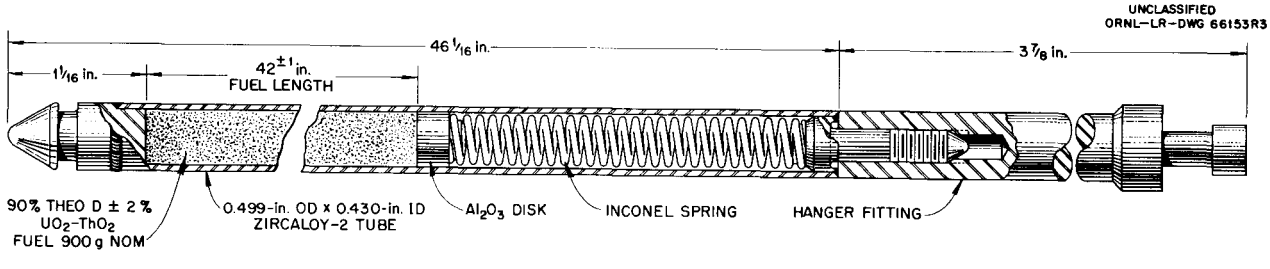

Fig. 29.1. Remotely Fabricated Th-^{233}U Oxide Fuel Rod.

The ^{233}U contained 37 ppm ^{232}U and thus required gamma shielding as well as alpha containment. Thus, the fabrication of these fuel rods has served as an excellent vehicle for demonstration of semiremote operation of a process that could be applied to refabrication of power reactor fuels. Valuable engineering and operational data were collected during the program, and these are already being applied to the design of equipment for the Thorium-Uranium Fuel Cycle Development Facility.

The fabrication process, which started with the delivery of bulk oxide to the rod fabrication facility, consisted of comminution, screening, and blending of sol-gel uranium-thorium oxide, vibratory compaction of the oxide in cladding tubes, end capping of the tubes, and inspection of the fuel rods.

The fuel rods were specified to be loaded to 90 ± 2% of theoretical density with not greater than 2% variation in density along their length as determined by gamma-scanning with a $\frac{1}{8} \times \frac{3}{8}$-in. beam. The 900 long fuel rods averaged 89.6% and the 200 short rods 90.4% of theoretical density, both with a range of 88 to 92%. To meet the required density profile, 8% of the rods required recycling between the vibratory-compaction step and the gamma-scanning step. No fuel rods were rejected because of unsatisfactory welds, as determined by helium leak testing. Surface contamination on completed fuel rods averaged approximately 500 dis min^{-1} cm^{-2} within the specified maximum of 2000 dis min^{-1} cm^{-2} transferable contamination.

The facility was operated in campaigns of 120 fuel rods each. At the end of each campaign, a material balance was made and the results of the campaign were assessed. Detailed preventive maintenance was accomplished and the facility was prepared for the next campaign. The facility required four operators and one operating supervisor for normal operation.

Before operations with ^{233}U, the final procedures to be used were determined by "cold" fabrication of fuel pins with thorium oxide containing depleted UO_2.

In the first operation powders were classified into three size fractions and later into only two. This change was for two reasons: (1) the binary powder could be compacted to a density as high as that produced from the ternary, and (2) the binary distribution was easier to produce, especially in the remote system. Determined from the cold operation, the optimum binary powder was 55% classified −6 +16 mesh and 45% of an unclassified fraction that was essentially half −50 +140 mesh and half −140 mesh and was produced with controlled charge and milling time.

Also as part of the cold runs, final equipment adjustments were made. In spite of these measures, during the first pilot hot runs (i.e., with ^{233}U), considerable difficulty was experienced with meeting fuel-rod specifications and with equipment failures. The remote ball mill and the pneumatic vibratory compactor gave the most trouble. After we corrected a number of design deficiencies, the operations became more routine. In the later campaigns, the facility performed at rated capacity.

During the first campaign, equipment on-stream time averaged about 30% and the facility operated at only 16% of its ultimate capability of 15.5 rods per day. During the last five campaigns, equipment on-stream time averaged 74% and the facility operated at from 51 to 62% of the ultimate capability. We conclude that when staffed with properly trained personnel, the facility in its present state can be operated for an extended period at a capacity of 15 rods per day with an on-stream time of 70%.

In the processing of approximately 1 metric ton of fuel, 89.5% of the fuel was loaded into acceptable fuel rods. Unrecoverable process losses accounted for 0.33%, 5.4% was returned for chemical processing because of spillage and consequent contamination by extraneous material, and analytical samples consumed 4.7%.

In summary, the feasibility of semiremote fabrication of fuel rods containing Th-^{233}U oxide has been demonstrated. Sustained production at the design rate has been attained, and the engineering of both facility and equipment has been proved.

Th-^{233}U PELLET FABRICATION

J. D. Sease A. J. Taylor

Approximately 300 close-tolerance (Th–3% $^{233}U)O_2$ pellets, 0.4251 in. in diam by $\frac{3}{8}$ in. long, were required for ^{233}U criticality experiments at BNL. Unfortunately, the fabrication is complicated by alpha and penetrating radiation associated

with ^{233}U. However, the quantity of oxide handled was small enough to permit the use of gloved fabrication techniques with controlled personal radiation doses. The procedure developed for the fabrication of the pellets is shown in Fig. 29.2.

All of the fabrication operations are accomplished in two alpha-tight glove boxes. The powder is prepared and pressed in a 6-ft-long glove box and sintered in a 3-ft glove box. We have procured all of the equipment for the fabrication line and checked out the equipment, and currently the line is operating in an alpha facility.

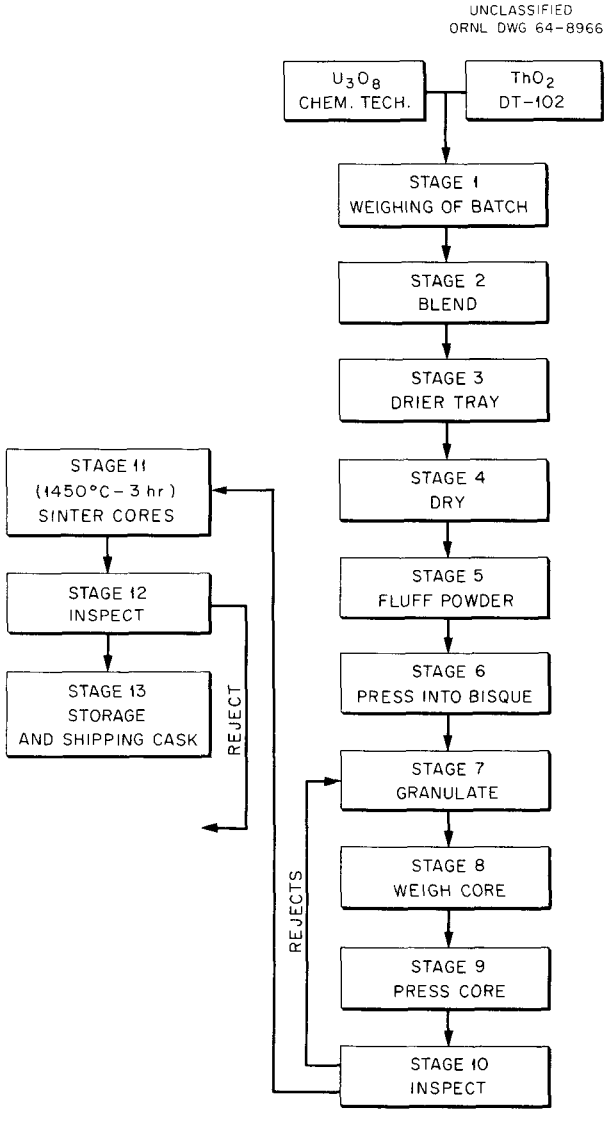

Fig. 29.2. Flow Sheet for Fabrication of Th-^{233}U Oxide Pellets.

THORIUM-URANIUM FUEL CYCLE DEVELOPMENT FACILITY

Development of the thorium fuel cycle must include an economic analysis of various fuel element reprocessing and fabrication techniques at pilot production levels. Since an economic advantage appears to result from reducing the amount of decontamination in reprocessing and because the decay of ^{232}U builds up activity in reprocessed fuels, a heavily shielded facility is desired for development and economic evaluation of a variety of integrated fuel reprocessing and fabrication schemes. The Thorium-Uranium Fuel Cycle Development Facility will be constructed to fulfill this need.

Title I design of the facility was completed in December 1963. Title II design is currently progressing and is expected to be completed in October 1964. The design of the facility is essentially the same as that previously reported.[2,3]

Building

R. A. Irvin[4] A. L. Lotts
A. R. Olsen

The facility will be located in the Melton Valley area near the Transuranium Processing Plant and the High Flux Isotope Reactor. The building will be irregular in shape, three stories in height, and approximately 124 ft wide by 162 ft long. The structure contains chemical processing, mechanical processing, contaminated fabrication, and clean fabrication cells (Fig. 29.3).

The first floor provides space for offices, cell-operating area, a receiving area, and change rooms. The second floor provides space for mechanical and electrical equipment, chemical makeup, a development laboratory, a warm shop, and a maintenance operating area. The third floor is a high-bay area equipped with a 50-ton crane for cell

[2]A. R. Irvine and A. L. Lotts, *Metals and Ceramics Div. Ann. Progr. Rept. May 31, 1963*, ORNL-3470, pp. 198–201.

[3]A. R. Irvine and A. L. Lotts, "The Thorium Fuel Cycle Development Facility Conceptual Design," pp. 333–50 in *Proceedings of Thorium Fuel Cycle Symposium, Gatlinburg, Tennessee, December 5–7, 1962*, TID-7650, bk 1 (July 1963).

[4]Chemical Technology Division.

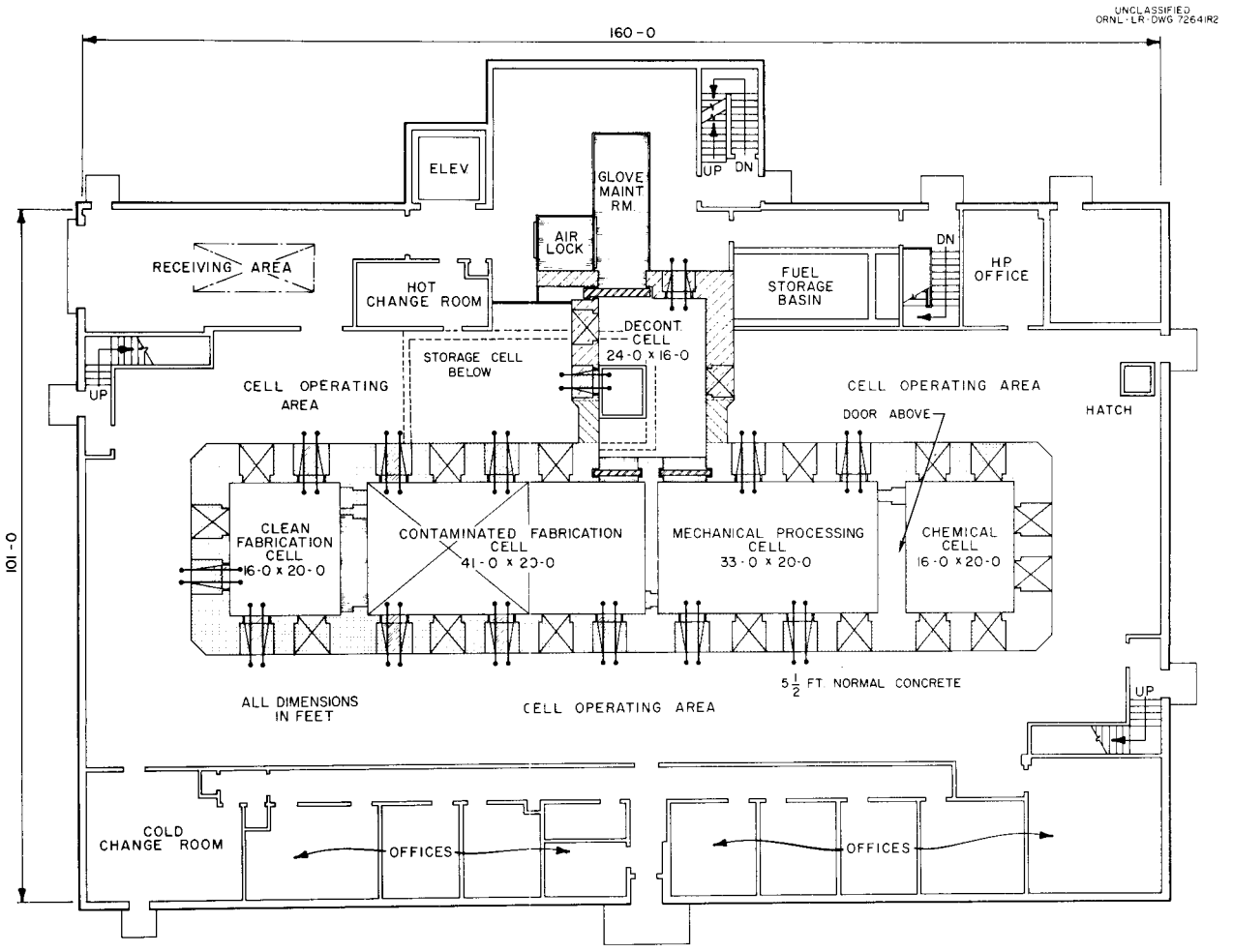

Fig. 29.3. First Floor Plan of Thorium-Uranium Fuel Cycle Development Facility.

entry and service. Four of the cells provide operating space for the process equipment. Two additional cells provide support functions for the cells.

The mechanical processing and the contaminated fabrication cells are designed for remote maintenance, the chemical processing cell is designed for either direct or remote maintenance, and the clean fabrication cell is designed for direct maintenance.

The cells are capable of use for processing and refabricating fuel assemblies as long as 12 ft and containing as much as 35 kg of thorium-uranium fuel irradiated to 25,000 Mwd/tonne and decayed for 90 days. They are equipped with a modular arrangement of windows and master-slave manipulators. Additional in-cell manipulation is provided by bridge cranes and electromechanical manipulators mounted on bridges. We are currently preparing specifications for this equipment. A cell mockup is being designed for evaluating building and process equipment details.

Oxide-Fabrication Equipment

R. B. Pratt J. D. Sease
A. L. Lotts

We are developing[5] fabrication equipment to demonstrate, on a pilot plant scale in the Thorium-Uranium Fuel Cycle Development Facility, the technical and economic feasibility of remote fabrication and assembly of rod-cluster fuel elements

[5]A. L. Lotts, *Metals and Ceramics Div. Ann. Progr. Rept. May 31, 1963*, ORNL-3470, pp. 201–202.

containing (Th-^{233}U)O_2. The method that has been selected for fabrication of these elements is to vibratorily compact bulk oxide into stainless steel or Zircaloy-2 tubes and then to mechanically assemble the rods into a fuel element bundle. We intend that the machinery for this process be very flexible and capable of scaling to larger capacities.

The fabrication and inspection equipment is to be capable of processing fuel rods 2 to 10 ft long and $\frac{1}{4}$ to $\frac{3}{4}$ in. in diameter. A slightly modified Elk River Reactor fuel element (Fig. 29.4) was recently chosen as the design reference for the assembly equipment. All equipment has been conceptually designed, and preliminary design and development is currently progressing.

As shown in Fig. 29.5, the selected fabrication procedure consists of (1) sizing of the sol-gel oxide, (2) vibratory compaction of fuel rods, (3) welding and inspection of fuel rod end caps, (4) fuel rod decontamination, (5) assembly of fuel rods into fuel elements, and (6) final inspection.

Fabrication operations that involve direct contact with the fuel material are done in the contaminated fabrication cell of the TUFCDF, as shown in the equipment layout (Fig. 29.6). Operations that are done after the fuel material is sealed in fuel rods are done in the clean fabrication cell. Powder-preparation and fabrication equipment is designed to process 40 kg of fuel material per 8-hr day.

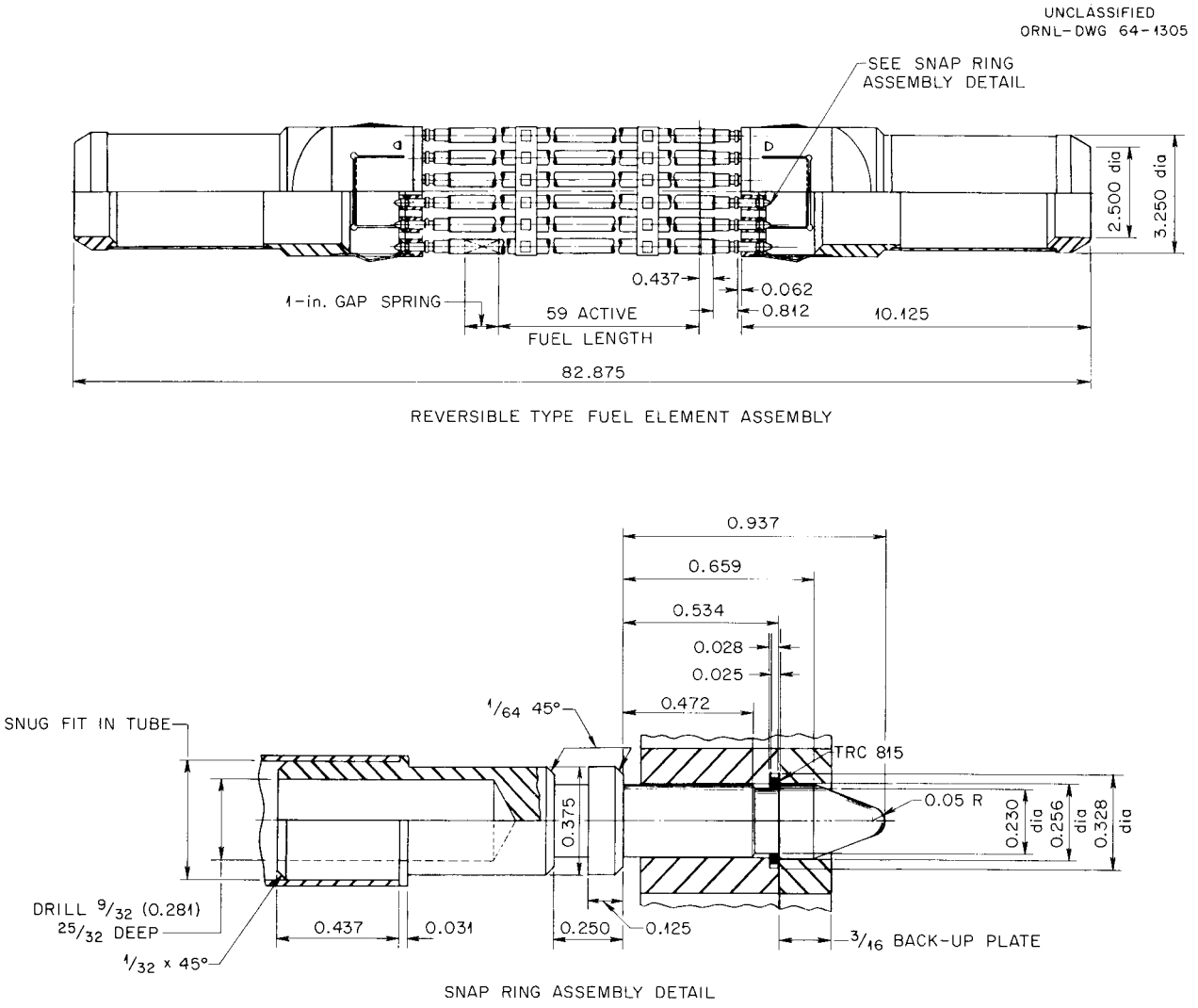

Fig. 29.4. Elk River Reactor Fuel Element.

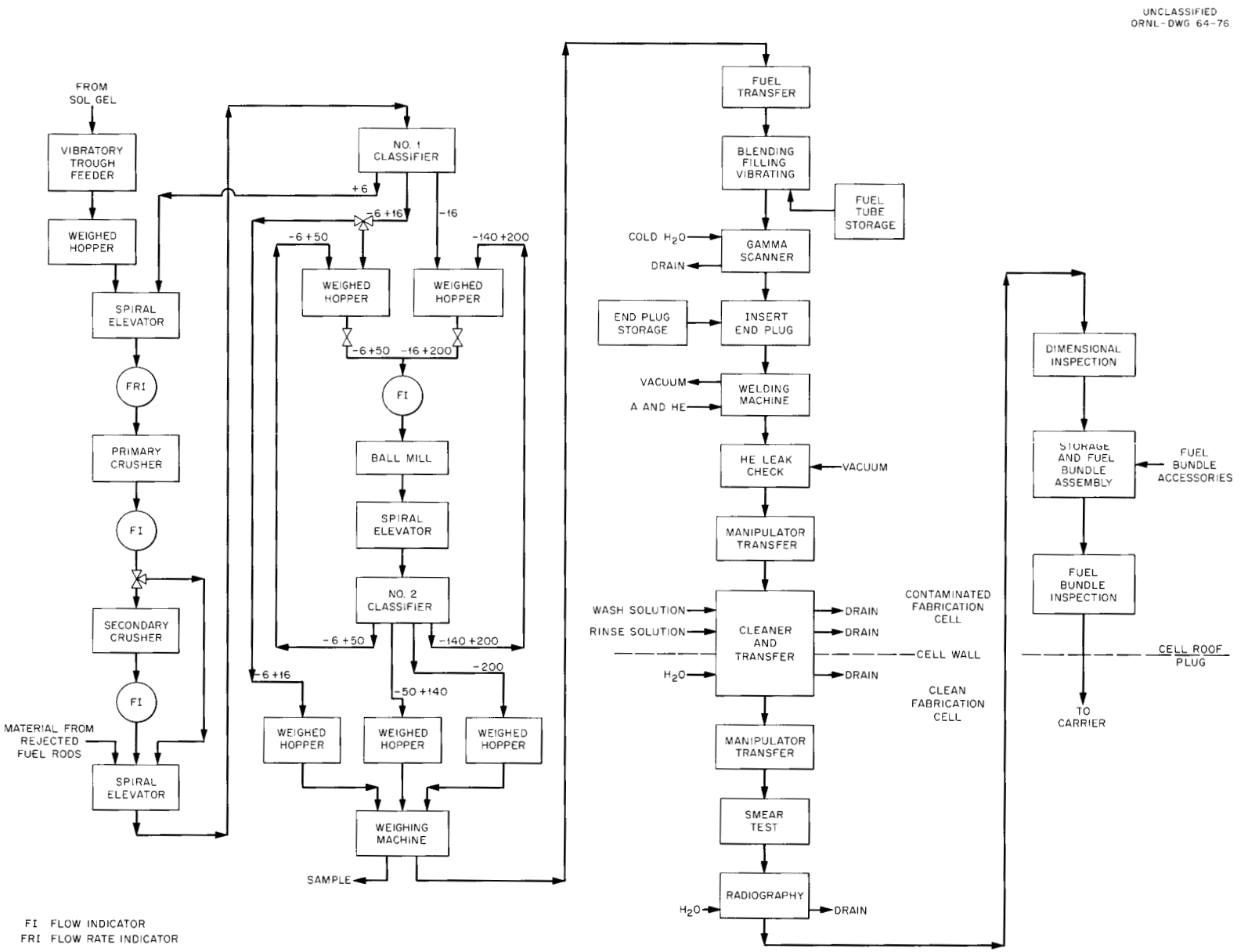

Fig. 29.5. Flow Sheet for Fabrication of Oxide Fuel Elements.

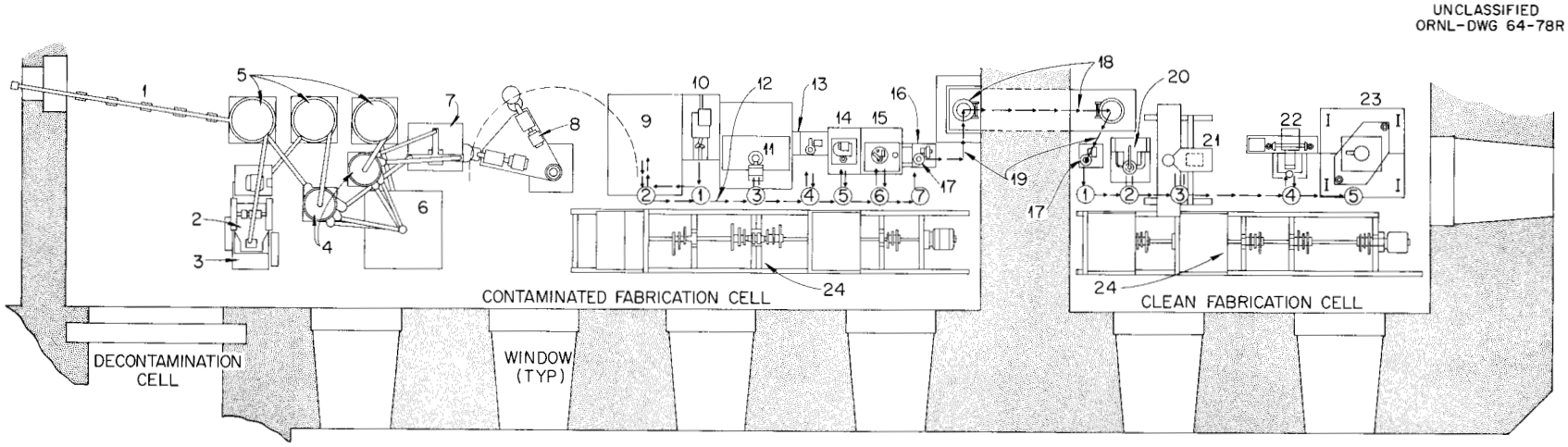

① TRANSFER STOP POSITIONS
1. VIBRATORY TROUGH FEEDER
2. JAW CRUSHER
3. ROLL CRUSHER
4. CLASSIFIERS
5. VIBRATORY SPIRAL ELEVATORS
6. BALL MILL
7. WEIGHING MACHINE
8. FUEL TRANSFER MACHINE
9. VIBRATORY COMPACTOR
10. FUEL ROD MAGAZINE
11. GAMMA SCANNER
12. FUEL ROD FLOW
13. REJECT RACK
14. CAPPING MACHINE
15. WELDING MACHINE
16. INDEXING MACHINE
17. FUEL ROD BASKET
18. CLEANER TRANSFER MACHINE
19. TRANSFER IN FUEL ROD BASKET
20. LEAK CHECK MACHINE
21. WELD RADIOGRAPHY MACHINE
22. FUEL ROD DIMENSIONAL CHECK
23. FUEL ELEMENT ASSEMBLY AND INSPECTION MACHINE
24. FUEL ROD TRANSFER MACHINE

Fig. 29.6. Oxide Fabrication Equipment Layout.

Bulk powder received from the sol-gel process is prepared for vibratory compaction in equipment that includes hoppers, crushers, classifiers, vibratory conveyors, and a batch weighing device. The batch weighing device dumps its contents into the blend can, which is mounted on the fuel transfer machine. Once the material is blended, it is moved to the vibratory compactor and dispensed into a feed mechanism. Meanwhile, a tube is removed from a tube magazine and inserted into the vibratory compactor. The fuel is fed into the tube while a pneumatic vibrator compacts it to approximately 90% of theoretical density. Next a gamma adsorptiometer checks the fuel tube for density and fuel distribution. Tubes are to be transferred between machines by electromechanical manipulators.

The fuel tube is then moved to the capping machine, where the end plug assembly is inserted and pressed into place. Next, the tube is moved to the welder where a fusion weld is made by tungsten inert-gas procedures.

The rod is then moved to a fuel rod basket and indexer, which consists of an indexable basket with clips for holding ten tubes. When the basket is filled, the cell crane moves it to the cleaner-transfer device, where the rods are decontaminated in an ultrasonic bath and spray rinse. Once cleaning is completed, the ultrasonic cleaning tank is transferred to the clean fabrication cell and unloaded.

The fuel tubes are checked for alpha contamination. Clean fuel rods are moved to the weld-radiography device, where an x-ray sensitive television system inspects the end-cap weld. Acceptable rods are then moved to a dimensional inspection device, which checks for compliance with length, diameter, and waviness specifications.

Completed fuel rods are assembled along with prefabricated structural components into a complete fuel element. Finally, the fuel element is inspected for rod-to-rod spacing.

Vibratory Compaction

W. S. Ernst, Jr.

The development of pneumatic vibrators for compaction of oxide particles in metal tubes is one of the key items in the fabrication process being developed for the Thorium-Uranium Fuel Cycle Development Facility. We are trying to understand the importance of several variables and to improve the efficiency of this type of machine.

Bulk densities of 90% of theoretical were obtained on a pneumatic impact vibrator as compared with 87% on an electrodynamic shaker. Details of the experiment have previously been reported.[6]

Simplified methods for generating particle-size distributions that can be vibratorily compacted to high bulk densities were studied. In general, these distributions are continuous from a controlled maximum particle size. The distributions examined were generated by either ball-milling or jaw-crushing crude sol-gel ThO_2–3% UO_2 and then scalping the run-of-the-mill product through a suitable coarse screen. Bulk densities of 90 and 87% of theoretical were obtained for the crude sol-gel materials after milling for only one hour and jaw crushing for one pass respectively.

Results of these experiments indicated that the bulk density is relatively insensitive to large variations in particle-size distributions. This means that batches large compared to a single fuel-rod loading can be blended at one time. In general, this is not so for discrete three- and two-size fraction distributions.

Vibratory compaction of sol-gel ThO_2–3% UO_2 in stainless steel tubes 8 ft long × $\frac{3}{4}$-in. OD × 0.010-in. wall failed because the thin wall could not absorb the vibratory energy without failure. Failure has usually occurred within several inches of the tube-to-vibrator coupling. Extremely high radial acceleration levels have been indicated in this area. Failure is by complete circumferential cracking due to fatigue of work-hardened material. This kind of failure can be obtained as well with the electrodynamic shaker at a resonance frequency of the tube.

We started to characterize the minimum vibration energy necessary for compacting a given configuration. Because the impact pulses lead to extremely high acceleration levels and are of short duration (100 μsec), experimental measurements are difficult. Systems for coupling tubes to reciprocating pneumatic vibrators have been developed that may lead to a general characterization of the vibration energy necessary for compaction. These coupling schemes use variations of fixed-anvil and floating-anvil wave guides.

[6]W. S. Ernst, Jr., *Status and Progress Report for Thorium Fuel Cycle Development December 31, 1963*, ORNL-3611 (in press).

Inspection Development

B. E. Foster S. D. Snyder
R. W. McClung

Quality control is an essential step in the production of any manufactured object. It is most important in the fabrication of fuel elements and the problem of making such inspections remotely but economically offers an interesting challenge.

During the past year, we have completed the design of a prototype model to scan the length of fuel rods remotely and record changes in fuel density. This machine will be capable of inspecting rods 10 ft long with diameters ranging from $\frac{1}{4}$ to $\frac{3}{4}$ in. Scanning speeds up to 24 in./min will be attempted and ^{60}Co and ^{137}Cs will be used as the radiation sources.

The development of reference standards for vibratorily compacted fuel rods has been difficult. We finally succeeded by two routes. We cast a series of lead-tin alloys varying in density in the range desired, and we obtained a series of carefully pressed and sintered pellets of ThO_2. Each type proved adequate, but we prefer the ThO_2 pellets at present.

COATED-PARTICLE DEVELOPMENT

One attractive class of reactors that utilize thorium is fueled with a homogeneous distribution of fuel particles throughout a graphite matrix and cooled by helium. The homogeneity of the mixture of fuel and moderator improves the conversion ratio, and the refractory nature of the graphite body promotes high thermal efficiency. The success of such a concept depends to a large extent on the strength and integrity of a pyrolytically deposited carbon coating on spherical fuel particles. Much of our research on this problem is reported in Chap. 25 of this report.

We are attempting to develop a process that is amenable to remote fabrication, is economical, and produces a final product comparable in performance to the elements that have been evaluated.

Prototype Fabrication Line

R. L. Pilloton J. W. Snider[7]
A. L. Lotts

We are assembling equipment developed by engineers in the Metals and Ceramics and Chemical Technology Divisions into a prototype fabrication line to study the problems involved in the remote production of coated particles. We shall produce engineering data in two main fields, (1) preparation of oxide microspheres by the sol-gel technique and (2) preparation and inspection of coated microspheres.

Corresponding areas are shown in the layout of Fig. 29.7. The equipment on the left is that of the oxide microsphere process. In this process a colloidal dispersion of thorium oxide is mixed with a solution of uranium nitrate in adequate ratios and partially neutralized to produce a sol; this sol will then be introduced at the top of a "sphere formation" column in which the sol droplets will be progressively dehydrated by an organic liquid to produce gel microspheres. These microspheres will be dried at 120°C and calcined to 1200°C.

The preparation of coated particles will be investigated in the area shown on the right in Fig. 29.7. The equipment will consist initially of a small fluidized-bed apparatus for coating microspheres by hydrocarbon cracking. Later, a high-temperature furnace for calcination of the oxides and a large fluidized-bed coater will be installed.

Fluidized-Bed Studies

R. L. Pilloton A. L. Lotts

To prepare for new engineering studies on particle coating, background information on fluidization has been collected through calculations[8] and through actual observations of fluidization characteristics in glass models.

Several equations and a nomogram were prepared to indicate the minimum flows of gas necessary to fluidize various spherical particles made

[7]Chemical Technology Division.

[8]R. L. Pilloton, *Gas Flow Calculations for Fluidized-Bed Coating of Nuclear Fuel Particles*, ORNL-3639 (June 1964).

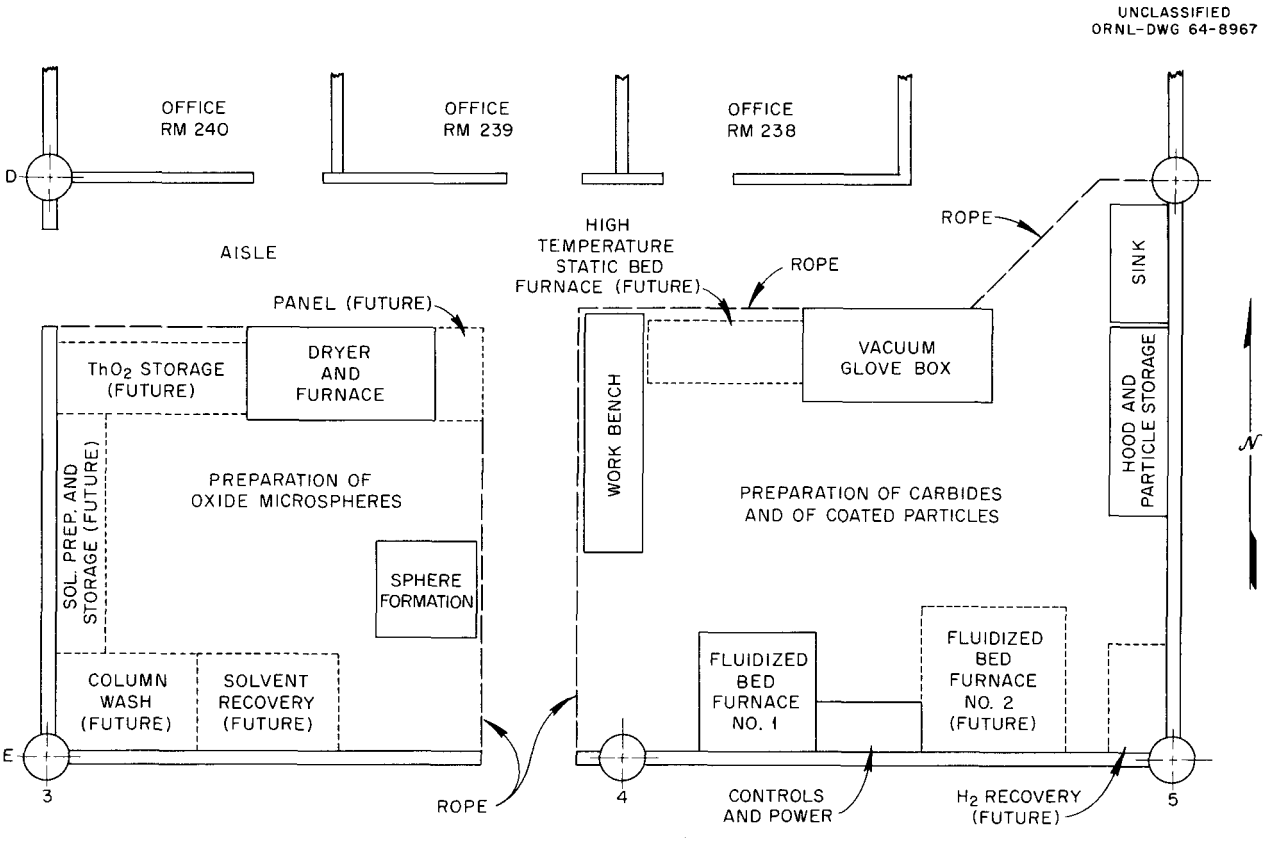

Fig. 29.7. Proposed Layout of Particle Coating Development Laboratory.

of heavy cores and covered with light or heavy coatings. On the basis of these equations a computer program was used to obtain minimum gas flows G_{mf} for fluidization by helium and argon at room temperature and temperature coefficients for temperatures up to 2200°C. These curves show that G_{mf} first decreases and then increases as the coating of particles proceeds in the fluidized bed (see Fig. 29.8). They also indicate that G_{mf} decreases very sharply with increasing temperatures.

We also plotted particle diameter as a function of time for constant flows of coating gas (e.g., methane) and variations of the coating gas flows necessary to maintain constant coating growth rates. Comparing these two sets of curves we concluded that coating times could, in theory, be shortened appreciably by programming the flow of coating gas.

Glass columns were built to study the effect of the geometry of the fluidized-bed apparatus on gas-solid contact and on particle motion. Each column consisted of a cylindrical tube connected by a conical section to a single gas inlet tube or to a gas-distributor plate. Iron and glass beads having diameters of 100 to 400 μ were suspended in the columns by various flows of air at room temperature, and motion pictures were taken to study the movement of the particles in the fluidized beds. Examples of typical bed characteristics are shown in Figs. 29.9 and 29.10. These observations showed that a cylindrical column with a single gas outlet and a conical intermediate section would be difficult to scale up because excessive slugging and poor gas-solid contact would occur when the charges of particles are large. We also condluded that a multiple-orifice flat gas-distributor plate with vertical gas channels would leave many particles static and, therefore, lead to nonuniform and inefficient coating. We developed a bed with greatly improved geometry, consisting of a cylindrical column connected by a 30° contained-angle cone to a multiorifice gas-distribution plate.

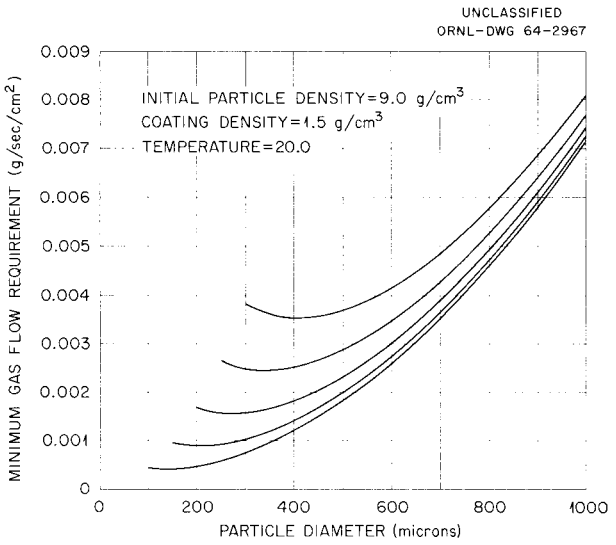

Fig. 29.8. Minimum Flow of Helium for Fluidization at Room Temperature.

coated state was noted by macroscopic, radiographic, or metallographic examination.[9]

In 2 to 4 hr at 1800 to 2000°C, no significant reaction could be detected between fuel particles and coatings 65 μ or thicker. Some thinner coatings, however, particularly those applied at low temperatures (900 to 1100°C), ruptured and subsequently reacted with the fuel. The thinner coatings probably ruptured because they could not contain the equilibrium carbon monoxide pressure.

The results of these laboratory studies indicate that the use of carbon-coated mixed-oxide spheres is promising for remote fabrication of fueled graphite elements. The oxide particles are more refractory than the carbides and have certain inherent economic and performance advantages. Their performance under irradiation must be ascertained and an experimental program using the ORR is currently under way.

Thermal Stability of Pyrolytic-Carbon-Coated Oxide Fuel Particles

R. L. Hamner R. L. Beatty
R. E. Meadows

We have started to investigate coating sol-gel ThO_2 and $(Th,U)O_2$ particles with pyrolytic carbon and to determine the thermal and irradiation behavior of the coated particles under conditions likely to be encountered during the fabrication of a fuel body and during operation as a fuel element.

Thermogravimetric experiments on intimately mixed powders showed that UO_2 and ThO_2 started to react with carbon at approximately 1260 and 1360°C, respectively, during heating at a rate of approximately 20°C/min at a pressure of 1×10^{-6} torr. Weight losses due to release of carbon monoxide showed that after 2 hr at 1750°C, UO_2 was essentially completely converted to the carbide but ThO_2 was converted only 52%.

Conventionally prepared spheroidal UO_2 particles and spheroidal sol-gel ThO_2 particles, 100 to 250 μ in diameter, were coated with pyrolytic carbon at 900 and 1400°C in thicknesses ranging from 20 to 120 μ. After heat treatment at 1100°C for 1000 hr or at 1400°C for 200 hr at a pressure of 10^{-5} torr, no significant change from the as-

IRRADIATION STUDIES

Powder-Packed Sol-Gel Oxide

S. A. Rabin[10] J. W. Ullmann[11]
D. A. Douglas

We are continuing to evaluate the irradiation behavior of sol-gel oxide for application as a nuclear fuel. We hope to learn the answers to the following questions:

1. Does this chemically produced ceramic meet the basic requirements of a nuclear fuel?
2. Do variations in the manufacturing process affect the irradiation performance?
3. How does sol-gel oxide compare with arc-fused material?
4. How do vibratorily compacted fuels behave under irradiation?
5. What are the maximum performance character- of vibratory compacted oxides?

---

[9]R. L. Hamner, R. L. Beatty, and R. E. Meadows, *GCR Program Semiann. Progr. Rept. March 31, 1964*, ORNL-3619, pp. 79–81.

[10]Now with General Electric Company, Atomic Power Equipment Department, San Jose, California.

[11]Chemical Technology Division.

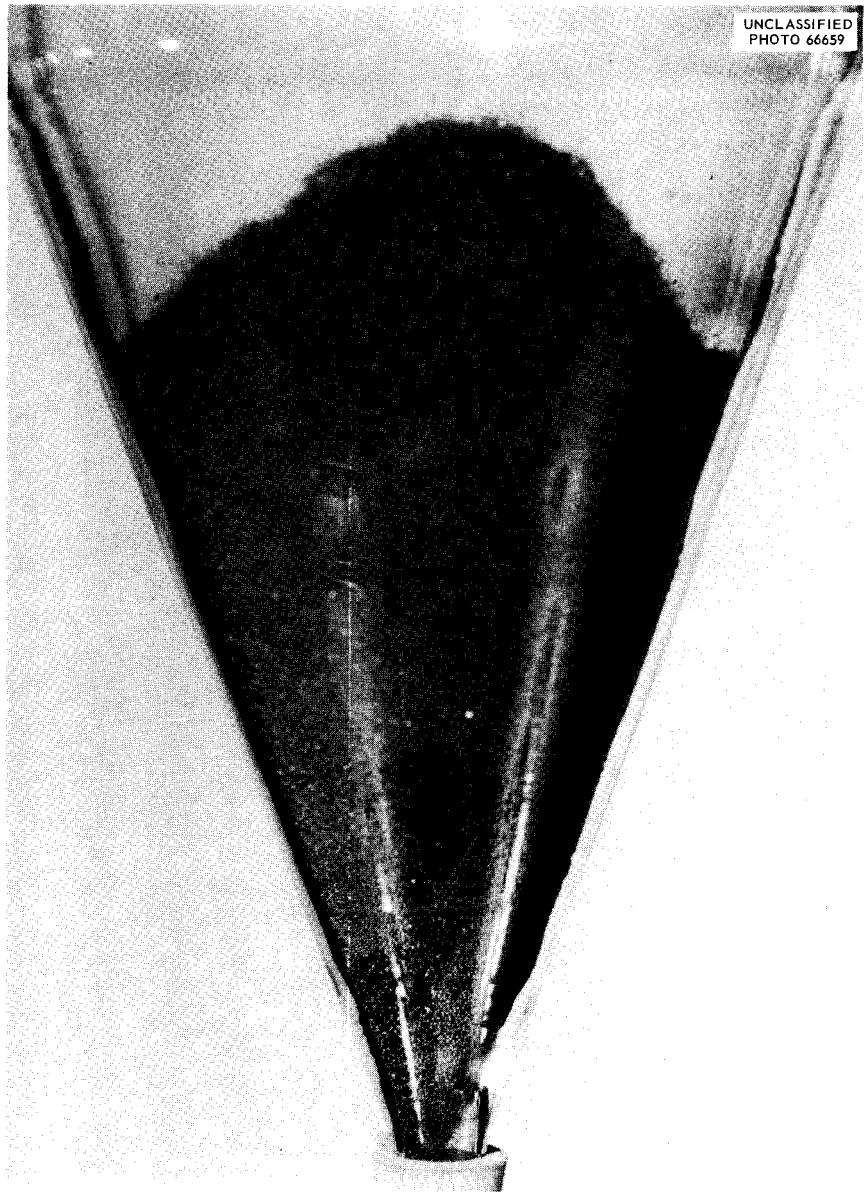

Fig. 29.9. Typical Fluidized-Bed Characteristics in a Conical Column with a Single Gas Inlet.

Previously,[12,13] we found that only slight variations in properties resulted from variations in the sol-gel process, and we demonstrated that sol-gel power compared favorably with pulverized arc-melted oxide. Currently we are comparing sol-gel fragments calcined in three different atmospheres: Ar–4% H_2 (standard atmosphere), air, and nitrogen. Significantly, the type of gas evolved, as well as the quantity, depended on the calcining atmosphere.

Table 29.1 summarizes the experimental conditions for the irradiation tests. The initial surveillance tests conducted in the MTR and NRX, in which the heat rating and fuel exposure were relatively modest, clearly showed that the chemically produced fuel was an excellent nuclear material and that the irradiation behavior was not

[12]S. A. Rabin, *Metals and Ceramics Div. Ann. Progr. Rept. May 31, 1963*, ORNL-3470, pp. 205–209.

[13]S. A. Rabin, S. D. Clinton, and J. W. Ullmann, *Status and Progress Report for Thorium Fuel Cycle Development December 31, 1963*, ORNL-3611 (in press).

Fig. 29.10. Typical Fluidized-Bed Characteristics in a Conical Column with Eight Gas Inlets.

sensitive to small variations in the processing steps. Test results also revealed that the sol-gel fuel was equivalent in performance to arc-fused oxide. Very little fission gas was released in these tests; in postirradiation examination we found 2 to 4% of the ^{85}Kr theoretically generated. Dimensional changes were negligible and microstructural effects were only minor.

Experiments to examine the behavior of the material at higher heat ratings were started in the ORR (see Table 29.1). The peak values of $\int_{\theta_0}^{\theta_c} k(\theta)d\theta$ on the three samples ranged from 47 to 57 w/cm and the surface temperature was 260°C. Less than 5% of the fission gas was released from these rods. Sintering and growth of equiaxed grains occurred in each of the fuel rods. Columnar grains and lenticular voids were found only in the capsule that operated at the highest thermal rating; these structures compare with those found in powder-packed UO_2 irradiated at a peak value of about 48 w/cm, and a central void would be generated under comparable conditions.

Also, we conducted experiments in the ORR using thermocouples to measure the central and surface temperatures. The maximum cladding temperature was 700°C and the peak central temperature was 1925°C with an external pressure of 315 psia of helium. We observed sintering across some 75% of the fuel region but no columnar grain growth. The fuel achieved about 5000 Mwd/tonne of metal and released about 18% of the fission gas.

Now we can compare sol-gel and arc-fused oxides as a function of fuel depletion. The effects of burnup on fission-gas release are illustrated in Table 29.2. As expected, the gas release increased with exposure. Since these fuels operated in a temperature range in which the diffusion mechanism is prominent, the increase in fission-gas release with time is expected.

No significant dimensional or gross microstructural changes were observed for the powder-packed rods at the higher burnups. The latter

Table 29.1. Summary of Irradiations of Powder-Packed Capsules (Rods) in Type 304 Stainless Steel[a]

Designation	No. of Rods	Type of Oxide	Density (% TD)	Fuel Rod Dimensions, in.			Linear Heat Rating (Btu hr^{-1} ft^{-1})	Peak Burnup Mwd/tonne metal	Status	Objective
				Length	OD	Wall				
MTR-I	7	Arc-fused Sol-gel E	86 to 87	11	0.312	0.025	45,000	15,000 to 100,000	2 examined; 2 being examined; 3 in-pile	Provide base-line data to use in comparing sol-gel and arc-fused oxide
MTR-II	2	Sol-gel S	88 to 89	22	0.312	0.025	62,000	100,000	In-pile	Obtain higher heat rating by increasing enrichment
MTR-III	6	Sol-gel 35	86 to 89	12	0.438	0.025	85,000	100,000	In-pile	Compare oxide calcining atmospheres and higher heat ratings obtained by increasing dimaeter
ETR-I	4	Sol-gel 35	86 to 89	12	0.438	0.025	>100,000	22,000	Being examined	Same as for MTR-III
NRX-I	8	Sol-gel A and B	86 to 87	11	0.312	0.025	17,000	16,000	Examined	Provide base-line data
NRX-II	4	Sol-gel C Arc-fused	83 to 86	22	0.312	0.025	22,000	5,000	Examined	Study effect of increased length
NRX-III	6	Sol-gel S	88 to 89	39	0.312	0.025	28,000	23,000	Being examined	Study effect of increased length
NRX-III	3	Sol-gel ThO_2-PuO_2	74 to 76[b]	11	0.312	0.025	27,000	22,000	Being examined	Study ThO_2-PuO_2 and lower packed density
ORR Loop	3	Sol-gel 26	84 to 85	22	0.460	0.015	52,000	2,100	Examined	Study in pressurized water at 260°C and 1750 psi
ORR Poolside	2	Sol-gel D	85	7	0.625	0.020	35,000	5,000	Examined	Measure effective thermal conductivity using a central thermocouple in Na-K at 315 psi; 540 and 705°C

[a]Two of the three ORR loop specimens were zircaloy clad.

[b]Tamp packed.

Table 29.2. Effect of Burnup on Fission-Gas Release of Vibratorily Compacted ThO_2-UO_2 Fuels

Fuel Oxide Source	Peak Linear Heat Rating, Time Averaged (Btu hr^{-1} ft^{-1})	Maximum Burnup (Mwd/tonne U + Th)	Maximum Burnup (Fissions/cm^3)	^{85}Kr Release (%)
			$\times 10^{20}$	
Sol-gel E	35,500	14,000	3.08	0.5
Sol-gel E	30,000	39,900	8.74	13.2
Arc-fused	31,100	12,300	2.70	2.4
Arc-fused	31,500	42,400	9.30	7.2

point is especially important because the time dependence of sintering and grain growth, unlike the temperature dependence, is all too frequently overlooked. At the higher burnups, the grain structure in sol-gel oxide was slightly more evident and slightly larger grains were observed in arc-fused oxide (see Figs. 29.11 and 29.12). In addition, white particles were precipitated at grain boundaries in the central regions of both fuels. Since the arc-fused oxide had contained white inclusions prior to irradiation, the postirradiation presence of a precipitate in this oxide cannot be interpreted. However, these particles decidedly were not present in the sol-gel oxide before irradiation or at lower burnups. We believe the white globules are alloys of fission-product oxides. One change unique to the sol-gel oxide with the longer exposure was the presence of a gray acicular phase at the periphery of the fuel. This phase has not as yet been identified, but x-ray diffraction analyses and electron metallography are in progress. In general, the irradiation behavior of sol-gel oxide has been excellent.

The tests that are still in-pile or being examined are expected to define the operating limits for sol-gel fuel. These experiments bracket severe thermal ratings and neutron exposures, as shown in Table 29.1. All of the specimens have performed satisfactorily. The four very highly rated rods in the ETR were recently discharged, so we should soon learn more about the limiting capabilities of the sol-gel fuel.

High-Burnup ThO_2-UO_2 Pellet Rods

S. A. Rabin[10] J. W. Ullmann[11]

Several years ago, ORNL started a program to provide irradiated fuel for dissolution studies. As a consequence, ThO_2-UO_2 pellet specimens have been irradiated in the MTR, ETR, and NRX to burnups up to 95,000 Mwd/tonne (2.43×10^{21} fissions/cm^3).

At the inception of the project, we did not intend to evaluate the performance of the fuel *per se*. However, in view of our present interest in thorium-bearing fuels and in high-burnup fuels in general, we decided to examine in detail several of the irradiated ThO_2-UO_2 fuel rods and glean as much information as possible about their behavior. Three such rods have been examined to date.

Pertinent design parameters of the thoria-urania fuel rods (not sol-gel) are 4.45% UO_2, 93.2% uranium enrichment, 4.5-in. overall length, 3.5-in. active length (less insulating plug when used), seven 93%-dense 0.260-in.-diam × 0.500-in.-long pellets per tube, 0.3125-in.-OD × 0.025-in.-wall type 304 stainless steel cladding, two 0.4375-in.-long end plugs, and 31 g oxide fuel per tube. The pellets were fabricated by an outside vendor. The ceramic end spacers were incorporated in only one of the three rods.

Chemical analyses indicated high contents of aluminum, silicon, and calcium impurities. The microstructure of an unirradiated specimen revealed

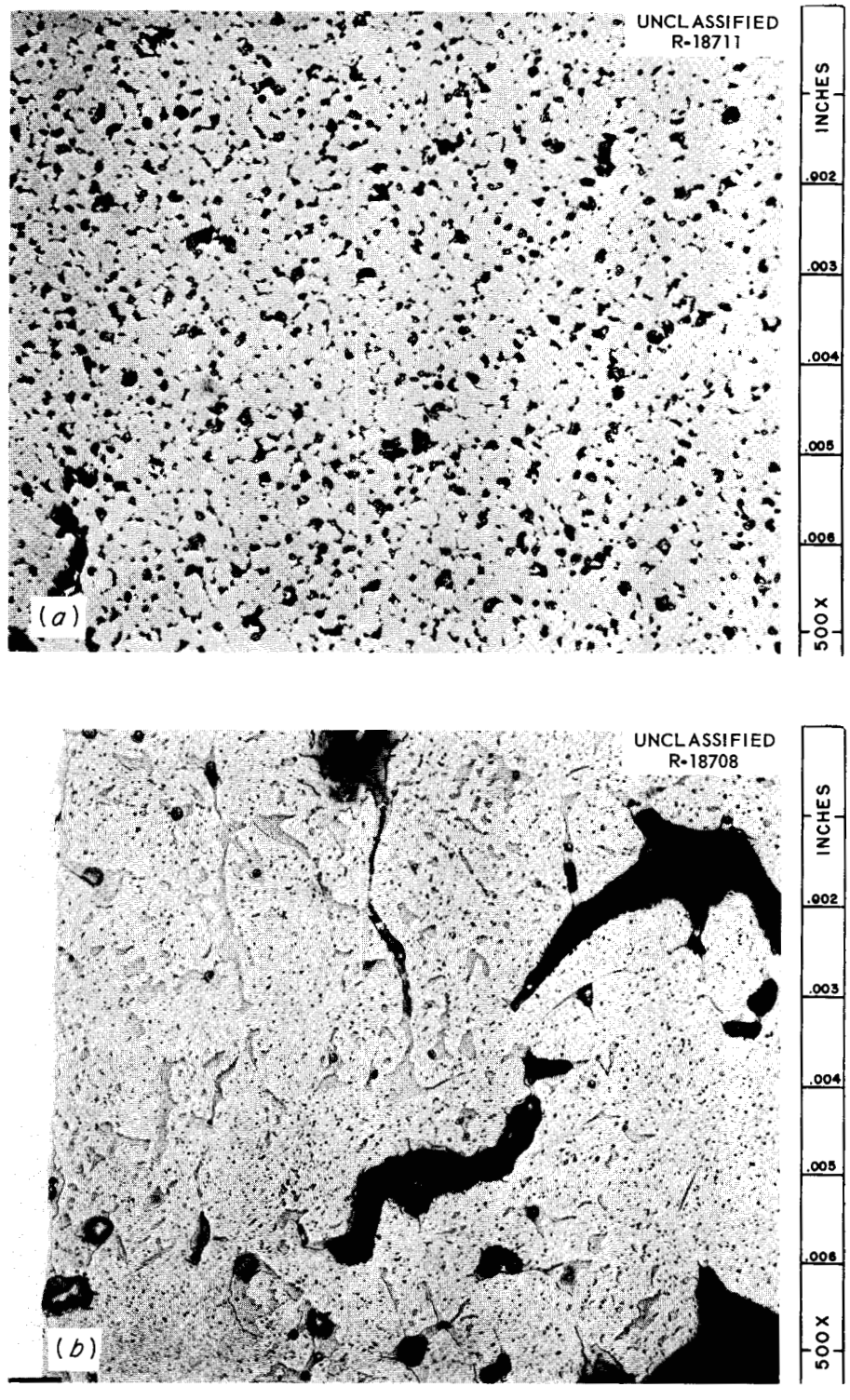

Fig. 29.11. Vibratorily Compacted Sol-Gel ThO_2-UO_2 Irradiated to 8.74×10^{20} Fissions/cm^3 at 30,000 Btu/hr-ft. 500×. (a) Central region of fuel. Etched. (b) Outer region of fuel. As polished.

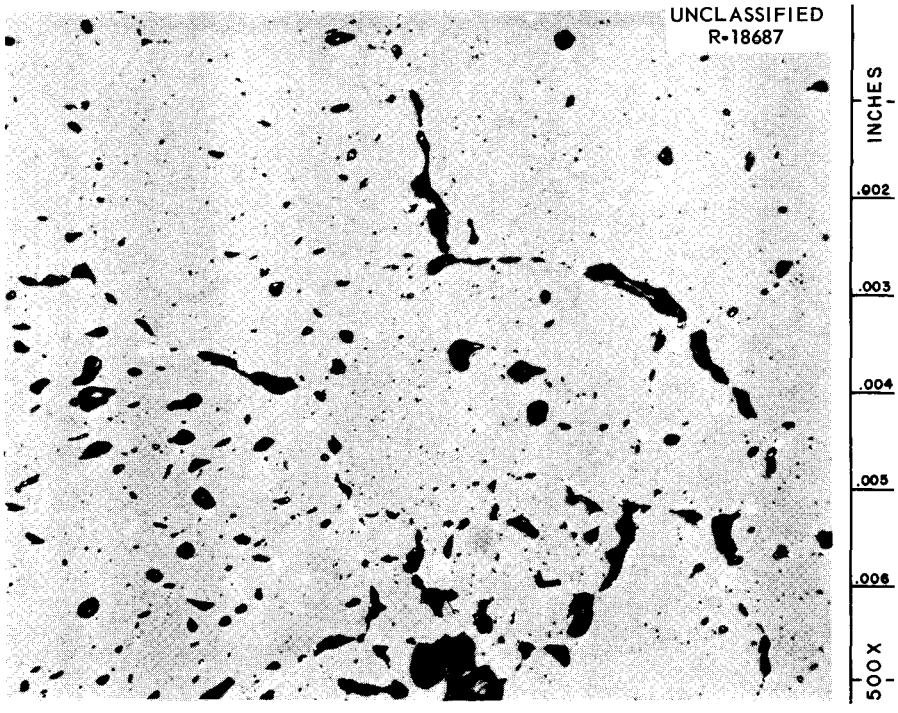

Fig. 29.12. Vibratorily Compacted Arc-Fused ThO_2-UO_2 Irradiated to 9.30×10^{20} Fissions/cm^3 at 31,500 Btu/hr-ft. Central region of fuel. Etched. 500×.

an appreciable quantity of a glassy gray second phase located primarily at the grain boundaries. X-ray diffraction analyses substantiated these findings by detecting Al_2O_3 and $6Al_2O_3 \cdot CaO$ in addition to the solid solution ThO_2-UO_2. Furthermore, application of the electron probe confirmed that an aluminum-bearing phase was prevalent at the grain boundaries.

Two of the pins were irradiated in MTR process water and the third in ETR process water. Reactor operating parameters and calculations are summarized in Table 29.3. The irradiation was completed as scheduled and without incident.

Although the dimensional data were not precisely documented for the individual rods before irradiation, we conclude that fuel swelling could not have exceeded 0.5% per 10^{20} fissions/cm^3; else the cladding would have deformed perceptibly. Calculations had predicted that the highest burnup capsule would swell, but remarkable dimensional stability was noted. These and other observations indicate that some of the fission products were apparently accommodated in the cubic fluorite crystal lattice.

Although a valid measurement of fission-gas release was obtained for only one specimen, fortunately it was for the rod exposed to the highest dose. The measured release of 12.4% is comparable to that from other oxide fuels irradiated under similar conditions. At such a high fuel depletion one would anticipate enhanced gas release because of fission-fragment damage to the lattice and changes in fuel composition. Of course, the absence of major structural changes would account for much of the observed stability.

The fuel pellets had fractured into several pieces each, but this behavior is typical of oxide exposed to severe thermal gradients and cycling.

The microstructure of the oxide approximated that of high-burnup UO_2 and ZrO_2-UO_2 irradiated at thermal ratings below which columnar grains grow or central voids form.[14,15] The structural

[14] R. C. Daniel *et al.*, *Effects of High Burnup on Zirconium-Clad, Bulk UO_2, Plate Fuel Element Samples*, WAPD-263 (September 1962).

[15] B. F. Rubin *et al.*, *The Irradiation Behavior of ZrO_2-UO_2 Fuels*, WAPD-264 (October 1962).

Table 29.3. Irradiation Operating Data for ThO_2-UO_2 Pellet Capsules

	Capsules		
	MTR 43-40	MTR 43-41	ETR 43-44
Irradiation starting date	5-12-60	6-23-60	6-4-60
Discharge date	9-17-62	4-2-62	11-26-62
Reactor operation, Mwd	26,400	19,874	71,078
Full-power days	660	497	406
Surface cladding temperature, °F	~200	~200	~200
Maximum exposure, neutrons/cm^2 (advertised, unperturbed)	1.13×10^{22}	7.15×10^{21}	5.88×10^{21}
Maximum burnup, Mwd/tonne metal	95,000	42,000	50,000
Fissions/cm^3	2.43×10^{21}	1.08×10^{21}	1.28×10^{21}
Peak linear heat rating,[a] Btu hr^{-1} ft^{-1}	47,800	28,100	41,000
Peak surface heat flux,[a] Btu hr^{-1} ft^{-2}	586,000	344,000	502,000
Peak heat generation rate,[a] w/cm^3	1310	770	1120
Peak integral of $k d\theta(T_c, T_s)$,[a] w/cm	38.0	21.5	31.3
Center line temperature,[a,b] °F	2500	1560	2180

[a]Calculated time-average value (peak refers to position of maximum burnup).
[b]Assuming effective $k_{fuel} = 1.7$ Btu/(hr ft^2 °F/ft).

stability of the ThO_2-UO_2 is notable. The most significant changes were the disruption of the grain boundary structure and the increased presence of the white spherical precipitate in the most severely tested rod (compare Fig. 29.13 with Fig. 29.14). At the higher temperatures the impurity phase, which formerly outlined the grain boundaries, went into solution and reprecipitated as fine particles. Some of the fission products had migrated to grain boundaries and voids, but others had undoubtedly been retained in the lattice.

In x-ray diffraction patterns, the overall intensity of the peaks changed little with burnup, implying that a relatively crystalline structure was maintained. The doublets in the peak were obscured, showing that the lattice was strained. This was further evidenced by the perceptible decrease in the lattice parameter from 5.590 A for the unirradiated material and specimen 43-44 to 5.584 A for specimen 43-40, which had the highest burnup. We postulate that at lower burnups the fission products are swept out to grain boundaries and pores. Eventually, these sites are filled, and the particles must then remain in the lattice unless new volume is provided by swelling. Bettis workers[14] observed no changes in the lattice parameter of UO_2, but this must be considered fortuitous in view of the numerous irradiation effects that are associated with highly irradiated ceramic fuels. We conclude that x-ray diffraction analyses confirm the conspicuous structural stability of ThO_2-UO_2 fuels.

Thorium Alloy Fuels

S. A. Rabin[10] D. A. Douglas

We have met numerous difficulties in irradiation testing the Th-U-Zr alloy fuel capsules designed

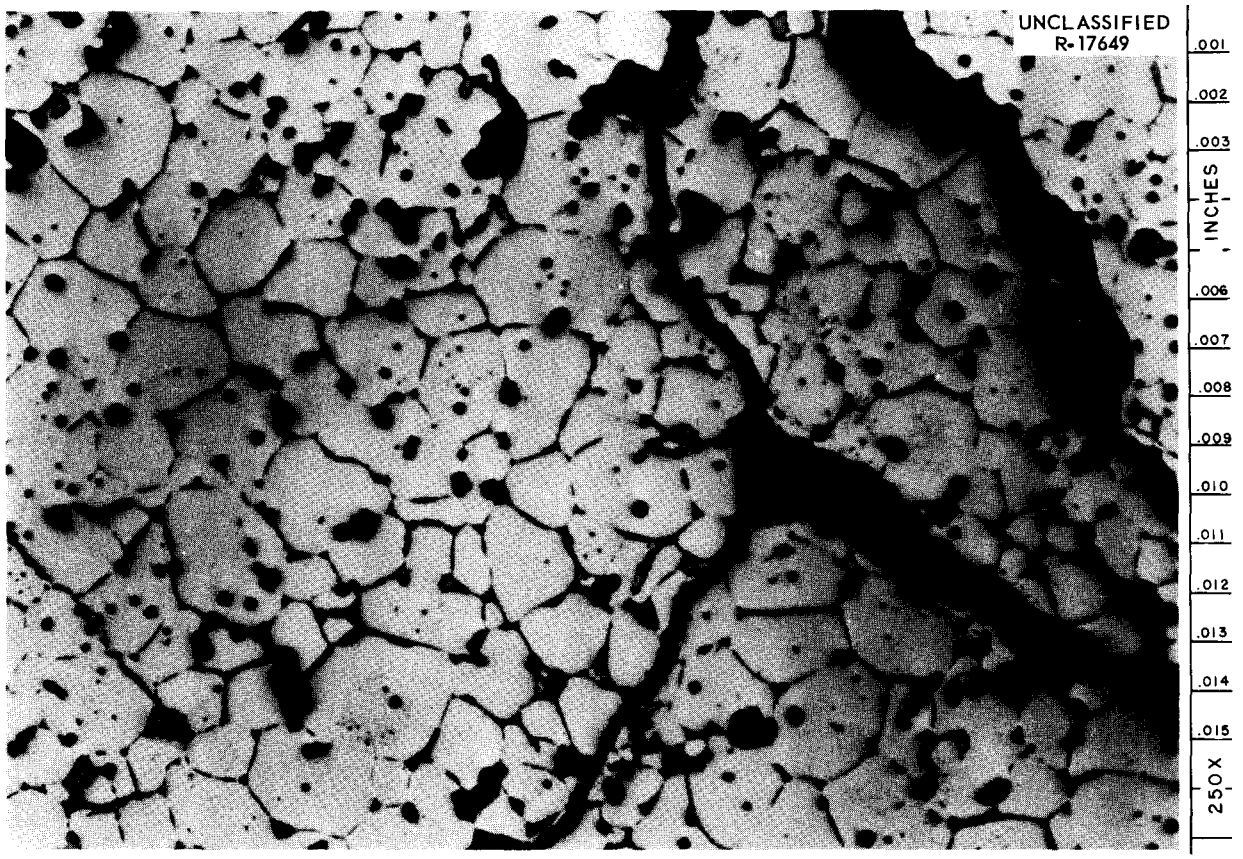

Fig. 29.13. Microstructure at Midradius of Fuel from Pellet Rod Irradiated to 50,000 Mwd per tonne of Metal at 41,000 Btu hr^{-1} ft^{-1}. Etched. 250×.

and fabricated by Advanced Technology Laboratories (ATL).[16] Initially, we planned to irradiate the group ATL-3 capsules (3-1, 3-2, 3-3) at 800°C central temperature to burnups of 10,000, 20,000, and 30,000 Mwd per metric ton of fuel respectively. Capsules 2-1, 2-2, and 2-3 were to be held in reserve. Subsequently, all of the specimens were used. At present, none of the capsules is being irradiated, and we doubt if any of them can be irradiated further. The status of the capsules is summarized in Table 29.4.

Capsules 3-3 and 2-2 performed the best, but were removed indefinitely when an interim examination revealed that the container had bowed appreciably. We are testing whether these capsules can be operated in this condition, but the outlook is not promising. The remaining capsules either have been disassembled or are considered irreparable.

[16]S. A. Rabin, *Metals and Ceramics Div. Ann. Progr. Rept. May 31, 1963*, ORNL-3470, pp. 208–10.

Fission-Gas Release from Ceramic Fuels

R. B. Fitts

The release of fission gas from ceramic fuels is being studied by low-temperature neutron activation and postirradiation heat treatment. Our experimental techniques have been described previously.[17,18] The mechanisms and characteristics of fission-gas release from various fuels are needed for evaluation and optimum utilization of reactor fuels. As described previously,[19] fission gas is released in two general situations. The

[17]Staff of the Oak Ridge National Laboratory, *GCR Program Quart. Progr. Rept. December 31, 1959*, ORNL-2888, pp. 68–72.

[18]D. F. Toner and J. L. Scott, "Study of Factors Controlling the Release of Xenon-133 from Bulk UO_2," pp. 86–99 in *Am. Soc. Testing Mater. Spec. Tech. Publ. 306* (1961).

[19]R. B. Fitts, *Metals and Ceramics Div. Ann. Progr. Rept. May 31, 1963*, ORNL-3470, p. 149.

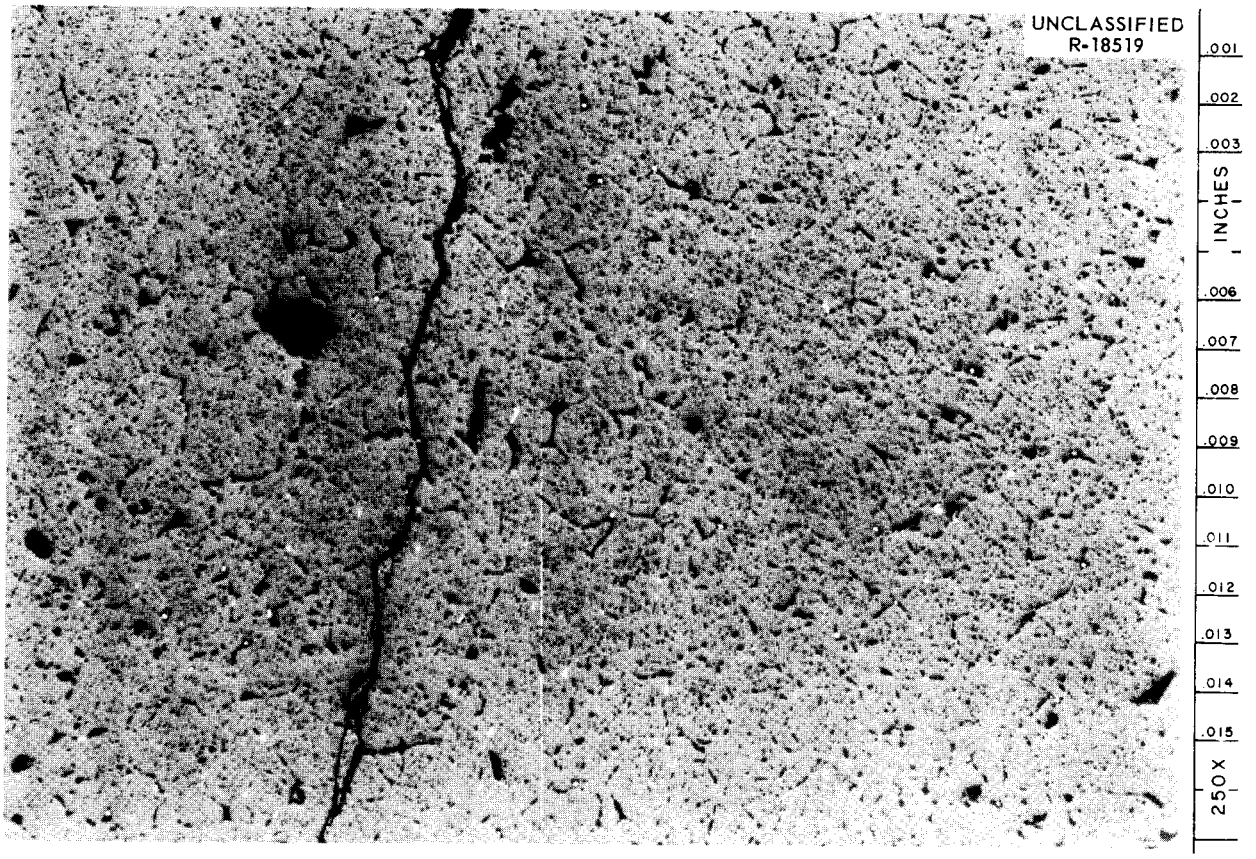

Fig. 29.14. Microstructure at Central Area of Fuel from Pellet Rod Irradiated to 95,000 Mwd per tonne of Metal at 47,800 Btu hr^{-1} ft^{-1}. Etched. 250×.

Table 29.4. Irradiation of ATL Capsules

Capsule	Central Temperature (°C)	Irradiation Time (Months)	Reasons for Removal
3-1	800	2	Thermocouples failed, leading to excessively high temperatures
3-2	800	1/4	Top weld cracked and failed
3-3	800	4	Capsule bowed
2-1	800	0	Erratic temperature response
2-2	700	2	Capsule bowed
2-3	800	1/2	Capsule leaked

first of these is the low-temperature (<100°C) in-pile release and the second is release during post-irradiation isothermal annealing.

Low-Temperature In-Pile Fission-Gas Release. – During irradiation at low temperature to low burnup (10^{15} fissions/cm^3), ^{133}Xe is apparently released from ceramic fuels due to a "boiling out" of gas atoms located near the points at which fission fragments cut an open surface in the fuel. In this mechanism the fractional release of gas should be proportional to the fraction of the recoil atoms that cut an open surface and, therefore, to the BET surface area of the sample. The equation relating that fraction to the BET surface area has been reported,[20] along with some data that show a good correlation between the surface area and the low-temperature in-pile release of fission gas. Since that time, we have extended the range of surface areas covered to include UO_2 samples having BET surface areas from 10 to 60,000 cm^2/g. The logarithm of the fractional ^{133}Xe release is a linear function of the logarithm of the BET surface area. The ratio of fractional ^{133}Xe release to the BET surface ranges from 2.50 ppm cm^{-2} g at low surface areas to 1.25 at high surface areas. The relationship between the fraction of fission fragments cutting an open surface and the surface area predicts a break in the plot at about 1000 cm^2/g, where every recoil fragment will cut at least one surface. This break was not observed, probably because ^{133}Xe was not released from the whole recoil range when a surface was cut. As a surface is intersected, atoms will be released from only a small portion of the end of the recoil track.

Elevated-Temperature Postirradiation Release of Fission Gas. – We have been trying mainly to define the mechanisms of fission-gas release through examination of the effects of stress on the release rates.

Morgan observed that the kinetics of the release of fission gas from ceramic fuels during postirradiation annealing are similar to the kinetics of densification of thoria compacts during sintering. Since dislocation motion appears responsible for the initial stages of densification of a powder compact,[21] we felt that this mechanism might also play a part in the release of fission gases from ceramic fuels. In particular, the motion of dislocations might be responsible for part or all of the so far unexplained "burst" release of fission gas observed as the temperature of an irradiated sample is raised for the first time. For this reason we decided to investigate the effects of stress, which produces dislocation motion, on the steady-state release of fission gas at elevated temperatures from ThO_2 containing approximately 2% UO_2 and from some other fuel materials. Some preliminary results of these tests and the experimental apparatus employed have been reported.[22]

The application of stress sufficient to cause creep has increased the rate of fission-gas release from samples of UO_2, ThO_2-UO_2, ThO_2-UO_2-CaO, Al-U, and V-U, the only materials tested to date. Representative temperatures and loads for the ceramic samples were 1500°C and 10,000 psi. A burst of gas was released from UO_2 and ThO_2-UO_2 samples when the load was applied but not from the other materials. The observed bursts and rate changes appear to increase with increasing load and temperature and to decrease with time at temperature and with the second and third application of a load. These are the behavior patterns associated with creep and dislocation motion at these temperatures.

In connection with the stress tests, two other methods of producing dislocation motion in ceramic samples were used. Samples of ThO_2-UO_2 were quenched from high temperature in an inert atmosphere, and the effects of this treatment on the release during subsequent heating to 1500°C were noted. The release of fission gas during heating of a sample increased markedly. These results support the hypothesis that the presence of dislocations and stress may play a major part in the burst of fission gas released when ceramic fuels are heated. The final method of producing dislocation motion was to heat a sample beyond the temperature at which it had previously been sintered. The rate of fission-gas release increased as the sintering temperature was passed.

We were concerned that these results might be due primarily to cracking of the samples by the applied stress. Metallographic examination revealed no gross cracking. To reduce the effects

---

[20] R. B. Fitts, *GCR Program Semiann. Progr. Rept. Sept. 30, 1963*, ORNL-3523, pp. 98–99.

[21] C. S. Morgan and C. S. Yust, *J. Nucl. Mater.* 10(3), 182–90 (1963).

[22] R. B. Fitts, J. L. Scott, and C. S. Morgan, *Stress-Induced Release of Fission Gases from UO_2 and ThO_2-UO_2*, ORNL-TM-740 (January 28, 1964).

of cracking, we tested low-density sintered ThO_2-UO_2 compacts and found no change in the results. The metal samples were tested because they were known not to crack. After removal of the load from a sample, the rate of release returned to the pre-stress rate, thereby indicating no increase in surface area. For these reasons, we believe cracking plays an insignificant part in the observed results.

We plan to correlate the creep rate and fission-gas release rate in ceramic fuels and to investigate the relationship of fission-gas release with the structure of dislocation networks and radiation-induced defects in metallic fuel. Use of metallic samples will also allow a better knowledge of sample variables such as stress, strain, strain rate, and pretesting conditions than is possible with the ceramic samples. These studies should help establish whether the effects of stress on ceramic fuels may be an important consideration in fuel element design. They should also establish the role of dislocations in the release of fission gases from ceramic fuels and help to define the possible mechanisms of such release. Also, the behavior of fission gases and the nature of possible fission-gas traps within fuels should be elucidated.

HIGH-TEMPERATURE THORIUM-BASE ALLOYS

J. A. Burka J. P. Hammond

Continuing our investigation of methods to obtain dispersion hardening in thorium, we measured mechanical properties of dispersion-hardened thorium and thorium-base alloys prepared by powder metallurgy.

To dispersion-harden thorium, we needed to develop methods for making submicron thorium powder and distribute ultrafine thorium oxide in it. Two approaches were attempted. One was ball milling of thorium hydride, a friable compound, which can be easily ground and decomposed to metal; the other was milling of calcium-reduced metal powder using various grinding aids. The latter method failed because thorium reacted with the grinding aids tested, forming thorium carbide or other compounds. With alcohol, thorium formed an unstable compound, which exploded violently upon being disturbed. Because of these adverse results, we abandoned the grinding of metal powders.

Previously, we have reported[23] the effects of milling time on the particle size of ThH_4 and the hot-hardness and stress-rupture behavior of extruded hot-pressed compacts of Th–10 vol % ThO_2. To determine the optimum thoria content, we extruded compacts containing 0, 4, 7, 10, and 13 vol % ThO_2. Hardness and tensile properties of the products at 800°C are compared in Table 29.5 with results on arc-melted thorium. No direct correlation was found between hardness or strength and oxide addition. We believe this is due to the wide variation of total oxide and carbon content resulting from the ball milling, handling in the vacuum dry box, and hot pressing. The strongest and hardest alloy contained 4 vol % ThO_2 (B1-2).

The strengthening of thorium by the combination of alloying and dispersion hardening was attempted by the addition of 10 vol % ThO_2 to alloys containing 2 and 5% Zr. The alloys were prepared from the hydrides using the same procedure as for the thoria-containing alloys. Hot-tensile results shown in Table 29.6 indicate that addition of ThO_2 weakened the thorium-zirconium alloys.

Indium, an effective strengthener of thorium, was alloyed with thorium in amounts from 2 to 5% by powder metallurgy. This method circumvents the problems imposed by high indium vapor pressure when the alloys are prepared by melting. Indium powder was prepared by milling in alcohol and was blended with calcium-reduced thorium powder. The mixture was hot pressed, homogenized, and extruded. Figure 29.15 gives hot-hardness curves for these alloys, while Table 29.7 gives tensile test results at 800°C. The alloy with the highest indium content appears best on the basis of hardness, strength, and ductility.

Indium strengthens thorium more at elevated temperature than does zirconium and imparts properties comparable to those from ThO_2 additions. Thorium-indium alloys are prepared easily by powder metallurgy. Consistent behavior of thorium dispersion-hardened with ThO_2 was difficult to obtain because contamination was hard to control. Nevertheless, creep results previously obtained for a ThO_2 dispersion[23] are superior to any others reported to date for thorium-base materials.

---

[23] J. A. Burka and J. P. Hammond, *Metals and Ceramics Div. Ann. Progr. Rept. May 31, 1963*, ORNL-3470, pp. 210–12.

Table 29.5. Tensile Properties and Hardness of Th–ThO_2 Alloys at 800°C

Alloy		Ultimate Tensile Strength (psi)	Yield Strength[a] (psi)	Elongation (%)	Hot Hardness[b] (DPHN)
Designation	Composition (vol %)				
Arc-melted	Thorium	2885	2140	40.0	
B1-1	Thorium	4040	2630	45.0	10
B1-2	Th–4 ThO_2	7960	7170	6.5	21
B5-1	Th–4 ThO_2	6425	5360	11.0	15
B2-1	Th–7 ThO_2	4835	4530	33.0	14
B2-2	Th–10 ThO_2	4245	3415	15.5	15
B2-3	Th–13 ThO_2	4685	4510	15.5	13
B5-3	Th–13 ThO_2	7010	6265	23.5	13

[a]0.2% offset.
[b]1-kg load.

Table 29.6. Tensile Tests at 800°C on Thorium-Zirconium Alloys

Alloy Composition	Ultimate Tensile Strength (psi)	Yield Strength[a] (psi)	Elongation (%)
Th–2 wt % Zr	5350	4245	55
Th–2 wt % Zr–10 vol % ThO_2	5190	4810	16.5
Th–5 wt % Zr[b]	4570	No yield	0.4
Th–5 wt % Zr–10 vol % ThO_2	2385	2210	5.0

[a]0.2% offset.
[b]Average of two tests.

Table 29.7. Tensile Results at 800°C on Thorium-Indium Alloys

Indium Content (wt %)		Ultimate Tensile Strength (psi)	Yield[a] Strength (psi)	Elongation (%)
Nominal	Actual			
2	1.78	6475	5550	10.0
3	2.60	7315	6330	6.0
4	3.68	6940	6120	5.5
5	4.38	7810	7130	20.0

[a]0.2% offset.

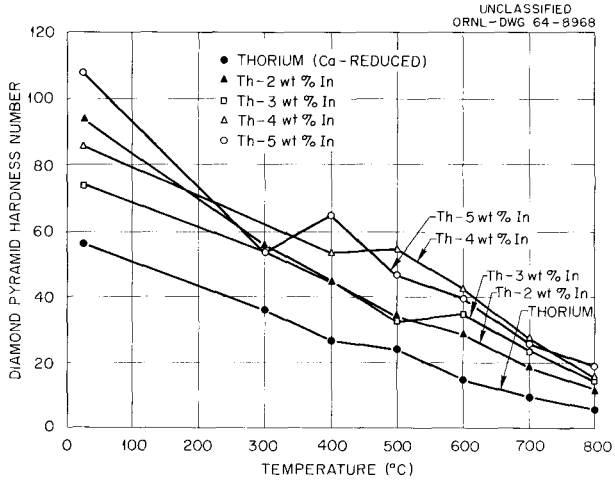

Fig. 29.15. Hardness (1-kg load) of Thorium and Thorium-Indium Alloys at Elevated Temperatures.

30. Water Desalination and General Reactor Economic Evaluations

D. A. Douglas, Jr.

We have evaluated the anticipated performance of fuel elements and calculated fuel fabrication costs for desalination reactors and several advanced converter reactors.

DESALINATION

D. A. Douglas, Jr. R. E. Adams
N. Pienaar[1] J. L. Scott

Our study of the problem of obtaining pure water from salt water by use of nuclear heat for evaporation was continued at a very modest level. Some fuel fabrication costs were calculated for new fuel element concepts, and in the process an interesting facet of manufacturing costs was established. Last year the importance of production levels was described. We now know that an additional important factor is the fuel density per unit length of cladding. One infers then that elements containing metallic fuel should be cheaper to fabricate than those containing ceramic fuel. A literature survey was conducted to ascertain known temperature and burnup limitations on metal fuels.

In desalination reactor economics, it is generally agreed that minimum costs are achieved by minimizing the costs per unit of heat (i.e., $\$/10^6$ Btu). The thermodynamic efficiency, which increases with increasing fuel surface temperature, is of secondary importance. Since this is true, it makes sense to reevaluate metal fuels, which are cheap to fabricate but have temperature limitations, to determine if they will result in lower overall costs in desalination plants than metal-clad oxide elements.

Toward this end we surveyed extensively the available information on the irradiation behavior of metal fuels. The types of metal fuels considered included unalloyed uranium, uranium with small alloy additions, U–10% Mo, and thorium-base uranium alloys. The erratic behavior of "unalloyed" uranium observed in the early days is attributable either to variations in trace element content or to uncontrolled operating conditions during irradiation. Recent British work on adjusted uranium (200 to 500 ppm Fe and 500 to 1200 ppm Al, beta-quenched) showed good irradiation stability (and reproducibility) up to 600°C. Careful control of the metallurgical processing is required to get the fine distribution of precipitate particles (10^{13} to 10^{14} particles/cm^3) that is responsible for the good behavior. Other uranium-base alloys such as U–1% Zr and U–1% Nb showed no real advantage over unalloyed uranium.

Uranium–10% Mo shows excellent radiation stability at high fission rates to temperatures above 600°C, but it swells excessively in the temperature range 350 to 400°C at low fission rates.

Thorium-base uranium alloys have shown excellent irradiation stability to temperatures in excess of 600°C, but the amount of information on these alloys is much more limited than that on the uranium-base alloys. Thus, additional metallurgical development and irradiation testing will be required to assess their ultimate potential.

We are now starting to consider questions of fuel-cladding and fuel-coolant compatibility.

[1] Visitor from Africa.

GENERAL REACTOR ECONOMIC EVALUATIONS

D. A. Douglas, Jr.

Reactors can conveniently be categorized into three general groups: burners, converters, and breeders. Essentially all of the privately owned and operated central power stations now in existence use burners. That is, little or no new fuel is recovered when the operating life of a core is complete. Studies of future energy requirements compared with known and estimated nuclear ore reserves indicate that reactors that produce more fuel than is consumed will be needed by the end of this century to ensure the continuance of low power costs. This need could be markedly delayed by the early development of converter reactors, which offer better net fuel utilization than the present reactor types.

The purpose of the ORNL study of advanced converter reactors was to compare six reactor concepts and designs as proposed by various sponsoring organizations with regard to power costs and fuel utilization.[2] A particular set of economic ground rules was adopted, and a range of economic parameters was employed. The design and operating characteristics of each reactor were evaluated and capital, fuel cycle, and operating costs were calculated. From these data, power costs and the fuel utilization capability were derived.

The advanced converters are based on the attractive thermal conversion characteristics of the thorium fuel cycle. Thus, with the exception of a pressurized-water uranium-fueled reactor, which was included to provide a standard of reference, all the reactors were fueled with thorium and uranium. The reactor types evaluated were pressurized-water, seed-blanket, spectral-shift-control, pressure-tube heavy-water moderated and cooled, high-temperature gas-cooled, and sodium-cooled graphite-moderated. The size of the reference plants was selected as 1000 Mw (electrical).

Our task was to evaluate the claims made for the fuel element performance by each designer and to estimate the cost of fabricating these fuel elements for each reactor. The following sections summarize our contributions.

[2]M. W. Rosenthal *et al.*, *A Comparative Evaluation of Advanced Converters*, ORNL-3686 (in press) (Official Use Only).

Fuel Element Performance Evaluation

R. E. Adams

The fuel element performance of each reactor was analyzed to determine the extent to which it conforms to current fuel technology and to identify areas of concern that might be expected to limit the life of the fuel element. All the reactors represent some advance in fuel technology. The performance characteristics of a fuel element are not reliably established by a few successful experiments or by those in which only one or two of the several important factors are tested. Rather, the determination of reliability must await the statistical accounting afforded by a multitude of tests that simulate operational conditions. For some of the proposed reactors, test data and operating experience are sufficient to predict that the objectives can be obtained. For others, considerably more testing will be required before the design is proved and the operational limitations are established.[3] Fuel element characteristics for the different reactors are listed in Table 30.1.

The advanced converter reactors submitted for evaluation use three categories of core designs from the viewpoint of design conservatism. These are: (1) reactors designed on the basis of current technology, (2) reactors designed on the basis of current technology with assumptions regarding the outcome of development efforts currently in progress, and (3) reactors designed on the basis of extrapolations well beyond existing data.

The spectral-shift control and pressurized-water reactors are based on current technology.

The seed-blanket reactor falls into the second category, for which successful completion of the current developmental work within a few years should make available data on the performance of the seed fuel to design burnups. Although we estimate that the cladding will absorb more than 250 ppm H during the 10-year life, we regard this standard, which was set by Bettis Laboratory, as very conservative, and we believe that hydriding need not curtail the desired life expectancy.

The third category includes the heavy-water reactor, the high-temperature gas-cooled reactor, and the sodium-graphite reactor. Although these reactors are adequately designed for heat transfer, many assumptions regarding other performance

[3]*Ibid.*, chap. 4.

Table 30.1. Fuel Element Characteristics of Advanced Converter Reactors

	Reactor Type						
	Pressurized Water	Seed Blanket	Spectral-Shift Control	Heavy Water, Thorium Fuel	Heavy Water, Thermal Fuel	High Temperature, Gas Cooled	Sodium, Graphite
Fuel element configuration	Square array, 16 × 16 rods	Cylindrical with three chevrons	238-rod bundle	Three concentric tubes	Three concentric tubes	Graphite cylinder	Rod cluster, Na annulus
Active core length, ft	11.0	7.2	10.92	15.0	15.0	15.5	14
Fuel rod or tube diameter, in.	0.378 0.320	0.280 (seed) 0.674 (blanket)	0.420	Up to 3.630	Up to 3.830	4.5	0.590
Fuel life, years	3	10.7	2.1	1	1.7	6	2.68
Fuel	UO_2	UO_2-ZrO_2 (seed) ThO_2 (blanket)	UO_2-ThO_2	UO_2	ThO_2-UO_2	ThC_2-UC_2	UC
Fuel fabrication	Pelletized		Vibratory compaction	Vibratory compaction and swaging	Vibratory compaction and swaging	Coated particles	Cast, 0.50 in. in diameter
Fuel theoretical density, %	96.5	80	88	92	92		
Maximum $\int k\, d\theta$ at rated power	41.2 35	39.5 (seed) 40 (blanket)	39.5	34	25	2900°F	2000°F
Average burnup in maximum power rod, Mwd/metric ton	30,000	813,000[a] (seed) 81,000[b] (blanket)	45,000	19,100	27,600	80–90 at. % U 6–10 at. % Th	40,000
Core average burnup, Mwd/metric ton	25,000	569,000[c] (seed) 35,000[d] (blanket)	30,000	15,400	22,200		35,000
Cladding material	Zircaloy-4	Zircaloy-4	Zircaloy-4	Zircaloy-2	Zircaloy-2	Pyrolytic carbon coating	Zircaloy-2
Cladding thickness, in.	0.020	0.018 0.038	0.025	0.025	0.025		0.020
Maximum cladding surface temperature, °F	640	640	650	626	626		1250
Maximum cladding surface heat flux at rated power, Btu hr^{-1} ft^{-2}	544,000	669,000 (seed) 300,000 (blanket)	470,000	820,000	621,000	140,000	760,000
Coolant	H_2O	H_2O	H_2O-D_2O	D_2O	D_2O	He	Na
Coolant inlet pressure, psi	2050	1980	2200	1900	1874	450	
Coolant inlet temperature, °F	546	520	535	507	507	720	750
Coolant outlet temperature, °F	598	568	594	579	579	1470	1150

[a] 30×10^{20} fissions/cm^3.
[b] 15×10^{20} fissions/cm^3.
[c] 20×10^{20} fissions/cm^3.
[d] 6.5×10^{20} fissions/cm^3.

factors are well beyond demonstrated technology, and these fuel concepts will require extensive development and testing.

The fuel element for the heavy-water reactor is nested. One problem with it is that the cladding may fail by nonuniform collapse. Since a complete fuel element assembly has never been tested, the possibility of ratchetting and fretting corrosion has not been explored.

Although the Sodium Reactor Experiment and the Hallam Reactor have been operated, the current proposal for a large sodium-cooled power reactor is based on some major extrapolation of the demonstrated technology. The use of vented zirconium cladding and outlet coolant temperature some 300°F above previous experience raises numerous questions that must be resolved.

The fuel element for the high-temperature gas-cooled reactor is still being evolved. The one proposed for this study departs markedly from the one being fabricated for the Peach Bottom Reactor, which is still many months from even going critical, much less reaching full-power operation. A great deal of development and test is under way, but much remains to be done to fully demonstrate the capability of the fuels proposed for a gas-cooled fueled-graphite reactor.

We concluded that all of these fuel elements could be successfully developed and would meet the proposed operating goals in the time period 1970–80. Thus, the fuel cycle cost estimates were based on the sponsor's proposals with no penalty for the present embryonic state of technology in certain concepts.

Fuel Fabrication Costs for Advanced Converter Reactors

A. L. Lotts

We calculated the costs of fuel fabrication for the six reactors being evaluated in the Advanced Converter Reactor study.[4] In addition to the differences in fuel element design imposed by these different reactor concepts, added variations were introduced for each reactor, because of changes in fuel material during the fuel cycle and because of a needed evaluation of the relative costs of fuel materials.

Fuel element designs proposed by proponents of the reactors were used as a basis for calculation of costs. We used computer programs specifically devised for this study (next subsection). Data were obtained for a range of plant capacities and plant amortization rates; Table 30.2 gives representative data for plants amortized at 22%.

Computer Programs for Calculation of Fuel Fabrication Costs

A. L. Lotts

In the evaluation and comparison of various proposed reactors, the cost of fuel element fabrication is an important consideration. Therefore, we need to calculate and predict fuel fabrication costs for reactor systems that may be used many years in the future.

The prediction of these costs involves the selection of fabrication procedures or flowsheets, the calculation of operating and capital costs, and the cost of materials used in the processes. Also, certain factors that are based upon the environment in which the fabrication must be done, upon the degree of optimism being employed, and upon the method of financing must be applied to these costs.

Because of the large number of variables in calculating fabrication costs, three computer programs, FABCOST 1, FABCOST 2, and FABSUM, were written to perform the calculations. Basic information on operating and capital costs of individual steps in the various fabrication flowsheets and on the cost of materials were collected for use in the programs.

The programs work in the following way. The fuel element is described in terms of its parameters; for example, outside diameter of the tubing, the fuel diameter, the length of the fuel rods, the length of the fuel element, the type of fuel, and the type of cladding. These data are used as input for the computer program. Also, the amortization rates to be applied, the type of fabrication plant to be used, the number of operating days for the plant, and other factors are selected and used as additional input data. The computer programs

[4] M. W. Rosenthal *et al.*, *A Comparative Evaluation of Advanced Converters*, chap. 8, ORNL-3686 (in press) (Official Use Only).

then select the proper flowsheet for application to the particular fuel element and compute operating, capital, hardware, and fuel-preparation costs for that particular case. The results are tabulated as dollars per kilogram and mills per kilowatt hour for different plant capacities.

Our programs calculate costs for fuel elements of three general types: (1) rod bundles, which are clusters of small-diameter metal-clad fuel rods; (2) nested fuel elements, which consist of concentric metal tubes filled with a fuel material; and (3) fueled graphite fuel elements, which consist of graphite bodies filled with a fuel material. Each of these general types of fuel elements can have a variety of cladding materials, fuel materials, and shapes. The use of our codes permits the evaluation of effects of single or several interacting parameters on fabrication costs.

Table 30.2. Fabrication Costs for Nonrecycle Fuel in Single-Purpose Plants, Amortized at 22%

Type of Fuel Element	Fuel	Plant Capacity (kg of heavy metal/day)					Type of Plant
		500	1000	3000	5000	10,000	
		Cost ($/kg heavy metal)					
PWR (vibratory compaction)	$(^{235}U\text{-}^{238}U)O_2$	114	71	50	45		Contact
PWR (pellets)	$(^{235}U\text{-}^{238}U)O_2$	127	85	60	53		Contact
Seed-Blanket	$(^{235}U\text{-}Th)O_2$	305	200	126	110		Hooded
SSCR	$(^{235}U\text{-}Th)O_2$	106	65	45	40		Hooded
HWR	$(^{235}U\text{-}Th)O_2$		52	28	23.5	18.5	Hooded
HWR	$(^{235}U\text{-}^{238}U)O_2$		47	27.5	23	18	Contact
HTGR (250-μ particles, virgin BeO)	$(^{235}U\text{-}Th)C_2$	180	160				Hooded
HTGR (250-μ particles, recycle BeO)	$(^{235}U\text{-}Th)C_2$	102	92				Hooded
HTGR (1000-μ particles, virgin BeO)	$(^{235}U\text{-}Th)C_2$	182	161				Hooded
HTGR (1000-μ particles, recycle BeO)	$(^{235}U\text{-}Th)C_2$	108	94				Hooded
SGR (Zr clad, vented)	$(^{235}U\text{-}^{238}U)C$	100	64	35	28		Contact
SGR (stainless steel clad, nonvented)	$(^{235}U\text{-}^{238}U)C$	96	58	30	23.5		Contact
Seed-Blanket	$(^{233}U\text{-}Th)O_2$	370	250	165	144		Remote
SSCR	$(^{233}U\text{-}Th)O_2$	132	80	57	50		Remote
HWR	$(^{233}U\text{-}Th)O_2$		58	32.5	26.5	21	Remote
HTGR (250-μ particles, virgin BeO)	$(^{233}U\text{-}Th)C_2$	195	175				Remote
HTGR (250-μ particles, recycle BeO)	$(^{233}U\text{-}Th)C_2$	120	103				Remote
HTGR (1000-μ particles, virgin BeO)	$(^{233}U\text{-}Th)C_2$	205	180				Remote
HTGR (1000-μ particles, recycle BeO)	$(^{233}U\text{-}Th)C_2$	130	112				Remote

Part IV.
Other Program Activities

31. SNPO-C NERVA Program Assistance

E. A. Franco-Ferreira

The Metals and Ceramics Division is providing materials and fabrication technology support to the NASA Space Nuclear Propulsion Office on the NERVA Nuclear Rocket Program. In general, we are providing technical liaison between NASA and its contractors and, where necessary, performing appropriate experimental studies. To date, the assistance on this program has been directed entirely toward the fabrication of nozzles to be used in static reactor test firings at the Nevada test site. Our work may be divided into two broad categories: studies in direct support of NASA contractor operations and studies aimed at developing a generalized rocket materials technology. Some aspects of this general experimental program will be discussed below. Table 31.1 gives the compositions of two alloys we are studying.

Table 31.1. Composition of Nickel-Base Alloys for Rocket Nozzles

Element	Content (%)	
	René 62	Inconel X-750
Chromium	15.00	14.0–17.0
Iron	22.50	5.0–9.0
Molybdenum	9.00	
Titanium	2.50	2.25–2.75
Niobium	2.25	0.70–1.20
Aluminum	1.25	0.40–1.00
Manganese		1.0 max
Silicon		0.5 max
Copper		0.5 max
Carbon	0.05	0.08 max
Boron	0.010	
Sulfur		0.01 max

BRAZING OF RENÉ 62

E. A. Franco-Ferreira

René 62, a precipitation-hardenable nickel-base alloy, is of interest as a construction material for advanced-performance nuclear nozzles. Since furnace brazing is widely used for nozzle fabrication, the brazability of the material is of importance and we studied it.

In essence, we brazed numerous René 62 T-joints, using a variety of brazing alloys and atmospheres. Table 31.2 shows some of the data. Based on these data, we concluded that René 62 is brazable with most commercially available brazing alloys. However, the brazing conditions used are of great importance, particularly the atmospheric protection of the joint during brazing. The hardening constituents of René 62 are aluminum and titanium, which form oxides that are extremely difficult to reduce and impede the flow of brazing alloy. Thus, for optimum results vacuum brazing should be used. If brazing either in an inert-gas or hydrogen atmosphere is necessary, the joint should be protected by prebraze nickel plating.

HOT-DUCTILITY OF INCONEL X-750

R. G. Gilliland

The use of Inconel X-750 for the fabrication of rocket nozzles requires that its weldability be

Table 31.2. Results of Brazing Studies on Rene´ 62 T-Joints

Brazing Alloy	Composition (wt %)	Specimen Pretreatment	Brazing Temperature (°C)	Atmosphere	Remarks
Coast Metals 52	4 Si–3 B–93 Ni	0.002-in. Ni plate	1060	Hydrogen	Good wetting and flow
Copper		0.002-in. Ni plate	1100	Hydrogen	Fair wetting and flow
Gold-nickel	82 Au–18 Ni	0.002-in. Ni plate	1010	Hydrogen	Good wetting and flow
Nicrobraz 50	10 P–12 Cr–78 Ni	0.002-in. Ni plate	1000	Hydrogen	Fair wetting and flow
Coast Metals 52	4 Si–3 B–93 Ni	Bare specimen	1060	Helium	Fair wetting, no flow
GE-8600	4 Si–32 Cr–24 Pd–40 Ni	Bare specimen	1170	Helium	Fair wetting, no flow
Gold-nickel	82 Au–18 Ni	Bare specimen	1010	Helium	Fair wetting, no flow
GE-8102	15 Cr–8 Si–77 Ni		1170	Vacuum	Fair wetting and flow
GE-8400	18 Cr–16 Ni–8 Si–4 W–1 B–53 Co		1170	Vacuum	Poor wetting and flow
GE-8600	4 Si–32 Cr–24 Pd–40 Ni		1170	Vacuum	Good wetting and flow
Gold-nickel	82 Au–18 Ni		1010	Vacuum	Very good wetting and flow
Nicrobraz 50	10 P–12 Cr–78 Ni		1010	Vacuum	Fair wetting, no flow
Coast Metals 52	4 Si–3 B–93 Ni		1060	Vacuum	Excellent wetting and flow
Coast Metals 62	16 Ni–16 Co–1 B–67 Mn		1100	Vacuum	Poor wetting and flow; skulling
GE-8202	2 Cr–2.5 Si–1.5 B–94 Ni		1100	Vacuum	Good wetting and flow

demonstrated. Both to define this property and provide elevated-temperature mechanical properties, a useful method is the hot-ductility technique developed at Rensselaer Polytechnic Institute.[1] We used this method to measure the weldability of Inconel X-750, heat No. 3977X.

This study was performed by tensile testing $\frac{1}{4}$-in.-diam samples during progression through a predetermined thermal cycle. The temperature cycle was automatically controlled and represents the thermal history experienced by a point in the heat-affected zone of a weld as the welding arc passes nearby. We assumed that the thermal properties of Inconel X-750 were similar to those of stainless steel. Therefore, we used thermal cycles that had been calculated and measured for $1\frac{1}{2}$-in. stainless steel plate with a welding energy input of 70,000 joules/in. and a preheat of 80°F.

The elevated nil ductility temperature (NDT) of heat No. 3977X was found to be 2300°F. This temperature was established, as shown in Fig. 31.1*a*, *b*, and *c*, by determination of the point at which the reduction in area, tensile strength, and total strain become zero during the heating portion of the welding thermal cycle. The ability of this material to withstand loading and straining while cooling from the NDT is exhibited in Fig. 31.1*d*, *e*, and *f*. This property measures the weldability of the material; these tests indicate that it possesses excellent base-metal weldability characteristics. The results of the hot-ductility test showed that the Inconel X-750 deteriorated negligibly in properties after being subjected to a simulated weld thermal cycle.

[1]E. F. Nippes *et al.*, *Welding J.* **34**(4), 183–85 (1955).

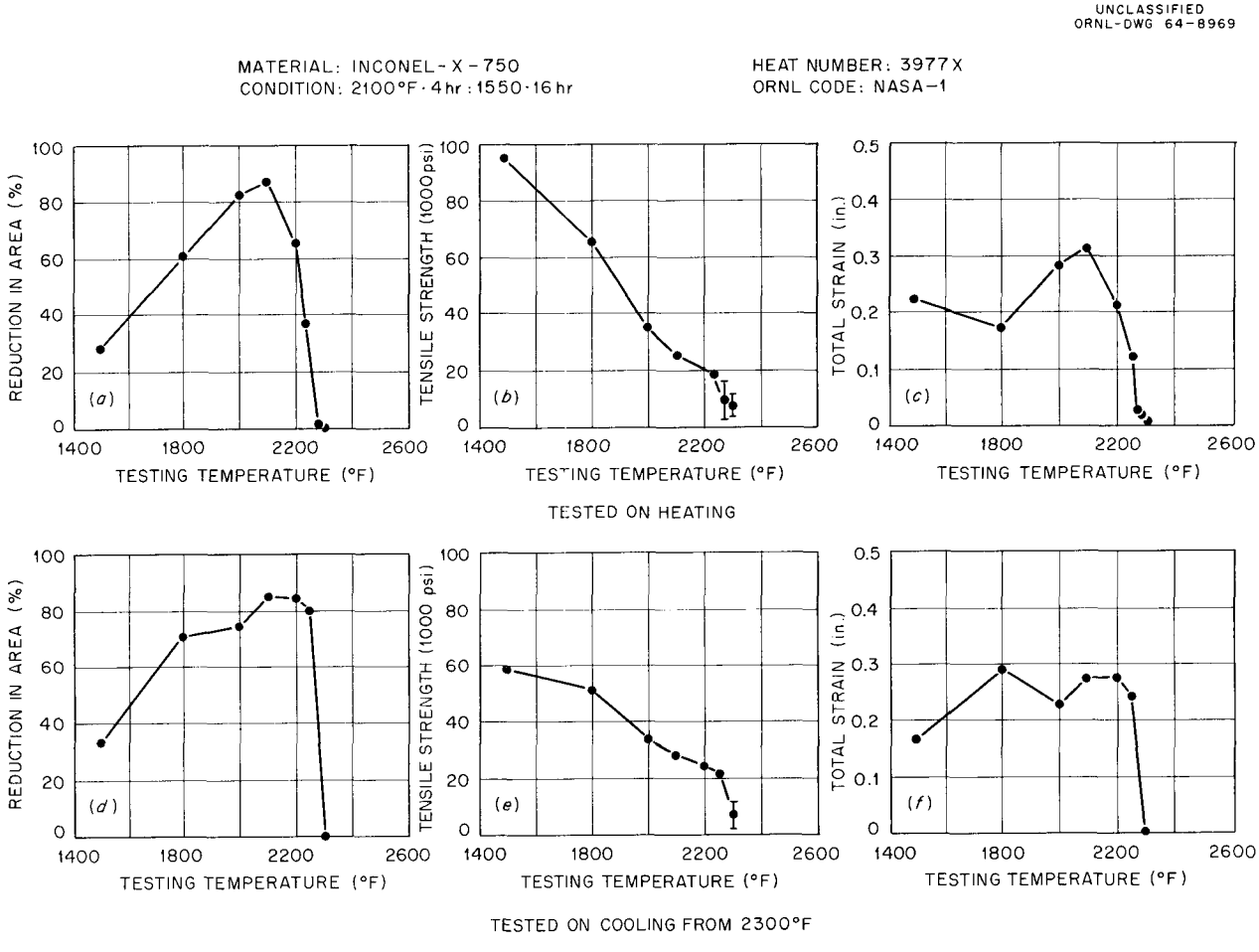

Fig. 31.1. Results of Hot-Ductility Studies on Inconel X-750.

32. Thermonuclear Project

R. E. Clausing

The goal of the Thermonuclear Project is to make the energy released by the fusion of the deuterium and tritium isotopes of hydrogen available in a tractable way. Progress toward this goal continues to be paced primarily by developments in plasma physics. The "fuel element" for a thermonuclear reactor will likely be a dense high-temperature plasma contained by magnetic fields. The experimental program at ORNL consists of several large and complex experiments whose immediate goals are to find ways of generating and containing such plasmas.

METALLURGICAL SUPPORT

The metallurgical support is in three areas: (1) consultation and other forms of help with the metallurgical problems encountered in the design and construction of experimental equipment, (2) research and development in the field of superconductivity, and (3) research and development in the field of vacuum technology.

The first area is increasingly important as equipment becomes more complex and the designs more demanding. Because of its diverse nature this effort does not lend itself to discussion here. The research and development work in superconductivity, which is no longer part of the Thermonuclear Project, is reported in Part I, Chap. 5, this report. However, since it is aimed at control of metallurgical variables in the construction of superconducting magnets, it is still of vital interest to the Sherwood project.

VACUUM STUDIES

The creation and containment of high-energy high-density plasmas requires an ultrahigh vacuum environment as free as possible of all materials, especially those with high atomic numbers or large molecular weights. Past efforts have been to decrease this contamination and the partial pressure of hydrogen simultaneously through the use of sorption on titanium films. The hydrogen results from the neutralization of ions escaping from the plasmas. This technology is now well developed and has been applied in the space program and in commercial vacuum systems as well as in thermonuclear research. We are now investigating the interaction of electrons with vacuum interfaces (i.e., material surfaces bounding the vacuum regions). These interactions are important both because they may play an important role in the relationship of plasmas with material boundaries and because electrons may be used to desorb gases from surfaces and thereby provide a means of cleaning vacuum systems.

We are determining both the amounts and species of gases released by bombardment of surfaces with electrons with energies from a few electron volts to 70 kev. Depending upon the conditions of the experiment, the number of gas molecules released has varied from 10^{-4} to 10 for each electron incident upon the surface. The large yields occurred in very "dirty" systems and are apparently due to the decomposition of hydrocarbon molecules. Yields of gas molecules as large as 10^{-2} per electron were observed in systems not detectably contaminated with hydrocarbons. These results are not merely due to heating by the electron bombardment. These experiments and their results have been reported elsewhere.[1]

The experimental apparatus now in use is shown schematically in Fig. 32.1. The chamber in which electron bombardment takes place has a volume

[1] R. E. Clausing, *Thermonuclear Div. Semiann. Progr. Rept. April 30, 1964*, ORNL-3652, pp. 132–36.

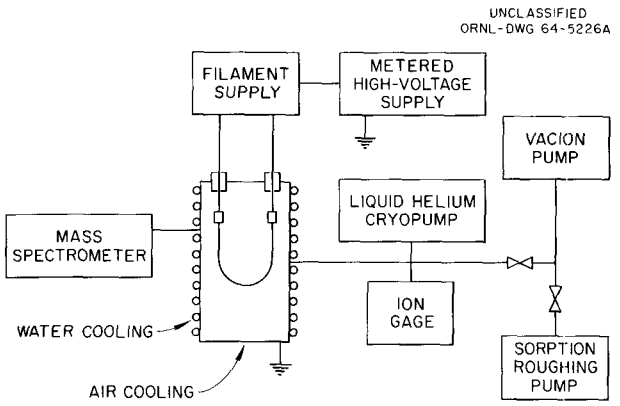

Fig. 32.1. Block Diagram of the EB-IV Electron Bombardment Apparatus.

of approximately 2.5 liters and a surface area of nearly 1000 cm^2. The chamber wall that is bombarded with electrons is made of type 304 stainless steel. Its temperature is held constant by combined water and air cooling. The system is assembled with metal gaskets to avoid introduction of hydrocarbons. The electron source is a simple tungsten wire filament. Several filament sizes have been used ranging from 0.005 to 0.015 in. in diameter with heated lengths from 2 to 15 cm. The smaller filaments are preferred since they require less heater power. Electron currents from 0.5 μa to 30 ma have been used resulting in average fluxes on the surface of 10^9 to 10^{14} electrons cm^{-2} sec^{-1}. The mass spectrometer is a General Electric model 22 PT 120 capable of detecting partial pressures of less than 10^{-13} torr without special care. The liquid helium cryopump was designed and built for this experiment. It evaporates less than 100 cm^3 of liquid helium per 8-hr day and should have a base pressure considerably below 10^{-10} torr. The pumping speed is equivalent to the conductance of a 2-cm^2 orifice for the helium-cooled surface and a 5-cm^2 orifice for the liquid-nitrogen-cooled surface. Normally an orifice with a 0.1-cm^2 opening will be placed over the pump opening to give a known pumping speed for all molecular weights. The Vacion pump is valved off during measurements. In normal operation the filament is kept at emitting temperature and the high voltage is pulsed on and off while the change in partial pressure of the various gases is observed with the mass spectrometer. Knowing the pumping speeds and change in pressure, one can calculate the amount of gas released. Dividing this amount by the electron current gives the yield of gas molecules per electron. This yield is then determined as a function of current, voltage, and surface conditions. Data from this experiment have been used primarily to confirm earlier data obtained without the mass spectrometer.

Figure 32.2 shows data on yields obtained in a wide variety of earlier experiments. The data marked EB-I are typical of those obtained thus far in the newer experiment, EB-IV, described above. These data illustrate the wide range of yields obtained and the relationship of system cleanliness to yield values. The data from the Ultrahigh Vacuum Test Facility show the yield curves for a copper system seriously contaminated with diffusion pump oil and for the same system after a mild thermal bake (20 hr at temperatures between 100 and 145°C). The yield after the bake was $\frac{1}{20}$ that before. In these two experiments, the yield did not depend greatly on electron energy. Additional baking decreased the yields in this system still further, but a change in the experimental techniques precludes direct comparison. The data from the DCX-1 end region illustrate the yields obtained after extensive electron bombardment in a complex system of stainless steel and copper. The yields at 3 kev were initially about 10 gas molecules per electron but decayed to the curve shown after electron bombardment of the exposed surfaces preceded by baking some of the copper parts, a small fraction of the total surface involved. The data for the DCX-1 liner were obtained after a 12-hr bake at 400°C. Although the surface had previously been coated with titanium, the getter film was no longer active, and no fresh titanium was evaporated. The surface was probably not seriously contaminated with oil. The data labeled EB-I, EB-II, and EB-III are representative of those obtained in systems built to avoid contamination with hydrocarbons; these systems also show electronic cleaning (i.e., the initial yields decrease as bombardment progresses). The curves for the cleaner surfaces all show an increase in yield in the region near 1 kev electron energy. The data in Fig. 32.2 are shown only for comparison and are not quantitatively accurate. They are computed from ion-gage readings and estimated pumping speeds with the assumption that the gases are "nitrogen-like" (i.e., the ion-gage sensitivity

and pumping speeds for nitrogen were used). If the gases are predominantly hydrogen, the yields shown may be as little as one-eighth the correct values. In fact, the gases released from systems contaminated with hydrocarbons may be mostly hydrogen as discussed below.

The gases released during bombardment of stainless steel have been hydrogen and carbon monoxide in a ratio increasing from 6 to 30 (with a corresponding decrease in yield from approximately 10^{-1} to 5×10^{-3}) as bombardment progressed at an electron energy of 5 to 10 kev. These data are probably typical of what can be expected from surfaces with small amounts of hydrocarbons initially present. No data are yet available on clean stainless steel surfaces. Bombardment of a "clean" tungsten surface released approximately five carbon monoxide molecules to one of hydrogen. This probably reflects the contamination of the "clean" surface by residual gases in the system.

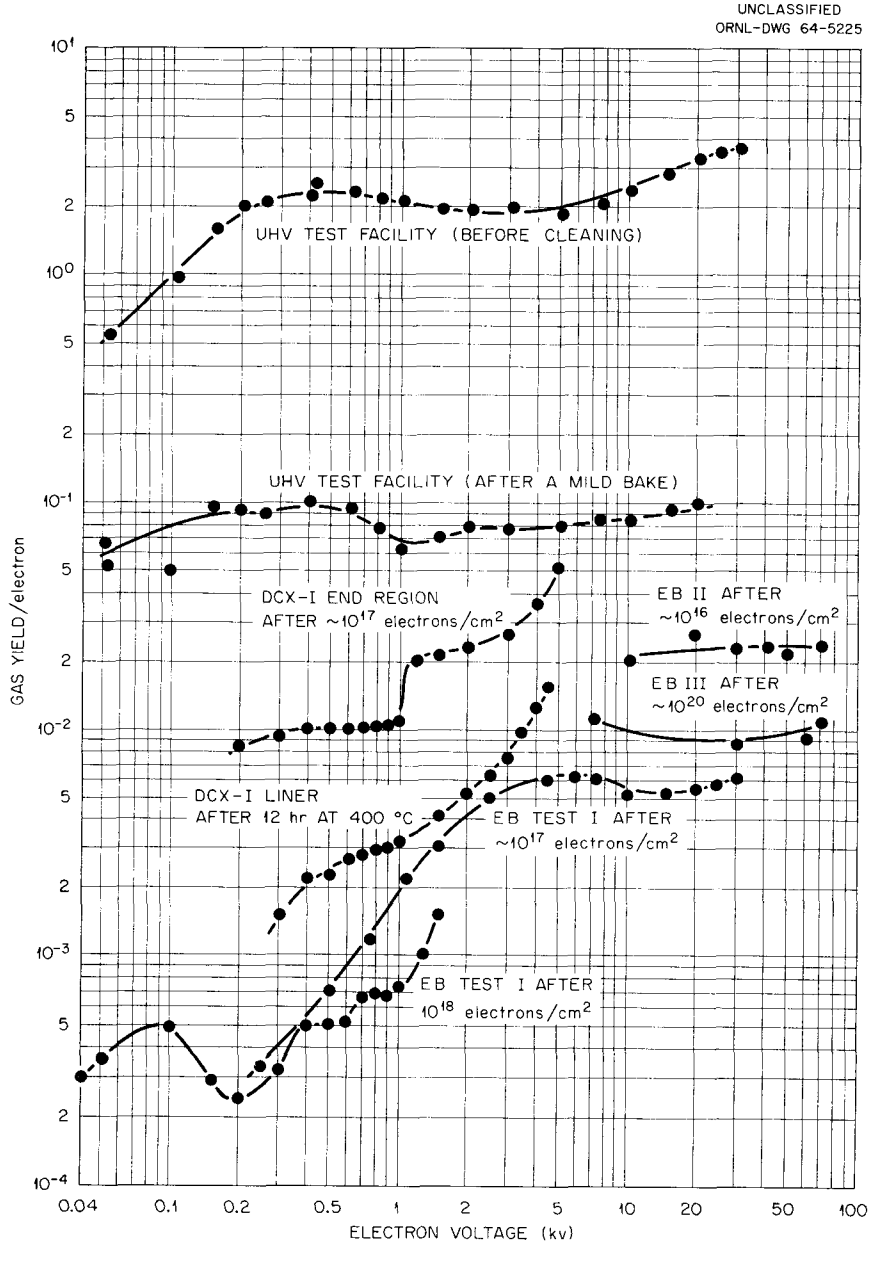

Fig. 32.2. Comparison of the Results of the Various Electron Bombardment Experiments.

Based on the preliminary experiments summarized above, the following conclusions seem reasonable.

1. Reduction of partial pressures of hydrocarbon vapors in vacuum systems by electron bombardment is both feasible and practical.
2. Both the kind and quantity of gases evolved during electron bombardment depend upon the type and amount of contamination on the surface and thus provide a means of characterizing the condition of the surface.
3. Electronic desorption is not a bulk heating effect. A combination of thermal baking and electron bombardment may be used advantageously.
4. Electronic desorption may be capable of producing clean surfaces without heating or causing radiation damage to the substrate. If hydrocarbons are present, however, a nonvolatile residue of carbonaceous material may be formed on the surface.

33. Transuranium Program

D. A. Douglas

The Transuranium Program is being carried out in two parts. One is the design and construction of the High Flux Isotope Reactor (HFIR), for which the development of the fuel and control elements is a responsibility of the Metals and Ceramics Division. This work is described in Part III, Chap. 26 of this report. The second phase of the program is the development of remote fabrication of the target elements and the requisite equipment. Progress on this phase is reported below.

The initial targets will contain plutonium oxide. Following their exposure in the reactor, desired isotopes will be chemically separated and suitably processed to provide material for inclusion in new targets for additional exposure. Through these sequential steps, gram quantities of the higher actinide oxides (americium, curium, berkelium, and californium) can be produced. Since the material to be processed will be highly radioactive and toxic, a heavily shielded and contained facility is required for carrying out the chemical processing and fabrication steps.

Our work consists of developing procedures for fabrication of satisfactory target elements, conducting irradiation tests to demonstrate the adequacy of the fabrication techniques, and inventing or adapting equipment to carry out the fabrication in enclosed and shielded cubicles.

TRANSURANIUM TARGET FABRICATION EQUIPMENT

M. K. Preston, Jr.[1] A. L. Lotts
R. I. Deaderick[2]

The HFIR target element shown in Fig. 33.1 consists of a $\frac{3}{8}$-in.-OD intermittently finned tube and a hex-can sheath, which is mechanically attached to the fins at the bottom of the target rod and acts as a spacer and coolant channel. The 35-in. elements contain 0.250-in.-diam, 0.571-in.-long pellets in the 20-in. active length. The remainder of the length is occupied by end caps and void space for the accumulation of fission gas. The pellets, which are completely encapsulated in aluminum, are compacts of actinide oxides and aluminum powder pressed to a density of 89 to 91% of theoretical.

The fabrication and inspection of the target elements employs a combination of powder-metallurgical, welding, inspection, and chemical techniques which will be carried out in three cubicles. The basic criteria and methods of operations have not changed substantially from that outlined previously.[3] All equipment is to be designed to operate semiautomatically, requiring minimum use of the manipulators. To minimize the spread of contamination, special devices will be used to transfer materials between steps in the process, and auxiliary enclosures around some equipment items will eliminate recontamination of cleaned components. All equipment is to be designed for easy removal via the 35- by 18-in. equipment-transfer opening in the cell roof. Further, many equipment components are to be designed for removal via the 8-in.-diam, 8-in.-deep intercell conveyor.

Figure 33.2 shows the layout of the target fabrication and inspection equipment for the Transuranium Facility. A résumé of the status of the

[1]On loan from General Engineering and Construction Division.

[2]Oak Ridge Gaseous Diffusion Plant.

[3]M. K. Preston, *Metals and Ceramics Div. Ann. Progr. Rept. May 31, 1962*, ORNL-3313, pp. 108–11.

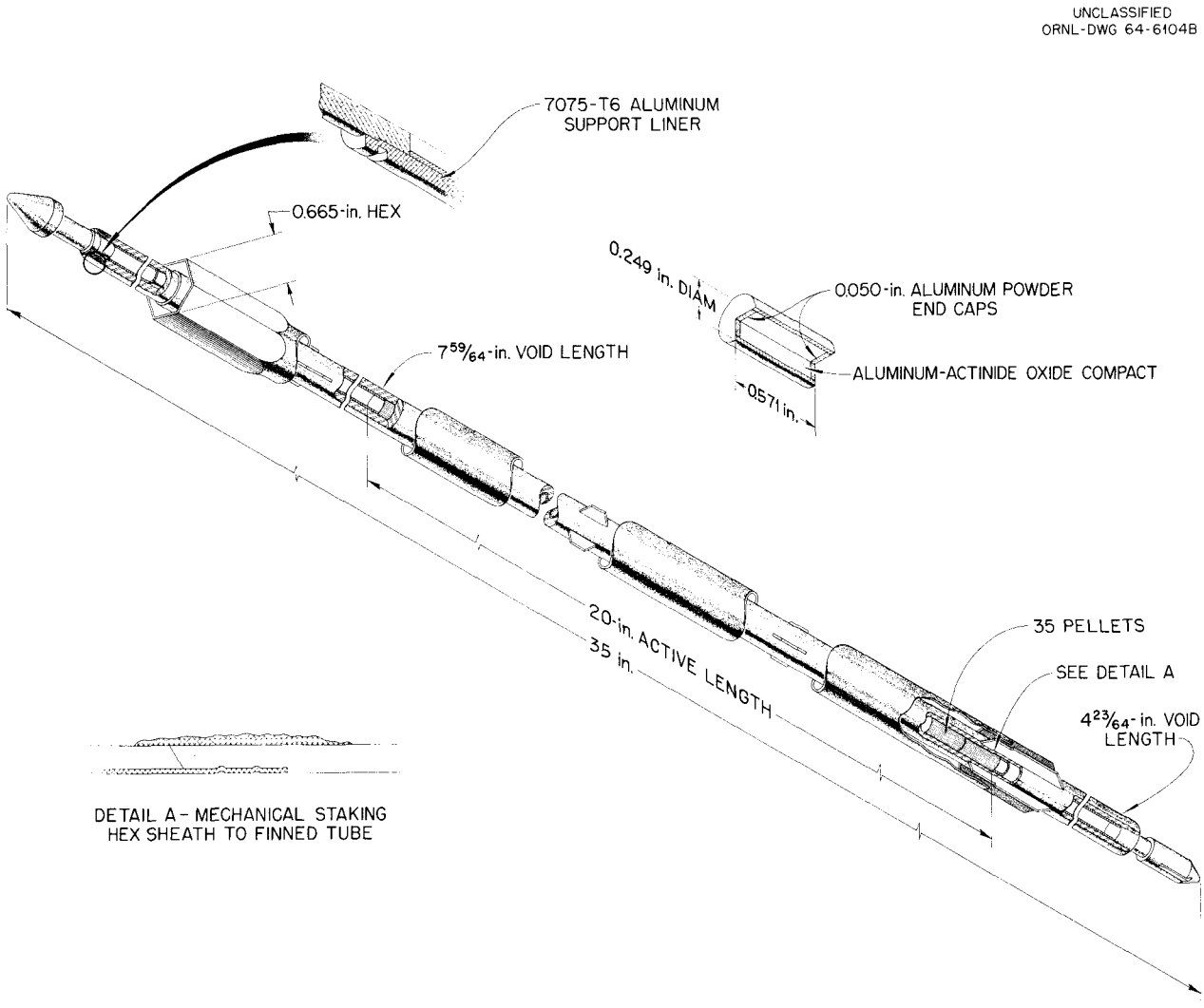

Fig. 33.1. Target Element for the High Flux Isotope Reactor.

design and development follows. More detailed information is reported elsewhere.[4-6]

Cubicle 3

Design and development of equipment for cubicle 3, which includes all operations up to completion of the pellets, are further advanced than that for the other two cubicles. Conceptual design of equipment is 87% complete, detailed design is 77% complete, and procurement is 65% complete. Table 33.1 depicts the status of equipment design or test. Items 3, 4, and 16 are new equipment pieces called for by recent changes and additions to the process. Items 6 and 15 are being redesigned because the original equipment design did

[4]M. K. Preston, R. I. Deaderick, and A. L. Lotts, *Transuranium Quart. Progr. Rept. Aug. 31, 1963*, ORNL-3358, pp. 76–83.

[5]M. K. Preston, R. I. Deaderick, and A. L. Lotts, *Transuranium Quart. Progr. Rept. Nov. 30, 1963*, ORNL-3597, pp. 50–63.

[6]M. K. Preston, R. I. Deaderick, and A. L. Lotts, *Transuranium Quart. Progr. Rept. Feb. 29, 1964*, ORNL-3651 (in press).

UNCLASSIFIED
ORNL-DWG 64-1442R1

CUBICLE 1
1. TUBE RECEIVING AND SURFACE SMEAR
2. X-RAY STATION
3. X-RAY UNIT
4. DIMENSIONAL INSPECTION STATION
5. HEX CAN ATTACHMENT
6. ULTRASONIC CLEANER
7. HYDROSTATIC COLLAPSE
8. PUMP FOR HYDROSTATIC COLLAPSE
9. HELIUM LEAK TEST STATION
10. TARGET REMOVAL STATION
11. TRANSFER ARM

CUBICLE 2
1. PELLET DIAMETER GAGE
2. STACK LENGTH GAGE
3. PELLET FEEDING ASSEMBLY
4. SECONDARY ENCLOSURE
5. TUBE HOLDER AND UPENDING STATION
6. HELIUM LEAK TEST CHAMBER
7. TRANSFER ARM
8. ASSEMBLY AND WELDING STATION
9. ULTRASONIC CLEANER
10. PASS-THRU TUBES

CUBICLE 3
1. CALCINER
2. PRESS STATION
3. PELLET TRANSFER CONTAINER
4. DIE FEED STATION
5. CAP-POWDER STATION
6. DIE HOLDER, DIE HOLDER STATION
7. BLENDER-DISPENSER
8. BLENDER-DISPENSER ELEVATING MECHANISM
9. DIE SCALE ASSEMBLY
10. BATCH SCALE
11. SCALES SUPPORT PLATFORM
12. ALUMINUM POWDER ADD STATION
13. TRANSFER ARM
14. PELLET TRANSFER TUBE
15. ULTRASONIC CLEANER
16. THERMAL CLEANER

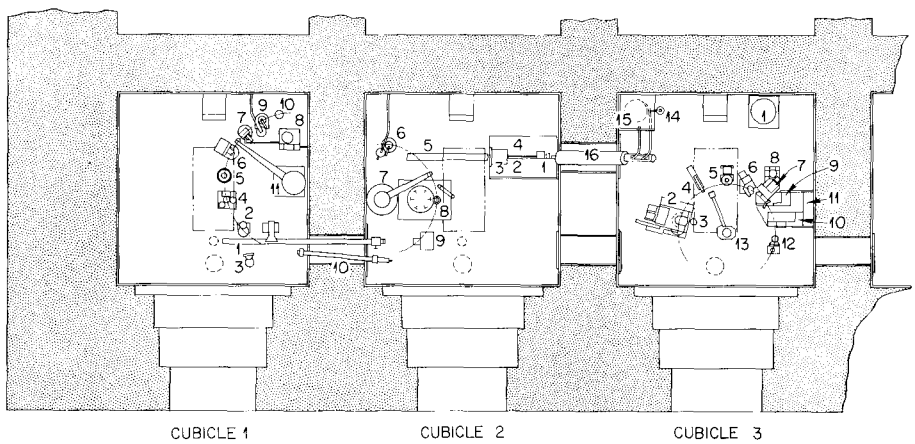

Fig. 33.2. Target Fabrication Equipment Plan.

not function properly. The equipment design has progressed so far that design and layout for electrical and in-cell piping are now under way.

Cubicle 2

Conceptual design of equipment for cubicle 2 is 80% complete, detailed design is 65% complete, and procurement is 35% complete. Table 33.2 summarizes the equipment status. Conceptual and detailed design is centered around the target assembly machine, which is to make the last preparations and the closure weld on the assembled rod. Bench testing of the pellet inspection and loading equipment showed that all components are satisfactory except the pellet-diameter gage. A redesigned gage is being fabricated.

Cubicle 1

Conceptual design of equipment for cubicle 1 is 70% complete, detailed design is 25% complete, and procurement is 10% complete. Table 33.3 shows the status of equipment design. The major effort is to complete the equipment design with the emphasis on that for dimensional inspection of the rod. A new device for hot collapse of the target rod is to replace the hydrostatic collapse equipment so as to reduce the radial gap between pellet and rod from 0.0005 to 0.0001 in. and thus improve the heat transfer characteristics of the rod.

All in-cell equipment is now being designed or procured for test, the design is approximately 62% complete, and all equipment should be designed by next September. Approximately 1200 man-days will be required to finish the design, and an additional 800 man-days will be required for testing and modifications of the equipment to ensure a workable production line for the fabrication and inspection of the HFIR targets.

Table 33.1. Cubicle 3 Equipment Percentage Completion[a]

Item No.	Description	Conceptual Design	Detailed Design	Procurement	Bench Test and Modify
1	Actinide calciner	100	90		
2	Pellet press	100	100	100	100
3	Pellet check weigh and length measurement	100			
4	Pellet storage container	50			
5	Die feed station	100	100	100	100
6	Cap powder station	25			
7	Die holder and die holder station	100	100	25	
8	Blender-dispenser	100	100	100	100
9	Blender-dispenser elevating mechanism	100	100	25	
10	Die-scale assembly	100	100	25	
11	Batch-scale assembly	100	100	25	
12	Scales support platform	100	100	25	
13	Aluminum powder addition station	100	100		
14	Transfer arm	100	100	100	100
15	Pellet ultrasonic cleaner	25			
16	Pellet vacuum anneal	25			
17	Pellet transfer	25			
18	Equipment mounting base	100	100	100	100
19	Cell crane	100	100	25	

[a]Mockup operation and any required redesign and modification are not started on any of these items.

PLUTONIUM TARGET FABRICATION

J. D. Sease A. L. Lotts

Target elements containing ^{242}Pu are to be fabricated for the initial and part of the subsequent target loadings of the HFIR. The design of the ^{242}Pu-containing elements is identical to that of the elements to be fabricated in the Transuranium Processing Facility. However, the low amount of penetrating radiation from plutonium allows relatively simple fabrication in glove boxes rather than the complex remote fabrication that will be carried out in the TRU Facility. The steps in plutonium target-element fabrication are shown in Fig. 33.3.

Table 33.2. Cubicle 2 Equipment Percentage Completion[a]

Item No.	Description	Conceptual Design	Detailed Design	Procurement	Bench Test and Modify
1	Pellet-diameter gage	100	100	100	75
2	Stacked length gage	100	100	100	100
3	Pellet feeding assembly	100	100	100	100
4	Secondary enclosures	100	100	100	100
5	Tube-loading station	100	50		
6	Void measurement	100	25		
7	Assembly and welding station	100	25		
8	Helium leak test chamber	100	100	25	
9	Helium leak test console	100	100	25	
10	Target transfer arm	75			
11	Target ultrasonic cleaner and transfer	100	25		
12	Equipment mounting base	50			
13	Cell crane	100	100	25	

[a]Mockup operation and any required redesign and modification are not started on any of these items.

The plutonium target fabrication line consists of a series of alpha-tight gloved enclosures, in which all operations involving direct contact with PuO_2 are carried out, and a work bench where the final inspection and assembly operations are performed. The fabrication equipment includes an automatic pellet-weighing station, a pellet press, a furnace for thermal cleaning of pellets, an end-closure welding apparatus, a hydrostatic collapse rig, and a helium mass-spectrometer-type leak tester. The only operation not carried out in the fabrication line is radiography.

Detailed descriptions of the equipment are contained in several documents.[7-9]

During the year, procurement of the target-line fabrication equipment was completed, its operation was checked, and the line was placed in operation in an alpha facility. The equipment was used[10] in fabrication of four ^{239}Pu-containing prototype target elements currently being irradiated in the MTR and seven ^{242}Pu-containing elements for irradiation testing in one of the Savannah River Laboratory's production reactors. The fabrication of these irradiation samples was an excellent demonstration of the entire fabrication line.

---

[7]J. D. Sease and A. L. Lotts, *Transuranium Quart. Progr. Rept. Aug. 31, 1963,* ORNL-3558, pp. 69–83.

[8]J. D. Sease and A. L. Lotts, *Transuranium Quart. Progr. Rept. Nov. 30, 1963,* ORNL-3597, pp. 45–50.

[9]J. D. Sease and A. L. Lotts, *Transuranium Quart. Progr. Rept. Feb. 29, 1964,* ORNL-3651 (in press).

[10]J. D. Sease and D. M. Hewette II, *Fabrication and Preirradiation Data for High Flux Isotope Reactor Prototype Target Rods,* ORNL-TM-811 (June 1964).

Table 33.3. Cubicle 1 Equipment Percentage Completion[a]

Item No.	Description	Conceptual Design	Detailed Design	Procurement
1	Target tube receiver	75		
2	Target x-ray station	75		
3	Target x-ray unit	100	100	25
4	Target dimensional inspection	90		
5	Target ultrasonic cleaner	100	50	
6	Target dryer and surface smear	100		
7	Target high-temperature collapse station	100		
8	Helium leak test chamber	100	100	25
9	Hex-can sheath attachment station	100	75	
10	Target transfer arm	50		
11	Equipment mounting base	25		
12	Cell crane	100	100	25

[a]Bench test and required modification, mockup operation, and any required redesign and modification are not yet started on any of these items.

WELDING DEVELOPMENT

C. H. Wodtke

Efforts toward producing highly reliable welded closures[11] for remote fabrication of target rods have continued. We are attempting to facilitate welding by changes in joint geometry, mechanization of equipment, automation of the weld cycle, and employment of electron-beam welding as an alternative process.

Gas Tungsten-Arc Welding

In preliminary work, summarized in Table 33.4, we showed that gas tungsten-arc welds having good appearance and fair soundness can be produced using several joint geometries.[12] However, gas tungsten-arc welds in these joints often have defects such as incomplete fusion in the root.

To improve reliability and to adapt the process for remote operation, we have automated the weld cycle, using the equipment shown in Fig. 33.4. Shown in Fig. 33.4 is a program time-control unit having very good setting and repeat accuracy. A modification of a commercial programmer was built to ORNL specifications to automate the welding power source; this programmer is shown in Fig. 33.4*b*. Modifications included precision 10-turn potentiometers and dials to provide setting resolution and direct calibration in time. The programmer is based on a highly accurate solid-state, time-delay relay having an *RC* circuit. The precision

[11]C. H. Wodtke, *Metals and Ceramics Div. Ann. Progr. Rept. May 31, 1963,* ORNL-3470, pp. 244–46.

[12]C. H. Wodtke, *Transuranium Quart. Progr. Rept. Aug. 31, 1963,* ORNL-3558, pp. 63–66.

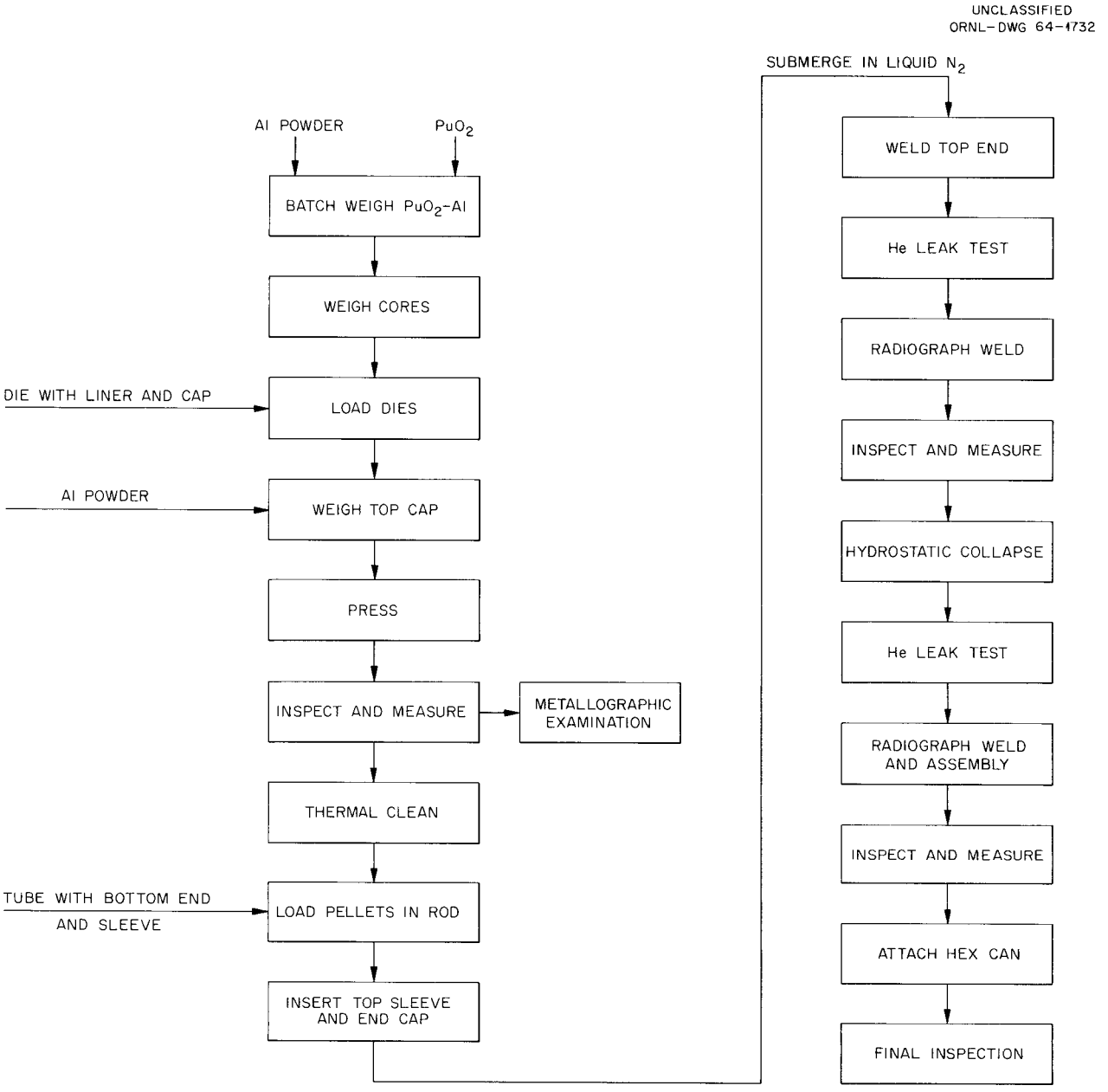

Fig. 33.3. Flow Diagram for Fabricating Plutonium Target Elements.

Table 33.4. Gas Tungsten-Arc Welding Conditions for Welds in Various Groups

Weld Group	Joint Geometry and Electrode Angle	Weld Cycle Control and Torch Type	Weld Cycle		Rotating Fixture		
			Current at Start/ Taper to (amps)	Time to Start of Tail Slope (sec)	Revolutions to Start of Tail Slope	Tube rpm	Type
A	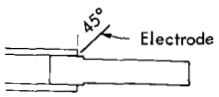	Manual and Stationary Torch	~60/~50	~8.4	~1-1/6	~8.3	Lathe
B	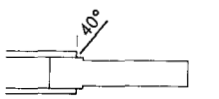	Automatic and Stationary Torch	~97/~52	~8.4	~1-1/6	~8.3	Lathe
C	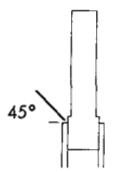	Automatic and Stationary Torch	~90/~50	~8.4	~1-1/6	~8.3	Vertical Chuck
D	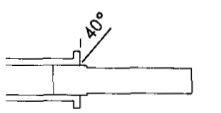	Automatic and Stationary Torch	~90/~50	~8.4	~1-1/6	~8.3	Lathe
D	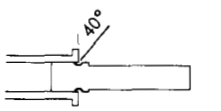	Automatic and Stationary Torch	~110/~60	~8.4	~1-1/6	~8.3	Lathe
E	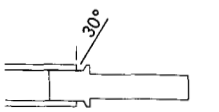	Automatic and Stationary Torch	~110/~60	~8.4	~1-1/6	~8.3	Lathe
F	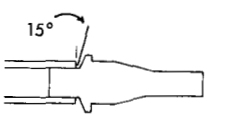	Automatic and Stationary Torch	115/70	~8.4	~1-1/6	~8.3	Lathe
F	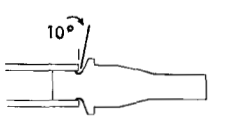	Automatic and Stationary Torch	110/65	~8.4	~1-1/6	~8.3	Lathe
G	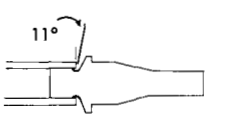	Automatic and Semiautomatic Torch	200/120	1.4 - 1.5	1.4 - 1.5	60 = 1 rps	Lathe
H	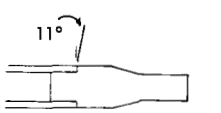	Automatic and Semiautomatic Torch	225/125[a]	1.4 - 1.5	1.4 - 1.5	60 = 1 rps	Lathe

[a] At approximately 12 to 14 v.

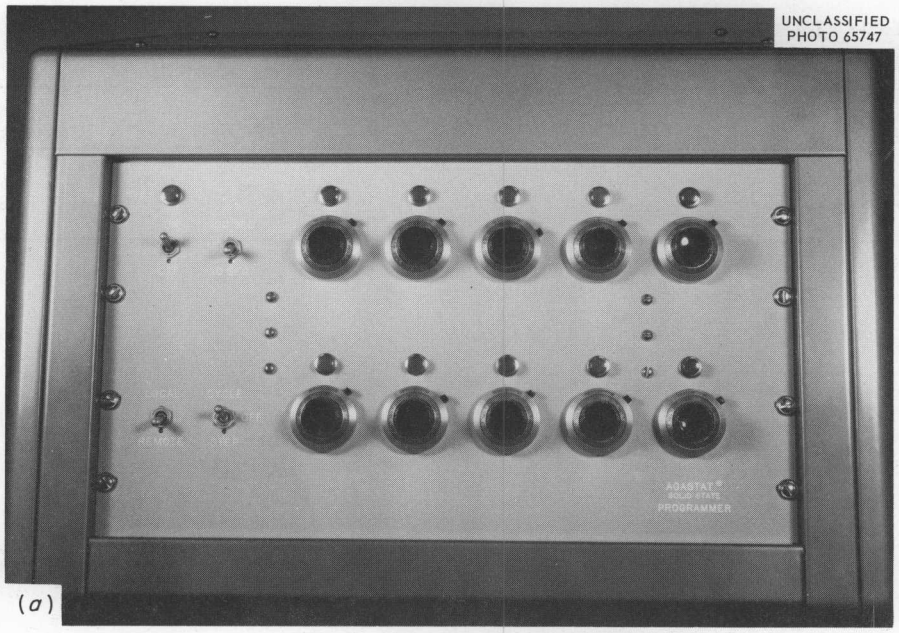

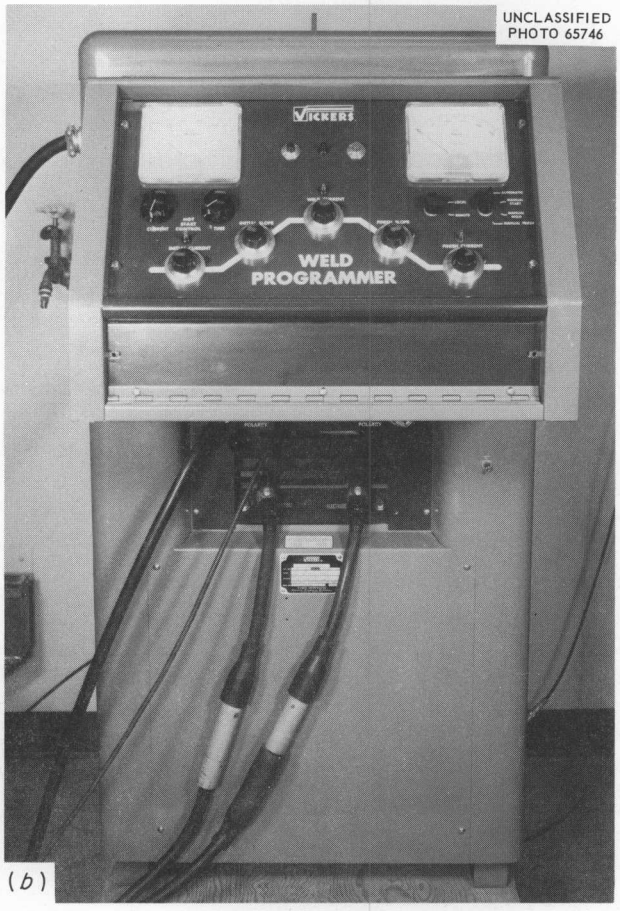

Fig. 33.4. Equipment for Welding HFIR Target Rods. (*a*) Program control unit. (*b*) Power source.

potentiometers in combination with the time-delay relay provided direct time calibration with resolution of 0.01 sec in one range and 0.10 sec in the other. The program control can repeat a weld cycle very reliably and also conveniently enable one to rapidly preset either a new weld cycle or a recorded previously used cycle.

We plan to determine the most desirable joint geometry, improve the welding apparatus, optimize the welding cycle, and mechanically test the welded joints.

Electron-Beam Welding

Electron-beam welding was explored as a process having several inherent advantages for sealing target elements. Two advantages are that the apparatus is readily adaptable for remote automatic welding and that extremely high power densities are developed. In joints of three geometries, we made[13] welds of very good appearance and penetration. The incomplete fusion common to gas tungsten-arc welds was eliminated. In addition, superior control of the fused zone permitted a butt joint to be readily welded in the 0.060-in.-wall, $\frac{3}{8}$-in.-OD tube. However, this process cannot be incorporated in the cell layout for the target line because design and construction were too far advanced.

PELLET PRESSING

D. M. Hewette II

Six batches of irradiation prototype target pellets were fabricated.[10] The pellets consisted of an Al–14 vol % PuO_2(–70 +325 mesh) core, covered top and bottom with pure aluminum powder caps. The first five batches of pellets were pressed to 90% of theoretical density, and the sixth was pressed to 97%.

A metallographic examination of six control pellets verified that aluminum was the continuous phase. This assured us that the pellets had adequate thermal conductivity; conductivities of 138 $w\ m^{-1}(^{\circ}C)^{-1}$ had been measured[14] on similar cermet structures containing rare-earth oxides as stand-ins. This value is nearly 10 times that previously determined[15] for a 15–vol % 325-mesh Gd_2O_3 dispersed in aluminum, in which the oxide was the continuous phase.

IRRADIATION TESTING

S. A. Rabin
S. D. Clinton[16]
J. W. Ullmann[16]
D. A. Douglas

Four prototype target elements containing PuO_2 were fabricated in a glove box line and inserted into the ETR to test the adequacy of the design and the fabrication techniques at the operating conditions expected in the HFIR. They operated for 6 months at a calculated heat flux that averaged 6.4×10^5 Btu hr^{-1} ft^{-2}, peaked at 7.0×10^5, and reached over 1×10^6 at hot spots.

One of the targets was removed in April after a burnup of about 40% of the original plutonium atoms at an integrated flux of 1.2×10^{21} neutrons/cm^2. Postirradiation examination established that all of the design innovations and fabrication techniques were successful. Very little fission gas escaped from the individual pellets into the tubular cladding. We detected no gross swelling and no changes in the spacing between the hex can and the tubing. From the microstructure of the pellets and reference standards, we estimate that the central temperature in the pellet was approximately 875°F.

These encouraging results have prompted us to propose operating one element in excess of expected HFIR service conditions, and we have arranged to expose a target at an average heat flux of 1×10^6 Btu hr^{-1} ft^{-2}.

Seven other irradiation prototypes were subsequently fabricated and inserted into a reactor to provide material for chemical processing studies. This provided us with an opportunity to improve the efficiency of the fabrication process and to test some new equipment. The irradiation conditions are less severe than those expected in the HFIR.

---

[13]C. H. Wodtke, *Transuranium Quart. Progr. Rept. Feb. 29, 1964*, ORNL-3651 (in press).

[14]D. M. Hewette II, *Transuranium Quart. Progr. Rept. Aug. 31, 1963*, ORNL-3558, p. 63.

[15]D. M. Hewette II, *Transuranium Quart. Progr. Rept. Aug. 31, 1962*, ORNL-3375, p. 25.

[16]Chemical Technology Division.

Papers, Oral Presentations, and Open-Literature Publications

Papers and Oral Presentations Given at Scientific and Technical Meetings

Atomic Energy Commission Coated Particle Fuels Working Group, Fifth, Cincinnati, Ohio, June 6–7, 1963

W. O. Harms* and E. S. Bomar,* "Summary of Coated Particle Fuel Development at the Oak Ridge National Laboratory for Period Nov. 15, 1962–May 15, 1963"

Symposium on Nucleation Processes in the Reactions of Gases on Metals, Paris, France, June 10–15, 1963

J. V. Cathcart,* G. F. Petersen, and C. J. Sparks, Jr., "Lattice Disregistry in Very Thin Oxide Films on Copper"

Vacuum Metallurgy Conference, New York, June 17–18, 1963

R. E. Clausing* and H. Inouye, "Vacuum as a Means of Protection for Refractory Metals at High Temperature"

American Nuclear Society, 19th Annual Meeting, Salt Lake City, Utah, June 17–19, 1963

F. L. Carlsen, Jr.,* W. O. Harms, J. A. Conlin, V. A. DeCarlo, J. G. Morgan, and D. F. Toner, "Irradiation Experiments on Graphite Matrix Fuel Elements Containing Pyrolytic-Carbon Coated Fuel Particles"

Institute of Nuclear Materials Management, Annual Meeting, Buffalo, N. Y., June 18, 1963

R. W. McClung, "Nondestructive Testing in the Control of Nuclear Materials"

American Society for Testing and Materials, 66th Annual Meeting, Atlantic City, N. J., June 23–28, 1963

R. W. McClung, "Studies in Contact Microradiography"

Conference on Refractory Metals, AGARD, Oslo, Norway, June 23–29, 1963

E. E. Hoffman* and J. R. DiStefano, "Corrosion Mechanisms in Refractory Metal–Alkali Metal Systems"

Libby/Cockcroft Exchange Meeting on Graphite Physics, Hanford, Wash., June 24–26, 1963

J. R. Weir* and C. R. Kennedy, "Radiation Creep of Graphite"

J. R. Weir* and C. R. Kennedy, "Mechanical Properties of Moderator Graphites"

International Congress of Pure and Applied Chemistry, 19th, London, England, July 10–17, 1963

G. P. Smith and C. R. Boston,* "The Structure of Nickel (II) Complexes in Alkali Halide Melts"

---

*Speaker.

Joint International Conference on Creep, New York, August 25–28, 1963

R. W. Swindeman, "The Interrelation of Cyclic and Monotonic Creep Rupture" Gordon Research Conference on Molten Salts, Meriden, N. H., Aug. 26–30, 1963

G. P. Smith, "Recent Advances in UV and Visible Spectroscopy of Fused Salts"

Symposium on the Ellipsometer and Its Use in the Measurement of Surface and Thin Films, Washington, D. C., Sept. 5–6, 1963

J. V. Cathcart* and G. F. Petersen, "Studies on Thin Oxide Films on Copper Crystals Using a Polarizing Spectrometer"

Nondestructive Testing, Fourth International Conference, London, England, Sept. 9–13, 1963

C. V. Dodd, "Recent Eddy-Current Development at the Oak Ridge National Laboratory"

B. E. Foster,* S. D. Snyder, and R. W. McClung, "Measurement and Application of X- and Gamma-Ray Attenuation to Reactor Materials Evaluation"

R. W. McClung and K. V. Cook, "Ultrasonic Detection of Nonbond in Clad Structures" (presented by a rapporteur)

International Union of Crystallography, Sixth General Assembly, Rome, Italy, Sept. 9–18, 1963

B. S. Borie* and C. J. Sparks, Jr., "The Short-Range Structure of Copper–16 Atomic Percent Aluminum"

Faraday Society, Discussion on Solvation of Molecules and Ions, Bradford Institute of Technology, England, Sept. 26–27, 1963

T. R. Griffiths, "The Orientation of the Solvent Shell Around Iodide in Non-Aqueous Solvents as Determined by Ultraviolet Spectroscopy"

Electrochemical Society, New York, Sept. 29–Oct. 3, 1963

R. J. Gray, "Application of Optical Microscopy and Related Techniques in Corrosion Studies"

J. O. Stiegler, "The Application of Electron Metallography to Problems in Surface Chemistry"

R. E. Pawel,* J. V. Cathcart, and J. J. Campbell, "Electron Microscope Observations of the Crystallization of Anodically Formed Tantalum and Niobium Oxide Films"

American Welding Society, National Fall Meeting, Boston, Mass., Sept. 30–Oct. 3, 1963

R. G. Donnelly* and G. M. Slaughter, "Fabrication of the Molten-Salt Reactor Experiment Heat Exchanger Core"

C. W. Fox* and G. M. Slaughter, "Brazing of Ceramics"

Symposium of Physics and Nondestructive Testing, San Antonio, Tex., Oct. 1–3, 1963

C. V. Dodd* and W. E. Deeds, "Eddy-Current Coil Impedance Calculated by a Relaxation Method"

NASA-AEC Liquid Metal Corrosion Meeting, Fourth, Cleveland, Ohio, Oct. 2–4, 1963

J. H. DeVan,* A. Taboada, and W. C. Thurber, "Liquid Metal Corrosion Test Summary"

Atomic Energy Commission, Problems in Irradiation-Capsule Experiments Meeting, Germantown, Md., Oct. 8–10, 1963

J. R. Weir, "Irradiation of Non-Fissile Materials in the ORR Core and Pool Facilities"

E. A. Franco-Ferreira, "Fabrication of Instrumented Irradiation Capsules for Gas-Cooled Reactor Program at the Oak Ridge National Laboratory"

*Speaker.

Thermal Conductivity Conference, Gatlinburg, Tenn., Oct. 16–18, 1963

T. G. Kollie, R. S. Graves, and D. L. McElroy,* "Progress Report for the Physical Properties Group of the Metals and Ceramics Division at the Oak Ridge National Laboratory"

M. L. Picklesimer, "Microstructural Examination"

T. G. Godfrey, W. Fulkerson,* D. L. McElroy, and J. P. Moore, "Thermal Conductivity of UO_2 and Armco Iron by a Radial Heat Flow Apparatus"

American Vacuum Society, Tenth National Vacuum Symposium, Boston, Mass., Oct. 16–18, 1963

D. T. Bourgette, "Vaporization of Iron-, Nickel-, and Cobalt-Base Alloys Between 760–980°C and 5×10^{-7} to 1×10^{-9} Torr"

American Society for Metals Seminar on Thin Films, Cleveland, Ohio, Oct. 19–20, 1963

B. S. Borie* and C. J. Sparks, Jr., "Methods for the Structural Investigation of Thin Films"

International Conference on Beryllium Oxide, Newport, Sydney, Australia, Oct. 21–25, 1963

R. L. Hamner, A. T. Chapman, and W. O. Harms,* "Fabrication Development and Irradiation Testing of Fueled Beryllium Oxide"

W. D. Manly, "Utilization of BeO in Reactors" (presented by W. O. Harms)

G. W. Keilholtz, J. E. Lee, Jr., R. E. Moore, and R. L. Hamner, "Behavior of BeO Under Neutron Irradiation" (presented by G. M. Watson)

American Institute of Mining, Metallurgical, and Petroleum Engineers, Metallurgical Society, Fall Meeting, Cleveland, Ohio, Oct. 21–25, 1963

R. J. Arsenault, "Effect of Strain Rate on Yield Points"

R. O. Williams, "The Effect of Grain Size on the Stored Energy of Copper Deformed at 24°C"

B. King* and H. A. B. Wiseman, "A Dispersion-Strengthened Iron-Aluminum-Chromium Alloy"

J. O. Betterton, Jr.* and J. O. Scarbrough, "Low Temperature Specific Heats of Ti-Zr and Hf-Zr Alloys"

R. E. Pawel* and T. S. Lundy, "A Submicron Sectioning Technique for Analyzing Diffusion Specimens of Tantalum and Niobium"

Society of Nondestructive Testing, 23rd National Fall Meeting, Cleveland, Ohio, Oct. 21–25, 1963

R. W. McClung, "Factors in Radiography at Energies Below 400 kvp"

Metals Division of Special Libraries Association, Fall Meeting, Cleveland, Ohio, Oct. 25, 1963

J. H. DeVan, "Compatibility Problems in High-Temperature Nuclear Energy Systems"

Symposium on Powder Filled Uranium Dioxide Fuel Elements, Worcester, Mass., Nov. 5–6, 1963

J. E. Van Cleve, Jr.* and A. L. Lotts, "Operation of a Lightly Shielded Facility at the Oak Ridge National Laboratory for Fabrication of Fuel Rods Bearing Uranium-233 and Thorium Oxide"

W. S. Ernst, Jr., "Recent Studies in Vibratory Compaction at ORNL"

S. A. Rabin,* S. D. Clinton, and J. W. Ullmann, "Irradiation of Nonsintered ThO_2-UO_2 and ThO_2-PuO_2 Fuel Rods for Power Reactor Applications"

International Conference on Carbides in Nuclear Energy, Harwell, England, Nov. 5–7, 1963

J. P. Hammond* and G. M. Adamson, Jr., "Fabrication of Uranium Monocarbide with a Volatile Sintering Temperature Depressant"

*Speaker.

American Chemical Society, 15th Annual Southeastern Regional Meeting, Charlotte, N. C., Nov. 14–16, 1963

G. P. Smith* and T. R. Griffiths, "Recent Evidence for Tetrahedral $CuCl_4^{-2}$ in Liquid Solutions"

American Society of Mechanical Engineers, Annual Winter Meeting, Philadelphia, Pa., Nov. 17–22, 1963

E. C Hise,* F. W. Cooke, and R. G. Donnelly, "Remote Fabrication of Brazed Structural Joints in Radioactive Piping"

American Nuclear Society, Winter Meeting, New York, Nov. 18–21, 1963

F. L. Carlsen, Jr., E. S. Bomar, and W. O. Harms,* "Development of Fueled Graphite Containing Pyrolytic-Carbon Coated Carbide Particles for Nonpurged, Gas-Cooled Reactor Systems"

J. D. Sease,* A. L. Lotts, and F. C. Davis, "New Remote Facility and Equipment at the Oak Ridge National Laboratory for Fabrication of Fuel Rods Bearing Uranium-233 and Thorium Oxide"

High-Temperature Fuels Committee Meeting, 17th, San Ramon, Calif., Dec. 3–5, 1963

G. W. Keilholtz, J. E. Lee, Jr., R. E. Moore, and R. L. Hamner, "Behavior of BeO Under Neutron Irradiation" (presented by J. L. Scott)

C. Michelson, V. A. DeCarlo, M. F. Osborne, and J. L. Scott,* "Coated Particle and Fueled Graphite Irradiation Tests at ORNL"

W. R. Martin and J. R. Weir, Jr., "Postirradiation Tensile Properties of Stainless Steel" (presented by J. L. Scott)

S. A. Rabin,* S. D. Clinton, and J. W. Ullmann, "Irradiation Behavior of Nonsintered ThO_2-Base Fuels"

Atomic Energy Commission Contractors Meeting on Measurement and Consequences of Preferred Orientation, Cincinnati, Ohio, Dec. 5–6, 1963

P. L. Rittenhouse* and M. L. Picklesimer, "The Effect of Preferred Orientation and Stress on the Directional Precipitation of Hydrides in Zircaloy-2"

Symposium on the Applied Aspects of Refractory Metals, Metallurgical Society, AIME, Los Angeles, Calif., Dec. 9–10, 1963

R. E. McDonald and C. F. Leitten, Jr.,* "Production of Refractory-Metal Tube Shells by Extrusion and Flow-Turning Techniques"

H. Inouye, "The Contamination of Refractory Metals in Vacua Below 10^{-6} Torr"

T. K. Roche, "The Effect of Degree of Vacuum on the Slow-Bend Creep Behavior of Columbium–0.6% Zirconium at 1000°C" (presented by H. Inouye)

E. A. Franco-Ferreira, "The Fabrication of a Large Columbium–1% Zirconium Pumped Loop for Boiling-Potassium Service"

R. G. Gilliland, "The Development of Refractory-Metal Brazing Alloys for Elevated-Temperature Service" (presented by W. C. Thurber)

R. L. Heestand* and C. F. Leitten, Jr., "Parameters for the Production of Refractory-Metal Tubing by the Vapor Deposition Process"

American Institute of Chemical Engineers, 52nd National Meeting, Memphis, Tenn., Feb. 2–5, 1964

G. M. Adamson, "Fabrication of High Flux Isotope Reactor Fuel Elements"

---

*Speaker.

Irradiation Effects on Reactor Structural Materials, San Antonio, Tex., Feb. 11–13, 1964

W. R. Martin* and J. R. Weir, "Effect of Irradiation Temperature and Strain Rate on the Post Irradiation Tensile Properties of Stainless Steel"

National Association of Corrosion Engineers, Edmonton, Alberta, Canada, Feb. 12–14, 1964

H. Inouye, "The Influence of Gaseous Corrosion on the Properties of Metals"

American Institute of Mining, Metallurgical, and Petroleum Engineers, Annual Meeting, New York, Feb. 16–20, 1964

F. R. Winslow, "Computer Plotting Applied to Self-Diffusion Data"

R. E. Pawel* and T. S. Lundy, "'Anomalous' Penetration Behavior During Diffusion of Cb^{95} into Tantalum Single Crystals"

T. S. Lundy* and T. L. Boswell, "Diffusion of Cb^{95} in Columbium"

D. Heitkamp* and W. K. Biermann, "Effect of α-Bombardment on Diffusion"

W. K. Biermann* and D. Heitkamp, "Diffusion in a Temperature Gradient"

W. C. Thurber,* J. R. DiStefano, T. G. Kollie, H. Inouye, H. E. McCoy, and R. L. Stephenson, "Recent Studies on the Columbium–1% Zirconium Alloy"

J. V. Cathcart,* G. F. Petersen, and C. J. Sparks, Jr., "Lattice Disregistry in Very Thin Oxide Films on Copper"

P. L. Rittenhouse* and M. L. Picklesimer, "Microhardness Anisotropy in Zr and Zircaloy-2 Single Crystals"

D. T. Bourgette* and H. E. McCoy, Jr., "Vaporization and Its Effect on the Total Emittance and Creep-Rupture Properties of Type 316 Stainless Steel"

R. J. Arsenault, "Stress-Induced Short-Range Order"

D. A. Douglas* and A. L. Lotts, "Cost of Remote Fabrication of Fuel Elements"

T. G. Godfrey, W. Fulkerson,* T. G. Kollie, J. P. Moore, and D. L. McElroy, "The Thermal Conductivity of Iron Between 100 and 1000°C Determined by a Radial Heat Flow Method"

M. L. Picklesimer* and G. R. Love, "Transformation Kinetics in Niobium-Rich Niobium-Zirconium Alloys"

R. A. Vandermeer, "Non-Steady State Grain Boundary Migration During Recrystallization in Aluminum"

National Association of Corrosion Engineers, Chicago, Ill., Mar. 9–13, 1964

J. R. DiStefano* and A. P. Litman, "The Effect of Impurities in Some Refractory Metal–Alkali Metal Systems"

Society of Nondestructive Testing, Albuquerque, N.M., Mar. 12, 1964

R. W. McClung, "Nondestructive Testing at the Oak Ridge National Laboratory"

Metallurgy of High-Field Superconductors Discussion, Institute of Metals, London, England, Mar. 17–18, 1964

M. L. Picklesimer* and G. R. Love, "Transformation Kinetics in Niobium-Rich Niobium-Zirconium Alloys"

Symposium on Joining Processes in Reactor Components, Institute of Metals, London, England, Mar. 17–19, 1964

P. Patriarca* and G. M. Slaughter, "Welding Problems in the Experimental Gas-Cooled Reactor"

*Speaker.

Atomic Energy Commission Symposium on Advanced Converter Reactor Prototypes, Washington, D. C., Mar. 19–20, 1964

W. O. Harms, "Oak Ridge National Laboratory Graphite Fuel Element Development Program for High-Temperature Gas-Cooled Reactors"

D. E. Ferguson, O. C. Dean, and D. A. Douglas, "Status of Thorium Fuel Cycle Technology" (presented by J. A. Lane)

American Ceramic Society, Augusta, Ga., Mar. 21, 1964

R. L. Hamner,* A. T. Chapman, and W. O. Harms, "Fabrication Development and Irradiation Testing of Fueled Beryllium Oxide"

Conference on Industrial Applications of New Technology, Atlanta, Ga., Apr. 2–3, 1964

R. W. McClung, "Recent Developments in Nondestructive Testing"

US/UK Libby-Cockcroft Gas-Metal Compatibility Meeting, Richland, Wash., Apr. 6–7, 1964

A. T. Chapman* and R. E. Meadows, "The Volatility of $UO_{2\pm x}$ and Phase Relations in the Uranium-Oxygen System"

W. R. Martin, "Influence of Chromium Content on Carburization of Chromium-Nickel-Iron Alloys in Carbon Dioxide"

J. V. Cathcart,* G. F. Petersen, and C. J. Sparks, Jr., "Lattice Disregistry in Very Thin Oxide Films on Copper"

H. Inouye, "The Oxidation of High Temperature Alloys in Air"

American Ceramic Society, 66th Annual Meeting, Chicago, Ill., Apr. 18–23, 1964

C. S. Morgan,* R. B. Fitts, and J. L. Scott, "Influence of Stress on Fission Gas Release"

A. P. Malinauskas* and F. L. Carlsen, Jr., "Gas Transport Characteristics of Uranium-Fueled Graphites"

R. L. Hamner,* A. T. Chapman, and W. O. Harms, "Fabrication Development and Irradiation Testing of Fueled Beryllium Oxide"

N. A. Hill* and O. B. Cavin, "Structures in the ThC_2-UC_2 System"

T. G. Godfrey,* W. Fulkerson, T. G. Kollie, J. P. Moore, and D. L. McElroy, "Thermal Conductivity of UO_2 Between −60 and 1100°C by an Improved Radial Heat Flow Apparatus"

A. T. Chapman, "The Volatility of $UO_{2\pm x}$ in Vacuum and Controlled Oxygen Pressures"

Rare Earth Research Conference, Fourth, Phoenix, Ariz., Apr. 22–25, 1964

C. B. Finch,* L. A. Harris, and G. Wayne Clark, "Single Crystal Synthesis and Properties of Lanthanide Germano-Molybdates"

H. L. Yakel, W. C. Koehler,* E. O. Wollan, and J. W. Cable, "The Magnetic Structures of Rare Earth Manganites, Mixed Oxides of Rare Earth Metals, and Trivalent Manganese"

American Physical Society, Washington, D. C., Apr. 27–30, 1964

J. S. Faulkner, "One-Dimensional Random Alloys"

International Conference on Electron and Ion Beam Science and Technology, Toronto, Canada, May 6–8, 1964

J. C. Wilson* and M. L. Picklesimer, "Variable-Gradient, Electron-Beam Heating Methods for Growing Single Crystals of Zirconium"

*Speaker.

American Welding Society, 45th Annual Meeting, Detroit, Mich., May 4–8, 1964

J. W. Tackett* and G. M. Slaughter, "Welding of Fuel Elements for the High-Flux Isotope Reactor"

G. M. Slaughter* and T. R. Housley, "The Welding of Ferritic Steels to Austenitic Stainless Steels"

High-Temperature Fuels Committee, 18th Meeting, Middletown, Conn., May 19–21, 1964

Compiled by J. L. Scott, "Thorium Utilization and Clad Fuel Work at the Oak Ridge National Laboratory"

C. Michelson and J. L. Scott,* "Fueled-Graphite Irradiation Tests at the Oak Ridge National Laboratory"

American Society for Mechanical Engineers, Idaho Falls, Idaho, May 21, 1964

R. W. Swindeman, "What We Know About Low-Cycle Fatigue in Metals"

Atomic Energy Commission 13th Annual Corrosion Symposium, Argonne National Laboratory, May 20–22, 1964

D. H. Jansen, "Forced-Convection Niobium–1% Zirconium Boiling-Potassium Loop Test"

J. R. DiStefano, "Status of Boiling-Potassium Refluxing Capsule Experiments"

B. Fleischer,* A. Taboada, W. R. Huntley, H. W. Savage, R. E. MacPherson, "Snap-8 Corrosion Loop Test Program"

Refractory Metal Sheet Rolling Panel, Sacramento, Calif., June 8–9, 1964

W. C. Thurber, "Preliminary Evaluation of Fansteel Powder-Metallurgy-Route Tungsten Sheet"

American Society for Testing and Materials, 67th Annual Meeting, Chicago, Ill., June 21–26, 1964

W. R. Martin* and J. R. Weir, "The Effect of Irradiation Temperature on the Postirradiation Stress-Strain Behavior of Stainless Steel"

H. E. McCoy and J. R. Weir,* "The Effect of Irradiation on the Bend Transition Temperatures of Molybdenum- and Niobium-Base Alloys"

M. L. Picklesimer, "Discussion of 'Effects of Neutron Irradiation on the Flow and Fracture of Zircaloy-2' by A. L. Bement, J. C. Tobin, and R. G. Hoagland"

J. W. Hendricks and D. L. McElroy,* "High-Temperature High-Vacuum Thermocouple Drift Tests"

J. T. Venard* and J. R. Weir, "In-Reactor Stress-Rupture Properties of a 20 Cr–25 Ni, Niobium-Stabilized Stainless Steel"

Atomic Energy Commission Metallographic Group Meeting, 18th, Canoga Park, Calif., June 22–24, 1964

T. M. Kegley, Jr.* and B. C. Leslie, "Metallographic Preparation of Dicarbides of Thorium and Thorium-Uranium"

C. K. H. DuBose* and J. O. Stiegler, "Electron Metallography of Pyrolytic Carbon Coatings on Fuel Particles"

---

*Speaker.

Publications

Arsenault, R. J., "Comments on the Yield Point in Iron," *Acta Met.* **11**(9), 1111–13 (1963).

Arsenault, R. J., "Low-Temperature Creep of Alpha Iron," *Acta Met.* **12**(5), 547–54 (1964).

Arsenault, R. J., "Reply to Discussion of 'Comments on the Yield Point in Iron'," *Acta Met.* **12**(6), 758 (1964).

Arsenault, R. J., and J. Weertman, "Incubation Creep Effect in Alpha Iron," *Acta Met.* **11**(10), 1119–28 (1963).

Beaver, R. J., G. M. Adamson, and P. Patriarca, *Procedures for Fabricating Aluminum-Base ATR Fuel Elements*, ORNL-3632 (June 1964). Available from OTS.

Beaver, R. J., and C. F. Leitten, Jr., *A Survey of the Corrosion of Martensitic and Ferritic Stainless Steels in Pressurized Water*, ORNL-TM-539 (July 16, 1963). Available from OTS.

Biermann, W., F. R. Winslow, and T. S. Lundy, "Comments on 'Diffusion of Iron, Cobalt and Nickel in Silver'," *Acta Met.* **12**(3), 328 (1964).

Borie, B., "The Correction of Diffuse Scattering Measurements for Thermal Effects," *Acta Cryst.* **17**(2), 212–13 (1964).

Boston, C. R., G. P. Smith, and L. C. Howick, "Spectra of Dilute Solutions of Bismuth Metal in Molten Bismuth Trihalides. II. Formulation of Solute Equilibrium in Bismuth Trichloride," *J. Phys. Chem.* **67**(9), 1849–52 (1963).

Bourgette, D. T., "Vaporization of Iron-, Nickel-, and Cobalt-Base Alloys Between 760–980°C and 5×10^{-7} to 1×10^{-9} Torr," pp. 497–502 in *1963 Transactions, The Tenth National Vacuum Symposium, American Vacuum Society* (ed. by G. H. Bancroft), Macmillan, New York, 1964.

Carlsen, F. L., Jr., W. O. Harms, J. A. Conlin, J. G. Morgan, V. A. DeCarlo, and D. F. Toner, "Irradiation Experiments on Graphite Matrix Fuel Elements Containing Pyrolytic-Carbon-Coated Fuel Particles," *Trans. Am. Nucl. Soc.* **6**, 157–58 (1963).

Chapman, A. T., and R. L. Hamner, "Fueled Beryllium Oxide," pp. 225–41 in *Materials and Fuels for High-Temperature Nuclear Applications* (ed. by M. T. Simnad and L. R. Zumwalt), MIT Press, Cambridge, Mass., 1964.

Chapman, A. T., and R. E. Meadows, *The Volatility of $UO_{2\pm x}$ and Phase Relations in the Uranium-Oxygen System*, ORNL-3587 (April 1964).

Clausing, R. E., *Sorption of Gases by Vapor-Deposited Titanium Films*, ORNL-3481 (March 1964) Available from OTS.

Cook, J. L., and R. L. Hamner, *The Removal of Uranium and Thorium from Fueled-Graphite Materials by Chlorination*, ORNL-3586 (April 1964). Available from OTS.

Cook, K. V., and R. W. McClung, *Nondestructive Evaluation of D-43 Alloy Tubing by Oak Ridge National Laboratory*, ORNL-TM-843 (June 1964).

Dean, O. C., R. E. Brooksbank, and A. L. Lotts, *A New Process for the Remote Preparation and Fabrication of Fuel Elements Containing Uranium-233 Oxide–Thorium Oxide*, ORNL-TM-588 (June 10, 1963). Available from OTS.

DeVan, J. H., A. Taboada, and W. C. Thurber, "Liquid Metal Corrosion Test Summary," pp. 3–41 in *NASA-AEC Liquid Metals Corrosion Meeting Vol. II*, NASA SP-42 (1964) (Classified).

DiStefano, J. R., *Corrosion of Refractory Metals by Lithium*, ORNL-3551 (March 1964). Available from OTS.

DiStefano, J. R., and E. E. Hoffman, *Corrosion Mechanisms in Refractory Metal–Alkali Metal Systems*, ORNL-3424 (Aug. 30, 1963); *At. Energy Rev.* **2**(1), 3–33 (1964).

DiStefano, J. R., and E. E. Hoffman, *A Survey of the Compatibility of Some Potential Refractory-Metal Fuel Cladding Materials with Potassium*, ORNL-TM-708 (Dec. 13, 1963) (Classified).

Dodd, C. V., *Design and Construction of Eddy-Current Coolant-Channel Spacing Probes*, ORNL-3580 (April 1964).

Dodd, C. V., "Applications of a Phase-Sensitive Eddy-Current Instrument," *Mater. Evaluation* **22**(6), 260 (1964).

Dodd, C. V., and W. E. Deeds, "Eddy-Current Coil Impedance Calculated by a Relaxation Method," pp. 300–14 in *Symposium on Physics and Nondestructive Testing*, Southwest Research Institute, San Antonio, Tex., 1964.

Donnelly, R. G., and G. M. Slaughter, *Fabrication of the Heat Exchanger Tube Bundle for the Molten-Salt Reactor Experiment*, ORNL-3500 (Nov. 22, 1963).

Donnelly, R. G., and G. M. Slaughter, "Fabrication of the Molten-Salt Reactor Experiment Heat Exchanger Core," *Welding J.* **43**(2), 118–24 (1964).

DuBose, C. K. H., and R. J. Gray, *Metallographic Examination of Pyrolytic-Carbon Coated and Uncoated Uranium Carbide Particles*, ORNL-TM-521 (June 25, 1963). Available from OTS.

Engel, N., "Device to Control the Temperature Profile in Tubular Furnaces," *Rev. Sci. Instr.* **34**(10), 1146–48 (1963).

Ernst, W. S., Jr., "Recent Vibratory-Compaction Studies on Thoria-Urania," pp. 585–605 in *Proceedings of the Thorium Fuel Cycle Symposium, Gatlinburg, Tennessee*, December 5–7, 1962, TID-7650, Bk II (July 1963).

Evans, R. M., and Goldman, A. E., "Status of Gas Cooled Reactor Program," *Metal Progr.* **85**(3), 118–22 (1964).

Federer, J. I., and T. S. Lundy, "Diffusion of Zr^{95} and Cb^{95} in Bcc Zirconium," *Trans. Met. Soc. AIME* **227**(3), 592–97 (1963).

Finch, C. B., L. A. Harris, and G. W. Clark, "The Thorite→Huttonite Phase Transformation as Determined by Growth of Synthetic Thorite and Huttonite Single Crystals," *Am. Mineralogist* **49** May–June, 782–85 (1964).

Fitts, R. B., J. L. Scott, and C. S. Morgan, *Stress-Induced Release of Fission Gases from UO_2 and ThO_2-UO_2*, ORNL-TM-740 (Jan. 28, 1964). Available from OTS.

Foster, B. E., and J. W. Evans, *X-Ray Mass Attenuation Coefficients in the Range of 50 to 150 kvp with Data for Several Reactor Materials*, ORNL-3552 (February 1964).

Fox, C. W., *Fabrication of Critical Assembly Calandria*, ORNL-TM-779 (March 1964) (Classified).

Fox, C. W., R. G. Gilliland, and G. M. Slaughter, "Development of Alloys for Brazing Columbium," *Welding J.* **42**(12), 535-s–40-s (1963).

Franco-Ferreira, E. A., *Fabrication of Radiators for Boiling Heat-Transfer Experiments*, ORNL-TM-602 (Aug. 23, 1963). Available from OTS.

Gilliland, R. G., "Wetting of Beryllium by Various Pure Metals and Alloys," *Welding J.* **43**(6), 248-s–57-s (1964).

Godfrey, T. G., W. Fulkerson, T. G. Kollie, J. P. Moore, and D. L. McElroy, *Thermal Conductivity of Uranium Dioxide and Armco Iron by an Improved Radial Heat Flow Technique*, ORNL-3556 (June 1964). Available from OTS.

Griffiths, T. R., "Diffuse Reflectance Spectra of Potassium Iodate and Some Mercuric Iodide Complexes," *Anal. Chem.* **35**(8), 1077–79 (1963).

Griffiths, T. R., "Densities of Some Molten Organic Quaternary Halides," *J. Chem. Engr. Data* **8**(4), 568–69 (1963).

Hallerman, G., and R. J. Gray, *Equipment for Hardness Testing at Elevated Temperatures*, ORNL-3448 (July 17, 1963).

Hallerman, G., and R. J. Gray, *Instrument for Determining Crushing Strength of Particles*, ORNL-3512 (Nov. 14, 1963).

Hallerman, G., and R. J. Gray, "Age Hardening of Haynes Alloy No. 25 Determined by Elevated-Temperature Hardness Testing," *Trans. Met. Soc. AIME* **230**(3), 593–94 (1964).

Hamner, R. L., *Fabrication and Characterization of High-Purity Beryllium Oxide Specimens for Irradiation Testing*, ORNL-TM-767 (March 1964). Available from OTS.

Hammond, J. P., J. D. Sease, and C. Hamby, Jr., "Uranium Monocarbide Fabrication with UAl_2 as Sintering Aid," pp. 145–53 in *The 4th Uranium Carbide Conference, East Hartford, Connecticut, May 20–21, 1963*, TID-7676 (1964).

Handler, G. S., and H. W. Joy, "Radial Correlation in Helium," *J. Chem. Phys.* **40**(8), 2408 (1964).

Harrington, F. E., E. D. Arnold, D. C. Brater, D. A. Douglas, S. H. Smiley, W. G. Stockdale, J. W. Ullmann, and A. L. Lotts, *Fuel Cycle Costs for a Plutonium Recycle System*, ORNL-3501 (Jan. 6, 1964). Available from OTS.

Hill, N. A., and O. B. Cavin, *Monoclinic-Cubic Transformation in Thorium Dicarbide*, ORNL-3588 (April 1964).

Hobson, D. O., "Aging Phenomena in Columbium-Base Alloys," pp. 325–34 in *High Temperature Materials*, Interscience, New York, 1963.

Irvine, A. R., and A. L. Lotts, "The Thorium Fuel Cycle Development Facility Conceptual Design," pp. 333–50 in *Proceedings of the Thorium Fuel Cycle Symposium, Gatlinburg, Tennessee, December 5–7, 1962*, TID-7650, Bk I (July 1963).

James, D. W., *Vibrational Spectra of Molten Salts*, ORNL-3413 (July 11, 1963); pp. 507–33 in *Molten Salt Chemistry* (ed. by M. Blander), Interscience, New York, 1964.

James, D. W., C. R. Boston, and G. P. Smith, "Far-UV Spectra of NO_3^- and I^- in Molten Salt Media," *J. Chem. Phys.* **40**(2), 609–10 (1964).

James, D. W., and C. H. Liu, "Densities of Some Molten Alkali Nitrate and Sulphate Mixtures," *J. Chem. Engr. Data* **8**(3), 469 (1963).

Jansen, D. H., and E. E. Hoffman, *Niobium–1% Zirconium Natural-Circulation, Boiling-Potassium Corrosion Loop Test*, ORNL-3603 (May 1964) (Classified).

Kegley, T. M., Jr., and B. C. Leslie, "How to Measure Hardness of Pyrolytic Carbon," *Nucleonics* **21**(12), 62–64 (1963).

Keilholtz, G. W., J. E. Lee, Jr., R. E. Moore, and R. L. Hamner, *Behavior of BeO Under Neutron Irradiation*, ORNL-TM-742 (Dec. 11, 1963). Available from OTS.

Kennedy, C. R., "The Effect of Stress State on High-Temperature Low-Cycle Fatigue," *Am. Soc. Testing Mater. Spec. Tech. Publ.* 338, pp. 92–107 (1963).

Kneip, G. D., Jr., J. O. Betterton, Jr., and J. O. Scarbrough, "Low-Temperature Specific Heats of Titanium, Zirconium, and Hafnium," *Phys. Rev.* **130**(5), 1687–92 (1963).

Kneip, G. D., Jr., J. O. Betterton, Jr., and J. O. Scarbrough, "Specific Heats of Zirconium Alloys at Low Temperatures," *Phys. Rev.* **131**(6), 2425–32 (1963).

Koehler, W. C., H. L. Yakel, E. O. Wollan, and J. W. Cable, "The Magnetic Structures of Rare Earth Manganites $RMnO_3$," *Fourth Rare Earth Research Conference, Phoenix, Arizona, April 22–5, 1964,* Session I.

Kopp, O. C., G. W. Clark, and T. G. Reynolds, "Replaceable Liner-Type Autoclave with Modified Bridgman Closures," *Rev. Sci. Instr.* **34**(11), 1262–63 (1963).

Kucera, W. J., C. F. Leitten, Jr., and R. J. Beaver, *Specifications and Procedures Used In Manufacturing U_3O_8-Aluminum Dispersion Fuel Elements for Core I of the Puerto Rico Research Reactor,* ORNL-3458 (Oct. 7, 1963). Available from OTS.

Lotts, A. L., and D. A. Douglas, Jr., *A Preliminary Study of Fuel Fabrication Costs for Large Heavy-Water-Moderated Reactors,* ORNL-TM-587 (April 1964). Available from OTS.

Lotts, A. L., J. D. Sease, R. E. Brooksbank, and A. R. Irvine, "The Oak Ridge National Laboratory Kilorod Facility," pp. 351–83 in *Proceedings of the Thorium Fuel Cycle Symposium, Gatlinburg, Tennessee, December 5–7, 1962,* TID-7650, Bk I (July 1963).

Lotts, A. L., W. C. Thurber, M. K. Preston, Jr., and D. A. Douglas, Jr., "Development of Procedures and Equipment for Fabrication of the High Flux Isotope Reactor Target Rods," *Nucl. Sci. Eng.* **17**(3), 468–78 (1963).

Love, G., "Dislocation Pipe Diffusion," *Acta Met.* **12**(6), 731–37 (1964).

Love, G., and P. G. Shewmon, "Self-Diffusivity of Silver in Twist Boundaries," *Acta. Met.* **11**(8), 899–906 (1963).

Lundy, T. S., *Diffusion in Body-Centered Cubic Metals Zirconium, Vanadium, Niobium, and Tantalum,* ORNL-3617 (June 1964).

Martin, W. R., and J. R. Weir, *Mechanical Properties of X8001 and 6061 Aluminum Alloys and Aluminum-Base Fuel Dispersion at Elevated Temperatures,* ORNL-3557 (February 1964). Available from OTS.

Martin, W. R., and J. R. Weir, "Effect of Post-irradiation Heat Treatment on the Elevated Temperature Embrittlement of Irradiated Stainless Steel," *Nature* **202**(4936), 997 (1964).

McClung, R. W., *Studies in Contact Microradiography, ORNL-3511* (Oct. 1, 1963); *Mater. Res. Std.* **4**(2), 66–68 (1964).

McClung, R. W., "Inspección de componentes nucleares," *Ingenieria* **XII**(144), 11–17 (1963).

McClung, R. W., "Development of Non-Destructive Techniques for Thin-Wall Beryllium Tubing," pp. 480–96 in *International Conference on the Metallurgy of Beryllium, London, 1961, Proceedings,* Chapman & Hall, London, 1963.

McClung, R. W., "Nondestructive Testing in Control of Special Nuclear Materials," pp. 9–19 in *Institute of Nuclear Materials Management, Proceedings of 4th Annual Meeting* (Buffalo, N.Y., June 1963), Institute of Nuclear Materials Management, Columbus, Ohio, 1964.

McClung, R. W., E. S. Bomar, and R. J. Gray, *Use of Microradiography Combined with Metallography for Evaluation of Coated Particles,* ORNL-3577 (June 1964).

McCoy, H. E., Jr., *Observations on the Oxidation of Beryllium in CO_2 by Use of $C^{14}O_2$ and Autoradiographic Techniques,* ORNL-TM-622 (Aug. 22, 1963). Available from OTS.

McCoy, H. E., Jr., *Effects of Hydrogen on the High-Temperature Flow and Fracture Characteristics of Metals,* ORNL-3600 (June 1964).

McCoy, H. E., Jr., R. L. Stephenson, and J. R. Weir, Jr., *Mechanical Properties of Some Refractory Metals and Their Alloys,* ORNL-3593 (April 1964). Available from OTS.

McDonald, R. E., and J. L. Wilson, *In-Cell Sound Transmission System*, ORNL-TM-565 (June 12, 1963). Available from OTS.

McElroy, D. L., and T. G. Kollie, "The Total Hemispherical Emittance of Platinum, Columbium–1% Zirconium, and Polished and Oxidized INOR-8 in the Range 100° to 1200°C," pp. 365–79 in *Measurement of Thermal Radiation Properties of Solids*, NASA SP-31, National Aeronautics and Space Administration, Washington, D. C., 1963.

McHargue, C. J., and H. E. McCoy, "Effect of Interstitial Elements on Twinning in Columbium," *Trans. Met. Soc. AIME* **227**(5), 1170–74 (1963).

Morgan, C. S., L. L. Hall, and C. S. Yust, "Sintering of Sodium Chloride," *J. Am. Ceram. Soc.* **46**(11), 559–60 (1963).

Morgan, C. S., and C. S. Yust, "Material Transport During Sintering of Materials with the Fluorite Structure," *J. Nucl. Mater.* **10**(3), 182–90 (1963).

Morgan, J. G., M. F. Osborne, and E. L. Long, Jr., *Examination of UO_2 Irradiated at High Temperatures*, ORNL-TM-763 (March 1964). Available from OTS.

Murdock, J. F., *Diffusion of Titanium-44 and Vanadium-48*, ORNL-3616 (June 1964).

Naruki, K., "Vibratory Compaction of Uranium Dioxide (I) Effect of Vibration Character," *J. Nucl. Sci. Technol.* **1**(2), 58–67 (1964).

Olsen, A. R., J. P. Nichols, and S. Peterson, *Safety Analysis of the Operation of the High-Radiation-Level Examination Laboratory*, ORNL-3479 (Nov. 20, 1963). Available from OTS.

Pawel, R. E., J. V. Cathcart, and J. J. Campbell, "Stress Generation in Tantalum During Oxidation," *J. Electrochem. Soc.* **110**(6), 551–57 (1963).

Pawel, R. E., and T. S. Lundy, "A Submicron Sectioning Technique for Analyzing Diffusion Specimens of Tantalum and Niobium," *J. Appl. Phys.* **35**(2), *435–38 (1964).*

Peterson, S., "Integrity of Reactor Fuels," *Nucl. Safety* **4**(4), 60–67 (1963).

Peterson, S., "Chemical Reactions of Graphite," *Nucl. Safety* **5**(1), 47–49 (1963).

Peterson, S., and R. G. Wymer, *Chemistry in Nuclear Technology*, Addison-Wesley, Reading, Mass., 1963.

Pilloton, R. L., *Gas Flow Calculations for Fluidized-Bed Coating of Nuclear Fuel Particles*, ORNL-3639 (June 1964).

Prados, J. W., and J. L. Scott, *Models for Fission-Gas Release from Coated Fuel Particles*, ORNL-3421 (June 6, 1963). Available from OTS.

Prados, J. W., and J. L. Scott, *Analysis of Stress and Strain in Spherical Shells of Pyrolytic Carbon*, ORNL-3553 (June 1964). Available from OTS.

Rabin, S. A., *Status of Fuel Cycle Irradiation Program at Oak Ridge National Laboratory*, ORNL-TM-610 (July 8, 1963).

Rabin, S. A., *Procurement and Evaluation of Hardware for the Brookhaven National Laboratory Fuel Rods*, ORNL-TM-739 (February 1964). Available from OTS.

Rabin, S. A., A. L. Lotts, and J. P. Hammond, *Swaging of Uranium-Molybdenum Alloy Powders Containing 10 to 15 wt % Molybdenum*, ORNL-TM-455 (Sept. 11, 1963). Available from OTS.

Rabin, S. A., M. M. Martin, A. L. Lotts, and J. P. Hammond, *Fabrication Development of U-Mo-UO_2 and U-Mo-UC Dispersion Fuels for the Enrico Fermi Fast-Breeder Reactor*, ORNL-3437 (June 10, 1963). Available from OTS.

Rabin, S. A., M. F. Osborne, S. D. Clinton, and J. W. Ullmann, "Thorium Fuel Cycle Irradiation Program at the Oak Ridge National Laboratory," pp. 643–74 in *Proceedings of the Thorium Fuel Cycle Symposium, Gatlinburg, Tennessee, December 5–7, 1962*, TID-7650, Bk II (July 1963).

Reagan, P. E., F. L. Carlsen, and R. M. Carroll, "Fission-Gas Release from Pyrolytic-Carbon-Coated Fuel Particles During Irradiation," *Nucl. Sci. Eng.* **18**(3), 301 (1964).

Richt, A. E., C. F. Leitten, Jr., and R. J. Beaver, *Postirradiation Evaluation of Stainless Steel-Clad Plate-Type Specimens Containing 3 wt % Enriched Boron in Iron*, ORNL-TM-815 (June 1964). Available from OTS.

Riddle, J. R., and R. J. Gray, *Metallography and Aging Characteristics of Hastelloy B*, ORNL-2496 (June 1964). Available from OTS.

Rittenhouse, P. L., and M. L. Picklesimer, *The Effect of Preferred Orientation and Stress on the Directional Precipitation of Hydrides in Zircaloy-2*, ORNL-TM-844 (June 1964).

Roche, T. K., *Effect of Degree of Vacuum on the Slow-Bend Creep Behavior of Columbium–0.6% Zirconium at 1000°C*, ORNL-3569 (June 1964).

Saturno, A. F., H. W. Joy, and L. C. Snyder, "Computations to Evaluate Dewar's Split P-Orbital (SPO) Method," *J. Chem. Phys.* **38**(10), 2494–99 (1963).

Scott, J. L., "Fission Product Release from Uranium-Graphite," *Nucl. Safety* **4**(4), 49–54 (1963).

Sease, J. D., F. C. Davis, and A. L. Lotts, "New Remote Facilities and Equipment at the Oak Ridge National Laboratory for Fabrication of Fuel Rods," pp. 33–43 in *Proceedings of the 11th Conference on Hot Laboratories and Equipment, ANS Winter Meeting, New York, December 28–31, 1963*, American Nuclear Society, New York, 1963.

Sease, J. D., and D. M. Hewette II, *Fabrication and Preirradiation Data for High Flux Isotope Reactor Prototype Target Rods*, ORNL-TM-811 (June 1964). Available from OTS.

Sease, J. D., A. L. Lotts, and F. C. Davis, *Thorium-Uranium-233 Oxide (Kilorod) Facility – Rod Fabrication Process and Equipment*, ORNL-3539 (April 1964). Available from OTS.

Slaughter, G. M., "Inspection," pp. 119–29 and "Ceramics and Graphite," pp. 237–42 in *Brazing Manual*, American Welding Society, New York, 1963.

Slaughter, G. M., *Welding and Brazing Techniques for Nuclear Reactor Components*, Rowman and Littlefield, Inc., New York, 1964.

Smith, G. P., *Review of Electronic Absorption Spectra of Molten Salts*, ORNL-3411 (Aug. 13, 1963).

Smith, G. P., "Electron Absorption Spectra of Molten Salts," pp. 427–505 in *Molten Salt Chemistry* (ed. by M. Blander), Interscience, New York, 1964.

Smith, G. P., and T. R. Griffiths, "Tetrahedral Tetrachlorocopper(II) Complex in Molten Salt Solutions," *J. Am. Chem. Soc.* **85**(24), 4051 (1963).

Smith, P. G., J. H. DeVan, and A. G. Grindell, "Cavitation Damage to Centrifugal Pump Impellers During Operation with Liquid Metals and Molten Salt at 1050–1400 F," *J. Basic Eng.* **85**(3), 329–37 (1963).

Sparks, C. J., Jr., and B. S. Borie, "An X-Ray Determination of the Debye-Waller Factors for Cu_2O and UO_2 and the Atomic Scattering Factor for Cu in Cu_2O," pp. 177–84 in *Advances in X-Ray Analysis*, vol. 6 (ed. by W. M. Mueller and Marie Fay), Plenum, New York, 1963.

Stiegler, J. O., C. K. H. DuBose, and C. J. McHargue, "The Effect of Interstitials on Mechanical Twinning in Body-Centered Cubic Metals," *Acta Met.* **12**(2), 263–64 (1964).

Stiegler, J. O., C. K. H. DuBose, R. E. Reed, Sr., and C. J. McHargue, "Dislocations in Deformed and Annealed Niobium Single Crystals," *Acta Met.* **11**(8), 851–60 (1963).

Stiegler, J. O., J. T. Houston, and M. L. Picklesimer, "Transmission Electron Microscopy of Omega Phase in a Zr–15% Nb Alloy," *J. Nucl. Mater.* **11**(1), 32–40 (1964).

Swindeman, R. W., *Mechanical Properties of INOR-8 Cast Metal*, ORNL-TM-607 (Aug. 6, 1963). Available from OTS.

Thurber, W. C., K. J. Kelly, C. J. Klamut, L. Rosenblum, and J. W. Semmel, Jr., "Corrosion of High-Temperature Materials in Alkali Metals," *Nucleonics* **22**(3), 37–42 (1964).

Tolson, G. M., and M. G. Arlotti, "The Manufacture of EGCR Core I Fuel Assemblies," *Welding J.* **43**(4), 280–86 (1964).

Vandermeer, R. A., and P. Gordon, "The Influence of Recovery on Recrystallization in Aluminum," pp. 211–40 in *Recovery and Recrystallization in Metals*, Interscience, New York, 1963.

Vandermeer, R. A., and C. J. McHargue, "The Nature of the <001> Fiber-Texture Component in Extruded Aluminum Rods," *Trans. Met. Soc. AIME* **230**(4), 667–75 (1964).

Venard, J. T., *Stress-Rupture Properties of Type 304 Stainless Steel Tubing*, ORNL-TM-535 (June 6, 1963). Available from OTS.

Venard, J. T., and A. E. Carden, *Thermal-Fatigue Analysis of the HFIR Target Irradiation Prototype*, ORNL-TM-661 (Feb. 17, 1964). Available from OTS.

Venard, J. T., and R. W. Swindeman, *Mechanical Properties of the UO_2-Type 347 Stainless Steel Cermet for Core B of the Fermi Reactor*, ORNL-TM-665 (Oct. 24, 1963). Available from OTS.

Watts, T. D., and K. K. Sinha, *Compatibility of Cadmium-Bearing Materials with the High Flux Isotope Reactor Fuel Plate Constituents*, ORNL-TM-647 (Oct. 1, 1963). Available from OTS.

Weir, J. R., "The Effect of High-Temperature Reactor Irradiation on Some Physical Properties of Beryllium," pp. 395–409 in *International Conference on the Metallurgy of Beryllium, London, 1961, Proceedings*, Chapman & Hall, London, 1963.

Werner, W. J., and H. Inouye, "The Reaction of Beryllium with Wet Carbon Dioxide," pp. 283–93 in *International Conference on the Metallurgy of Beryllium, London, 1961, Proceedings*, Chapman & Hall, London, 1963.

Williams, R. O., "Liquid-Gas Film Calorimeter for Deformation of Metals," *Rev. Sci. Instr.* **34**(6), 639–43 (1963).

Williams, R. O., "The Changes in Internal Energy of a Copper-Aluminum Alloy and a Copper-Zinc Alloy Resulting from Deformation and Recovery near 25°C," *Trans. Met. Soc. AIME* **227**(6), 1290–96 (1963).

Williams, R. O., "The Increase in Internal Energy of Copper Crystals During Deforming at 25°C," *Acta Met.* **12**(6), 745–47 (1964).

Winslow, F. R., "Basic Studies of Irradiation Effects on Fuel Materials," *Reactor Mater.* **6**(2), 44–45 (1963).

Winslow, F. R., *A Fortran Program for Calculating Diffusion Coefficients and Plotting Penetration Curves*, ORNL-TM-726 (Dec. 6, 1963). Available from OTS.

Winslow, F. R., and K. H. Osthagen, "Diffusion Today," *J. Metals* **15**(11), 855–60 (1963).

Winslow, F. R., and P. G. Shewmon, "Orientation Dependence of the Surface Free Energy on Silver by a New Method," *Trans. Met. Soc. AIME* **227**(5), 1078–80 (1963).

Wittels, M. C., J. O. Stiegler, and F. A. Sherrill, "An Investigation of Transmutation Effects in Crystalline Solids," *Phys. Stat. Sol.* **4**, 533 (1964).

Yakel, H. L., *ORSTAT, A Fortran Program for the Statistical Analysis of Diffraction Data*, ORNL-TM-750 (Feb. 3, 1964). Available from OTS.

Yakel, H. L., and B. Borie, "Structural Changes in Irradiated BeO," *Acta Cryst.* **15**(7), 589–93 (1963).

Yakel, H. L., W. C. Koehler, E. F. Bertaut, and E. F. Forrat, "On the Crystal Structure of the Manganese (III) Trioxides of the Heavy Lanthanides and Yttrium," *Acta. Cryst.* **16**(10), 957–62 (1963).

Young, J. P., and G. P. Smith, "Coordination of Fluoride Ions About Nickel(II) Ions in the Molten LiF-NaF-KF Eutectic," *J. Chem. Phys.* **40**(3), 913–14 (1964).

Fixation of Fission Products in Aluminum Nitrate Wastes by Ceramic Masses, ORNL-2611 (Sept. 27, 1963). Available from OTS.

ORNL-3670
UC-25 – Metals, Ceramics, and Materials
TID-4500 (34th ed.)

INTERNAL DISTRIBUTION

1. Biology Library
2–4. Central Research Library
5. Reactor Division Library
6–7. ORNL – Y-12 Technical Library, Document Reference Section
8–57. Laboratory Records Department
58. Laboratory Records, ORNL R.C.
59. ORNL Patent Office
60. Laboratory Shift Supervisor
61. G. M. Adamson, Jr.
62. L. G. Alexander
63. R. J. Beaver
64. J. O. Betterton, Jr.
65. D. S. Billington
66. A. L. Boch
67. E. G. Bohlmann
68. E. S. Bomar
69. B. S. Borie
70. R. B. Briggs
71. J. V. Cathcart
72. G. W. Clark
73. J. H. Coobs
74. J. A. Cox
75. F. L. Culler
76. J. E. Cunningham
77. G. V. Czjzek
78. J. H. DeVan
79. D. A. Douglas, Jr.
80. J. H. Erwin
81. G. W. Flack
82. A. P. Fraas
83. J. H Frye, Jr.
84. J. H. Gillette
85. A. E. Goldman
86. R. J. Gray
87. W. R. Grimes
88. J. P. Hammond
89. W. O. Harms
90. C. S. Harrill
91–100. M. R. Hill
101. N. E. Hinkle
102. A. Hollaender
103. A. S. Householder
104. A. P. Huber (K-25)
105. H. Inouye
106. R. G. Jordan (K-25)
107. M. T. Kelley
108. E. M. King
109. R. B. Korsmeyer
110. J. A. Lane
111. C. E. Larson
112. C. F. Leitten, Jr.
113. R. S. Livingston
114. A. L. Lotts
115. T. S. Lundy
116. H. G. MacPherson
117. R. W. McClung
118. H. C. McCurdy
119. D. L. McElroy
120. C. J. McHargue
121. A. J. Miller
122. E. C. Miller
123. C. S. Morgan
124. K. Z. Morgan
125. M. L. Nelson
126. A. R. Olsen
127–128. R. B. Parker
129. P. Patriarca
130. S. Peterson
131. M. L. Picklesimer
132. H. W. Savage
133. A. W. Savolainen
134. J. L. Scott
135. H E. Seagren
136. G. M. Slaughter
137. C. O. Smith
138. G. P. Smith, Jr.
139. P. E. Stein (K-25)
140. J. O. Steigler
141. J. A. Swartout
142. A. Taboada
143. E. H. Taylor
144. W. C. Thurber
145. D. B. Trauger
146. M. S. Wechsler
147. A. M. Weinberg
148. J. R. Weir, Jr.
149. G. D. Whitman
150. G. C. Williams
151. R. O. Williams
152. J. C. Wilson
153. H. L. Yakel
154. M. B. Bever (consultant)
155. A. A. Burr (consultant)
156. J. R. Johnson (consultant)
157. A. R. Kaufmann (consultant)

EXTERNAL DISTRIBUTION

158. C. M. Adams, Jr., MIT
159. R. B. Burlin, AEC, Washington
160–161. D. F. Cope, AEC, ORO
162. J. F. Elliott, MIT
163. N. Engel, Georgia Institute of Technology
164. H. B. Finger, AEC, Washington
165. J. D. Fleming, Georgia Institute of Technology
166. V. D. Frechette, Alfred Univ.
167. Angelo Giambusso, AEC, Washington
168. J. L. Gregg, Bard Hall, Cornell Univ.
169. E. G. Haas, Dept. of the Navy, Washington
170. R. F. Hehemann, Case Institute of Technology
171. E. E. Hoffman, GE, Cincinnati
172. O. C. Kopp, Univ. of Tenn.
173. J. Korringa, Ohio State Univ.
174. J. J. Lombardo, NASA, Lewis Research Center
175. W. D. Manly, Union Carbide Corp., N.Y.
176. R. S. Mateer, Univ. of Kentucky
177. P. W. McDaniel, AEC, Washington
178. R. W. McNamee, Union Carbide Corp., N.Y.
179. Peter Murray, AERE, Harwell
180. R. R. Nash, NASA, Washington
181. E. F. Nippes, Rensselaer Polytechnic Inst.
182. H. M. Otte, RIAS Research Inst.
183. R. E. Pahler, AEC, Washington
184. J. Pheline, Centre d'Etudes Nucleaires de Saclay
185. J. W. Prados, Univ. of Tenn.
186. J. M. Prosser, AEC, Washington
187. H. B. Rahner, Savannah River Operations
188. T. A. Read, Univ. of Illinois
189. R. E. Reed-Hill, Univ. of Florida
190. F. N. Rhines, Univ. of Florida
191. A. F. Saturno, Univ. of Tenn.
192. R. W. Schroeder, NASA, Lewis Research Center
193. F. C. Schwenk, AEC, Washington
194. A. A. Shoudy, Atomic Power Development Associate, Inc.
195. J. Simmons, AEC, Washington
196. E. E. Sinclair, AEC, Washington
197. L. M. Slifkin, Univ. of N.C.
198. E. E. Stansbury, Univ. of Tenn.
199. D. K. Stevens, AEC, Washington
200. Dorothy Smith, AEC, Washington
201. A. Van Echo, AEC, Washington
202. J. B. Wagner, Massachusetts Institute of Technology
203. Watt Webb, Union Carbide Metals
204. J. Weertman, Northwestern Univ.
205. G. W. Wench, AEC, Washington
206. M. J. Whitman, AEC, Washington
207. C. H. T. Wilkins, Univ. of Ala.
208. Division of Research and Development, AEC, ORO
209–792. Given distribution as shown in TID-4500 (34th ed.) under Metals, Ceramics, and Materials category (75 copies – CFSTI)